# AN ABSTRACT OF A DISSERTAION

# AN INVESTIGATION OF DUAL STATOR WINDING INDUCTION MACHINES

**Zhiqiao Wu**

**Doctor of Philosophy in Engineering**

A design procedure including the evaluation of the magnetic load for the dual stator winding induction machine is clearly laid out and the method to estimate the equivalent parameters of the dual winding machine has been presented.

The computer simulation model of the dual stator winding induction machine with constant air gap in which the space harmonics of the stator windings and rotor circuits are accounted for has been presented. The winding function method is used to calculate the self and mutual inductances in the stator windings, the rotor circuits and the mutual inductances between the stator windings and the rotor circuits. The phase voltage and torque equations thus obtained are further transformed to the rotor reference frame to facilitate simplicity of model and ease computational efforts using a n x n complex variable reference frame transformation. Computer simulation results of the no-load starting transient were presented with the response of the machine for a change in the load torque. A novel approach, in which the stator windings and rotor bar currents determined from the coupled-circuit model and the winding functions of the stator windings and the rotor loops are used to generate the air gap flux density, has been proposed. A simplified correction scheme, using the B-H curve of the magnetic steel material to account for magnetic saturation in the air gap was introduced, improving the prediction accuracy. Some measurements of no-load and full load flux densities confirm the computer simulation and FEA results.

An analysis method of a dual stator winding induction machine with a squirrel-cage rotor under static, dynamic and mixed rotor eccentricity conditions has been presented. The nature of the inductances under rotor eccentricity conditions calculated using a general winding function definition is comprehensively presented. Following the conceptual framework of multiple coupled circuit model of an induction machine, a circuit simulation model for the dual stator winding induction machines has been set forth which accounts for rotor static, dynamic and mixed eccentricities. Because of the asymmetries in the inductance matrices, the Manley-Rowe Power-Frequency relationships are used for the calculation of the developed electromagnetic torques. Computer simulation results for the machine's starting transient and steady-state

operation are given to demonstrate the consequences of the rotor eccentricities. Spectral analysis results of key waveforms are shown to illustrate the harmonic components generated by the air-gap length asymmetry.

Based on concepts the rotating-field and coupling magnetic circuit concepts, the field analysis method is applied to understand the operation of the dual stator winding squirrel-cage induction machine having two stator windings with dissimilar pole numbers. When the fundamental current components are considered, the frequency components of induced voltages at the two winding terminals are determined in addition to those arising from the interactions between them. The development of the torque equations gives clarity to the fact that under certain operating stator frequencies and rotor speeds, additional average torque components can be developed.

The air-gap flux linkage of a dual stator winding squirrel cage induction machine comprises of four fundamental flux components due to the currents flowing in the two stator windings with $P_1$ and $P_2$ pole numbers and the currents they induce in the squirrel-cage. In view of the dissimilar pole numbers of the stator windings and frequencies of the supply voltages, the air-gap flux linkage waveform is complex especially when the stator and rotor teeth are saturated. This complexity has been explored using analytic, computer simulation, Finite Elements Analysis and some experimental results. Furthermore, a fundamental component circuit model of the machine is set forth, which with the use of a specially defined reference frame transformation permits an accurate simulation of the transient and dynamic characteristics. Computer simulation results are validated by some experimental results obtained from a 2hp dual stator winding induction machine.

The steady state analysis of dual stator winding induction machine to explore the operability regimes of the machine under constant Volt/Hz control scheme has firstly been presented using the steady state machine model in complex form. The relationship between the slip frequencies of two stator windings and the power contributions from each winding have been clearly shown while the operating conditions for minimum copper loss conditions have been determined.

The use of a dual stator winding squirrel-cage induction machine for generating dc power using series or parallel connected ac-dc PWM rectifiers have been presented. The operating principles and constraints are explored using the steady-state model of machine and converter considering magnetizing flux saturation effects. Regulation of the dc voltage using concepts of the nonlinear input-output linearization method including the design of the controllers are set forth and confirmed to be effective by computer simulation results. Some experimental waveforms of the generator under load are also included.

A speed sensorless control scheme based on full-order flux observer using MRAS technique has been analyzed. A torque partition factor K has been introduced to distribute the electromagnetic torque of each winding set. By changing the value of K, one winding set can move smoothly from motoring condition into generating condition. The principles of input-output linearization have been applied to the control system design such that the

coupling and interaction terms are removed and the classic linear design method can be applied for controller design. The Butterworth method is used to design the controller parameters and observer gains. The transfer function of the estimated and actual speeds is derived based on the error analysis, which is used to determine the parameters of speed estimator. The D-decomposition method is adopted as the design methodology for both speed estimator and speed controller. The proposed sensorless design scheme is validated by computer simulation and experimental results for operations in the motoring and regeneration modes.

# AN INVESTIGATION OF

# DUAL STATOR WINDING INDUCTION MACHINES

---

A Dissertation

Presented to

The Faculty of the Graduate School

Tennessee Technological University

by

Zhiqiao Wu

---

In Partial Fulfillment

Of the Requirements for the Degree

DOCTOR OF PHILOSOPHY

Engineering

---

December 2006

**CERTIFICATE OF APPROVAL OF DISSERTATION**

**AN INVESTIGATION OF DUAL STATOR WINDING**

**INDUCTION MACHINES**

by

Zhiqiao Wu

Graduate Advisory Committee:

| | |
|---|---|
| _____ | _____ |
| Dr. Joseph O. Ojo, Chairperson | date |
| _____ | _____ |
| Dr. Sastry Munukutla | date |
| _____ | _____ |
| Dr. Arun Sekar | date |
| _____ | _____ |
| Dr. Brian M. O'Connor | date |
| _____ | _____ |
| Dr. Mohamed A. Abdelrahman | date |

Approved for the Faculty:

_____
Francis Otuonye
Associate Vice President for
Research and Graduate Studies

_____
Date

# DEDICATION

To GOD, Lirong, Daniel and my parents

My soul finds rest in God alone;

my salvation comes from him.

He alone is my rock and my salvation;

he is my fortress, I will never be shaken.

Psalm 62:1-2

# ACKNOWLEDGEMENTS

I would like to express my sincere appreciation to my advisor and the chairperson of my committee, Dr. Joseph O. Ojo, for his professional guidance and support through the period of my PhD Program. I would like to thank the other members of my committee, Dr. Sastry Munukutla, Dr. Arun Sekar, Dr. Brian M. O'Connor and Dr. Mohamed A. Abdelrahman for their wonderful courses and their efforts in evaluating my research works.

I would also like to thank Gan Dong, Conard Murray, L.V. Randolph, David Walker and Robert (Bob) Peterson for their invaluable help during the course of this project. I would also like to thank the Office of Naval Research (ONR) and Center for Energy Systems Research for the financial support provided during my study.

I am also grateful to Dr. Jiahong Zhu, Dr. Ying Zhang and some Chinese friends in Cookeville for their help and support during my study.

I would like to thank my parents for a lifetime support, selfless love, endless patience and encouragement.

Finally, I would like to give my most sincere thanks to my wife Lirong and my son Daniel for their moral support, invaluable help and encouragement during the course of my PhD Program.

# TABLE OF CONTENTS

Page

Page

Page

Page

Page

Page

Page

Page

Page

# LIST OF FIGURES

Page

Page

Page

Page

Page

Page

Page

Page

Page

Page

Page

Page

Page

Page

Page

Page

Page

Page

Page

Page

# LIST OF TABLES

Page

# CHAPTER 1

# INTRODUCTION AND LITERATURE REVIEW

## 1.1 Introduction

The idea of using dual stator winding machines can be found in some papers published as early as the beginning of 20th century. However, high performance control of the machines was difficult. Reasons included the absence of power electronic converters and the incomplete analysis of the machines due to the immaturity of machine theory, numerical simulation and analytical methodologies. Recently, dual-winding machines of various types are being considered for various motor and generating applications since two stator winding sets offer the possibility of more flexible energy conversion. For example, energy can be transferred not only between stator and rotor like what is found in single winding machines, but also indirectly between stator winding sets.

Generally speaking, dual winding machines can be divided into the following categories. The first is the oldest machines in the machine history and it is always called a wound rotor induction machine. In this type, the rotor winding is always called the secondary winding, and both the stator and rotor windings have the same number of poles and number of phases. The most significant advantages of this machine lie in its ability to achieve a constant output frequency at variable rotor speeds. This is useful in wind power generation. The ability to send the rotor slip energy back to the system improves the efficiency of the whole system.

From the point of view of the stator winding, dual winding machines have been categorized as “split-wound” and “self-cascaded” [1.1]. The split-wound dual winding machine was introduced in 1920s to increase the power capability of large synchronous generators and has recently found utility as part of uninterruptible power supplies, generators of both dc and ac electric power and stand-alone power supplies. Its inherent redundancy has also been exploited to achieve better drive reliability [1.2-1.5]. The split-wound synchronous machine with either round or salient-pole rotor structure has two similar but separate three-phase winding sets wound for the same number of poles. The squirrel-cage machine version also has two symmetric but separate three-phase stator winding sets having the same pole number. Since the two windings have the same pole number, they are coupled together resulting in significant circulating currents in the presence of unavoidable unbalances in the supply voltages.

The third dual winding machine, the “self-cascaded machine”, recently christened the brushless doubly-fed machine (BDFM) was introduced by Hunt in 1907. It has two stator winding sets with dissimilar pole numbers, the same number of phases and sharing the same stator core. This requires a special rotor structure that has nested loops on the rotor to incorporate the effects of cascade connection. [1.6-1.8]. Because of the different rotor structures, the brushless doubly-fed machine can be further divided into brushless doubly-fed induction machines and brushless doubly-fed synchronous reluctance machines. The special rotor structure increases the cost of the machine, the efficiency is relatively low, but has potential utility in drive applications with a narrow speed range [1.9].

The last is the recently developed dual stator winding squirrel-cage induction machine. This type is claimed to offer advantages of ease of sensor-less control (especially at low speed), high reliability, full utilization of the stator windings and absence of circulating currents. It is the structure considered in this dissertation [1.1, 1.10]. It consists of a stator with two separate symmetric three-phase winding sets, having different numbers of poles $P_1$ and $P_2$ (e.g., 2/6 or 4/12) and a standard squirrel-cage rotor. In principle, any combination of different pole numbers could be used, however to better utilize the magnetic material, avoid localized saturation and additional stator losses, it is found that the most advantageous configuration should have a pole ratio of 1: 3 [1.1]. Since a standard squirrel cage rotor is utilized, the cost of the machine decreases and the advantages of squirrel cage rotor are inherited. Advantages include simple structures, easy connections, durability under severe operating conditions, low cost and low maintenance. All these features make this kind of machine attractive in real industry applications.

It is known from previous works that the dual stator winding squirrel-cage induction machine can be treated as two induction machines coupled through rotor shaft [1.1, 1.10], although, strictly speaking, some couplings between two stator winding sets are possible during the transient process of the machine as shown in the chapter 5 of this dissertation. Hence the control methodologies applied to the single winding set squirrel-cage induction machine can also be used to control this dual stator winding induction machine as shown in [1.1].

The extensive industry applications of induction machines greatly benefit from the development of power electronics. At the very beginning, induction machines were used

in applications where only a fixed speed is required. Although several speed levels can be obtained by changing the connections of the stator winding sets, speed control of induction machines was difficult compared to the DC machines. As a result, DC machines were always used for high performance speed or torque control. The advantage of DC machines lies in the independent regulation of the air-gap field and armature current. The air-gap flux linearly depends on field current while the torque is proportional to the armature current when air gap flux level is fixed. A precise speed control can be achieved by regulating the torque of the machine. However, the torque control of the induction machine is apparently complicated due to the coupling characteristic between air-gap flux and stator currents while electromagnetic torque is the cross-product of them.

The development of power electronics provides a novel method of energy conversion such that one kind of electrical energy can be freely converted to another kind of electrical energy with acceptable small losses. The conversions of electrical power can be broadly classified as DC-to-DC, DC-to-AC, AC-to-DC and AC-to-AC and the converters corresponding to each energy conversion are generally called DC-DC converter, inverter, rectifier and AC-AC converters respectively. A diagram of a three-phase Voltage Source Converter (VSC) is shown in Figure 1.1.

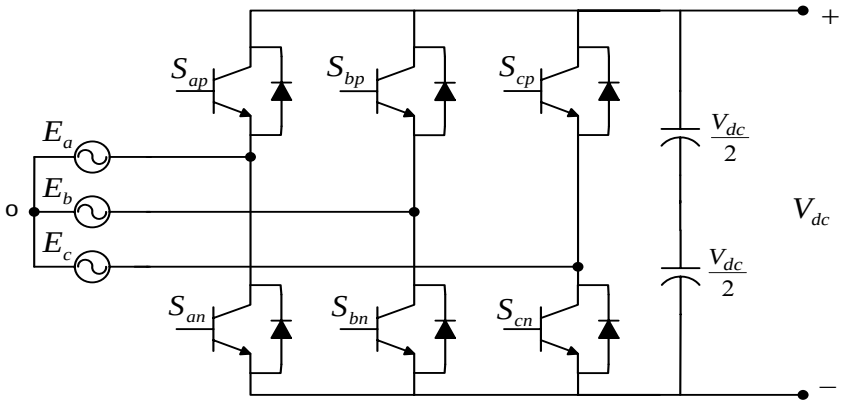


Figure 1.1 The diagram of a three-phase voltage source converter

It should be noted that at any time the power flowing in the converters could be bi-direction with the same hardware topology. For example, the voltage source converter shown in Figure 1.1 is called as voltage source inverter when power is flowing from dc side to ac side and it can also be called as voltage source rectifier when power is flowing from ac side to dc side. The power direction is dominated by the direction of dc current in the voltage source converter while dc voltage direction is unchanged.

Energy conversion in converters is achieved by the Pulse Width Modulation (PWM) technique. The turn on and turn off time of each switching device is calculated from a control scheme and when these PWM pluses are applied, the fundamental voltages embedded in the output PWM voltages are the same as the desired ones. The PWM technique can be generally divided into Carrier-based PWM (CPWM) and Space Vector PWM (SVPWM). In the CPWM method, the modulation signals which contain certain magnitude, frequency and angle information are compared with a high frequency carrier signal to generate the switching pulses. The pulses are "one" when modulation signals are larger than the carrier signal and "zero" when modulation signal are smaller than carrier signal. However, the turn on and turn off times of each device are calculated and then sent to the PWM generator directly in the SVPWM method.

The development of fast switching devices in power converters and microcontrollers provides the possibility of implementing complex control schemes to the induction machine. Generally speaking the variable speed control of an induction machine can be classified into two main categories: scalar control and vector control.

The scalar control is the first control scheme applied to the induction machine. The constant volts per Hertz (Constant V/Hz) control is the simplest and most robust scalar

control method, and is still widely used by most of the drives in industry applications. The significant advantage of the method is its simplicity while the disadvantages are low speed inaccuracy and slow torque response.

The vector control is classified into three main categories—direct flux field orientation control, indirect flux field orientation control and direct torque control. The direct field orientation control is based on the position signal of the rotor flux such that a sensor for flux measurement is necessary. This increases the cost and complexity of the system. For indirect flux orientation control, the flux sensor is eliminated and performance similar to DC machines can be achieved. The rotor position signal in an indirect flux orientation control is necessary and the synchronous speed or stator frequency is obtained by adding the slip frequency to the rotor speed. The flux estimation in this method is machine parameters dependent. Direct torque control, in which the torque and flux are regulated directly, is based on the estimation of electromagnetic torque and flux. Torque ripple in the low speed range is the main drawback of direct torque control.

The control methods for induction machines seems to be a mature technology now. Future development in this area lies in the elimination of various kinds of sensors while keeping the high performance unchanged. The installation of speed sensors not only increases the system cost, but also reduces the system reliability and increases the size of the drive, hence the elimination of speed sensor has been intensively studied for about 14 years. Speed sensorless control methods can be broadly classified into two categories: machine model based methods and magnetic structure based methods. The methods of sensorless control are abundant however very few industry applications are found.

A. R. Munoz and T.A. Lipo are pioneers in the research of this machine. A detail report of their work can be found in Munoz's Ph.D dissertation [1.11]. The same work in the dissertation also led to a U.S. patent 6,242,884 in 2001 and two journal publications [1.1, 1.10].

## 1.2 Literature Review

Since the dual stator winding squirrel-cage rotor induction machine considered in this research is relatively new, publications regarding this machine are limited. However, since the analytic methodologies on electric machines are common, the methods applied to the analysis of other types of electric machines provide a good base for the studies on this new machine. Hence some work related to induction machines and other machines, which may be used in the study of this dual stator winding squirrel-cage machine, will be included in this literature review.

This section is organized as follows: the design of the dual stator winding squirrel-cage rotor induction machine is the first item that needs to be studied. Then the machine modeling methodologies are introduced, including the coupled-circuit based full model simulation, the machine model under rotor eccentricity conditions, the field analysis method based machine analysis and the machine model including saturation effect. The literature related to the induction generator and parallel/series connected PWM boost rectifiers is reviewed. Finally the work related to induction machine drive and speed sensorless control is discussed.

### 1.2.1 Machine Design

The dual stator winding induction machine (DSWIM) studies in this research has a normal squirrel cage rotor design and the standard stator laminations. Therefore it is different from the one that is called Brushless Doubly-Fed Induction Machine (BDFM), which has a special rotor design. As a result, the dual stator winding induction machine design based on the standard single stator winding induction machine frame is possible. The only modification is the different interconnection of the stator coils. This idea of the dual winding induction machine design provides some advantages such as reducing the cost of the dual winding induction machine. This is very important for real applications of a new machine, so that the manufacturing process and cost will be similar to the standard single induction machine.

The research on electric machines has been ongoing for more than 100 years and induction machines as one of the oldest and widely used machines have been manufactured for a long time. The machine design methods for the induction machine are very mature. Fortunately, since the dual stator winding induction machine under consideration has some common characteristics with the normal single winding induction machine, some of the machine design methods for an induction machine can be used in the design process of this machine. One of the basic differences between a dual stator winding induction machine and a normal induction machine from the machine design point of view lies in the determination of air gap flux densities. Since the air gap flux linkage of the dual stator winding induction machine has two different components, in which the frequencies, magnitudes and phase angles of these two components are generally independent, the traditional method that considers only one air gap flux linkage

has to be modified to adapt to these changes. The challenge is how to avoid the deep saturation problem when the designed dual stator winding machines are working under different load conditions. The answers lie in finding a proper way to evaluate the flux density for the dual stator-winding machine and design the flux density for each stator winding. This important issue for the dual stator-winding machine has been addressed in few papers.

In [2.1], the author discusses this issue for a specific example, however the general conclusions are not presented. In [2.2], the author lists three methods that can be used to evaluate the magnetic flux density of a BDFM. The first method is a conservative one, in which the peak value of flux density of the dual stator-winding machine can be found by adding the peak values of flux densities of two stator winding sets together. In the second approach, the combined magnetic loading is defined as the square root of two components. It has been shown in [2.2] that the value of the combined flux density obtained by the second approach will be much less than the value obtained from the first one. The last evaluation method was proposed by the author in [2.2], which is called a new generalized method. The results show that the value of the magnetic loading obtained by the third method are independent of pole number combinations and offset angles, except one special case-- $p_1 = 2,\ p_2 = 4$. The magnetic loading calculated by the proposed method is close to the second approach and the advantages and disadvantages of these two methods have been addressed in [2.2]. It should be noted, however, that all the methods can only be used to evaluate the combined magnetic loading and can not be used to determine the magnetic loading for each stator winding set.

A straightforward method that can be used to design the magnetic loading of each stator winding set has been discussed in [1.11]. To avoid deep saturation of the core material, the peak magnetic loading produced by the combined effect of the two MMFs is designed to be the same as that of an equivalent single stator winding design, which means the peak flux density in the air gap must remain constant and the maximum flux density per pole must be identical in both the dual stator and single stator design.

### 1.2.2 Full Model Simulation

In the pioneering works on the dual stator winding induction machines, computer simulation was based on the q-d model and only the fundamental components of the stator winding set are considered [1.1, 1.10]. The qd model expressed in the complex variable form permits the calculation of the rotor bar currents, which is a significant achievement of this work [1.10]. It is well known that the conventional q-d model of an ac machine has a basic assumption that the stator windings are sinusoidally distributed around the stator surface. The machine models based on this assumption are generally acceptable for the control and fundamental component dynamic and steady state analysis of the machine. However, if the focus of study is on the influence of high order harmonic MMFs on machine performance, fault condition analysis, performance analysis when there is rotor eccentricity or the study of a general machine with arbitrary winding connections, the conventional q-d model is not adequate. A model based on machine geometry and winding layouts of an arbitrary n phase machine is required for a general machine analysis. This is the motivation for the development of the multiple coupled

circuit model of an induction machine set forth in [3.5]. The inductance calculation has been carried out on a coil-to-coil basis. The stator winding of each phase and rotor circuit are generally modeled as circuit $m$ and circuit $n$, which have $k$ and $l$ coils respectively, then the inductance calculation between circuit $m$ and circuit $n$ is given, which looks complicated. The input line-to-line voltages are the only excitation needed for this model. This model has been proven to be useful for fault analysis where the fault occurs in the winding itself [3.5].

Finite Element Analysis (FEA) is a well-known method of plotting the steady state magnetic fields of various parts of electric machines. Repeated and time consuming simulations are needed, using FEA to obtain comprehensive performance profiles of electric machines. Although FEA yields very accurate results, its use to study the dynamics of electric machines and machines with multiple windings and excitations of different frequencies is still a tough task.

Another advantage of the coupled-circuit model is the possibility of calculating the currents flowing in the component parts of the machine, such as stator coils and rotor bars during transient, dynamic and steady state operating conditions. In view of this possibility, the approximate flux densities in the air gap and cores of the machine can be deduced.

### 1.2.3 Machine Model under Eccentricity Conditions

Induction machines have small air gap lengths, although the actual length may be variable. They usually assumed to be constant for the purpose of ease of analysis, however, the air-gap lengths of real machines are not constant because of problems

associated with rotor misalignment, rotor shaft bending, weak bearings and manufacturing tolerances. The behavior and the performance of induction machines under rotor eccentricity conditions have been a subject of recent investigations.

Generally speaking, the air gap eccentricity can be classified as: static eccentricity, dynamic eccentricity and mixed eccentricity [4.4]. The diagram of different eccentricity conditions are shown in Figure 1.2. In the uniform air gap condition, the center of the rotor and the center of the stator have the same location as shown in Figure 1.2(a). However, the location of the centers of the rotor and stator are not the same under all eccentricity conditions. The differences between the eccentricity conditions are explained as: under static eccentricity condition, the rotor still rotates around its own center axis and the air gap is not uniform as shown in Figure 1.2(b). The rotor rotates around the stator's center axis under dynamic eccentricity condition. The central axis shown in Figure 1.2(c) is the one for the stator. For mixed eccentricity condition, the rotor will still rotate around the rotor's central axis while the rotor's central axis rotates around stator central axis. Both the central axis of the rotor and stator are shown in Figure 1.2(d) and the possible rotating behaviors are represented by arrows.

Some of the previous works focus on the definitions of the air gap and the approximation of the inverse of the air gap, the determination of the harmonic components present in the machine variables (currents, torques etc.) due to rotor eccentricity, the computer simulation of the machine under eccentricity and the evaluation of the inductances [3.7-3.9, 4.1-4.6]. Based on the winding function method and coupled-circuit model simulation, the modeling methodology of the induction machine under eccentricity conditions has been proposed in [3.7].

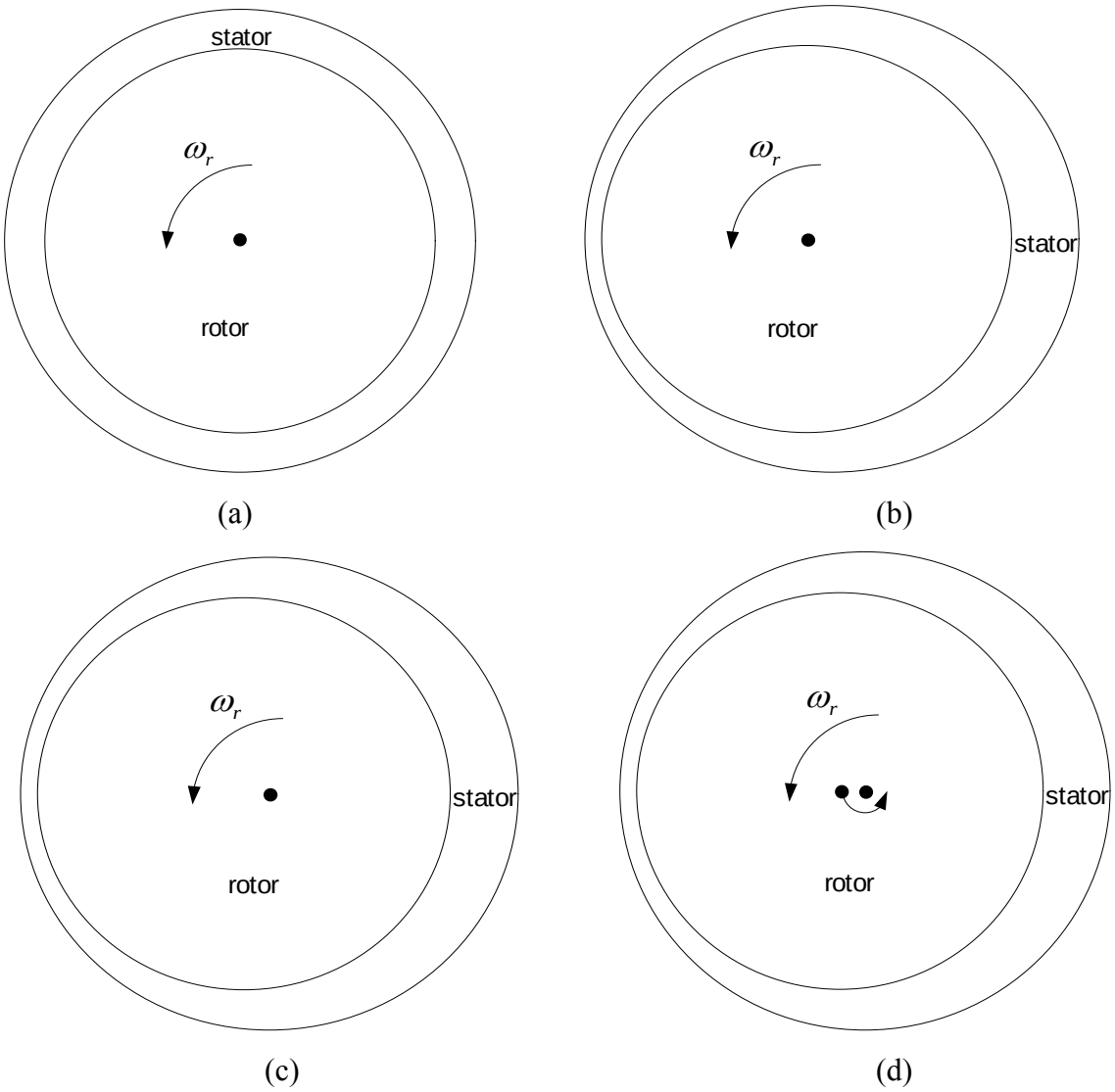


Figure 1.2 The diagrams of uniform air gap and air gap eccentricity conditions. (a) uniform air gap condition, (b) static eccentricity condition, (c) dynamic eccentricity condition, (d) mixed eccentricity condition

However, the winding function definition under eccentricity conditions is different from the one under uniform air gap length condition, which is an important issue that was ignored by previous authors. As a result the inductance calculation and simulation results have questionable credibility. The proposed methodology for the study of eccentricity conditions has been adopted for the future work. The same methodology has been applied for a synchronous reluctance machine as shown in [3.8]. An extension of the winding

function definition under general air gap length condition has been presented in [3.9]. In [4.1], the rotor slot and other eccentricity related harmonic components in the line currents were determined. The effects of pole pair and rotor slot numbers under healthy and different eccentricity conditions are presented. The equations that described the principal slot harmonic and eccentricity harmonics have been developed. The simulation results are validated by both the Finite Element Analysis (FEA) method and experimental results. The dynamic simulation of an induction machine has been presented in [4.2], in which the inductance calculation method is not correct. Then written by the same first author, the simulation model for an induction machine under eccentricity condition has been emphasized with correct inductance calculation methodology in [4.6]. A new comprehensive method for the calculation of systems inductances based on combined winding function and magnetic equivalent circuit has been presented in [4.3] where the rotor skewing, stator and rotor slots effects can be taken into account. In [4.4], a precise geometrical model of an induction machine under mixed eccentricity condition has been determined and the inductance calculation based on the precise model has been evaluated. A theoretical analysis explaining the presence of certain harmonics under eccentricity condition has been given in [4.5]. It has also been shown in [4.5] that the high frequency harmonic components found in the line-current spectrum are caused by the low frequency component.

### 1.2.4 Field Analysis Method

In [5.1], rotating-field theory has been used to develop a general model of a squirrel-cage induction machine having a general winding connection and any supply configuration. Hence, this methodology is called the field analysis method in this dissertation. The coupling impedance model that relates the EMF induced in any circuit of the machine to the current flowing in all the other circuits is the basis of this analysis method. Although the original idea of the author in [5.1] is to study the power factor issue of a cage rotor induction machine, this method can be applied to study the rotating field of electric machines in other areas. The application of this method to the understanding of the asynchronous and synchronous operation of the "brushless doubly-fed machine" has been demonstrated in [1.8]. A mathematical model based on the field analysis method for the analysis of a brushless doubly-fed machine is the contribution of that work.

### 1.2.5 Saturation Effects

In a dual stator winding induction machine, since the air-gap flux linkages created by the two stator winding sets and the induced rotor currents share the same magnetic loop, the main air-gap flux saturation phenomenon is more complicated than that of the normal single stator winding squirrel-cage induction machine [6.3, 6.5]. Because of this complexity, a reconsideration of main flux linkage saturation effect is called for in the design of the machine and in the development and practical implementation of speed/torque control algorithms. To avoid deep magnetic saturation in the stator and rotor cores, rotor and stator teeth, magnetic design methodologies have been suggested both for

the dual-stator winding and brushless doubly-fed induction machines [1.11, 6.5]. An approach to include the influence of magnetic saturation and iron loss using time-stepping Finite Element Analysis in the performance prediction of the brushless doubly-fed induction machine was set forth in [6.3], in which the authors believed that the proposed finite element model provides very good steady-state predictions and can be used for the sizing and design optimization of the machine. In [6.5], the performance of brushless doubly-fed machine is analysed using an equivalent circuit which has been developed in [6.6]. The magnetic loading of a brushless doubly-fed machine is considered in detail. A 25% reduction of the power rating in comparison to comparable single stator winding induction machine with the same volume of material and the same designed speed has been reported.

How the time-varying, multi-frequency flux linkages derivable from the currents flowing in the stator winding sets and rotor bars can be appropriately selected for an optimal machine design is yet a challenging question since these flux linkages combine additively in some regions and subtractively in others engendering non-uniform main flux magnetic saturation.

### 1.2.6 Induction Generator

Although the synchronous generators are still used in most of the power plants, induction generators are being used increasingly in the new nonconventional energy systems such as wind power, hydro, etc [8.3]. The advantages of an induction generator are reduced system cost and system size, brushless, ease of maintenance and absence of

separated dc source, etc. From the rotor structure viewpoint, the induction generator can be classified into two types: wound rotor induction generator and squirrel-cage rotor induction generator. One of the significant advantages of a wound rotor induction generator lies in the ability to operate under variable speed constant frequency condition. The other unique advantage of this machine is the ability to send the slip energy back to the system. Hence the use of this type of machine in wind power generation has become an increasing emphasis on renewable energy system recently. However, problems with brushes become the main disadvantage of this machine. The squirrel-cage rotor induction generator is the one considered in this review.

A squirrel-cage rotor induction generator with capacitor excitation is known as self-excited induction generator (SEIG). The diagram of capacitor-excited SEIG is shown in Figure 1.3.

The self-excitation phenomenon in induction machines was discovered in the 1930s. Current interest in this topic is due to the potential applications of SEIG. When the induction machine works as a generator, the real power flows out of the machine but the machine needs reactive power to build up the voltages across the machine terminals.

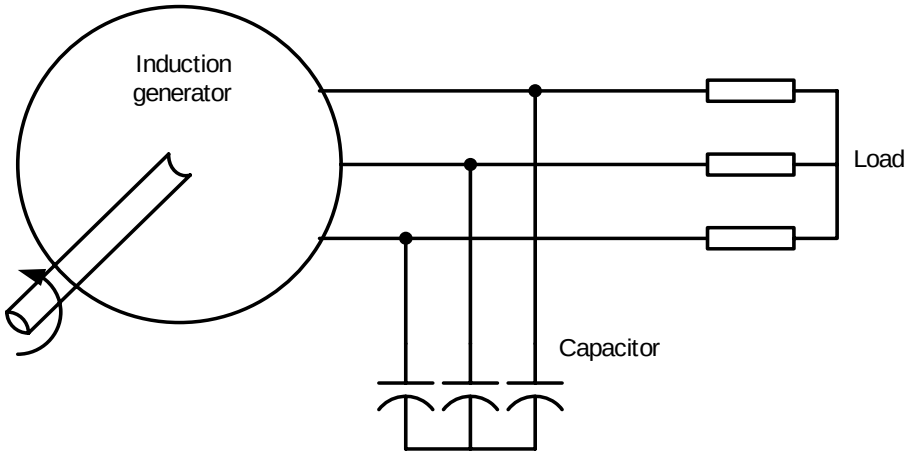


Figure 1.3 The diagram of self-excited induction generator

The reactive power can either be provided by the power system when it is connected to the grid or by capacitors when it is working as isolated generating system. The capacitance requirement is so important that much work has been done on this area. In [8.4], a comparative study of steady state performance of both long-shunt and short-shunt configuration of SEIG under various loads was presented. The analyzed results show that the short-shunt connection has better voltage regulation under higher load voltages while long-shunt connection will be better under low load voltages. A methodology has been explained to choose appropriate set of values of capacitors for desired voltage regulation in [8.5]. Only the pure resistive load was used in the analysis and studies, although the effectiveness of the proposed methodology under reactive load has been claimed by the authors. A formula for determining minimum self-excited capacitor requirement for induction generators is also presented in [8.6]. A minimum air gap flux linkage that is required for the self-excitation and stable operation of and SEIG feeding an impedance load has also been studied in [8.7]. The performance of a self-excited induction generator is another interesting topic since the performance and operating limitations of this kind of machine depend on the output voltage, frequency, rotor speed, load condition and terminal capacitances. An analytic method for steady state analysis of this machine was reported in [8.8]. The performance of a self-excited induction generator under a wide range of varying conditions has also been studied in [8.9-8.10]. The use of damping resistors across series capacitors is proposed to damp out the starting transients and for the stable operation in [8.11]. The performance improvement of self-excited induction generators from the machine parameters and machine design view points can be found in [8.12, 8.13]. The stability analysis of self-excited induction generators has been reported

in [8.14]. In [8.15-8.17], the studies on single-phase self-excited induction generators have been presented. The equivalent circuit model is used to analyze the induction generators in most of the works reported [8.3-8.17].

With the development of power electronics, more and more studies have been focused on PWM converter excited induction generators [8.18-8.23]. Two system topologies are found and their diagrams are shown in Figure 1.4.

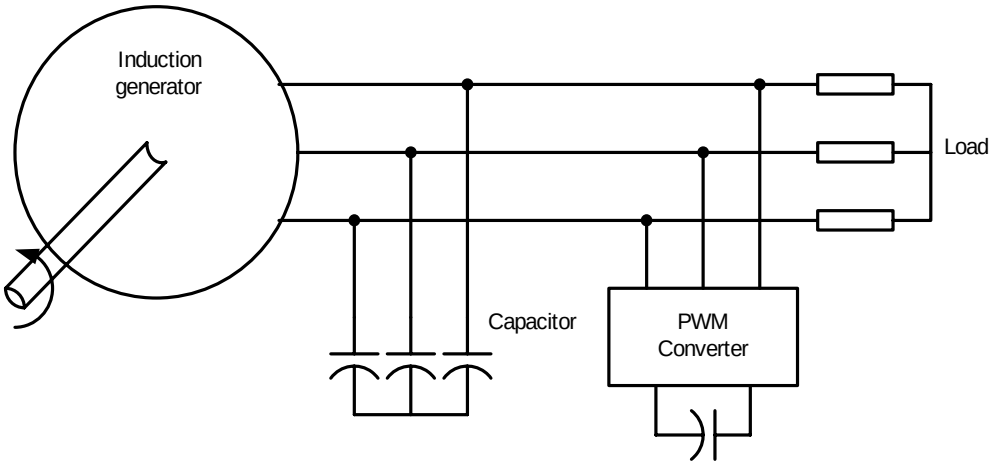


(a)

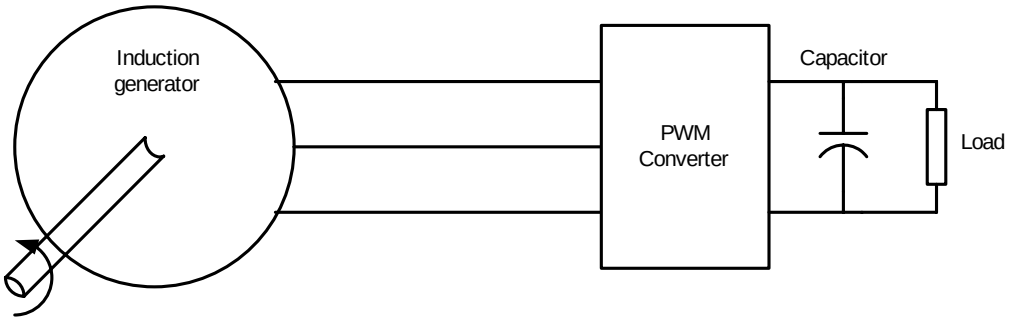


(b)

Figure 1.4 The diagrams of PWM converter excited induction generators. (a) PWM converter assisted induction generators, (b) PWM converter driven induction generators

The system in which a PWM converter is shunt connected with capacitors and loads is called PWM converter assisted induction generators as shown in Figure 1.4(a). The PWM converter with dc capacitor in this topology functions as a variable and controllable three-phase capacitor. The advantage of this topology is that with the reduced power rating of the PWM converter the system cost can be reduced. However, the complexity of the system is increased. The other one with absence of a three-phase excitation capacitor is called PWM converter driven induction generator, in which the three terminals of induction generator are connected to PWM converter only as shown in Figure 1.4(b).

The PWM converter assisted induction generator system was proposed in [8.18], where an indirect stator flux control strategy is adopted and the system steady state and dynamic operation is studied. Similar system topology is found in [8.19], where the analysis, design and selection of PWM converter components were presented for five different power rating machines with varying power factor loads. However, the PWM converter in [8.18] and [8.19] can only absorb or inject reactive power into the system because of the absence of dc sources. In [8.20], a battery bank is paralleled with dc capacitor such that it can absorb and inject both active power and reactive power thus increasing the efficiency and availability of the system.

In [8.21], an inverter driven induction generator has been proposed and a theoretical treatment based on a first harmonic approximation of inverter performance was presented. It has been concluded that the inverter makes the development of efficient induction generators capable of operating over wide speed ranges [8.21]. A strategy to control an induction generator working with variable speed and load was presented in

[8.22] and the total losses of the generator are minimized by proper control of the PWM converter. In [8.23], a comprehensive control method that addressed three control objectives in a wind power generation system was presented. By regulating the currents of rectifier and inverter, the local bus voltage is controlled to avoid voltage rise, the maximum winding power is captured while losses are minimized. The back-to-back connection of two PWM converters were used in the system [8.23]. The application of induction generator in electric automotives was reported in [8.24], where three different system topologies were proposed for different system cost and system objectives. A control methodology has also be proposed to achieved the objectives.

### 1.2.7 Parallel and Series Connected Boost Rectifiers

The parallel connected rectifiers are normally used to increase the output power of the system. Traditionally, the input sources of a parallel connected rectifier system have been isolated from each other using a transformer in ac side as shown in [9.1] or using separate power supplies. In [9.1], different topologies of series and parallel connections of the hysteresis current controlled PWM rectifiers have been investigated. The unity power factor (or leading power factor) operation of each rectifier has been reported. The particular concerns about the system stability and the capability of sharing voltage (series connection) and current (parallel connection) between the modular units have been addressed.

The disadvantages of the system configuration with independent power sources lie in a relatively bulky size and higher system cost because of the line-frequency transformer

and additional power supplies. Directly connected parallel three-phase converters from on source is the way to overcome those problem, however since the two three-phase PWM converters share the same voltage sources, circulating currents can exist in all of the phases. To avoid the circulating current, inter-phase reactors are used as zero-sequence current damper, however the reactors can only provide high impedance at high frequency level and can not dampen the low-frequency circulating current. In [9.4], it is found that the zero-sequence excitation of parallel connected rectifiers comes from the discontinuous point of the Space Vector Modulation (SVM) method. Since the conventional control method with only q- and d-axis components cannot eliminate the disturbance, a SVM without using zero vectors is used to reduce the pure zero-sequence current. By using the proposed modulation method, a circulating current at switching frequency on each phase can still be observed, which can be considered as small disturbances. Another synchronized current control method has been proposed in [9.7], in which two parallel connected three-phase converters are controlled as a three-phase six-leg converter. The switching frequency and harmonic current content were reduced in steady state while the quick response has been observed at transient state. The circulating current and zero sequence current can be regulated to be zero, however, the control of the system will be very complicated if more converters are paralleled. In [9.2], a zero-sequence model is developed based on an average model of parallel connected converters. Then a control variable associated with space vector modulation was introduced for the control of zero sequence current. A high performance zero sequence current control was proposed to suppress the circulating current. In [9.8], a method combining the space-vector modulation scheme with a variable-structure control was

proposed. The switching frequency is kept constant and satisfactory dynamic performance can be achieved. Three control schemes for parallel connected PWM rectifiers have been proposed and the system performances of the three proposed controllers have also been compared.

In the parallel voltage source inverter area, different system configurations have been studied in [9.9]. The control strategy for parallel operation and the system protection methods have been discussed in detail. In [9.10], a simple control scheme that regulates the current of each inverter independently has been used. Current instability has been reported when a dual-winding three-phase motor was driven by parallel connected voltage source inverters. It was discovered that the nonlinearities of the system, including the modulator, inverter and machine, result in a chaotic transient into the instability, which is not predictable or repeatable. Parallel connected five-level PWM inverters have also been studied in [9.11] to increase the power rating of the inverter system. The dc current was found to be controllable by means of phase shifting of the injected third order harmonics.

Very few published papers have focused on the use of series connected ac-dc boost rectifiers when compared to the relatively large body of work on paralleled ac-dc boost converters [9.1-9.5, 9.7-9.11]. In [9.1], both parallel and series connected AC-DC rectifier systems using hysteresis current control have been studied and stability analysis results based on a very simplified converter model have also been shown under unity power factor condition.

### 1.2.8 Induction Machine Drive---Scalar Control

Generally speaking the variable speed control of induction machine can be classified into three main categories: scalar control, vector control and direct torque control.

Scalar control is used in low cost drives and there is no direct control of either air-gap flux or electromagnetic torque. The simplest and most robust scalar control method is constant Volts per Hertz (Constant V/Hz), in which the magnitude of input stator voltage is adjusted in proportion to the frequency of input voltage. The stator flux linkage is kept approximately constant by keeping this proportional relationship between the magnitude and frequency of input phase voltages. In constant V/Hz method, the speed of the rotating magnetic field of the machine is controlled by changing the supply frequency. The electromagnetic torque developed in the machine depends only on the slip frequency. The general configuration of a speed control system using constant V/Hz method is given in Figure 1.5.

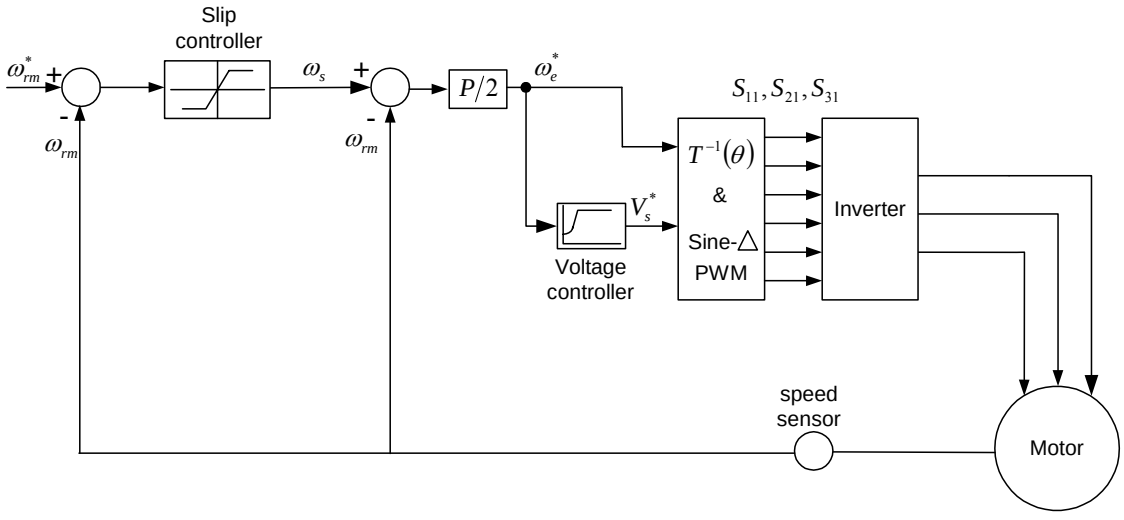


Figure 1.5 The general diagram of a speed control system using constant V/Hz method

The actual rotor mechanical speed is obtained from a speed sensor coupled on the rotor shaft. The error of the reference rotor speed and the actual rotor speed is applied to a slip controller whose output represents a reference slip frequency signal. Then the reference electric frequency is obtained by adding the reference slip frequency to the actual rotor speed. A small voltage boost is necessary to compensate the relatively large voltage drop on stator resistance at the low speed region and to improve the controllability. The disadvantages of this control method are the low speed accuracy and poor torque responses. In [10.1], currents and speed feedback are used to regulate the frequency and the magnitude of applied voltages. A current regulated PWM inverter was found in [10.2]. The stability issue of an induction machine driven by constant V/Hz inverter has been studied in [10.3].

Scalar torque control is another scalar control method, in which the magnitude and frequency of the stator current are regulated so that the steady state torque of the machine is controlled. In this case, the feedback currents are required and the current-controlled type of inverter is used. The block diagram of a scalar torque control system is shown in Figure 1.6.

The current controller performs the computation of the reference torque current $I_T^*$ and the reference flux-producing current $I_\phi^*$ from the torque command $T^*$ and rotor flux linkage command $\lambda_r^*$. The expression of reference torque current calculation is given as:

$$I_T^* = \frac{T^*}{1.5P\lambda_r^*} \tag{1.1}$$

where, $P$ is the pole number of the machine.

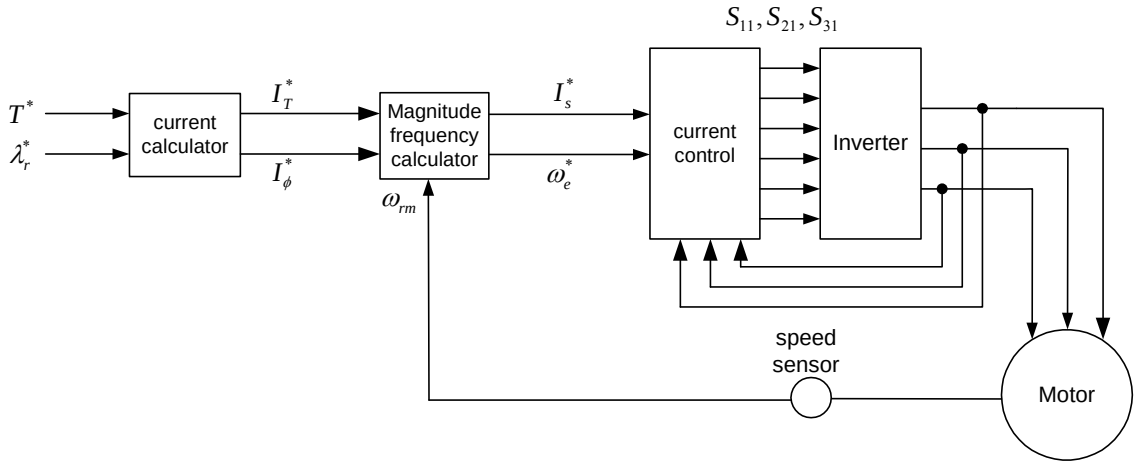


Figure 1.6 The block diagram of a scalar torque control system

The reference flux-producing current is calculated as:

$$I_\phi^* = \frac{\lambda_r^*}{L_m} \tag{1.2}$$

where, $L_m$ is the magnetizing inductance.

The magnitude of the stator current is given as:

$$I_s^* = \sqrt{I_T^{*2} + I_\phi^{*2}} \tag{1.3}$$

and the reference frequency of the stator current is expressed as:

$$\omega_e^* = \frac{P}{2}\omega_{rm} + \frac{I_T^*}{\tau_r I_\phi^*} \tag{1.4}$$

where, $\tau_r = \frac{L_m}{r_r}$ is the time constant of the rotor.

The torque developed by the machine is limited by the maximum value of current. Only under transient conditions and for a limited time, is a higher than rated current allowed. The current sensors increase the system cost and the control scheme is more complicated than the constant V/Hz method.

### 1.2.9 Induction Machine Drive---Vector Control

The vector control method is also called the Field Orientation Control (FOC) method, in which the air-gap flux vector is kept orthogonal to current vector so that effective decoupling between flux and current can be obtained and instantaneous torque control is achieved. The vector control method is divided into three categories: indirect vector control, direct vector control and direct torque control.

Indirect rotor field orientation is basically achieved by controlling the slip frequency to satisfy the following slip condition.

$$\omega_s = \frac{r_r L_m i_{qs}}{L_r \lambda_{dr}} \tag{1.5}$$

where, $i_{qs}$ and $\lambda_{dr}$ are the q-axis current and rotor d-axis flux linkage in synchronous reference frame. The synchronous speed or stator frequency is obtained by adding the slip frequency to the rotor speed. The disadvantages of this method are the need for a speed or position sensor and accurate knowledge of machine parameters. Unfortunately the machine parameters are subject to change for different operating conditions, so certain machine parameter estimation methods or adaptive parameters modification scheme are necessary for high performance control which increases the complexity of the control structure. The slip calculation is critical in the control method. Unfortunately, the rotor time constant of the machine, which is variable during different operation conditions, is involved in the slip calculation. Several adaptive schemes have been proposed to overcome this problem [10.4-10.7]. In [10.4], the rotor time constant of an induction machine has been measured by injecting a single-phase ac current and observing the

voltage transient when this test current is switched to dc. A self-tuning system based on this measurement method has also been demonstrated. An adaptive control has been presented in [10.5] to correct the rotor time constant estimation. The one step prediction of the correction that is necessary for the slip calculation can be obtained by using the proposed controller. The control scheme depends on the value magnetizing inductance which is a varying component under practical circumstances. Hence a magnetizing inductance correction strategy has been adopted by the authors. In [10.6], three rotor time constant estimation methods based on Model Reference Adaptive System (MRAS) have been proposed and the performances of those methods have been compared. It has been found that depending on the application, any one of those estimation methods may be the most suitable one. The method based on regulating the energy stored in the magnetizing inductance has been proposed to estimate the rotor time constant in [10.7]. The input voltages and currents are all needed to calculate the magnetizing inductance energy. The authors found that the proposed method can solve the thermal variation problems of both rotor time constant and stator resistance.

The direct field orientation control is based on the position signal of the rotor flux. The advantages of this method are elimination of rotor position sensor and less machine parameter sensitivity. However, a sensor that can measure the rotor flux position is required, which increases the cost and the complexity of machine and seems impractical. Although the alternative methods for flux measurement, such as searching coil and tapped stator windings [10.8-10.9], have been introduced, the performance most likely degrades at the low speed region. In [10.8], a low cost direct field orientation control that requires little knowledge of machine parameters has been presented, in which the tapped

stator windings were used as flux sensors. The searching coil has been used in the control of an induction machine in [10.8]. The problems in flux measurement have been identified. Optimal flux coil configuration has been developed to overcome those problems.

### 1.2.10 Induction Machine Drive---Direct Torque Control

Direct torque control, in which the torque and flux are regulated directly by the hysteresis controller, is based on the estimation of electromagnetic torque and flux. The PWM generator and the coordinate transformations that are required in the field orientation control are not necessary, becoming the main advantages of the method. The control scheme itself requires little machine parameter information, however the knowledge of those machine parameters are required for the torque and flux estimation. Hence the similar problem--machine parameters dependency can also be found in this control method. Some significant torque ripples are also found in the low speed range and are difficult to eliminate.

From the above discussion, it seems that the control methods for induction machine are a mature technology. Future development of this area lies in the elimination of all kinds of sensors without degrading the performance.

### 1.2.11 Sensorless Control of Induction Machine

After the intensive study all around the world in the past 15 years, the development of sensorless induction motor drives has become a mature technology. However, a standardized solution does not emerge, which indicates that the maturing process of this technology will continue.

The obvious advantages of sensorless drives are system cost reduction and increasing overall system ruggedness and reliability, especially in hostile environments. Generally speaking, sensorless control is achieved by the extensive use of state observation techniques, in which the measurements of currents and voltages are used to estimate the flux position or velocity. Several sensorless control techniques have been tried over the years and the methods can be broadly classified into two categories: equivalent circuit based methods and magnetic structure based methods [1.11].

For the equivalent circuit based method, well known machine dynamic equations are used to produce relationships between the measured quantities and estimated variables. The voltage model flux estimation method is one of the oldest methods. The estimation method is based on the stator voltage equation, in which the rotor speed independent variables--stator voltages and currents are utilized. From the stator voltage equation, the stator flux is estimated by the integration as:

$$p\hat{\lambda}_s^s = v_s^s - r_s \cdot i_s^s \tag{1.6}$$

where, the subscript "s" represents the variables of stator and the superscript "s" represents the variables in stationary reference frame; the superscript "$\wedge$" represents the estimated variable; p represents the operator $\frac{d}{dt}$.

The rotor flux can be obtained by:

$$\hat{\lambda}_r^s = \frac{\hat{L}_r}{\hat{L}_m}\left[\hat{\lambda}_s^s - \left(\hat{L}_s - \frac{\hat{L}_m^2}{\hat{L}_r}\right)\cdot i_s^s\right] \tag{1.7}$$

Sensorless control of induction machine based on voltage model flux estimation has been proposed in [10.10], where two lag-circuits were inserted into the estimator for better estimation. The integration of (1.2) by pure integrator involves the drift and saturation problems [10.12]. A Low Pass Filter (LPF) was proposed to solve the problems, the pure integrator is replaced by LPF and the transfer function becomes $\frac{1}{s+a}$ compared with that of a pure integrator $\frac{1}{s}$.

The current-based model is another flux estimation method. The motor flux is identified by solving a set of equations where machine parameters and rotor speed are required [10.13]. The estimation equation is given as:

$$p\hat{\lambda}_r^s = -\left(\frac{\hat{r}_r}{\hat{L}_r} - j\omega_r\right)\cdot\hat{\lambda}_r^s + \hat{r}_r\frac{\hat{L}_m}{\hat{L}_r}i_s^s \tag{1.8}$$

In [10.14], a clear classification of open loop flux observers has been given with the analysis of their advantages and disadvantages. A design methodology based on the physical model of induction machine model has been presented. Four open loop flux observers and a closed loop Gopinath flux observer are evaluated using Frequency Response Function (FRF) analysis method. The voltage model flux observer utilizes the measured stator voltages and currents, but not the rotor velocity. From FRF analysis, the accuracy of this observer is sensitive to stator resistance at low rotor velocities, which is a well known limitation of this observer.

For the current model flux observer, the measured stator currents and rotor speed are used. The influence of parameter estimation errors on the estimated flux linkage are studied using FRF analysis. It is found that under high slip condition, the magnitude of rotor flux linkage is sensitive to rotor resistance while the phase angle of the estimated rotor flux linkage is very insensitive. Both the magnitude and phase angle of estimated rotor flux linkage are sensitive to the rotor resistance and magnetizing inductance under rated slip condition. It should be noted that the accuracy can be affected by the rotor leakage inductance under any operating condition.

The measured stator voltages and rotor speed are utilized in the full order open loop flux observer, in which the stator currents are estimated as intermediary quantities. It has been found that the sensitivity to stator resistance decreases with increasing rotor speed and the influence of leakage inductance is relatively small and nearly constant. However, the need for accurately measured stator voltages are low and zero speed range is a main limitation of this observer.

In addition to these, a cancellation method open loop flux estimator has been presented, in which stator voltages and currents as well as rotor speed are used. The inherent drawback of this observer lies in huge flux estimation error when the rotor speed is near zero due to the division by rotor speed. In this range, the quantization noise due to the numerical differentiation will be significant. Based on the above analysis, an improved closed loop Gopinath model for flux estimation has been proposed in [10.14], in which the voltage model and current model were combined to be a closed loop observer. A similar flux observer with a generalized analysis method can be found in [10.15].

The basic idea of a closed loop flux observer is that the current error can be driven to zero through the use of proper feedback acting on the estimated rotor flux linkage since the rotor flux linkage acts as a state feedback of stator current. In the design of the observer, the limitations on gains and eigenvalues selection are given in [10.14] as the disturbances in the form of measured signal quantization noise and harmonic noise. It should be noted that an interesting conclusion about the accuracy of the observer has been given in [10.14] also. For the closed loop flux observer, the accuracy of the estimated quantities is determined by the accuracy of the open loop observer model, observer topology and observer controller gains. The conclusion is that the accuracy of a closed loop estimator is primarily determined by the accuracy of the measured variables (sensor and signal conditioning accuracy) and secondarily by the controller design in the way the controller rejects disturbances.

The extended Kalman filter based speed estimation algorithm is another equivalent circuit based method, in which a complete mathematical model of the induction machine is used [10.16]. The Kalman filters have the ability to obtain accurate estimation under noisy conditions. However, the intensive computation makes this approach less attractive and difficult for real implementation.

The most popular speed estimation methodology in the first category is based on Model Reference Adaptive System (MRAS). The MRAS for sensorless control was firstly proposed by Schauder in [10.17], where the adaptive mechanism of MRAS has been explained clearly and an error function based on q- and d-axis rotor fluxes has been proposed. Popov's criterion has been used to prove the stability of the adaptive algorithm. A similar method was presented in [10.18] with discussion of flux observer design. The

most recent work on this estimation algorithm includes an improved closed-loop stator flux estimator which adjusts the value of stator resistance on-line [10.19]. The cross product of estimated and actual currents is utilized in the resistance estimation. Almost starting at the same time, another adaptive estimation methodology called full-order flux observer has been presented in [10.20-10.23]. In [10.20], the Lyapunov's theorem was utilized to derive the adaptive scheme, which is similar to the error function in [10.17]. Since the adaptive control theorem is applied to both estimation algorithms, the boundary between them is not clear and both of these estimation schemes can be considered to be one although some authors call it MRAS-based speed estimation and the others call it a full-order flux observer based speed estimation as found in many publications in this area. In this dissertation, both speed estimation algorithms will be combined and called MRAS-based speed estimation scheme.

From the definitions of reference model and adaptive model point of view, the MRAS-based speed estimation schemes are broadly classified into two categories. In the first type, the rotor speed independent stator equations are used as a reference model while the rotor speed dependent rotor equation is assumed to be an adaptive model. The errors between these models are used to formulate an error function or adaptive scheme, which passes through a PI controller and yields the estimated rotor speed [10.17, 10.18, 10.19, 10.24]. However, the actual machine itself is considered to be the reference model and the flux observer becomes the adaptive model in the second approach. The error between the measured stator currents from reference model and the estimated stator currents from adaptive model are combined with rotor fluxes to be the error function [10.20-10.21]. This MRAS scheme is called full-order flux observer based speed

estimation. It has been claimed in [10.27] that the conventional MRAS scheme in [10.17] is a special case of operating point of a full-order flux observer. Most of the studies in sensorless control of induction machines utilized the full-order flux observer-based speed estimation scheme.

From the error function point of view, the MRAS-based speed estimation schemes can be divided into several categories. In the first type, q- and d-axis rotor fluxes are estimated using two different machine models and the error of the rotor fluxes from the two models are used to estimate the rotor speed [10.17-10.19]. The expression of the speed adaptive algorithm of the first type is expressed as;

$$\hat{\omega}_r = \left( K_p + \frac{K_i}{S} \right) \cdot \left( \lambda_q \cdot \hat{\lambda}_d - \lambda_d \cdot \hat{\lambda}_q \right) \tag{1.9}$$

In the second type, the stator current is estimated and compared with the measured stator current. The error between the estimated and measured stator current is used to produce the speed adaptive scheme [10.20-10.23, 10.25-10.29, 10.31 -10.34]. This type of error function is the most popular one and the speed estimation scheme is given as:

$$\hat{\omega}_r = \left( K_p + \frac{K_i}{S} \right) \cdot \left( e_{iq} \cdot \hat{\lambda}_d - e_{id} \cdot \hat{\lambda}_q \right) \tag{1.10}$$

Another speed adaptive scheme has been proposed in [10.29] by adding a rotating angle into the error function. It was claimed that the angle can change the direction of the error projection and this angle will be adjusted online to stabilize the regenerating-mode at low speed range. The expression of this MRAS scheme is:

$$\hat{\omega}_r = \left( K_p + \frac{K_i}{S} \right) \cdot \mathrm{Im}\left[ \hat{\lambda}^*_{qdr} \cdot \left( i_s - \hat{i}_s \right) \cdot e^{-j\phi} \right] \tag{1.11}$$

The third type of error function was proposed in [10.24]. The cross product of the back-EMF from the reference model and the adaptive model is used to calculate the estimation speed as expressed in the following equation.

$$\hat{\omega}_r = \left( K_p + \frac{K_i}{S} \right) \cdot \left( \hat{e}_m \otimes e_m \right) \tag{1.12}$$

In the forth type of error function, the cross product of the back-EMF and the stator current vector was used [10.24]. This type of error function is not well known and the expression of speed adaptive scheme is:

$$\hat{\omega}_r = \left( K_p + \frac{K_i}{S} \right) \cdot \left( i_s \otimes e_m \right) \tag{1.13}$$

The fifth type of error function can be found in [10.36], where the error function is composed of two components. The first component is the cross product of the estimated rotor flux vector and the error in the estimated back-EMF, while second component is the dot product of those two quantities. A variable coefficient k has been inserted into the error function as a partition factor between these two components. Better speed estimation result has been claimed in [10.36]. The speed adaptive scheme for this error function is given as:

$$\hat{\omega}_r = \left( K_p + \frac{K_i}{S} \right) \cdot \left( \hat{\psi}_r \otimes \Delta e_m + k \cdot \hat{\psi}_r \cdot \Delta e_m \right) \tag{1.14}$$

Similar to the fifth error function, another error function has been proposed in [10.39]. The real and imaginary part of the product of estimated rotor flux vector and error in the stator current are used to formulate the speed adaptive scheme. A partition factor k is also adopted to change the effect of each component to the output of error function. The expression of speed estimation is:

$$\hat{\omega}_r = \left( K_p + \frac{K_i}{S} \right) \cdot \left\{ k \,\mathrm{Im}\left[ \hat{\lambda}^*_{qdr} \cdot \left( i_{qds} - \hat{i}_{qds} \right) \right] + (1-k)\,\mathrm{Re}\left[ \hat{\lambda}^*_{qdr} \cdot \left( i_{qds} - \hat{i}_{qds} \right) \right] \right\} \tag{1.15}$$

By minimizing the squared error $\left| i_s - \hat{i}_s \right|^2$, a voltage error-based speed estimator has been proposed in [10.30].

The instability problem at low speed is the main limitation of MRAS schemes especially when the machine is working under generating mode or braking mode. To overcome the problem, different error functions have been proposed [10.23-10.24, 10.29, 10.33, 10.36]. The design methodologies of properly choosing the observer gain and speed estimation controller parameters become another way to solve the instability issue such that the instability region can be reduced or even eliminated by using the right observer parameters [10.20-10.21, 10.25-10.32, 10.38]. The approach that the observer poles are placed proportionally to the poles of induction machine has been reported in [10.20-10.21]. In [10.25], a different pole-placement technique was proposed in which the observer poles correspond to the induction machine poles shifted to the left in the s plane by an amount $k_s$, which is a machine parameters dependent constant. Similar approach has been adopted in [10.34]. Speed-adaptive gains have been proposed in [10.27] to give enough damping at high speed. The expression of observer gain in complex form is given as:

$$K = \lambda \begin{bmatrix} 1 + j \cdot sign(\hat{\omega}_m) \\ -1 + j \cdot sign(\hat{\omega}_m) \end{bmatrix} \tag{1.16}$$

where, $\lambda = \begin{cases} \lambda' \dfrac{\hat{\omega}_m}{\omega_\lambda}, & if \ |\hat{\omega}_m| < \omega_\lambda \\ \lambda', & if \ |\hat{\omega}_m| \geq \omega_\lambda \end{cases}$, $\hat{\omega}_m$ is estimated rotor speed, $\lambda'$ and $\omega_\lambda$ are positive constants. The instability of sensorless control under low speed generating condition has

been discussed in [10.31-10.32] using Routh-Hurwitz criterion while a design strategy of both observer gains and speed estimator parameters has been proposed and discussed. It has been shown that the instability region can be reduced by properly designing the observer gains and speed estimator parameters. In [10.39], the Butterworth method was used to select the observer gains and the D-decomposition method [10.66, 10.67] defines the boundary of stability area and instability area. However, the effectivities of the observer gains and speed estimator parameters within the whole speed range have not been ensured and checked by author.

Since the effect of stator resistance is so significant at low speed while temperature affects the stator resistance value so much, the machine parameter adaptive scheme becomes one of the ways to improve the MRAS adaptive algorithm at low speed range. The MRAS scheme has also been used to estimate the stator resistance. This estimation method was firstly presented in [10.21] and then adopted in [10.34, 10.36, 10.37]. The design methods for observer gains and estimator parameters can only ensure the stability of two estimators individually, however the overall estimation algorithm may be unstable. To solve this problem, in [10.33, 10.36], the speed and stator resistance estimators are combined to be a multi-input, multi-output system (MIMO) so that the observer gains and the parameters of estimators can be designed properly to ensure the stability of the whole system. A comparison study of three different MRAS schemes has been presented in [10.35].

The speed identification problem at low speed range has received considerable attention and some new approaches can be found in the recent publications. In [10.40], a different speed adaptive scheme has been proposed, in which the current difference, its

integral and a new stretch-turn operator have been used to ensure the operation at very low speed. Another sensorless scheme has been proposed in [10.41], in which the error of q-axis current is used to feed a PI control and the output of this PI control is the estimated slip frequency. Then the estimated rotor speed is obtained by subtracting the estimated slip from the synchronous speed. The sliding-mode control and variable-structure control have been adopted into the MRAS system to offer robust performance and overcome the parameters uncertainties [10.42-10.47]. The induction machine sensorless control using the Luenberger observer have been found in [10.48-10.49].

It is also found that in addition to the emergence of new approaches, some "new" techniques have been applied into the old approaches to yield better results. For example, the Phase Locked Loop (PLL) technique is combined with a low-pass filter to obtain better flux estimation results from the simple voltage model approach [10.50]. In [10.51], the MRAS scheme and the saliency-based flux orientation are used at different speed ranges and the combination scheme offers the synergetic effect between these two methods. The MRAS adaptive scheme has also been applied to study the induction generator and wound-rotor induction machine in wind energy applications [10.52-10.54].

The magnetic structure method is based on using second order effects due to the physical structure of the machine [1.11]. The third harmonic voltages due to the saturation effects were used to estimate the flux angle in [10.55]. Another technique that uses the effect of the rotor slots to track position has been presented by Lorenz. This method achieves zero speed estimation by using high frequency excitations adding to the main signals. The high frequency injection method, which is based on saturation induced saliency, has been proposed in [10.56-10.58]. It is claimed that the local saturation due to

rotating flux vector can be related to the position and the rotor. For example, the difference of the impedance of the motor between the flux axis and the quadrature axis is measurable at injected high frequency due to the skin effect [10.58]. The flux position can be estimated from this difference of impedance. A recent speed estimation method based on high frequency current due to the high frequency injected voltages was found in [10.59]. Different high frequency injection techniques for sensorless control of induction machine have been reviewed and experimentally investigated in [10.60]. One of the conclusions of this paper is that high frequency injection techniques can outperform observer-based methods at low speed range. The variation of the leakage inductance due to either saturation or rotor slotting has been used to estimate the flux position by measuring the zero sequence current in [10.61]. However, an appropriate test voltage needs to be injected and an extra sensor is necessary in this application. The low-frequency signal injection method for sensorless induction machine drive has been proposed in [10.62], in which a zero-sequence voltage component due to the low frequency injected signal is used to estimate the position of the air-gap flux. Another low frequency current injection method has been proposed to estimate the rotor flux position, in which an oscillation component in back electromotive force (EMF) due to the small speed oscillation caused by injected current signal is used to form an error signal. The error signal is regulated to be zero. As a result the test signal and rotor flux are aligned [10.63]. A sensorless position estimation method for double-cage induction machine using the resistance variation of the outer-cage has been proposed in [10.64]. The special double-cage rotor structure makes this method less attractive for the application.

The most recent overview paper is given as [10.65], in which different sensorless methods have been analyzed and their merits and drawbacks have been discussed. The mechanism of the voltage model open loop flux observer and its improved model have been clearly explained. The performance improvement of the voltage model at the low-speed region including the effect of inverter nonlinearity has been addressed. For the closed loop observer, only the full-order flux observer and the sliding model observer have been included in [10.65]. The basic ideas of those observers have been explained; however the shortcomings have not been noted. For the signal injection method, the injected signal excites the machine at a much higher frequency than the fundamental. The resulting high frequency currents generate flux linkages that only pass through the leakage path of the machine and do not influence the fundamental mutual flux linkage. The magnetic anisotropy, which is caused by the saturation of the leakage paths or the special rotor structure, serves to identify the rotor position angle. It should be noted that the existing rotor anisotropies have different spatial orientations such as the actual angular position of the fundamental field and position of the rotor bars within a rotor bar pitch. The response to the injected signal reflects all anisotropies, so it is required to extract information on one particular anisotropy while the other anisotropies act as disturbances. The injection of a rotating carrier signal is the first method used. The useful information is separated by a bandpass filter (BPF) from the fundamental current and from the switching harmonics of higher frequency. However the axis leakage inductance ratio $L_{\sigma q}/L_{\sigma d}$ is so closed to unity value such that the angular information is difficult to identify. A direct extraction of the current signal is also problematic since the characterizing components in current are very small and being superimposed by the large

positive sequence current and switching harmonics. Then a dynamic model of the mechanical subsystem of the drive motor has been proposed to enable spectral separation, however a custom designed rotor is required. The revolving carrier scans the whole anisotropies that exist in a machine, but only one of them is useful. Why not just achieve the targeted anisotropy? Then an alternative class of methods that inject not a rotating, but alternating carrier in a specific time-variable spatial direction has been proposed to achieve maximum sensitivity in the targeted anisotropy. The method that utilizes high-frequency impedance is one of the approaches. However, the identification of the d-axis is based on the symmetric assumption of the machine, which may not be guaranteed for every motor. An asymmetric characteristic would increase the estimation error. The injection of elliptic current is another approach for the estimation of anisotropy characteristic. The good speed estimation at zero speed can be obtained while the undesired ripple is the problem of this method. The anisotropy induced by PWM signal has also been considered for the speed estimation, however the speed estimation will be worse at higher rotor speed which limits the maximum operating speed of this method.

# CHAPTER 2

# DUAL STATOR WINDING INDUCTION MACHINE DESIGN

## 2.1 Introduction

The dual stator winding induction machine (DSWIM) under taken in this research has the normal squirrel cage rotor design and standard stator laminations. As a result, the same squirrel cage rotor, which is used in the normal single stator winding induction machine, can be shared by the dual stator winding induction machine without any modification. Then a design of the dual stator winding induction machine using the existed standard single stator winding induction machine frame can greatly reduced the cost of this new machine.

In this chapter, a dual stator-winding machine is designed using the stator frame of a standard 3-hp induction machine. The same rotor as the one for the standard 3-hp induction machine is utilized in the dual stator winding machine. Since the stator and rotor dimensions, which are the important parameters in the machine design, are already known, the design progress is different from the one based on unknown stator and rotor dimensions.

This chapter is organized as follows. In Section 2.2, two stator winding configurations are compared and the one has two independent stator winding sets is chosen in this design. Then an air gap flux densities determination process is given based

on the constant peak air gap flux density constraint and the constant yoke flux linkage constraint, in which the peak value of the air gap flux density and the stator yoke flux linkage value of the designed dual stator winding induction machine are required to be the same as those for the standard single winding induction machine. A power estimation of the designed machine is given in the last part of Section 2.2. A detailed process of the machine parameter estimation is given in Section 2.3. If the two stator winding sets are connected to PWM converters and controlled using the vector control scheme, the magnitude and the frequency of the air gap flux density of each winding set can be controlled independently. The saturation of the dual stator winding induction machine can be reduced, if the phase angles of the air gap flux densities of two stator winding set are 180 degrees apart from each other, which is also called "out of phase" in some publications. At this condition, the stator frame is fully used and the output power of the dual stator winding induction machine can be increased. A design procedure of the dual winding induction machine working under this condition is given in Section 2.4. The conclusions are included in Section 2.5.

The standard 3-hp 4-pole induction machine, which provided by A. O. Smith Electrical Products Company, is rewound to be a prototype of the dual winding induction machine having the pole combination 2/6.

Some known parameters of the machine are shown in Table 2.1.

Table 2.1 Parameters of machine design

| | |
|---|---|
| Core length: | 2.25 (in) 57.15 (mm) |
| Inside diameter of stator: | 5 (in) 127 (mm) |
| Outside diameter of stator: | 8.25 (in) 209.55 (mm) |
| Power factor (pf): | 0.8 |
| Efficiency ($\eta$) | 87% |
| Pole number (P): | 2/6 |
| Number of slot (S): | 36 |
| Frequency (f): | 60 HZ |
| Input voltage ($V_{ll}$): | 110/330 (rms) |
| Stator winding factor ($k_1$) | 0.96 |

## 2.2 Machine Design I

The two essential factors that need to be designed are stator winding type and air gap flux density of each stator winding.

### 2.2.1 Stator Winding

The essential function of the stator winding sets of the dual stator winding induction machine is to produce two simultaneous sinusoidal flux distributions with dissimilar numbers of poles. Two different approaches can obtained the same goal; one is by using a

single winding capable of producing two flux distributions of different numbers of poles, the other is by using two isolated windings of different numbers of poles.

The first approach can be found in the 70's [1.7]. The motivation of the stator winding study came from the self-cascaded machine, which also has two dissimilar flux distributions in the air gap. In this type of winding distribution, the balanced three-phase currents flowing through terminals ABC produce p pole flux distribution in the air gap, whereas the currents flowing through terminals XYZ produce q pole flux distribution. The advantage of this approach is better utilization of the slot area such that the resistance is reduced and the efficiency is improved. The disadvantages are the existence of circulating currents under unbalanced condition and the limitation of the voltage ratio between the two sets of terminals. An example of this kind of winding is shown in Figure 2.1.

Two-isolated winding sets having different numbers of poles are used in two-isolated winding approach. For example, if the stator winding has two layers, the p pole winding set may use the inner layer and the q pole winding set uses the outer layer. This approach avoids the circulating current problem under unbalance conditions, however more space harmonic components may be observed from the winding set having higher number of pole because of the less number of slots per pole per phase. More flexibilities are provided by the second approach, it is chosen in this design.

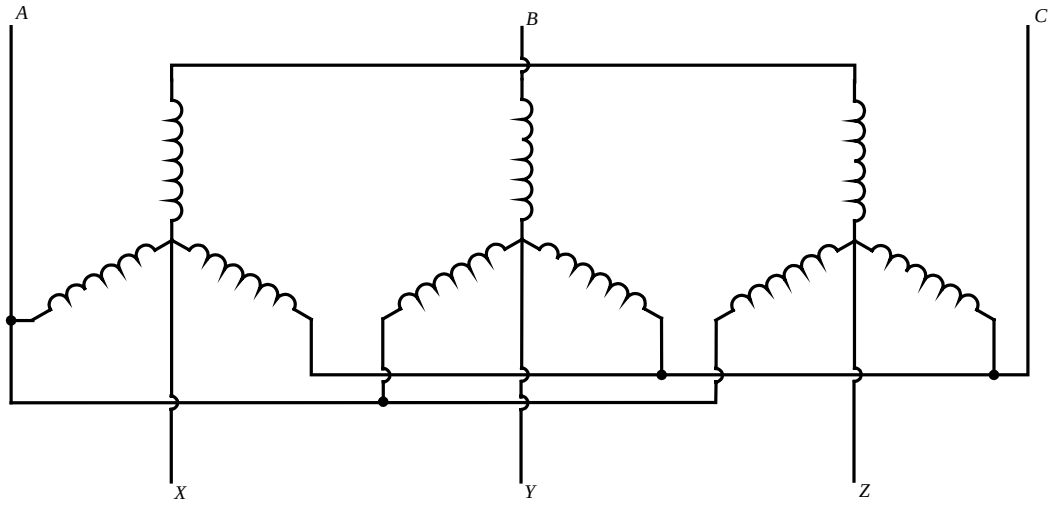


Figure 2.1 Single winding dissimilar pole number distribution

### 2.2.2 Air Gap Flux Density

In the dual stator winding induction machine, the common stator core is shared by two sets of stator windings, which implies the presence of two simultaneous MMF distributions along the air gap. The question is how to avoid the deep saturation problem when the designed dual stator winding machines are working under different load conditions. The answers lie in finding an appropriate method to evaluate the flux density for the dual stator-winding machine and designing the flux density for each stator winding set. In [2.1], the issue was considered for a specific example, however the general conclusions were not presented. In [2.2], three methods are listed that can be used to evaluate the magnetic flux density of a BDFM. The first method is a conservative one, in which the peak value of flux density of the dual stator-winding machine can be found by adding the peak value of flux densities of two stator winding sets together. The expression is shown as:

$$B_{dual} = B_{ABC} + B_{XYZ} \tag{2.1}$$

where, $B_{ABC}$ is the peak value of the flux density of the ABC winding set and $B_{XYZ}$ is the peak value of the flux density of the XYZ winding set. It is claimed that since the peak value occurs infrequently, this result will be too conservative [2.2].

The second approach defines the combined magnetic loading as:

$$B_{dual} = \sqrt{B_{ABC}^2 + B_{XYZ}^2} \tag{2.2}$$

It is found from the results shown in [2.2] that the combined flux density by using second approach will be much less than the value obtained from the first one.

The last evaluation method is called a new generalized method. This method is based on the idea of the conventional induction machine, in which the magnetic loading is evaluated by the mean absolute flux per pole, the proposed generalized definition is:

$$B = \lim_{T\to\infty} \frac{1}{T} \int_0^T \frac{1}{2\pi} \int_0^{2\pi} |B(\theta)| d\theta dt \tag{2.3}$$

The magnetic fields in the dual stator-winding machine can be written as:

$$B = B_1 \cos(\omega_1 t - p_1\theta) + B_2 \cos(\omega_2 t - p_2\theta + \gamma) \tag{2.4}$$

where, $B_1$, $\omega_1$ and $p_1$ are the magnitude of flux density, electric speed and pole pair number of the ABC winding set respectively; $B_2$, $\omega_2$ and $p_2$ are the magnitude of flux density, electric speed and pole pair number of the XYZ winding set respectively; $\theta$ is the stator angle and $\gamma$ is the shifted angle between ABC winding and XYZ winding.

If the magnetic field of dual stator-winding machine is referred to the rotor reference frame, the expression for field is:

$$B_r = B_1 \cos(\omega_{s1} t - p_1\phi) + B_2 \cos(\omega_{s2} t - p_2\phi + \gamma) \tag{2.5}$$

where, $\omega_{s1}$ and $\omega_{s2}$ are the slip frequency of ABC winding and XYZ winding respectively.

Substituting (2.5) into (2.3), the magnetic load can be found. The results show that the value of the magnetic load obtained by this method is independent of the pole numbers combination and offset angles, except one special case-- $p_1 = 2, p_2 = 4$ [2.2]. The magnetic load calculated by the proposed method is close to the second approach and the advantages and disadvantages of these two methods have been addressed in the paper. However, all the methods that have been mentioned can only be used to evaluate the combined magnetic load and can not be used to determine the magnetic load of the stator winding sets.

It should be noted that once the stator winding sets are fixed in the stator, the mechanical angle between these two stator winding sets can not change any more. However, the electrical angle between the voltage vectors and the current vectors of two stator winding sets are variable and controllable. Then it can be found that at some particular load conditions, the peak value that claim to occur relatively infrequently in [2.2] can always be found at that kind of load. Hence it is better to consider the worst operating case in the design of the dual stator winding machine.

A straightforward method that can be used to design the magnetic load of each stator winding has been discussed in [1.11]. To avoid deep saturation of the core material, the peak magnetic loading produced by the combined effect of the two MMFs must be the same as that of an equivalent single stator winding design, which means the peak flux density in the air gap must remain constant and the maximum flux density per pole must be identical in both the dual stator and single stator design. Since dissimilar pole numbers

are applied in this kind of dual stator winding induction machine and the input voltage frequency of each stator winding depends on the control objectives and is not required to be fixed. Generally, the two simultaneous MMFs have different rotating speeds and the peak value of the combination of two simultaneous MMFs changes with time. The machine design is to make sure that even in the worst case, the machine can still avoid operating in deep magnetic saturation.

Assuming the dual stator machine is wound for 2/6 pole and neglecting the saturation, the flux density in the air gap at a given instant time can be expressed as:

$$B_{g2/6}(\theta) = B_2\left[\cos(\theta) - K_1\cos(3\theta + \delta_1)\right] \tag{2.6}$$

where the magnitude of the flux density induced by the 2-pole winding set is $B_2$, the ratio of the magnitude of the flux density induced by the 6-pole winding set and the 2-pole winding set is $K_1$ and the phase angle between two flux densities, which may be a time varying number , is $\delta_1$. In the worst case, the peak value of $B_{g2/6}$ will be obtained when $\theta = \theta_p$; $K_1$ is a positive value and the delay angle $\delta_1$ is zero.

On the other hand, the 4-pole single stator winding set induction machine has a flux distribution expressed as:

$$B_{g4}(\theta) = B_4\cos(2\theta) \tag{2.7}$$

To maintain the same magnetic saturation level produced by peak flux density, the peak flux density value of the dual-winding design will be equal to the peak flux density of the single 4-pole machine, which can be expressed as:

$$B_4 = B_2\left[\cos(\theta_p) - K_1\cos(3\theta_p)\right] \tag{2.8}$$

There are two unknown variables in (2.8). One equation cannot solve two unknowns, hence the stator yoke flux is chosen as the second objective function in this design. The stator yoke flux corresponds to the integral of the air gap flux density, for the dual-winding design:

$$\phi_{y2/6} = rlB_2 \int_0^{\theta} \left[\cos(\theta) - K_1 \cos(3\theta + \delta_1)\right] d\theta \tag{2.9}$$

where, $r$ is the mean air gap radius and $l$ is the stator core length. After the integration, the stator yoke flux can be written as:

$$\phi_{y2/6} = rlB_2 \left[\sin(\theta) - \frac{K_1}{3}\sin(3\theta + \delta_1)\right] \tag{2.10}$$

At the peak point of yoke flux, the derivative of $\phi_{y2/6}$ with respect to angle $\theta$ is equal to zero, which can be expressed as:

$$\frac{d\phi_{y2/6}}{d\theta} = rlB_2\left[\cos(\theta) - K_1 \cos(3\theta + \delta_1)\right] = 0 \tag{2.11}$$

When $\theta = \frac{\pi}{2}$ and $\delta_1 = 0$, the peak value of the stator yoke flux can be found as:

$$\phi_{y2/6} = rlB_2\left(1 + \frac{K_1}{3}\right) \tag{2.12}$$

The peak value of the flux in the yoke for the 4-pole machine can be written as:

$$\phi_{y4} = \frac{rlB_4}{2} \tag{2.13}$$

To maintain the same level of saturation, the peak yoke flux value of the 2/6 pole design and the 4-pole design should be the same, which can be expressed as:

$$rlB_2\left(1 + \frac{K_1}{3}\right) = \frac{rlB_4}{2} \tag{2.14}$$

Equation (2.8) and (2.14) need be solved simultaneously for $K_1$ and $B_2/B_4$. The result can only be achieved by using a numerical method. Both the curves for constant air gap flux density and constant yoke flux density are shown in Figure 2.2. From the figure, it is found that the coefficient $K_1$ should be 4.4875 and the ratio $B_2/B_4$ should be 0.2. Therefore the peak values of the air gap flux densities of two stator winding sets of the dual winding induction machine are:

$$\begin{aligned} B_2 &= 0.2B_4 \\ B_6 &= 0.8975B_4 \end{aligned} \tag{2.15}$$

The maximum value for tooth flux density is typically in the range 1.55 to 2.0 Tesla for common steel while the flux density in the core normally ranges from 1.4 to 1.7 Tesla. All these values are for 60 Hz. Since the width of the teeth is almost half of the slot pitch, the maximum value of $B_4$ is typically in the range from 0.75 to 1.0 Tesla.

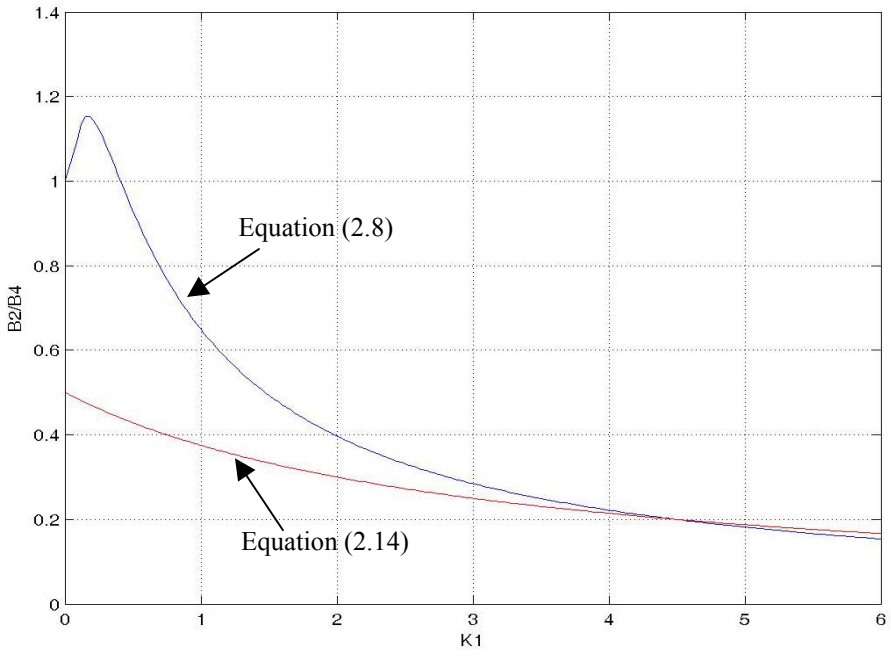


Figure 2.2 Flux density as a function of $K_1$ to determine operating condition

Since small machines typically have lower value of gap flux density than large machines, the peak fundamental air gap flux density $B_4$ for the 4-pole induction machine is finally chosen to be 0.8 Tesla. Then the air gap flux densities for each stator winding are:

$$\begin{aligned} B_2 &= 0.16 \quad Tesla \\ B_6 &= 0.718 \quad Tesla \end{aligned} \tag{2.16}$$

The air gap flux density and the yoke flux of the dual stator winding induction machine are shown in Figure 2.3 and Figure 2.4 respectively. The air gap flux density and the yoke flux of the 4-pole induction machine are also shown for the comparison. The result clearly shows that the dual winding machine design does achieve the same peak air gap flux density and yoke flux as the 4-pole induction machine.

### 2.2.3 Number of Turns per Phase

The EMF generated in the armature winding can be expressed as:

$$E = 4.44 f K_1 N_s \phi_m \tag{2.17}$$

where, $f$ is the frequency of the input voltage; $K_1$ is the stator winding factor; $N_s$ is the number of turns per phase and $\phi_m$ is the magnetic flux per pole. If the voltage across the stator resistance is negligible, the EMF will be equal to the input voltage. The only unknown in the above is the turns per phase $N_s$, hence its value can be expressed as:

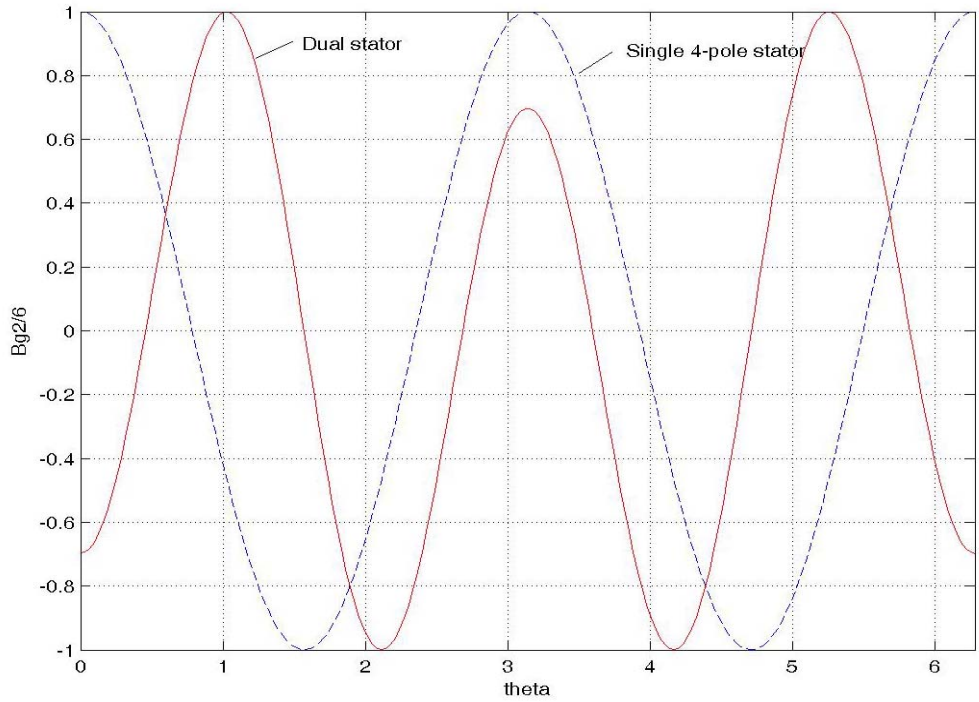


Figure 2.3 Normalized air gap flux density

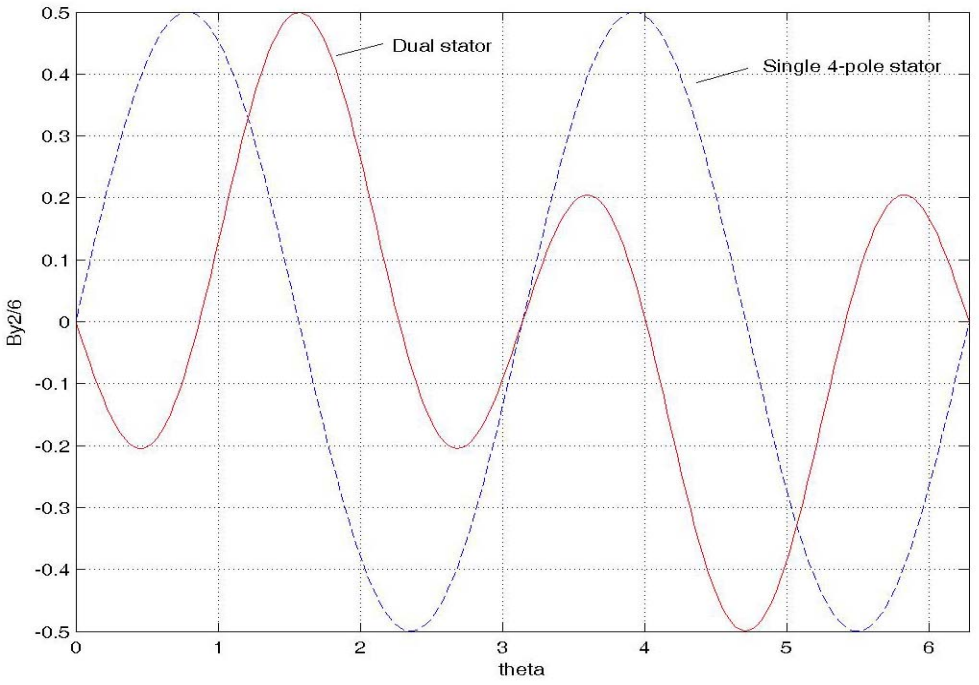


Figure 2.4 Normalized yoke flux

$$N_s = \frac{E}{4.44\, f K_1 \phi_m} \tag{2.18}$$

Flux per pole can be written as:

$$\phi_m = \frac{2}{\pi} B_g \left( \frac{\pi D_{is} l_e}{P} \right) \tag{2.19}$$

where, $B_g$ is the peak value of air gap flux density; $D_{is}$ is the inner diameter of the stator; $l_e$ is the effective length of the stator core and $P$ is the number of pole.

Substituting (2.19) into (2.18),

$$N_s = \frac{E \cdot P}{8.88\, f K_1 B_g D_{is} l_e} \tag{2.20}$$

For the 2-pole winding set, the number of turns per phase is:

$$N_{s1} = 214 \tag{2.21}$$

For the 2-pole three-phase machine set, number of slot per pole per phase is:

$$Z_s = \frac{S}{3P} = 6 \tag{2.22}$$

Since the number of turns per slot can only be an integer, the number of turns per phase is finally chosen as 216.

Proceeding as above, the number of turns per phase of the 6-pole winding set is calculated to be:

$$N_{s2} = 142 \tag{2.23}$$

### 2.2.4 Power Estimation

From the general induction machine design point of view, the power of the machine is one of the design objectives that are known from the beginning of the design progress. The Essen's rule is used to calculate the important dimensions of the machine—inner diameter of stator $D_{is}$ and the effective length of the stator core $l_e$. However, in the design of the dual stator winding induction machine, the dimensions of the machine are known, hence the Essen's rule is used to estimate the power of the dual winding machine [2.3].

The equation of Essen's rule can be expressed as:

$$P_{mech} = \left( \frac{\sqrt{2}\pi^2}{120} \right) \Omega_s k_1 \left( D_{is}^2 l_e \right) B_g K_{s(rms)} \eta_{gap} \cos\phi_{gap} \tag{2.24}$$

where, $\Omega_s$ is the rotor mechanical speed; $K_{s(rms)}$ is the value of the surface current density in the stator winding; $\eta_{gap}$ is the air gap efficiency and $\cos\phi_{gap}$ is the air gap power factor.

Although the gap efficiency $\eta_{gap}$ is different from the terminal efficiency and the gap power factor $\cos\phi_{gap}$ is different from terminal power factor $\cos\phi$, the difference between both pairs, which depends on the parameters of the stator resistance $r_s$ and leakage inductance $L_{ls}$, is normally small. It is assumed that they are equal in the power estimation.

Using Essen's rule for the power estimation, the only variable in equation (2.19) that is not clear is the surface current density $K_{s(rms)}$. The surface current density is based on the steady state value, which could be constrained by the ability of the cooling system to

conduct away the heat produced in the stator under the temperature limit of the winding insulation. After the machine is rewound, the value of $K_{s(rms)}$ in the dual winding machine is not expected to be bigger than the one in the standard single stator-winding machine. If it is assumed that the partition of the surface current density $K_{s(rms)}$ follows the pattern of the air gap flux density, then the surface current density of each winding can be figured out.

The surface current density of the standard 4-pole 3-hp induction machine can be calculated as:

$$K_{s(rms)} = \frac{P_{mech}}{\left(\frac{\sqrt{2}\pi^2}{120}\right)\Omega_s k_1 \left(D_{is}^2 l_e\right) B_g \eta \cos\phi} = 212.5\ A/cm^2 \tag{2.25}$$

Then the surface current density of the 2-pole winding and the 6-pole winding can be expressed as:

$$\begin{aligned} K_{s2(rms)} &= 0.2 \cdot K_{s(rms)} \\ K_{s6(rms)} &= 0.8 \cdot K_{s(rms)} \end{aligned} \tag{2.26}$$

The power of the dual stator winding induction machine can be written as:

$$\begin{aligned} P_{2/6} &= P_2 + P_6 \\ &= \left(\frac{\sqrt{2}\pi^2}{120}\right) k_1 \left(D_{is}^2 l_e\right) \eta \cos\phi \left(\Omega_{s2} B_{g2} K_{s2(rms)} + \Omega_{s6} B_{g6} K_{s6(rms)}\right) \\ &= 1.126\ kW \end{aligned} \tag{2.27}$$

## 2.3 Machine Parameter Estimation

To evaluate the performance of the dual stator winding induction machine, the equivalent circuit parameters need to be determined. Furthermore, in the full model simulation of the dual stator winding induction machine, the estimated parameters of the designed machine can be used to check the parameter calculations in the full model simulation. Magnetic circuit analysis method, which is the general method to determine the parameters of the equivalent circuit, is used here [2.3]. Only the calculation progress for the 2-pole winding set is shown here, the one for the 6-pole winding set can be found by using exactly the same way.

### 2.3.1 Magnetizing Inductance $L_{m2}$

2.3.1.1 Calculation of MMF

The effective length of the stator (and rotor in this case) is expressed as:

$$l_{ef} = l_e + 2l_g \tag{2.28}$$

From which

$$l_{ef} = 57.15 + 2 \cdot 0.33 = 57.81\, mm$$

Let us now determine the MMF per pole necessary to produce a peak value of the fundamental component of air gap flux density $B_{g2}$.

A) MMF of air gap $F_g$

The Carter's coefficient for the stator slot can be expressed as:

$$k_{cs} = \frac{\tau_s}{\tau_s - \frac{2b_0}{\pi}\left\{a\tan\frac{b_0}{2g} - \frac{g}{b_0}\log\left[1+\left(\frac{b_0}{2g}\right)^2\right]\right\}} \tag{2.29}$$

The stator slot opening $b_0 = 0.0027\ m$. From which

$$k_{cs} = \frac{0.0174}{0.0111 - \frac{0.0054}{\pi}\left\{a\tan\frac{0.0027}{0.00066} - \frac{0.00033}{0.0027}\log\left[1+\left(\frac{0.0027}{0.00066}\right)^2\right]\right\}}$$
$$= 1.179$$

Since the rotor slot is chosen to be closed type, the carter's coefficient for the rotor slots is:

$$k_{cr} = 1.0$$

The effective air gap is therefore

$$g_e = k_{cs}k_{cr}l_g$$
$$= 1.179 \cdot 1.0 \cdot 0.33 \tag{2.30}$$
$$= 0.389 \quad mm$$

The amplitude of flux density at the point $30^o$ away from the maximum is:

$$B_{g2(30^o)} = \frac{\sqrt{3}}{2}B_{g2}$$
$$= 0.866 \cdot 0.16 \tag{2.31}$$
$$= 0.139 \quad T$$

Therefore, the MMF required to overcome the air gap is given as:

$$F_{g(30^o)} = \frac{B_{g2(30^o)}}{\mu_0}g_e \tag{2.32}$$
$$= 42.9\ At$$

B) MMF of stator tooth $F_{ts}$

The tooth width at the top is given as

$$t_{ts} = \frac{\pi D_{is}}{2S} = 0.00554\ m \tag{2.33}$$

The tooth width at the root is:

$$t_{rs} = \frac{\pi\left(D_{is} + 2d_s\right)}{S} - \frac{\pi D_{is}}{2S} = 0.00956\ m \tag{2.34}$$

Therefore, the tooth width mid-way down the stator tooth is:

$$\begin{aligned} t_{ms} &= t_{ts} + \frac{1}{2}\left(t_{rs} - t_{ts}\right) \\ &= 0.0075\ m \end{aligned} \tag{2.35}$$

The flux density at the top of the stator tooth is calculated as:

$$\begin{aligned} B_{ts} &= B_{g2(30^o)} \frac{\tau_s l_{ef}}{t_{ts} k_{is} l_e} \\ &= 0.28\,T \end{aligned} \tag{2.36}$$

The corresponding flux densities at the mid point and at the root of the tooth are found from the following ratios.

$$\begin{aligned} B_{ms} &= \frac{B_{ts} t_{ts}}{t_{ms}} \\ &= 0.21\,T \end{aligned} \tag{2.37}$$

$$\begin{aligned} B_{rs} &= \frac{B_{ts} t_{ts}}{t_{rs}} \\ &= 0.163\,T \end{aligned} \tag{2.38}$$

Assuming the B-H characteristic of 3% silicon steel is linear, the average field intensity along the stator tooth is expressed as

$$\begin{aligned} H_{ts(ave)} &= \frac{1}{6} H_{ts} + \frac{2}{3} H_{ms} + \frac{1}{6} H_{rs} \\ &= 87\ At/m \end{aligned} \tag{2.39}$$

The corresponding average MMF drop in the stator tooth is calculated as:

$$F_{ts(ave)} = H_{ts(ave)} d_s \\ = 2.0\ At \tag{2.40}$$

C) MMF of stator core $F_{cs}$

The maximum flux in the stator core is obtained from

$$\phi_{cs} = \left(\frac{2}{\pi} B_{g2}\right)\left(\frac{\tau_p}{2} l_e\right) \\ = 0.58\ mWb \tag{2.41}$$

Therefore, the peak fundamental component of flux density in the core is,

$$B_{cs(90^o)} = \frac{\phi_{cs}}{d_{cs} k_{is} l_e} \\ = 0.56\ T \tag{2.42}$$

The corresponding values of core flux density points $30^o$ and $60^o$ from the maximum are:

$$B_{cs(60^o)} = \frac{\sqrt{3}}{2} B_{cs(90^o)} \\ = 0.48\ T \tag{2.43}$$

and

$$B_{cs(30^o)} = \frac{1}{2} B_{cs(90^o)} \\ = 0.28\ T \tag{2.44}$$

Assume the B-H characteristic of 3% silicon steel is linear, the average field intensity along the stator core is calculated as

$$H_{cs(ave)} = \frac{1}{6} H_{cs(90^o)} + \frac{2}{3} H_{cs(60^o)} + \frac{1}{6} H_{cs(30^o)} \\ = 208\ At/m \tag{2.45}$$

The length of one pole pitch at the center line of the stator core can be computed from

$$l_{cs} = \frac{\pi\left(D_{os} - d_{cs}\right)}{P} = 0.301\,m \tag{2.46}$$

The corresponding MMF drop in the stator core is given as:

$$F_{cs(ave)} = H_{cs(ave)} l_{cs} = 62.67\ At \tag{2.47}$$

D) MMF of rotor core $F_{cr}$

If the leakage flux has been neglected, the flux per pole in the rotor core is the same as in the stator core.

$\phi_{cr} = 0.58\,mWb$

Then, the peak fundamental component of flux density in the core is,

$$B_{cr(90^o)} = \frac{\phi_{cr}}{d_{cr} k_{ir} l_r} = 0.56\,T \tag{2.48}$$

The corresponding values of core flux density points $30^o$ and $60^o$ from the maximum are:

$$B_{cr(60^o)} = \frac{\sqrt{3}}{2} B_{cr(90^o)} = 0.48\,T \tag{2.49}$$

and

$$B_{cr(30^o)} = \frac{1}{2} B_{cr(90^o)} = 0.28\,T \tag{2.50}$$

Assume the B-H characteristic of 3% silicon steel is linear, the average field intensity along the stator core is given as:

$$H_{cr(ave)} = \frac{1}{6}H_{cr(90^o)} + \frac{2}{3}H_{cr(60^o)} + \frac{1}{6}H_{cr(30^o)} \\ = 208\ At/m \tag{2.51}$$

The length of one pole pitch at the center of the rotor core can be computed from:

$$l_{cr} = \frac{\pi(D_{ir} - d_{cr})}{P} = \frac{\pi(D_{is} - 2l_g - d_{cr})}{P} \\ = 0.17\ m \tag{2.52}$$

The corresponding average MMF drop in the rotor core is:

$$F_{cr(ave)} = H_{cr(ave)}l_{cr} \\ = 35.3\ At \tag{2.53}$$

The total MMF drop around the magnetic circuits is obtained by summing up the individual MMF drops around the entire magnetic circuit comprising of two air gaps, two stator teeth, the stator core and the rotor core. The required MMF per pole at the $30^o$ point needed to produce the specified air gap flux density is:

$$F_{p(30^o)} = \frac{2F_g + 2F_{ts} + F_{cs} + F_{cr}}{2} \\ = 93.9\ At \tag{2.54}$$

The corresponding value of MMF per pole at the maximum value of air gap flux density is expressed as:

$$F_{p(0^o)} = F_{p1} = \frac{2}{\sqrt{3}}F_{p(30^o)} \\ = 108.4\ At \tag{2.55}$$

2.3.1.2 Calculation of winding factor $k_1$

A) Pitch factor $k_{p1}$

The pitch of the machine is 1. The pitch factor for the fundamental component of MMF can be expressed as:

$$k_{p1} = \sin\left(\frac{W}{\tau_p} \cdot \frac{\pi}{2}\right) = \sin\left(1 \cdot \frac{\pi}{2}\right) = 1 \tag{2.56}$$

B) Distribution factor $k_{d1}$

Assume the phase belt is $60^o$. Then the slots per phase belt will be 6 in this machine. The phase belt in per unit of a pole pitch can be expressed by taking the appropriate ratio of slots.

$$\frac{Z}{\tau_p} = \frac{6}{18} = \frac{1}{3} \tag{2.57}$$

Hence from Table 2.1 the distribution factor is:

$$k_{d1} = 0.966 \tag{2.58}$$

C) Slot opening factor $k_{\chi 1}$

The slot opening factor is determined from:

$$k_{\chi 1} = \frac{\sin(\chi/2)}{\chi/2} \tag{2.59}$$

where, $\chi = \frac{b_{os}}{\tau_p}\pi = 0.0742$.

Therefore,

$$k_{\chi 1} = \frac{\sin(0.0371)}{0.0371} = 0.9991 \tag{2.60}$$

D) Skew factor $k_{s1}$

The skew of the stator winding is not supplied in this design, the skew factor is unity, which is expressed as:

$$k_{s1} = 1.0 \tag{2.61}$$

The overall winding factor for the stator winding of this design is given as:

$$\begin{aligned} k_1 &= k_{p1} k_{d1} k_{\chi 1} k_{s1} \\ &= 1 \cdot 0.966 \cdot 0.9991 \cdot 1.0 \\ &= 0.965 \end{aligned} \tag{2.62}$$

2.3.1.3 Calculation of magnetizing inductance per phase $L_{ms}$

The magnetizing inductance per phase can be found from equation as:

$$\begin{aligned} L_{ms2} &= \frac{3}{2}\frac{4}{\pi}\frac{k_1^2 N_{s2}^2}{P}\frac{\left(\frac{2}{\pi}B_{g2}\right)\left(\tau_p l_e\right)}{F_{p1}} \\ &= 0.218\,H \end{aligned} \tag{2.63}$$

## 2.3.2 Stator Leakage Inductance $L_{ls}$

Although it is called leakage inductance, it plays an important role in the machine performance. The stator and rotor currents are primarily a function of the leakage inductance of the machine and some key performance characteristics such as starting torque, breakdown torque and inrush current are dependent on it. In addition, the electromagnetic time constant almost only depends on the leakage inductance.

The leakage inductance is composed of five components—slot leakage inductance, stator end winding leakage inductance, belt leakage inductance, zigzag leakage inductance and skew leakage inductance.

2.3.2.1 Slot leakage inductance

The detailed stator slot configurations are shown in Figure 2.5.

The values of these dimensions are:

$b_0 = 2.76\ mm$ $d_0 = 0.9\ mm$ $d_1 = 1\ mm$

$d_2 = 1\ mm$ $d_3 = 9\ mm$ $d_4 = 2\ mm$

$d_5 = 9\ mm$ $d_6 = 2\ mm$ $b_s = 6.2\ mm$

The specific permeances $p_T$, $p_B$ and $p_{TB}$ are given as:

$$p_T = \mu_0 \left[ \frac{d_3}{3b_s} + \frac{d_2}{b_s} + \frac{d_1}{b_s - b_0} \log_e \left( \frac{b_s}{b_0} \right) + \frac{d_0}{b_0} \right] \tag{2.64}$$
$$= 1.52 \times 10^{-6}\ H/m$$

$$p_B = \mu_0 \left[ \frac{d_5}{3b_s} + \frac{d_2 + d_3 + d_4}{b_s} + \frac{d_1}{b_s - b_0} \log_e \left( \frac{b_s}{b_0} \right) + \frac{d_0}{b_0} \right] \tag{2.65}$$
$$= 3.75 \times 10^{-6}\ H/m$$

$$p_{TB} = \mu_0 \left[ \frac{d_3}{2b_s} + \frac{d_2}{b_s} + \frac{d_1}{b_s - b_0} \log_e \left( \frac{b_s}{b_0} \right) + \frac{d_0}{b_0} \right] \tag{2.66}$$
$$= 1.82 \times 10^{-6}\ H/m$$

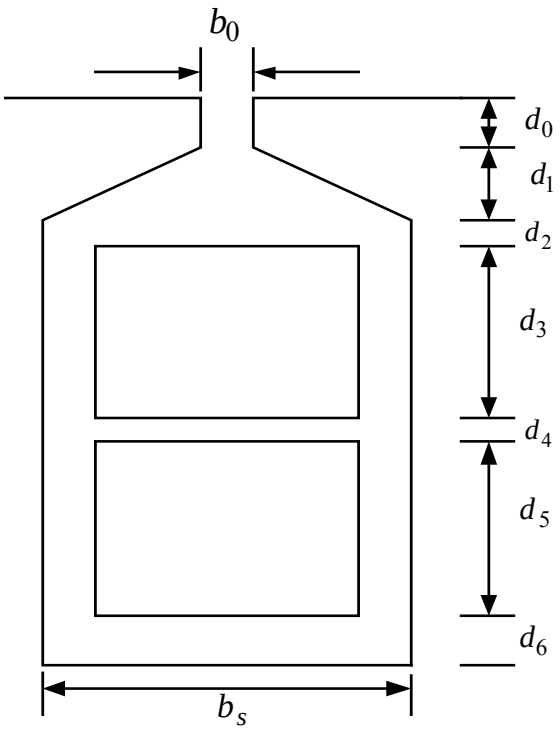


Figure 2.5. Detailed stator slot configuration

The slot leakage inductance per phase for the top, bottom and the mutual coupling between top and bottom coils can be obtained from the following equations:

$$L_{lT} = \frac{3N_{s2}^2 l_e}{S} p_T = 0.33\ mH \tag{2.67}$$

$$L_{lB} = \frac{3N_{s6}^2 l_e}{S} p_B = 0.36\ mH \tag{2.68}$$

$$L_{lM} = \frac{3N_s^2 l_e}{S} p_{TB} = 0.18\ mH \tag{2.69}$$

Since the pitch of the stator coils is 1, the slot factor for mutual coupling is

$$k_{sl} = 3p - 1$$
$$= 3 \cdot 1 - 1 \qquad (2.70)$$
$$= 2$$

The total slot leakage inductance per phase is:

$$L_{lsl} = L_{lT} + L_{lB} + k_{sl} L_{lM}$$
$$= 0.96\ mH \qquad (2.71)$$

2.3.2.2 Stator end winding leakage inductance

Assume the additional information has been given in Figure 2.6. The length $l_{e2}$ is 0.005 m. The space between adjacent coil sides in the slot is specified as 0.008 m. If this minimum spacing is maintained in the end winding region then $t_e$ is also 0.008 m. The width of the coil $b_c$ is 0.005 m.

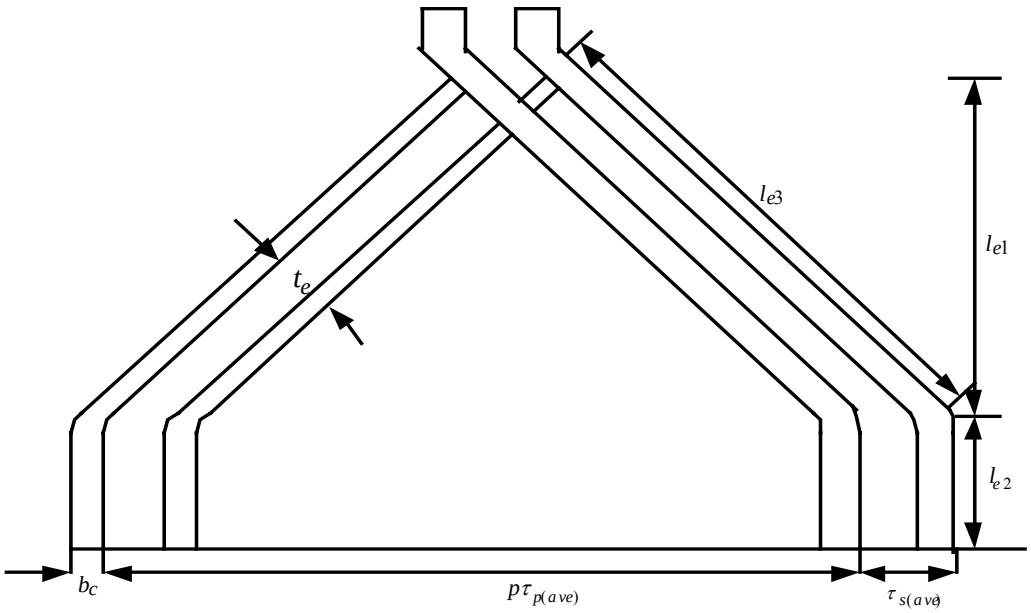


Figure 2.6 End winding configuration

The pole pitch at the mid point of the stator slot is given as:

$$\tau_{p1} = \frac{\pi}{P}\left(D_{is} + d_s\right) = 0.236\ m \tag{2.72}$$

Then the slot pitch at the mid point of the stator slot is:

$$\tau_{s1} = \frac{P\tau_{p1}}{S} = 0.013\ m \tag{2.73}$$

Hence the length of the end winding extension over the diagonal region is calculated by:

$$l_{e1} = \frac{p\tau_{p1}\left(b_c + t_e\right)}{2\sqrt{\tau_{s1}^2 - \left(b_c + t_e\right)^2}} = 0.09\ m \tag{2.74}$$

The stator end winding leakage inductance per phase is expressed as:

$$L_{lew} = 4\mu_0 \frac{N_s^2}{P} k_{p1}^2 k_{d1}^2 (2.4)\left(l_{e2} + \frac{l_{e1}}{2}\right) = 12\ mH \tag{2.75}$$

Since the number of poles of the machine is small, the corresponding length of the end winding extension is big and the end winding leakage inductance per phase for 2-pole winding is bigger. For 6-pole winding, this component will be expected to be much smaller.

2.3.2.3 Belt leakage inductance

The belt leakage inductance is essentially zero since the machine is equipped with a squirrel cage rotor.

2.3.2.4 Zigzag leakage inductance

For this machine, some of the parameters used to calculate the zigzag leakage inductance are:

Stator slot pitch: $\tau_s = \frac{\pi D_{is}}{S} = 0.0111\ m$

Stator slot width: $t_1 = \frac{\tau_s}{2} = 0.0055\ m$

Since closed type rotor slot is chosen, the rotor tooth width is equal to the rotor slot width, which can be expressed as:

$t_2 = 0.0058\ m$

The specific permeance corresponding to zigzag leakage flux is given as:

$$p_{zz} = \frac{\mu_0 t_1 t_2 \left(t_1^2 + t_2^2\right)}{6 g_e \tau_s^3} = 0.82 \times 10^{-6}\ H/m \tag{2.76}$$

Hence the zigzag leakage inductance is:

$$L_{zz} = \frac{12 N_s^2}{S} l_{es} \frac{21p - 5}{16} p_{zz} = 0.56\ mH \tag{2.77}$$

2.3.2.5 Skew leakage inductance

Since the rotor slots are skewed half stator slot pitch. The inductance due to skew is found as:

$$
\begin{aligned}
L_{lsk} &= L_m \left\{ 1 - \left[ \frac{\sin(\alpha/2)}{\alpha/2} \right]^2 \right\} \\
&= L_m \left\{ 1 - \left[ \frac{\sin(\pi/28)}{\pi/28} \right]^2 \right\} \\
&= 0.91\ mH
\end{aligned}
\tag{2.78}
$$

The total stator leakage inductance can be calculated as the sum of the slot, end winding, belt, zigzag and skew leakage inductances as:

$$
\begin{aligned}
L_{ls2} &= L_{lsl} + L_{lew} + L_{lbt} + L_{lzz} + L_{lsk} \\
&= 13\ mH
\end{aligned}
\tag{2.79}
$$

### 2.3.3 Rotor Leakage Inductance

In the full model simulation, the rotor model is based on the individual rotor loop, which is composed of two adjunct rotor bars and two end ring pieces that connect the two rotor bars. The rotor slot leakage inductance per bar and the end ring leakage inductance per bar are essential parameters that need to be calculated.

2.3.3.1 Rotor slot leakage inductance per bar

For each rotor slot, the specific permeance is given as:

$$
\begin{aligned}
p_{sl} &= \mu_0 \int_0^{\pi} \left( \frac{\alpha - \frac{1}{2}\sin 2\alpha}{\pi} \right)^2 \frac{r \sin\alpha}{2r \sin\alpha} d\alpha \\
&= \frac{\mu_0}{2\pi^2} \int_0^{\pi} \left( \alpha - \frac{1}{2}\sin 2\alpha \right)^2 d\alpha = \mu_0 \left( \frac{\pi}{6} + \frac{5}{16\pi} \right) \\
&= 0.78 \times 10^{-6}\ H/m
\end{aligned}
\tag{2.80}
$$

The length of the rotor bar takes into account the slight additional length of the bar due to skew:

$$l_{er} = \frac{l_e}{\cos\left(\frac{2\pi}{S}\right)} = 0.059\ m \tag{2.81}$$

Then the slot leakage per bar is:

$$\begin{aligned} L_b &= n_r^2 l_{er} p_{sl} \\ &= 0.0457 \times 10^{-6}\ H/bar \end{aligned} \tag{2.82}$$

2.3.3.2 Rotor end winding inductance per bar

The end winding leakage inductance per segment of the end ring is obtained as:

$$L_e = \mu_0 \left(\frac{4}{9}\right)\left(l_{be} + k\tau_{pr(ave)}\right) \tag{2.83}$$

The length of the bar extension from the surface of the core to the start of the end ring is:

$$l_{be} = 0.003\ m$$

The rotor pole pitch measured at the middle of the end ring is:

$$\begin{aligned} \tau_{pr(ave)} &= \frac{\pi}{P}\left(D_{or} - 2d_{sr} - d_{re}\right) \\ &= 0.097\ m \end{aligned} \tag{2.84}$$

$$\begin{aligned} L_e &= \mu_0 \left(\frac{4}{9}\right)\left(l_{be} + k\tau_{pr(ave)}\right) \\ &= 9.6 \times 10^{-9}\ H \end{aligned} \tag{2.85}$$

### 2.3.4 Rotor Bar Resistance $r_b$

The length of one rotor bar not including the end ring is:

$$l_b = \frac{l_e + 2l_{be}}{\cos\alpha} = 0.065\ m \tag{2.86}$$

Therefore, the resistance of one rotor bar is given as:

$$r_b = \rho\frac{l_b}{A_b} = \frac{1.6\times10^{-8}\cdot 0.065}{63.4\times10^{-6}} = 14.5\ \mu\Omega \tag{2.87}$$

### 2.3.5 End Ring Resistance $r_e$

The tooth pitch at the middle of the end ring can be obtained as:

$$\tau_{r2} = \frac{P\tau_{pr(ave)}}{S_r} = 0.0069\ m \tag{2.88}$$

The resistance of the end winding portion over one rotor slot pitch is:

$$r_e = \rho_{al}\frac{\tau_{r2}}{a_{er}} = 1.8\ \mu\Omega \tag{2.89}$$

### 2.3.6 Stator Resistance $r_s$

By properly using stranding and transposition, the eddy current in a stator coil can usually be reduced to a small value such that it can be neglected in our calculation. The

resistance can be calculated by first estimating an average length for each coil, then adding up the coil in series and parallel as appropriate.

The mean length of the coil is approximately:

$$l_c = 2l_s + 4l_{e2} + 4l_{e3} \tag{2.90}$$

where $l_s$ is the length of the stator stack including ducts; $l_{e2}$ is the straight extension of the coils beyond the stack; $l_{e3}$ is the diagonal portion of the end winding.

$$\begin{aligned} l_{e3} &= \frac{p\tau_{p(ave)}}{2} \frac{\tau_{s(ave)}}{\sqrt{\tau_{s1}^2 - (b_c + t_e)^2}} \\ &= 0.064\ m \end{aligned} \tag{2.91}$$

The mean length of a coil is therefore,

$l_c = 0.529\ m$

The stator resistance is:

$$\begin{aligned} r_{s2} &= \left(\frac{N_s}{C}\right)\rho\frac{l_c}{a_c} \\ &= 0.5\ \Omega \quad @75^o \end{aligned} \tag{2.92}$$

Follow the same progress, the parameters for the 6-pole winding can be calculated as:

$L_{ms6} = 0.06\ H$

$L_{ls6} = 2.5\ mH$

$r_{s6} = 0.3\ \Omega \quad @75^o$

Because the length of the end winding extension for 6-pole winding is much shorter than that of the 2-pole, the leakage inductance is much smaller which matches our expectation.

### 2.3.7 Rotor Resistance Referred to the Stator $r'_{r2}$

The effective bar resistance is:

$$r_{be} = r_b + \frac{r_e}{2\sin^2\left(\frac{\pi P}{2S_r}\right)} \qquad (2.93)$$
$$= 89.93\ \mu\Omega$$

The resistance per rotor mesh is:

$$r_r = 2r_{be} = 179.86\ \mu\Omega \qquad (2.94)$$

The rotor resistance referred to the stator is obtained as:

$$r'_{r2} = \frac{12k_1^2 N_{s2}^2}{S_r} r_r \qquad (2.95)$$
$$= 3.28\ \Omega$$

To the XYZ winding, the rotor resistance is:

$$r'_{r6} = \frac{12k_1^2 N_{s6}^2}{S_r} r_r \qquad (2.96)$$
$$= 0.68\ \Omega$$

## 2.4 Machine Design II

The general definition of the total air gap flux density produced by both of the stator winding sets has been given in (2.4), which depends on time, the stator circumferential angle and the phase angle between the two flux density components. The maximum value of the total flux density is independent of time. Hence for the purpose of the analysis that follows the total air gap flux density is expressed as:

$$B = B_1 \cos(p_1\theta) + B_2 \cos(p_2\theta + \delta) \qquad (2.97)$$

where, $\delta$ is the phase angle, which varies within [0, $2\pi$ ]. The maximum value of the air gap flux density ($B_{max}$) under different pole ratios and different flux density values are found numerically. The simulation results are shown in Figure 2.7. It is found from the figure that when the pole ratio is odd number (1, 3 and 5), the minimum $B_{max}$ value is found at $\delta = \pi$. The $B_{max}$ value for pole ratio = 1 is the least followed by the value when the pole ratio = 3. When the pole ratio is three, the maximum air gap flux density reaches its minimum point when the two air gap flux density components are out of phase. Under this condition, the magnetic material of the machine is fully utilized and the saturation level is reduced. Using different values of $B_1$ and $B_2$ for this analysis yield similar results. For the dual stator winding induction machine design proposed in this chapter the pole ratio of 3 is selected.

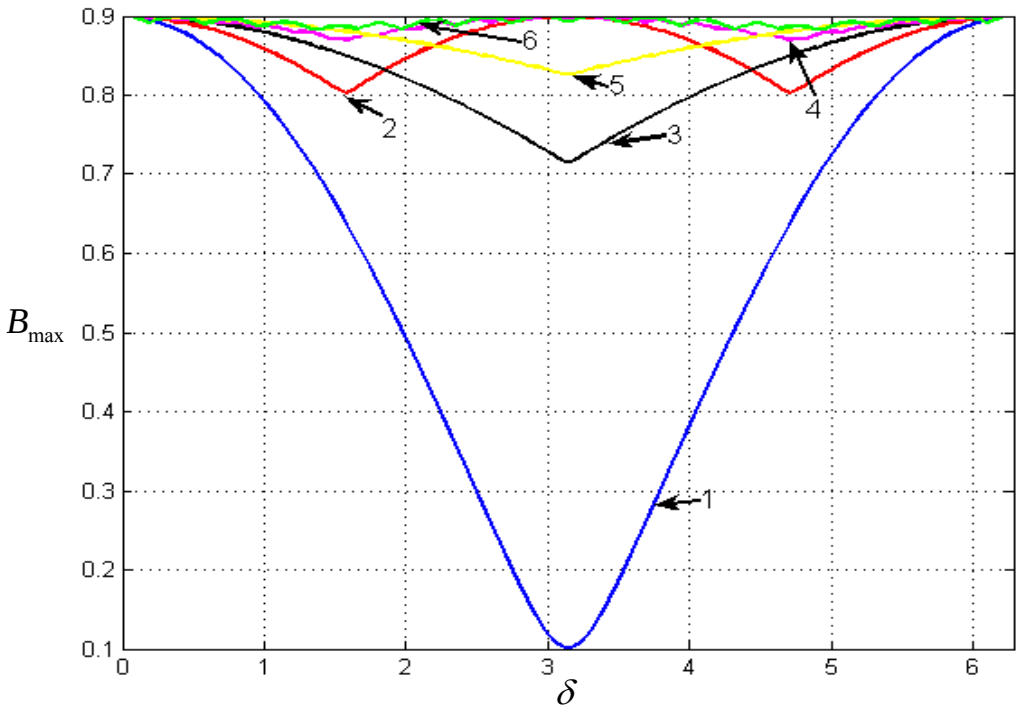


Figure 2.7 The maximum value of the air gap flux density under different pole ratios (the value of pole ratio has been given as numbers) and different $\delta$ values when $B_1 = 0.4\,T$ and $B_2 = 0.5\,T$.

Substituting $\delta = \pi$ into (2.97) and assume $\theta = \theta_p$ is the position in which the peak air gap flux density occurs then,

$$B_{\max} = B_1 \cos(p_1\theta_p) - B_2 \cos(p_2\theta_p) \tag{2.98}$$

If both sides of equation (2.98) are multiplied by $\frac{1}{B_2}$, equation (2.98) becomes

$$\frac{B_{\max}}{B_2} = \frac{B_1}{B_2}\cos(p_1\theta_p) - \cos(p_2\theta_p) \tag{2.99}$$

From (2.99), it is found that if the flux densities ratio ($\frac{B_1}{B_2}$) is given and the numbers of poles of both stator winding sets are known, the value of $\frac{B_1}{B_2}\cos(p_1\theta_p) - \cos(p_2\theta_p)$ is fixed. Then if the peak value of the air gap flux density ($B_{\max}$) is given, the air gap flux density of each stator winding set can be determined.

The equation of Essen's rule has been given in (2.24). If the Essen's rule is applied to two stator winding sets, the output mechanical power equations of both winding sets are:

$$P_{ABC} = \alpha \cdot P_{mech} = \left(\frac{\sqrt{2}\pi^2}{120}\right)\Omega_s k_{11}\left(D_{is}^2 l_e\right)B_1 K_{s1(rms)}\eta_{gap1}\cos\phi_{gap1} \tag{2.100}$$

$$P_{XYZ} = (1-\alpha)\cdot P_{mech} = \left(\frac{\sqrt{2}\pi^2}{120}\right)\Omega_s k_{12}\left(D_{is}^2 l_e\right)B_2 K_{s2(rms)}\eta_{gap2}\cos\phi_{gap2} \tag{2.101}$$

where, $\alpha$ is the mechanical power partition factor that allocates the output powers to the two winding sets; $K_{si(rms)}$ is the value of the surface current density in the $i$ stator winding set; $\eta_{gapi}$ and $\cos\phi_{gapi}$ are the air gap efficiency and the air gap power factor of the $i$ stator winding set respectively. The symbol $i$ can be either the ABC winding set or

the XYZ winding set. The designed rotor mechanical speeds of both stator winding sets are the same to improve the efficiency of the system.

If the air gap efficiency and the air gap power factor of both winding sets are assumed to be equal, the output mechanical power ratio is expressed as:

$$\frac{P_{ABC}}{P_{XYZ}} = \frac{\alpha}{1-\alpha} = \frac{B_1 K_{s1(rms)}}{B_2 K_{s2(rms)}} \tag{2.102}$$

The value of the mechanical power partition factor $\alpha$ determines the mechanical power generated by each of the two winding sets and its value varies from 0 to 1. This mechanical power partition factor is given as part of the design requirements, however, the value of $\alpha$ may be changed for different design objectives.

If the surface current density ratio is expressed as:

$$\varepsilon = \frac{K_{s1(rms)}}{K_{s2(rms)}} \tag{2.103}$$

The ratio of the air gap flux densities due to the two winding sets from (2.102) is given :

$$\frac{B_1}{B_2} = \frac{\alpha}{(1-\alpha)\varepsilon} \tag{2.104}$$

The values of the air gap flux densities $B_1$ and $B_2$ are determined by solving (2.99) and (2.104). The simulation results of the air gap flux densities under different values of $\alpha$ and $B_{\max}$ are given in Figure 2.8. It is found from the simulation results that the air gap flux density due to the ABC winding set increases to output more power when $\alpha$ increases from 0 to 1. The air gap flux density due to the ABC winding set under the same mechanical power partition factor condition increases as the surface current density

ratio also increases. The air gap flux densities of both winding sets decrease when the maximum air gap flux density value $B_{max}$ decreases.

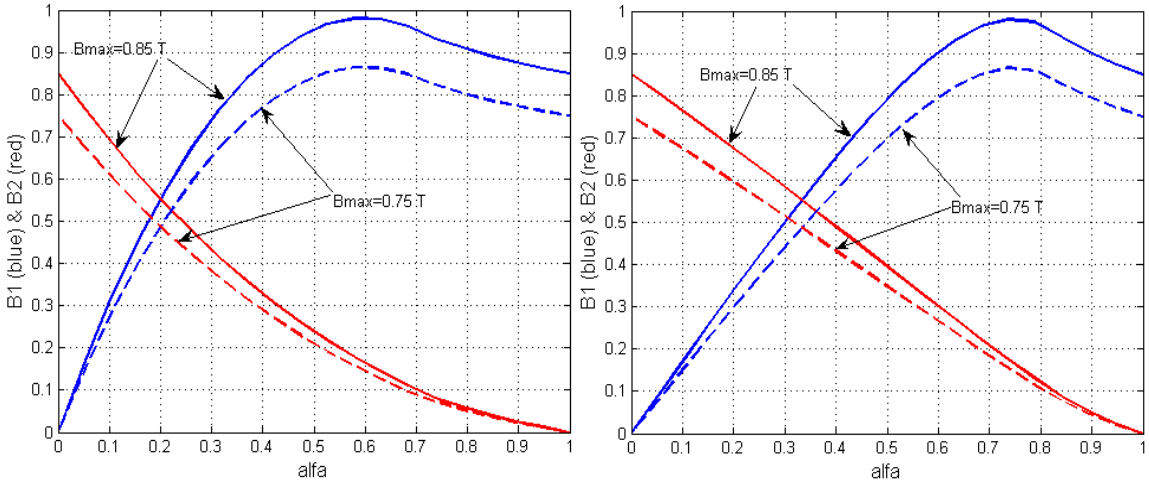


(a) $K_{s1}/K_{s2} = 0.25$ (b) $K_{s1}/K_{s2} = 0.5$

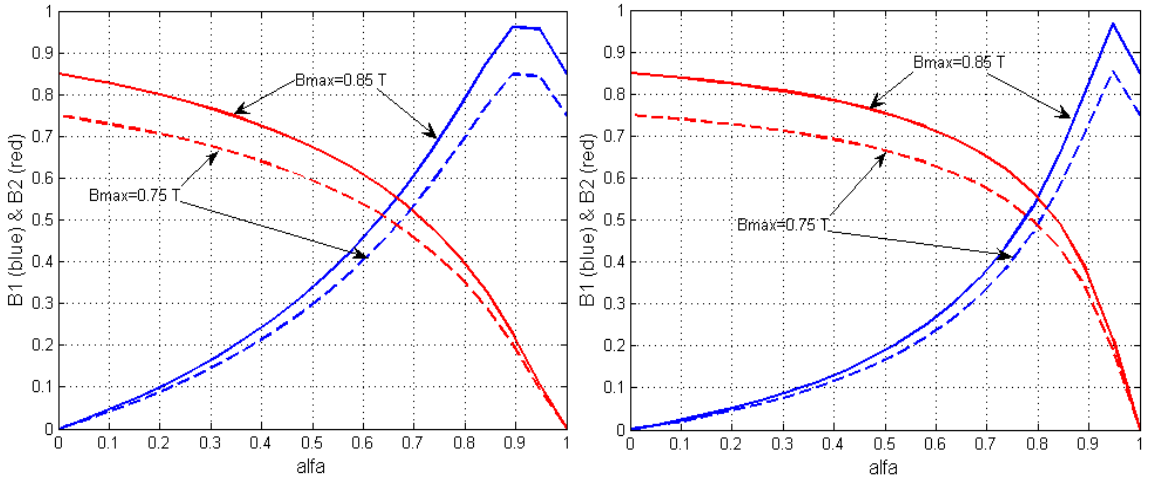


(c) $K_{s1}/K_{s2} = 2$ (d) $K_{s1}/K_{s2} = 4$

Figure 2.8 The air gap flux densities of both winding set for different values of $\alpha$ under two different $B_{max}$ values

The stator current density is defined as:

$$J_{si} = \frac{N_{sloti} I_{si}}{A_{si}} \tag{2.105}$$

where, $N_{sloti}$ is the number of conductors in one slot, $I_{si}$ is the phase current per conductor, $A_{si}$ is the area of the conductors, $i = 1 \, or \, 2$ represents the variables of the ABC and XYZ winding sets respectively.

The number of conductors per slot of each winding set is given as:

$$N_{sloti} = \frac{6 N_{si} p_i}{S} \tag{2.106}$$

where, $N_{si}$ is the number of conductors per phase, $p_i$ is the pole pair number and $S$ is the number of stator slots.

The stator coils of different winding sets are located at different layers within the stator slots, the width of the slots housing the winding sets is assumed to be constant. The depths of the slots occupied by each of the conductors of the two winding sets are different in general. Then, the ratio of the conductor areas can be expressed in terms of the depths as:

$$\frac{A_2}{A_1} = \frac{d_{s2}}{d_{s1}} \tag{2.107}$$

where, $d_{si}$ is the depth of the conductor area for either the ABC winding set or the XYZ winding set.

Since the total usable area of the slot is fixed, the sum of the depths of the conductor areas is also given.

$$d_s = d_{s1} + d_{s2} \tag{2.108}$$

From (2.105-2.108), the ratio of the stator current densities of both stator winding sets is given as:

$$\begin{aligned}\frac{J_1}{J_2} &= \frac{N_{s1}I_{s1}}{N_{s2}I_{s2}} \cdot \frac{p_1}{p_2} \cdot \frac{d_{s2}}{d_{s1}} \\ &= \frac{K_{s1}}{K_{s2}} \cdot \frac{p_1}{p_2} \cdot \frac{d_{s2}}{d_{s1}} \\ &= \frac{K_{s1}}{K_{s2}} \cdot \frac{p_1}{p_2} \cdot \frac{d_{s2}}{d_s - d_{s2}}\end{aligned} \tag{2.108}$$

If the percentage of the slot area used by the XYZ winding set is represented by

$$\tau_2 = A_2/(A_1 + A_2) \tag{2.109}$$

Equation (2.108) can be expressed in term of $\tau_2$ as:

$$\frac{J_1}{J_2} = \frac{K_{s1}}{K_{s2}} \cdot \frac{p_1}{p_2} \cdot \frac{\tau_2}{1-\tau_2} \tag{2.110}$$

The simulation results of (2.110) under different surface current density ratios condition are shown in Figure 2.9.

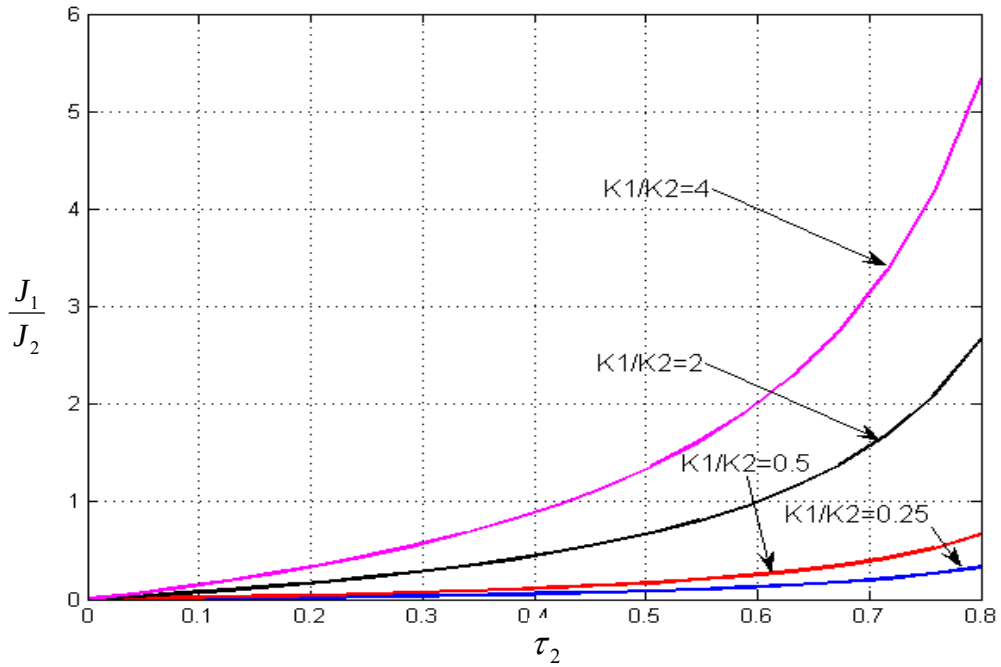


Figure 2.9 Stator current density ratios for various values of $K_{s1}/K_{s2}$ and $\tau_2$.

From the simulation results given in Figure 2.9, it is found that the ratio of the stator current densities increases when $\tau_2$ increases while the ratio of the stator current densities decreases when the ratio of the surface current density decreases.

Using the outlined design procedures, the design of a 3hp dual winding machine with specifications given in Table 2.1 and three mechanical power partition factors are given in Table 2.2. The sum of the air flux densities of two stator winding sets is greater than the design given in Section 2.1 while the surface current density of each winding set is slightly lower than the one for the normal single winding induction machine.

Table 2.2 Machine design results

| Power partition factor | | $\alpha = 0.4$ | $\alpha = 0.5$ | $\alpha = 0.6$ |
|---|---|---|---|---|
| Given parameters | $B_{\max}$ (T) | 0.85 | 0.85 | 0.85 |
| | $K_{s1}/K_{s2}$ | 1 | 1 | 1 |
| | $J_1/J_{s2}$ | 1 | 1 | 1 |
| Calculated parameters | $B_1$ (T) | 0.42 | 0.55 | 0.69 |
| | $B_2$ (T) | 0.63 | 0.55 | 0.46 |
| | $K_{s1}$ ($A/cm^2$) | 182.4 | 173.2 | 165.3 |
| | $K_{s2}$ ($A/cm^2$) | 182.4 | 173.2 | 165.3 |
| | $N_{s1}$ | 141 | 107 | 85 |
| | $N_{s2}$ | 282 | 322 | 384 |
| | $J_1$ ($A/mm^2$) | 7.8 | 7.4 | 7.1 |
| | $J_2$ ($A/mm^2$) | 7.8 | 7.4 | 7.1 |

## 2.5 Conclusions

In this chapter, a design process of the dual stator winding induction machine is clearly laid out. The idea of rewinding the standard cage-rotor induction machine stator to be the stator suitable for dual winding induction machine reduces the cost of the machine and simplifies the producing progress. The methods to evaluate the magnetic loading have been summarized and the process to design the magnetic loading for each winding has clearly been presented. As the second part of this chapter, a method to estimate the equivalent parameters of the dual winding machine has been presented. The resultant parameters are used to check the parameters calculated online by the extensive winding function approach and some parameters such as leakage inductances and resistances are used directly in the full model simulation of the dual winding induction machine. In section 3, a novel alternative design method has been proposed to design the dual stator winding induction machine based on a particular air gap flux distribution. The output power of each winding set is determined by the mechanical power partition factor and the maximum flux density of the dual winding induction machine is within the limit. The advantage of this proposed method is the power of the designed dual winding induction machine can be maximized within the same air gap flux density constraint.

# CHAPTER 3

# FULL MODEL SIMULATION OF DUAL STATOR WINDING INDUCTION MACHINE

## 3.1 Introduction

The conceptual idea of dual stator winding machines can be traced to publications in the early 1900's [1.6, 3.1, 3.2]. From the point of view of the stator winding, dual stator winding machines have been categorized as “split-wound” and “self-cascaded” [1.1]. The split-wound dual winding machine was introduced in the 1920s to increase the power capability of large synchronous generators. Its inherent redundancy has also been exploited to achieve better drive reliability. The split-wound synchronous machine and squirrel-cage machine have different rotor structures and the same stator structure with two similar but separate three-phase winding sets wound for the same number of poles. Since the two windings have the same pole number, they are mutually coupled resulting in significant circulating currents in the presence of unavoidable unbalances in the supply voltages. The second kind of dual winding machine, the “self-cascaded machine”, recently christened the brushless doubly-fed machine (BDFM) was introduced by Hunt in 1907. It requires a special rotor structure that has some nested loops on the rotor to incorporate the effects of the cascade connection. [1.7, 1.8, 3.3]. The special rotor structure increases the cost of the machine, its efficiency is relatively low, but has potential utility in drive applications with a narrow speed range [1.7, 3.3].

A recently developed dual stator winding squirrel-cage induction machine is considered in this chapter [1.1, 1.10]. It is claimed that this innovation offers the advantages of ease of sensor-less control (especially at low speeds), high reliability, full utilization of the stator windings and absence of circulating currents. It consists of a stator with two separate symmetric three-phase windings, having different numbers of poles $P_1$ and $P_2$ (e.g., 2/6 or 4/12) and a standard squirrel-cage rotor. The machine used for the analysis reported in this chapter has the number of poles as 2/6. The design process of this machine has been clearly laid out in chapter 2.

A model based on the machine geometry and the winding layouts of an arbitrary n phase machine is required for a general machine analysis. This is the motivation for the development of the multiple coupled circuit model of an induction machine set forth in [3.5]. Following this conceptual framework, this chapter presents a coupled circuit and air gap field calculation model for the dual stator winding induction machine with squirrel-cage rotor. The inductances of the stator windings and rotor bars are calculated using the winding function methodology based on the actual distributions of the windings and the bars [3.6]. Unlike the technique based on the fundamental component of the stator winding distributions, the space harmonic components are included in the analysis that follows. Another advantage of the model developed in this chapter is the possibility of calculating the currents flowing in the component parts of the machine. This includes stator coils and rotor bars during transient, dynamic and steady state operating conditions. In view of this possibility, the approximate flux densities in the air gap and cores of the machine can be deduced.

Finite Element Analysis (FEA) is the favored method of plotting the steady state magnetic fields of various parts of electric machines. Using FEA, repeated and time-consuming simulations are needed to obtain comprehensive performance profiles of electric machines. Although FEA yields very accurate results, its use to study the dynamics of electric machines and machines with multiple windings and excitations of different frequencies is still a difficult task. With the benefit of the winding function approach in which the winding distributions are accounted for, and the proposed coupled circuit model of the dual stator winding machines which yields currents in stator coils and rotor bars, the air gap flux density can be approximately determined under all operating conditions. The influence of the air gap magnetic saturation is approximated using the B-H curve of the magnetic core material of the machine. Both the FEA and the experimental results on a 3 hp 2/6 dual winding, squirrel-cage induction machine confirm the accuracy and utility of the air gap flux linkage calculation scheme.

The arrangement of the chapter is as follows: Some preliminaries are listed in section 3.2. The winding function approach used for the calculations of the machine inductances with a general non-constant air gap length is presented in Section 3.3. Sections 3.4, 3.5, 3.6, respectively outline the calculations of the stator inductance, rotor inductance and stator-rotor mutual inductance matrices. The dual stator winding induction machine model is presented in section 3.7. A general complex variable transformation for n-phase systems is outlined in Section 3.8 and is utilized to transform the phase variable voltage and electromagnetic torque equations (set forth in Section 3.7) of the machine to the rotor reference frame. This transformation retains the space harmonics in the rotor currents and enables the determination of the bar currents. Computer simulation results of the dual

stator winding induction machine based on the proposed model are given in Section 3.9. The steady state simulation results are used in Section 3.10 to calculate the air gap flux density of the machine. FEA and experimental results validate the approximate field calculation technique. Conclusions are drawn in Section 3.11. Although the proposed analysis tools are applied to 2/6 dual stator winding, squirrel-cage induction machines, they have wider applicability to other multi-phase machines with multi-frequency excitations.

## 3.2 Preliminaries

The following definitions are fundamental to the magnetic circuit analysis.

**Definition 3.1: Gauss 's Law**

If $E$ is the electric field in the space and $\rho(r)$ is a distribution of charge density, then the Gauss's Law is expressed as:

$$\Phi = \oint_S E \cdot ds = \oint_V (\nabla \cdot E) \cdot dv = \frac{1}{\varepsilon_0} \oint_V \rho(r) \cdot dv \tag{3.1}$$

Since the total charge density within the space is zero, then from Gauss theorem we get:

$$\oint_S B \cdot ds = 0 \tag{3.2}$$

where, $B$ is the magnetic field in the space and $S$ enclosed a volume $V$ ,

**Definition 3.2:**

If $E$ is the electric field in the area, $O$ is the boundary of the area S, then from Stoke's theorem, the following property can be established:

$$\oint_O E \cdot dl = 0 \tag{3.3}$$

**Definition 3.3: Ampere's Law**

Ampere's law is the fundamental basis on which we begin our electric machine design and analysis. It can be expressed as:

$$\nabla \times B = \mu_0 \cdot J \tag{3.4}$$

where, $B$ is the magnetic flux density, $J$ is the current density and $\mu_0$ is the permeability of free space.

Doing integration on both sides of equation (3.4) over an arbitrary finite open surface:

$$\int_S \nabla \times B \cdot ds = \mu_0 \int_S J \cdot ds \tag{3.5}$$

By Stoke's theorem, the left side of equation (3.5) can be altered to the form:

$$\int_S \nabla \times B \cdot ds = \oint_O B \cdot dl \tag{3.6}$$

The right side of equation (3.5) is obviously proportional to the current flowing through the surface $S$. Then a simple format of the integration of Ampere's law can be expressed as:

$$\oint_O B \cdot dl = \mu_0 I \tag{3.7}$$

If the behavior of the magnetic field in the material bodies is considered, the usual format of the integration of Ampere's law can be expressed as:

$$\oint_O H \cdot dl = \int_S J \cdot ds = N \cdot I \tag{3.8}$$

where, $O$ is a closed boundary of area $S$, $N$ is the number of conductors carrying current $I$.

**Definition 3.4:**

The Magneto-Motive Force (MMF) of any closed path $C$ is defined as:

$$F_c = \int_S J \cdot ds = N \cdot I \tag{3.9}$$

where, $S$, $N$ and $I$ are as defined in definition 3.3.

**Definition 3.5:**

The magnetic flux passing through the area $S$ is defined as:

$$\phi_s = \int_S B \cdot ds \tag{3.10}$$

If there are $N$ coincident conductors bounding the area $S$, the linkage flux can be expressed as:

$$\psi_s = N \cdot \int_S B \cdot ds \tag{3.11}$$

**Definition 3.6: Faraday's Law**

Faraday's law is very important since it gives a way to understand and explain the links between magnetic field and electric field. It can be expressed as:

$$\oint_O E \cdot dl = -\frac{d}{dt} \int_S B \cdot ds = -\frac{d\psi}{dt} \tag{3.12}$$

This expression shows that an additional electric field will be induced by a time varying magnetic field and consequently a voltage is produced in a closed coil placed in the magnetic field. If the Electro-Motive Force (EMF) in equation (3.12) is replaced by the negative of the voltage $-v$, a conventional expression will be found as:

$$v = \frac{d\psi}{dt} \tag{3.13}$$

## 3.3 General Winding Function Expression

The winding function theory which is used to calculate the inductances of induction machines was developed in the 1960's. The winding function theory has been used with success to calculate the inductances of induction and synchronous machines with constant or variable air gap length with or without rotor eccentricities [3.6-3.8]. It can be found from previously published papers that the winding function is only considered after the average of the turn function is removed from itself. This winding function definition yields correct results when the air gap of the machine is constant around the inner surface of the stator. However, if the same definition of the winding function is applied under rotor eccentricity conditions, in which the air gap length of the machine is no longer constant, the equality of $L_{12} = L_{21} = L$ cannot be observed by using the winding function definition for inductance calculation under rotor eccentricity conditions. This inequality, which does not agree with the equality that we can find in the linear magnetic circuit, was first reported in [3.7]. It is very difficult to find a proper explanation for this inequality. As a result, a method called the modified winding function approach and extension of winding function theory were proposed in [3.8, 3.9]. The winding function

theory itself is correct. The inaccuracy under rotor eccentricity conditions comes from some simplification or assumption during the equation derivation. Hence the name "extension of the winding function theory" may not be proper.

The derivation of the general winding function from the fundamental relationships is the subject of this section. With all the assumptions or simplifications removed, a general equation for the winding function of a winding distribution can be obtained.

A general diagram of an electric machine is given in Figure 3.1, in which the air gap length may not be constant. A closed area which includes the stator core, the air gap and the rotor core can be found and its boundary is shown as a dash line in the figure, where AB is in the stator core; O is the central point of stator; OA and OB go through the rotor, the air gap and the stator core and can be considered to be orthogonal to the inner surface of the stator. Based on the Ampere's Law, the magnetic field (H) of the boundary AOB can be expressed in terms of the current density J, the differential length ∂l and the area ∂s as:

$$\oint_C H \cdot dl = \int_S J \cdot ds \tag{3.14}$$

If the turn function of an arbitrary winding A is $n_A(\theta)$, where $\theta$ is the angle around the inner surface of the stator, then equation (3.14) can be written as:

$$\oint_C H \cdot dl = n_A(\theta) \cdot i_A \tag{3.15}$$

There are two assumptions that need to be clarified before the next step. The first one is: The air gap is so small compared to the stator or the rotor core that the magnetic field in the air gap can be considered to be orthogonal to the inner surface of the stator. This is a very fundamental assumption in electric machine analysis. The second one is:

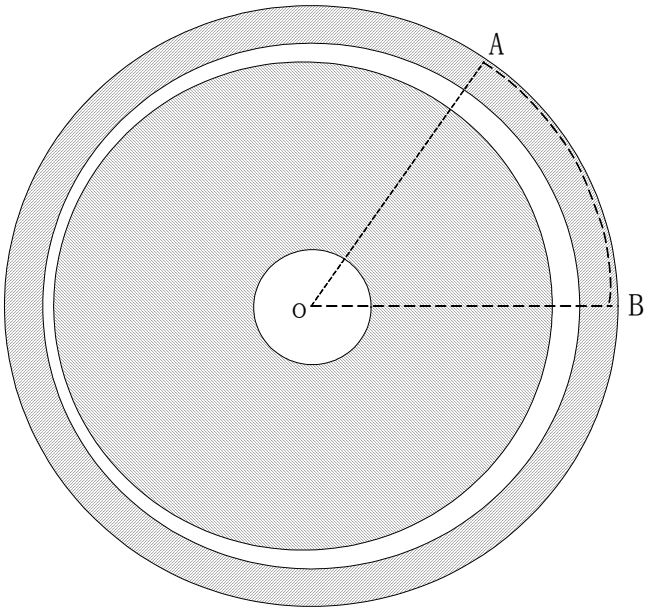


Figure 3.1 General diagram for an electric machine showing non-constant air gap length

The permeability of iron is much greater than that of air, hence the magneto-motive force drops on the stator and the rotor cores can be ignored. A general definition for the air gap is expressed as [3.9]:

$$g(\theta,\theta_{rm}) = g_0\left[1 - a_1\cos(\theta+\gamma) - a_2\cos(\theta-\theta_{rm}+\gamma)\right] \tag{3.16}$$

where, $a_1$ and $a_2$ are constants, which represent the degree of static and dynamic eccentricity respectively; $\theta_{rm}$ is the rotor mechanical angle; $g_0$ is the average air gap length and angle $\gamma$ defines the changes of the distribution of the air gap length around the inner stator surface.

It is clear from (3.16) that the air gap length not only depends on the angle around the stator, but also on the rotor angle, which will be true under almost all possible conditions. The constant air gap length condition can be achieved by setting $a_1$ and $a_2$ to be zero. Applying the above two assumptions to equation (3.15), the integration part of the equation (3.15) can be restated as:

$$\oint_C H \cdot dl = H_A(\theta) \cdot g(\theta, \theta_{rm}) - H_A(0) \cdot g(0, \theta_{rm}) \tag{3.17}$$

where, $g(0, \theta_{rm})$ is the air gap length at the starting point and the value of $\theta$ at the starting point is assumed to be zero. $H_A(0)$ is the magnetic field at the starting point while $g(\theta, \theta_{rm})$ and $H_A(\theta)$ are the air gap length and magnetic field at $\theta$ angle point respectively.

Substituting (3.17) into (3.15),

$$H_A(\theta) \cdot g(\theta, \theta_{rm}) - H_A(0) \cdot g(0, \theta_{rm}) = n_A(\theta) \cdot i_A \tag{3.18}$$

An expression for the magnetic field around the stator can be found from (3.18) as:

$$H_A(\theta) = \frac{n_A(\theta) \cdot i_A + H_A(0) \cdot g(0, \theta_{rm})}{g(\theta, \theta_{rm})} \tag{3.19}$$

The $H_A(\theta)$ and $H_A(0)$ are unknown and must be solved. Hence Gauss's Law is applied to determine the unknown quantity.

If a cylinder passing through the air gap is considered, Gauss's Law can be expressed as:

$$\int_0^{2\pi} \mu_0 H_A(\theta) r_{is} l_s d\theta = 0 \tag{3.20}$$

where, $r_{is}$ is the radius of the inner stator surface; $l_s$ is the length of the machine.

Substituting (3.19) into (3.20),

$$\int_0^{2\pi} \mu_0 r_{is} l_s \frac{n_A(\theta) \cdot i_A + H_A(0) \cdot g(0, \theta_{rm})}{g(\theta, \theta_{rm})} d\theta = 0 \tag{3.21}$$

Rearranging equation (3.21) gives,

$$H_A(0)\cdot g(0,\theta_{rm}) = -\frac{\int_0^{2\pi}\frac{n_A(\theta)}{g(\theta,\theta_{rm})}d\theta}{\int_0^{2\pi}\frac{1}{g(\theta,\theta_{rm})}d\theta}\cdot i_A \tag{3.22}$$

Substituting (3.22) into (3.19),

$$H_A(\theta) = \frac{n_A(\theta)\cdot i_A}{g(\theta,\theta_{rm})} - \frac{1}{g(\theta,\theta_{rm})}\frac{\int_0^{2\pi}\frac{n_A(\theta)}{g(\theta,\theta_{rm})}d\theta}{\int_0^{2\pi}\frac{1}{g(\theta,\theta_{rm})}d\theta}\cdot i_A \tag{3.23}$$

Simplification of (3.23) yields (3.24),

$$N_A(\theta)\cdot i_A = H_A(\theta)\cdot g(\theta,\theta_{rm}) \tag{3.24}$$

$N_A(\theta)$ is called the winding function. Then the winding function $N_A(\theta)$ is expressed as:

$$N_A(\theta) = n_A(\theta) - \frac{\int_0^{2\pi}\frac{n_A(\theta)}{g(\theta,\theta_{rm})}d\theta}{\int_0^{2\pi}\frac{1}{g(\theta,\theta_{rm})}d\theta} \tag{3.25}$$

If the air gap length is constant,

$$g(\theta,\theta_{rm}) = g_0$$

The winding function in equation (3.25) can be simplified as:

$$\begin{aligned} N_A(\theta) &= n_A(\theta) - \frac{\int_0^{2\pi}\frac{n_A(\theta)}{g_0}d\theta}{\int_0^{2\pi}\frac{1}{g_0}d\theta} \\ &= n_A(\theta) - \frac{\int_0^{2\pi} n_A(\theta)d\theta}{2\pi} \\ &= n_A(\theta) - \langle n_A(\theta)\rangle \end{aligned} \tag{3.26}$$

where $\langle n_A(\theta)\rangle$ is the average of the turn function. Equation (3.26) is similar to the definition of the winding function traditionally used for constant air gap length.

To simplify the integration in the winding function calculation, the inverse of the air gap is approximated as:

$$\frac{1}{g(\theta,\theta_{rm})} = A_0 + \sum_{i=1}^{\infty} A_i \cos\left(i\theta - i\theta_{rm}^{'} + i\gamma\right) \tag{3.27a}$$

where, $A_0 = \dfrac{1}{g_0\sqrt{1-a_3^2}}$, $A_i = \dfrac{2}{g_0\sqrt{1-a_3^2}} \cdot \left(\dfrac{1-\sqrt{1-a_3^2}}{a_3}\right)^i$,

$a_3 = \sqrt{a_1^2 + 2a_1a_2\cos\theta_{rm} + a_2^2}$, $\theta_{rm}^{'} = \arctan\left(\dfrac{a_2\sin\theta_{rm}}{a_1 + a_2\cos\theta_{rm}}\right)$.

The other approximations of the inverse of the air gap function are given as:

$$\frac{1}{g(\theta,\theta_{rm})} = \frac{1}{g_0}\left[\begin{array}{l}\left(1+\dfrac{\rho^2}{2}\right) + \rho\cos(\theta-\sigma) + \dfrac{\rho^2}{2}\cos^2(\theta-\sigma) \\ + \dfrac{\rho^3}{4}\cos^3(\theta-\sigma) + \cdots\end{array}\right] \tag{3.27b}$$

where, $\rho = \dfrac{\sqrt{\alpha^2+\beta^2}}{g_0}$, $\sigma = \arctan\left(\dfrac{\beta}{\alpha}\right)$, $\alpha$ and $\beta$ are the displacement of rotor center respected to the stator central point.

If the first two terms in (3.27a) are used in the approximation, the inverse of the air gap length function is expressed as:

$$\frac{1}{g(\theta,\theta_{rm})} = A_0 + A_1\cos\left(\theta - \theta_{rm}^{'} + \gamma\right) \tag{3.28}$$

When the expression for the inverse of the air gap is used in the general winding function equation, a new simplified expression of winding function will results:

$$N_A(\theta) = n_A(\theta) - \langle n_A(\theta) \rangle - \sum_{i=1}^{\infty} \frac{A_i}{2\pi A_0} \int_0^{2\pi} n_A(\theta) \cos\left(i\theta - i\theta'_{rm} + i\gamma\right) d\theta \tag{3.29}$$

## 3.4 Stator Inductances Calculation

The expression for winding inductances is calculated using the winding function and the turn function of the windings. If the winding function of $i^{th}$ winding is expressed as $N_i(\theta)$, where $\theta$ is the angle around the stator, then from (3.22) the magnetic field around the stator can be expressed as:

$$H_i(\theta) = \frac{N_i(\theta)}{g(\theta, \theta_{rm})} \cdot i_i \tag{3.30}$$

where, $g(\theta, \theta_{rm})$ is the air gap function and $i_i$ is the current flowing through the $i^{th}$ winding.

Then the flux density in the air gap can be written as:

$$B_i(\theta) = \mu_0 \frac{N_i(\theta)}{g(\theta, \theta_{rm})} \cdot i_i \tag{3.31}$$

Assume the mutual inductance between $i^{th}$ winding and $j^{th}$ winding is the objective and the turn function of $j^{th}$ winding is $n_j(\theta)$. The flux linkage induced in $j^{th}$ winding due to the $i^{th}$ winding current $i_i$ can be expressed as:

$$\lambda_{ji} = \mu_0 r l \cdot i_i \cdot \int_0^{2\pi} \frac{1}{g(\theta, \theta_{rm})} \cdot n_j(\theta) \cdot N_i(\theta) \cdot d\theta \tag{3.32}$$

where, $r$ is the mean value of radius of the air gap middle line and $l$ is the effective length of the stator core.

Since the definition of the mutual inductance is:

$$L_{ji} = \frac{\lambda_{ji}}{i_i} \tag{3.33}$$

The general expression for the mutual inductance calculation is:

$$L_{ji} = \mu_0 rl \int_0^{2\pi} \frac{1}{g(\theta, \theta_{rm})} \cdot n_j(\theta) \cdot N_i(\theta) \cdot d\theta \tag{3.34}$$

The stator inductances considered include the stator winding self-inductances and the mutual inductances between the stator windings. Since the numbers of poles of two stator winding sets are different, the mutual inductances between two stator winding sets are zero. Hence the inductances that will be calculated in this section are self and mutual inductances of the ABC winding set and the self and mutual inductances of the XYZ winding set. Because only the uniform air gap condition is considered in this chapter, the air gap function is a constant:

$$g(\theta, \theta_{rm}) = g_0 \tag{3.35}$$

### 3.4.1 Self Inductances of the ABC Winding Set

The general expression to calculate the self-inductance of $i^{th}$ winding is:

$$L_{ii} = \mu_0 rl \int_0^{2\pi} \frac{1}{g_0} \cdot n_i(\theta) \cdot N_i(\theta) \cdot d\theta \tag{3.36}$$

where, $n_i(\theta)$ is the turn function of $i^{th}$ winding; $N_i(\theta)$ is the winding function of $i^{th}$ winding; $g_0$ is the constant air gap.

The clock diagram of the dual stator winding induction machine is given in Figure 3.2. The turn and winding functions of the ABC winding set are shown in Figure 3.3 (I) and Figure 3.3 (II) respectively, where $C_{s1}$ is the number of coils per slot for the ABC winding set and $C_{s1} = N_{s1}/6$. $N_{s1}$ is the number of turns per phase.

For phase A, the self-inductance is:

$$L_{AA} = \mu_0 rl \int_0^{2\pi} \frac{1}{g_0} \cdot n_A(\theta) \cdot N_A(\theta) \cdot d\theta \tag{3.37}$$

Since the turn function of phase A is a piecewise linear equation, the integration can only be done in each linear region and the results of each linear region are added to obtain the final result.

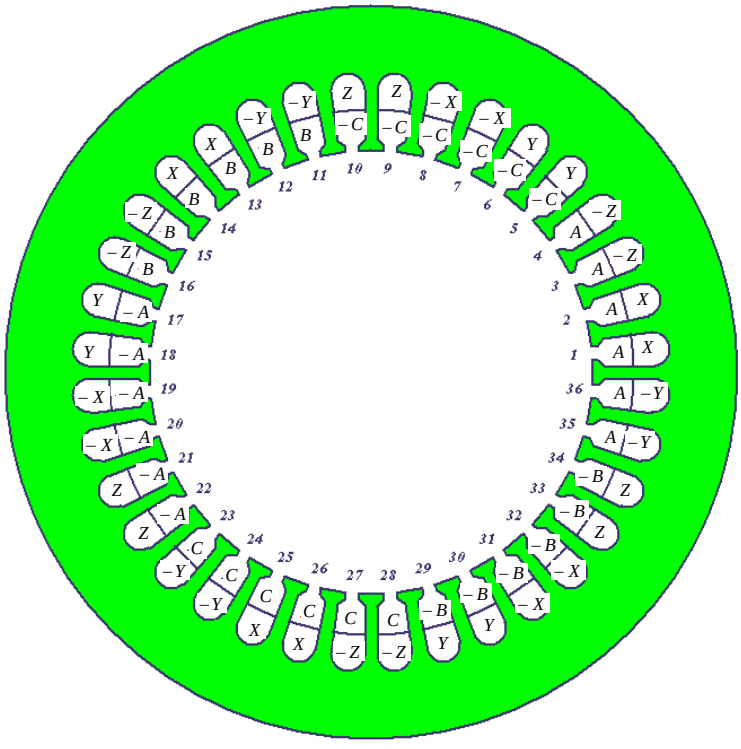

Figure 3.2 The clock diagram of dual stator winding induction machine

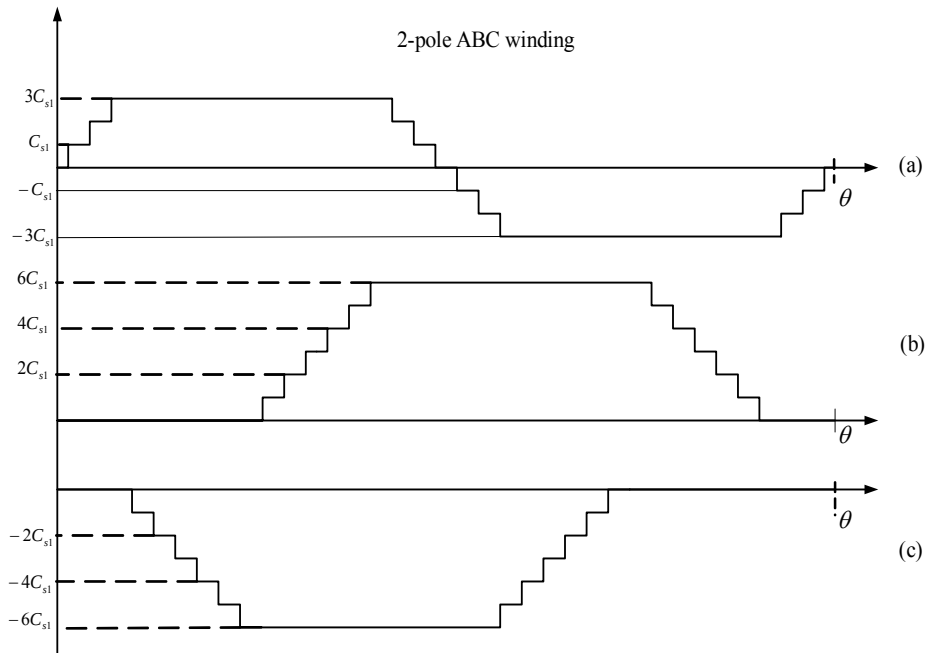


(I) Turn function

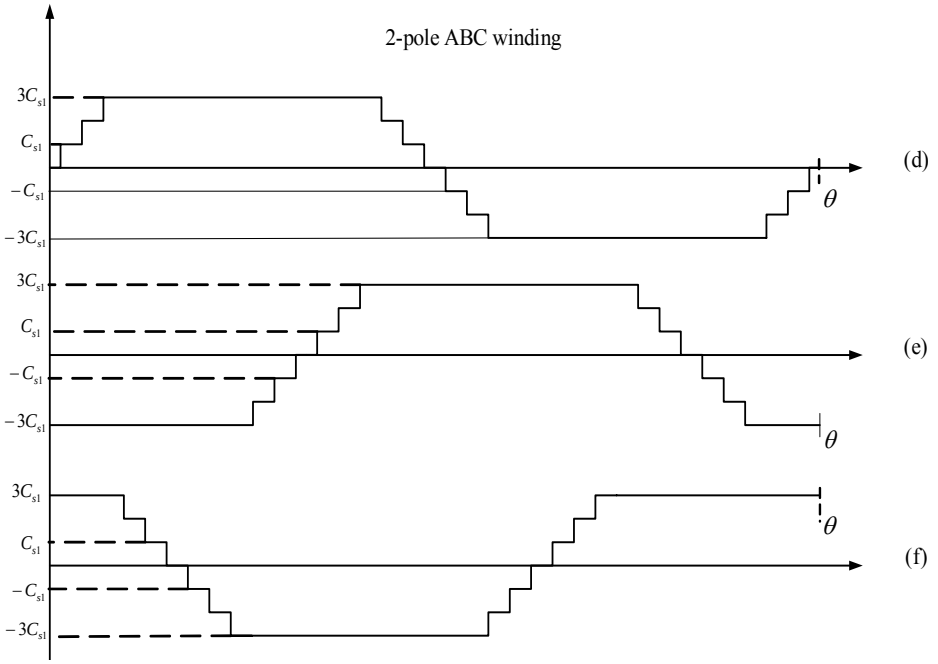


(II) Winding function

Figure 3.3 The turn and winding functions of the ABC winding set, (a) the turn function of phase A, (b) the turn function of phase B, (c) the turn function of phase C, (d) the winding function of phase A, (e) the winding function of phase B, (f) the winding function of phase C.

The expressed for the self-inductance of phase A can be simplified as:

$$L_{AA} = \frac{\mu_0 rl}{g_0} \int_0^{2\pi} n_A(\theta) \cdot \left[ n_A(\theta) - \langle n_A(\theta) \rangle \right] \cdot d\theta \tag{3.38}$$

where, $\langle n_A(\theta) \rangle$ is the averages of the phase A winding functions.

Similar expressions can be found for phases B and C.

$$L_{BB} = \frac{\mu_0 rl}{g_0} \int_0^{2\pi} n_B(\theta) \cdot \left[ n_B(\theta) - \langle n_B(\theta) \rangle \right] \cdot d\theta \tag{3.39}$$

$$L_{CC} = \frac{\mu_0 rl}{g_0} \int_0^{2\pi} n_C(\theta) \cdot \left[ n_C(\theta) - \langle n_C(\theta) \rangle \right] \cdot d\theta \tag{3.40}$$

where, $\langle n_B(\theta) \rangle$ and $\langle n_C(\theta) \rangle$ are the averages of the phases B and C winding functions respectively.

The self-inductances of three phases have the same value and the value of the self-inductances is:

$$\begin{aligned} L_{AA} = L_{BB} = L_{CC} &= \frac{\mu_0 rl}{g_0} \int_0^{2\pi} N_A(\theta) \cdot N_A(\theta) \cdot d\theta \\ &= \frac{2\mu_0 rl}{g_0} \left[ \int_{\frac{3\cdot\pi}{2\cdot 18}}^{\frac{5\cdot\pi}{2\cdot 18}} C_{s1}^2 d\theta + \int_{\frac{5\cdot\pi}{2\cdot 18}}^{\frac{7\cdot\pi}{2\cdot 18}} (2C_{s1})^2 d\theta + \int_{\frac{7\cdot\pi}{2\cdot 18}}^{\frac{33\cdot\pi}{2\cdot 18}} (3C_{s1})^2 d\theta + \int_{\frac{33\cdot\pi}{2\cdot 18}}^{\frac{35\cdot\pi}{2\cdot 18}} (2C_{s1})^2 d\theta + \int_{\frac{35\cdot\pi}{2\cdot 18}}^{\frac{37\cdot\pi}{2\cdot 18}} C_{s1}^2 d\theta \right] \\ &= \frac{127\pi\mu_0 rl}{9g_0} C_{s1}^2 \end{aligned} \tag{3.41}$$

where, $C_{s1}$ is the number of turns per slot for the ABC winding set; $P_1$ is the number of pole for ABC stator winding set and $S$ is the number of stator slots. This expression of self-inductance calculation is only good for this particular machine design.

### 3.4.2 Mutual Inductances of the ABC Winding Set

The general expression for the mutual inductance is:

$$L_{ij} = \mu_0 rl \int_0^{2\pi} \frac{1}{g_0} \cdot n_i(\theta) \cdot N_j(\theta) \cdot d\theta \tag{3.42}$$

where, $n_i(\theta)$ is the turn function of $i^{th}$ winding; $N_j(\theta)$ is the winding function of $j^{th}$ winding, $i, j = A, B, C$ and $i \neq j$.

The calculation method and process are similar to the one for self-inductance, but the number of linear region is much more than that. All the mutual inductances of the stator windings have the same constant value for constant air gap length. The expression for the mutual inductance is:

$$L_{ij} = -\frac{S^2 \pi \mu_0 rl}{54 P_1^2 g_0} \left( \frac{3 P_1 C_{s1}}{S} \right)^2 = -\frac{6\pi \mu_0 rl}{g_0} C_{s1}^2 \tag{3.43}$$

where, $i, j = A, B, C$ and $i \neq j$.

### 3.4.3 Self Inductances of the XYZ Winding Set

The turn and winding functions of the XYZ winding set are shown in Figure 3.4 (I) and Figure 3.4 (II) respectively, where $C_{s2} = N_{s2}/2$ is the number of coils per slot for XYZ stator winding set. $N_{s2}$ is the number of turns per phase for the XYZ winding set.

For phase X, the self-inductance is:

$$L_{XX} = \mu_0 rl \int_0^{2\pi} \frac{1}{g_0} \cdot n_X(\theta) \cdot N_X(\theta) \cdot d\theta \tag{3.44}$$

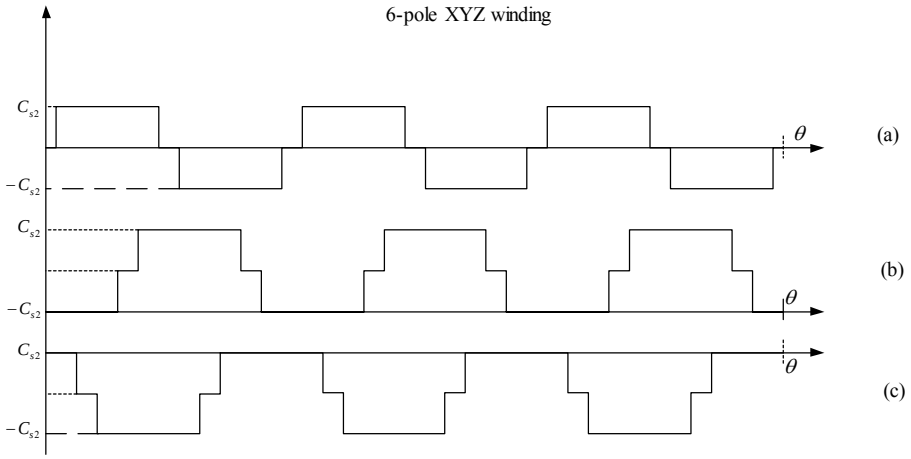


(I)

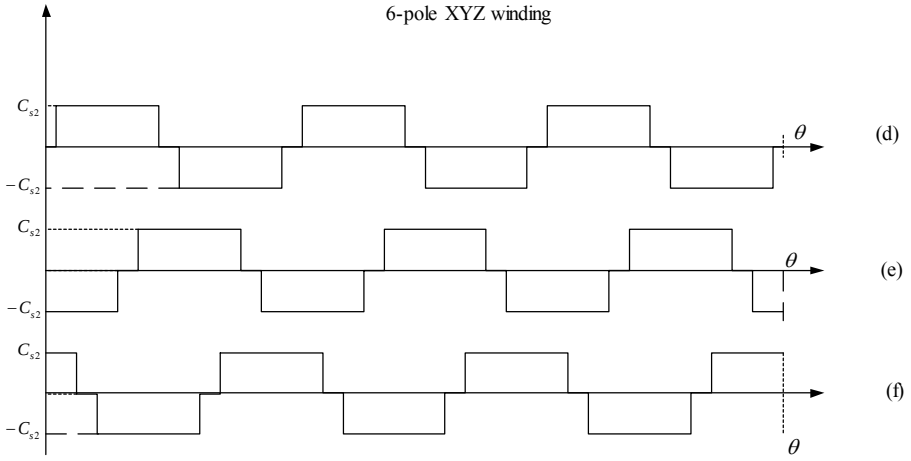


(II)

Figure 3.4 The winding function of the XYZ winding set, (a) the turn function of phase X, (b) the turn function of phase Y, (c) the turn function of phase Z, (d) the winding function of phase X, (e) the winding function of phase Y, (f) the winding function of phase Z.

Similar to the integrations in the ABC winding set, the integration can only be done in each linear region and the results of each linear region are added to achieve the final result. The expression for self-inductance of phase X can be simplified as:

$$L_{XX} = \frac{\mu_0 rl}{g_0} \int_0^{2\pi} n_X(\theta) \cdot \left[ n_X(\theta) - \langle n_X(\theta) \rangle \right] \cdot d\theta \tag{3.45}$$

where, $\langle n_X(\theta)\rangle$ is the average of the phase A winding functions.

Similar equations can be found for phases Y and Z.

$$L_{YY} = \frac{\mu_0 rl}{g_0}\int_0^{2\pi} n_Y(\theta)\cdot\left[n_Y(\theta) - \langle n_Y(\theta)\rangle\right]\cdot d\theta \tag{3.46}$$

$$L_{ZZ} = \frac{\mu_0 rl}{g_0}\int_0^{2\pi} n_Z(\theta)\cdot\left[n_Z(\theta) - \langle n_Z(\theta)\rangle\right]\cdot d\theta \tag{3.47}$$

where, $\langle n_Y(\theta)\rangle$ and $\langle n_Z(\theta)\rangle$ are the averages of the phases Y and Z winding functions respectively.

The self-inductances of three phases have the same value and the value of the self-inductances is obtained using the similar method shown for (3.41):

$$L_{XX} = L_{YY} = L_{ZZ} = \frac{5\pi\mu_0 rl}{3g_0}C_{s2}^2 \tag{3.48}$$

where, $C_{s2}$ is the number of turns per slot for the XYZ winding set; $P_2$ is the number of pole for the XYZ stator winding set and $S$ is the number of slots.

.

### 3.4.4 Mutual Inductances of the XYZ Winding Set

Substituting the turn and winding functions of the XYZ winding set into the general mutual inductance calculation equation (3.34) and performing the integration for piecewise linear equations, the mutual inductances of the XYZ winding set are obtained. Since all the mutual inductances of the XYZ winding set have the same constant value for a uniform air gap, it is expressed as:

$$L_{ij} = -\frac{S^2 \pi \mu_0 rl}{54 P_2^2 g_0}\left(\frac{3P_2 N_{s2}}{S}\right)^2 = -\frac{2\pi\mu_0 rl}{3g_0} N_{s2}^2 \tag{3.49}$$

where, $i, j = X, Y, Z$ and $i \neq j$.

## 3.5 Calculation of Rotor Inductances

A method to adequately model a squirrel cage rotor has been set forth in [1.10, 2.3]. The squirrel cage rotor with $n$ (even or odd) bars and two end rings to short circuit all the bars together is considered as $n$ identical magnetically coupled circuits. Each circuit is composed of two adjunct rotor bars and segments of the end rings connect two adjacent bars together at both ends of the bars. Each bar and end ring segment of the rotor loop is equivalently represented by a serial connection of a resistor and an inductor as shown in Figure 3.5.

The resistance and the inductance of the rotor bar are represented by $r_b$ and $l_b$ respectively; the resistance and inductance of the partial end winding in the rotor loop are represented by $r_e$ and $l_e$ respectively. Three rotor loops are shown in Figure 3.5 and the current flowing through the rotor loops are represented by $i_{k-1}$, $i_k$ and $i_{k+1}$ respectively. Since every rotor loop is treated as an independent phase, a healthy cage rotor having $n$ rotor bars becomes a $n$ phases balanced system.

The turn function of $i^{th}$ rotor loop is shown in Figure 3.6 (a). Since a constant air gap length is considered in this chapter, the winding function of the $i^{th}$ rotor loop can be easily found with Figure 3.6 (b).

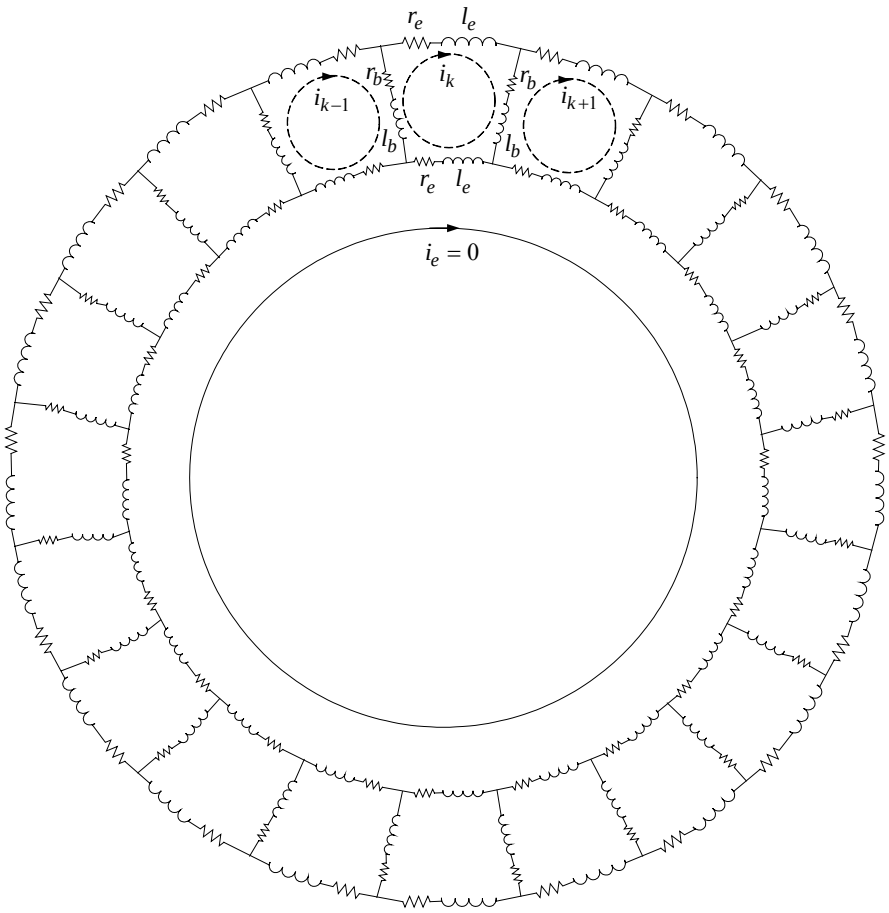


Figure 3.5 Squirrel cage rotor equivalent circuit

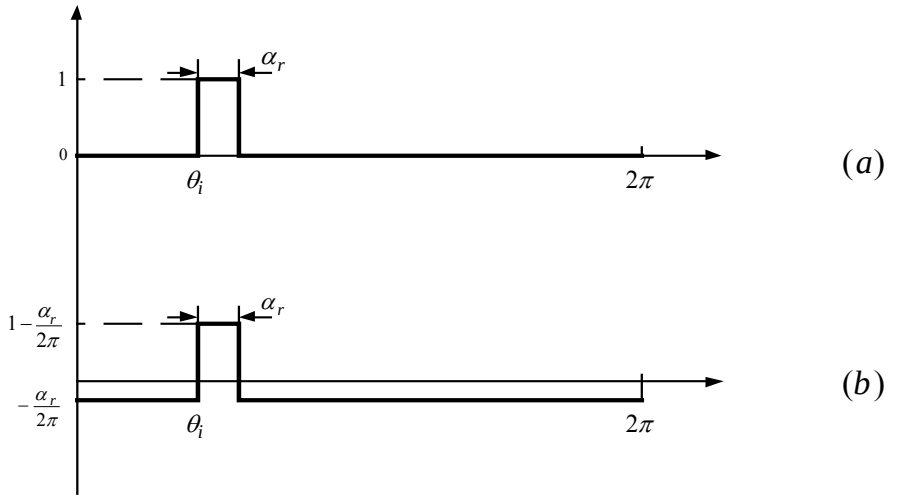


Figure 3.6 Rotor $i^{th}$ rotor loop turn and winding function, (a) turn function, (b) winding function.

The turn function of the $i^{th}$ rotor loop is:

$$n_i(\theta)=\begin{cases}0 & \theta\in[0,\ \theta_i)\\ 1 & \theta\in[\theta_i,\ \theta_i+\alpha_r)\\ 0 & \theta\in[\theta_i+\alpha_r,\ 2\pi)\end{cases} \tag{3.50}$$

The winding function can be expressed as:

$$N_i(\theta)=\begin{cases}-\dfrac{\alpha_r}{2\pi} & \theta\in[0,\ \theta_i)\\ 1-\dfrac{\alpha_r}{2\pi} & \theta\in[\theta_i,\ \theta_i+\alpha_r)\\ -\dfrac{\alpha_r}{2\pi} & \theta\in[\theta_i+\alpha_r,\ 2\pi)\end{cases} \tag{3.51}$$

where, $\alpha_r$ is the $i^{th}$ rotor loop pitch. Since a symmetrical equally spaced rotor bar structure is considered in the analysis, all the rotor loops have the same pitch $\alpha_r$.

None of the turn and winding functions shown in Figure 3.6 take the skew of the rotor into the consideration. If the rotor is skewed, the turn function and winding function are shown in Figure 3.7.

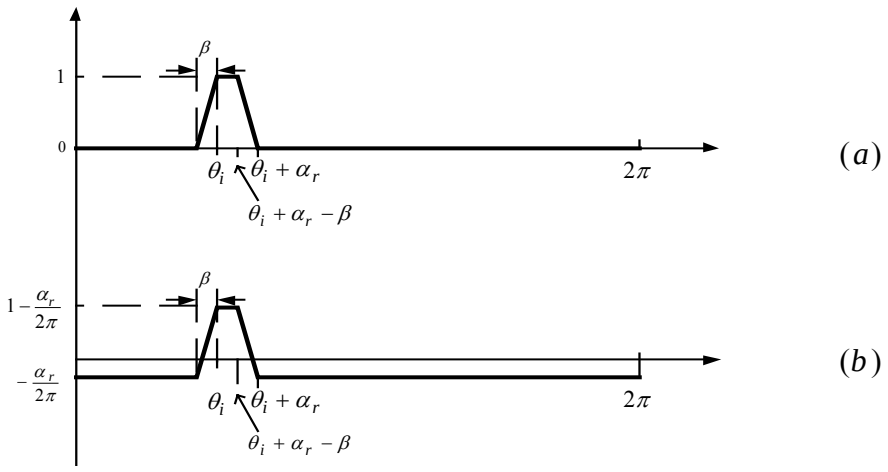


Figure 3.7 Rotor $i^{th}$ rotor loop turn and winding function for skewed rotor, (a) turn function, (b) winding function.

When the skewing factor of the rotor is considered, the expressions for the turn and winding functions become (3.52) and (3.53) respectively:

$$n_i(\theta)=\begin{cases}0 & \theta\in[0,\ \theta_i-\beta)\\ \frac{1}{\beta}(\theta-\theta_i+\beta) & \theta\in[\theta_i-\beta,\ \theta_i)\\ 1 & \theta\in[\theta_i,\ \theta_i+\alpha_r-\beta)\\ \frac{1}{\beta}(\theta_i+\alpha_r-\theta) & \theta\in[\theta_i+\alpha_r-\beta,\ \theta_i+\alpha_r)\\ 0 & \theta\in[\theta_i+\alpha_r,\ 2\pi)\end{cases} \tag{3.52}$$

$$N_i(\theta)=\begin{cases}-\frac{\alpha_r}{2\pi} & \theta\in[0,\ \theta_i-\beta)\\ \frac{1}{\beta}(\theta-\theta_i+\beta)-\frac{\alpha_r}{2\pi} & \theta\in[\theta_i-\beta,\ \theta_i)\\ 1-\frac{\alpha_r}{2\pi} & \theta\in[\theta_i,\ \theta_i+\alpha_r-\beta)\\ \frac{1}{\beta}(\theta_i+\alpha_r-\theta)-\frac{\alpha_r}{2\pi} & \theta\in[\theta_i+\alpha_r-\beta,\ \theta_i+\alpha_r)\\ 0-\frac{\alpha_r}{2\pi} & \theta\in[\theta_i+\alpha_r,\ 2\pi)\end{cases} \tag{3.53}$$

where, $\beta = skew\ \ factor\cdot\alpha_r$.

Substituting the turn function and winding function of the $i^{th}$ rotor loop into the general expression for the self-inductance given in (3.36), the self-inductance for the $i^{th}$ rotor loop can be determined. Since all the rotor loops have the same self-inductance under the uniform air gap condition, its expression is:

$$
\begin{aligned}
L_{rr} &= \frac{\mu_0 rl}{g_0}\int_0^{2\pi} N_i(\theta)\cdot N_i(\theta)d\theta \\
&= \frac{\mu_0 rl}{g_0}\int_0^{2\pi}\left(n_i(\theta)-\frac{\alpha_r}{2\pi}\right)^2 d\theta \\
&= \frac{\mu_0 rl}{g_0}\left(\alpha_r-\frac{\beta}{3}-\frac{\alpha_r^2}{2\pi}\right)
\end{aligned}
\tag{3.54}
$$

The winding functions of the adjacent rotor loops will overlap each other when the rotor is skewed, such that the mutual inductances between $i^{th}$ and $i+1^{th}$ will be different from $i^{th}$ and $i+k^{th}$ $\left(k\in[2,\,n-1]\right)$, where $n$ is the number of rotor bar.

The mutual inductance between $i^{th}$ and $i+1^{th}$ rotor loop is:

$$
\begin{aligned}
L_{rm1} &= \frac{\mu_0 rl}{g_0}\left\{\begin{aligned}
&\int_0^{\theta_i-\beta}\left(-\frac{\alpha_r}{2\pi}\right)^2 d\theta+\int_{\theta_i-\beta}^{\theta_i}\left(-\frac{\alpha_r}{2\pi}\right)\left[\frac{1}{\beta}(\theta-\theta_i+\beta)-\frac{\alpha_r}{2\pi}\right]d\theta \\
&+\int_{\theta_i-\beta}^{\theta_i+\alpha_r-\beta}\left(-\frac{\alpha_r}{2\pi}\right)\cdot\left(1-\frac{\alpha_r}{2\pi}\right)d\theta+\int_{\theta_{i+1}}^{\theta_{i+1}+\alpha_r-\beta}\left(-\frac{\alpha_r}{2\pi}\right)\cdot\left(1-\frac{\alpha_r}{2\pi}\right)d\theta \\
&+\int_{\theta_i+\alpha-\beta}^{\theta_i+\alpha_r}\left[\frac{1}{\beta}(\theta-\theta_i+\beta)-\frac{\alpha_r}{2\pi}\right]\cdot\left[\frac{1}{\beta}(\theta_i+\alpha_r-\theta)-\frac{\alpha_r}{2\pi}\right]d\theta \\
&+\int_{\theta_{i+1}+\alpha_r-\beta}^{\theta_{i+1}+\alpha_r}\left(-\frac{\alpha_r}{2\pi}\right)\left[\frac{1}{\beta}(\theta_i+\alpha_r-\theta)-\frac{\alpha_r}{2\pi}\right]d\theta+\int_{\theta_{i+1}+\alpha_r}^{2\pi}\left(-\frac{\alpha_r}{2\pi}\right)^2 d\theta
\end{aligned}\right\} \\
&= \frac{\mu_0 rl}{g_0}\left(\frac{\beta}{6}-\frac{\alpha_r^2}{2\pi}\right)
\end{aligned}
\tag{3.55}
$$

All the mutual inductance between $i^{th}$ and $i+k^{th}$ rotor loop have the same value and it can be calculated by:

$$
\begin{aligned}
L_{rm2} &= \frac{\mu_0 rl}{g_0}\int_0^{2\pi}\left(n_i(\theta)-\frac{\alpha_r}{2\pi}\right)\cdot\left(n_{i+k}(\theta)-\frac{\alpha_r}{2\pi}\right)d\theta \\
&= \frac{\mu_0 rl}{g_0}\int_0^{2\pi}\left[n_i(\theta)n_{i+k}(\theta)-\frac{\alpha_r}{2\pi}\left(n_i(\theta)+n_{i+k}(\theta)\right)-\frac{\alpha_r^2}{4\pi^2}\right]d\theta \\
&= \frac{\mu_0 rl}{g_0}\left(-\frac{\alpha_r^2}{2\pi}\right)
\end{aligned}
\tag{3.56}
$$

## 3.6 Calculation of Stator-Rotor Mutual Inductances

Both the stator and the rotor loop winding functions are represented by piecewise linear equations while the position of the $i^{th}$ rotor loop depends on the rotor angle. Using the expression for the mutual inductance in (3.57), the mutual inductances between $i^{th}$ rotor loop and the stator winding set are shown in Figure 3.8 and Figure 3.9.

$$L_{ij} = \mu_0 rl \int_0^{2\pi} \frac{1}{g_0} \cdot n_i(\theta) \cdot N_j(\theta) \cdot d\theta \tag{3.57}$$

where, $i = A, B, C$ and $j = 1,2,\cdots,n$, $n$ is the rotor bar number.

The results shown above are for the mutual inductance between $i^{th}$ rotor loop and the stator winding set. The mutual inductances between $i+1^{th}$ rotor loop and stator have exactly the same shape, except there is a phase shift angle $\alpha_r$.

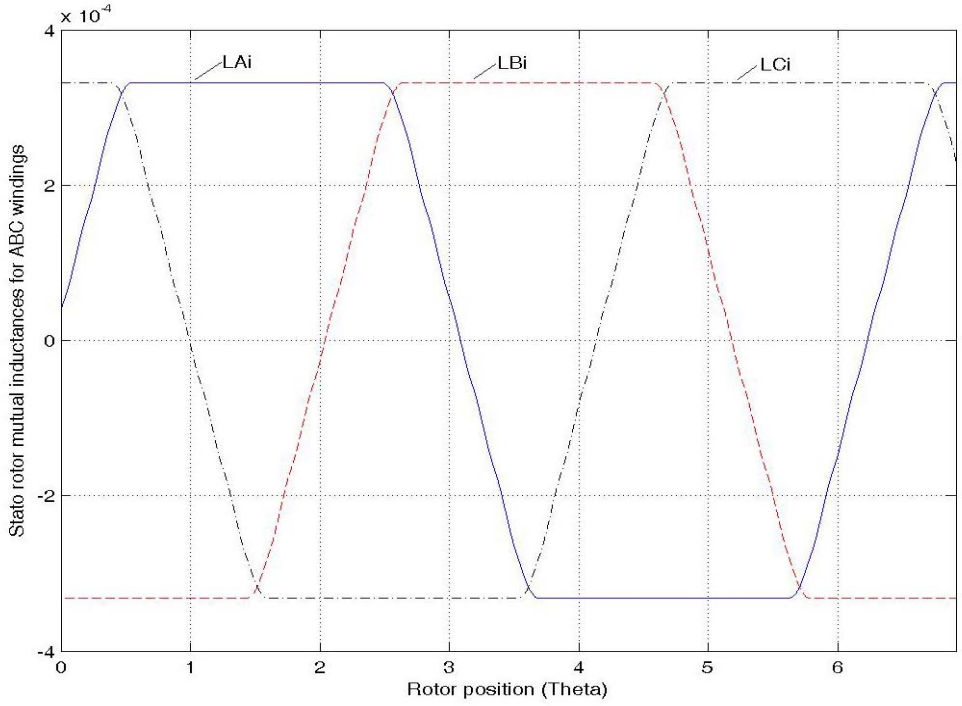


Figure 3.8 Stator rotor mutual inductance in the ABC winding set

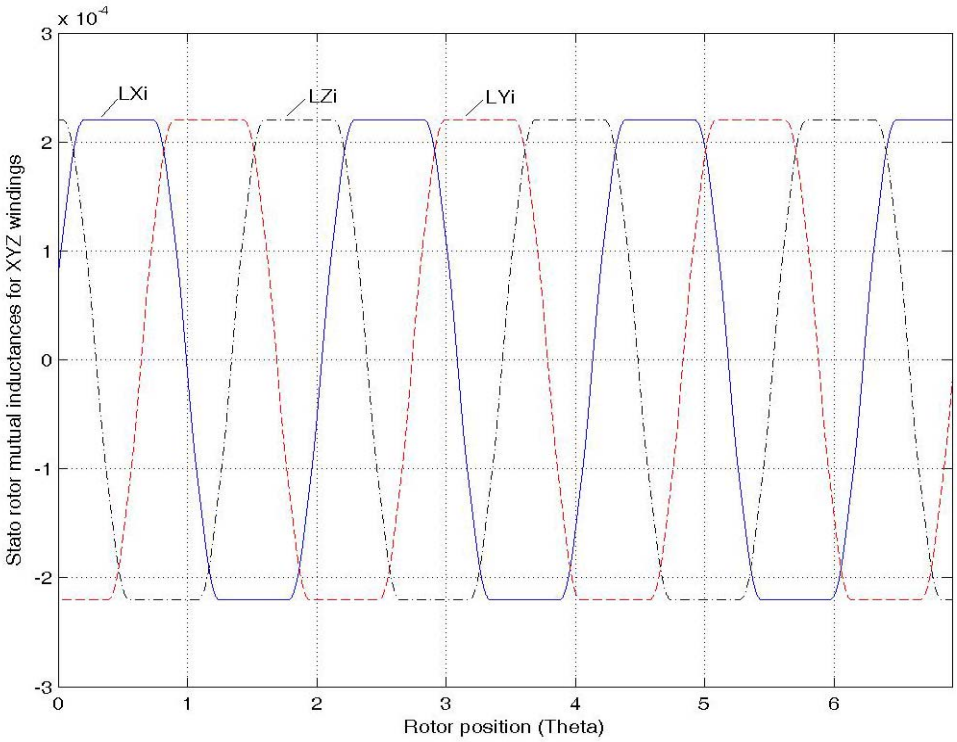


Figure 3.9 Stator rotor mutual inductance in the XYZ winding set

Since the number of pole of the XYZ winding set is three times that of the ABC winding set, the frequency of the mutual inductance for the XYZ winding set should be three times that of the ABC winding set.

## 3.7 Model of the Dual Stator Winding Machine

Based on the magnetic circuit theory, a full model of the induction machine can be developed. The reason it is called a full model is that this model is not based on any assumptions of stator windings or rotor bars distribution. Hence all the harmonics are included into the model.

The general coupled circuit model can be expressed as:

$$v = R \cdot i + \frac{d\lambda}{dt} \tag{3.58}$$

where, $v$, $i$ and $\lambda$ are the terminal voltage, current flow and flux linkage in each circuit; $R$ is the matrix of resistance. Applying this general equation to the dual stator winding induction machine leads to the full model.

### 3.7.1 Stator Voltage Equation

For the ABC winding set, the stator voltage equation is expressed as:

$$v_{abc} = R_{abc} i_{abc} + p\lambda_{abc} \tag{3.59}$$

where, $R_{abc}$ is a diagonal $3 \times 3$ matrix, in which the diagonal value depends on the resistances per phase of the ABC winding set; $p$ represents the operator $\frac{d}{dt}$ and

$$v_{abc} = \begin{pmatrix} v_a \\ v_b \\ v_c \end{pmatrix},\ i_{abc} = \begin{pmatrix} i_a \\ i_b \\ i_c \end{pmatrix},\ \lambda_{abc} = \begin{pmatrix} \lambda_a \\ \lambda_b \\ \lambda_c \end{pmatrix}.$$

The flux linkage can be written as the contribution of three components as:

$$\lambda_{abc} = \lambda_{s1s1} + \lambda_{s1s2} + \lambda_{s1r} \tag{3.60}$$

The first term in equation (3.60) represents the ABC winding set stator flux linkage due to the ABC winding stator currents, the second term is the flux linkage due to the XYZ winding set stator currents and the last term is the contribution of the rotor current. More detailed explanations of each term will be developed separately in the following sub-sections.

3.7.1.1 Stator flux linkage in the ABC winding set due to ABC winding currents. The stator flux linkage of the ABC winding set due to the ABC winding currents can be expressed as:

$$\lambda_{s1s1} = \begin{pmatrix} \lambda_{as1} \\ \lambda_{bs1} \\ \lambda_{cs1} \end{pmatrix} = \begin{pmatrix} L_{ls1} + L_{AA} & L_{AB} & L_{AC} \\ L_{BA} & L_{ls1} + L_{BB} & L_{BC} \\ L_{CA} & L_{CB} & L_{ls1} + L_{CC} \end{pmatrix} \cdot i_{s1} = L_{s1s1} \cdot i_{abc} \tag{3.61}$$

The stator self and mutual inductances in the above inductance matrix have been worked out in the previous sections and the leakage inductance calculation method is given in Section 3.4.

3.7.1.2 Stator flux linkage in the ABC winding set due to XYZ winding currents. The two stator winding sets have dissimilar numbers of poles. Hence the mutual inductances between the stator winding sets are zero, which means that these two stator winding sets are naturally decoupled. The only possible coupling between these two winding sets comes from the leakage inductance. A proof has been given clearly in [1.10] that even the leakage inductance coupling doesn't exist. Since the two stator winding set are fully decoupled, the stator flux linkage in the ABC winding set due to the XYZ winding currents is always zero.

$$\lambda_{s1s2} = 0 \tag{3.62}$$

3.7.1.3 Stator flux linkage in ABC winding set due to the rotor currents. The cage rotor having $n$ rotor bars can be modeled as a $n$ phase system. The total stator flux linkage due to the rotor currents can be written as:

$$\lambda_{s1r} = \begin{pmatrix} \lambda_{ar} \\ \lambda_{br} \\ \lambda_{cr} \end{pmatrix} = \begin{pmatrix} L_{a1} & L_{a2} & \cdots & L_{a(n-1)} & L_{an} \\ L_{b1} & L_{b2} & \cdots & L_{b(n-1)} & L_{bn} \\ L_{c1} & L_{c2} & \cdots & L_{c(n-1)} & L_{cn} \end{pmatrix} \cdot \begin{pmatrix} i_{r1} \\ i_{r2} \\ \vdots \\ i_{rn} \end{pmatrix} = L_{s1r} \cdot i_r \tag{3.63}$$

where, $L_{ai}$ is the mutual inductance between the phase A and $i^{th}$ rotor loop, $L_{bi}$ is the mutual inductance between the phase B and $i^{th}$ rotor loop, $L_{ci}$ is the mutual inductance between the phase C and $i^{th}$ rotor loop.

For the XYZ winding set, the stator voltage equation is expressed as:

$$v_{xyz} = R_{xyz} i_{xyz} + p\lambda_{xyz} \tag{3.64}$$

where, $R_{xyz}$ is a diagonal $3 \times 3$ matrix, in which the diagonal values depend on the resistance per phase of the XYZ winding set; $p$ represents the operator $\frac{d}{dt}$ and

$$v_{xyz} = \begin{pmatrix} v_x \\ v_y \\ v_z \end{pmatrix},\ i_{xyz} = \begin{pmatrix} i_x \\ i_y \\ i_z \end{pmatrix},\ \lambda_{xyz} = \begin{pmatrix} \lambda_x \\ \lambda_y \\ \lambda_z \end{pmatrix}.$$

$$\lambda_{xyz} = \lambda_{s2s2} + \lambda_{s2s1} + \lambda_{s2r} \tag{3.65}$$

Stator flux linkage in the XYZ winding set due to the XYZ winding currents is:

$$\lambda_{s2s2} = \begin{pmatrix} \lambda_{xs2} \\ \lambda_{ys2} \\ \lambda_{zs2} \end{pmatrix} = \begin{pmatrix} L_{ls2} + L_{XX} & L_{XY} & L_{XZ} \\ L_{YX} & L_{ls2} + L_{YY} & L_{YZ} \\ L_{ZX} & L_{ZY} & L_{ls2} + L_{ZZ} \end{pmatrix} \cdot i_{s2} = L_{s2s2} \cdot i_{xyz} \tag{3.66}$$

Stator flux linkage in the XYZ winding set due to the ABC winding currents is:

$$\lambda_{s2s1} = 0 \tag{3.67}$$

Stator flux linkage in the XYZ winding set due to the rotor currents is:

$$\lambda_{s2r} = \begin{pmatrix} \lambda_{xr} \\ \lambda_{yr} \\ \lambda_{zr} \end{pmatrix} = \begin{pmatrix} L_{x1} & L_{x2} & \cdots & L_{x(n-1)} & L_{xn} \\ L_{y1} & L_{y2} & \cdots & L_{y(n-1)} & L_{yn} \\ L_{z1} & L_{z2} & \cdots & L_{z(n-1)} & L_{zn} \end{pmatrix} \cdot \begin{pmatrix} i_{r1} \\ i_{r2} \\ \vdots \\ i_{rn} \end{pmatrix} = L_{s2r} \cdot i_r \tag{3.68}$$

### 3.7.2 Rotor Voltage Equation

The equivalent circuit of the cage rotor and the detailed modeling information has been clearly laid out in Section 3.5.

The voltage equation for the $k^{th}$ rotor loop can be represented as:

$$0 = 2(r_b + r_e) \cdot i_k - r_b \cdot i_{k+1} - r_b \cdot i_{k-1} + p\lambda_{rk} \tag{3.69}$$

where, $r_b$ is the bar resistance; $r_e$ is the resistance of the segment of end ring; $i_k$, $i_{k-1}$ and $i_{k+1}$ are the currents of the $k^{th}$, $k-1^{th}$ and $k+1^{th}$ loop respectively; $\lambda_{rk}$ is the flux linkage of the $k^{th}$ rotor loop. This equation is valid for all the rotor loops, therefore the total rotor voltage equation can be written in the matrix form as:

$$\begin{pmatrix} 0 \\ 0 \\ \vdots \\ 0 \end{pmatrix} = \begin{pmatrix} 2(r_b + r_e) & -r_b & \cdots & -r_b \\ -r_b & 2(r_b + r_e) & \cdots & 0 \\ \vdots & \vdots & \ddots & \vdots \\ -r_b & 0 & \cdots & 2(r_b + r_e) \end{pmatrix} \cdot \begin{pmatrix} i_{r1} \\ i_{r2} \\ \vdots \\ i_{rn} \end{pmatrix} + p \begin{pmatrix} \lambda_{r1} \\ \lambda_{r2} \\ \vdots \\ \lambda_{rn} \end{pmatrix} \tag{3.70}$$

The compact form of the above equation is:

$$0 = R_r \cdot i_r + p\lambda_r \tag{3.71}$$

where, $R_r$ is the resistance matrix, $i_r$ is the rotor loop current vector and $\lambda_r$ is the rotor loop flux linkage vector.

The rotor flux linkage can be divided into three components, the first is due to the ABC winding currents, the second is due to the XYZ winding currents while the third component is due to the rotor currents. The expression for rotor flux linkage can be expressed as:

$$\lambda_r = \lambda_{rs1} + \lambda_{rs2} + \lambda_{rr} \tag{3.72}$$

The expression for each term of (3.72) can be written as:

$$\lambda_{rs1} = \begin{pmatrix} \lambda_{r1s1} \\ \lambda_{r2s1} \\ \vdots \\ \lambda_{rns1} \end{pmatrix} = \begin{pmatrix} L_{ar1} & L_{br1} & L_{cr1} \\ L_{ar2} & L_{br2} & L_{cr2} \\ \vdots & \vdots & \vdots \\ L_{arn} & L_{brn} & L_{crn} \end{pmatrix} \cdot \begin{pmatrix} i_a \\ i_b \\ i_c \end{pmatrix} = L_{rs1} \cdot i_{abc} \tag{3.73}$$

$$\lambda_{rs2} = \begin{pmatrix} \lambda_{r1s2} \\ \lambda_{r2s2} \\ \vdots \\ \lambda_{rns2} \end{pmatrix} = \begin{pmatrix} L_{xr1} & L_{yr1} & L_{zr1} \\ L_{xr2} & L_{yr2} & L_{zr2} \\ \vdots & \vdots & \vdots \\ L_{xrn} & L_{yrn} & L_{zrn} \end{pmatrix} \cdot \begin{pmatrix} i_x \\ i_y \\ i_z \end{pmatrix} = L_{rs2} \cdot i_{xyz} \tag{3.74}$$

$$\lambda_{rr} = \begin{pmatrix} L_{rr} + 2(l_b + l_e) & L_{rm1} - l_b & \cdots & L_{rm1} - l_b \\ L_{rm1} - l_b & L_{rr} + 2(l_b + l_e) & \cdots & L_{rm2} \\ \vdots & \vdots & \ddots & \vdots \\ L_{rm1} - l_b & L_{rm2} & \cdots & L_{rr} + 2(l_b + l_e) \end{pmatrix} \cdot \begin{pmatrix} i_{r1} \\ i_{r2} \\ \vdots \\ i_{rn} \end{pmatrix} = L_{rr} \cdot i_r \tag{3.75}$$

where, $L_{irj}$ is the mutual inductance between the stator $i^{th}$ winding and $j^{th}$ rotor loop, $i = A, B, C, X, Y, Z$ and $j = 1,2,\cdots n$, $n$ is the number of rotor loop; $L_{rr}$ is the self-inductance of the rotor loops; $L_{rm1}$ is the mutual inductance between the adjunct rotor loops; $L_{rm2}$ is the mutual inductance between the rotor loops that are not adjunct; $l_b$ and $l_e$ are the leakage inductance of the rotor bar and the segment of end ring respectively.

### 3.7.3 Torque Equation

The electro-magnetic force developed by the machine is the only one that couples the electrical equation with the mechanical equation. From the energy point of view, the torque is determined by the instantaneous power transferred in the electromechanical system.

The coenergy in a magnetic field is defined as:

$$W_c = \sum_{j=1}^{J} i_j \lambda_j - W_f \text{ and } W_f = \int \sum_{j=1}^{J} i_j \cdot d\lambda_j \tag{3.76}$$

where, $i_j$ and $\lambda_j$ are the current and flux linkage of $j^{th}$ circuit respectively. $W_f$ is the total field energy in the system. In the dual stator winding inductance machine, the currents in the system include two stator currents and one rotor current. Hence for dual stator winding induction machine, the total field energy can be expressed as:

$$\begin{aligned} W_f = & \frac{1}{2} {i_{abc}}^T \cdot L_{s1s1} \cdot i_{abc} + \frac{1}{2} {i_{xyz}}^T \cdot L_{s2s2} \cdot i_{xyz} + \frac{1}{2} {i_{abc}}^T \cdot L_{s1s2} \cdot i_{xyz} \\ & + \frac{1}{2} {i_{xyz}}^T \cdot L_{s2s1} \cdot i_{abc} + \frac{1}{2} {i_{abc}}^T \cdot L_{s1r} \cdot i_r + \frac{1}{2} {i_{xyz}}^T \cdot L_{s2r} \cdot i_r \\ & + \frac{1}{2} {i_r}^T \cdot L_{rs1} \cdot i_{abc} + \frac{1}{2} {i_r}^T \cdot L_{rs2} \cdot i_{xyz} + \frac{1}{2} {i_r}^T \cdot L_{rr} \cdot i_r \end{aligned} \tag{3.77}$$

The electromagnetic torque can be obtained from the magnetic coenergy as:

$$T_e = \frac{\partial W_c}{\partial \theta_{rm}} = -\frac{\partial W_f}{\partial \theta_{rm}} \tag{3.78}$$

where, $\theta_{rm}$ is the mechanical angle of the rotor.

The coupling inductance between two stator winding sets is zero.

$$L_{s1s2} = L_{s2s1} = 0 \tag{3.79}$$

Only terms in equation (3.77) which are the functions of the rotor angle can contribute the electromagnetic torque. So applying (3.78) to (3.77), the electromagnetic torque can be expressed as:

$$T_e = -\frac{1}{2} i_{abc}^{\ T} \cdot \frac{\partial L_{s1r}}{\partial \theta_{rm}} \cdot i_r - \frac{1}{2} i_{xyz}^{\ T} \cdot \frac{\partial L_{s2r}}{\partial \theta_{rm}} \cdot i_r - \frac{1}{2} i_r^{\ T} \cdot \frac{\partial L_{rs1}}{\partial \theta_{rm}} \cdot i_{abc} - \frac{1}{2} i_r^{\ T} \cdot \frac{\partial L_{rs2}}{\partial \theta_{rm}} \cdot i_{xyz} \tag{3.80}$$

For a linear magnetic circuit,

$$L_{ij} = L_{ji} \tag{3.81}$$

Hence the torque equation is simplified as:

$$T_e = -i_{abc}^{\ T} \cdot \frac{\partial L_{s1r}}{\partial \theta_{rm}} \cdot i_r - i_{xyz}^{\ T} \cdot \frac{\partial L_{s2r}}{\partial \theta_{rm}} \cdot i_r \tag{3.82}$$

## 3.8 Complex Variable Reference Frame Transformation

The circuit model derived in the previous sections can be used to simulate the dynamic and steady state characteristics of the machine. Unfortunately, the model of the machine is complicated due to the time-varying mutual inductances and it is desirable to simplify it to simplify computation. The $q-d$ reference frame transformation for three-phase electric machines is widely and traditionally used to simplify phase models of electric machines to facilitate their analysis and control, since they eliminate the time variance of the mutual inductances. However, for multi-phase systems including space harmonics, the proper reference frame transformation is complicated [3.11]. Since the rotor model is actually a $n$ phase system, where $n$ is the number of rotor bars, an appropriate n x n arbitrary reference transformation for multi-phase system is required if

all the possible harmonic currents are to be included in the analysis. When the space harmonics in the rotor circuits are ignored, a simplified reference frame transformation given in [1.10] is proposed which drastically reduces the computation time.

A general arbitrary reference frame transformation matrix and its inverse for the $n$ phase system expressed in complex variable form are [3.12]:

$$T(\theta)=\frac{2}{n}\begin{bmatrix} 1/2 & 1/2 & 1/2 & \cdots & 1/2 \\ e^{j\theta_1} & a^1e^{j\theta_1} & a^2e^{j\theta_1} & \cdots & a^{(n-1)}e^{j\theta_1} \\ e^{j\theta_2} & a^2e^{j\theta_2} & a^4e^{j\theta_2} & \cdots & a^{2(n-1)}e^{j\theta_2} \\ \vdots & \vdots & \vdots & \ddots & \vdots \\ e^{j\theta_{n-1}} & a^{(n-1)}e^{j\theta_{n-1}} & a^{2(n-1)}e^{j\theta_{n-1}} & \cdots & a^{(n-1)^2}e^{j\theta_{n-1}} \end{bmatrix} \tag{3.83}$$

$$T(\theta)^{-1}=\begin{bmatrix} 1/2 & 1/2 & 1/2 & \cdots & 1/2 \\ e^{-j\theta_1} & a^{-1}e^{-j\theta_1} & a^{-2}e^{-j\theta_1} & \cdots & a^{-(n-1)}e^{-j\theta_1} \\ e^{-j\theta_2} & a^{-2}e^{-j\theta_2} & a^{-4}e^{-j\theta_2} & \cdots & a^{-2(n-1)}e^{-j\theta_2} \\ \vdots & \vdots & \vdots & \ddots & \vdots \\ e^{-j\theta_{n-1}} & a^{-(n-1)}e^{-j\theta_{n-1}} & a^{-2(n-1)}e^{-j\theta_{n-1}} & \cdots & a^{-(n-1)^2}e^{-j\theta_{n-1}} \end{bmatrix} \tag{3.84}$$

where, $a=e^{j\alpha}$, $\alpha=2\pi/n$, $\theta_i=\omega_i t+\theta_{0i}$, $\omega_i$ is the reference frame angular speed and $\theta_{0i}$ is an initial condition.

The transformation matrixes and their inverses for 3 phases, 5 phases and 6 phases systems are given in equation (3.85), (3.86) and (3.87) respectively.

$$T(\theta)=\frac{2}{3}\begin{bmatrix} 1/2 & 1/2 & 1/2 \\ e^{j\theta_1} & e^{j\left(\theta_1+\frac{2\pi}{3}\right)} & e^{j\left(\theta_1+\frac{4\pi}{3}\right)} \\ e^{j\theta_2} & e^{j\left(\theta_2+\frac{4\pi}{3}\right)} & e^{j\left(\theta_2+\frac{2\pi}{3}\right)} \end{bmatrix} \tag{3.85a}$$

$$T(\theta)^{-1}=\begin{bmatrix} 1/2 & 1/2 & 1/2 \\ e^{-j\theta_1} & e^{-j\left(\theta_1+\frac{2\pi}{3}\right)} & e^{-j\left(\theta_1+\frac{4\pi}{3}\right)} \\ e^{-j\theta_2} & e^{-j\left(\theta_2+\frac{4\pi}{3}\right)} & e^{-j\left(\theta_2+\frac{2\pi}{3}\right)} \end{bmatrix} \tag{3.85b}$$

$$T(\theta)=\frac{2}{5}\begin{bmatrix} 1/2 & 1/2 & 1/2 & 1/2 & 1/2 \\ e^{j\theta_1} & e^{j\left(\theta_1+\frac{2\pi}{5}\right)} & e^{j\left(\theta_1+\frac{4\pi}{5}\right)} & e^{j\left(\theta_1+\frac{6\pi}{5}\right)} & e^{j\left(\theta_1+\frac{8\pi}{5}\right)} \\ e^{j\theta_2} & e^{j\left(\theta_2+\frac{4\pi}{5}\right)} & e^{j\left(\theta_2+\frac{8\pi}{5}\right)} & e^{j\left(\theta_2+\frac{2\pi}{5}\right)} & e^{j\left(\theta_2+\frac{6\pi}{5}\right)} \\ e^{j\theta_3} & e^{j\left(\theta_3+\frac{6\pi}{5}\right)} & e^{j\left(\theta_3+\frac{2\pi}{5}\right)} & e^{j\left(\theta_3+\frac{8\pi}{5}\right)} & e^{j\left(\theta_3+\frac{4\pi}{5}\right)} \\ e^{j\theta_4} & e^{j\left(\theta_4+\frac{8\pi}{5}\right)} & e^{j\left(\theta_4+\frac{6\pi}{5}\right)} & e^{j\left(\theta_4+\frac{4\pi}{5}\right)} & e^{j\left(\theta_4+\frac{2\pi}{5}\right)} \end{bmatrix} \tag{3.86a}$$

$$T(\theta)^{-1}=\begin{bmatrix} 1/2 & 1/2 & 1/2 & 1/2 & 1/2 \\ e^{-j\theta_1} & e^{-j\left(\theta_1+\frac{2\pi}{5}\right)} & e^{-j\left(\theta_1+\frac{4\pi}{5}\right)} & e^{-j\left(\theta_1+\frac{6\pi}{5}\right)} & e^{-j\left(\theta_1+\frac{8\pi}{5}\right)} \\ e^{-j\theta_2} & e^{-j\left(\theta_2+\frac{4\pi}{5}\right)} & e^{-j\left(\theta_2+\frac{8\pi}{5}\right)} & e^{-j\left(\theta_2+\frac{2\pi}{5}\right)} & e^{-j\left(\theta_2+\frac{6\pi}{5}\right)} \\ e^{-j\theta_3} & e^{-j\left(\theta_3+\frac{6\pi}{5}\right)} & e^{-j\left(\theta_3+\frac{2\pi}{5}\right)} & e^{-j\left(\theta_3+\frac{8\pi}{5}\right)} & e^{-j\left(\theta_3+\frac{4\pi}{5}\right)} \\ e^{-j\theta_4} & e^{-j\left(\theta_4+\frac{8\pi}{5}\right)} & e^{-j\left(\theta_4+\frac{6\pi}{5}\right)} & e^{-j\left(\theta_4+\frac{4\pi}{5}\right)} & e^{-j\left(\theta_4+\frac{2\pi}{5}\right)} \end{bmatrix} \tag{3.86b}$$

$$T(\theta)=\frac{2}{6}\begin{bmatrix} 1/2 & 1/2 & 1/2 & 1/2 & 1/2 & 1/2 \\ e^{j\theta_1} & e^{j\left(\theta_1+\frac{\pi}{3}\right)} & e^{j\left(\theta_1+\frac{2\pi}{3}\right)} & e^{j(\theta_1+\pi)} & e^{j\left(\theta_1+\frac{4\pi}{3}\right)} & e^{j\left(\theta_1+\frac{5\pi}{3}\right)} \\ e^{j\theta_2} & e^{j\left(\theta_2+\frac{2\pi}{3}\right)} & e^{j\left(\theta_2+\frac{4\pi}{3}\right)} & e^{j(\theta_2)} & e^{j\left(\theta_2+\frac{2\pi}{3}\right)} & e^{j\left(\theta_2+\frac{4\pi}{3}\right)} \\ e^{j\theta_3} & e^{j(\theta_3+\pi)} & e^{j(\theta_3)} & e^{j(\theta_3+\pi)} & e^{j(\theta_3)} & e^{j(\theta_3+\pi)} \\ e^{j\theta_4} & e^{j\left(\theta_4+\frac{4\pi}{3}\right)} & e^{j\left(\theta_4+\frac{2\pi}{3}\right)} & e^{j(\theta_4)} & e^{j\left(\theta_4+\frac{4\pi}{3}\right)} & e^{j\left(\theta_4+\frac{2\pi}{3}\right)} \\ e^{j\theta_5} & e^{j\left(\theta_5+\frac{5\pi}{3}\right)} & e^{j\left(\theta_5+\frac{4\pi}{3}\right)} & e^{j(\theta_5+\pi)} & e^{j\left(\theta_5+\frac{2\pi}{3}\right)} & e^{j\left(\theta_5+\frac{\pi}{3}\right)} \end{bmatrix} \tag{3.87a}$$

$$T(\theta)^{-1}=\begin{bmatrix} 1/2 & 1/2 & 1/2 & 1/2 & 1/2 & 1/2 \\ e^{-j\theta_1} & e^{-j\left(\theta_1+\frac{\pi}{3}\right)} & e^{-j\left(\theta_1+\frac{2\pi}{3}\right)} & e^{-j(\theta_1+\pi)} & e^{-j\left(\theta_1+\frac{4\pi}{3}\right)} & e^{-j\left(\theta_1+\frac{5\pi}{3}\right)} \\ e^{-j\theta_2} & e^{-j\left(\theta_2+\frac{2\pi}{3}\right)} & e^{-j\left(\theta_2+\frac{4\pi}{3}\right)} & e^{-j(\theta_2)} & e^{-j\left(\theta_2+\frac{2\pi}{3}\right)} & e^{-j\left(\theta_2+\frac{4\pi}{3}\right)} \\ e^{-j\theta_3} & e^{-j(\theta_3+\pi)} & e^{-j(\theta_3)} & e^{-j(\theta_3+\pi)} & e^{-j(\theta_3)} & e^{-j(\theta_3+\pi)} \\ e^{-j\theta_4} & e^{-j\left(\theta_4+\frac{4\pi}{3}\right)} & e^{-j\left(\theta_4+\frac{2\pi}{3}\right)} & e^{-j(\theta_4)} & e^{-j\left(\theta_4+\frac{4\pi}{3}\right)} & e^{-j\left(\theta_4+\frac{2\pi}{3}\right)} \\ e^{-j\theta_5} & e^{-j\left(\theta_5+\frac{5\pi}{3}\right)} & e^{-j\left(\theta_5+\frac{4\pi}{3}\right)} & e^{-j(\theta_5+\pi)} & e^{-j\left(\theta_5+\frac{2\pi}{3}\right)} & e^{-j\left(\theta_5+\frac{\pi}{3}\right)} \end{bmatrix} \tag{3.87a}$$

The reference frame transformation produces n complex variables in the arbitrary reference frame for n variables in the phase variable system. However, it is observed that when n is odd, there is a zero sequence real component, (n-1)/2 forward rotating complex variable components which are complex conjugates of the remaining (n-1)/2 backward

rotating complex variable components. When n is even, there is a zero sequence and another zero-sequence real components, (n-2)/2 forward rotating complex variable components which are complex conjugates of the remaining (n-2)/2 backward rotating complex variable components. If the analysis is undertaken in the complex variable form, all the elements of the n x n complex variable transformations in (3.83-84) are required. However, if the analysis is done using the real variables, a n x n reference frame transformation matrix comprised of the zero sequence and the (n-1)/2 forward rotating components expressed in real variables (for n = odd) or the two zero sequence real components and the (n-2)/2 forward rotating complex variable components expressed in real variables (for n = even) is used. Further simplification is achieved by setting the reference frame speed as the rotor speed in which case the inductances of the rotor circuit in the model equations become invariant to the rotor position.

For the ABC stator winding set, the voltage equation transformed to the rotor reference frame becomes :

$$v_{qds1} = \left(T_{abc} R_{s1} T_{abc}^{-1}\right) \cdot i_{qds1} + T_{abc}\left(pT_{abc}^{-1}\right) \cdot \lambda_{qds1} + p\lambda_{qds1} \tag{3.88}$$

where, $v_{qds1} = T_{abc} v_{abc}$, $i_{qds1} = T_{abc} i_{abc}$, $i_{qdr} = T_r i_r$, $\lambda_{qds1} = T_{abc} L_{s1s1} T_{abc}^{-1} i_{qds1} + T_{abc} L_{s1r} T_r^{-1} i_{qdr}$.

Similarly, for the voltage equation of the XYZ winding set, the transformed equation to the rotor reference frame is given as :

$$v_{qds2} = \left(T_{xyz} R_{s2} T_{xyz}^{-1}\right) \cdot i_{qds2} + T_{xyz}\left(pT_{xyz}^{-1}\right) \cdot \lambda_{qds2} + p\lambda_{qds2} \tag{3.89}$$

where, $v_{qds2} = T_{xyz} v_{xyz}$, $i_{qds2} = T_{xyz} i_{xyz}$, $\lambda_{qds2} = T_{xyz} L_{s2s2} T_{xyz}^{-1} i_{qds2} + T_{xyz} L_{s2r} T_r^{-1} i_{qdr}$.

Rotor voltage equation:

$$0 = T_r R_r T_r^{-1} i_{qdr} + p\lambda_{qdr} \tag{3.90}$$

where, $\lambda_{qdr} = T_r L_{rr} T_r^{-1} i_{qdr} + T_r L_{rs1} T_{abc}^{-1} i_{qds1} + T_r L_{rs2} T_{xyz}^{-1} i_{qds2}$

Finally the equation for the electromagnetic torque expressed in terms of the transformed variables is :

$$T_e = -i_{qds1}{}^T \cdot \left[ \left(T_{abc}^{-1}\right)^T \frac{\partial L_{s1r}}{\partial \theta_{rm}} T_r^{-1} \right] \cdot i_{qdr} - i_{qds2}{}^T \cdot \left[ \left(T_{xyz}^{-1}\right)^T \frac{\partial L_{s2r}}{\partial \theta_{rm}} T_r^{-1} \right] \cdot i_{qdr} \qquad (3.91)$$

## 3.9 Simulation Results

The dual stator winding induction machine is treated as two independent machines coupled by the rotor shaft with only the fundamental component considered. The system can be simulated using MATLAB/SIMULINK. All the inductances except the leakage inductances are calculated on-line.

In the first case, both of the windings are working as motors. Some of the system parameters used for the simulation are listed in Table 3.1.

Table 3.1 Designed machine parameters

| | ABC winding | XYZ winding |
|---|---|---|
| Number of pole | 2 | 6 |
| Stator resistance ($\Omega$) | 0.5 | 0.3 |
| Number of coils per slot | 36 | 71 |
| Stator leakage inductance (H) | 0.013 | 0.009 |
| Rotor bar resistance ($\Omega$) | $1.45\times10^{-5}$ | |
| Rotor bar inductance (H) | $4.57\times10^{-8}$ | |
| End ring segment resistance ($\Omega$) | $1.0\times10^{-6}$ | |
| End ring segment inductance (H) | $9.6\times10^{-9}$ | |

The no-load starting transient simulation results are shown in Figure 3.10 when the machine is fed with voltages satisfying the constant voltage/Hertz open-loop control algorithm in which the ratios of the frequency of the 6-pole stator winding set to those of the 2-pole stator winding set is 3. The frequencies of the ABC (2-pole) and XYZ (6-pole) stator winding sets are 30 Hz and 90 Hz respectively. The line-to-line voltages of the ABC (2-pole) and XYZ (6-pole) stator winding set are 67 V and 202 V respectively. The rotor speed starts from zero and ramps up to steady state smoothly. The transient current is big, but all the currents are reduced to almost zero at the no load steady state condition. During the steady-state operation, a 3Nm load torque is added to the machine to check the dynamic response of the system. The simulation results of the dynamic response are shown in Figure 3.11. It is observed that the ABC stator winding set contributes a smaller percentage of the generated electromagnetic torque to meet the load demand. This torque distribution is determined by the machine design.

Three of the rotor bar currents are chosen for illustration. The rotor bar currents during the starting process are shown in the Figure 3.12 and the rotor bar currents during the steady state at loaded condition are shown in the Figure 3.13.

In the second case, the frequency of the input voltages of the ABC winding set is set to 27 Hz while that of the XYZ winding set is set at 90 Hz, both operating with the same Voltz/Hz ratio. It is observed that the 2-pole (ABC) winding set is generating with negative electromagnetic torque, the XYZ (6-pole) winding set needs to provide load torque and counteract the negative torque produced by the ABC winding set. The simulation results for both the starting process and dynamic response are shown in Figure 3.14 and Figure 3.15 respectively. Three of the rotor bar currents are shown in Figure

3.16 and Figure 3.17. It is found from the simulation that the rotor bar currents are almost zero under no-load condition. However, under the load condition, the rotor bar current is closed to sinusoidal waveform.

## 3.10 Air Gap Field Calculation

Finite Element Analysis (FEA) is the favored method of plotting the magnetic fields in various parts of electric machines, most especially, the flux density of the air gap. The calculation time for FEA is long and involved if it is required to generate sufficient performance data. Using the stator winding and rotor bar currents obtained from the computer simulation results set forth in Section 8 and the winding functions of the stator windings and rotor loops, the air gap magnetic field contributions from all the stator windings and rotor bars can be calculated using (3.31). This approach, augmented with the B-H curve of the core magnetic material to approximately account for the saturation of the air-gap flux linkage, enables the estimation of the air gap flux density.

When the machine is running under rated load at steady state condition, at any instant time, the stator currents and rotor loop currents can be found in the full model simulation. From the rotor model, the bar current is actually the subtraction of the two adjacent rotor loops that share that rotor bar.

At an instant time, the phase currents of the ABC winding set are $i_a = -1.03\,A$, $i_b = 0.52\,A$ and $i_c = 0.51\,A$ while the phase currents of the XYZ winding set are given as $i_x = 1.65\,A$, $i_y = 0.21\,A$ and $i_z = -1.86\,A$. Then the total air gap flux density and its components are shown in Figures 3.18-3.24.

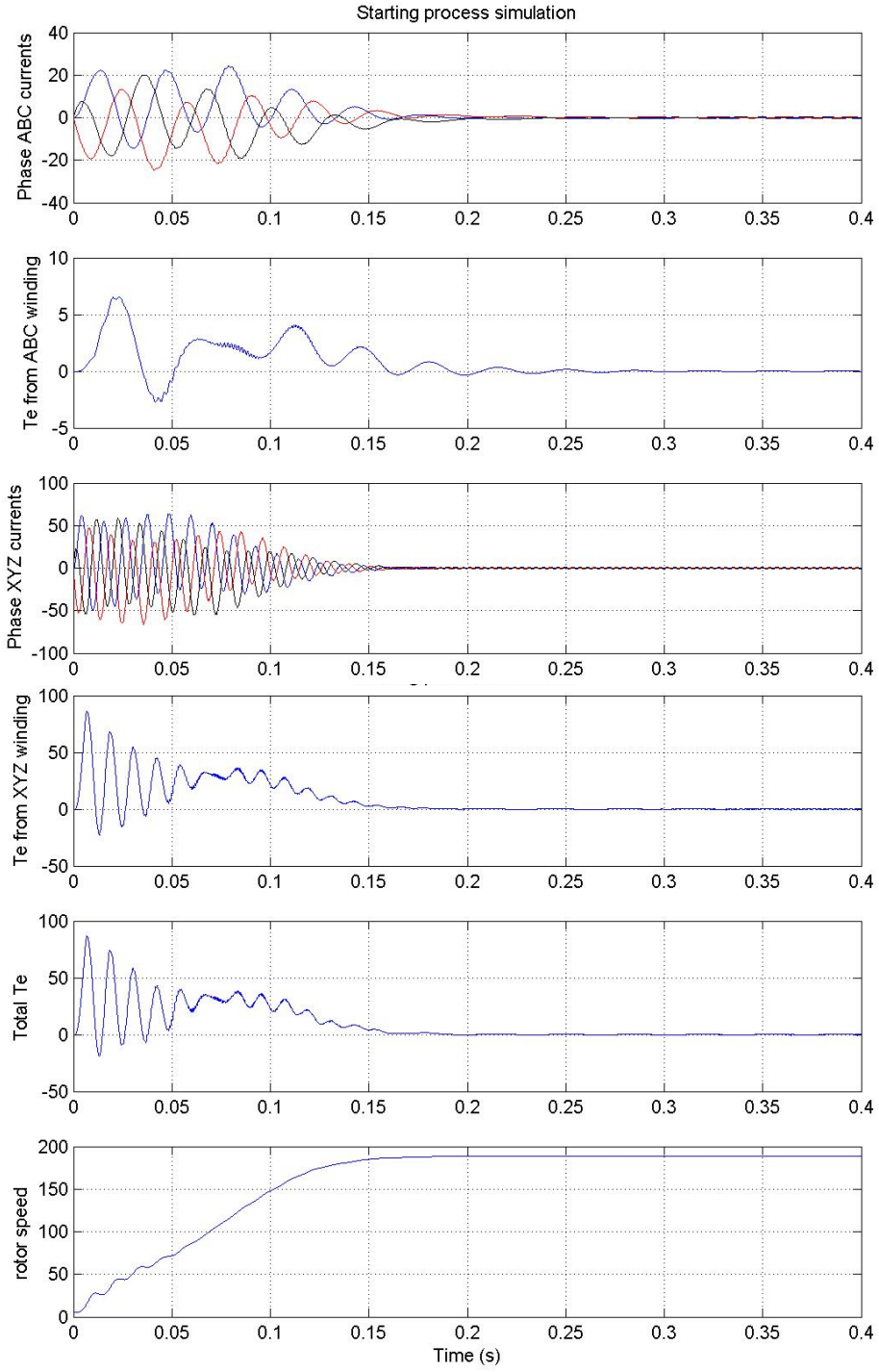


Figure 3.10 The simulation of the starting process of the dual stator winding induction machine, a) phase ABC currents, b) electromagnetic torque from ABC windings, c) phase XYZ currents, d) electromagnetic torque from XYZ windings; e) total electromagnetic torque, f) rotor speed.

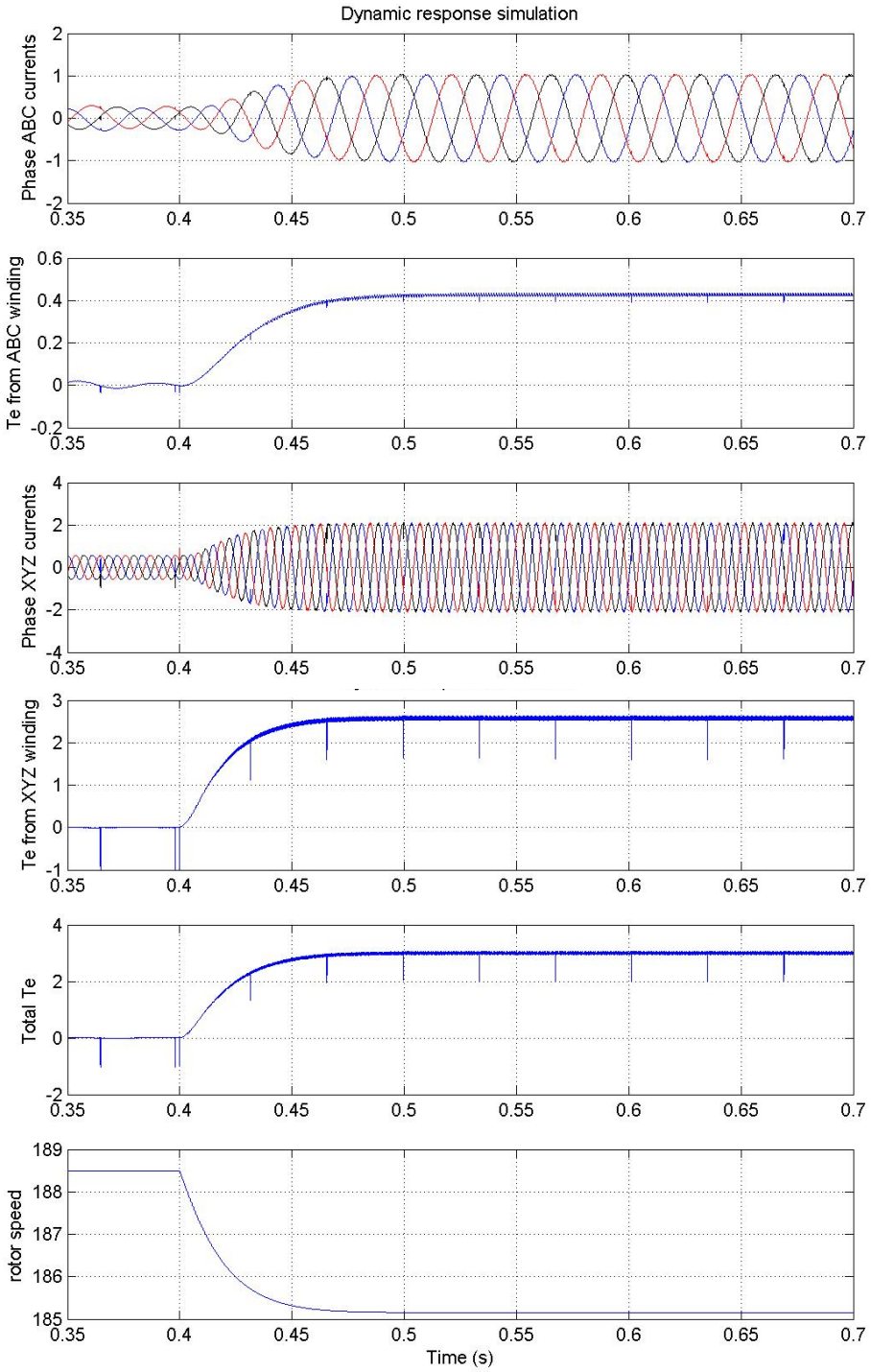


Figure 3.11 The simulation of the dynamic response of the dual stator winding induction machine, a) phase ABC currents, b) electromagnetic torque from ABC windings, c) phase XYZ currents, d) electromagnetic torque from XYZ windings; e) total electromagnetic torque, f) rotor speed.

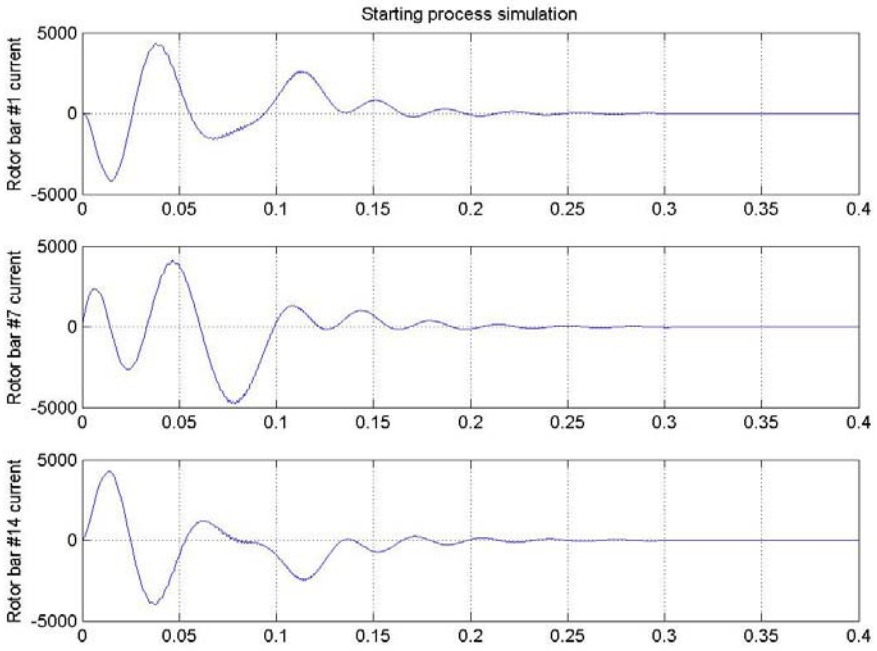


Figure 3.12 Rotor bar currents during the starting process, a) #1 rotor bar current, b) #7 rotor bar current, c) #14 rotor bar current.

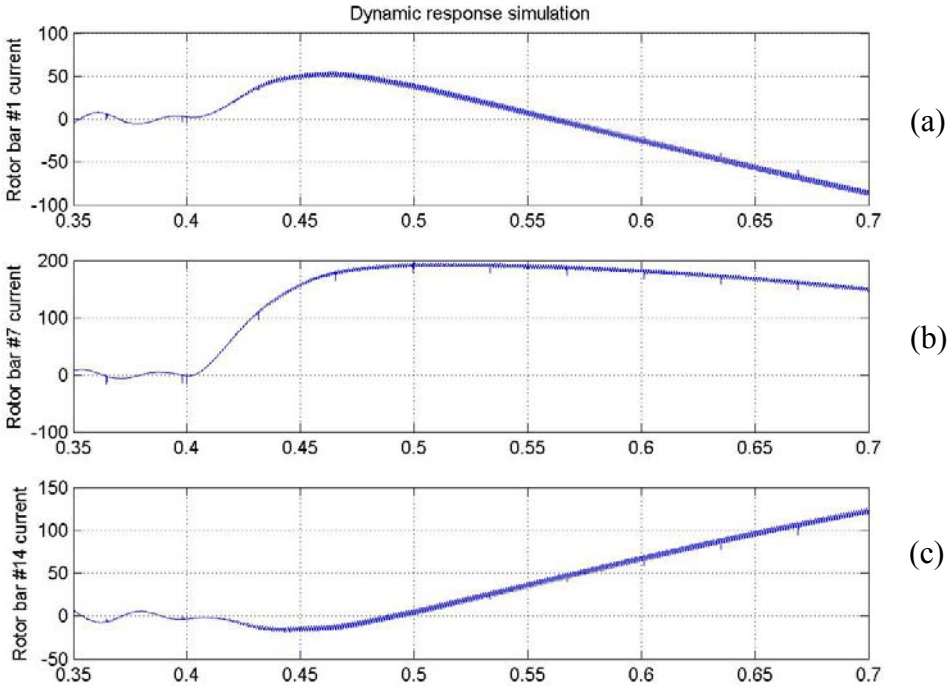


Figure 3.13 Rotor bar currents during the steady state at rated load condition, a) #1 rotor bar current, b) #7 rotor bar current, c) #14 rotor bar current.

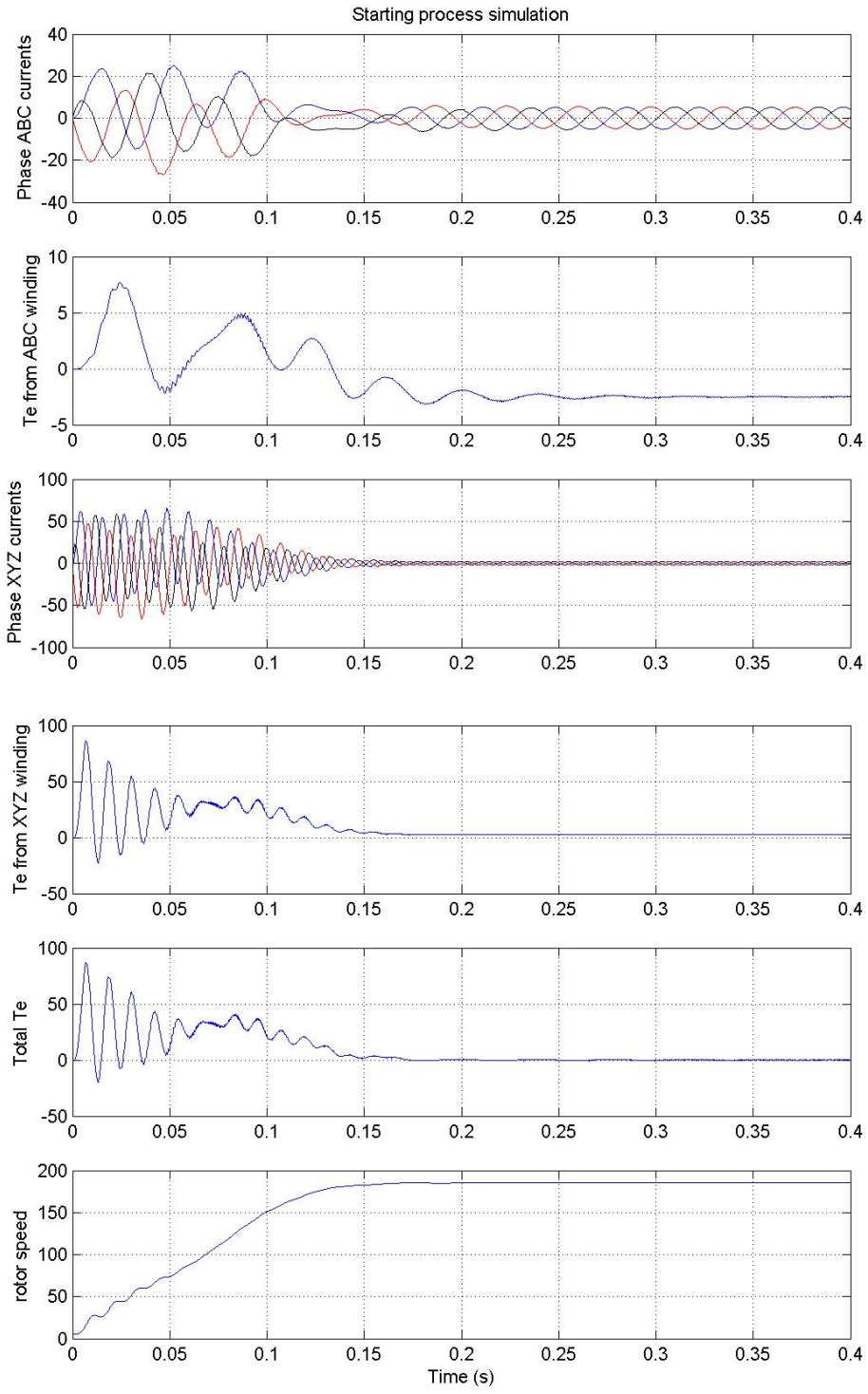


Figure 3.14 The simulation of the starting process of the dual stator winding induction machine, a) phase ABC currents, b) electromagnetic torque from ABC windings, c) phase XYZ currents, d) electromagnetic torque from XYZ windings; e) total electromagnetic torque, f) rotor speed.

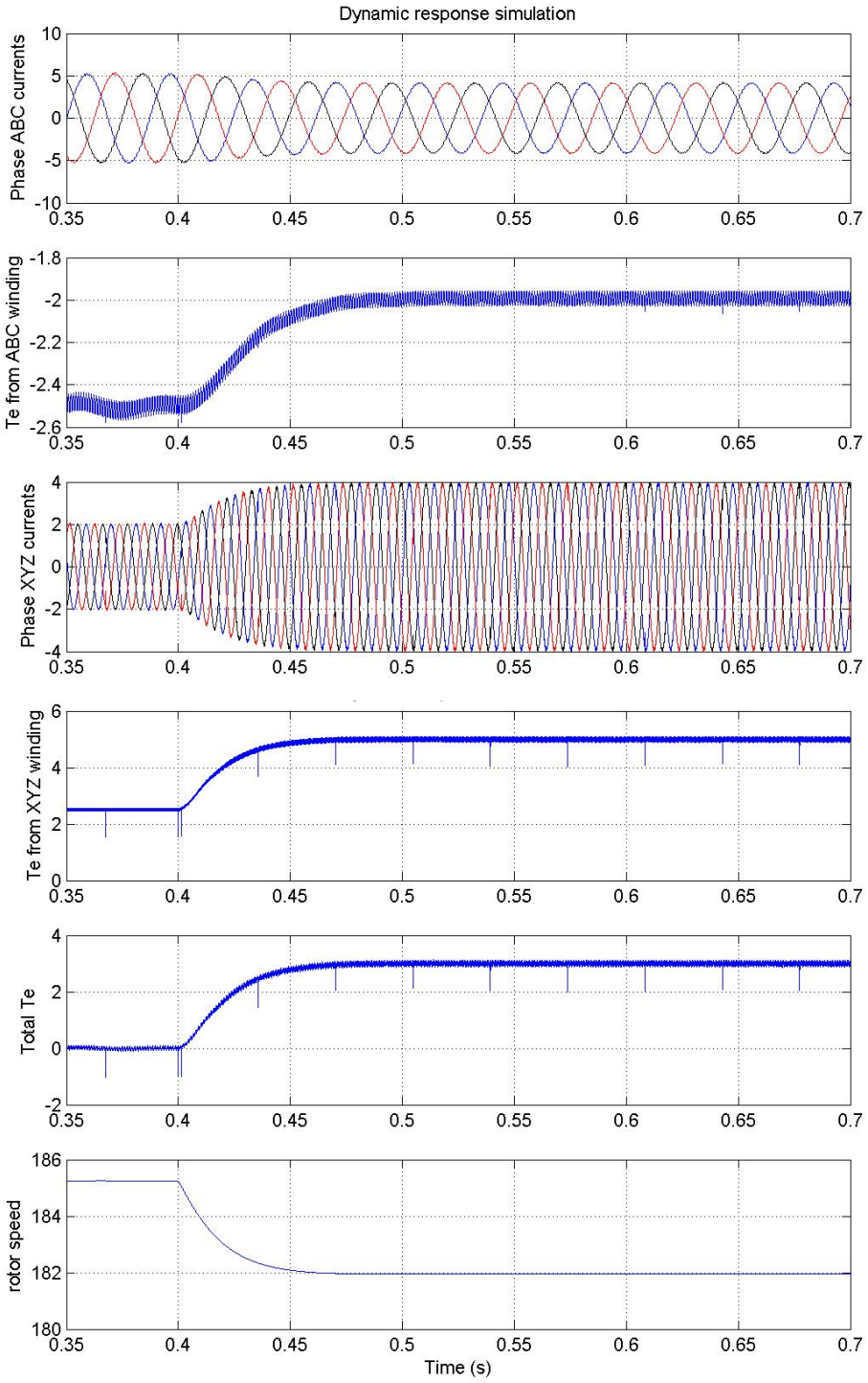


Figure 3.15 The simulation of the dynamic response of the dual stator winding induction machine, a) phase ABC currents, b) electromagnetic torque from ABC windings, c) phase XYZ currents, d) electromagnetic torque from XYZ windings; e) total electromagnetic torque, f) rotor speed.

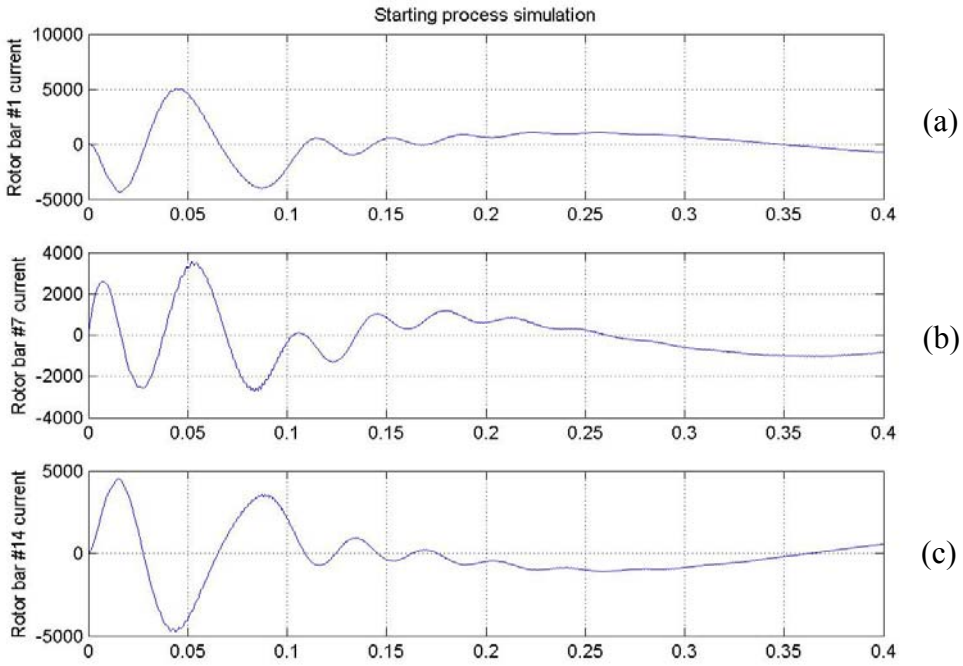


Figure 3.16 Rotor bar currents during the starting process, a) #1 rotor bar current, b) #7 rotor bar current, c) #14 rotor bar current.

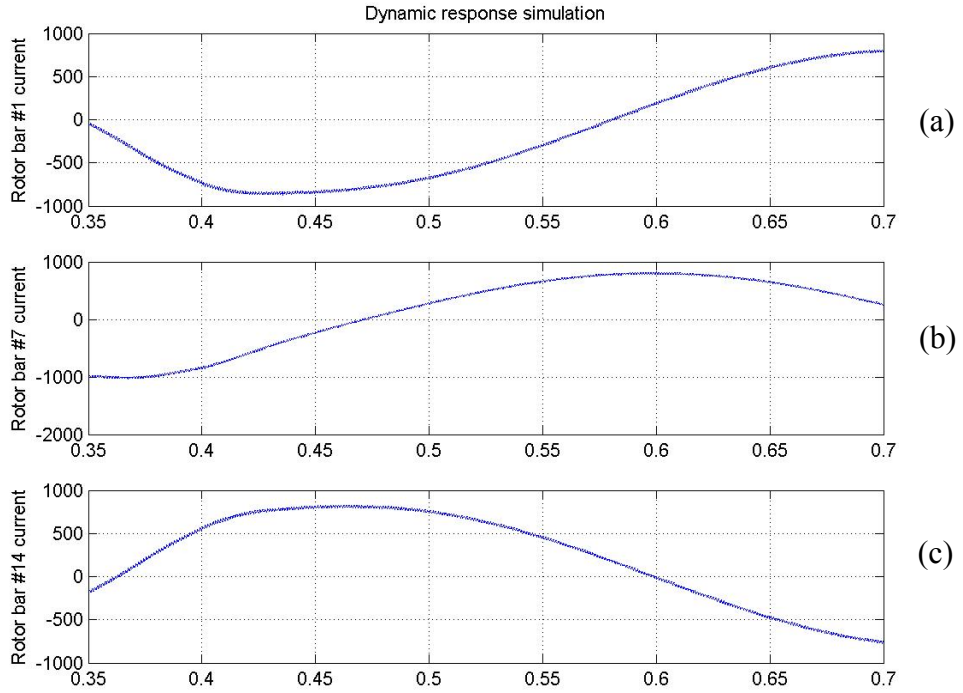


Figure 3.17 Rotor bar currents during the steady state at rated load condition, a) #1 rotor bar current, b) #7 rotor bar current, c) #14 rotor bar current.

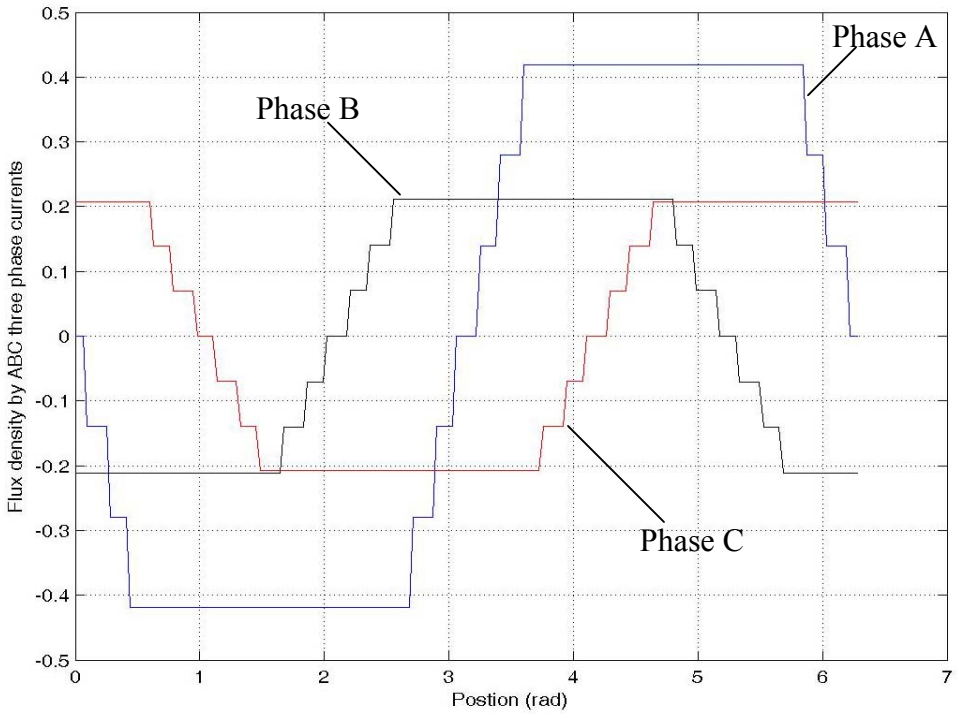


Figure 3.18 Air gap flux density contributed by each phase of the ABC winding set

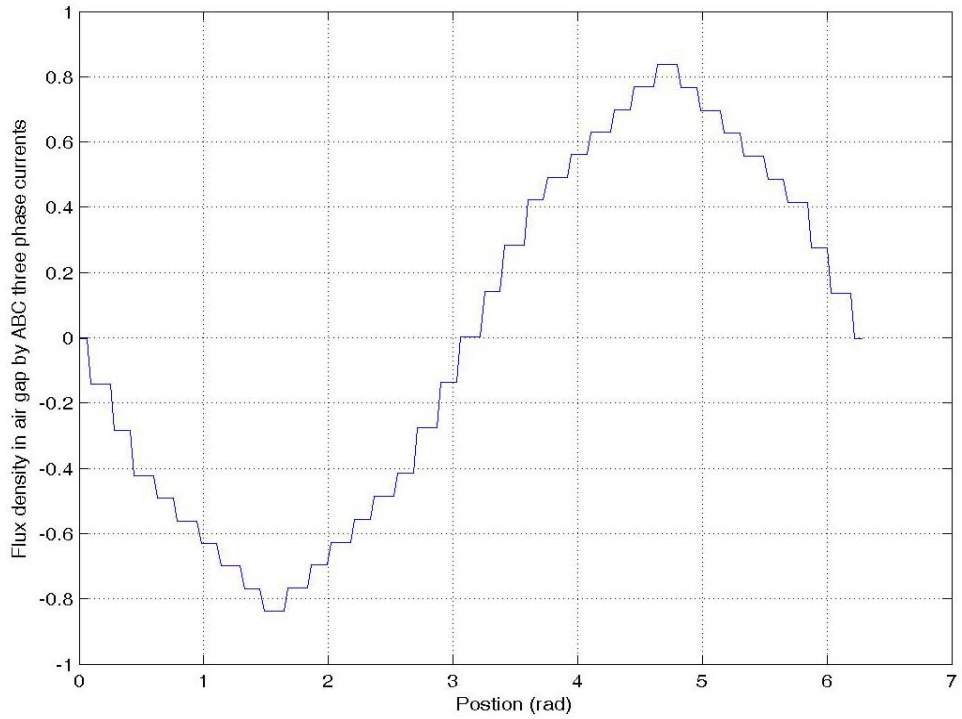


Figure 3.19 Air gap flux density contributed by the ABC winding set

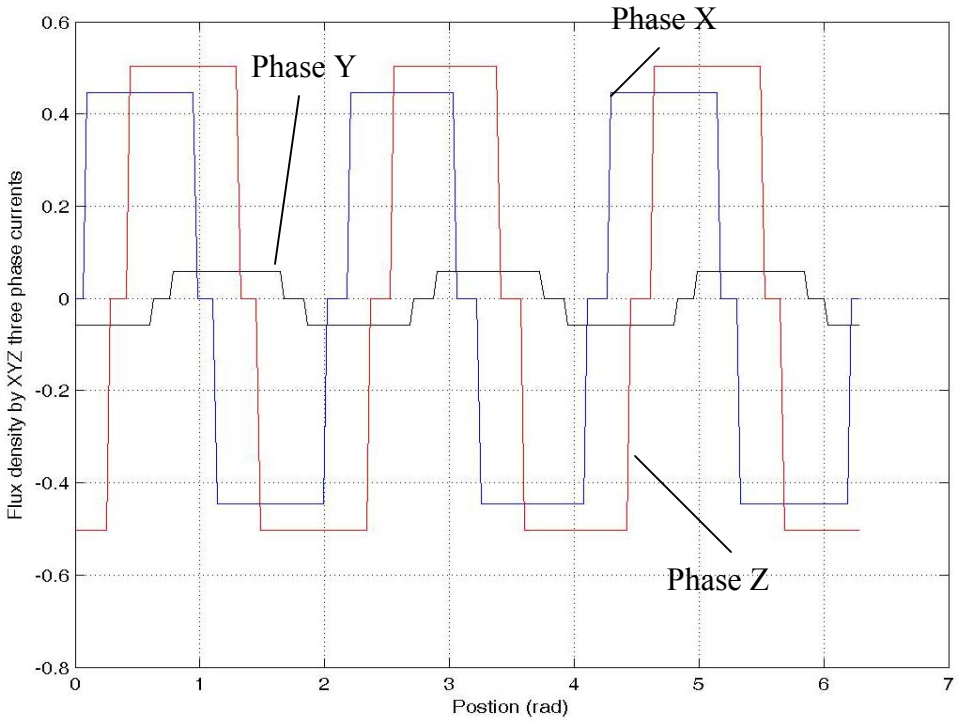


Figure 3.20 Air gap flux density contributed by each phase of the XYZ winding set

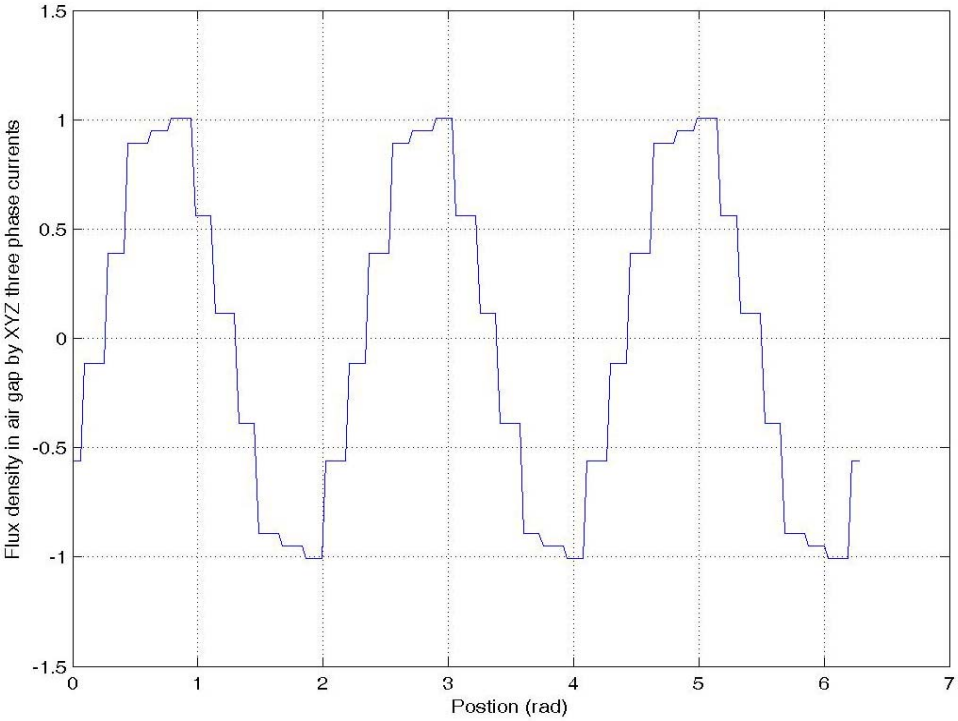


Figure 3.21 Air gap flux density contributed by the XYZ winding set

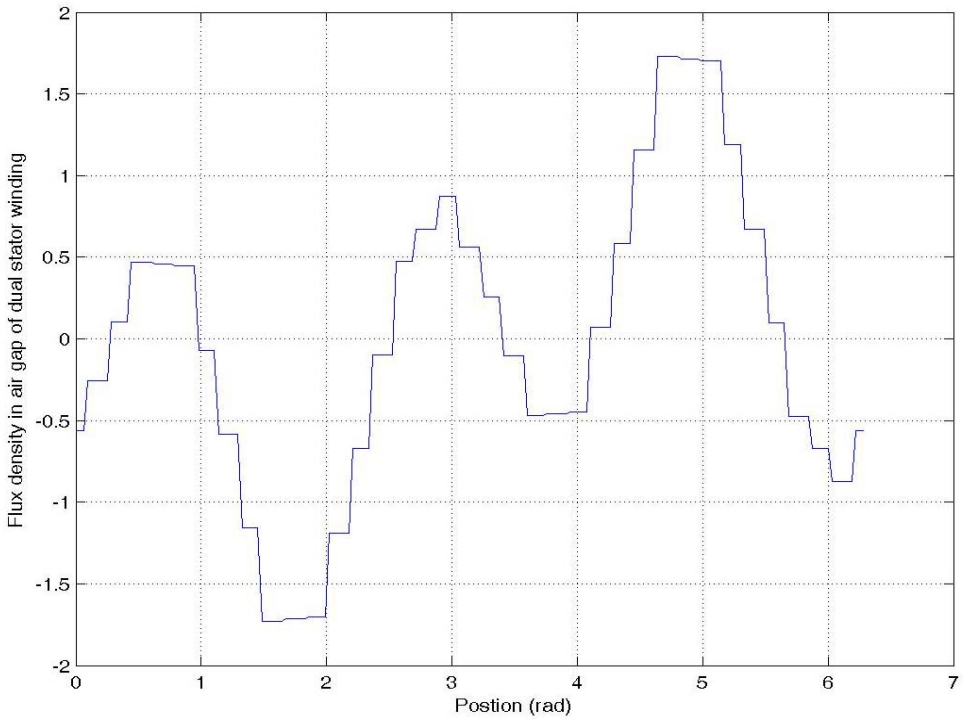


Figure 3.22 Air gap flux density contributed by the two stator winding sets

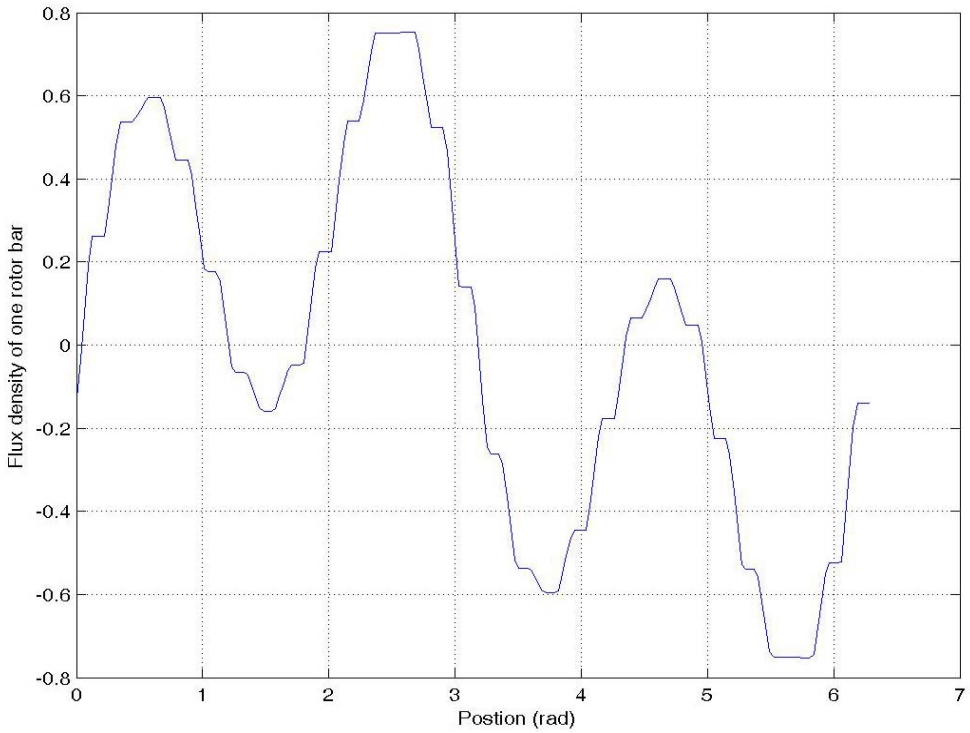


Figure 3.23 Air gap flux density contributed by the rotor currents

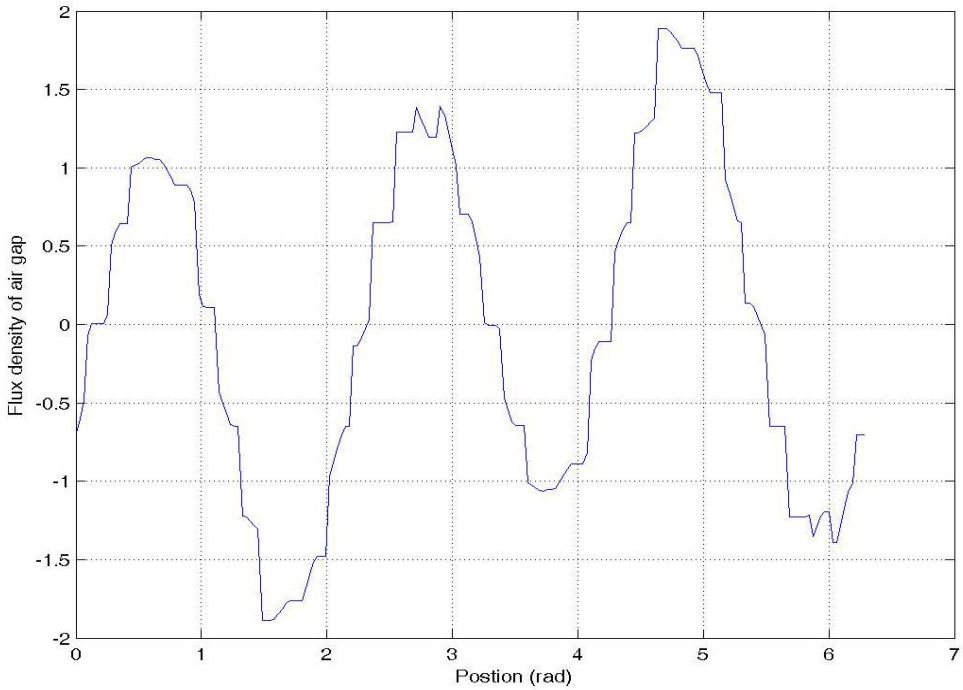


Figure 3.24 Total air gap flux density without considering saturation

The air gap flux density shown above is the one without considering the saturation factor. The saturation is included by implementing the B-H curve of the material given in Figure 3.25.

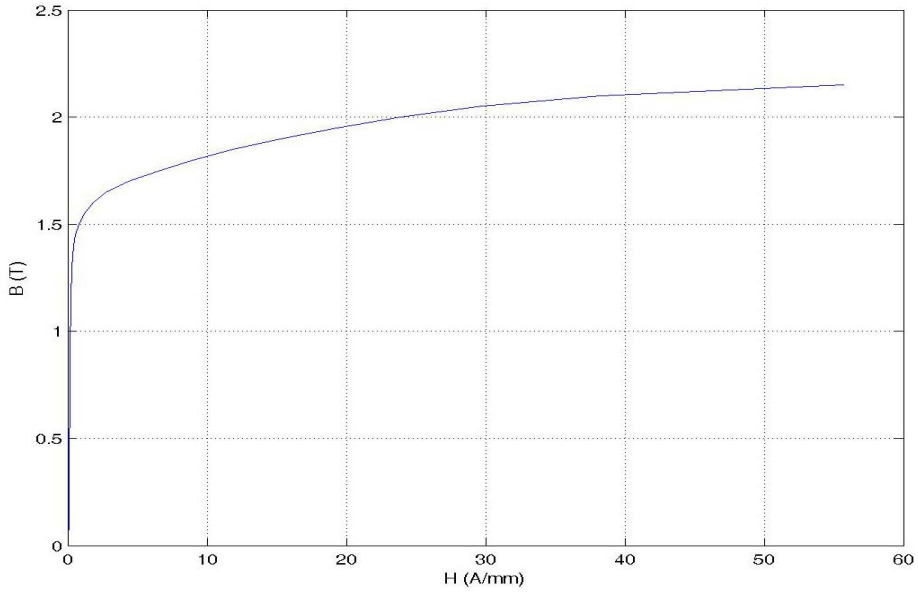


Figure 3.25 The B-H curve of the steel

From the B-H curve, the relationship between the linear flux density and the saturated flux density is shown in Figure 3.26. The blue curve is the actual one calculated from the material data and the red curve is the function approximation that is used to approximate the actual data in the simulation. Flux density with consideration the saturation effect given in Figure 3.27 is used to compare the results.

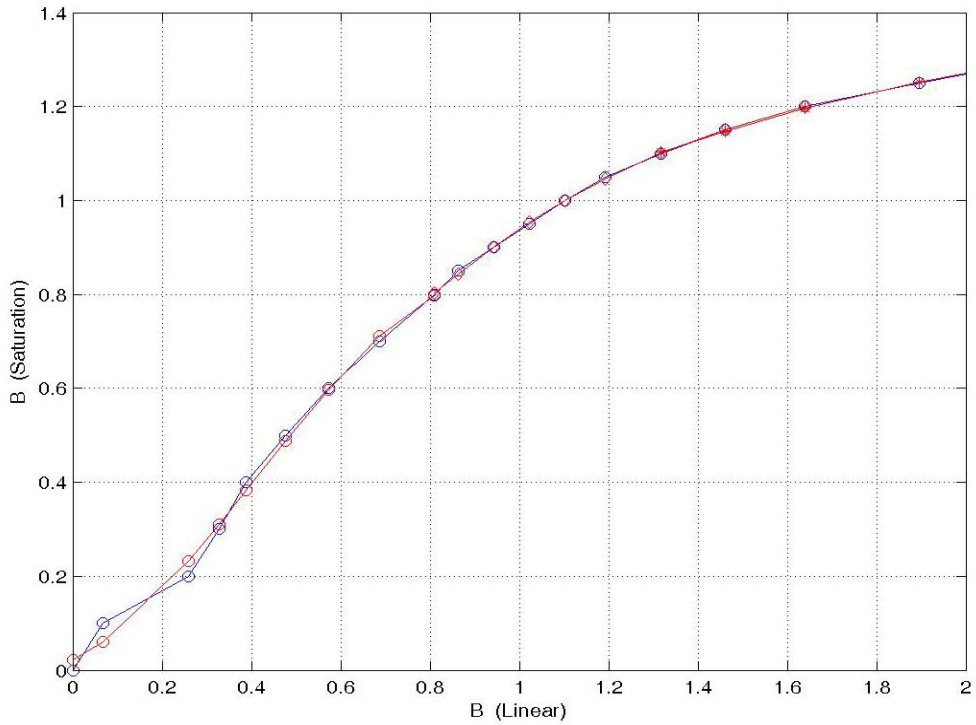


Figure 3.26 The relationship between the linear and saturated flux density

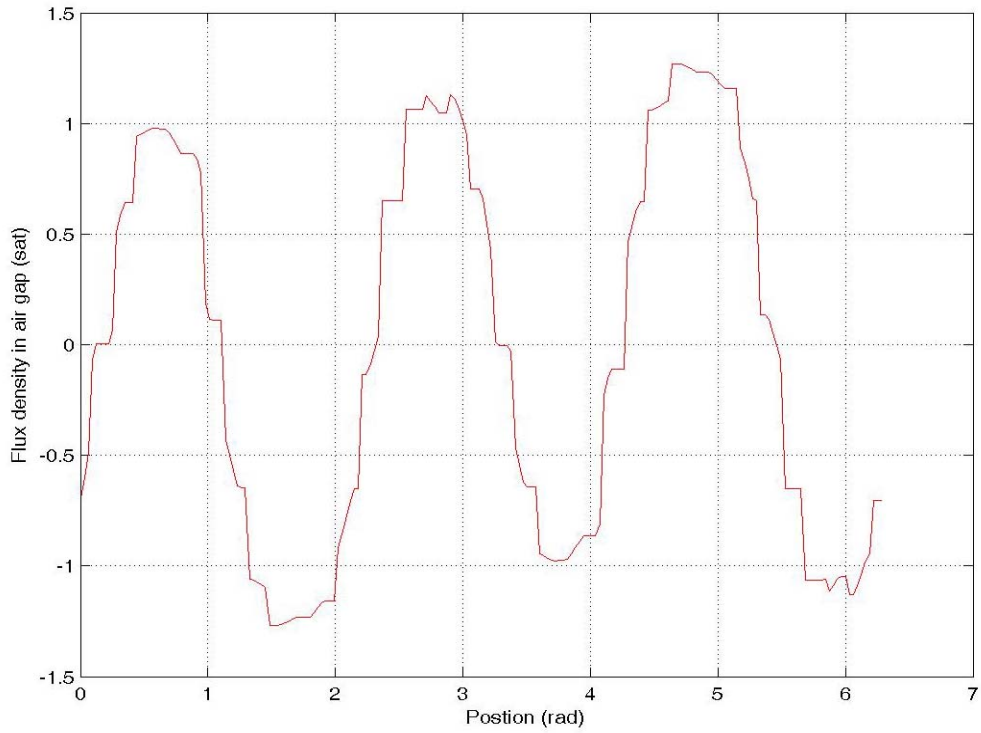


Figure 3.27 The air gap flux density considering the saturation

The corresponding finite element analysis has also been done to check the results obtained from the winding function method. The finite element analysis result for the XYZ winding set is slightly smaller than the one found from the winding function method since in the winding layout, the XYZ winding are arranged in the second layer which is far from the rotor. It also proves that the winding function method cannot adequately account for the distance to the air gap or the winding distributed in different layer. In addition, the slot effect cannot be seen in the simulation because the slot opening affection is not included in the winding function method. If the slot opening is included in the analysis, this method will be able to give a better result to approximate the actual air gap flux density.

Except for what has been mentioned above, the comparison clearly shows that the full model simulation in addition with the winding function method can approximate the air gap flux density very well.

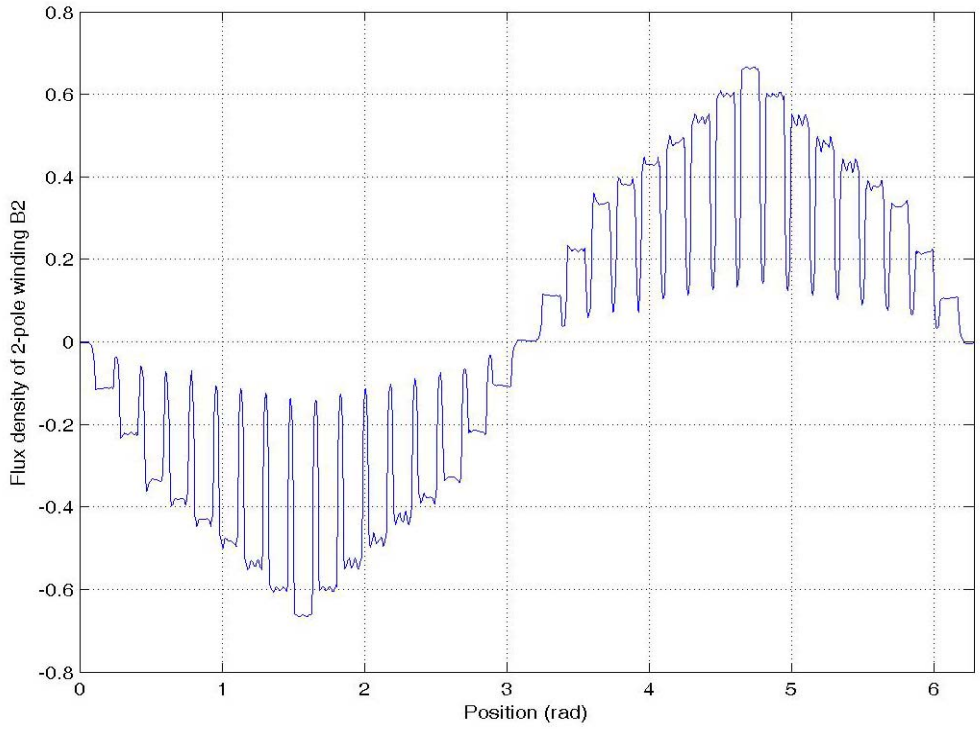


Figure 3.28 Air gap flux density contributed by the ABC winding set using FEA method

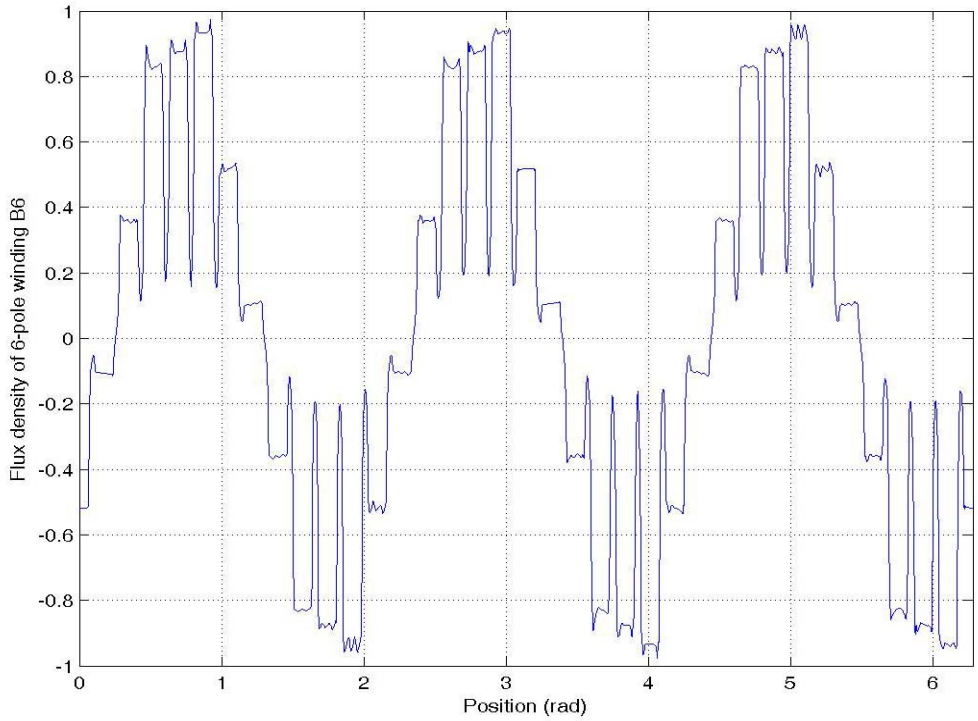


Figure 3.29 Air gap flux density contributed by the XYZ winding set using FEA method

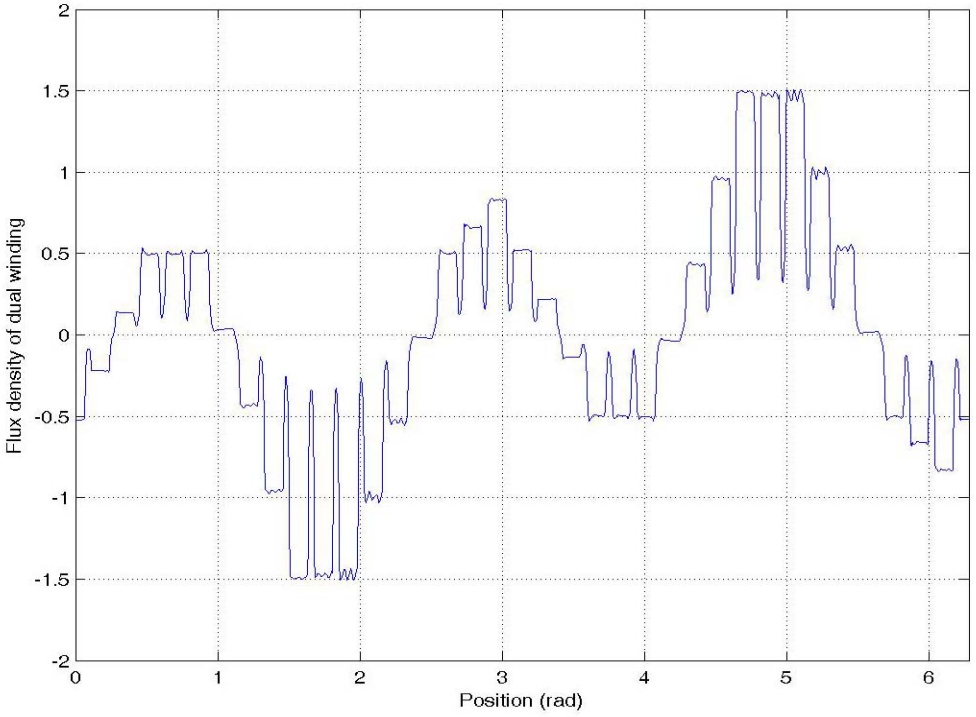


Figure 3.30 Air gap flux density contributed by two stator winding sets using FEA method

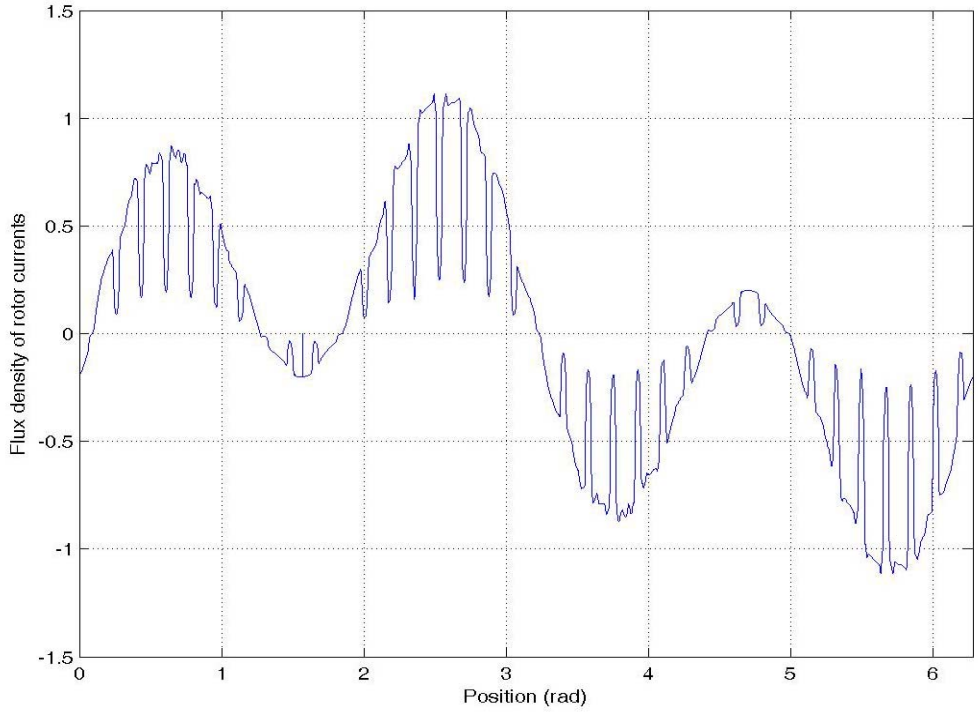


Figure 3.31 Air gap flux density contributed by rotor currents using FEA method

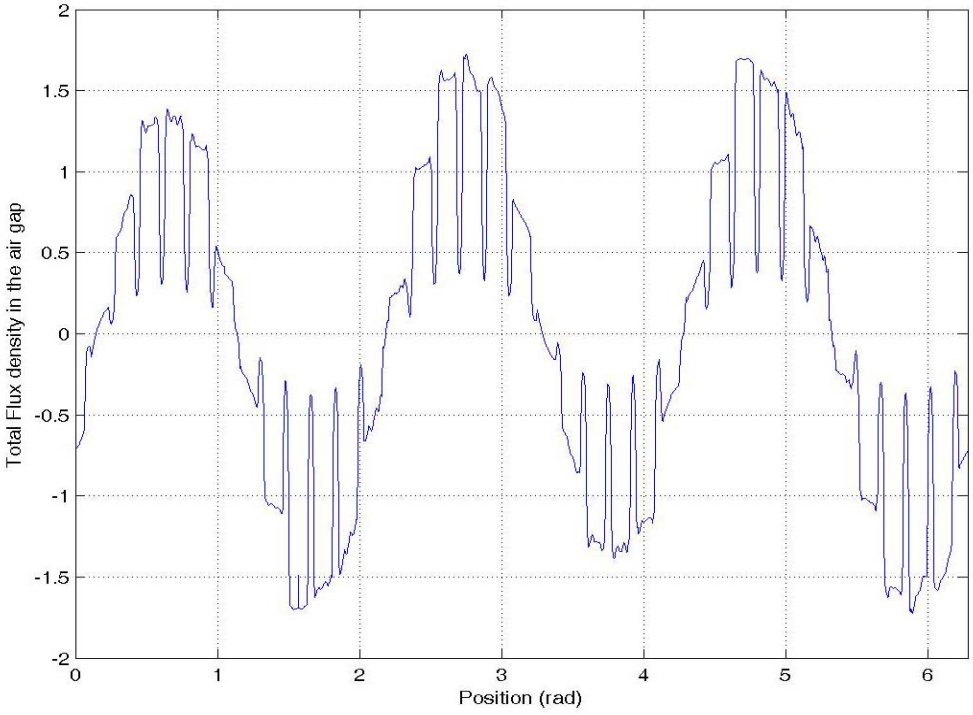


Figure 3.32 Air gap flux density without considering saturation using FEA method

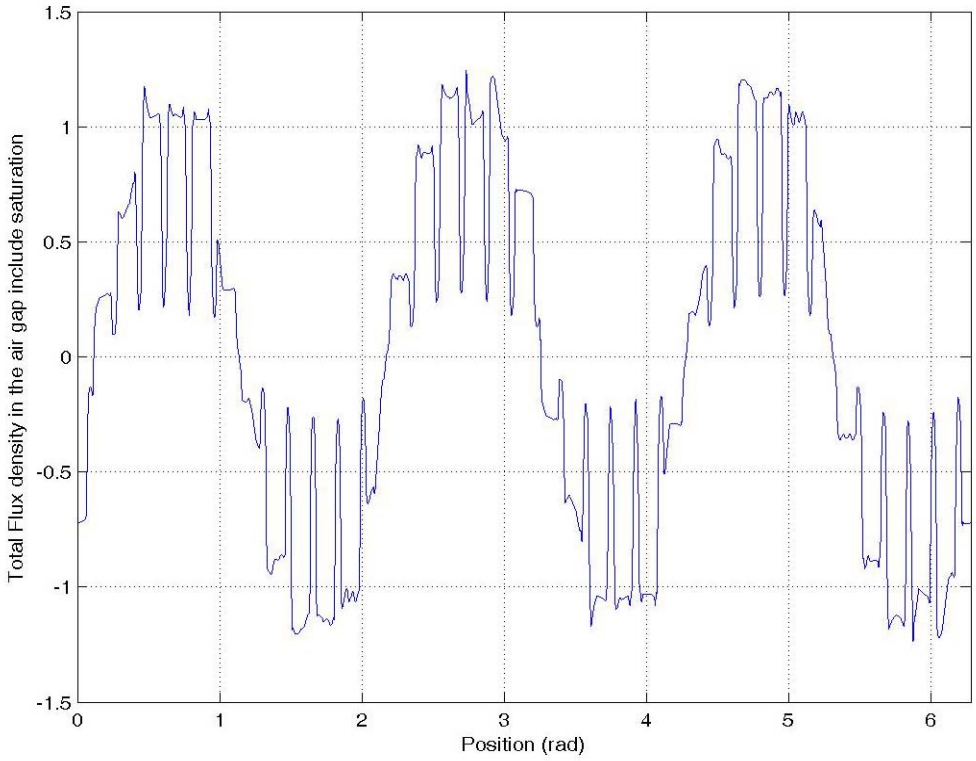


Figure 3.33 Air gap flux density include saturation using FEA method

The air gap flux density of the experimental machine was measured with search coils when both of the stator windings are excited with the same voltages and frequencies used in the computer simulations of Figure 3.10. Three search coils were inserted in the stator slots: one has a full coil pitch for the two-pole stator winding set, the second also has a full-pitch span for the six-pole winding set while the third is placed to measure flux density in the stator yoke. In Figure 3.34, the flux densities are shown when the machine operates in the linear magnetic region or no load. When the machine is loaded to the rated torque, the air gap flux density profile changes to Figure 3.35.

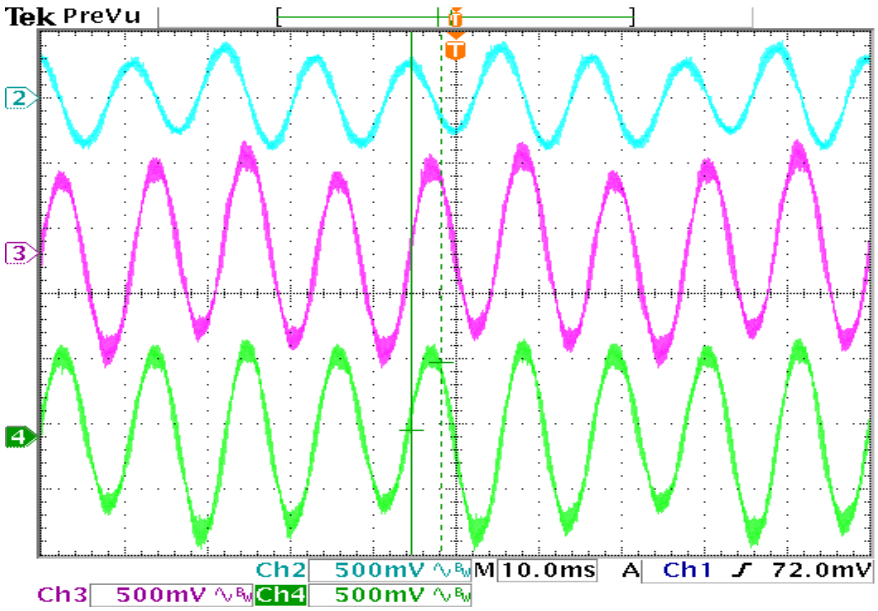


Figure 3.34 Measured flux densities of the dual stator winding induction machine at no-load condition. From top: (2) stator core flux density (0.76 Tesla/div), (3) output of a searching coil with two-pole full pitch (0.86 Tesla/div), (4) output of a searching coil with six-pole full pitch (0.86 Tesla/div).

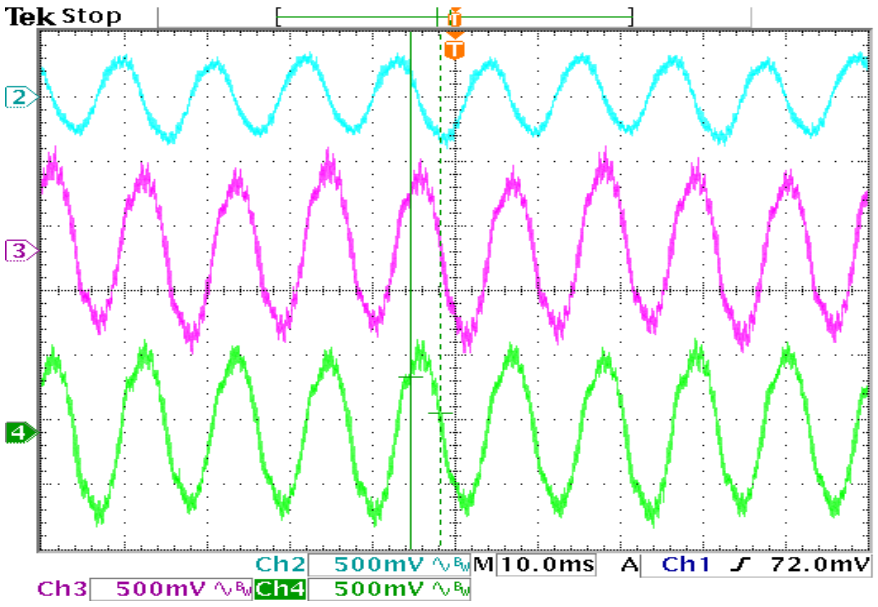


Figure 3.35 Measured flux densities of the dual stator winding induction machine at full load condition. From top: (2) stator core flux density (0.76 Tesla/div), (3) output of a searching coil with two-pole full pitch (0.86 Tesla/div), (4) output of a searching coil with six-pole full pitch (0.86 Tesla/div).

All the waveforms shown above are the flux density in the air gap at an instant of time. How the flux density changes with time can be seen in the following 3D figures 3.36-3.409, from which it is found that as time passes, the flux density in the air gap keeps the same shape but moves around the inner surface of the stator.

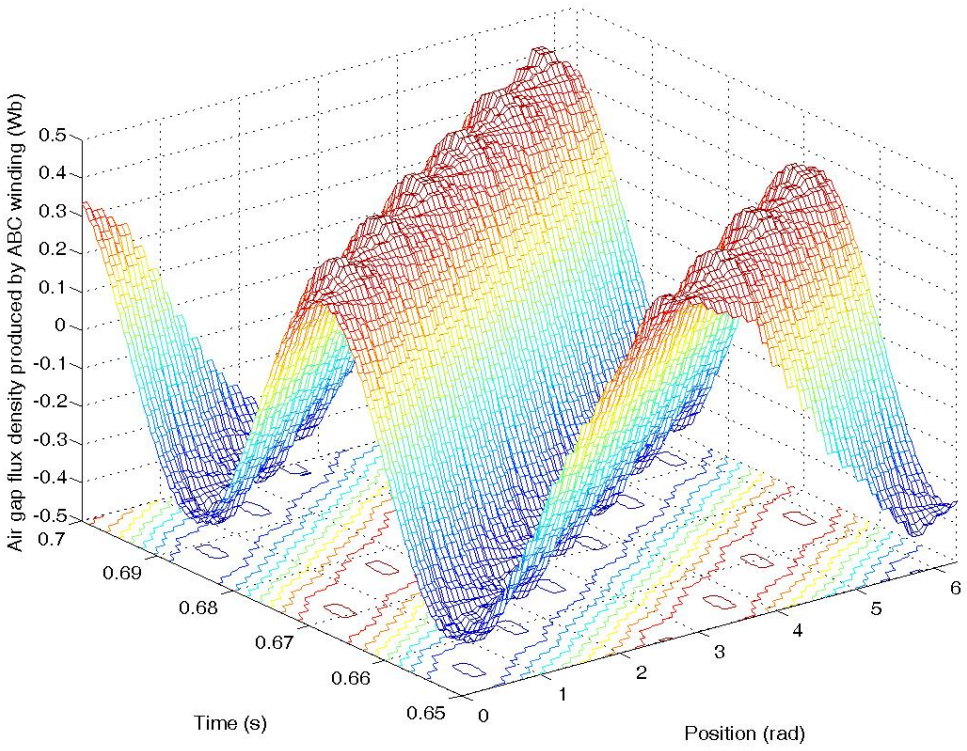


Figure 3.36 Air gap flux density produced by the ABC winding set

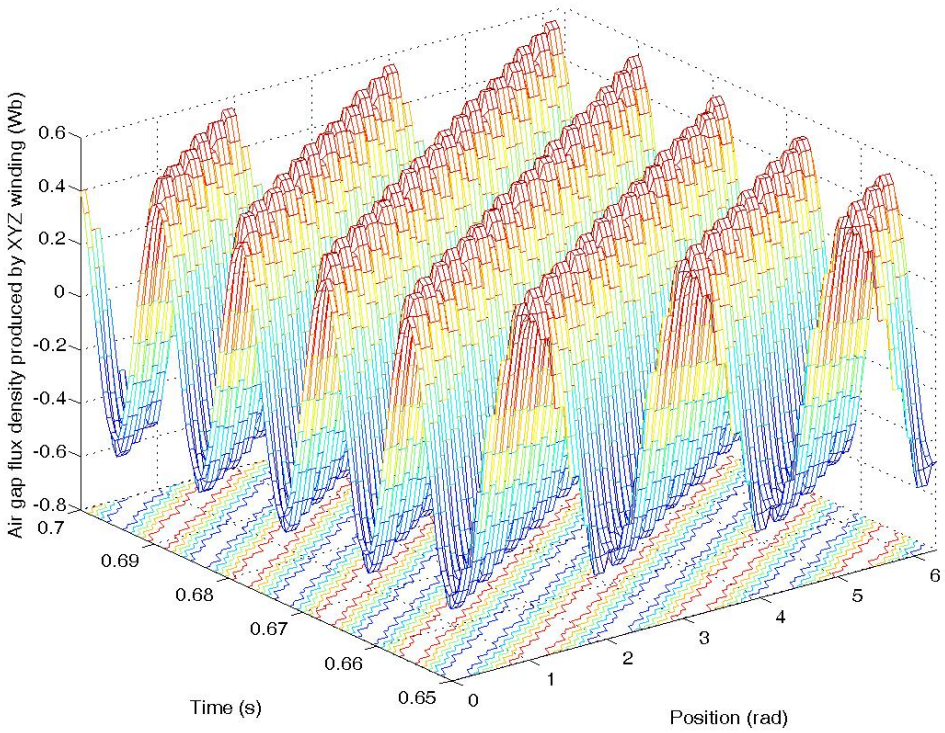


Figure 3.37 Air gap flux density produced by the XYZ winding set

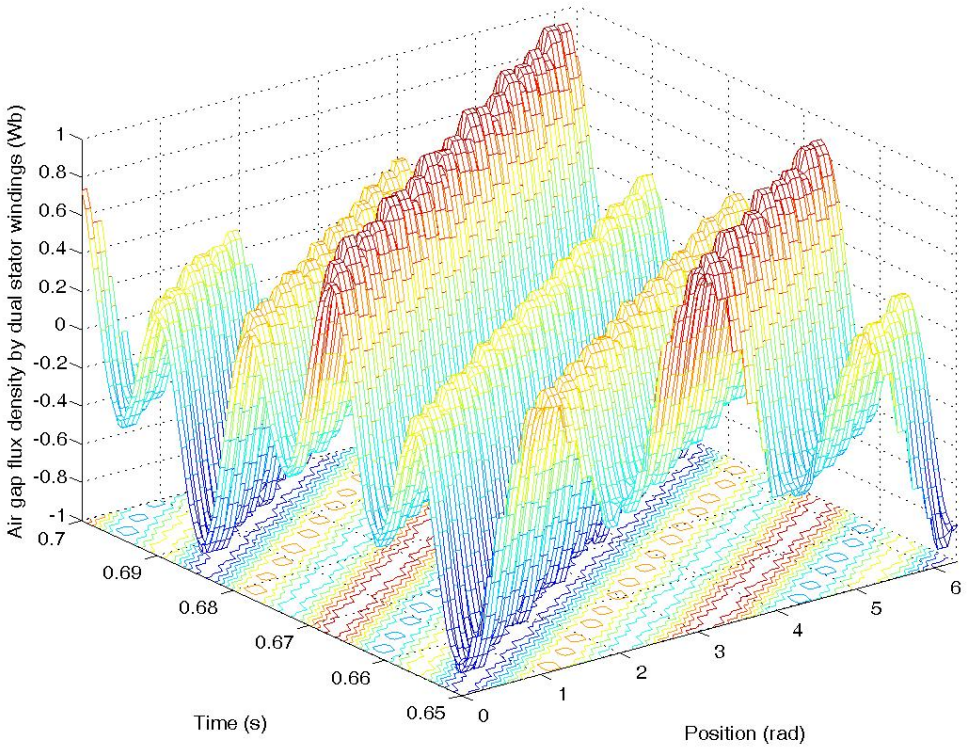


Figure 3.38 Air gap flux density produced by the two stator winding sets

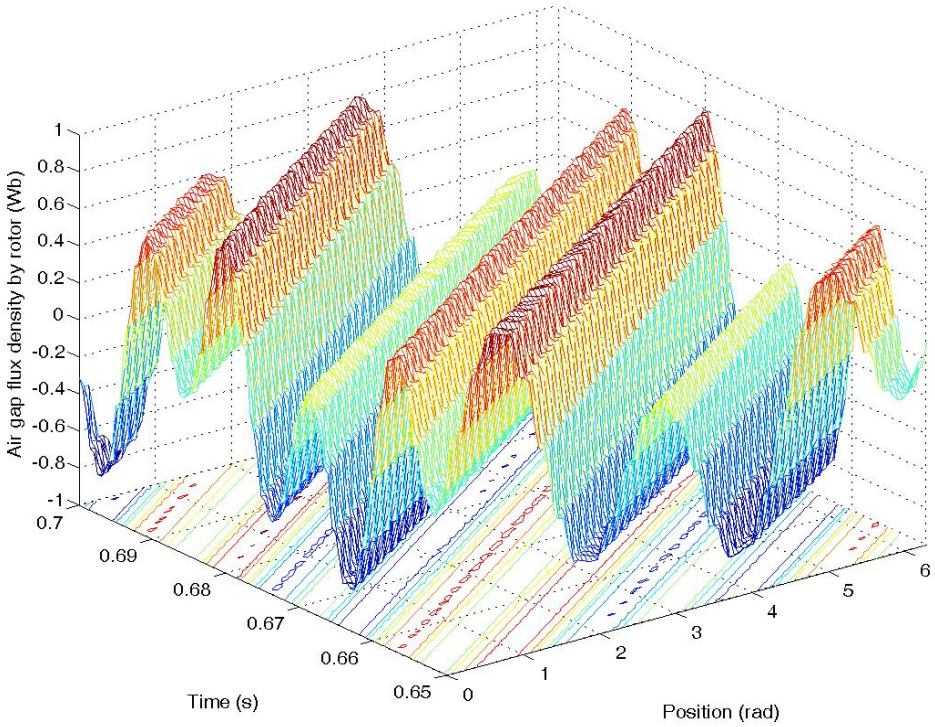


Figure 3.39 Air gap flux density produced by the rotor currents

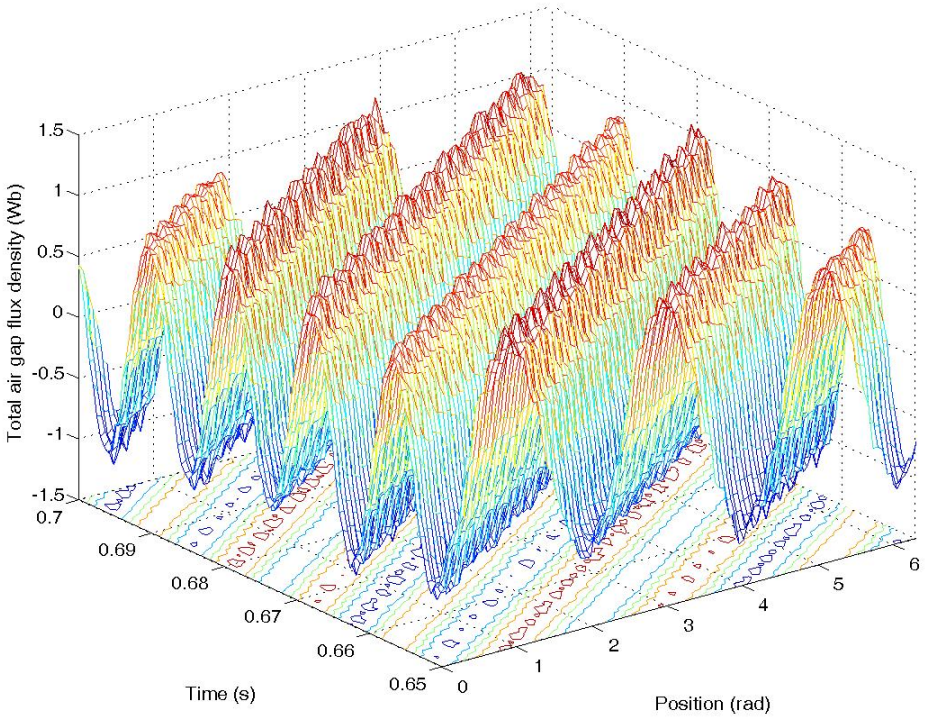


Figure 3.40 Total air gap flux density in the dual winding induction machine

The Fourier analysis results of the field plots obtained using the winding function approach are shown in Figure 3.41-3.47. The normalized spectrum of the air gap flux density contributed by the two stator winding sets is shown in Figure 3.41-3.44, in which the frequency of the fundamental component of the ABC winding set is one while the frequency of the fundamental component of the XYZ winding set is three. In Figure 3.41 and 3.42, the fundamental component is reduced 10 times to highlight the other harmonic components. The spectrum of the air gap flux density contributed by the rotor currents and the total air gap flux density are shown in Figure 3.45-3.47. Two major frequencies and their harmonic components in the air gap are significant in those figures. The comparisons between the spectrum with and without the saturation effect show that saturation increases the magnitudes of 3$^{rd}$ harmonic components of both winding sets.

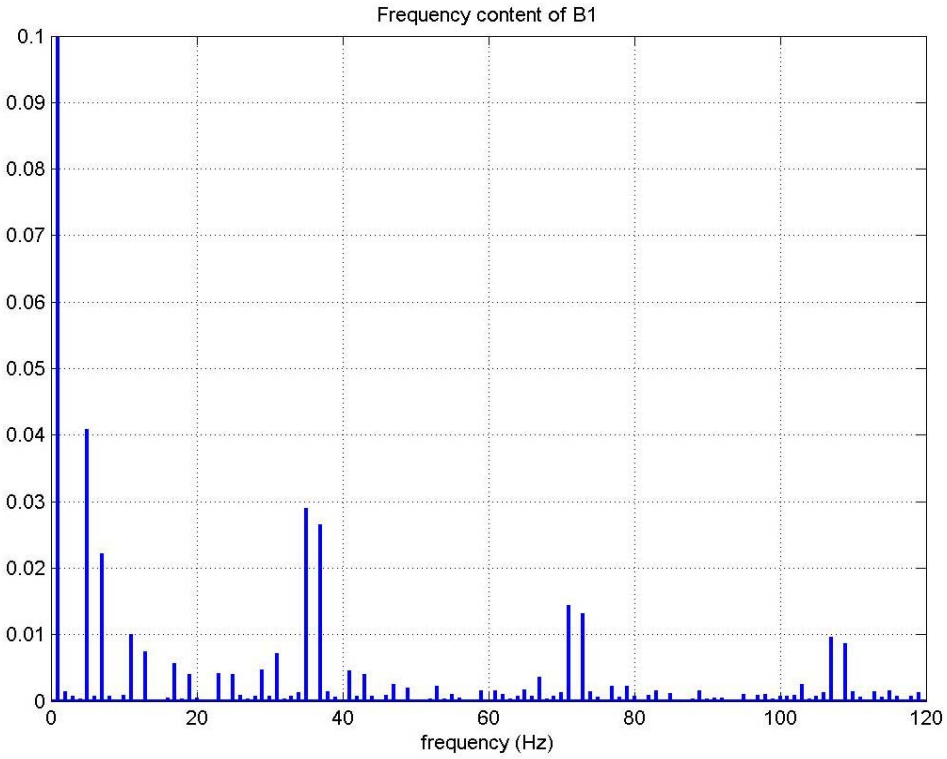


Figure 3.41 Normalized spectrum of the air gap flux density contributed by the ABC winding set

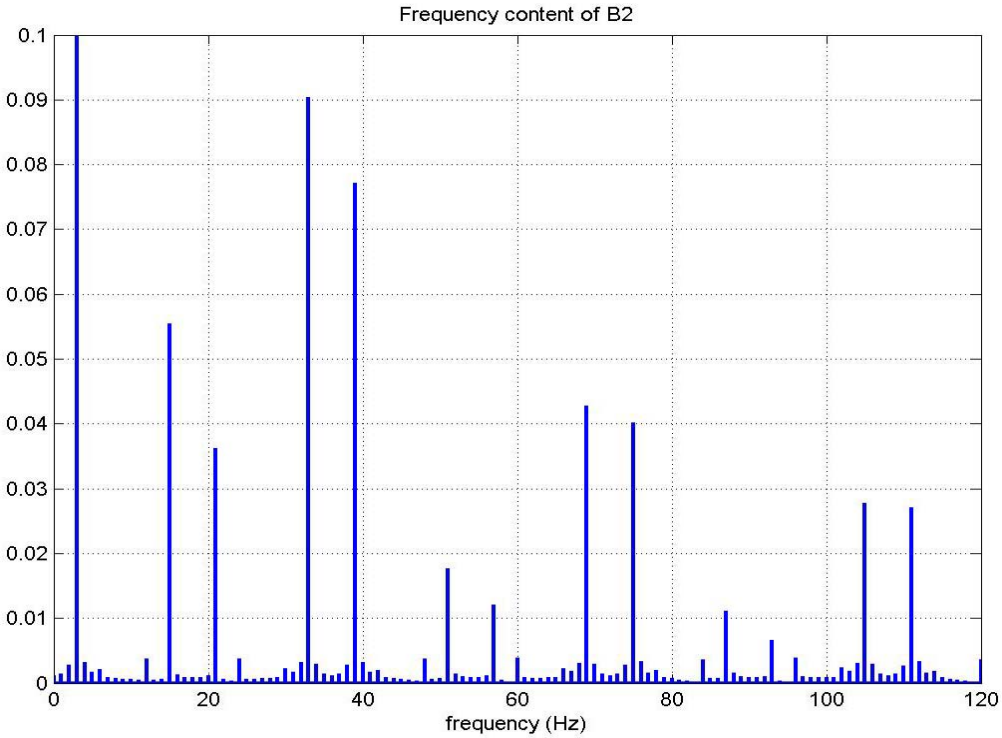

Figure 3.42 Normalized spectrum of the air gap flux density contributed by the XYZ winding set

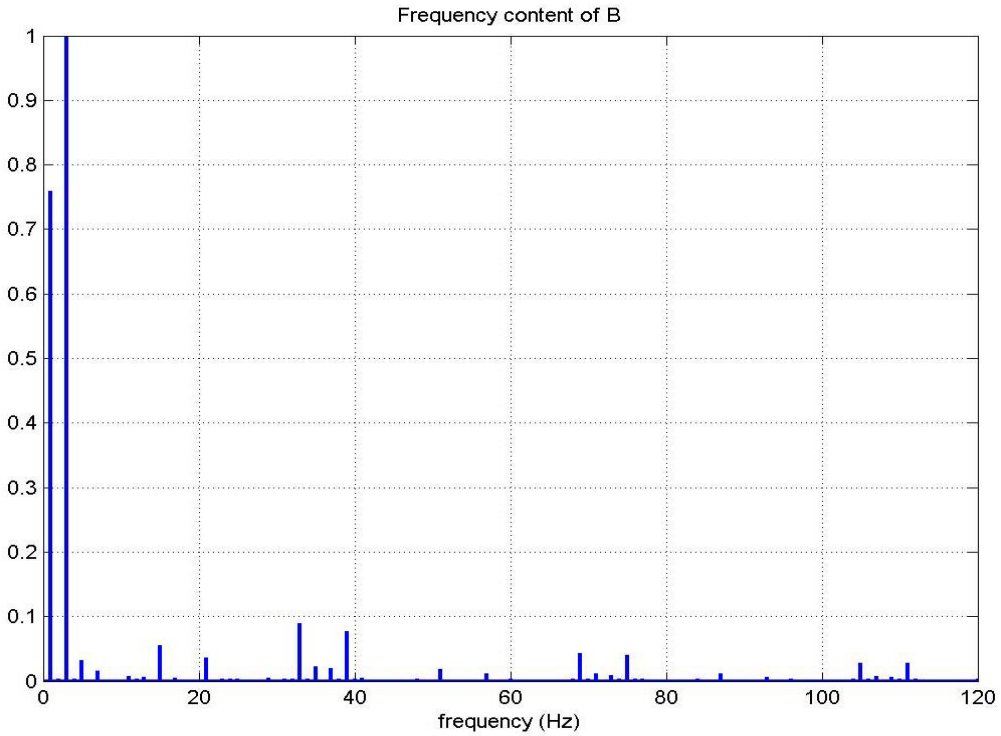

Figure 3.43 Normalized spectrum of the air gap flux density contributed by two stator winding sets

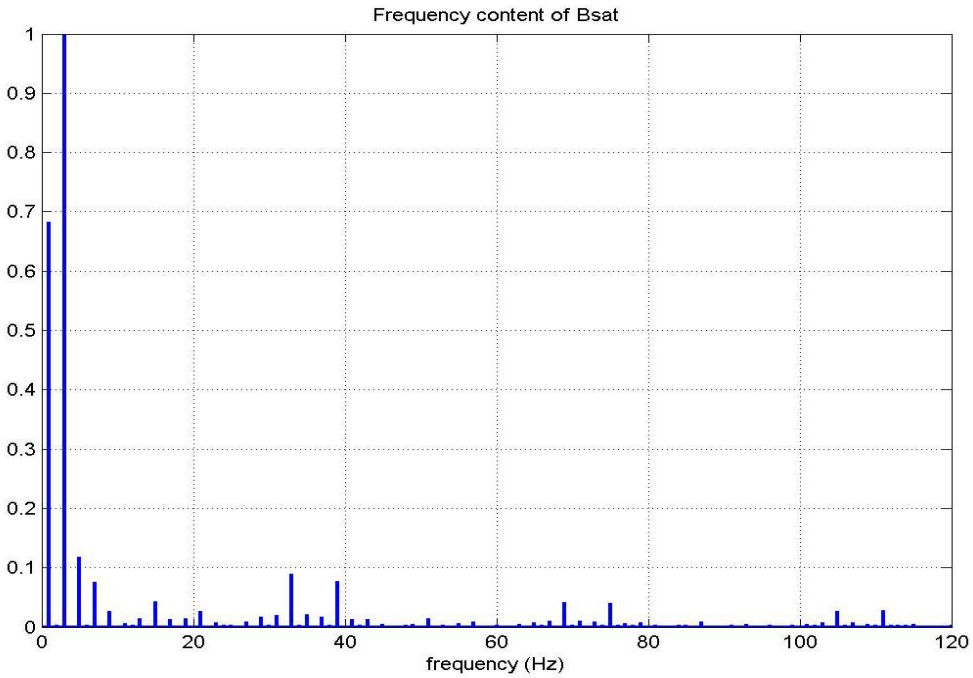


Figure 3.44 Normalized spectrum of the air gap flux density contributed by two stator winding set including saturation effect

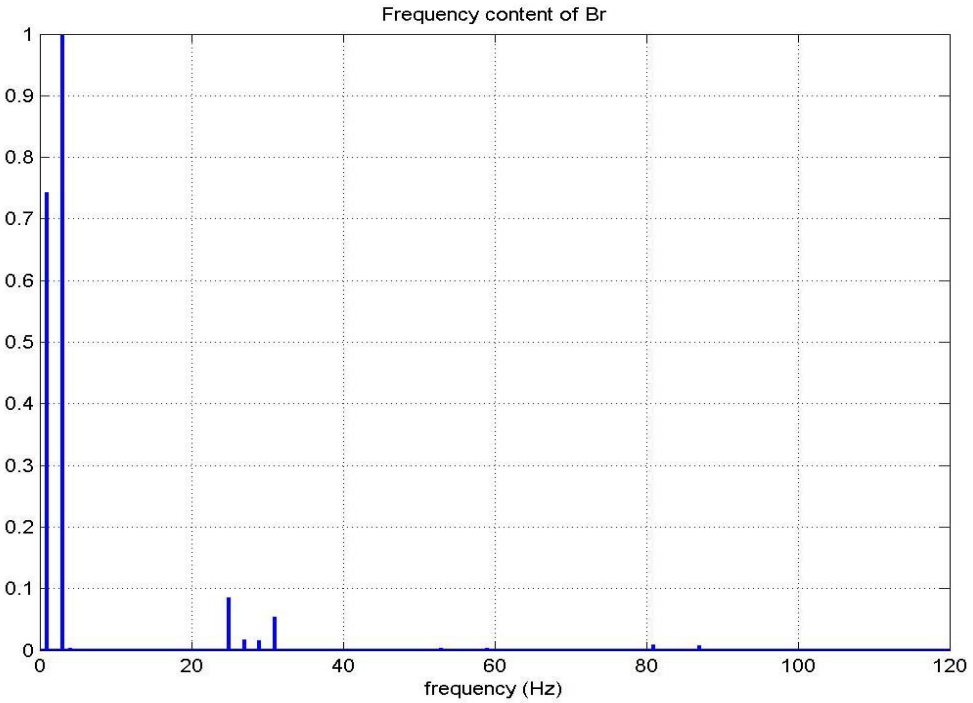


Figure 3.45 Normalized spectrum of the air gap flux density contributed by the rotor currents

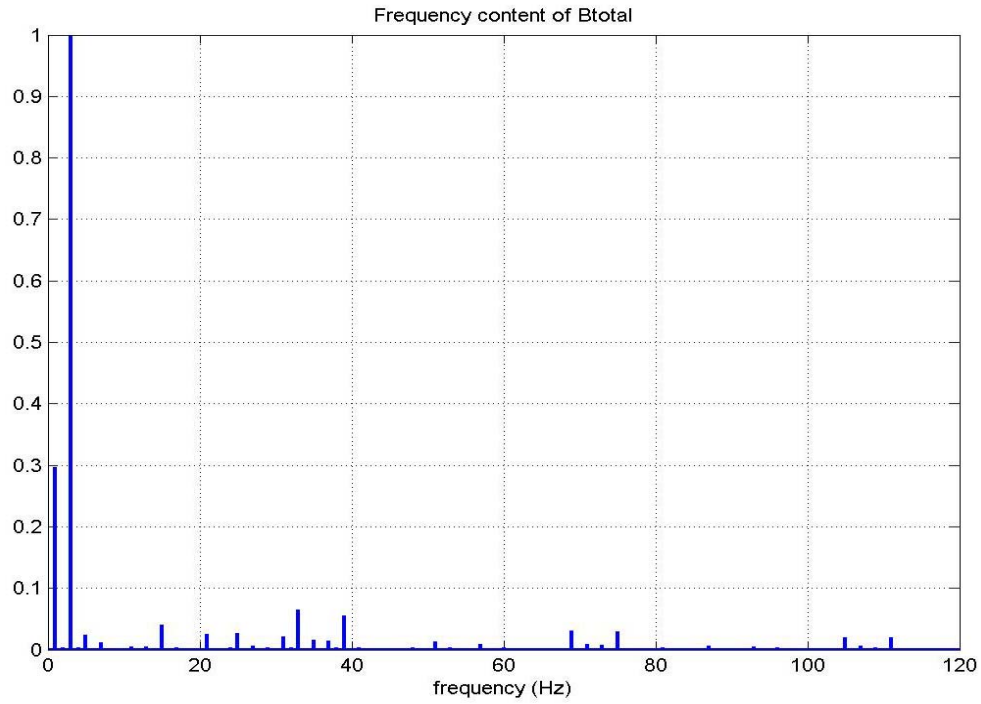


Figure 3.46 Normalized spectrum of the total air gap flux density

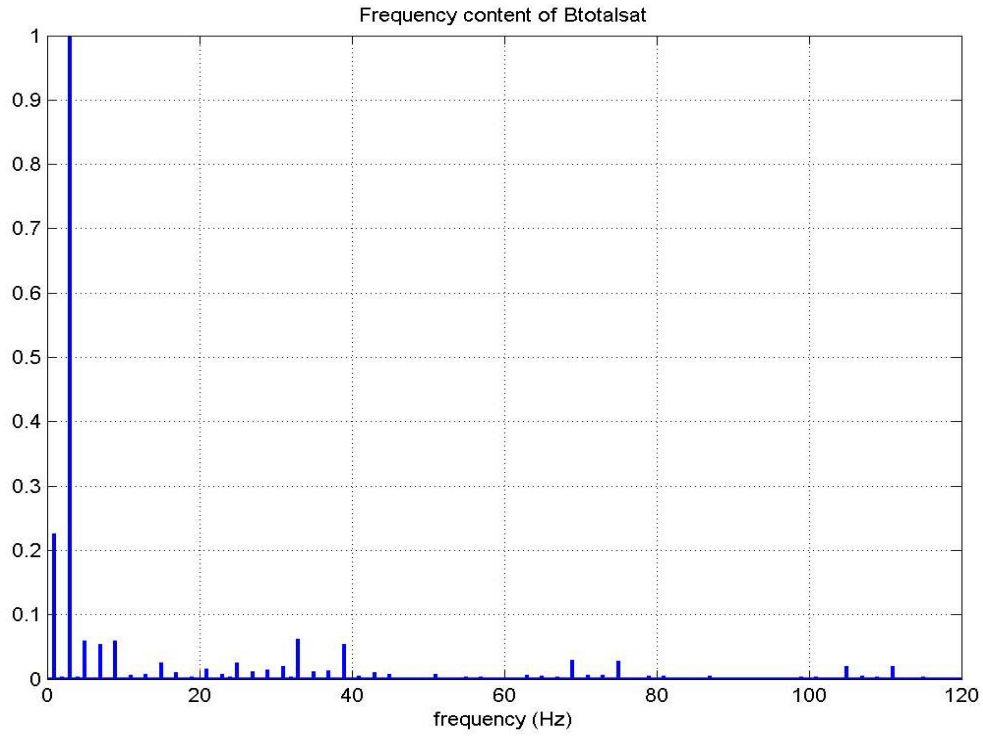


Figure 3.47 Normalized spectrum of the total air gap flux density including saturation

The Fourier analysis results of the field plots obtained by the finite element analysis method are shown in Figure 3.48-3.53. The comparisons between the Fourier analysis results of the winding function approach and the finite element analysis show that the frequency components are similar, however the magnitudes of the components have slight differences, which maybe due to the opening slot effects and the factor that the two stator winding sets are arranged at different layers of the stator slots. The magnitude of the flux density contributed by the ABC winding set in the finite element analysis is smaller than that is in the winding function approach. The normalized spectrum is obtained by dividing all the components with the peak value of magnitudes so that the largest value in the spectrum is one.

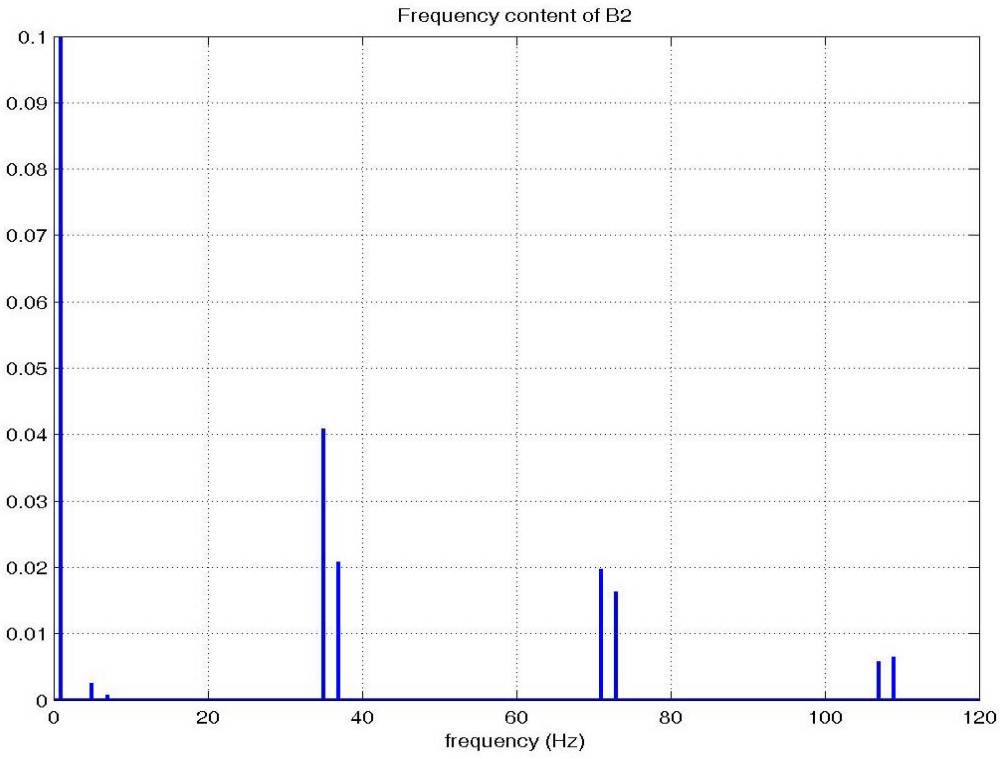


Figure 3.48 Normalized spectrum of the air gap flux density contributed by the ABC winding set

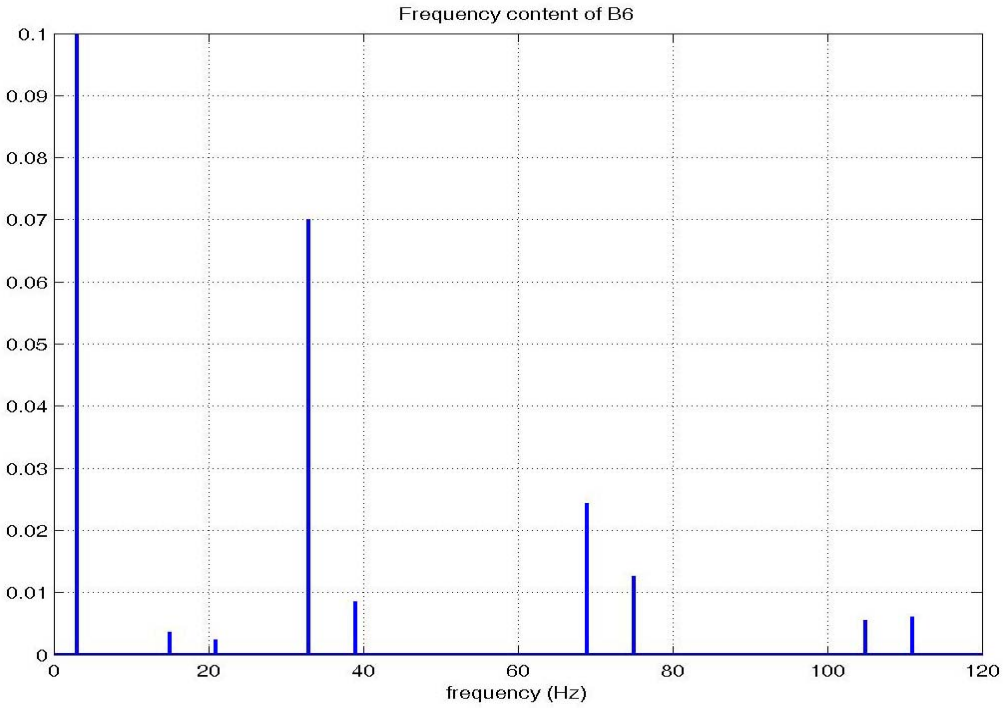


Figure 3.49 Normalized spectrum of the air gap flux density contributed by the XYZ winding set

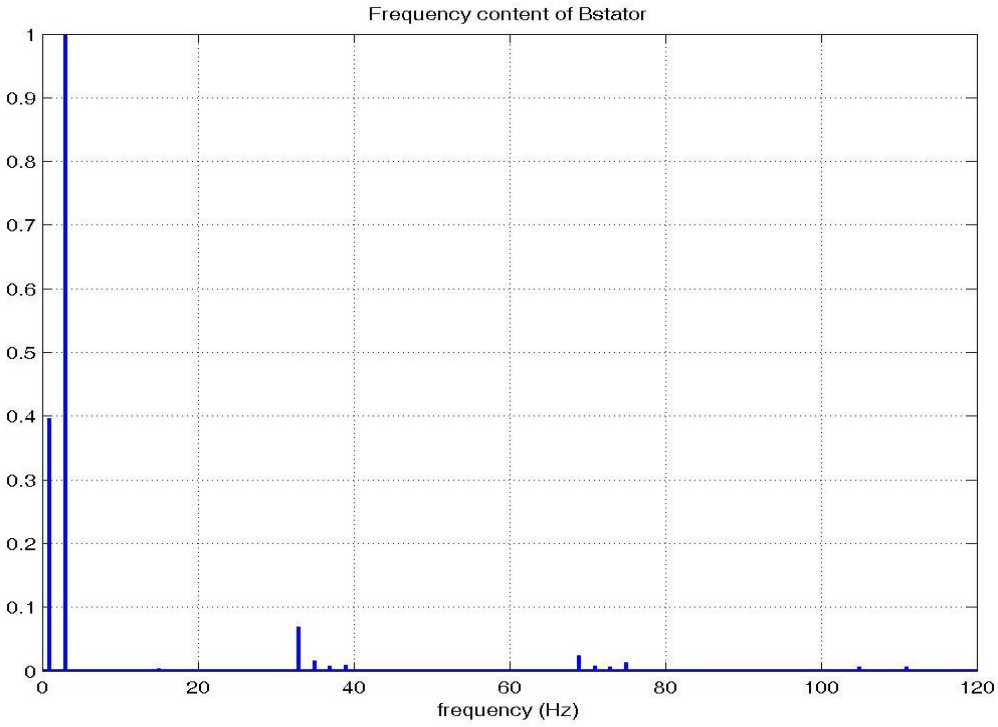


Figure 3.50 Normalized spectrum of the air gap flux density contributed by two stator winding set

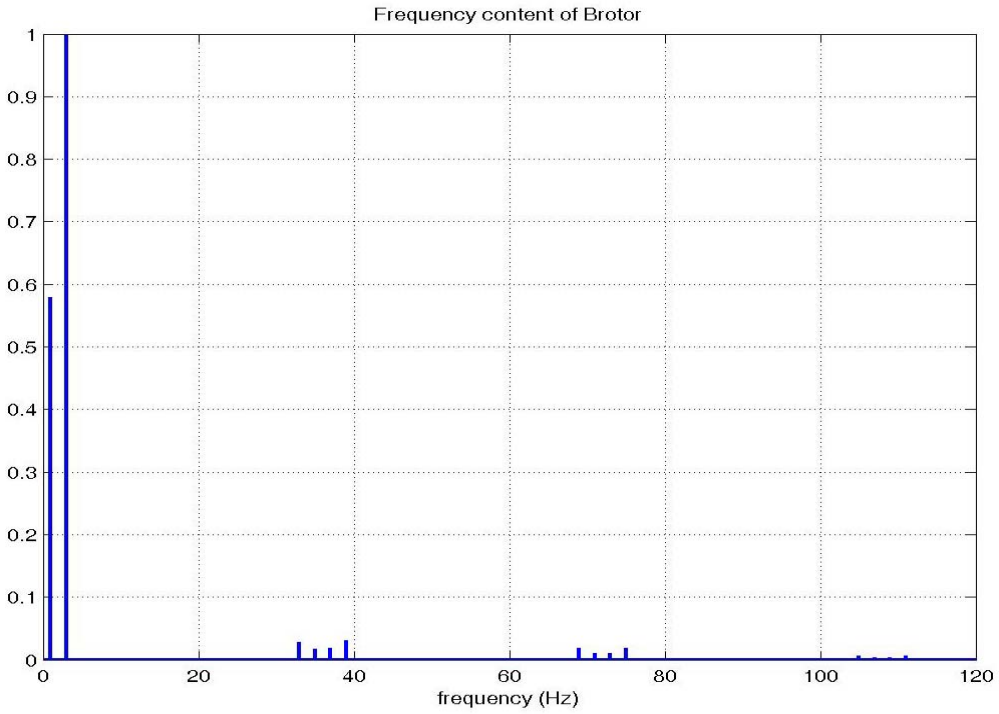


Figure 3.51 Normalized spectrum of the air gap flux density contributed by the rotor currents

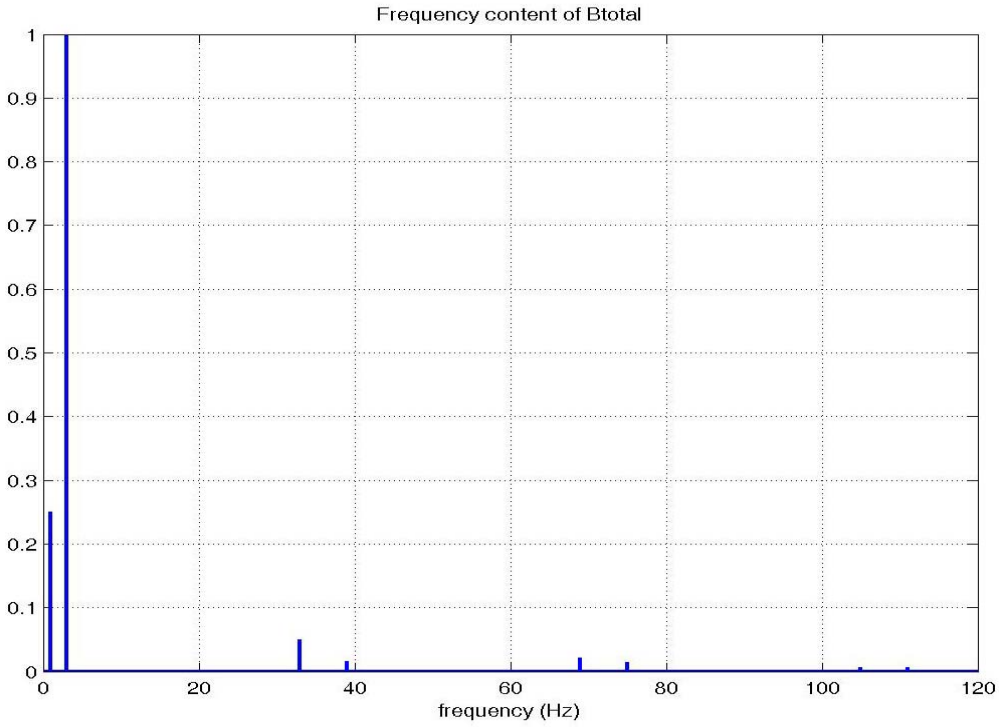


Figure 3.52 Normalized spectrum of the total air gap flux density

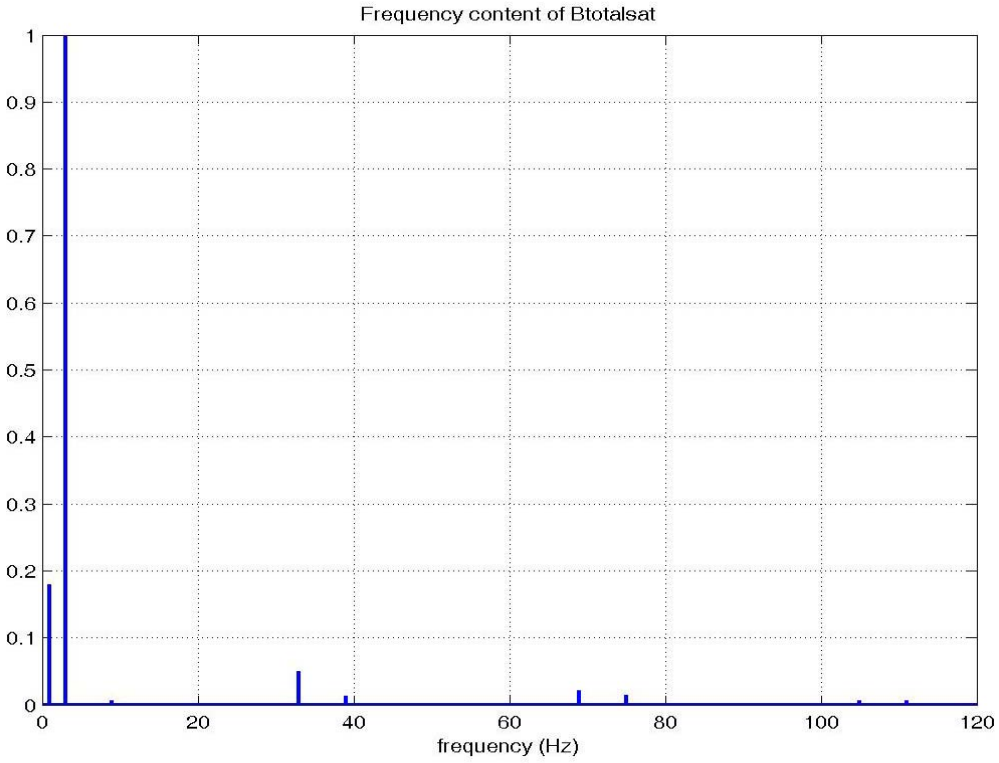


Figure 3.53 Normalized spectrum of the total air gap flux density including saturation effect

## 3.11 Conclusions

The simulation model of the dual stator winding induction machine in which the space harmonics of the stator windings and those of the rotor circuits are accounted has been presented. The complications involved with the definition of the winding function when the air gap length is not constant have been highlighted. The method is used to calculate the self and mutual inductances in the stator windings, the rotor circuits and the mutual inductances between the stator windings and the rotor circuits. The phase voltage and torque equations thus obtained are further transformed to the rotor reference frame to facilitate simplicity of model and ease computational efforts. If it is desirable to include the effects of the space harmonics in the stator windings and in the rotor bars, an n x n

reference frame transformation has to be used for the rotor circuits. Computer simulation results of the no-load starting transient were presented as well as the responses of the machine to a change in the load torque.

The balance of the chapter presents an approach, using the stator windings and rotor bar currents determined from the coupled-circuit model, the winding functions of the stator windings and the rotor loops to generate the air gap flux density. A simplified correction scheme, using the B-H curve of the magnetic steel material to account for magnetic saturation in the air gap was introduced, improving the prediction accuracy. The measurements of no-load and full load flux densities shown in Figure 3.33 and Figure 3.34 largely confirm the simulation and FEA results.

# CHAPTER 4

# FULL MODEL SIMULATION OF DUAL STATOR WINDING INDUCTION MACHINE UNDER ROTOR ECCENTRICITY CONDITIONS

## 4.1 Introduction

Induction machines have small air gap lengths to enhance their energy transfer capability. Air gap eccentricities can greatly influence machine performance. The rotor eccentricities are classified into three categories: static eccentricity, dynamic eccentricity and mixed eccentricity. The diagrams of different rotor eccentricities and previous work reviews have been given in Section 1.2.3. However, the eccentricity analysis of dual stator winding induction machines has not been investigated.

This chapter considers the effect of rotor eccentricities in the performance of the dual stator winding squirrel-cage induction machine. Based on the general winding function approach laid out in Section 3.3, the calculations of all the mutual and self inductances under the static, dynamic and mixed eccentricity conditions are presented comprehensively in Sections 4.2-4.4. The waveforms of the inductances under different eccentricity conditions are fully displayed for the first time in Section 4.4. Using these calculated inductances, the computer simulation method to study the starting transient and steady-state operations is provided in Section 4.5. Spectral analysis of the steady-state waveforms shows the presence of high-order currents and the high frequency

electromagnetic torque components that brought about by the presence of rotor eccentricities.

## 4.2 Stator Inductances Calculation

The stator inductances considered here include the stator winding self-inductances and the mutual inductances between the stator winding sets. Since the pole numbers of the two stator winding sets are different, the mutual inductances between the two stator winding sets are zero. The inductances calculated in this section are self and mutual inductances of the ABC and XYZ winding sets.

### 4.2.1 Self Inductances of the ABC winding Set

The general expression to calculate the self-inductance of $i^{th}$ winding is:

$$L_{ii} = \mu_0 rl \int_0^{2\pi} \frac{1}{g(\theta, \theta_{rm})} \cdot n_i(\theta) \cdot N_i(\theta) \cdot d\theta \tag{4.1}$$

where, $n_i(\theta)$ is the turn function of $i^{th}$ winding; $N_i(\theta)$ is the winding function of $i^{th}$ winding; $g(\theta, \theta_{rm})$ is the air gap function.

The clock diagram of the ABC winding set is shown in Figure 3.2 while the turn function of the ABC winding set is given in Figure 3.3. For phase A, the self-inductance is:

$$L_{AA} = \mu_0 rl \int_0^{2\pi} \frac{1}{g(\theta, \theta_{rm})} \cdot n_A(\theta) \cdot N_A(\theta) \cdot d\theta \tag{4.2}$$

Substituting (3.28) and (3.29) into the above equation and simplifying,

$$L_{AA} = \mu_0 rl \int_0^{2\pi} \left[A_0 + A_1 \cos\left(\theta - \theta'_{rm}\right)\right] \cdot n_A(\theta) \cdot \left[n_A(\theta) - \left\langle n_A(\theta)\right\rangle - K_A\left(\theta'_{rm}\right)\right] \cdot d\theta \qquad (4.3)$$

where, $K_A\left(\theta'_{rm}\right) = \dfrac{A_1}{2\pi A_0} \int_0^{2\pi} n_A(\theta)\cos\left(\theta - \theta'_{rm}\right) d\theta$.

Since the turn function of phase A is a piecewise linear equation, the integration can only be done in each linear region. The final result is obtained by adding the result of each linear region together.

Under rotor eccentricity conditions, similar equations can be found for phase B and phase C.

$$L_{BB} = \mu_0 rl \int_0^{2\pi} \left[A_0 + A_1 \cos\left(\theta - \theta'_{rm}\right)\right] \cdot n_B(\theta) \cdot \left[n_B(\theta) - \left\langle n_B(\theta)\right\rangle - K_B\left(\theta'_{rm}\right)\right] \cdot d\theta \qquad (4.4)$$

$$L_{CC} = \mu_0 rl \int_0^{2\pi} \left[A_0 + A_1 \cos\left(\theta - \theta'_{rm}\right)\right] \cdot n_C(\theta) \cdot \left[n_C(\theta) - \left\langle n_C(\theta)\right\rangle - K_C\left(\theta'_{rm}\right)\right] \cdot d\theta \qquad (4.5)$$

where, $K_B\left(\theta'_{rm}\right) = \dfrac{A_1}{2\pi A_0} \int_0^{2\pi} n_B(\theta)\cos\left(\theta - \theta'_{rm}\right) d\theta$, $K_C\left(\theta'_{rm}\right) = \dfrac{A_1}{2\pi A_0} \int_0^{2\pi} n_C(\theta)\cos\left(\theta - \theta'_{rm}\right) d\theta$.

Unlike the case where the self-inductances of the three phases have the same values when the air-gap length is constant, they are quite different under rotor eccentricity conditions. The simulation results of the self-inductances under different eccentricity conditions are shown in Figures 4.1, 4.2 and 4.3.

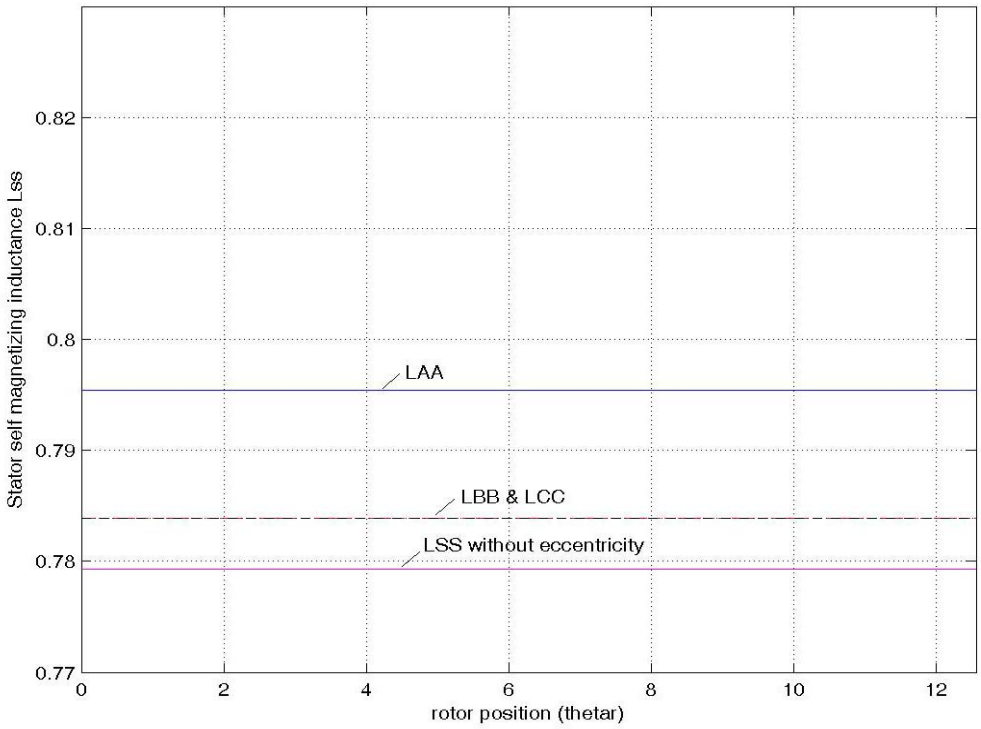


Figure 4.1 Self-inductance under 20% static rotor eccentricity

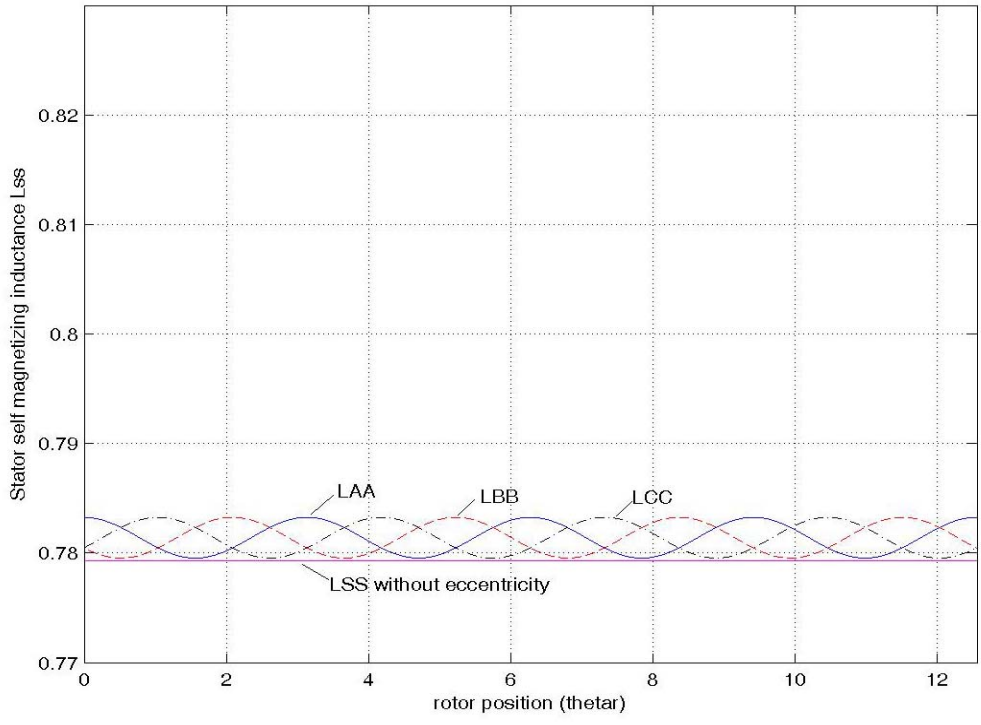


Figure 4.2 Self-inductance under 10% dynamic rotor eccentricity

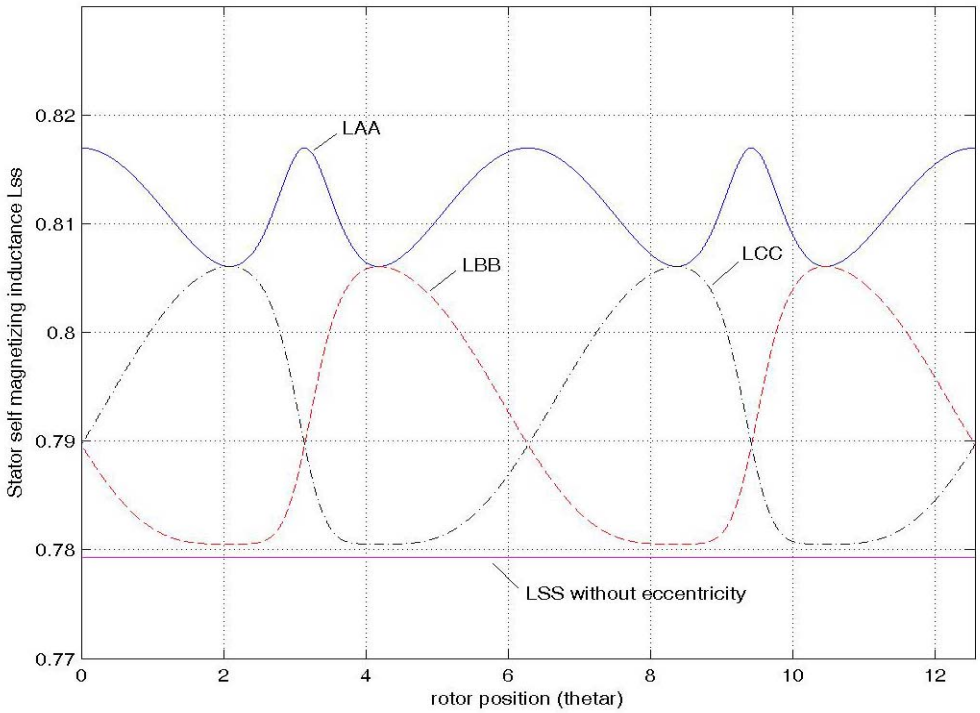


Figure 4.3 Self-inductance under 20% static and 10% dynamic rotor eccentricity

From the above simulation results it can be seen that the self-inductances of the ABC winding set do not depend on the rotor position under static rotor eccentricity condition. However the inductance value of each phase may be different from each other as determined by the nature of the variation of the air-gap length. Under the dynamic rotor eccentricity condition, the self-inductances of the stator windings are three sinusoidal waveforms with the same constant dc component. They have a 120 degree phase shift from each other as shown in Figure 4.2. In Figure 4.3, the inductances under the mixed rotor eccentricity condition lose the symmetric characteristic and have bigger peak-peak magnitudes than the case when the rotor is subjected to a pure dynamic rotor eccentricity. Irrespective of the eccentricity conditions the machine is subjected to, the self-inductances of the stator ABC winding set are greater than when the air-gap length is

constant. The offset angle $\lambda$ in (3.16) is zero for all the above calculations. Changing the value of angle $\lambda$ will only create a common phase shift in all the waveforms. All the figures have the same limit in the y-axis for better comparison.

### 4.2.2 Mutual Inductances of the ABC Winding Set

The general expression for the mutual inductance calculation is:

$$L_{ij} = \mu_0 rl \int_0^{2\pi} \frac{1}{g(\theta, \theta_{rm})} \cdot n_i(\theta) \cdot N_j(\theta) \cdot d\theta \tag{4.6}$$

where, $n_i(\theta)$ is the turn function of $i^{th}$ winding; $N_j(\theta)$ is the winding function of $j^{th}$ winding; $g(\theta, \theta_{rm})$ is the air gap function.

Substituting the inverse of the air gap equation and general winding function into (4.6) and simplifying,

$$L_{ij} = \mu_0 rl \int_0^{2\pi} \left[A_0 + A_1 \cos(\theta - \theta'_{rm})\right] \cdot n_i(\theta) \cdot \left[n_j(\theta) - \langle n_j(\theta) \rangle - K_j(\theta'_{rm})\right] \cdot d\theta \tag{4.7}$$

where, $K_j(\theta'_{rm}) = \frac{A_1}{2\pi A_0} \int_0^{2\pi} n_j(\theta) \cos(\theta - \theta'_{rm}) d\theta$, $n_j(\theta)$ is the turn function of $j$ winding.

The calculation method and process for mutual inductance calculation are similar to the one for self-inductance, except the number of linear regions needed for the calculation is more. The simulation results of the stator winding mutual inductances can be found in Figures 4.4, 4.5 and 4.6.

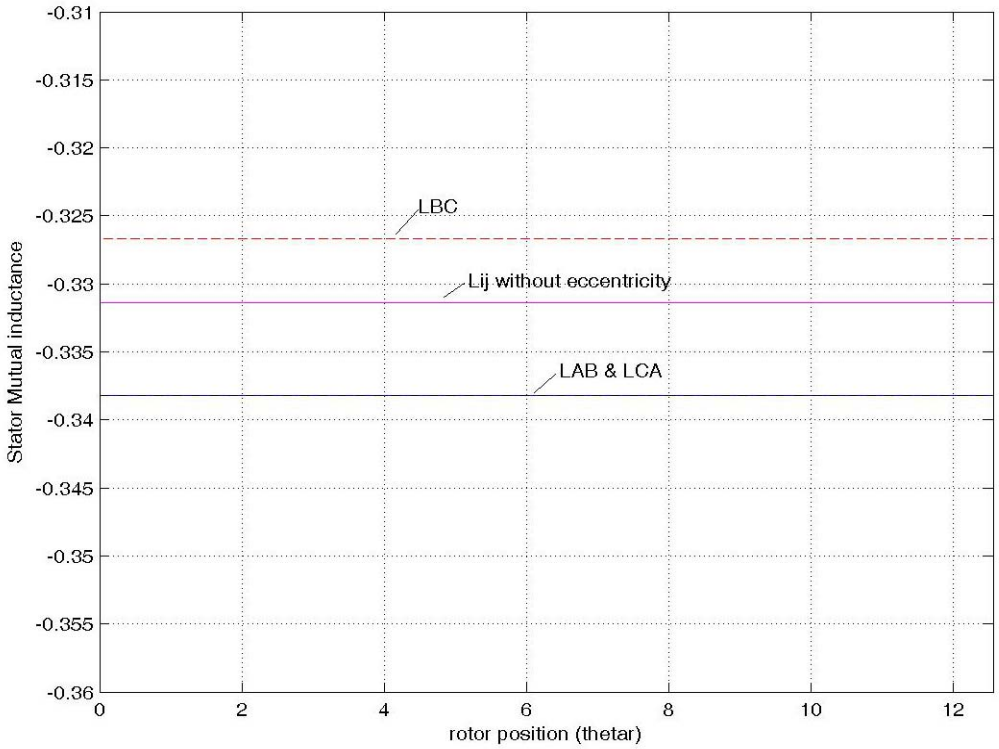


Figure 4.4 Mutual inductance under 20% static rotor eccentricity

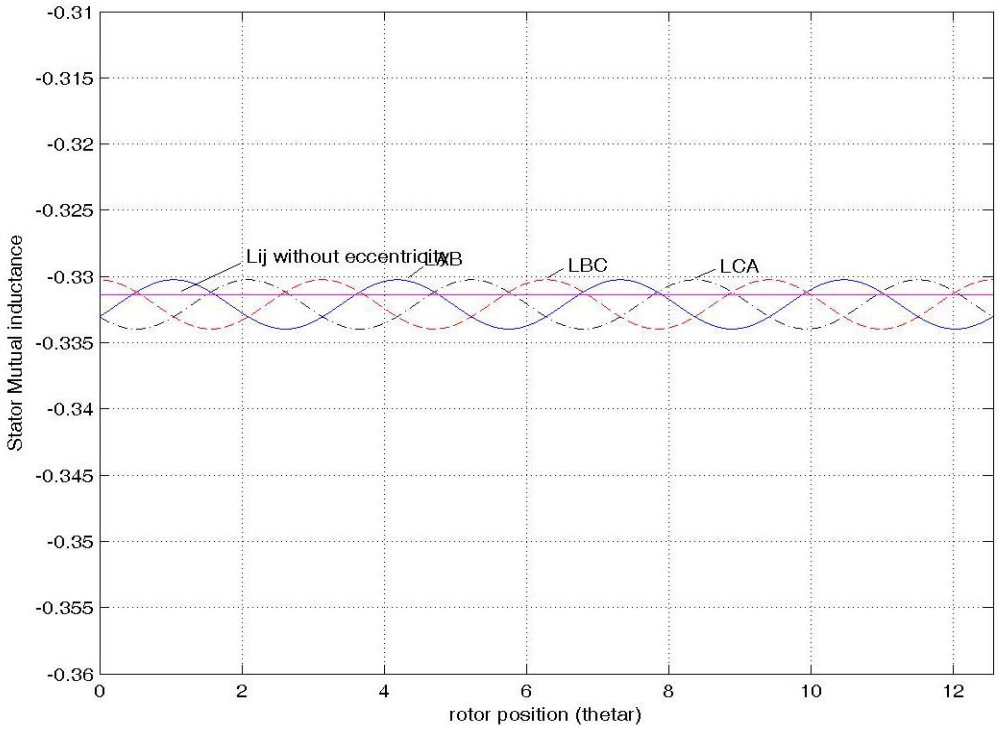


Figure 4.5 Mutual inductance under 10% dynamic rotor eccentricity

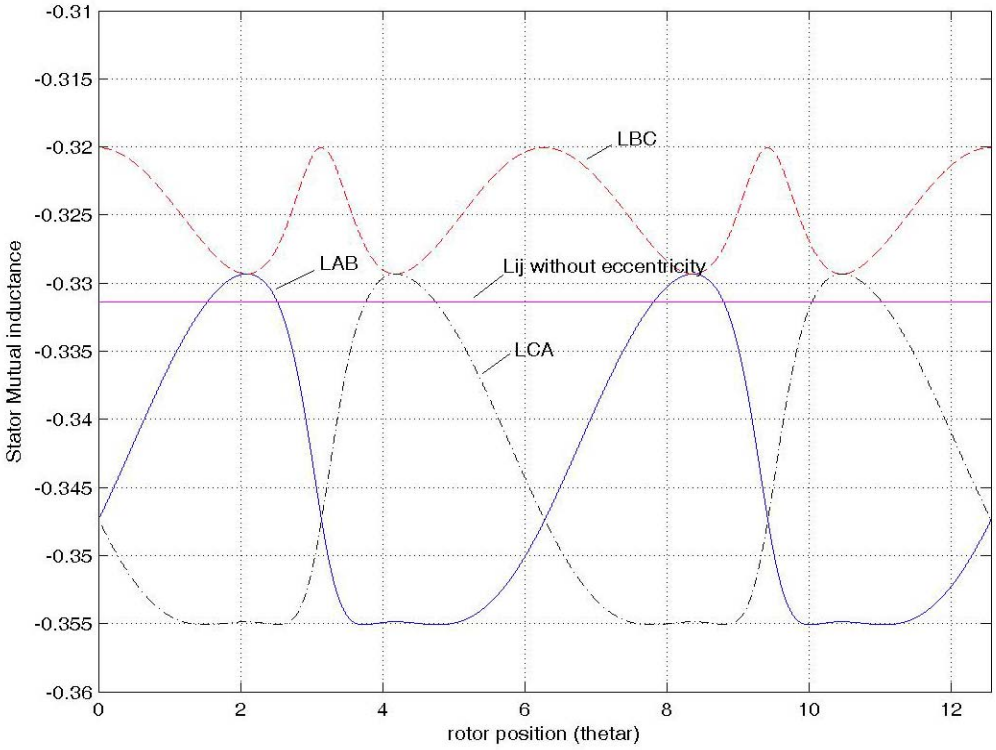


Figure 4.6 Mutual inductance under 20% static and 10% dynamic rotor eccentricity

The mutual inductances of the stator ABC winding set have the same constant values when the air gap length is constant. Under the static rotor eccentricity condition, the mutual inductances of the ABC winding set are constant, but their values are unequal depending on the air gap length distribution as shown in Figure 4.4. From Figure 4.5, the mutual inductances of the ABC winding set have sinusoidal components that have a 120 degree phase shift between each other under the dynamic rotor eccentricity condition. For the mixed rotor eccentricity condition, the mutual inductances are not symmetric and the peak-peak magnitudes are unequal as shown in Figure 4.6.

The equalities of $L_{AB}$ and $L_{BA}$, $L_{BC}$ and $L_{CB}$, $L_{CA}$ and $L_{AC}$ have been checked by the simulation and it is found that by applying the general winding function definition in the inductance calculation, the inequalities of the mutual inductances in [3.7] disappear, such

that $L_{AB} = L_{BA}$, $L_{BC} = L_{CB}$ and $L_{CA} = L_{AC}$ . These equations confirm expectations from the linear magnetic circuit theory.

### 4.2.3 Self Inductances of the XYZ Winding Set

Similar expression of the self-inductance calculation can be found for the XYZ winding set,

$$L_{ii} = \mu_0 rl \int_0^{2\pi} \left[A_0 + A_1 \cos\left(\theta - \theta'_{rm}\right)\right] \cdot n_i(\theta) \cdot \left[n_i(\theta) - \langle n_i(\theta)\rangle - K_i\left(\theta'_{rm}\right)\right] \cdot d\theta \qquad (4.8)$$

where, $K_i\left(\theta'_{rm}\right) = \dfrac{A_1}{2\pi A_0} \int_0^{2\pi} n_i(\theta)\cos\left(\theta - \theta'_{rm}\right) d\theta$ and $i = X, Y, Z$ .

Since the XYZ winding set is a 6 pole winding set, the Fourier series of the XYZ winding function is composed of $3\theta$ component, $6\theta$ component, …, $3k\theta$ component, etc, where $k = 1,2,\cdots,\infty$. The integration of the multiplication of two cosine functions will be zero except both have the same frequency. Therefore it is obvious that in the XYZ winding set, $K_i\left(\theta'_{rm}\right)$ will always be zero, which is not the case with the 2-pole ABC winding set. This explains why the stator self-inductances of the XYZ winding set are not simple three times repetition of the stator self-inductance waveform of the ABC winding set; they are quite different from each other. The same reason explains the difference between the mutual inductances of the ABC winding and XYZ winding sets. If a precise model of the inverse of the air gap function including more high order components is used in the analysis, the characteristics found in the mutual inductances of the ABC winding set may be observed in the mutual inductances of the XYZ winding set also.

However, it should be noticed that the magnitude of the high order component is reduced exponentially such that the influence of those high order components may not be as much as the fundamental one. It would appear a better model of the air-gap length is required for the analysis. The simulation results of the self-inductances of the XYZ winding set are shown in Figures 4.7, 4.8 and 4.9.

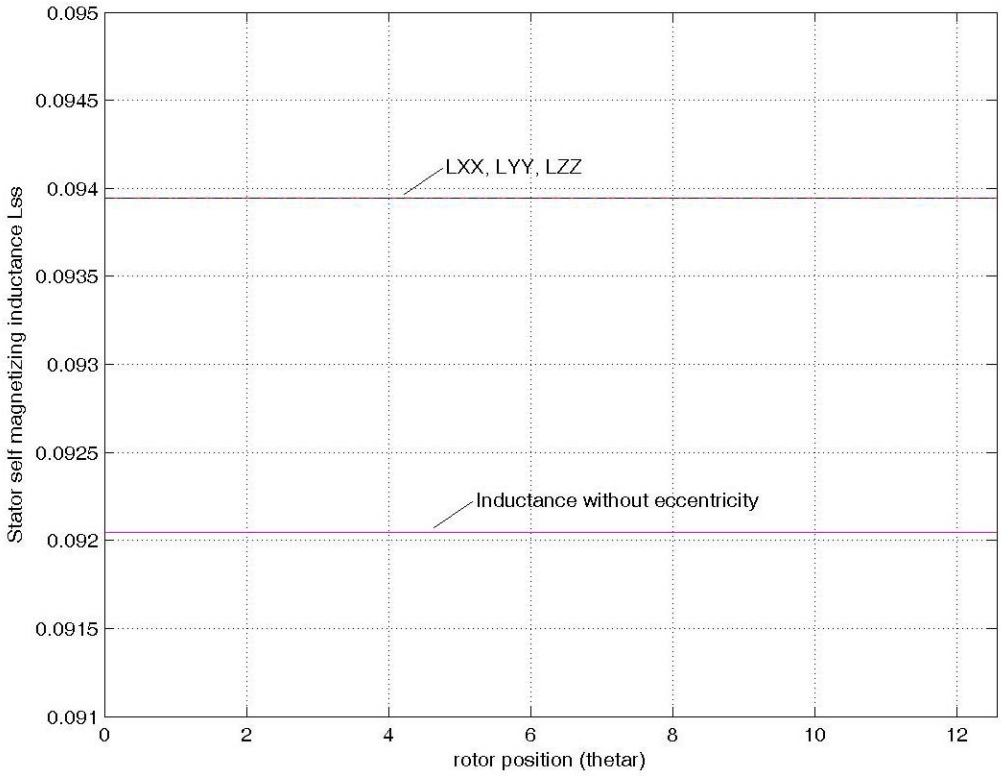


Figure 4.7 Self-inductance under 20% static rotor eccentricity

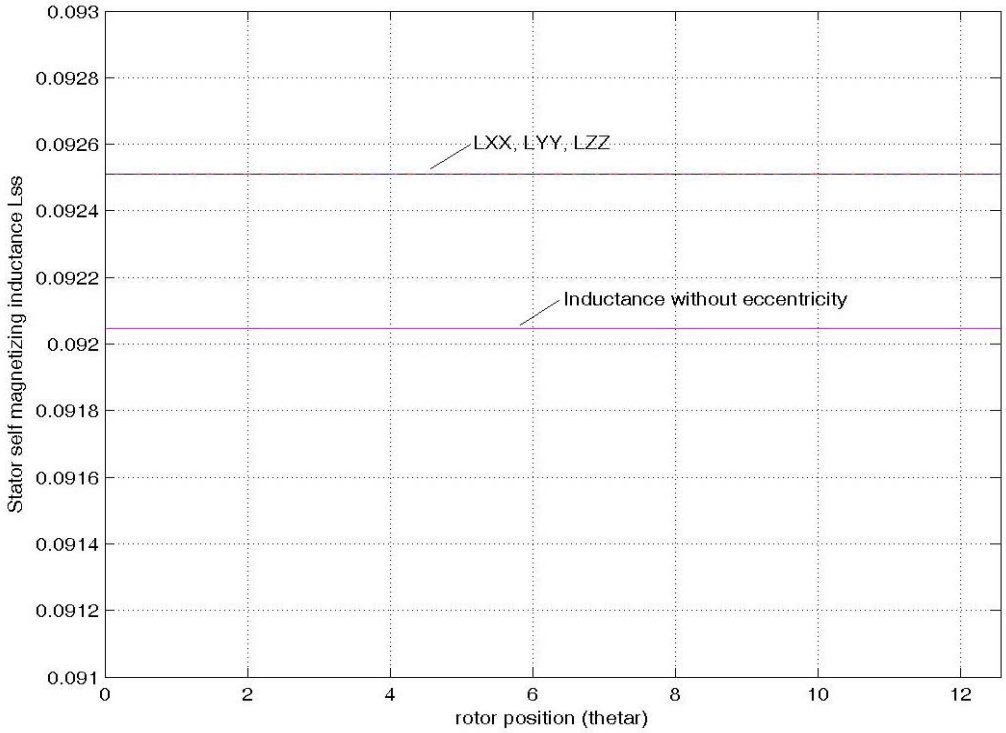


Figure 4.8 Self-inductance under 10% dynamic rotor eccentricity

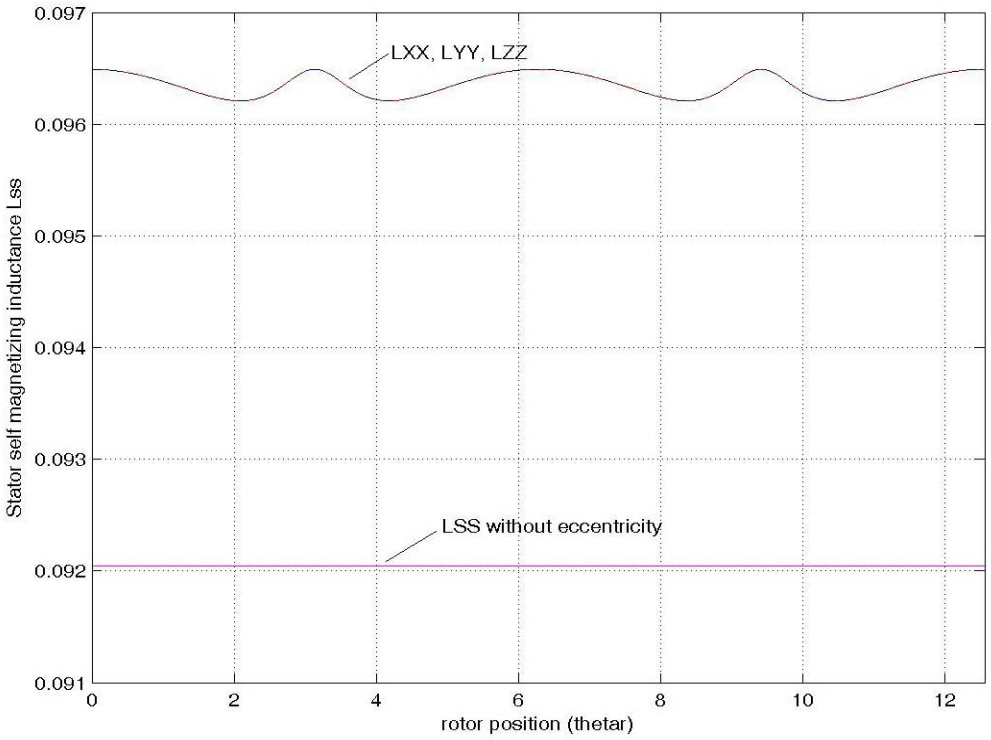


Figure 4.9 Self-inductance under 20% static eccentricity and 10% dynamic rotor eccentricity

The three phase self inductances of the XYZ winding set are equal and constant at both the static and dynamic rotor eccentricity conditions, however different constant values can be found in the static and dynamic rotor eccentricity conditions, as shown in Figures 4.7 and 4.8. The stator self inductances are quite different at the mixed rotor eccentricity condition as shown in Figure 4.9. No matter what rotor eccentricity condition it is, three phase stator self-inductances are equal to pr greater than that under the constant air gap condition.

### 4.2.4 Mutual Inductances of the XYZ Winding Set

Using the same calculation method, the stator mutual inductances of the XYZ winding set can be obtained. The results of the mutual inductance calculation for the XYZ winding set under different rotor eccentricity conditions are shown in Figure 4.10, Figure 4.11 and Figure 4.12 respectively.

The behaviors of the stator mutual inductances for the XYZ winding set are different from those for the ABC winding set and the explanation is the same as the one given in the self-inductance calculation (Section 4.2.3). As shown in Figures 4.10 and 4.11, the three phase mutual inductances of the XYZ winding set are equal and constant. However the constant values will be different at the static and dynamic rotor eccentricity conditions. The stator mutual inductances at the mixed rotor eccentricity condition are different from what is found under the static and dynamic eccentricity conditions as shown in Figure 4.12.

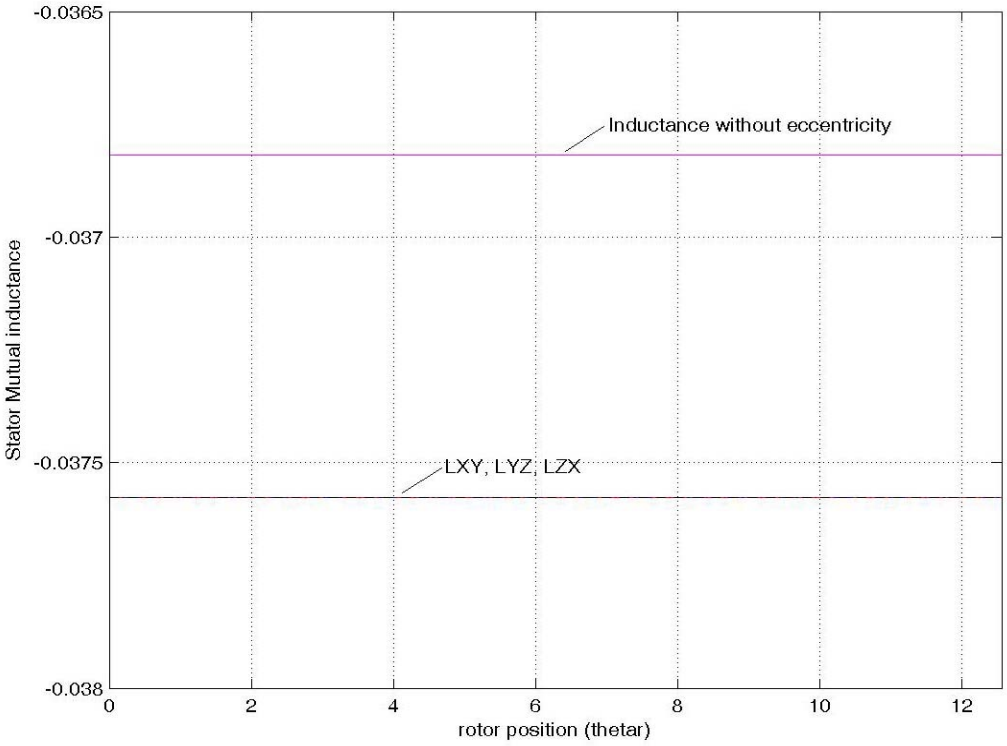


Figure 4.10 Mutual inductance under 20% static rotor eccentricity

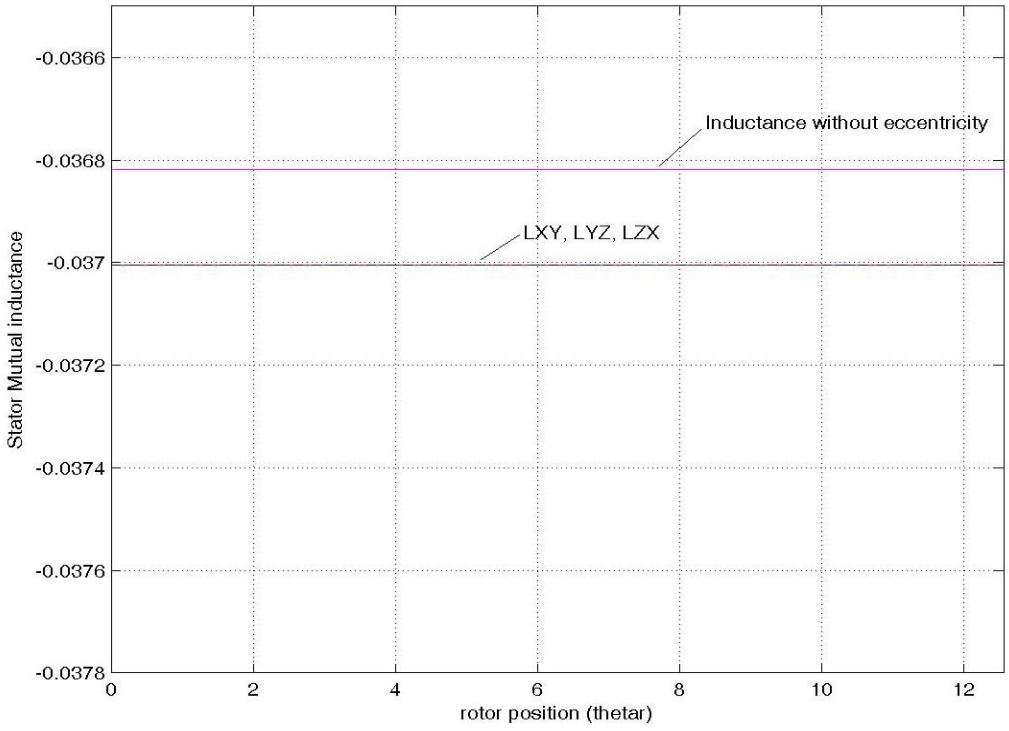


Figure 4.11 Mutual inductance under 10% dynamic rotor eccentricity

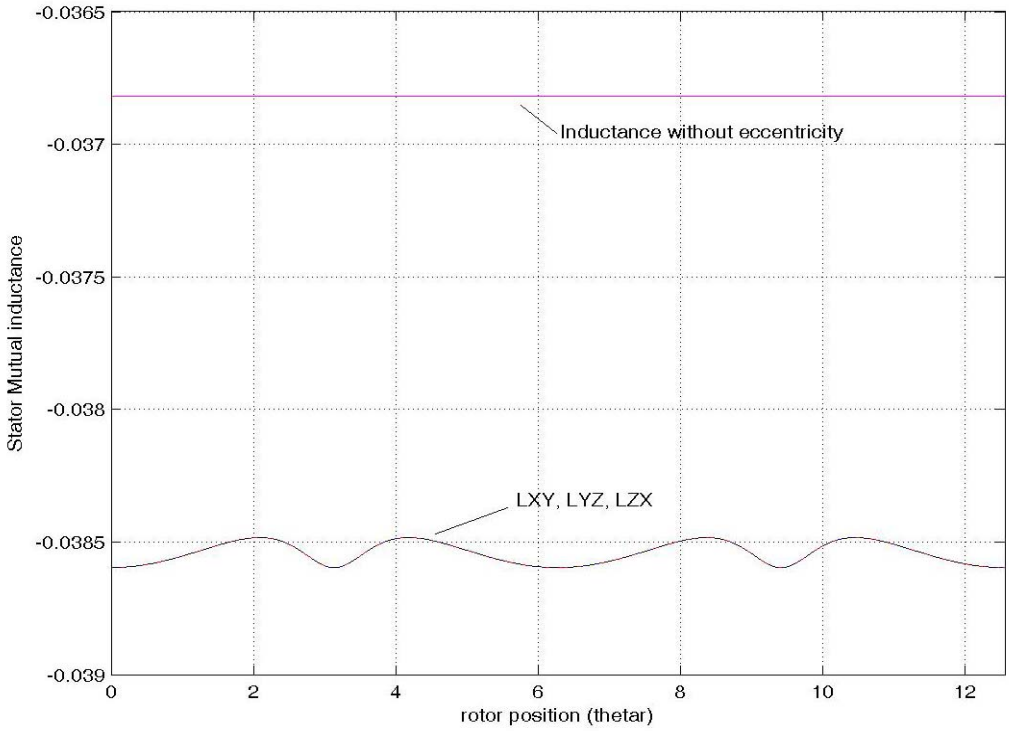


Figure 4.12 Mutual inductance under 20% static and 10% dynamic rotor eccentricity

## 4.3 Rotor Inductance Calculation

The rotor inductances calculation can be divided into three categories based on the relationship between the rotor loop winding function distributions. The first case is the self inductance of rotor loops. In this condition, the turn function and the winding function of the rotor loop will overlap each other in all the integration regions. The second case is the mutual inductance of rotor loops between $i^{th}$ loop and $i+1^{th}$ loop, in which the turn functions of the two rotor loops will overlap each other partially. The third case is the mutual inductance of rotor loops between $i^{th}$ loop and $i+k^{th}$ loop ($k \neq 1$). The turn function of the $i^{th}$ rotor loop will not overlap the turn function of $i+k^{th}$ loop at all, if k is not equal to 1. It should be noticed that all the above statements are based on

the assumption that the rotor skew factor is considered in the analysis. In the case that the rotor is no skewed, only two types of inductances can be found in the rotor self-inductance and mutual inductance. Since the rotor inductances calculation in this section has no relationship with the stator coil distribution, the results are valid for both the 2-pole and the 6-pole stator winding sets.

### 4.3.1 Self Inductance of Rotor Loops

The expression to calculate the self-inductance of $i^{th}$ rotor loop is:

$$L_{ii} = \mu_0 rl \int_0^{2\pi} \frac{1}{g(\theta, \theta_{rm})} \cdot n_i(\theta) \cdot N_i(\theta) \cdot d\theta \tag{4.9}$$

where, $n_i(\theta)$ is the turn function of $i^{th}$ rotor loop; $N_i(\theta)$ is the winding function of $i^{th}$ rotor loop; $g(\theta, \theta_{rm})$ is the air gap function; $i$ is the rotor loop number.

The rotor loop self inductance maybe a function of the rotor angle depending on the different eccentricity conditions. The waveforms of rotor loop self inductance under the static rotor eccentricity condition, the dynamic rotor eccentricity condition and the mixed rotor eccentricity condition are shown in the Figure 4.13, Figure 4.14 and Figure 4.15 respectively.

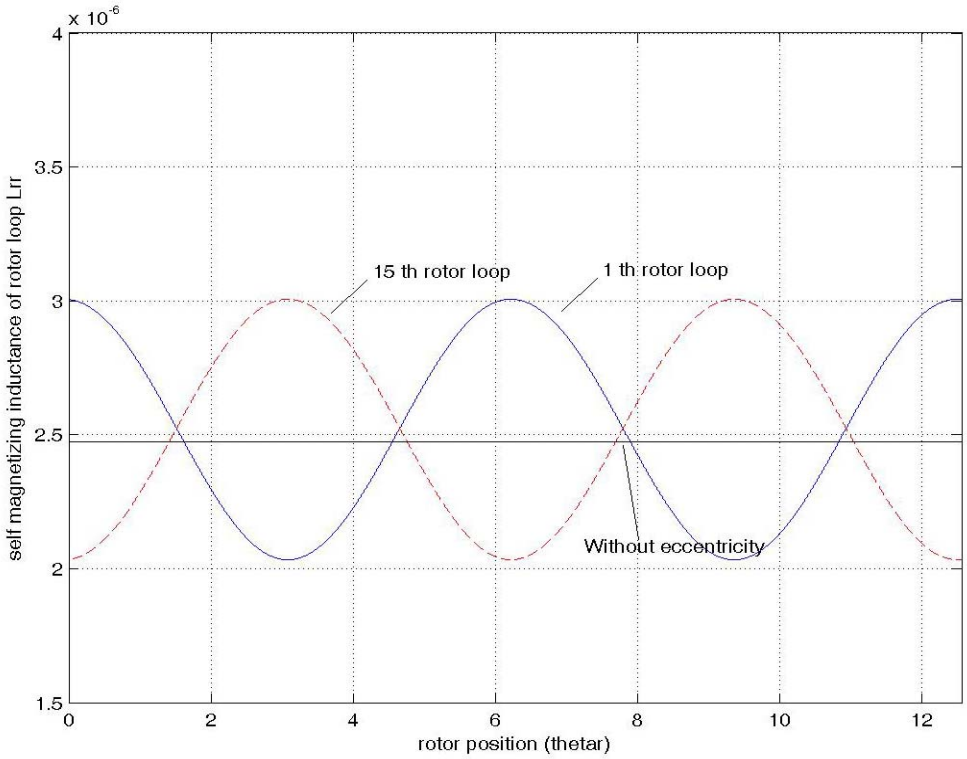


Figure 4.13 Self-inductance under 20% static rotor eccentricity

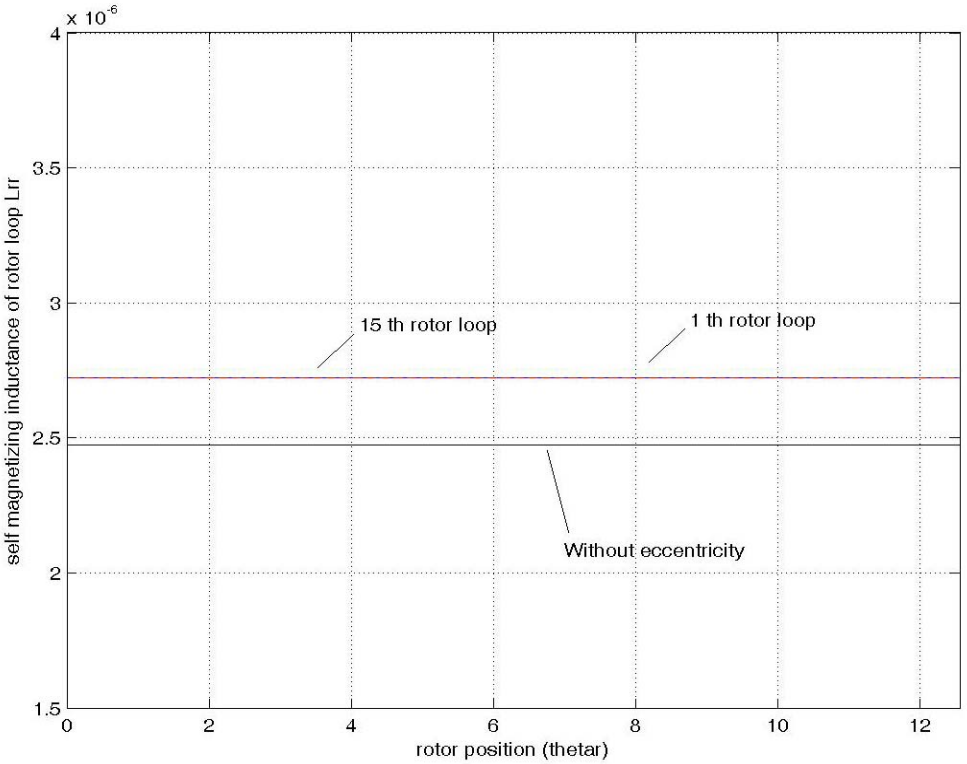


Figure 4.14 Self-inductance under 10% dynamic rotor eccentricity

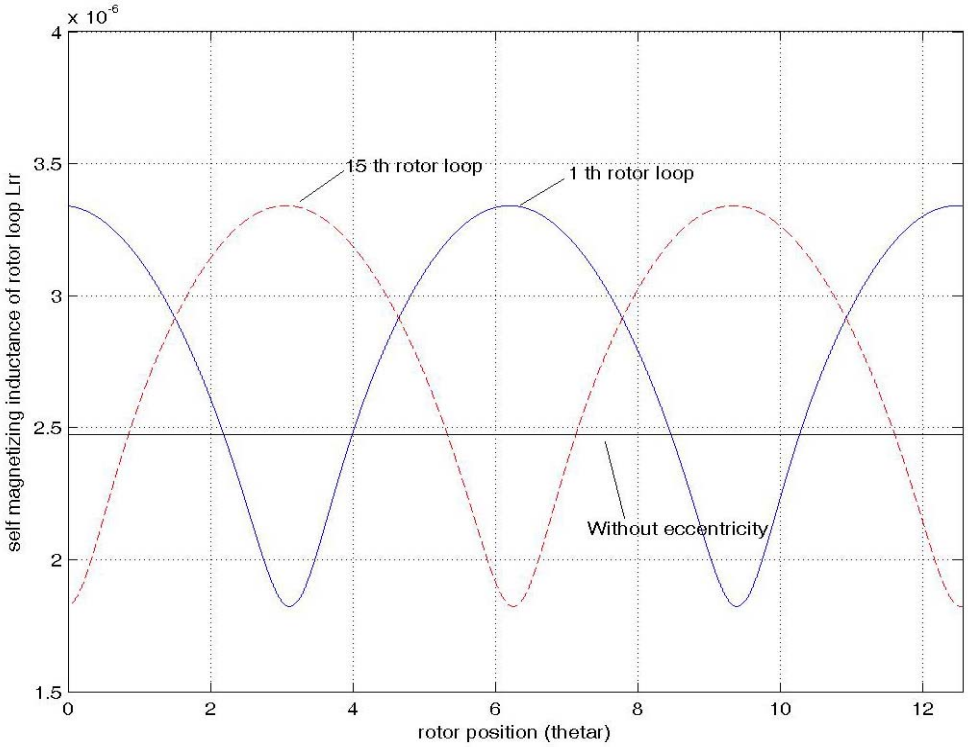


Figure 4.15 Self-inductance under 20% static and 10% dynamic rotor eccentricity

From the Figures 4.13, 4.14 and 4.15, it is found that the self-inductances of the rotor loops are sinusoidal waveforms under the static rotor eccentricity condition. However self-inductances are constant under the dynamic rotor eccentricity condition. The self-inductance under the mixed rotor eccentricity condition is not a simple addition of the inductances due to the static and dynamic rotor eccentricity conditions. Apart from the fundamental frequency component, some other high frequency harmonic components exist in the self-inductances, resulting in harmonic currents and high frequency torque disturbances. There are significant differences in these self inductances when they are compared to those of the constant air-gap condition.

### 4.3.2 Mutual Inductance Between $i^{th}$ Loop and $i+1^{th}$ Loop

The expression to calculate the Mutual inductance between $i^{th}$ loop and $i+1^{th}$ loop is:

$$L_{i,i+1} = \mu_0 rl \int_0^{2\pi} \frac{1}{g(\theta,\theta_{rm})} \cdot n_i(\theta) \cdot N_{i+1}(\theta) \cdot d\theta \tag{4.10}$$

where, $n_i(\theta)$ is the turn function of $i^{th}$ rotor loop; $N_{i+1}(\theta)$ is the winding function of $i+1^{th}$ rotor loop; $g(\theta,\theta_{rm})$ is the air gap function; $i$ is the rotor loop number.

The mutual inductance between rotor $i^{th}$ loop and $i+1^{th}$ loop changing by the rotor angle under the static rotor eccentricity, dynamic rotor eccentricity and mixed rotor eccentricity conditions are shown in Figure 4.16, Figure 4.17 and Figure 4.18 respectively.

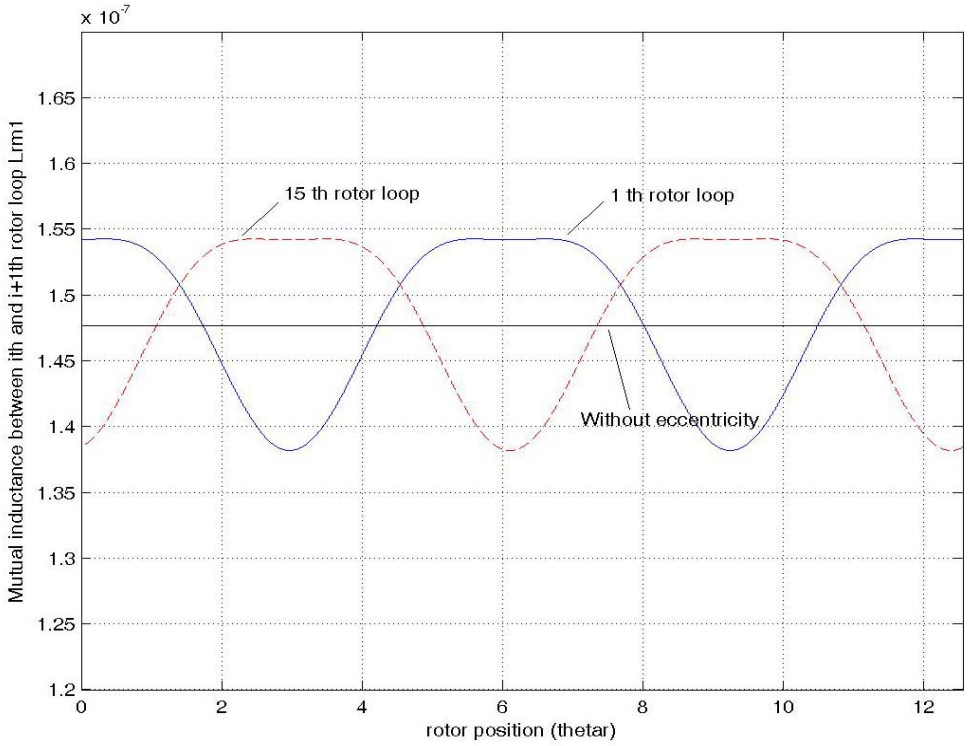


Figure 4.16 Mutual inductance under 20% static rotor eccentricity.

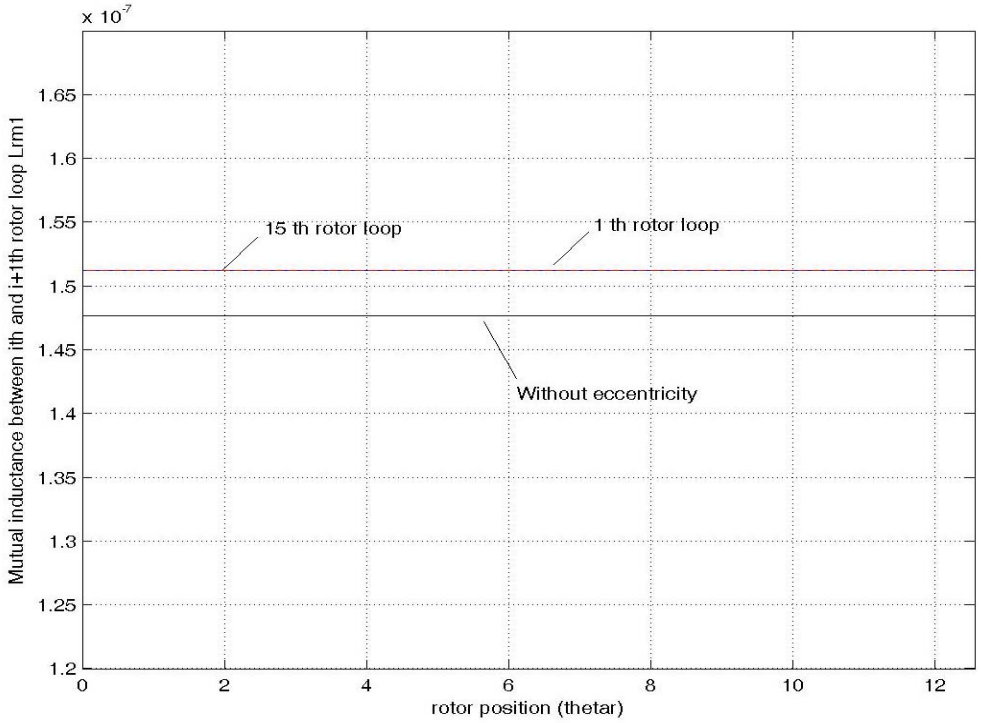


Figure 4.17 Mutual inductance under 10% dynamic rotor eccentricity

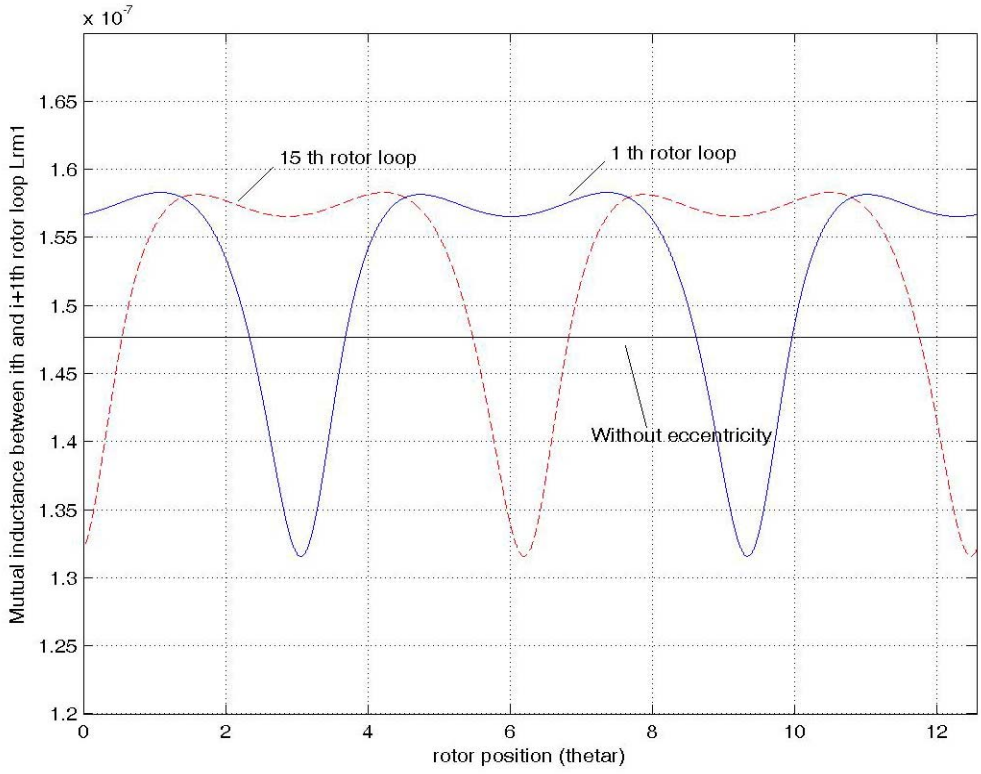


Figure 4.18 Mutual inductance under 20% static and 10% dynamic rotor eccentricity

As shown in Figure 4.16, the mutual inductance between rotor $i^{th}$ loop and $i+1^{th}$ loop under the static rotor eccentricity looks quite different from the self-inductance. Instead of a pure sinusoidal waveform, more harmonic components are found in the mutual inductance under the static rotor eccentricity condition. The magnitudes of the harmonic components of the mutual inductance under the mixed eccentricity are greater than those under the static eccentricity condition, as shown in Figure 4.18. However, it is seen from Figure 4.17 that the mutual inductance is a constant under dynamic rotor eccentricity.

### 4.3.3 Mutual Inductance Between $i^{th}$ Loop and $i+k^{th}$ Loop ($k \neq 1$)

The equation to calculate the Mutual inductance between $i^{th}$ loop and $i+k^{th}$ loop can be expressed as:

$$L_{i,i+k} = \mu_0 rl \int_0^{2\pi} \frac{1}{g(\theta,\theta_{rm})} \cdot n_i(\theta) \cdot N_{i+k}(\theta) \cdot d\theta \tag{4.11}$$

where, $n_i(\theta)$ is the turn function of $i^{th}$ rotor loop; $N_{i+k}(\theta)$ is the winding function of $i+k^{th}$ rotor loop; $g(\theta,\theta_{rm})$ is the air gap function; $i$ is the rotor loop number and $k$ is any integral number between 2 and $n$. $n$ is the rotor bar number.

The mutual inductances between rotor $i^{th}$ loop and $i+k^{th}$ loop under the static rotor eccentricity, dynamic rotor eccentricity and mixed rotor eccentricity conditions are shown in Figure 4.19, Figure 4.20 and Figure 4.21 respectively.

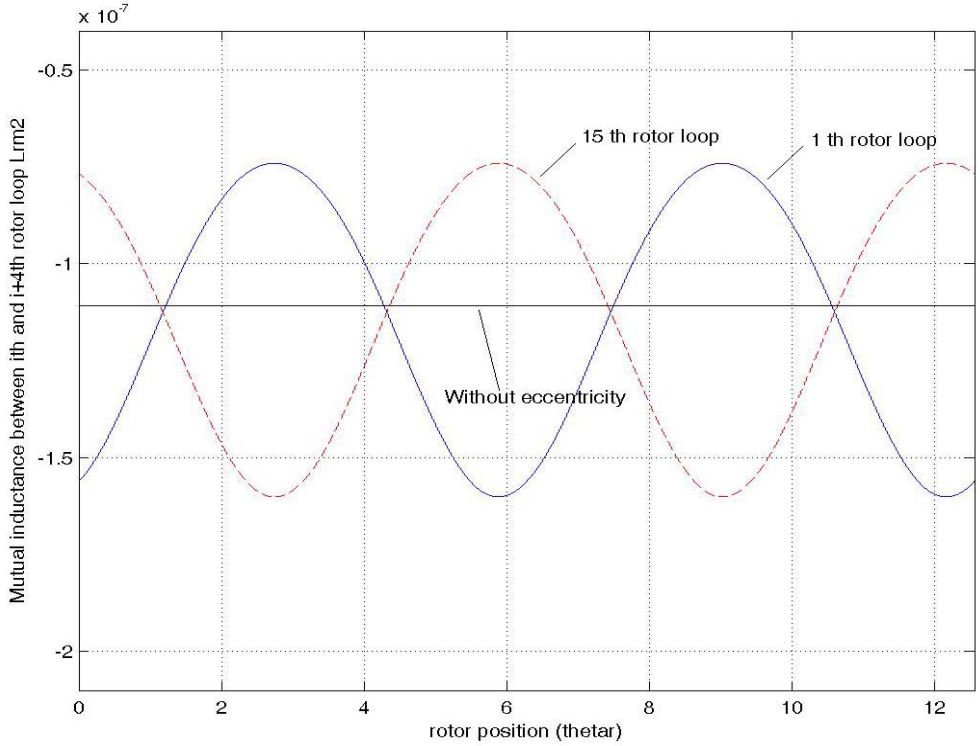


Figure 4.19 Mutual inductance under 20% static rotor eccentricity

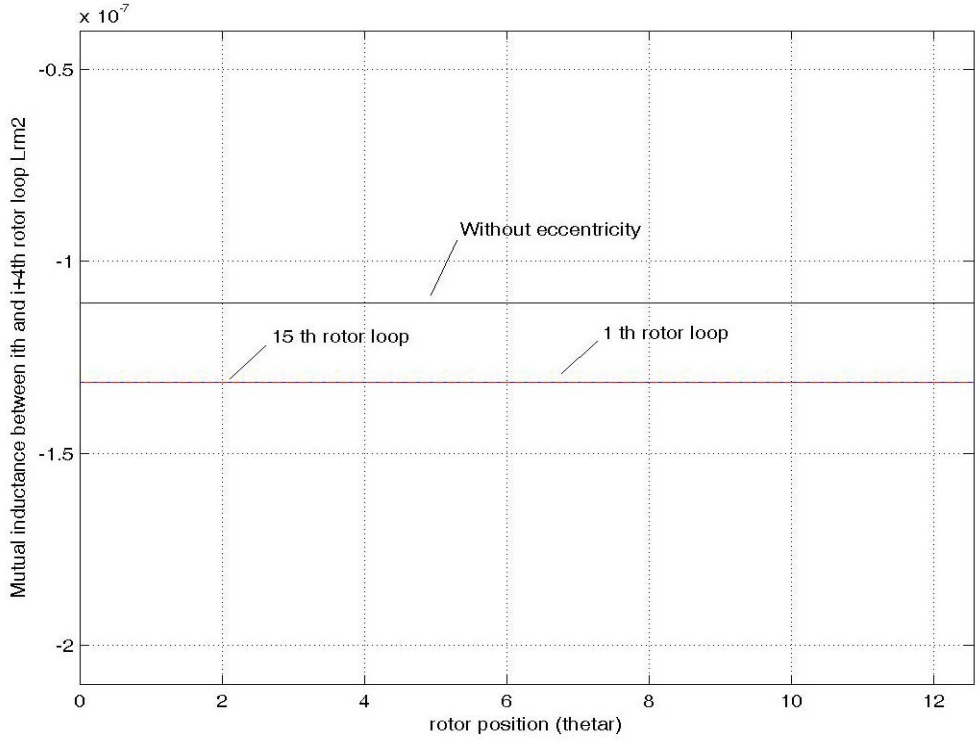


Figure 4.20 Mutual inductance under 10% dynamic rotor eccentricity

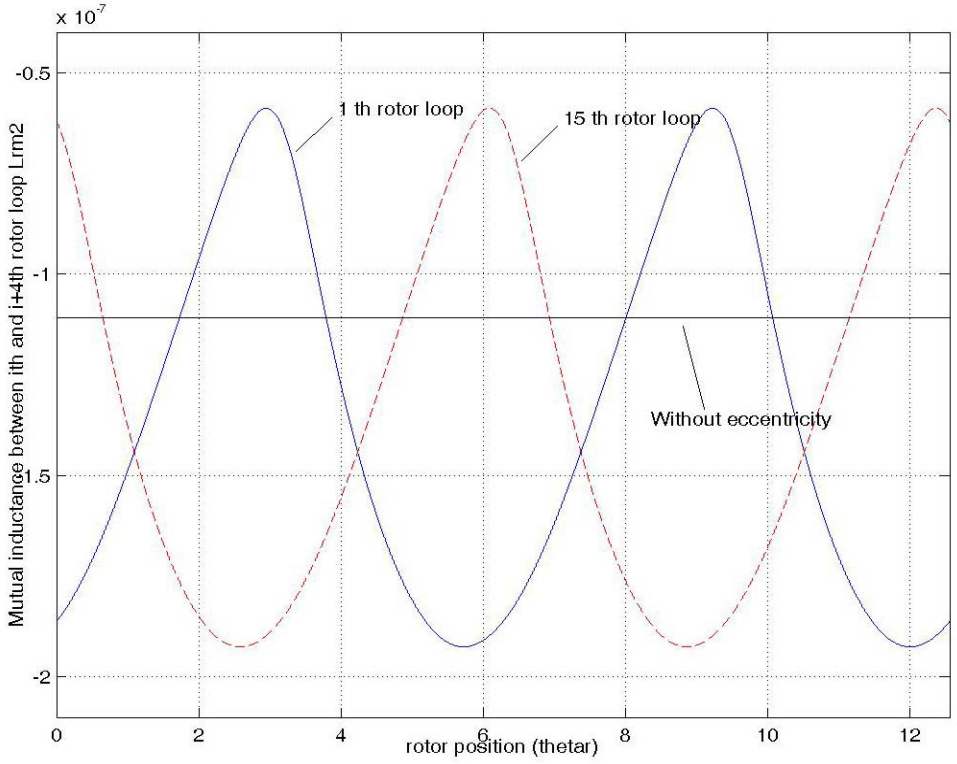


Figure 4.21 Mutual inductance under 20% static and 10% dynamic rotor eccentricity

It is interesting to note that the mutual inductance between rotor $i^{th}$ loop and $i+k^{th}$ loop under the static rotor eccentricity is a sinusoidal waveform, which is similar to the self-inductance but different from the mutual inductance between rotor $i^{th}$ loop and $i+1^{th}$ loop, as shown in Figure 4.19. The mutual inductance is a constant under the dynamic rotor eccentricity condition as given in Figure 4.20. More harmonic components are present in the mutual inductance when the machine is under the mixed rotor eccentricity condition, which is the same as the other rotor inductances.

## 4.4 Mutual Inductances Calculation

The mutual inductances are the inductances between stator windings and rotor loops, which is a very important and interesting part of the inductance calculation. Mutual inductances changing by the rotor angle under the constant air gap condition are shown in the previous chapter. The mutual inductances shown here are under different rotor eccentricity conditions. These mutual inductances are quite different from those when the machine is under the constant air gap condition as shown in the upcoming figures.

### 4.4.1 Stator Rotor Mutual Inductances of the ABC Winding Set

From the general winding function definition, the equation of stator rotor mutual inductance can be expressed as:

$$L_{ij} = \mu_0 rl \int_0^{2\pi} \left[A_0 + A_1 \cos\left(\theta - \theta_{rm}^{'}\right)\right] \cdot n_i(\theta) \cdot \left[n_j(\theta) - \left\langle n_j(\theta)\right\rangle - K_j\left(\theta_{rm}^{'}\right)\right] \cdot d\theta \qquad (4.12)$$

where, $K_j\left(\theta_{rm}^{'}\right) = \frac{A_1}{2\pi A_0} \int_0^{2\pi} n_j(\theta)\cos\left(\theta - \theta_{rm}^{'}\right) d\theta$, $n_i(\theta)$ is the turn function of $i^{th}$ rotor loop, $n_j(\theta)$ is the turn function of stator $j^{th}$ winding and $A_0 + A_1 \cos\left(\theta - \theta_{rm}^{'}\right)$ is the inverse of the air gap function.

The stator rotor mutual inductance under the static rotor eccentricity, dynamic rotor eccentricity and mixed rotor eccentricity conditions are shown in Figure 4.22, Figure 4.23 and Figure 4.24 respectively.

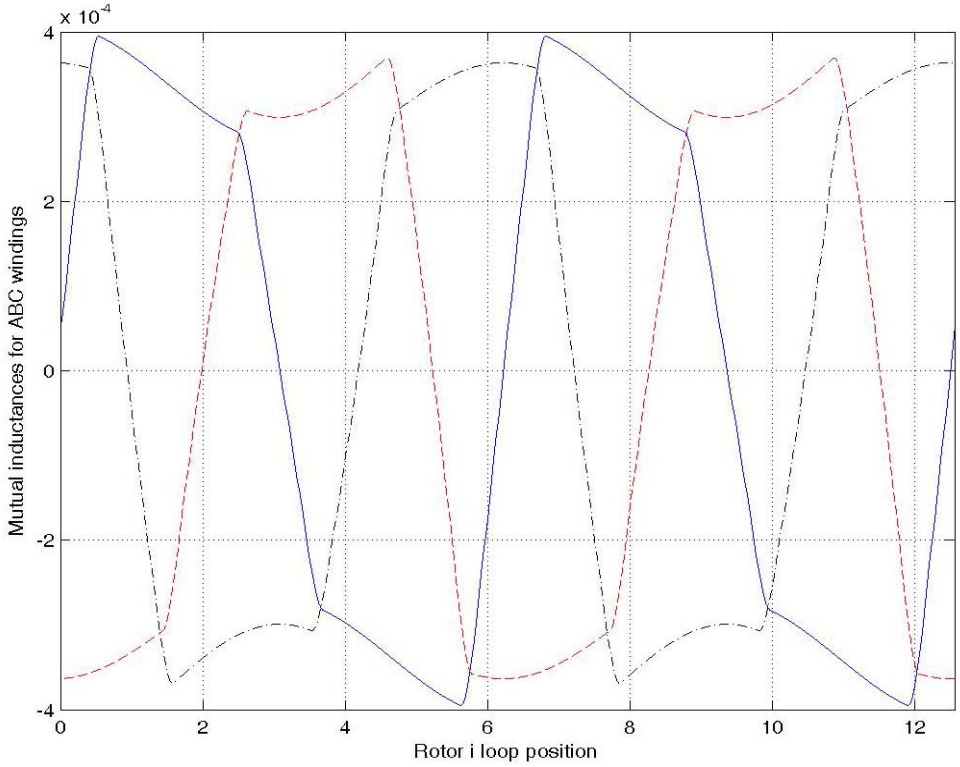


Figure 4.22 Stator rotor mutual inductance under 20% static rotor eccentricity

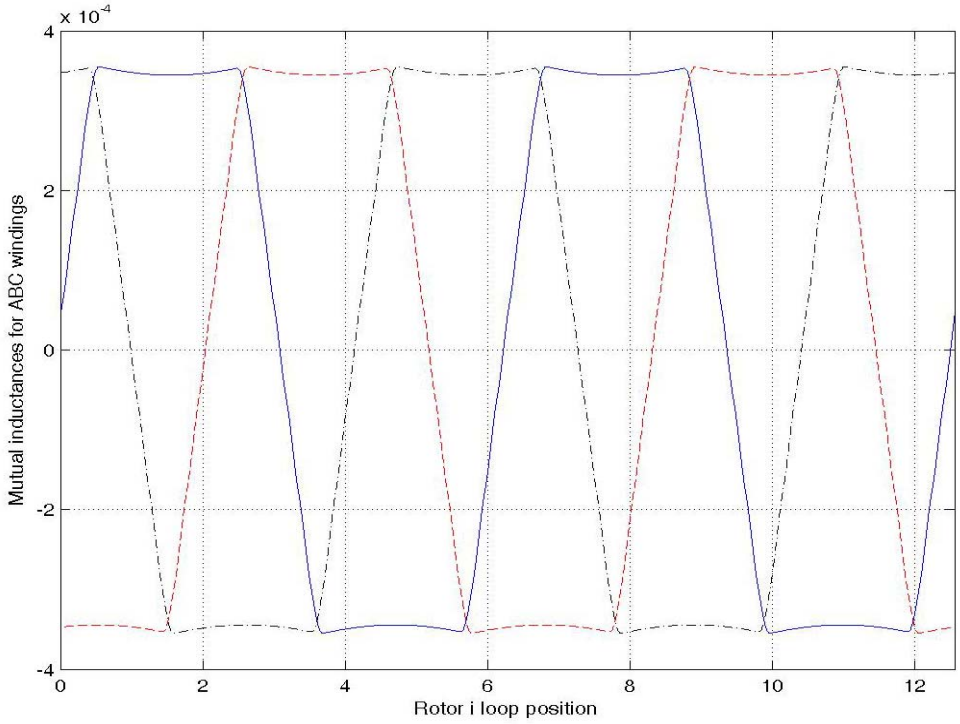


Figure 4.23 Stator rotor mutual inductance under 10% dynamic rotor eccentricity

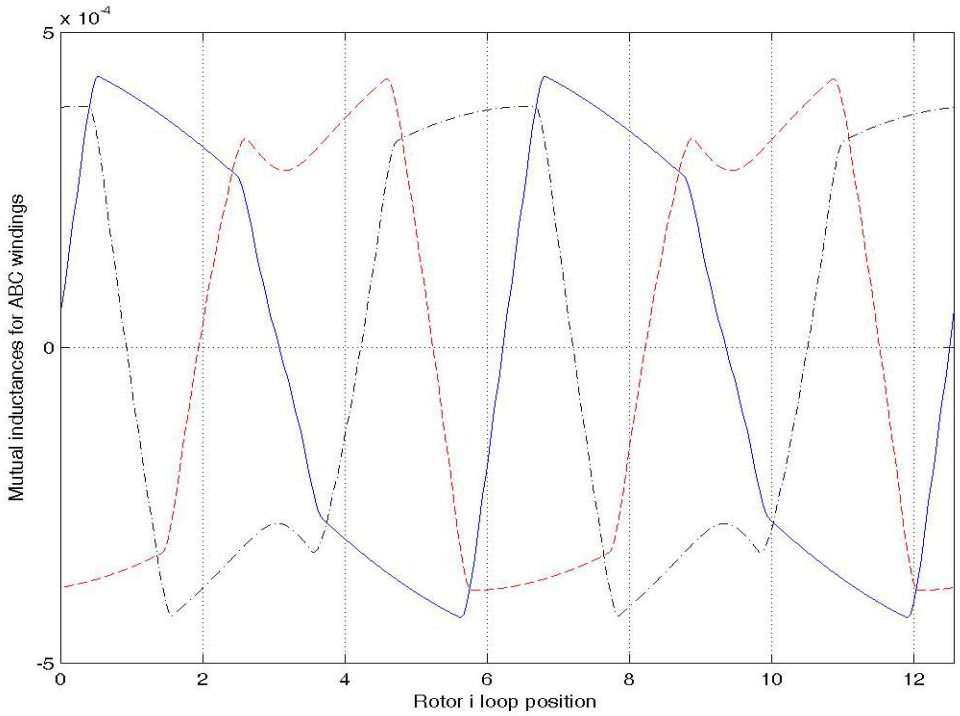


Figure 4.24 Stator rotor mutual inductance under 20% static and 10% dynamic rotor eccentricity

From the simulation results, it can be seen that the static rotor eccentricity and dynamic rotor eccentricity conditions influence the mutual inductances in various ways. Under both the static and mixed rotor eccentricity condition, the uniform envelope cannot be found and the mutual inductances will lose the symmetric characteristic. However, the mutual inductances are symmetric under the dynamic eccentricity condition. Comparing the waveforms under the static and mixed rotor eccentricity conditions, it is observed that the waveform distortion is worse in the mixed rotor eccentricity condition.

### 4.4.2 Stator Rotor Mutual Inductances of the XYZ Winding Set

The equation to calculate the mutual inductance is the same as the one for the ABC winding set, however, since the XYZ winding set has 6 pole, $K_j\left(\theta_{rm}^{'}\right)$ in the equation will be zero for the XYZ winding set, such that the difference between the waveforms of the ABC winding set and the XYZ winding set can be found not only in the frequency, but also in the envelope.

The stator rotor mutual inductance under the static rotor eccentricity, dynamic rotor eccentricity and mixed rotor eccentricity conditions for the XYZ winding set are shown in the Figure 4.25, Figure 4.26 and Figure 4.27 respectively. Differing from the mutual inductances in the ABC winding set, a uniform envelope can be found in this case and the magnitude of the envelope depends on the degree of the static rotor eccentricity. The waveform under the dynamic rotor eccentricity condition looks similar to the one in the constant air gap, however, the magnitude of the inductance under the dynamic rotor eccentricity condition is greater than the one under the static rotor eccentricity condition, and the magnitude of the inductance increases if the degree of the dynamic eccentricity increases. Under the mixed rotor eccentricity condition, the uniform envelope is no longer sinusoidal and the waveform contains more harmonic components.

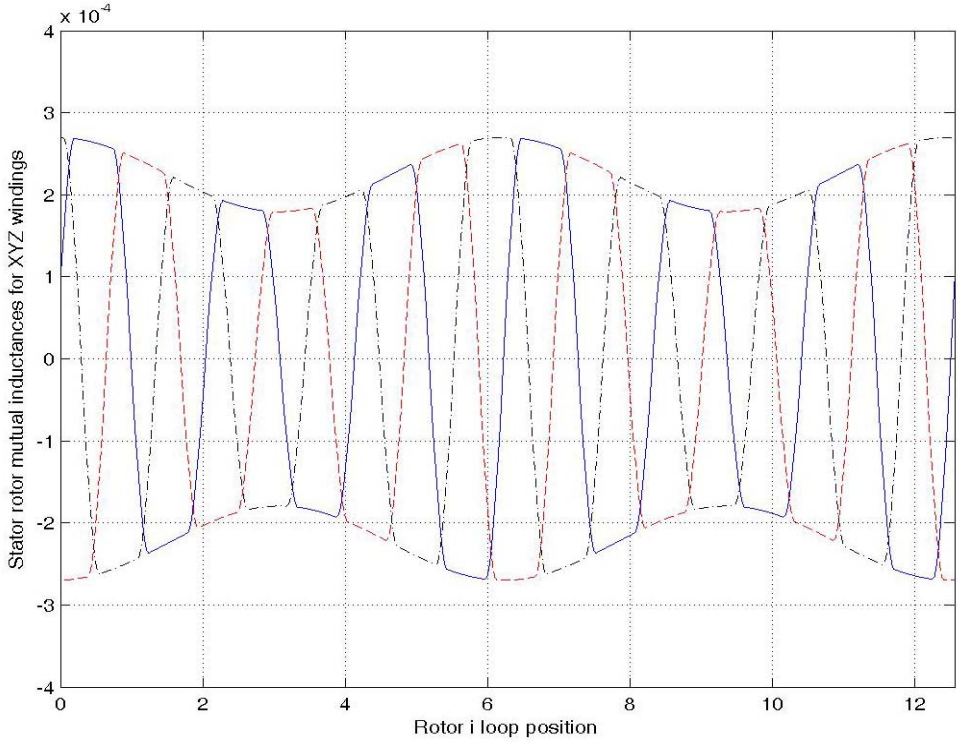


Figure 4.25 Stator rotor mutual inductance under 20% static rotor eccentricity

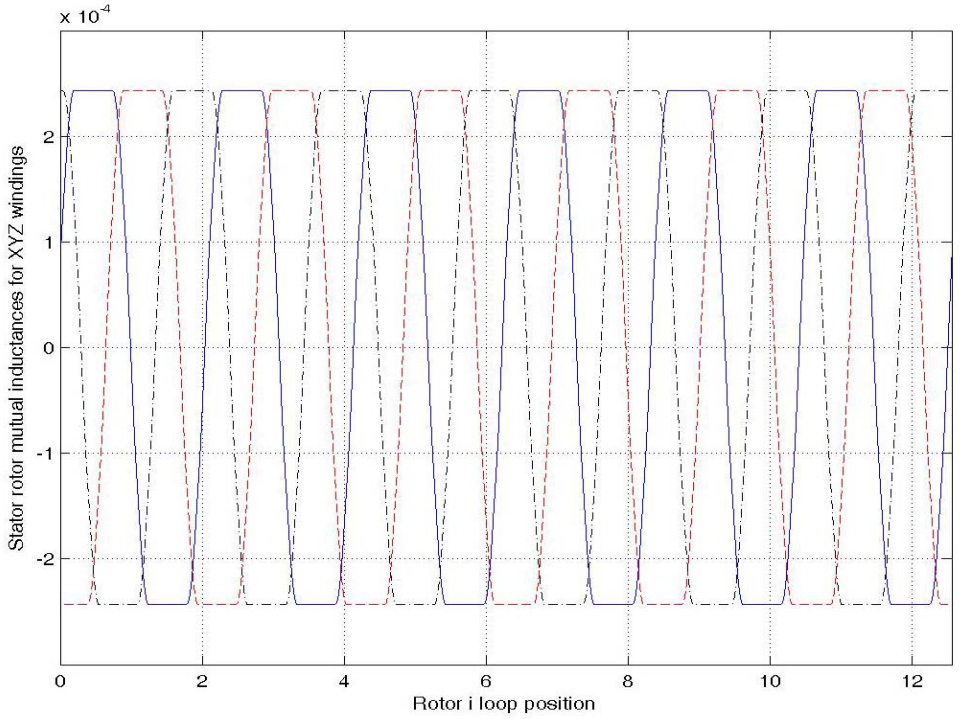


Figure 4.26 Stator rotor mutual inductance under 10% dynamic rotor eccentricity

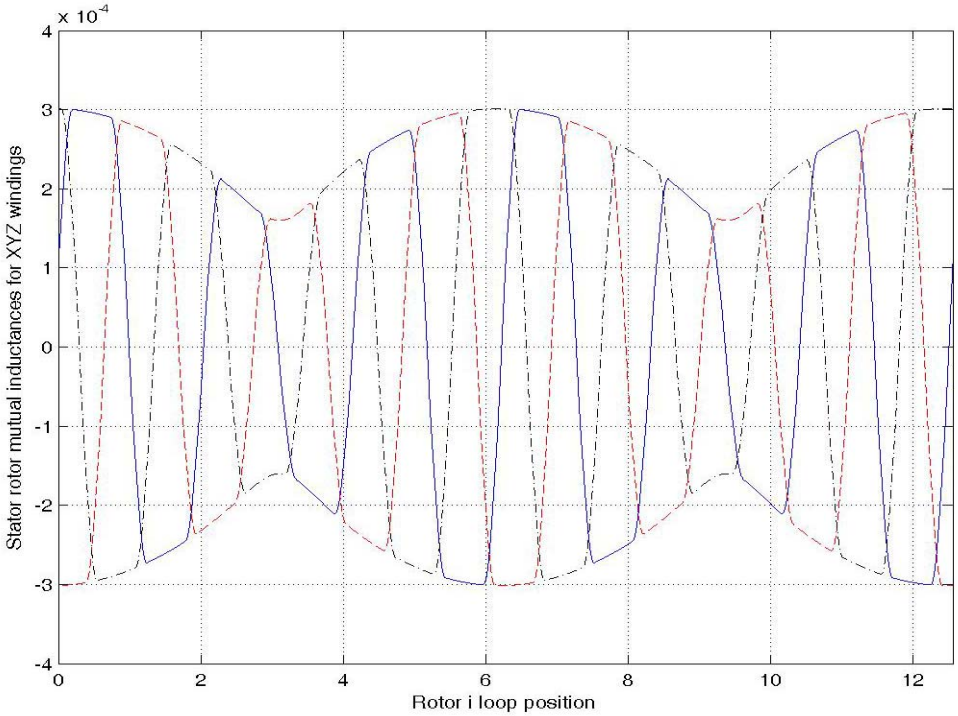


Figure 4.27 Stator rotor mutual inductance under 20% static and 10% dynamic rotor eccentricity

## 4.5 Model of the Dual Stator Winding Machine

The model of the dual stator winding machine used under rotor eccentricity conditions is the same as the one given in Chapter 3, except the torque calculation using the power balance method is used to simplify the calculation process.

The expression for the electromagnetic torque is derived using the Manley-Rowe power-frequency relationships for nonlinear circuits since electric machines are nonlinear energy-conversion circuits [4.7, 4.8]. The co-energy method was not used to determine the equation for the electromagnetic torque in view of the excessive computational burden occasioned by the need to find derivatives of rotor-angle dependent stator-rotor inductances and other components of the stator and rotor inductances. The Manley-Rowe real power-frequency relationship for a dissipation-less circuit with non-linear or time-

varying inductances excited by four independent angular frequencies ($\omega_1$, $\omega_2$, $\omega_{s1}$, $\omega_{s2}$) are expressed as :

$$\sum_{m=0}^{+\infty}\sum_{n=-\infty}^{+\infty}\sum_{k=-\infty}^{+\infty}\sum_{z=-\infty}^{+\infty}\frac{m\cdot P\left(m\omega_1+n\omega_2+k\omega_3+z\omega_4\right)}{m\omega_1+n\omega_2+k\omega_3+z\omega_4}=0$$

$$\sum_{n=0}^{+\infty}\sum_{m=-\infty}^{+\infty}\sum_{k=-\infty}^{+\infty}\sum_{z=-\infty}^{+\infty}\frac{n\cdot P\left(m\omega_1+n\omega_2+k\omega_3+z\omega_4\right)}{m\omega_1+n\omega_2+k\omega_3+z\omega_4}=0 \qquad (4.13)$$

$$\sum_{k=0}^{+\infty}\sum_{m=-\infty}^{+\infty}\sum_{n=-\infty}^{+\infty}\sum_{z=-\infty}^{+\infty}\frac{k\cdot P\left(m\omega_1+n\omega_2+k\omega_3+z\omega_4\right)}{m\omega_1+n\omega_2+k\omega_3+z\omega_4}=0$$

$$\sum_{z=0}^{+\infty}\sum_{m=-\infty}^{+\infty}\sum_{n=-\infty}^{+\infty}\sum_{k=-\infty}^{+\infty}\frac{z\cdot P\left(m\omega_1+n\omega_2+k\omega_3+z\omega_4\right)}{m\omega_1+n\omega_2+k\omega_3+z\omega_4}=0$$

The average input power into the machine is assumed to be positive, average power going out of the machine is negative and $P\left(\omega_a+\omega_b\right)=P\left(-\omega_a-\omega_b\right)$. $P\left(m\omega_1+n\omega_2+k\omega_3+z\omega_4\right)$ is the average real power flow at angular frequency $\left(m\omega_1+n\omega_2+k\omega_3+z\omega_4\right)$. In using (4.13), all sources of loss (such as copper and core losses in the electrical circuit and the mechanical and frictional losses in the mechanical subsystem) are considered to be external to the energy converting electric machines. Hence, (4.13) in the context of dual stator winding induction machines, the average powers are the input and output powers of the time varying inductances between the stator and rotor windings. The angular frequency of the voltages impressed on the ABC winding set is $\omega_1$ and the angular frequency of the rotor currents due to this voltage is $\omega_{s1}$, the angular frequency of the voltage connected to the XYZ winding set and the corresponding angular frequency of the rotor currents induced by this impressed voltage source are $\omega_2$, $\omega_{s2}$ respectively. The dependent angular frequency is the mechanical

rotor speed $\omega_m$ ($\omega_{r1} = 0.5P_1\omega_m$ for the ABC winding set, $\omega_{r2} = 0.5P_2\omega_m$ for the XYZ winding set) Then, the slip frequencies are $\omega_{s1} = \omega_1 - \omega_{r1}$ and $\omega_{s2} = \omega_2 - \omega_{r2}$, where the angular rotor speeds corresponding to the windings with $P_1$ and $P_2$ poles are $\omega_{r1}$ and $\omega_{r2}$ respectively. Since the interactions between $\omega_1$ and $\omega_{s2}$, $\omega_1$ and $\omega_2$, $\omega_{s2}$ and $\omega_1$, $\omega_{s1}$ and $\omega_{s2}$ are nonexistent, the corresponding terms such as $P(\omega_1 - \omega_{s2})$ should be eliminated and the final equations (4.14) are:

$$\frac{P(\omega_1)}{\omega_1} = -\frac{P(\omega_1 - \omega_{s1})}{\omega_1 - \omega_{s1}} \qquad \frac{P(\omega_2)}{\omega_2} = -\frac{P(\omega_2 - \omega_{s2})}{\omega_2 - \omega_{s2}} \tag{4.14}$$

$$\frac{P(\omega_{s1})}{\omega_{s1}} = -\frac{P(\omega_{s1} - \omega_1)}{\omega_{s1} - \omega_1} \qquad \frac{P(\omega_{s2})}{\omega_{s2}} = -\frac{P(\omega_{s2} - \omega_2)}{\omega_{s2} - \omega_2}$$

Hence,

$$\frac{P(\omega_1)}{\omega_1} = \frac{P(\omega_{s1})}{\omega_{s1}} = -\frac{P(\omega_{r1})}{\omega_{r1}} \qquad \frac{P(\omega_2)}{\omega_2} = \frac{P(\omega_{s2})}{\omega_{s2}} = -\frac{P(\omega_{r2})}{\omega_{r2}}$$

The electromagnetic torques from two stator windings and the total electromagnetic torques can be written as:

$$T_{e1} = \frac{P(\omega_1)}{\omega_1} \qquad T_{e2} = \frac{P(\omega_2)}{\omega_2} \qquad T_e = T_{e1} + T_{e2} \tag{4.15}$$

where, $\omega_1 = 2\pi f_1$ and $\omega_2 = 2\pi f_2$.

The average active powers going into the ABC and XYZ winding sets, which are $P(\omega_1)$ and $P(\omega_2)$, are given as :

$$\begin{aligned} P(\omega_1) &= v_a i_a + v_b i_b + v_c i_c - r_{s1}\left(i_a^2 + i_b^2 + i_c^2\right) \\ P(\omega_2) &= v_x i_x + v_y i_y + v_z i_z - r_{s2}\left(i_x^2 + i_y^2 + i_z^2\right) \end{aligned} \tag{4.16}$$

Equations similar to (4.15-4.16) were used in [4.9] to calculate the developed electromagnetic torque of the three-phase synchronous machine. Using the measured motor terminal voltages and phase currents to synthesize (4.15-4.16), the measured starting torque of the tested synchronous machine was shown to compare favorably with the calculated torque. Hence, the Manley-Rowe power-frequency relationships set forth in this paper to determine the electromagnetic torques of electric machines gives a firmer theoretical basis for the input power based electromagnetic torque determination and the experimental work in [4.9].

## 4.6 Simulation Results

Based on the full model of the dual winding induction machine and the calculation of the inductances shown in the previous Sections, the simulation of the dual stator winding induction machine under mixed eccentricity condition was undertaken, in which only the fundamental component of the rotor circuit q-d transformation is considered. The mixed eccentricity condition, in which 20% static rotor eccentricity and 5% dynamic rotor eccentricity are combined, is considered in the computer simulation results. Some of the calculated parameters which are constant are given in Table 3.1. The no-load starting transient simulation results are shown in Figure 4.28 and the corresponding rotor bar currents are shown in Figure 4.30 when the two sets of windings are fed with voltages satisfying constant voltage/Hertz in which the ratio of the frequency of the 6-pole stator winding set to those of the 2-pole stator winding set is 3. The frequencies of the ABC (2-pole) and XYZ (6-pole) stator winding sets are 30 Hz and 90 Hz respectively. The line-to-line voltages of the ABC (2-pole) and XYZ (6-pole) stator winding sets are 67 V and

202 V respectively. After the machine has achieved steady state operating condition at 0.4 second, a 3 Nm (rated load) load is added to the machine to stimulate a dynamic response. The simulation results for dynamic responses of the machine are shown in Figure 4.29 and the corresponding rotor bar currents are shown in Figure 4.31. When the simulation results are compared to those when the air-gap length is constant, it is observed in the waveforms of the developed electromagnetic torque, rotor currents and the stator currents that the waveforms under the mixed eccentricity condition contain more harmonic components. The stator currents for both the ABC winding set and the XYZ winding set are not pure sinusoidal under no load steady state condition and the current waveforms are not improved under the rated load condition. Obviously a pulsation torque component is observed in the waveform of the electromagnetic torque under the rated load condition. All the simulation results show that under rotor eccentricity conditions, more harmonic components appear in the machine developed electromagnetic torque and currents; harmonic components which can be used to diagnose the state of health of the dual stator winding induction machines. From the simulation results, the harmonic content of the current waveforms of the 2-pole stator set of windings are higher than those of the 6-pole stator winding set due to the frequency component match of the 2-pole winding set distribution and the approximate inverse gap function. Similar frequency component match, leading to increased harmonic current magnitude is also possible for the 6-pole winding set distribution if the approximate inverse gap function contains commensurate higher frequency components. However, the influence of this interaction is not as significant in the 6-pole winding set. In general, harmonic currents are obtained due to the harmonics in the inductances; they decrease as

the number of poles for the winding set increases. Hence, the 2-pole induction machine has the worst performance and much greater harmonic current components under rotor eccentricity conditions. Under the steady state operating condition, the Fourier series components of one phase current and the electromagnetic torque of both the ABC and the XYZ winding sets are shown in Fig. 4.32. It is observed that the two-pole winding set has lower frequency (torque, current) harmonic components when compared to the 6-pole winding set.

From [4.1], the principal slot harmonics (PSH) of the induction machine can be expressed as:

$$PSH = \left( R\frac{1-s}{p} \pm 1 \right) f \tag{4.17}$$

where, $R$ is the rotor bar number; $s$ is the slip; $p$ is the pole pair number of the machine and $f$ is the input voltage frequency. From the machine parameters shown in the Appendix for the ABC winding set, the calculated PSH is 853.2 Hz for $s = 0.02$. The spectrum of the simulated phase A current shown in Figure 4.32(a) shows that the PSH is significant. Some harmonic frequency components, because of the mixed rotor eccentricity can also be found around the PSH, which coincide with the results obtained in the previous work [4.1, 4.6]. For the XYZ winding set, the simulated current spectrum did show the principal slot harmonic. However, only the PSH is significant and the other harmonic frequencies around it are almost invisible. For this machine, under the rotor eccentricity condition it is easier for the PSH in the currents of the 2-pole ABC winding set to be detected.

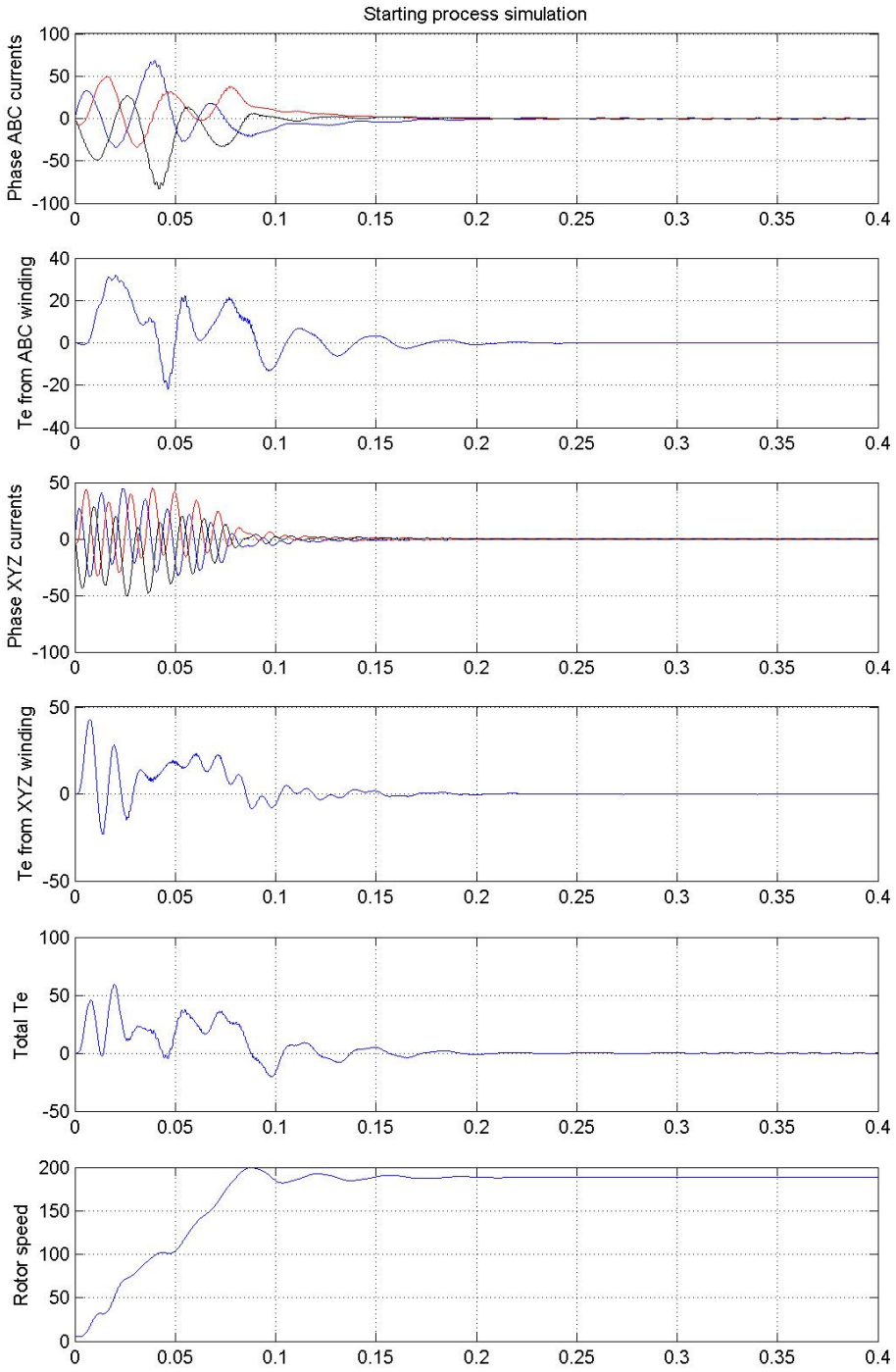


Figure 4.28 Starting simulation of dual stator winding induction machine under mixed rotor eccentricity condition, a) phase ABC currents, b) electromagnetic torque from ABC windings, c) phase XYZ currents, d) electromagnetic torque from XYZ windings; e) total electromagnetic torque, f) rotor speed.

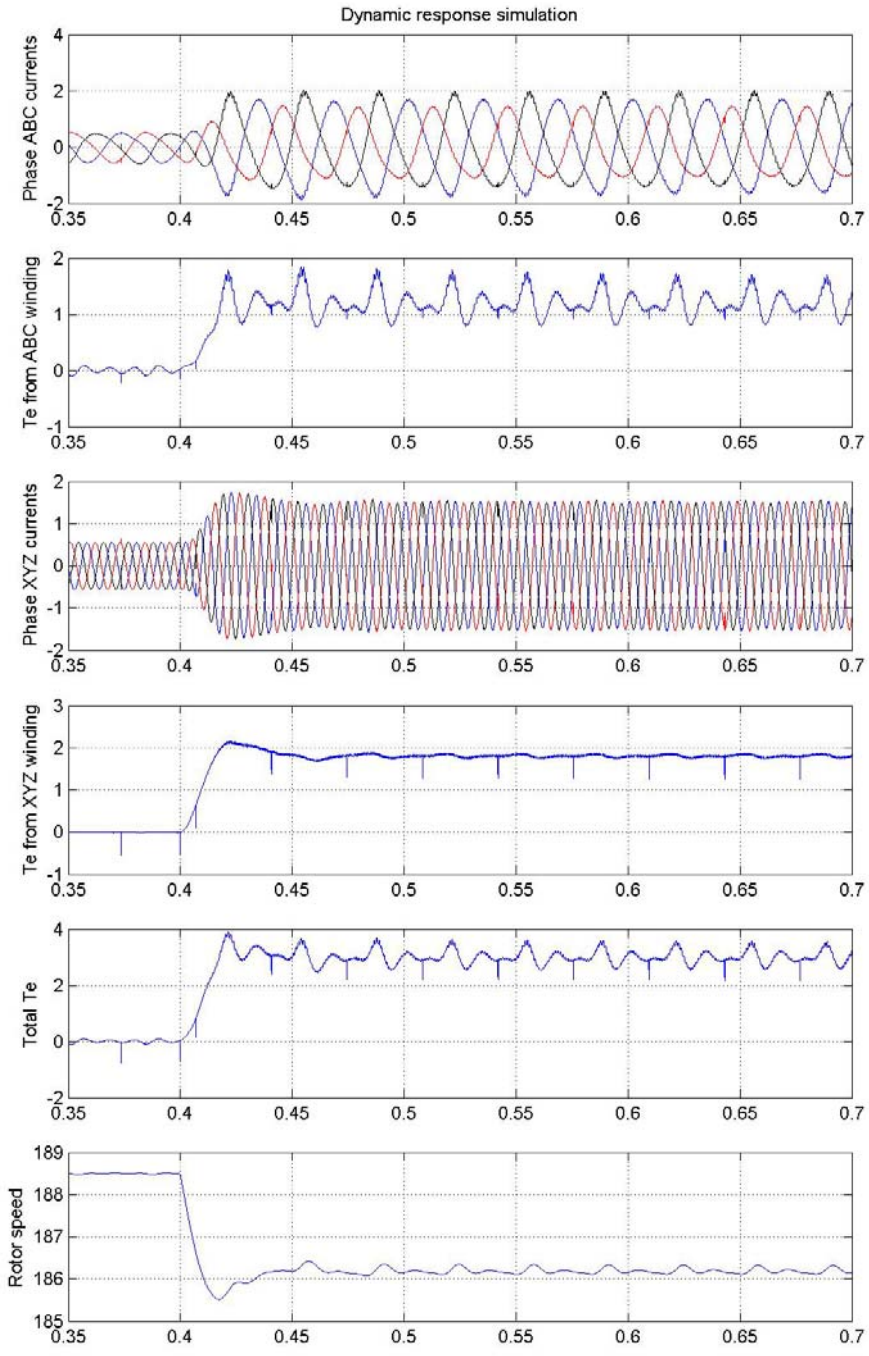


Figure 4.29 Dynamic response of dual stator winding induction machine under mixed rotor eccentricity condition, a) phase ABC currents, b) electromagnetic torque from ABC windings, c) phase XYZ currents, d) electromagnetic torque from XYZ windings; e) total electromagnetic torque, f) rotor speed.

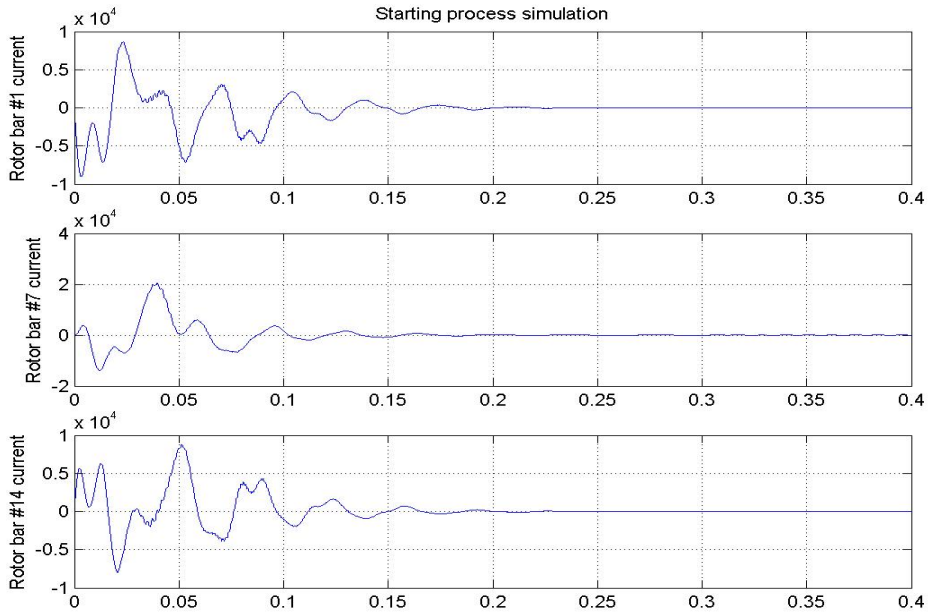


Figure 4.30 Rotor bar current during starting process of dual stator winding induction machine under mixed rotor eccentricity condition, a) #1 rotor bar current, b) #7 rotor bar current, c) #14 rotor bar current.

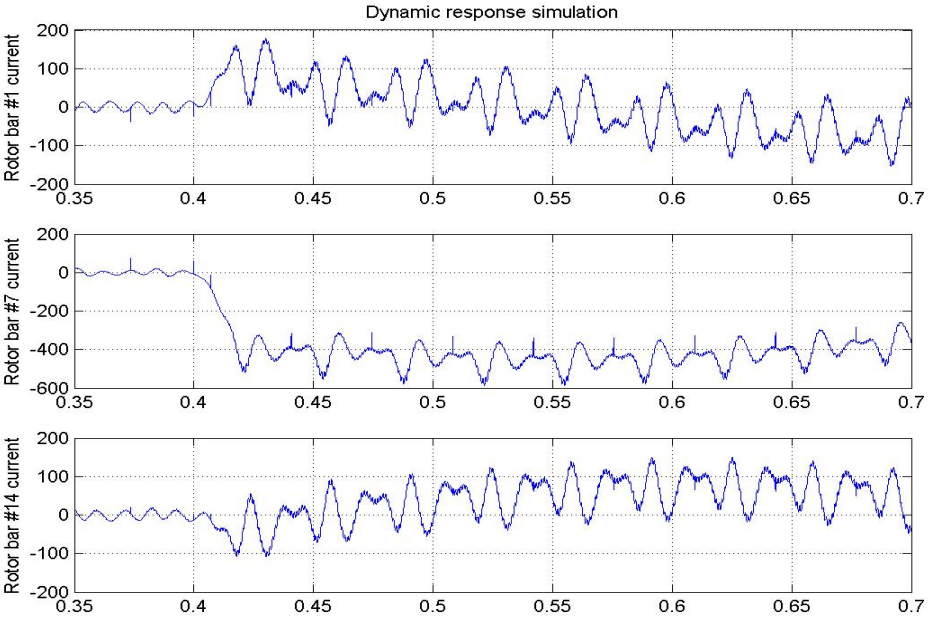


Figure 4.31 Rotor bar current during dynamic response of dual stator winding induction machine under mixed rotor eccentricity condition, a) #1 rotor bar current, b) #7 rotor bar current, c) #14 rotor bar current.

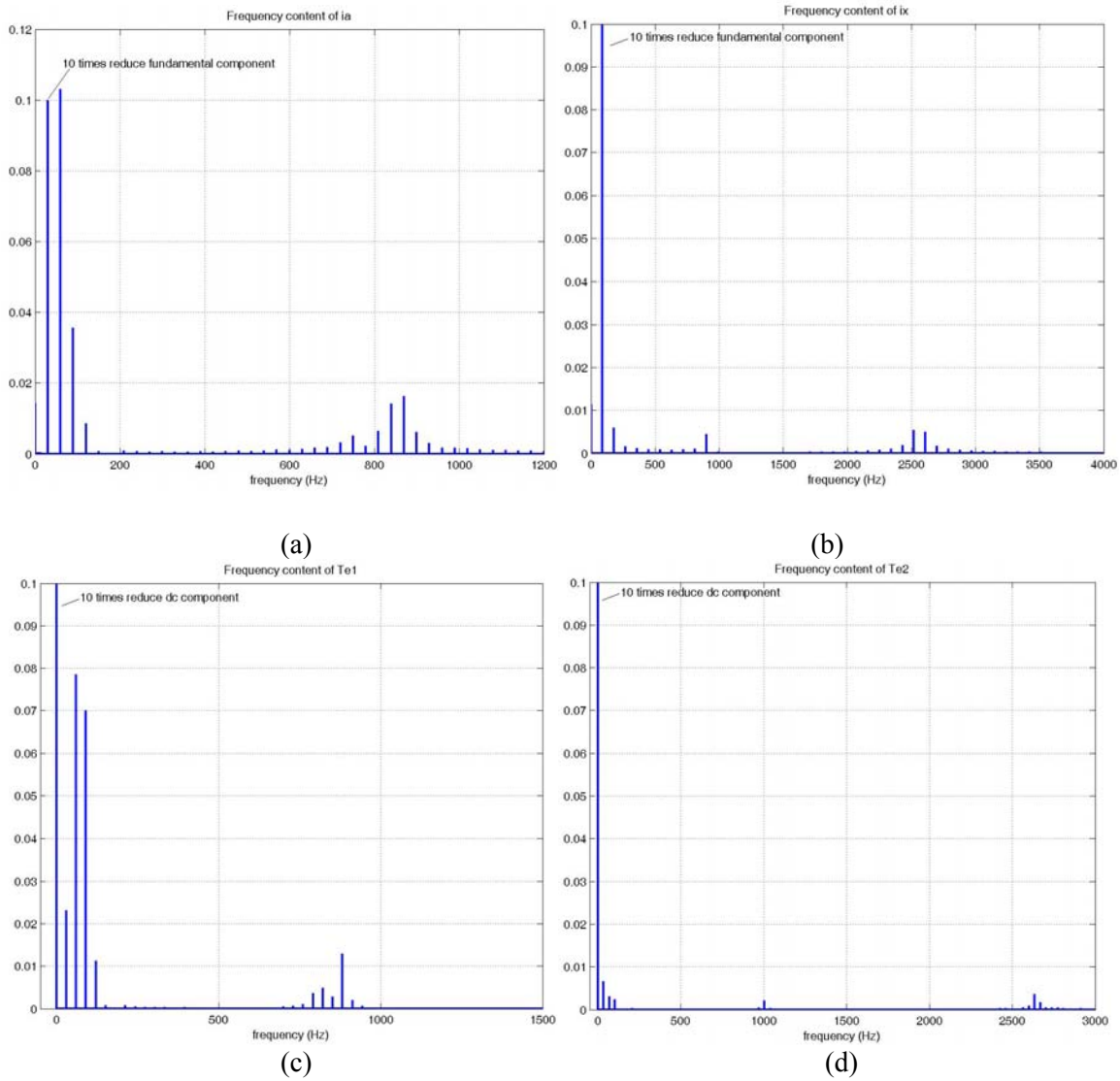


Figure 4.32. Normalized Fourier series analysis of the simulation results, (a) phase A current, (b) phase X current, (c) electromagnetic torque of the ABC winding set, (d) electromagnetic torque of the XYZ winding set

Since the stator rotor mutual inductance of the 2-pole ABC winding set has the highest harmonic components as shown and explained previously, the corresponding developed electromagnetic torque has greater harmonic components as shown in Figure 4.32 (c) while the torque spectrum found in the XYZ winding set have much lower harmonic components as shown in Figure 4.32(d). Both the form of the inductances and the simulation results show that the 2-pole induction machine or the 2-pole three-phase

winding set of the dual induction machine has more harmonic contents than the other winding set having more than 2 poles under the eccentricity conditions.

## 4.7 Conclusions

In this chapter, an analysis of a dual stator winding induction machine under rotor eccentricity conditions is presented. The method for calculating the inductances is based on the general winding function approach. The calculation and waveforms of stator, rotor and mutual inductances under the static, dynamic and mixed rotor eccentricity conditions are clearly set forth and illustrated for the first time. The 2-pole winding set of the induction machine has the worst performance in terms of generating more harmonic inductance components under rotor eccentricity conditions when it is compared to the other higher pole number stator winding set. Computer simulation of the starting transient is presented under the mixed eccentricity condition as well as the steady state and dynamics performances. Finally, the frequency components of the currents and electromagnetic torque are given indicating the presence of non-fundamental and low order harmonics in currents and torque induced by the presence of the eccentricity conditions.

# CHAPTER 5

# FIELD ANALYSIS OF DUAL STATOR WINDING INDUCTION MACHINE

## 5.1 Introduction

The dual stator winding induction machine is a special design based on the convention squirrel-cage induction machine. Two stator winding set with different numbers of poles share a common squirrel cage rotor. These two stator winding sets have been proven to be completely decoupled as shown in [1.11], however a potential coupling between the stator winding sets through the common rotor bar currents may exist. Are these two stator winding sets coupled or not? How do the fields interact with each other? Is there any electromagnetic torque component due to the coupling of two stator winding sets? All these questions are very relevant in this special machine and will be answered in this chapter.

The analysis method proposed by Williamson for an induction machine having a general winding connection and any supply configuration in [5.1] has been found to be suited to the field analysis of electric machines. The well-known rotating-field theory together with a coupling impedance model is used. The application of this method to the understanding of the asynchronous and synchronous operation of the "brushless doubly-fed machine" has been demonstrated in [1.8]. Recently, the brushless doubly-fed induction machine has been understood deeply through the development of the steady-state equivalent circuit, discussion of design issues and operation as either as a generator

or motor [5.2-5.3]. In this chapter, the first attempt at a deeper understanding of the dual winding stator induction machine with a squirrel-cage rotor using the field analysis method is reported. The advantages of this analytical tool are the representation of all the fields in the machine and their interactions as well as the opportunities to determine possible torque components and the conditions of stator frequencies and rotor speeds under which torque components can be developed. The coupled circuit modeling approach is used generate two models of this machine: In the first, the machine is treated as two separate machines coupled by the rotor speed with each stator winding set interacting independently with the rotor circuit. The second model presumes that there is only one rotor circuit (carrying the total current) to which the two stator windings mutually interact. Computer simulation of these models is used to highlight the additional torque component resulting from the mutual interactions of the stator winding and total rotor currents under transient condition.

## 5.2 Field Analysis Development

### 5.2.1 Voltages Equations

In the design of the dual stator winding induction machines, two stator winding sets are arranged to be totally decoupled [1.1]. However, two stator winding sets might couple with the same rotor circuit and generate an electromagnetic torque. The field analysis method is therefore used to determine the voltages induced by the stator windings and the rotor circuits including the interactions [1.8, 5.1].

In the analysis that follows the fundamental components of the stator winding distributions, stator and rotor currents and voltages are considered as these are sufficient to elucidate the fundamental operation of the machine. The two sets of three-phase windings with pole pair numbers $P_1$ and $P_2$ are henceforth called ABC and XYZ winding sets, respectively. The induced voltages found in the dual stator winding induction machine are:

A) Voltages in the ABC winding set by the stator currents flowing in the ABC winding set $u_{s1}$;

B) Voltages in the XYZ winding set by the stator currents flowing in the XYZ winding set $u_{s2}$;

C) Voltages in the ABC winding set by the stator currents flowing in the XYZ winding set $u_{qp}$;

D) Voltages in the XYZ winding set due to the stator currents flowing in the ABC winding set $u_{pq}$;

E) Voltages in the rotor loops due to the stator currents flowing in the ABC winding set $u_{rp}$;

F) Voltages in the rotor loops due to the stator currents following in the XYZ winding set $u_{rq}$;

G) Voltages in the ABC winding set due to the rotor currents induced by currents flowing in the ABC winding set $u_{prp}$;

H) Voltages in the XYZ winding set due to the rotor currents induced by currents flowing in the ABC winding set $u_{qrp}$;

I) Voltages in the XYZ winding set due to the rotor currents induced by currents flowing in the XYZ winding set $u_{qrq}$;

J) Voltages in the ABC winding set due to the rotor currents induced by currents flowing in the XYZ winding set $u_{prq}$;

The detail derivation for each component can be found in the following subsections.

5.2.1.1 Voltages in the ABC Winding Set by the Stator Currents flowing in the ABC Winding Set. If the stator currents and the winding distributions are known, the expressions for the stator voltages can be found as the function of the currents and winding distributions. The voltage expressions for the ABC winding set is firstly considered here.

The fundamental component of the winding distributions of the ABC winding set expressed in the complex variable form are given as:

$$\begin{cases} C_A(\theta) = \overline{C_{s1}}\, e^{-jP_1\theta} + \overline{C_{s1}}^{*}\, e^{jP_1\theta} \\ C_B(\theta) = \overline{C_{s1}} e^{-j\left(P_1\theta-\frac{2\pi}{3}\right)} + \overline{C_{s1}}^{*}\, e^{j\left(P_1\theta-\frac{2\pi}{3}\right)} \\ C_C(\theta) = \overline{C_{s1}} e^{-j\left(P_1\theta+\frac{2\pi}{3}\right)} + \overline{C_{s1}}^{*}\, e^{j\left(P_1\theta+\frac{2\pi}{3}\right)} \end{cases} \tag{5.1}$$

where, the subscripts A, B and C denote the phases of the ABC winding set; $P_1$ is the pole pair number of the ABC winding set; the angle θ is the circumferential angle of the stator and the symbol * depicts the complex conjugation of variables. The peak value of the winding function is given as:

$$\left|\overline{C_{s1}}\right| = \frac{C_{s1}}{\pi \cdot d} k_{s1} \tag{5.2}$$

where, $C_{s1}$ is the number of series connected turns per phase; $r$ is the mean air gap radius; $k_{s1}$ is the fundamental winding factor for the ABC winding set.

The three-phase balance currents flowing through the three-phase windings are represented as:

$$\begin{cases} i_A(t) = \mathrm{Re}\left(\sqrt{2}\,\overline{I_{s1}}\,e^{j\omega_1 t}\right) \\ i_B(t) = \mathrm{Re}\left(\sqrt{2}\,\overline{I_{s1}}\,e^{j\left(\omega_1 t-\frac{2\pi}{3}\right)}\right) \\ i_C(t) = \mathrm{Re}\left(\sqrt{2}\,\overline{I_{s1}}\,e^{j\left(\omega_1 t+\frac{2\pi}{3}\right)}\right) \end{cases} \tag{5.3}$$

where, $\overline{I_{s1}}$ is the complex value form of the current magnitude and phase angle, and the electric angular speed of the current is $\omega_1$. The symbol Re[] is the real part of the complex variable contained in the bracket. The surface current distribution of the winding set is the sum of the product of the winding distributions and stator currents and is given as:

$$J_1(\theta,t) = C_A(\theta)\cdot i_A(t) + C_B(\theta)\cdot i_B(t) + C_C(\theta)\cdot i_C(t) \tag{5.4}$$

Substituting (5.2) and (5.3) into (5.4) and simplifying, the surface current distribution due to the ABC winding set is given as:

$$J_1(\theta,t) = \mathrm{Re}\left\{\begin{array}{l} \sqrt{2}\,\overline{I_{s1}}\,e^{j\omega_1 t}\cdot\left(\overline{C_{s1}}\,e^{-jP_1\theta} + \overline{C_{s1}}^{*}\,e^{jP_1\theta}\right) + \\ \sqrt{2}\,\overline{I_{s1}}\,e^{j\left(\omega_1 t-\frac{2\pi}{3}\right)}\cdot\left(\overline{C_{s1}}\,e^{-j\left(P_1\theta-\frac{2\pi}{3}\right)} + \overline{C_{s1}}^{*}\,e^{j\left(P_1\theta-\frac{2\pi}{3}\right)}\right) + \\ \sqrt{2}\,\overline{I_{s1}}\,e^{j\left(\omega_1 t+\frac{2\pi}{3}\right)}\cdot\left(\overline{C_{s1}}\,e^{-j\left(P_1\theta+\frac{2\pi}{3}\right)} + \overline{C_{s1}}^{*}\,e^{j\left(P_1\theta+\frac{2\pi}{3}\right)}\right) \end{array}\right\} \qquad (5.5)$$
$$= \mathrm{Re}\left\{\sqrt{2}\left(3\overline{C_{s1}}\cdot\overline{I_{s1}}\right)e^{j(\omega_1 t-P_1\theta)}\right\}$$

The air gap field produced by the stator MMF is obtained by the application of Ampere's Law. The expression is:

$$\frac{\partial B_1}{\partial y} = \frac{\mu_0}{g}\cdot J_1(\theta,t) \qquad (5.6)$$

The illustrative diagram for the Ampere's Law is shown in Figure 5.1.

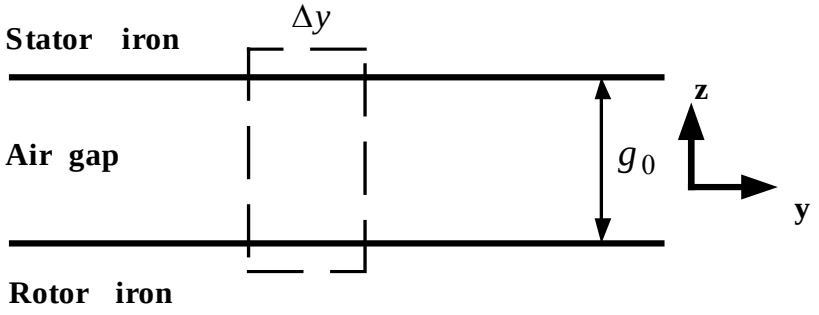


Figure 5.1 The diagram of Ampere's Law loop

The derivative of y can be expressed as:

$$\partial y = r\cdot\partial\theta \qquad (5.7)$$

where, $r$ is the mean air gap radius and $\theta$ is the stator angle.

Substituting (5.7) into (5.6),

$$\frac{\partial B_1}{\partial \theta} = \frac{\mu_0 r}{g} \cdot J_1(\theta, t) \tag{5.8}$$

Then the flux density is obtained by integrating (5.8) with respect to the stator angle $\theta$,

$$B_1 = \int \frac{\mu_0 r}{g} \cdot J_1(\theta, t) \cdot d\theta \tag{5.9}$$

Substituting the expression of surface current distribution (5.5) into (5.9),

$$B_1(\theta, t) = \mathrm{Re}\left\{ j \frac{\mu_0 r}{g P_1} \left[ \sqrt{2} \left( 3\overline{C_{s1}} \cdot \overline{I_{s1}} \right) e^{j(\omega_1 t - P_1 \theta)} \right] \right\} \tag{5.10}$$

The electric field induced at the stator surface is calculated by Faraday's Law. Since the air gap is z direction, the change only happens in the y direction:

$$\frac{\partial E}{\partial y} = \frac{\partial B}{\partial t} \tag{5.11}$$

Substituting (5.7) into (5.11),

$$\frac{\partial E_1}{\partial \theta} = r \frac{\partial B_1}{\partial t} = r B_1 \cdot j\omega_1 \tag{5.12}$$

Then the electric field is expressed as:

$$E_1 = \int j\omega_1 \cdot r \cdot B_1(\theta, t) \cdot d\theta \tag{5.13}$$

Substituting (5.10) into (5.13) and integrating, the electric field due to the ABC winding set is given as:

$$E_1(\theta, t) = \mathrm{Re}\left\{ - j \frac{\mu_0 \omega_1 r^2}{g P_1^2} \left[ \sqrt{2} \left( 3\overline{C_{s1}} \cdot \overline{I_{s1}} \right) e^{j(\omega_1 t - P_1 \theta)} \right] \right\} \tag{5.14}$$

The electromotive-force (EMF) induced in the stator phase A can be found by multiplying the electric field with the winding distribution of the phase A and is given as:

$$u_{s1}(t) = \int_{x=0}^{l} \int_{y=0}^{2\pi r} C_A(\theta) \cdot E_1(\theta, t)\, dy\, dx \tag{5.15}$$

Since the electric field and the winding distribution along the stator axial direction are uniform, the integration can be simplified as:

$$u_{s1}(t) = rl \int_{0}^{2\pi} C_A(\theta) \cdot E_1(\theta, t)\, d\theta \tag{5.16}$$

The expression of the induced phase 'A' voltage in the ABC winding set is determined by substituting the expression of winding distribution and electric field (5.1, 5.14) into (12) and integrating to yield,

$$u_{s1}(t) = 2\pi rl \,\mathrm{Re}\left\{ - j \frac{\mu_0 \omega_1 r^2}{g P_1^2} \overline{C_{s1}}^{*} \left[ \sqrt{2} \left( 3 \overline{C_{s1}} \cdot \overline{I_{s1}} \right) e^{j\omega_1 t} \right] \right\} \tag{5.17}$$

The fundamental currents flowing in the ABC winding set induce the same frequency voltage components in the stator ABC winding set if the stator windings are assumed to be sinusoidally distributed.

5.2.1.2 Voltages in the XYZ Winding Set by the Stator Currents Flowing in the XYZ Winding Set. For the XYZ winding set, the winding contribution is expressed as:

$$\begin{cases} C_X(\theta) = \overline{C_{s2}}\, e^{-jP_2\theta} + \overline{C_{s2}}^{*}\, e^{jP_2\theta} \\ C_Y(\theta) = \overline{C_{s2}} e^{-j\left(P_2\theta - \frac{2\pi}{3}\right)} + \overline{C_{s2}}^{*} e^{j\left(P_2\theta - \frac{2\pi}{3}\right)} \\ C_Z(\theta) = \overline{C_{s2}} e^{-j\left(P_2\theta + \frac{2\pi}{3}\right)} + \overline{C_{s2}}^{*} e^{j\left(P_2\theta + \frac{2\pi}{3}\right)} \end{cases} \tag{5.18}$$

where the subscripts X, Y and Z denote the phases of the XYZ winding set; $P_2$ is the pole pair number of the XYZ winding set; the absolute value of the magnitude is:

$$\left|\overline{C_{s2}}\right| = \frac{C_{s2}}{\pi \cdot d} k_{s2} \tag{5.19}$$

where, $C_{s2}$ is the number of series connected turns per phase; $d$ is the mean air gap diameter; $k_{s2}$ is the fundamental winding factor for the XYZ winding set.

The three-phase balance currents flowing through the phases can be expressed as:

$$\begin{cases} i_X(t) = \mathrm{Re}\left(\sqrt{2}\,\overline{I_{s2}}\, e^{j\omega_2 t}\right) \\ i_Y(t) = \mathrm{Re}\left(\sqrt{2}\,\overline{I_{s2}}\, e^{j\left(\omega_2 t - \frac{2\pi}{3}\right)}\right) \\ i_Z(t) = \mathrm{Re}\left(\sqrt{2}\,\overline{I_{s2}}\, e^{j\left(\omega_2 t + \frac{2\pi}{3}\right)}\right) \end{cases} \tag{5.20}$$

where, $\overline{I_{s2}}$ is the current magnitude in complex form and the electric speed of the current is $\omega_2$.

By using the same idea and process as the ABC winding set, the field equations for the XYZ winding set are given as:

$$J_2(\theta,t) = \mathrm{Re}\left\{\sqrt{2}\left(3\overline{C_{s2}} \cdot \overline{I_{s2}}\right) e^{j(\omega_2 t - P_2\theta)}\right\} \tag{5.21}$$

$$B_2(\theta,t) = \mathrm{Re}\left\{ j\frac{\mu_0 r}{gP_2}\left[\sqrt{2}\left(3\overline{C_{s2}} \cdot \overline{I_{s2}}\right) e^{j(\omega_2 t - P_2\theta)}\right]\right\} \tag{5.22}$$

$$E_2(\theta,t) = \mathrm{Re}\left\{ - j\frac{\mu_0 \omega_2 r^2}{gP_2^2}\left[\sqrt{2}\left(3\overline{C_{s2}} \cdot \overline{I_{s2}}\right) e^{j(\omega_2 t - P_2\theta)}\right]\right\} \tag{5.23}$$

$$u_{s2}(t) = 2\pi r l\, \mathrm{Re}\left\{ - j\frac{\mu_0 \omega_2 r^2}{gP_2^2}\overline{C_{s2}}^{*}\left[\sqrt{2}\left(3\overline{C_{s2}} \cdot \overline{I_{s2}}\right) e^{j\omega_2 t}\right]\right\} \tag{5.24}$$

The sinusoidal currents flowing in the XYZ winding set induce the same frequency voltage components in the stator XYZ winding set if the stator windings are assumed to be sinusoidally distributed.

5.2.1.3 Voltages in the XYZ Winding Set due to the Currents Flowing in the ABC Winding Set. The EMF induced in the stator phase X by the ABC winding set stator currents can be found by multiplying the electric field of the ABC winding set with the winding distribution of the phase X as:

$$u_{qp}(t) = rl \int_0^{2\pi} C_X(\theta) \cdot E_1(\theta, t)\, d\theta \tag{5.25}$$

Substituting the expression of winding distribution and electric field into equation and integrating, the voltage equation is given as:

$$u_{qp}(t) = rl\,\mathrm{Re}\left\{ \begin{array}{l} \int_0^{2\pi} \overline{C_{s2}} \left( -\frac{r\omega_1}{P_1} \right) \left( j\frac{\mu_0 r}{gP_1} \right) \left[ \sqrt{2} \left( 3\overline{C_{s1}} \cdot \overline{I_{s1}} \right) e^{j(\omega_1 t - P_1\theta - P_2\theta)} \right] d\theta \\ + \int_0^{2\pi} \overline{C_{s2}}^{*} \left( -\frac{r\omega_1}{P_1} \right) \left( j\frac{\mu_0 r}{gP_1} \right) \left[ \sqrt{2} \left( 3\overline{C_{s1}} \cdot \overline{I_{s1}} \right) e^{j(\omega_1 t - P_1\theta + P_2\theta)} \right] d\theta \end{array} \right\} \tag{5.26}$$

For the dual stator winding induction machine under study here, the pole numbers of two stator windings are dissimilar. Hence (5.26) becomes

$$u_{qp}(t) = 0 \tag{5.27}$$

The ABC winding set currents cannot induce any voltage in the XYZ winding set, confirming the conclusions in [1.1].

5.2.1.4 Voltages in the ABC Winding Set due to the Stator Currents Flowing in the XYZ Winding Set. The EMF in the stator phase A due to the stator currents flowing in

the XYZ winding set is obtained by multiplying the electric field of the XYZ winding set with the winding distribution of the phase A as:

$$u_{pq}(t) = rl \int_0^{2\pi} C_A(\theta) \cdot E_2(\theta, t)\, d\theta \tag{5.28}$$

Substituting the expression of phase A winding distribution and the electric field of the XYZ winding set into (5.28) and integrating, the voltage equation is given as:

$$u_{pq}(t) = rl\,\mathrm{Re}\left\{ \begin{array}{l} \int_0^{2\pi} \overline{C_{s1}} \left( -\frac{r\omega_2}{P_2} \right) \left( j\frac{\mu_0 r}{gP_2} \right) \left[ \sqrt{2} \left( 3\overline{C_{s2}} \cdot \overline{I_{s2}} \right) e^{j(\omega_2 t - P_2\theta - P_1\theta)} \right] d\theta \\ + \int_0^{2\pi} \overline{C_{s1}}^{*} \left( -\frac{r\omega_2}{P_2} \right) \left( j\frac{\mu_0 r}{gP_2} \right) \left[ \sqrt{2} \left( 3\overline{C_{s2}} \cdot \overline{I_{s2}} \right) e^{j(\omega_2 t - P_2\theta + P_1\theta)} \right] d\theta \end{array} \right\} \tag{5.29}$$

Since the pole numbers of two stator windings are dissimilar, (5.30) becomes:

$$u_{pq}(t) = 0 \tag{5.30}$$

The fundamental stator currents flowing in the XYZ winding set cannot induce any voltage in the ABC winding set. Hence the two stator winding set are decoupled and the currents flowing in one winding set cannot induce voltages in the other winding set.

5.2.1.5 Voltages in Rotor Loops due to the Stator Currents Flowing in the ABC Winding Set. Since the number of rotor bars is $N_r$, the rotor equivalent circuit is composed of $N_r$ rotor loops. The winding distribution of the rotor is rich in harmonic components. The $i^{th}$ rotor loop winding distribution is expressed in the rotor reference frame as:

$$C_{Ri}(\theta') = \sum_k \overline{C_R^k} \cdot e^{-jk\left[\theta' - (i-1)\alpha_r\right]} \tag{5.31}$$

where, $\alpha_r = \frac{2\pi}{N_r}$ is the bar spacing angle, $\theta'$ is the angle in rotor reference frame; $\overline{C_R^k}$ is the magnitude of the $k^{th}$ harmonics winding distribution and its peak value is expressed as:

$$\left|\overline{C_R^k}\right| = \frac{1}{\pi \cdot r} k_{wR}^k \tag{5.32}$$

where, $k_{wR}^k$ is the winding factor of a loop for $k^{th}$ harmonics winding distribution.

Then the flux density and electric field due to the currents flowing in the ABC winding set expressed in the rotor reference frame are given as:

$$B_{r1}\left(\theta', t\right) = \mathrm{Re}\left\{ j \frac{\mu_0 r}{g P_1} \left[\sqrt{2}\left(3\overline{C_{s1}} \cdot \overline{I_{s1}}\right) e^{j\left(s_1 \omega_1 t - P_1 \theta'\right)}\right]\right\} \tag{5.33}$$

$$E_{r1}\left(\theta', t\right) = \mathrm{Re}\left\{ - j \frac{\mu_0 s_1 \omega_1 r^2}{g P_1^2} \left[\sqrt{2}\left(3\overline{C_{s1}} \cdot \overline{I_{s1}}\right) e^{j\left(s_1 \omega_1 t - P_1 \theta'\right)}\right]\right\} \tag{5.34}$$

The slip frequency $s_1$ is defined as:

$$s_1 = \frac{\omega_1 - P_1 \omega_r}{\omega_1} \tag{5.35}$$

where, $\omega_r$ is the rotor mechanical speed.

The induced EMF in the $i^{th}$ rotor loop due to currents flowing in the ABC winding set is obtained by multiplying the $i^{th}$ rotor loop winding distribution function with the electric field function as:

$$u_{rpi}(t) = rl \int_0^{2\pi} C_{Ri}\left(\theta'\right) \cdot E_{r1}\left(\theta', t\right) d\theta' \tag{5.36}$$

Substituting the expression of the $i^{th}$ rotor loop winding distribution and the electric field into (5.36) to yield,

$$u_{rpi}(t) = rl\int_0^{2\pi}\sum_k \overline{C_R^k}\cdot e^{-jk\left[\theta'-(i-1)\alpha_r\right]}\cdot \mathrm{Re}\left\{-\frac{rs_1\omega_1}{P_1}\left(j\frac{\mu_0 r}{gP_1}\right)\left[\sqrt{2}\left(3\overline{C_{s1}}\cdot\overline{I_{s1}}\right)e^{j\left(s_1\omega_1 t-P_1\theta'\right)}\right]\right\}d\theta' \tag{5.37}$$

Unless $k=-P_1$, the induced EMF in the rotor loops (5.37) is zero. If

$$\overline{C_R^{-P_1}} = \overline{C_R^{P_1}}^* \tag{5.38}$$

Then the induced EMF in the $i^{th}$ rotor loops is given as:

$$u_{rpi}(t) = 2\pi\, rl\,\mathrm{Re}\left\{-j\frac{\mu_0 s\omega_1 r^2}{gP_1^2}\overline{C_R^{P_1}}^*\left[\sqrt{2}\left(3\overline{C_{s1}}\cdot\overline{I_{s1}}\right)e^{j\left[s_1\omega_1 t-P_1(i-1)\alpha_r\right]}\right]\right\} \tag{5.39}$$

The above equation shows that the field driving the ABC winding set only induces an EMF that has $P_1$ pole pair distribution in the $i^{th}$ rotor loop. If it is assumed that the currents flowing in the $i^{th}$ rotor loop has the same time relationship as the EMF, the $i^{th}$ rotor loop current equation becomes:

$$i_{rpi}(t) = \mathrm{Re}\left\{\sqrt{2}\cdot\overline{I_{iR1}}\cdot e^{js_1\omega_1 t}\right\} \tag{5.40}$$

5.2.1.6 Voltages in Rotor Loops due to the Stator Currents Flowing in the XYZ Winding Set. The induced voltage in the $i^{th}$ rotor loop by the XYZ winding set stator currents can be expressed as:

$$u_{rqi}(t) = 2\pi\, rl\,\mathrm{Re}\left\{-j\frac{\mu_0 s\omega_2 r^2}{gP_2^2}\overline{C_R^{P_2}}^*\left[\sqrt{2}\left(3\overline{C_{s2}}\cdot\overline{I_{s2}}\right)e^{j\left[s_2\omega_2 t-P_2(i-1)\alpha_r\right]}\right]\right\} \tag{5.41}$$

The slip frequency $s_2$ is defined as:

$$s_2 = \frac{\omega_2 - P_2\omega_r}{\omega_2} \tag{5.42}$$

The above equation shows that the XYZ winding set driven field only induces an EMF that has $P_2$ pole pair distribution in the $i^{th}$ rotor loop. Assuming that the currents flowing in the $i^{th}$ rotor loops follow the same pattern as the EMF, the $i^{th}$ rotor loop current that induced by the XYZ stator winding field is given as:

$$i_{rqi}(t) = \mathrm{Re}\left\{\sqrt{2}\cdot\overline{I_{iR2}}\cdot e^{js_2\omega_2 t}\right\} \tag{5.43}$$

5.2.1.7 Voltages in the ABC Winding Set due to the Rotor Currents induced by Currents Flowing in the ABC Windings Set. The $i^{th}$ rotor loop surface current density distribution is the product of the rotor winding distribution and rotor currents:

$$J_{r1}(\theta',t) = C_{Ri}(\theta')\cdot i_{rpi}(t) \tag{5.44}$$

Substituting (5.31) and (5.40) into the above equation yields,

$$J_{r1i}(\theta',t) = \mathrm{Re}\left\{\sum_k \sqrt{2}\cdot\overline{I_{iR1}}\cdot\overline{C_R^k}\cdot e^{j\left(s_1\omega_1 t - k\left[\theta' - (i-1)\alpha_r\right]\right)}\right\} \tag{5.45}$$

The above equation is written in the rotor reference frame, however the EMF induced by this field in the stator is in the stationary reference frame. Hence the equations may be referred to the stationary reference frame.

If the rotor angle $\theta'$ can be expressed in term of the stationary angle $\theta$ as:

$$\theta' = \theta - \omega_r t \tag{5.46}$$

Substituting (5.35) and (5.46) into (5.45),

$$J_{r1i}(\theta,t) = \mathrm{Re}\left\{\sum_k \sqrt{2}\cdot\overline{I_{iR1}}\cdot\overline{C_R^k}\cdot e^{j(\omega_1 t - k\theta + k(i-1)\alpha_r + (k-P_1)\omega_r t)}\right\} \tag{5.47}$$

The corresponding flux densities in the air gap induced by this current distribution are expressed as:

$$B_{prpi}(\theta,t) = \mathrm{Re}\left\{\sum_k \frac{j\mu_0 r}{k\,g}\sqrt{2}\cdot\overline{I_{iR1}}\cdot\overline{C_R^k}\cdot e^{j(\omega_1 t - k\theta + k(i-1)\alpha_r + (k-P_1)\omega_r t)}\right\} \tag{5.48}$$

The electric fields induced at the stator surface become:

$$E_{prpi}(\theta,t) = \mathrm{Re}\left\{\sum_k -\frac{j\mu_0\omega_1 r^2}{k\,g}\sqrt{2}\cdot\overline{I_{iR1}}\cdot\overline{C_R^k}\cdot e^{j(\omega_1 t - k\theta + k(i-1)\alpha_r + (k-P_1)\omega_r t)}\right\} \tag{5.49}$$

The induced EMFs in the stator windings due to rotor currents in the $i^{th}$ loop are given as the product of the electric field with the winding distributions of the phase windings. For phase A, the induced EMF is given as:

$$u_{prpi}(t) = rl\int_0^{2\pi} C_A(\theta)\cdot E_{prpi}(\theta,t)\,d\theta \tag{5.50}$$

Substituting (5.1) and (5.49) into (5.50) and integrating,

$$u_{prpi}(t) = rl\,\mathrm{Re}\left\{\begin{array}{l}\displaystyle\sum_k \int_0^{2\pi}\overline{C_{s1}}e^{-jP_1\theta}\cdot\frac{\mu_0\omega_1 r^2}{jk\,g}\sqrt{2}\cdot\overline{I_{iR1}}\cdot\overline{C_R^k}\cdot e^{j(\omega_1 t - k\theta + k(i-1)\alpha_r + (k-P_1)\omega_r t)}\,d\theta \\ \displaystyle+\sum_k \int_0^{2\pi}\overline{C_{s1}}^{*}e^{jP_1\theta}\cdot\frac{\mu_0\omega_1 r^2}{jk\,g}\sqrt{2}\cdot\overline{I_{iR1}}\cdot\overline{C_R^k}\cdot e^{j(\omega_1 t - k\theta + k(i-1)\alpha_r + (k-P_1)\omega_r t)}\,d\theta\end{array}\right\} \tag{5.51}$$

The first term in (5.51) is zero unless,

$k = -P_1$

The second term in (5.51) is zero unless,

$k = P_1$

Then the induced EMF equation is simplified as:

$$u_{prpi}(t) = 2\pi\, rl\, \mathrm{Re}\left\{ \begin{array}{l} j\dfrac{\mu_0 \omega_1 r^2}{P_1\, g}\sqrt{2}\cdot \overline{C_{s1}}\cdot \overline{I_{iR1}}\cdot \overline{C_R^{P_1}}^{*}\cdot e^{j(\omega_1 t - 2P_1\omega_r t - P_1(i-1)\alpha_r)} \\ -j\dfrac{\mu_0 \omega_1 r^2}{P_1\, g}\sqrt{2}\cdot \overline{C_{s1}}^{*}\cdot \overline{I_{iR1}}\cdot \overline{C_R^{P_1}}\cdot e^{j(\omega_1 t + P_1(i-1)\alpha_r)} \end{array} \right\} \tag{5.52}$$

For all the rotor loops, the total induced EMF in the stator winding A by the rotor loop currents is given in (5.53).

$$u_{prp}(t) = 2\pi rl\, \mathrm{Re}\left\{ \begin{array}{l} j\dfrac{\mu_0 \omega_1 r^2}{P_1\, g}\sqrt{2}\cdot \overline{C_{s1}}\cdot \overline{C_R^{P_1}}^{*}\cdot e^{j(\omega_1 t - 2P_1\omega_r t)}\cdot \sum_{i=1}^{N_r} \overline{I_{iR1}}\cdot e^{-j(P_1(i-1)\alpha_r)} \\ -j\dfrac{\mu_0 \omega_1 r^2}{P_1\, g}\sqrt{2}\cdot \overline{C_{s1}}^{*}\cdot \overline{C_R^{P_1}}\cdot e^{j(\omega_1 t)}\cdot \sum_{i=1}^{N_r} \overline{I_{iR1}}\cdot e^{j(P_1(i-1)\alpha_r)} \end{array} \right\} \tag{5.53}$$

A rotor speed dependent frequency component is induced in the ABC winding set by currents induced in the rotor circuit due to the fundamental currents flowing in the ABC winding set, whose frequency is given as $\omega_1 - 2P_1\omega_r$.

5.2.1.8 Voltages in the XYZ Winding Set due to the Rotor Currents induced by Currents Flowing in the ABC Winding Set. The EMF induced in the phase X of XYZ winding set is obtained by multiplying the electric field of $i^{th}$ rotor loop with the winding distribution of the phase X as:

$$u_{qrpi}(t) = rl\int_0^{2\pi} C_X(\theta)\cdot E_{prpi}(\theta, t)\, d\theta \tag{5.54}$$

Substituting (5.18) and (5.49) into (5.54) and integrating,

$$u_{qrpi}(t) = rl\, \mathrm{Re}\left\{ \begin{array}{l} \sum_k \int_0^{2\pi} \overline{C_{s2}} e^{-jP_2\theta}\cdot \dfrac{\mu_0 \omega_1 r^2}{jk\, g}\sqrt{2}\cdot \overline{I_{iR1}}\cdot \overline{C_R^{k}}\cdot e^{j(\omega_1 t - k\theta + k(i-1)\alpha_r + (k-P_1)\omega_r t)}\, d\theta \\ +\sum_k \int_0^{2\pi} \overline{C_{s2}}^{*} e^{jP_2\theta}\cdot \dfrac{\mu_0 \omega_1 r^2}{jk\, g}\sqrt{2}\cdot \overline{I_{iR1}}\cdot \overline{C_R^{k}}\cdot e^{j(\omega_1 t - k\theta + k(i-1)\alpha_r + (k-P_1)\omega_r t)}\, d\theta \end{array} \right\}$$

(5.55)

The first term in equation (5.55) is zero unless,

$k = -P_2$

The second term in equation (5.55) is zero unless,

$k = P_2$

Then the induced EMF equation is simplified as:

$$u_{qrpi}(t) = 2\pi rl \,\mathrm{Re}\left\{ \begin{array}{l} j\dfrac{\mu_0 \omega_1 r^2}{P_2\, g}\sqrt{2}\cdot\overline{C_{s2}}\cdot\overline{I_{iR1}}\cdot\overline{C_R^{P_2}}^{*}\cdot e^{j(\omega_1 t+(-P_2-P_1)\omega_r t-P_2(i-1)\alpha_r)} \\ -j\dfrac{\mu_0 \omega_1 r^2}{P_2\, g}\sqrt{2}\cdot\overline{C_{s2}}^{*}\cdot\overline{I_{iR1}}\cdot\overline{C_R^{P_2}}\cdot e^{j(\omega_1 t+(P_2-P_1)\omega_r t+P_2(i-1)\alpha_r)} \end{array} \right\} \quad (5.56)$$

For all the rotor loops, the total induced EMF in the stator winding X by the rotor loop currents is given in (5.57).

$$u_{qrqi}(t) = 2\pi rl \,\mathrm{Re}\left\{ \begin{array}{l} j\dfrac{\mu_0 \omega_1 r^2}{P_2\, g}\sqrt{2}\cdot\overline{C_{s2}}\cdot\overline{C_R^{P_2}}^{*}\cdot e^{j(\omega_1 t+(-P_1-P_2)\omega_r t)}\cdot\sum_{i=1}^{N_r}\overline{I_{iR1}}\cdot e^{-j(P_2(i-1)\alpha_r)} \\ -j\dfrac{\mu_0 \omega_1 r^2}{P_2\, g}\sqrt{2}\cdot\overline{C_{s2}}^{*}\cdot\overline{C_R^{P_2}}\cdot e^{j(\omega_1 t+(P_2-P_1)\omega_r t)}\cdot\sum_{i=1}^{N_r}\overline{I_{iR1}}\cdot e^{j(P_2(i-1)\alpha_r)} \end{array} \right\} \quad (5.57)$$

The rotor current due to the ABC winding set induces two new frequency components-- $\omega_1 + (-P_2 - P_1)\omega_r$ and $\omega_1 + (P_2 - P_1)\omega_r$ in the XYZ winding set. They are the products of the interactions between these two stator winding sets.

5.2.1.9 Voltages in the XYZ Winding Set due to the Rotor Currents induced by Currents Flowing in the XYZ Winding Set. The rotor surface current density distribution is the multiplication of the rotor winding distribution and rotor currents:

$$J_{r2i}(\theta', t) = C_{Ri}(\theta')\cdot i_{rqi}(t) \quad (5.58)$$

Substituting (5.31) and (5.43) into the above equation yields,

$$J_{r2i}\left(\theta',t\right)=\mathrm{Re}\left\{\sum_{k}\sqrt{2}\cdot\overline{I_{iR2}}\cdot\overline{C_R^k}\cdot e^{j\left(s_2\omega_2 t-k\left[\theta'-(i-1)\alpha_r\right]\right)}\right\} \tag{5.59}$$

Transform the above equation into the stationary reference frame,

$$J_{r2i}\left(\theta,t\right)=\mathrm{Re}\left\{\sum_{k}\sqrt{2}\cdot\overline{I_{iR2}}\cdot\overline{C_R^k}\cdot e^{j\left(\omega_2 t-k\theta+k(i-1)\alpha_r+(k-P_2)\omega_r t\right)}\right\} \tag{5.60}$$

The corresponding flux densities in the air gap induced by these currents are expressed as:

$$B_{qrqi}\left(\theta,t\right)=\mathrm{Re}\left\{\sum_{k}\frac{j\mu_0 r}{k\,g}\sqrt{2}\cdot\overline{I_{iR2}}\cdot\overline{C_R^k}\cdot e^{j\left(\omega_{21} t-k\theta+k(i-1)\alpha_r+(k-P_2)\omega_r t\right)}\right\} \tag{5.61}$$

The electric field induced at the stator surface is:

$$E_{qrqi}\left(\theta,t\right)=\mathrm{Re}\left\{\sum_{k}-\frac{j\mu_0\omega_2 r^2}{k\,g}\sqrt{2}\cdot\overline{I_{iR2}}\cdot\overline{C_R^k}\cdot e^{j\left(\omega_2 t-k\theta+k(i-1)\alpha_r+(k-P_2)\omega_r t\right)}\right\} \tag{5.62}$$

Then the EMF induced in the phase X of the XYZ winding set is obtained by multiplying the electric field with the winding distribution of the phase X as:

$$u_{qrqi}\left(t\right)=rl\int_0^{2\pi}C_X\left(\theta\right)\cdot E_{qrqi}\left(\theta,t\right)d\theta \tag{5.63}$$

Substituting (5.18) and (5.62) into (5.63) and integrating,

$$u_{qrqi}\left(t\right)=rl\,\mathrm{Re}\left\{\begin{array}{l}\displaystyle\sum_{k}\int_0^{2\pi}\overline{C_{s2}}e^{-jP_2\theta}\cdot\frac{\mu_0\omega_2 r^2}{jk\,g}\sqrt{2}\cdot\overline{I_{R2}}\cdot\overline{C_R^k}\cdot e^{j\left(\omega_2 t-k\theta+k(i-1)\alpha_r+(k-P_2)\omega_r t\right)}\,d\theta \\ \displaystyle+\sum_{k}\int_0^{2\pi}\overline{C_{s2}}^{*}e^{jP_2\theta}\cdot\frac{\mu_0\omega_2 r^2}{jk\,g}\sqrt{2}\cdot\overline{I_{R2}}\cdot\overline{C_R^k}\cdot e^{j\left(\omega_2 t-k\theta+k(i-1)\alpha_r+(k-P_2)\omega_r t\right)}\,d\theta\end{array}\right\} \tag{5.64}$$

The first term in (5.64) is zero unless,

$k=-P_2$

The second term in (5.64) is zero unless,

$k = P_2$

Then the induced EMF equation is simplified as:

$$u_{qrqi}(t) = 2\pi r l \,\mathrm{Re}\left\{ \begin{array}{l} j\dfrac{\mu_0 \omega_2 r^2}{P_2\, g}\sqrt{2}\cdot\overline{C_{s2}}\cdot\overline{I_{iR2}}\cdot\overline{C_R^{P_2}}^{*}\cdot e^{j(\omega_2 t - 2P_2\omega_r t - P_2(i-1)\alpha_r)} \\ \\ -j\dfrac{\mu_0 \omega_2 r^2}{P_2\, g}\sqrt{2}\cdot\overline{C_{s2}}^{*}\cdot\overline{I_{iR2}}\cdot\overline{C_R^{P_2}}\cdot e^{j(\omega_2 t + P_2(i-1)\alpha_r)} \end{array} \right\} \tag{5.65}$$

Then by adding the EMFs in the stator winding X due to all the rotor loop currents induced by the XYZ winding set, the total EMF is given as:

$$u_{qrq}(t) = 2\pi r l \,\mathrm{Re}\left\{ \begin{array}{l} j\dfrac{\mu_0 \omega_2 r^2}{P_2\, g}\sqrt{2}\cdot\overline{C_{s2}}\cdot\overline{C_R^{P_2}}^{*}\cdot e^{j(\omega_2 t - 2P_2\omega_r t)}\cdot\sum_{i=1}^{N_r}\overline{I_{iR2}}\cdot e^{-j(P_2(i-1)\alpha_r)} \\ \\ -j\dfrac{\mu_0 \omega_2 r^2}{P_2\, g}\sqrt{2}\cdot\overline{C_{s2}}^{*}\cdot\overline{C_R^{P_2}}\cdot e^{j(\omega_2 t)}\cdot\sum_{i=1}^{N_r}\overline{I_{iR2}}\cdot e^{j(P_2(i-1)\alpha_r)} \end{array} \right\} \tag{5.66}$$

A new frequency component except the fundamental one is induced in the XYZ winding set and it has a rotor speed dependent frequency given as $\omega_2 - 2P_2\omega_r$.

5.2.1.10 Voltages in the ABC Winding Set due to the Rotor Currents induced by Currents Flowing in the XYZ Winding Set. The EMF induced in the stator winding can be obtained by multiplying the electric field with the winding distribution of the phase A as:

$$u_{prqi}(t) = rl\int_0^{2\pi} C_A(\theta)\cdot E_{qrqi}(\theta, t)\, d\theta \tag{5.67}$$

Substituting (5.18) and (5.62) into (5.67) and integrating,

$$u_{prqi}(t) = rl\,\mathrm{Re}\left\{\begin{array}{l}\sum\limits_{k}\int\limits_{0}^{2\pi}\overline{C_{s1}}e^{-jP_1\theta}\cdot\dfrac{\mu_0\omega_2 r^2}{jk\,g}\sqrt{2}\cdot\overline{I_{R2}}\cdot\overline{C_R^k}\cdot e^{j(\omega_2 t-k\theta+k(i-1)\alpha_r+(k-P_2)\omega_r t)}\,d\theta \\ +\sum\limits_{k}\int\limits_{0}^{2\pi}\overline{C_{s1}}^{*}e^{jP_1\theta}\cdot\dfrac{\mu_0\omega_2 r^2}{jk\,g}\sqrt{2}\cdot\overline{I_{R2}}\cdot\overline{C_R^k}\cdot e^{j(\omega_2 t-k\theta+k(i-1)\alpha_r+(k-P_2)\omega_r t)}\,d\theta\end{array}\right\}$$

(5.68)

The first term in (5.68) is zero unless,

$k = -P_1$

The second term in (5.68) is zero unless,

$k = P_1$

Then the induced EMF equation is simplified as:

$$u_{prqi}(t) = 2\pi\, rl\,\mathrm{Re}\left\{\begin{array}{l}j\dfrac{\mu_0\omega_2 r^2}{P_1\,g}\sqrt{2}\cdot\overline{C_{s1}}\cdot\overline{I_{iR2}}\cdot\overline{C_R^{P_1}}^{*}\cdot e^{j(\omega_2 t+(-P_1-P_2)\omega_r t-P_1(i-1)\alpha_r)} \\ -j\dfrac{\mu_0\omega_2 r^2}{P_2\,g}\sqrt{2}\cdot\overline{C_{s1}}^{*}\cdot\overline{I_{iR2}}\cdot\overline{C_R^{P_1}}\cdot e^{j(\omega_2 t+(P_1-P_2)\omega_r t+P_1(i-1)\alpha_r)}\end{array}\right\} \qquad (5.69)$$

The total EMF in the stator winding A due to rotor loop currents induced by currents flowing in the XYZ winding set is given as:

$$u_{prq}(t) = 2\pi rl\,\mathrm{Re}\left\{\begin{array}{l}j\dfrac{\mu_0\omega_2 r^2}{P_1\,g}\sqrt{2}\cdot\overline{C_{s1}}\cdot\overline{C_R^{P_1}}^{*}\cdot e^{j(\omega_2 t+(-P_1-P_2)\omega_r t)}\cdot\sum\limits_{i=1}^{N_r}\overline{I_{iR2}}\cdot e^{-j(P_1(i-1)\alpha_r)} \\ -j\dfrac{\mu_0\omega_2 r^2}{P_1\,g}\sqrt{2}\cdot\overline{C_{s1}}^{*}\cdot\overline{C_R^{P_1}}\cdot e^{j(\omega_2 t+(P_1-P_2)\omega_r t)}\cdot\sum\limits_{i=1}^{N_r}\overline{I_{iR2}}\cdot e^{j(P_1(i-1)\alpha_r)}\end{array}\right\} \qquad (5.70)$$

The rotor current due to the XYZ winding set induces two new frequency components-- $\omega_2+(-P_1-P_2)\omega_r$ and $\omega_2+(P_1-P_2)\omega_r$ in the ABC stator winding set. They are the products of the interactions between these two stator winding sets.

### 5.2.2 Torque Equation

The calculation of the torque components of the dual stator winding induction machine is very important in the understanding of the machine. Developed torque can be calculated at the stator surface. The general expression of the developed electromagnetic torque is defined as:

$$T_e = -rl\int_0^{2\pi} J_S(\theta,t)\cdot B_g(\theta,t)d\theta \tag{5.71}$$

where $B_g(\theta,t)$ consists of the flux densities contributed by the currents flowing in the two stator winding sets and the rotor currents they induce in the rotor circuit. Since the magnitudes of the harmonic flux density components are much less than the fundamental components, only the fundamental flux densities contributed by the fundamental currents in the two stator winding set and rotor loops are considered. Hence, the expression of the total flux density is given as :

$$B_g(\theta,t) = B_1(\theta,t) + B_2(\theta,t) + B_{prp}(\theta,t) + B_{qrq}(\theta,t) \tag{5.72}$$

5.2.2.1 Torque components due to Currents Flowing in the ABC winding Set. The torque component from the stator ABC winding set can be calculated as:

$$\begin{aligned} T_{e1} &= -rl\int_0^{2\pi} J_1(\theta,t)\cdot B_g(\theta,t)d\theta \\ &= -rl\left[\begin{array}{l} \int_0^{2\pi} J_1(\theta,t)\cdot B_1(\theta,t)d\theta + \int_0^{2\pi} J_1(\theta,t)\cdot B_2(\theta,t)d\theta \\ + \int_0^{2\pi} J_1(\theta,t)\cdot B_{prp}(\theta,t)d\theta + \int_0^{2\pi} J_1(\theta,t)\cdot B_{qrq}(\theta,t)d\theta \end{array}\right] \end{aligned} \tag{5.73}$$

A) The first term of $T_{e1}$

Substituting the expressions of surface current distribution and the flux density into the first term, the integration result can be written as:

$$\int_0^{2\pi} J_1(\theta,t)\cdot B_1(\theta,t)d\theta = \frac{1}{2} rl\,\mathrm{Re}\left[ j2\pi \frac{\mu_0 r}{gP_1}\left(3\sqrt{2}\right)^2 \left(\overline{C_{s1}}\cdot \overline{C_{s1}}^{\,*}\right)\left(\overline{I_{s1}}\cdot \overline{I_{s1}}^{\,*}\right)\right] \tag{5.74}$$

Since both $\left(\overline{C_{s1}}\cdot \overline{C_{s1}}^{\,*}\right)$ and $\left(\overline{I_{s1}}\cdot \overline{I_{s1}}^{\,*}\right)$ are real number, then:

$$\int_0^{2\pi} J_1(\theta,t)\cdot B_1(\theta,t)d\theta = 0 \tag{5.75}$$

B) The second term of $T_{e1}$

Substituting the expressions of surface current distribution and the flux density into the first term,

$$\begin{aligned}&\int_0^{2\pi} J_1(\theta,t)\cdot B_2(\theta,t)d\theta \\ &= \int_0^{2\pi} \mathrm{Re}\left\{\sqrt{2}\left(3\overline{C_{s1}}\cdot \overline{I_{s1}}\right)e^{j(\omega_1 t - P_1\theta)}\right\}\cdot \mathrm{Re}\left\{ j\frac{\mu_0 r}{gP_2}\left[\sqrt{2}\left(3\overline{C_{s2}}\cdot \overline{I_{s2}}\right)e^{j(\omega_2 t - P_2\theta)}\right]\right\}d\theta\end{aligned} \tag{5.76}$$

If $x$ and $y$ are both the complex number, then the following identity is true,

$$\mathrm{Re}(x)\cdot \mathrm{Re}(y) \neq \mathrm{Re}(x\cdot y) \tag{5.77}$$

However each term in equation (5.76) can be expressed as:

$$\mathrm{Re}\left\{\sqrt{2}\left(3\overline{C_{s1}}\cdot \overline{I_{s1}}\right)e^{j(\omega_1 t - P_1\theta)}\right\} = \sqrt{2}\left|3\overline{C_{s1}}\cdot \overline{I_{s1}}\right|\cos\left(\omega_1 t - P_1\theta + \theta_1\right) \tag{5.78}$$

$$\mathrm{Re}\left\{ j\frac{\mu_0 r}{gP_2}\left[\sqrt{2}\left(3\overline{C_{s2}}\cdot \overline{I_{s2}}\right)e^{j(\omega_2 t - P_2\theta)}\right]\right\} = -\frac{\mu_0 r}{gP_2}\sqrt{2}\left|3\overline{C_{s2}}\cdot \overline{I_{s2}}\right|\sin\left(\omega_2 t - P_2\theta + \theta_2\right) \tag{5.79}$$

The multiplication of the two terms is:

$$\begin{aligned}&\mathrm{Re}\left\{\sqrt{2}\left(3\overline{C_{s1}}\cdot\overline{I_{s1}}\right)e^{j(\omega_1 t-P_1\theta)}\right\}\cdot\mathrm{Re}\left\{j\frac{\mu_0 r}{gP_2}\left[\sqrt{2}\left(3\overline{C_{s2}}\cdot\overline{I_{s2}}\right)e^{j(\omega_2 t-P_2\theta)}\right]\right\}\\&=-\frac{1}{2}\frac{\mu_0 r}{gP_2}\sqrt{2}^2\left|3\overline{C_{s1}}\cdot\overline{I_{s1}}\right|\left|3\overline{C_{s2}}\cdot\overline{I_{s2}}\right|\left[\begin{array}{l}\sin\left(\omega_1 t+\omega_2 t-P_1\theta-P_2\theta+\theta_1+\theta_2\right)\\+\sin\left(\omega_2 t-\omega_1 t-P_2\theta+P_1\theta+\theta_2-\theta_1\right)\end{array}\right]\end{aligned}\tag{5.80}$$

Equation (5.76) can be written as:

$$\frac{1}{2}\mathrm{Re}\left\{\begin{array}{l}\int_0^{2\pi} j\frac{\mu_0 r}{gP_2}\sqrt{2}^2\left(3\overline{C_{s1}}\cdot\overline{I_{s1}}\right)\left(3\overline{C_{s2}}\cdot\overline{I_{s2}}\right)e^{j(\omega_1 t+\omega_2 t-P_1\theta-P_2\theta)}d\theta\\+\int_0^{2\pi} j\frac{\mu_0 r}{gP_2}\sqrt{2}^2\left(3\overline{C_{s1}}^{*}\cdot\overline{I_{s1}}^{*}\right)\left(3\overline{C_{s2}}\cdot\overline{I_{s2}}\right)e^{j(\omega_2 t-\omega_1 t+P_1\theta-P_2\theta)}d\theta\end{array}\right\}\tag{5.81}$$

The above equation will be zero unless the pole numbers of two stator winding meet any of the following conditions.

$P_1=P_2$ or $P_1=-P_2$

Since dissimilar pole numbers are chosen in this special machine,

$$\int_0^{2\pi} J_1(\theta,t)\cdot B_2(\theta,t)d\theta=0\tag{5.82}$$

C) The third term of $T_{e1}$

For the $i^{th}$ rotor loop, substituting the expressions of the surface current distribution and the flux density due to the ABC winding set into the third term,

$$\begin{aligned}&\int_0^{2\pi} J_1(\theta,t)\cdot B_{prpi}(\theta,t)d\theta\\&=-\frac{1}{2}rl\,\mathrm{Re}\left\{\begin{array}{l}\sum_k\left[\int_0^{2\pi} j\frac{\mu_0 r}{gk}\sqrt{2}^2\left(3\overline{C_{s1}}\cdot\overline{I_{s1}}\right)\left(\overline{C_R^k}\cdot\overline{I_{iR1}}\right)e^{j(2\omega_1 t+(k-P_1)\omega_r t+k(i-1)\alpha_r-P_1\theta-k\theta)}d\theta\right]\\+\sum_k\left[\int_0^{2\pi} j\frac{\mu_0 r}{gk}\sqrt{2}^2\left(3\overline{C_{s1}}^{*}\cdot\overline{I_{s1}}^{*}\right)\left(\overline{C_R^k}\cdot\overline{I_{R1}}\right)e^{j((k-P_1)\omega_r t+k(i-1)\alpha_r+P_1\theta-k\theta)}d\theta\right]\end{array}\right\}\end{aligned}\tag{5.83}$$

The first component of the above equation is zero unless $k=-P_1$ and the second component is also zero except when $k=P_1$. Hence, the final result can be written as:

$$-\pi r l \,\mathrm{Re}\left\{\begin{array}{l} j\dfrac{\mu_0 r}{-gP_1}\sqrt{2}^2\left(3\overline{C_{s1}}\cdot\overline{I_{s1}}\right)\left(\overline{C_R^{P_1}}^*\cdot\overline{I_{iR1}}\right)e^{j(2\omega_1 t-2P_1\omega_r t-P_1(i-1)\alpha_r)} \\ +j\dfrac{\mu_0 r}{gP_1}\sqrt{2}^2\left(3\overline{C_{s1}}^*\cdot\overline{I_{s1}}^*\right)\left(\overline{C_R^{P_1}}\cdot\overline{I_{iR1}}\right)e^{jP_1(i-1)\alpha_r} \end{array}\right\} \tag{5.84}$$

Summing the torques due to all the rotor bars, the torque component becomes:

$$\begin{aligned} &\int_0^{2\pi} J_1(\theta,t)\cdot B_{prp}(\theta,t)d\theta \\ &=-\pi r l \,\mathrm{Re}\left\{\begin{array}{l} j\dfrac{\mu_0 r}{-gP_1}\sqrt{2}^2\left(3\overline{C_{s1}}\cdot\overline{I_{s1}}\cdot\overline{C_R^{P_1}}^*\right)e^{j(2\omega_1 t-2P_1\omega_r t)}\cdot\sum_{i=1}^{N_r}\overline{I_{iR1}}\cdot e^{-j(P_1(i-1)\alpha_r)} \\ +j\dfrac{\mu_0 r}{gP_1}\sqrt{2}^2\left(3\overline{C_{s1}}^*\cdot\overline{I_{s1}}^*\cdot\overline{C_R^{P_1}}\right)\cdot\sum_{i=1}^{N_r}\overline{I_{iR1}}\cdot e^{j(P_1(i-1)\alpha_r)} \end{array}\right\} \end{aligned} \tag{5.85}$$

D) The fourth term of $T_{e1}$

For the $i^{th}$ rotor loop, substituting the expressions of winding surface current distribution and the flux density into the last term,

$$\begin{aligned} &\int_0^{2\pi} J_1(\theta,t)\cdot B_{qrqi}(\theta,t)d\theta \\ &=-\frac{1}{2}rl\,\mathrm{Re}\left\{\begin{array}{l} \sum_k\left[\int_0^{2\pi} j\dfrac{\mu_0 r}{gk}\sqrt{2}^2\left(3\overline{C_{s1}}\cdot\overline{I_{s1}}\right)\left(\overline{C_R^k}\cdot\overline{I_{iR2}}\right)e^{j(\omega_1 t+\omega_2 t+(k-P_2)\omega_r t+k(i-1)\alpha_r-P_1\theta-k\theta)}d\theta\right] \\ +\sum_k\left[\int_0^{2\pi} j\dfrac{\mu_0 r}{gk}\sqrt{2}^2\left(3\overline{C_{s1}}^*\cdot\overline{I_{s1}}^*\right)\left(\overline{C_R^k}\cdot\overline{I_{iR2}}\right)e^{j(-\omega_1 t+\omega_2 t+(k-P_2)\omega_r t+k(i-1)\alpha_r+P_1\theta-k\theta)}d\theta\right] \end{array}\right\} \end{aligned} \tag{5.86}$$

The first component of the above equation is zero except $k=-P_1$ and the second component is zero unless $k=P_1$. The final result of (5.86) can be written as:

$$-\pi rl\,\mathrm{Re}\left\{\begin{array}{l} j\dfrac{\mu_0 r}{-gP_1}\sqrt{2}^2\left(3\overline{C_{s1}}\cdot\overline{I_{s1}}\right)\left(\overline{C_R^{P_1}}^{*}\cdot\overline{I_{iR2}}\right)e^{j(\omega_1 t+\omega_2 t+(-P_1-P_2)\omega_r t-P_1(i-1)\alpha_r)} \\ +\,j\dfrac{\mu_0 r}{gP_1}\sqrt{2}^2\left(3\overline{C_{s1}}^{*}\cdot\overline{I_{s1}}^{*}\right)\left(\overline{C_R^{P_1}}\cdot\overline{I_{iR2}}\right)e^{j(-\omega_1 t+\omega_2 t+(P_1-P_2)\omega_r t+P_1(i-1)\alpha_r)} \end{array}\right\} \tag{5.87}$$

For all the rotor loops, the torque becomes,

$$\begin{aligned} &\int_0^{2\pi} J_1(\theta,t)\cdot B_{qrq}(\theta,t)d\theta \\ &=-\pi rl\,\mathrm{Re}\left\{\begin{array}{l} j\dfrac{\mu_0 r}{-gP_1}\sqrt{2}^2\left(3\overline{C_{s1}}\cdot\overline{I_{s1}}\cdot\overline{C_R^{P_1}}^{*}\right)e^{j(\omega_1 t+\omega_2 t+(-P_1-P_2)\omega_r t)}\cdot\sum_{i=1}^{N_r}\overline{I_{iR2}}\cdot e^{-j(P_1(i-1)\alpha_r)} \\ +\,j\dfrac{\mu_0 r}{gP_1}\sqrt{2}^2\left(3\overline{C_{s1}}^{*}\cdot\overline{I_{s1}}^{*}\cdot\overline{C_R^{P_1}}\right)e^{j(-\omega_1 t+\omega_2 t+(P_1-P_2)\omega_r t)}\cdot\sum_{i=1}^{N_r}\overline{I_{iR2}}\cdot e^{j(P_1(i-1)\alpha_r)} \end{array}\right\} \end{aligned} \tag{5.88}$$

5.2.2.2 Torque Components due to Currents Flowing in the XYZ winding Set. The torque component due to currents flowing in the XYZ winding set can be calculated as:

$$\begin{aligned} T_{e2} &= -rl\int_0^{2\pi} J_2(\theta,t)\cdot B_g(\theta,t)d\theta \\ &= -rl\left[\begin{array}{l} \displaystyle\int_0^{2\pi} J_2(\theta,t)\cdot B_1(\theta,t)d\theta+\int_0^{2\pi} J_2(\theta,t)\cdot B_2(\theta,t)d\theta \\ +\displaystyle\int_0^{2\pi} J_2(\theta,t)\cdot B_{prp}(\theta,t)d\theta+\int_0^{2\pi} J_2(\theta,t)\cdot B_{qrq}(\theta,t)d\theta \end{array}\right] \end{aligned} \tag{5.89}$$

The calculation method for the developed torque components resulting from currents flowing in the XYZ winding set is the same as the approach used for the determination of the torque generated due to currents flowing in the ABC winding set. The results are given below.

A) The first term of $T_{e2}$

Substituting the expressions of surface current distribution and the flux density into the first term,

$$\int_0^{2\pi} J_2(\theta,t)\cdot B_1(\theta,t)d\theta$$
$$= \int_0^{2\pi} \mathrm{Re}\left\{\sqrt{2}\left(3\overline{C_{s2}}\cdot\overline{I_{s2}}\right)e^{j(\omega_2 t-P_2\theta)}\right\}\cdot \mathrm{Re}\left\{ j\frac{\mu_0 r}{gP_2}\left[\sqrt{2}\left(3\overline{C_{s1}}\cdot\overline{I_{s1}}\right)e^{j(\omega_1 t-P_1\theta)}\right]\right\}d\theta \tag{5.90}$$

Equation (5.90) can be written as:

$$\frac{1}{2}\mathrm{Re}\left\{\begin{array}{l}\int_0^{2\pi} j\frac{\mu_0 r}{gP_1}\sqrt{2}^2\left(3\overline{C_{s2}}\cdot\overline{I_{s2}}\right)\left(3\overline{C_{s1}}\cdot\overline{I_{s1}}\right)e^{j(\omega_2 t+\omega_1 t-P_2\theta-P_1\theta)}d\theta \\ +\int_0^{2\pi} j\frac{\mu_0 r}{gP_1}\sqrt{2}^2\left(3\overline{C_{s2}}^{\,*}\cdot\overline{I_{s2}}^{\,*}\right)\left(3\overline{C_{s1}}\cdot\overline{I_{s1}}\right)e^{j(\omega_1 t-\omega_2 t+P_2\theta-P_1\theta)}d\theta\end{array}\right\} \tag{5.91}$$

The above equation will be zero unless the pole numbers of two stator winding sets meet any of the following conditions.

$P_1 = P_2$ or $P_1 = -P_2$

Since the dissimilar pole numbers are chosen in this special machine,

$$\int_0^{2\pi} J_2(\theta,t)\cdot B_1(\theta,t)d\theta = 0 \tag{5.92}$$

B) The second term of $T_{e2}$

Substituting the expressions of surface current distribution and the flux density into the first term,

$$\int_0^{2\pi} J_2(\theta,t)\cdot B_2(\theta,t)d\theta$$
$$= \int_0^{2\pi} \mathrm{Re}\left\{\sqrt{2}\left(3\overline{C_{s2}}\cdot\overline{I_{s2}}\right)e^{j(\omega_2 t-P_2\theta)}\right\}\cdot \mathrm{Re}\left\{ j\frac{\mu_0 r}{gP_2}\left[\sqrt{2}\left(3\overline{C_{s2}}\cdot\overline{I_{s2}}\right)e^{j(\omega_2 t-P_2\theta)}\right]\right\}d\theta \tag{5.93}$$

Then (5.93) is rewritten as:

$$\frac{1}{2}\mathrm{Re}\left[ j2\pi\frac{\mu_0 r}{gP_2}\left(3\sqrt{2}\right)^2\left(\overline{C_{s2}}\cdot\overline{C_{s2}}^{\,*}\right)\left(\overline{I_{s2}}\cdot\overline{I_{s2}}^{\,*}\right)\right] \tag{5.94}$$

Since both $\left(\overline{C_{s2}}\cdot\overline{C_{s2}}^{*}\right)$ and $\left(\overline{I_{s2}}\cdot\overline{I_{s2}}^{*}\right)$ are real number,

$$\int_0^{2\pi} J_2(\theta,t)\cdot B_2(\theta,t)d\theta = 0 \tag{5.95}$$

C) The third term of $T_{e2}$

Substituting the expressions of winding surface current distribution and the flux density into the first term,

$$\begin{aligned}
&\int_0^{2\pi} J_2(\theta,t)\cdot B_{prp}(\theta,t)d\theta \\
&= \int_0^{2\pi} \mathrm{Re}\left\{\sqrt{2}\left(3\overline{C_{s2}}\cdot\overline{I_{s2}}\right)e^{j(\omega_2 t-P_2\theta)}\right\}\cdot \mathrm{Re}\left\{\sum_k \frac{j\mu_0 r}{k\,g}\sqrt{2}\cdot\overline{I_{R1}}\cdot\overline{C_R^k}\cdot e^{j(\omega_1 t-k\theta+(k-P_1)\omega_r t)}\right\}d\theta \\
&= \frac{1}{2}\mathrm{Re}\left\{\begin{array}{l}\displaystyle\sum_k\left[\int_0^{2\pi} j\frac{\mu_0 r}{gk}\sqrt{2}^2\left(3\overline{C_{s2}}\cdot\overline{I_{s2}}\right)\left(\overline{C_R^k}\cdot\overline{I_{R1}}\right)e^{j(\omega_2 t+\omega_1 t+(k-P_1)\omega_r t-P_2\theta-k\theta)}d\theta\right] \\ \displaystyle+\sum_k\left[\int_0^{2\pi} j\frac{\mu_0 r}{gk}\sqrt{2}^2\left(3\overline{C_{s2}}^{*}\cdot\overline{I_{s2}}^{*}\right)\left(\overline{C_R^k}\cdot\overline{I_{R1}}\right)e^{j(-\omega_2 t+\omega_1 t+(k-P_1)\omega_r t+P_2\theta-k\theta)}d\theta\right]\end{array}\right\}
\end{aligned} \tag{5.96}$$

The first component of the above equation is zero unless $k=-P_2$ and the second component is zero unless $k=P_2$. Hence,

$$\begin{aligned}
&\int_0^{2\pi} J_2(\theta,t)\cdot B_{prp}(\theta,t)d\theta \\
&= \pi\,\mathrm{Re}\left\{\begin{array}{l} j\dfrac{\mu_0 r}{-gP_2}\sqrt{2}^2\left(3\overline{C_{s2}}\cdot\overline{I_{s2}}\right)\left(\overline{C_R^{P_2}}^{*}\cdot\overline{I_{R1}}\right)e^{j(\omega_2 t+\omega_1 t+(-P_2-P_1)\omega_r t)} \\ +\,j\dfrac{\mu_0 r}{gP_2}\sqrt{2}^2\left(3\overline{C_{s2}}^{*}\cdot\overline{I_{s2}}^{*}\right)\left(\overline{C_R^{P_1}}\cdot\overline{I_{R1}}\right)e^{j(-\omega_2 t+\omega_1 t+(P_2-P_1)\omega_r t)}\end{array}\right\}
\end{aligned} \tag{5.97}$$

D) The fourth term of $T_{e2}$

Substituting the expressions of XYZ windings surface current distribution and the flux density into the first term,

$$
\begin{aligned}
&\int_0^{2\pi} J_2(\theta,t)\cdot B_{qrq}(\theta,t)d\theta \\
&= \int_0^{2\pi} \mathrm{Re}\left\{\sqrt{2}\left(3\overline{C_{s2}}\cdot\overline{I_{s2}}\right)e^{j(\omega_2 t-P_2\theta)}\right\}\cdot \mathrm{Re}\left\{\sum_k \frac{j\mu_0 r}{k\,g}\sqrt{2}\cdot\overline{I_{R2}}\cdot\overline{C_R^k}\cdot e^{j(\omega_2 t-k\theta+(k-P_2)\omega_r t)}\right\}d\theta \qquad (5.98)\\
&= \frac{1}{2}\mathrm{Re}\left\{\begin{array}{l}\displaystyle\sum_k\left[\int_0^{2\pi} j\frac{\mu_0 r}{gk}\sqrt{2}^2\left(3\overline{C_{s2}}\cdot\overline{I_{s2}}\right)\left(\overline{C_R^k}\cdot\overline{I_{R2}}\right)e^{j(2\omega_2 t+(k-P_2)\omega_r t-P_2\theta-k\theta)}d\theta\right] \\ \displaystyle+\sum_k\left[\int_0^{2\pi} j\frac{\mu_0 r}{gk}\sqrt{2}^2\left(3\overline{C_{s2}}^*\cdot\overline{I_{s2}}^*\right)\left(\overline{C_R^k}\cdot\overline{I_{R2}}\right)e^{j((k-P_2)\omega_r t+P_2\theta-k\theta)}d\theta\right]\end{array}\right\}
\end{aligned}
$$

The first component of the above equation is unless $k=-P_2$ and the second component is zero unless $k=P_2$. Hence,

$$
\begin{aligned}
&\int_0^{2\pi} J_2(\theta,t)\cdot B_{qrq}(\theta,t)d\theta \\
&= \pi\,\mathrm{Re}\left\{\begin{array}{l} j\dfrac{\mu_0 r}{-gP_2}\sqrt{2}^2\left(3\overline{C_{s2}}\cdot\overline{I_{s2}}\right)\left(\overline{C_R^{P_2}}^*\cdot\overline{I_{R2}}\right)e^{j(2\omega_2 t-2P_2\omega_r t)} \\ + j\dfrac{\mu_0 r}{gP_2}\sqrt{2}^2\left(3\overline{C_{s2}}^*\cdot\overline{I_{s2}}^*\right)\left(\overline{C_R^{P_2}}\cdot\overline{I_{R2}}\right)\end{array}\right\} \qquad (5.99)
\end{aligned}
$$

## 5.3 Equation Summary

The voltage and torque equations of the dual stator winding induction machine due to fundamental current components are now summarized.

### 5.3.1 Voltages in the ABC Winding Set

If only the fundamental component is considered, the voltages that can be found at the terminals of the ABC winding set are:

(A) Induced voltage in the ABC winding set due to the ABC winding set stator currents is :

$$u_{s1}(t) = 2\pi rl \,\mathrm{Re}\left\{ -j\frac{\mu_0 \omega_1 r^2}{g P_1^2} \overline{C_{s1}}^{\,*} \left[ \sqrt{2} \left( 3\overline{C_{s1}} \cdot \overline{I_{s1}} \right) e^{j\omega_1 t} \right] \right\} \tag{5.100}$$

(B) Induced voltage in the ABC winding set due to currents flowing through the XYZ winding set is :

$$u_{pq}(t) = 0 \tag{5.101}$$

(C) Induced voltage in the ABC windings set due to rotor currents induced by currents flowing in the ABC winding set is :

$$u_{prp}(t) = 2\pi rl \,\mathrm{Re}\left\{ \begin{array}{l} j\dfrac{\mu_0 \omega_1 r^2}{P_1\, g} \sqrt{2} \cdot \overline{C_{s1}} \cdot \overline{C_R^{P_1}}^{\,*} \cdot e^{j(\omega_1 t - 2P_1 \omega_r t)} \cdot \displaystyle\sum_{i=1}^{N_r} \overline{I_{iR1}} \cdot e^{-j(P_1(i-1)\alpha_r)} \\ -j\dfrac{\mu_0 \omega_1 r^2}{P_1\, g} \sqrt{2} \cdot \overline{C_{s1}}^{\,*} \cdot \overline{C_R^{P_1}} \cdot e^{j(\omega_1 t)} \cdot \displaystyle\sum_{i=1}^{N_r} \overline{I_{iR1}} \cdot e^{j(P_1(i-1)\alpha_r)} \end{array} \right\} \tag{5.102}$$

(D) Induced voltage in the ABC winding set due to rotor currents induced by currents flowing in the XYZ winding set is :

$$u_{prq}(t) = 2\pi rl \,\mathrm{Re}\left\{ \begin{array}{l} j\dfrac{\mu_0 \omega_2 r^2}{P_1\, g} \sqrt{2} \cdot \overline{C_{s1}} \cdot \overline{C_R^{P_1}}^{\,*} \cdot e^{j(\omega_2 t + (-P_1 - P_2)\omega_r t)} \cdot \displaystyle\sum_{i=1}^{N_r} \overline{I_{iR2}} \cdot e^{-j(P_1(i-1)\alpha_r)} \\ -j\dfrac{\mu_0 \omega_2 r^2}{P_1\, g} \sqrt{2} \cdot \overline{C_{s1}}^{\,*} \cdot \overline{C_R^{P_1}} \cdot e^{j(\omega_2 t + (P_1 - P_2)\omega_r t)} \cdot \displaystyle\sum_{i=1}^{N_r} \overline{I_{iR2}} \cdot e^{j(P_1(i-1)\alpha_r)} \end{array} \right\} \tag{5.103}$$

### 5.3.2 Voltages in the XYZ Winding Set

If only the fundamental component is considered, the voltages that can be found at the terminals of XYZ windings are:

A) Induced voltage in the XYZ winding set due to stator currents flowing in the XYZ winding set is :

$$u_{s2}(t) = 2\pi r l \,\mathrm{Re}\left\{ - j\frac{\mu_0 \omega_2 r^2}{g P_2^2} \overline{C_{s2}}^{\,*} \left[ \sqrt{2} \left( 3\overline{C_{s2}} \cdot \overline{I_{s2}} \right) e^{j\omega_2 t} \right] \right\} \tag{5.104}$$

B) Induced voltage in the XYZ winding set due to stator currents flowing in the ABC winding set is :

$$u_{qp}(t) = 0 \tag{5.105}$$

C) Induced voltage in the XYZ winding set due to the rotor currents induced by currents flowing in the ABC winding set is:

$$u_{qrp}(t) = 2\pi r l \,\mathrm{Re}\left\{ \begin{array}{l} j\dfrac{\mu_0 \omega_1 r^2}{P_2\, g} \sqrt{2} \cdot \overline{C_{s2}} \cdot \overline{C_R^{P_2}}^{\,*} \cdot e^{j(\omega_1 t + (-P_1 - P_2)\omega_r t)} \cdot \sum_{i=1}^{N_r} \overline{I_{iR1}} \cdot e^{-j(P_2(i-1)\alpha_r)} \\ - j\dfrac{\mu_0 \omega_1 r^2}{P_2\, g} \sqrt{2} \cdot \overline{C_{s2}}^{\,*} \cdot \overline{C_R^{P_2}} \cdot e^{j(\omega_1 t + (P_2 - P_1)\omega_r t)} \cdot \sum_{i=1}^{N_r} \overline{I_{iR1}} \cdot e^{j(P_2(i-1)\alpha_r)} \end{array} \right\} \tag{5.106}$$

D) Induced voltage in the XYZ winding set due to the rotor currents induced by currents flowing in the XYZ winding set is :

$$u_{qrq}(t) = 2\pi r l \,\mathrm{Re}\left\{ \begin{array}{l} j\dfrac{\mu_0 \omega_2 r^2}{P_2\, g} \sqrt{2} \cdot \overline{C_{s2}} \cdot \overline{C_R^{P_2}}^{\,*} \cdot e^{j(\omega_2 t - 2P_2\omega_r t)} \cdot \sum_{i=1}^{N_r} \overline{I_{iR2}} \cdot e^{-j(P_2(i-1)\alpha_r)} \\ - j\dfrac{\mu_0 \omega_2 r^2}{P_2\, g} \sqrt{2} \cdot \overline{C_{s2}}^{\,*} \cdot \overline{C_R^{P_2}} \cdot e^{j(\omega_2 t)} \cdot \sum_{i=1}^{N_r} \overline{I_{iR2}} \cdot e^{j(P_2(i-1)\alpha_r)} \end{array} \right\} \tag{5.107}$$

The developed electromagnetic torque in the dual stator winding induction machine is composed of the torque component produced by the ABC winding set and the torque component produced by the XYZ winding set.

$$T_e = T_{eABC} + T_{eXYZ} \tag{5.108}$$

The summary of the torque equations is shown in the following section.

### 5.3.3 Equation of Torque Contributed by the ABC Winding Set

$$T_{eABC} = -\pi r l \,\mathrm{Re}\left\{\begin{array}{l} j\dfrac{\mu_0 r}{-gP_1}\sqrt{2}^2\left(3\overline{C_{s1}}\cdot\overline{I_{s1}}\cdot\overline{C_R^{P_1}}^*\right)e^{j(\omega_1 t+\omega_2 t+(-P_1-P_2)\omega_r t)}\cdot\sum_{i=1}^{N_r}\overline{I_{iR2}}\cdot e^{-j(P_1(i-1)\alpha_r)} \\ +\ j\dfrac{\mu_0 r}{gP_1}\sqrt{2}^2\left(3\overline{C_{s1}}^*\cdot\overline{I_{s1}}^*\cdot\overline{C_R^{P_1}}\right)e^{j(-\omega_1 t+\omega_2 t+(P_1-P_2)\omega_r t)}\cdot\sum_{i=1}^{N_r}\overline{I_{iR2}}\cdot e^{j(P_1(i-1)\alpha_r)} \\ j\dfrac{\mu_0 r}{-gP_1}\sqrt{2}^2\left(3\overline{C_{s1}}\cdot\overline{I_{s1}}\cdot\overline{C_R^{P_1}}^*\right)e^{j(2\omega_1 t-2P_1\omega_r t)}\cdot\sum_{i=1}^{N_r}\overline{I_{iR1}}\cdot e^{-j(P_1(i-1)\alpha_r)} \\ +\ j\dfrac{\mu_0 r}{gP_1}\sqrt{2}^2\left(3\overline{C_{s1}}^*\cdot\overline{I_{s1}}^*\cdot\overline{C_R^{P_1}}\right)\cdot\sum_{i=1}^{N_r}\overline{I_{iR1}}\cdot e^{j(P_1(i-1)\alpha_r)} \end{array}\right\} \tag{5.109}$$

### 5.3.4 Equation of Torque Contributed by the XYZ Winding Set

$$T_{eXYZ} = -\pi r l \,\mathrm{Re}\left\{\begin{array}{l} j\dfrac{\mu_0 r}{-gP_2}\sqrt{2}^2\left(3\overline{C_{s2}}\cdot\overline{I_{s2}}\cdot\overline{C_R^{P_2}}^*\right)e^{j(\omega_1 t+\omega_2 t+(-P_1-P_2)\omega_r t)}\cdot\sum_{i=1}^{N_r}\overline{I_{iR1}}\cdot e^{-j(P_2(i-1)\alpha_r)} \\ +\ j\dfrac{\mu_0 r}{gP_2}\sqrt{2}^2\left(3\overline{C_{s2}}^*\cdot\overline{I_{s2}}^*\cdot\overline{C_R^{P_2}}\right)e^{j(-\omega_2 t+\omega_1 t+(P_2-P_1)\omega_r t)}\cdot\sum_{i=1}^{N_r}\overline{I_{iR1}}\cdot e^{j(P_2(i-1)\alpha_r)} \\ j\dfrac{\mu_0 r}{-gP_2}\sqrt{2}^2\left(3\overline{C_{s2}}\cdot\overline{I_{s2}}\cdot\overline{C_R^{P_2}}^*\right)e^{j(2\omega_2 t-2P_2\omega_r t)}\cdot\sum_{i=1}^{N_r}\overline{I_{iR2}}\cdot e^{-j(P_2(i-1)\alpha_r)} \\ +\ j\dfrac{\mu_0 r}{gP_2}\sqrt{2}^2\left(3\overline{C_{s2}}^*\cdot\overline{I_{s2}}^*\cdot\overline{C_R^{P_2}}\right)\cdot\sum_{i=1}^{N_r}\overline{I_{iR2}}\cdot e^{j(P_2(i-1)\alpha_r)} \end{array}\right\} \tag{5.110}$$

## 5.4 Discussion

From the summarized voltage equations in Section 5.3, it is observed that apart from the input voltage frequency $\omega_1$ induced in the ABC winding set, three rotor speed

dependent frequency voltage components are generated having frequencies which are $\omega_1 - 2P_1\omega_r$, $\omega_2 + (-P_1 - P_2)\omega_r$ and $\omega_2 + (P_1 - P_2)\omega_r$. The additional frequency voltage components induced in the XYZ winding set are $\omega_2 - 2P_2\omega_r$, $\omega_1 + (-P_2 - P_1)\omega_r$ and $\omega_1 + (P_2 - P_1)\omega_r$. All the voltages with harmonic frequencies (such as $\omega_1 - 2P_1\omega_r$, $\omega_2 + (-P_1 - P_2)\omega_r$ and $\omega_2 + (P_1 - P_2)\omega_r$) induce harmonic currents. These harmonic currents subsequently induce other higher-level harmonic voltages, and so on and so forth. However, since the magnitudes of the harmonic currents and voltages are much less than the fundamental components, they are insignificant and can be ignored.

From the torque equations, an average torque generated individually by the ABC and XYZ winding sets is given by the last terms of the equations (5.109-5.110). In addition, by constraining the supply voltage frequencies of the windings, a potential average torque can be obtained as discussed below.

(A) The first term in (5.109-5.110) potentially contributes to the average torque when the following frequency equation is met.

$$\omega_1 + \omega_2 + (-P_1 - P_2)\omega_r = 0 \quad \text{or} \quad \omega_1 = (P_1 + P_2)\omega_r - \omega_2 \tag{5.111}$$

The frequency constraint in (5.111) is such that if the rotor speed and the input frequency of the ABC winding set are fixed, the frequency of the voltage in the XYZ winding set can be controlled according to (5.111) to create an additional torque component. If the slip frequencies of the stator windings are defined as $\omega_{s1} = \omega_1 - P_1\omega_r$, $\omega_{s2} = \omega_2 - P_2\omega_r$, then $\omega_{s1} + \omega_{s2} = 0$. It follows that an additional torque may be available when the slip frequencies of two stator windings have the same magnitude but of opposite signs. Under this constraint, one three-phase

winding set works as a generator, while the other three-phase winding set is working as a motor. This operating condition may be useful at low speeds.

Then the expression of the average torque is the next step. If the inverse slip condition is applied, the first term of torque from ABC winding is expressed as:

$$T_{eABC1} = -\pi r l \,\mathrm{Re}\left\{ j \frac{\mu_0 r}{-gP_1} \sqrt{2}^2 \left( 3\overline{C_{s1}} \cdot \overline{I_{s1}} \cdot \overline{C_R^{P_1}}^* \right) \cdot \sum_{i=1}^{N_r} \overline{I_{iR2}} \cdot e^{-j(P_1(i-1)\alpha_r)} \right\} \tag{5.112}$$

Under steady state condition, the rotor current distribution follows the sinusoidal function, which is written as:

$$\overline{I_{iR2}} = \overline{I_{R2}} \cdot e^{j(P_2 \cdot (i-1)\alpha_r + \varepsilon)} \tag{5.113}$$

where, the complex number $\overline{I_{R2}}$ represents the magnitude of the rotor current induced by the XYZ winding set; $\varepsilon$ is a general shift angle between the rotor currents induced by the XYZ winding and physical rotor loops fixed by the ABC winding set.

Substituting (5.113) into (5.112), the first term of $T_{eABC}$ becomes,

$$T_{eABC1} = -\pi r l \,\mathrm{Re}\left\{ j \frac{\mu_0 r}{-gP_1} \sqrt{2}^2 \left( 3\overline{C_{s1}} \cdot \overline{I_{s1}} \cdot \overline{C_R^{P_1}}^* \right) \cdot \sum_{i=1}^{N_r} \overline{I_{R2}} \cdot e^{j[(P_2 - P_1)(i-1)\alpha_r + \varepsilon]} \right\} \tag{5.114}$$

Since the pole numbers of two stator windings are unequal, the sum of terms yield zero, i.e:

$$\sum_{i=1}^{N_r} e^{j[(P_2 - P_1)(i-1)\alpha_r + \varepsilon]} = 0 \tag{5.115}$$

Similar result is obtained for the first term of $T_{eXYZ}$. It can be concluded that the potential additional torque due to this term is zero under steady state operating condition. However, since the rotor current distribution assumption is only good

for the steady state condition, the additional average torque from the interaction of the two stator winding sets may be obtained during the transient condition.

(B) The second term in (5.109-5.110) contributes to the average torque only when the following conditions are meet :

$$\omega_1 - \omega_2 + (P_2 - P_1)\omega_r = 0 \qquad \text{or} \quad \omega_1 = (P_1 - P_2)\omega_r + \omega_2 \ , \ \omega_{s1} - \omega_{s2} = 0 \qquad (5.116)$$

If the rotor speed and the input frequency of the ABC winding set are fixed, the frequency of the supply voltage to the XYZ winding set can be controlled according to (5.116) to create a possible additional torque component. This additional torque component will be available when the slip frequencies of the two stator winding sets have the same value implying that both winding sets are either working as motors or generators. Following the same derivation process for case (A), the possible additional torque from the second term of $T_{eABC}$ is expressed as:

$$T_{eABC2} = \pi r l \,\mathrm{Re}\left\{ j\frac{\mu_0 r}{g P_1}\sqrt{2}^2 \left( 3\overline{C_{s1}} \cdot \overline{I_{s1}} \cdot \overline{C_R^{P_1}}^{*} \right) \cdot \sum_{i=1}^{N_r} \overline{I_{R2}} \cdot e^{j[(P_2+P_1)(i-1)\alpha_r + \varepsilon]} \right\} = 0 \qquad (5.117)$$

It is obvious that this possible additional torque term will also be zero under steady state condition although it may not be zero during the transient condition. The same result can be obtained for the second term of $T_{eXYZ}$ .

(C) The third term in (5.109-5.110) may contribute to the average torque when any the rotor angular speed is the same as the angular speed of the supply voltage corresponding to synchronous operating conditions. That is, $\omega_r p_1 = \omega_1$, $\omega_r p_2 = \omega_2$. Unfortunately at synchronous rotor speeds, the rotor currents are zero, hence no electromagnetic torque results. Synchronous operation, which is

possible for the brushless doubly-fed induction machine, is therefore not feasible for the dual-winding squirrel-cage induction machine.

(D) The fourth terms of (5.109-5.110) are the two average torque components which are present under any operating asynchronous condition. The expressions for the developed electromagnetic torques due to both winding sets are the same as the one obtained for a standard single winding squirrel-cage induction machine.

## 5.5 Coupled Circuit Machine Model with Common Rotor Currents

The additional torque components (5.114, 5.117) are due to the interaction of the currents of the ABC winding set and the rotor currents induced by the XYZ winding set and those of the currents in the XYZ winding set interacting with the rotor currents induced by the ABC stator winding set. To validate the field analysis and include the possible interactions between two stator windings into the analysis, a simulation model with common rotor circuit currents is developed in this section. The multiple coupled circuits modeling approach of an induction machine is used [1.8]. All the stator rotor mutual inductances are calculated on-line based on the winding functions of stator windings and rotor circuits without simplification [5.4]. However, unlike the previous work in which two independent rotor circuits are assumed and each of the two separate models for the machine predicts its corresponding rotor current components, only one rotor circuit is used so that the influence of the two separate stator currents on the total bar currents (not the components thereof) on the developed electromagnetic torque are properly accounted for.

From the general expression of coupled circuit model of electric machine, the matrix format of stator voltage equation set of the dual stator winding induction machine is expressed as:

$$v = R \cdot i + p\lambda \tag{5.118}$$

where, $R$ is the resistance matrix; $p$ represents the operator $\frac{d}{dt}$

$$v = \begin{pmatrix} v_a & v_b & v_c & v_x & v_y & v_z & v_{r1} & v_{r2} & \cdots & v_{rn} \end{pmatrix}^T,$$

$$i = \begin{pmatrix} i_a & i_b & i_c & i_x & i_y & i_z & i_{r1} & i_{r2} & \cdots & i_{rn} \end{pmatrix}^T,$$

$$\lambda = \begin{pmatrix} \lambda_a & \lambda_b & \lambda_c & \lambda_x & \lambda_y & \lambda_z & \lambda_{r1} & \lambda_{r2} & \cdots & \lambda_{rn} \end{pmatrix}^T.$$

The voltage equation for the $k^{th}$ rotor loop is represented as:

$$0 = 2(r_b + r_e) \cdot i_k - r_b \cdot i_{k+1} - r_b \cdot i_{k-1} + p\lambda_{rk} \tag{5.119}$$

where, $r_b$ is the bar resistance; $r_e$ is the resistance of the segment of end ring; $i_k$, $i_{k-1}$ and $i_{k+1}$ are the currents of the $k^{th}$, $k-1^{th}$ and $k+1^{th}$ rotor loops respectively; $\lambda_{rk}$ is the flux linkage of the $k^{th}$ rotor loop.

The resistance matrix $R$ is expressed as:

$$R = \begin{pmatrix} r_{s1} & 0 & 0 & 0 & 0 & 0 & 0 & 0 & \cdots & 0 \\ 0 & r_{s1} & 0 & 0 & 0 & 0 & 0 & 0 & \cdots & 0 \\ 0 & 0 & r_{s1} & 0 & 0 & 0 & 0 & 0 & \cdots & 0 \\ 0 & 0 & 0 & r_{s2} & 0 & 0 & 0 & 0 & \cdots & 0 \\ 0 & 0 & 0 & 0 & r_{s2} & 0 & 0 & 0 & \cdots & 0 \\ 0 & 0 & 0 & 0 & 0 & r_{s2} & 0 & 0 & \cdots & 0 \\ 0 & 0 & 0 & 0 & 0 & 0 & 2(r_b + r_e) & -r_b & \cdots & -r_b \\ 0 & 0 & 0 & 0 & 0 & 0 & -r_b & 2(r_b + r_e) & \cdots & 0 \\ \vdots & \vdots & \vdots & \vdots & \vdots & \vdots & \vdots & \vdots & \ddots & \vdots \\ 0 & 0 & 0 & 0 & 0 & 0 & -r_b & 0 & \cdots & 2(r_b + r_e) \end{pmatrix} \tag{5.120}$$

Since the number of rotor bar is n, the resistance matrix $R$ is a $(n+6)\times(n+6)$ matrix and the voltage vector $v$, current vector $i$ and flux vector $\lambda$ are all $(n+6)\times 1$ vectors.

With the two stator winding sets having dissimilar number of poles, the mutual inductances between the two sets of windings are zero and are therefore naturally decoupled. The flux linkages can be written as the contribution of two components: one of them is the flux linkages due to the stator winding currents; the other term represents the flux linkages that are due to the contribution of the rotor (bar) currents. The flux linkage equation is:

$$\lambda=\begin{pmatrix} L_{ls1}+L_{aa} & L_{ab} & L_{ac} & 0 & 0 & 0 & L_{ar1} & L_{ar2} & \cdots & L_{arn} \\ L_{ba} & L_{ls1}+L_{bb} & L_{bc} & 0 & 0 & 0 & L_{br1} & L_{br2} & \cdots & L_{brn} \\ L_{ca} & L_{cb} & L_{ls1}+L_{cc} & 0 & 0 & 0 & L_{cr1} & L_{cr2} & \cdots & L_{crn} \\ 0 & 0 & 0 & L_{ls2}+L_{xx} & L_{xy} & L_{xz} & L_{xr1} & L_{xr2} & \cdots & L_{xrn} \\ 0 & 0 & 0 & L_{yx} & L_{ls2}+L_{yy} & L_{yz} & L_{yr1} & L_{yr2} & \cdots & L_{yrn} \\ 0 & 0 & 0 & L_{zx} & L_{zy} & L_{ls2}+L_{zz} & L_{zr1} & L_{zr2} & \cdots & L_{zrn} \\ L_{r1a} & L_{r1b} & L_{r1c} & L_{r1x} & L_{r1y} & L_{r1z} & L_{rr}+2(l_b+l_e) & L_{rm1}-l_b & \cdots & L_{rm1}-l_b \\ L_{r2a} & L_{r2b} & L_{r2c} & L_{r2x} & L_{r2y} & L_{r2z} & L_{rm1}-l_b & L_{rr}+2(l_b+l_e) & \cdots & L_{rm2} \\ \vdots & \vdots & \vdots & \vdots & \vdots & \vdots & \vdots & \vdots & \ddots & \vdots \\ L_{rna} & L_{rnb} & L_{rnc} & L_{rnx} & L_{rny} & L_{rnz} & L_{rm1}-l_b & L_{rm2} & \cdots & L_{rr}+2(l_b+l_e) \end{pmatrix}\cdot\begin{pmatrix} i_a \\ i_b \\ i_c \\ i_x \\ i_y \\ i_z \\ i_{r1} \\ i_{r2} \\ \vdots \\ i_{rn} \end{pmatrix} \tag{5.121}$$

where, $L_{ls1}$ and $L_{ls2}$ are the leakage inductances of the ABC and XYZ winding sets respectively; $L_{mm}$ ($m=a,b,c,x,y,z$) is the self-inductance of the stator windings, $L_{mn}$ ($m\neq n=a,b,c,x,y,z$) is the mutual inductance between two stator windings, $L_{mri}$ and $L_{rim}$ ($m=a,b,c,x,y,z\,;i=1,2,\cdots,n$) are the mutual inductances between the phase m and $i^{th}$ rotor loop; $L_{rr}$ is the self-inductance of the rotor loops; $L_{rm1}$ is the mutual inductance between the adjunct rotor loops; $L_{rm2}$ is the mutual inductance between the rotor loops that are not adjunct; $l_b$ and $l_e$ are the leakage inductances of the rotor bar and the

segment of end ring respectively. The calculation of the inductances is based on the winding functions approach that has been given in Section 3.3-3.6.

The electromagnetic torque can be obtained from the magnetic co-energy as:

$$T_e = \frac{\partial W_c}{\partial \theta_{rm}} = -\frac{\partial W_f}{\partial \theta_{rm}} \tag{5.122}$$

where, $\theta_{rm}$ is the mechanical angle of the rotor. The total field energy equation for the dual stator winding induction machine is expressed as:

$$\begin{aligned} W_f = & \frac{1}{2} i_{abc}{}^T \cdot L_{s1s1} \cdot i_{abc} + \frac{1}{2} i_{xyz}{}^T \cdot L_{s2s2} \cdot i_{xyz} + \frac{1}{2} i_{abc}{}^T \cdot L_{s1s2} \cdot i_{xyz} \\ & + \frac{1}{2} i_{xyz}{}^T \cdot L_{s2s1} \cdot i_{abc} + \frac{1}{2} i_{abc}{}^T \cdot L_{s1r} \cdot i_r + \frac{1}{2} i_{xyz}{}^T \cdot L_{s2r} \cdot i_r \\ & + \frac{1}{2} i_r{}^T \cdot L_{rs1} \cdot i_{abc} + \frac{1}{2} i_r{}^T \cdot L_{rs2} \cdot i_{xyz} + \frac{1}{2} i_r{}^T \cdot L_{rr} \cdot i_r \end{aligned} \tag{5.123}$$

where, $L_{mm}$ $(m = s1, s2, r)$ represents the self-inductance matrix of m winding; $L_{mn}$ $(n \neq m = s1, s2, r)$ represents the mutual inductance matrix between m winding and n winding. Both $L_{mm}$ and $L_{mn}$ are sub-matrixes of the inductance matrix in given in (5.121).

Only the terms in equation (5.123) which are functions of the rotor angle contribute to the electromagnetic torque. Ignoring magnetic saturation i.e $L_{ab} = L_{ba}$, the electromagnetic torque becomes :

$$T_e = -i_{abc}{}^T \cdot \frac{\partial L_{s1r}}{\partial \theta_{rm}} \cdot i_r - i_{xyz}{}^T \cdot \frac{\partial L_{s2r}}{\partial \theta_{rm}} \cdot i_r \tag{5.124}$$

## 5.6 Computer Simulation and Experimental Results

The computer simulation of the conditions in (5.116) in which the slip frequencies of the two stator windings are equal has been undertaken using the MATLAB/SIMULINK software. The dual stator winding induction machine models with a common rotor circuit and with two independent rotor circuits are used in the computer simulations and the results are compared to show the differences. Some of the calculated machine parameters used are constant and are given in Table 3.1. The simulation results for stator-frequency and rotor speed condition in (5.116) are displayed in Figure 5.2. The two windings are fed with two sinusoidal voltage sources and operating under constant voltage/Hertz open loop control in which the ratio of the frequency of the 6-pole stator winding set to those of the 2-pole stator winding set is equal to 3. The frequencies of the ABC (2-pole) and XYZ (6-pole) stator winding sets are initially set to be 30 Hz and 90 Hz respectively. The constant voltage/Hertz coefficient of both the voltages supplied to the ABC (2-pole) and XYZ (6-pole) stator winding sets is at 2.23. The load torque is 3 Nm. During the steady-state operation, the frequency of the input voltage to the ABC winding set remains at 30 Hz, the measured rotor speed is used to adjust the frequency of the input voltage supplied to the XYZ winding set to satisfy (5.116) at t =1.5 seconds. If the motor is closed-loop speed controlled, the input phase voltages of the XYZ winding set are adjusted accordingly while maintaining equal slip frequency operation. The same simulation conditions are applied to both machine models and the simulation results are shown in Figure 5.2. In this figure, the blue solid line represents the results from the one rotor circuit model and the red dash-dot line represents the results from the independent rotor circuit model. The steady state rotor speeds of two models are different because of the

additional torque generated by the one-rotor circuit model during the transient process as shown in Figure 5.2(c). Greater oscillatory torque is observed in the results from the one rotor circuit model which is absent in two independent rotor circuit model as shown in Figure 5.2(d-f). It follows that the pulsating torque is due to the interaction of the two stator windings through a common rotor current. The power consumption distribution between the two stator winding sets (represented by the electromagnetic torques due to each winding set in Figure 5.2(e-f)) changes; however the total developed electromagnetic torque is constant as the load torque remains the same.

When the same operating equal slip frequency condition (5.116) as enforced in the computer simulation in Figure 5.2 is applied to a 2hp laboratory dual winding squirrel-cage induction machine, the experimental results are shown in Figure 5.3. The two stator winding sets are fed with two voltage source PWM inverters using the space vector PWM modulation scheme. The rotor speed is measured by a shaft mounted encoder. The open-loop control algorithm in (5.116) is implemented using a TI DSP TMS320LF2407 EVM board to determine the frequency of the XYZ winding set. The motor under load is initially running under steady state condition with a constant Volt/Hz operating condition at frequencies of 30 and 90 Hz for the ABC and XYZ winding sets respectively. Then the measured rotor speed is used to adjust the frequency of the XYZ winding set (the frequency of the ABC winding set is kept constant at 30 Hz) to force the values of slip frequency of the two windings to be equal. The rotor speed drops and the power drawn by the ABC winding set and the phase "A" current increases while the power drawn by the XYZ winding set and the phase X current decreases, validating the trends in the computer simulation results in Figure 5.3.

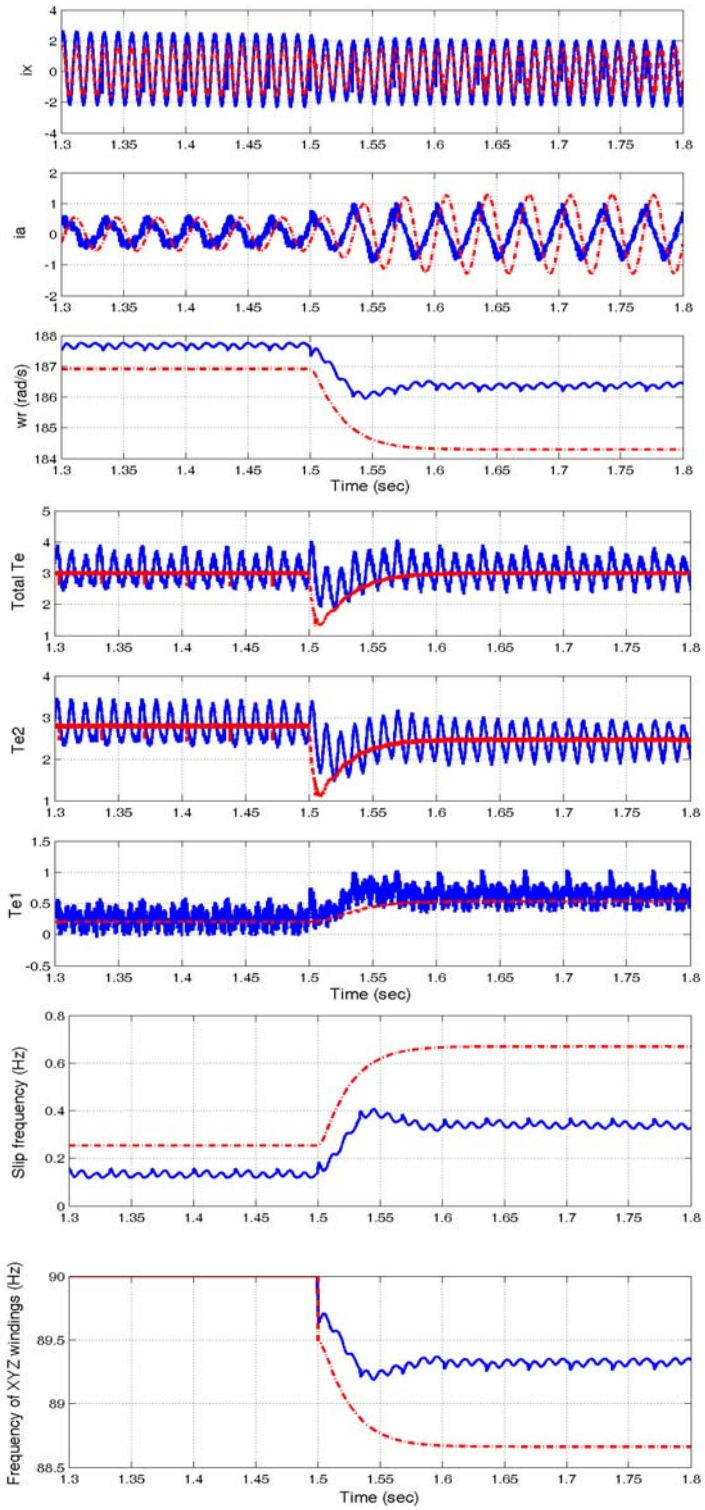


Figure 5.2. Simulation results for equal slip condition, the red dot-dash line is the result for two independent rotor circuit model and blue solid line is for one rotor circuit model. From top: (a) Phase X current, (b) phase A current, (c) rotor speed, (d) total electromagnetic torque, (e) electromagnetic torque from XYZ windings, (f) electromagnetic torque from ABC windings, (g) slip frequency, (h) frequency of XYZ windings.

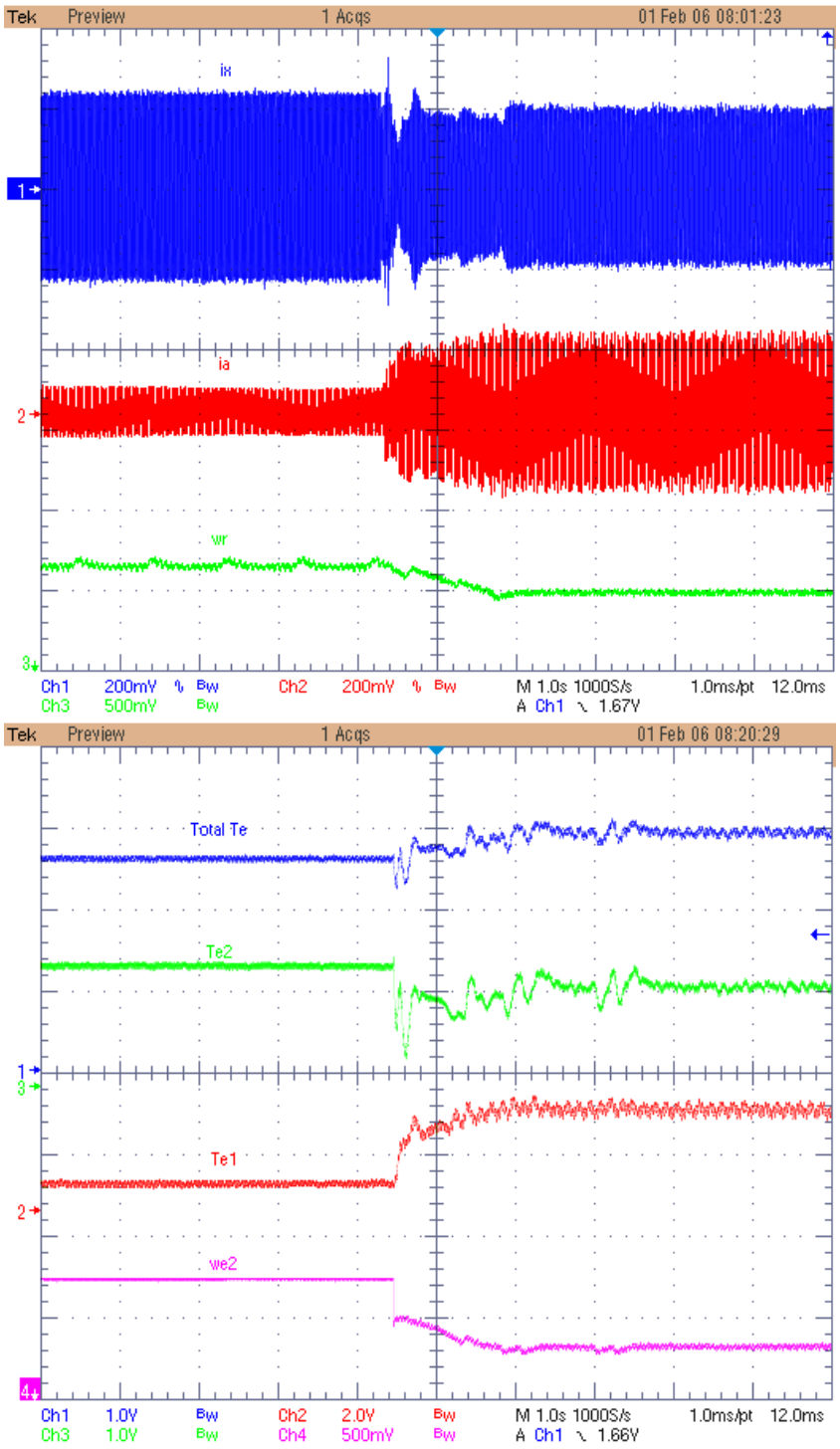


(a)

(b)

(c)

(d)

(e)

(f)

(g)

Figure 5.3. Experimental results for equal slip condition. In part (I), from top: (a) Phase X current (changes from 3.4A to 2.8A), (b) phase A current (changes from 0.7A to 2.1A), (c) rotor speed (changes from 1785 rpm to 1752 rpm); in part (II) from top: (d) total electromagnetic torque (changes from 3.2 Nm to 3.3 Nm), (e) electromagnetic torque from XYZ windings (changes from 2.95 Nm to 2.5Nm), (f) electromagnetic torque from ABC windings (changes from 0.25 Nm to 0.9 Nm), (g) electrical speed of XYZ windings (changes from 565 rad/s to 556 rad/s).

## 5.7. Conclusions

In this chapter, using the rotating-field theory and coupling magnetic circuit theory first used in [5.1] for the study of three-phase induction machines and later for the brushless doubly-fed machines [1.8], a fundamental understanding of the generated voltages and possible developed electromagnetic torque components of the dual stator winding squirrel-cage induction machine is set forth for the first time. The advantage of this method is the opportunity to clearly show all the frequency components and the corresponding magnitudes of induced voltages, unsaturated air-gap flux linkages and components of the developed electromagnetic torque. It may be possible to use some of these induced voltages and air-gap flux linkages by virtue of their dependencies on the rotor speed to estimate the rotor speeds (from zero to high speed) for use in sensorless speed and/or torque control. This possibility is a subject of future research and experimentation.

The development of the torque equations show that under certain operating conditions, some additional torque components may be created only during the transient process, however the average torque will disappear under steady state condition. Relevant computer simulation results from two different machine models are provided to show the possible equal slip frequency operating condition of the motor to yield an additional torque component during the transient process. This operational mode is not predicted when the dual stator winding induction machine is modeled and analyzed as two independent induction machines coupled by the rotor shaft since the generated torque components are due to the stator winding currents of the individual winding sets interacting with the total rotor currents [1.1].

# CHAPTER 6

# MODELING OF A DUAL STATOR WINDING INDUCTION MACHINE INCLUDING THE EFFECT OF MAIN FLUX LINKAGE MAGNETIC SATURATION

## 6.1 Introduction

Saturation analysis of single stator winding induction machines has been studied for many years. The techniques, including incorporating air gap flux saturation into the performance analysis and parameter estimation are mature. However, the saturation analysis for dual winding machines is still in early development. Since the air-gap flux linkages created by the two stator windings and the induced rotor currents share the same magnetic stator and rotor cores, the primary air-gap flux saturation phenomenon is more complicated than that of the normal single stator winding squirrel-cage induction machine [6.3, 6.5]. Because of this complexity, it is appropriate to reconsider the main flux linkage saturation effect in the design of the machine and in the development and practical implementation of speed/torque control algorithms. To avoid deep magnetic saturation in the stator and rotor cores, rotor and stator teeth, magnetic design methodologies have been suggested both for the dual-stator winding and brushless doubly-fed induction machines [6.5, 6.6, 1.11]. An approach to include the influence of magnetic saturation and iron loss using time-stepping Finite Element Analysis in the performance prediction of the brushless doubly-fed induction machine was set forth in [6.3]. It is the belief of the authors that the proposed finite element model produces very

good steady-state predictions and can be used for the sizing and design optimization of the machine. How the time-varying, multi-frequency flux linkages derivable from the currents flowing in the stator windings and rotor bars can be appropriately selected for an optimal machine design remains a challenging question. These flux linkages combine additively in some regions and subtractively in others engendering non-uniform main flux magnetic saturation.

This chapter reports on a study of the effects of magnetic saturation on the air-gap flux linkages and provides for the first time a methodology to include the main air-gap flux linkage saturation effect in the dynamic modeling of the dual winding induction machine. This is achieved by the definition of a common reference frame for the defining differential equations of the machine that ensures that the total air gap flux linkage lies on the d-axis of the reference frame. Thus, only the d-axis magnetizing inductances vary with the main air-gap flux linkage while the q-axis magnetizing inductances remain constant at the unsaturated values. The new dynamic machine model is validated by computer simulation and experimental results for two operating conditions.

## 6.2 Main Flux Linkage Saturation Effects

Since the two stator windings (ABC and XYZ winding sets) have dissimilar pole numbers, the mutual inductances between them are zero when the main-flux linkage path is unsaturated. Possible coupling may be found in the stator leakage inductances. However, it has been shown in [1.1] that the couplings between the leakage inductances do not exist in such a way as to allow the dual stator winding induction machine to be treated (on the fundamental frequency basis) as two independent squirrel-cage induction

machines coupling through the rotor circuit. The magneto-motive forces (MMFs) resulting in the air-gap flux linkage is the sum of the MMFs due to the currents flowing in the two stator winding sets and the MMFs arising from the induced rotor bar currents. If only the fundamental stator currents and their induced harmonic-rich rotor currents are considered, the air-gap flux density therefore has four components given as:

$$\begin{aligned} B = {} & B_{1s}\cos(\omega_{e1}t - P_1\theta) + B_{2s}\cos(\omega_{e2}t - P_2\theta + \alpha_1) \\ & + \sum_k B_{1rk}\cos(\omega_{e1}t + (k - P_1)\omega_r t - k\theta + \alpha_{2k}) \\ & + \sum_k B_{2rk}\cos(\omega_{e2}t + (k - P_2)\omega_r t - P_2\theta + \alpha_{3k}) \end{aligned} \tag{6.1}$$

where, $B_{1s}$ and $B_{2s}$ are the peak values of the air gap flux densities contributed by the stator ABC and XYZ winding sets, respectively. $B_{1rk}$ and $B_{2rk}$ are the flux densities due to the $k^{th}$ harmonic MMFs of rotor currents.

The dual stator winding squirrel-cage induction machines operate in the asynchronous mode for the development of torque components usually found in the single winding three-phase squirrel-cage induction machine, however additional average torque components can be produced during the transient process when the absolute values of the slip frequencies relative to the two stator windings are equal as shown in previous chapter; i.e

$$\omega_r = \frac{\omega_{e1} \mp \omega_{e2}}{P_1 \mp P_2} \tag{6.2}$$

$$\begin{aligned} B = {} & B_{1s}\cos(\omega_{e1}t - P_1\theta) + B_{2s}\cos(\omega_{e2}t - P_2\theta + \alpha_1) \\ & + B_{1rp1}\cos(\omega_{e1}t - P_1\theta + \alpha_{2p1}) + B_{2rp2}\cos(\omega_{e2}t - P_2\theta + \alpha_{3p2}) \end{aligned} \tag{6.3}$$

When the speed constraint in (6.2) is implemented in (6.1), the resulting fundamental air-gap flux density is given in (6.3), comprising of components of $P_1$ and $P_2$ poles upon

which are superimposed some space harmonics. When the magnetic circuit is saturated, new saturation induced air-gap flux densities are generated which may link one set of windings to the second set. In the case where the pole pair number combination of the two stator windings is 1/3, the 2-pole winding under main air-gap flux saturation produces a third harmonic component which is commensurate with the flux linkage originating from the 6-pole winding set. By virtue of the phase angle difference between the flux densities due to the 2 and 6-pole windings, the generated saturation flux linkage may reduce or enhance the fundamental air-gap flux linkage due to the 6-pole stator winding set. An understanding of the consequence of the main flux saturation on the air-gap flux density given in (6.3) is obtained by reviewing Figure 6.1.

Figure 6.1(a) shows the unsaturated and saturated air-gap flux density (at time t = 0) due to the sum of $B_1 \cos(\omega_{e1} t - P_1\theta + \alpha)$ and $B_2 \cos(\omega_{e2} t - P_2\theta)$ where $P_1 = 1$, $P_2 = 3$, $B_1 = 0.9$ T and $B_2 = 1.1$ T and $\alpha = 0$ is a phase shift angle. The 3-dimensional graph of the saturated air-gap flux density is given in Figure 6.1(c). The graph of the saturated air-gap flux density is obtained using the effective nonlinear B-H characteristics of the air-gap magnetic flux path. There are 5th and 7th harmonic components shown in Figure 6.1(b) resulting from the magnetic air-gap saturation effect. The fundamental and third harmonic flux density components reduce from 0.9 T to 0.647 T and 1.1 T to 0.879 T, respectively. The effect of the phase shift angle $\alpha$ on the magnitudes of the harmonic components for the saturated flux density is displayed in Figure 6.2. While the dominant harmonic components are present under all phase angles, the magnitudes change cyclically. Apart from the magnitudes of the flux densities, the phase angle between them affects the magnitudes of the generated harmonics and fundamental flux densities. For

the 2 hp machine operating under rated condition, Figure 6.3 shows the field plots obtained from the Finite Element Analysis in which magnetic circuit saturation has been accounted for. The Spectrums of the field plots have been given in Figure 6.3, in which the harmonic components are small. Apart from the slot harmonics, the dominant components of the air-gap and stator core flux densities are due to the $P_1$ and $P_2$ pole numbers.

Figure 6.4(a) gives the experimental waveforms of the no-load induced air-gap voltages obtained from an experimental machine using a 2-pole search coil when the two stator winding sets and when only one of the three-phase windings are connected to the voltage source(s). The machine main flux is saturated and the Volts/Hz for each winding set is kept the same while the supply frequencies are in the ratio of 1:3. The Fourier series of the induced voltages displayed in Figure 6.4(b) suggest the presence of the fundamental components in addition to the 5th and 7th harmonics. The slight change in the magnitude of the third harmonic component when the two windings and when the six-pole winding alone are powered may be due to the inter-winding saturation induced voltages. Figure 6.4(c) gives the increased saturation voltage induced on the 6-pole winding with variation of the 2-pole winding voltage under no-load condition. The magnitude is however reduced when the two stator winding sets are voltage fed.

In Figure 6.5, the induced air-gap voltages for three loading conditions are shown for the same input voltages applied in Figure 6.4. It would appear that the rotor MMFs under load tend to reduce the magnitudes of the components of the air-gap flux densities as the load increases.

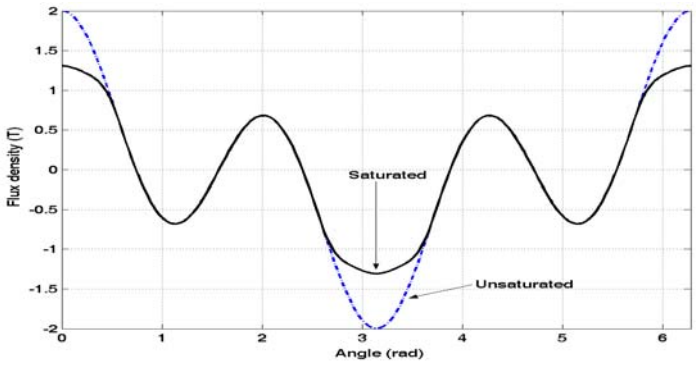


(a)

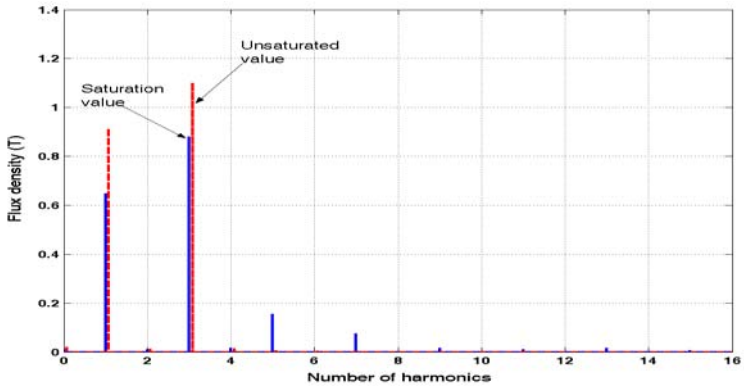


(b)

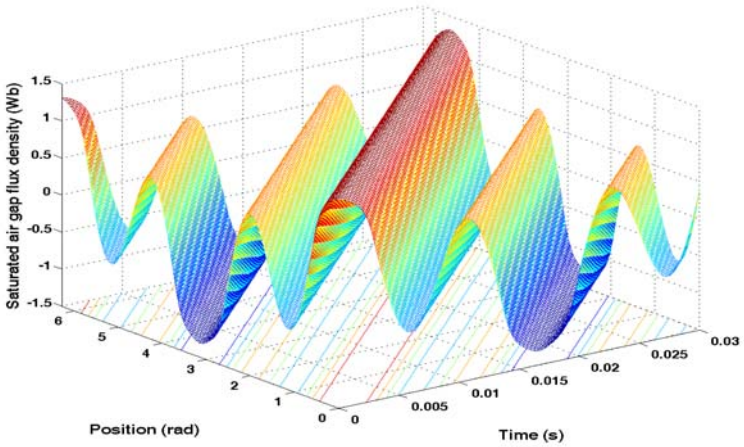


(c)

Figure 6.1: Main flux saturation. $B_1 = 0.9$ T, $B_3 = 1.1$T, $f_1 = 30$ Hz, $f_2 = 90$ Hz, (a) Unsaturated and saturated air-gap flux density at t = 0.0, (b) Fourier series of the unsaturated and saturated waveforms, (c) saturated air-gap flux density distribution as functions of time and circumferential angle.

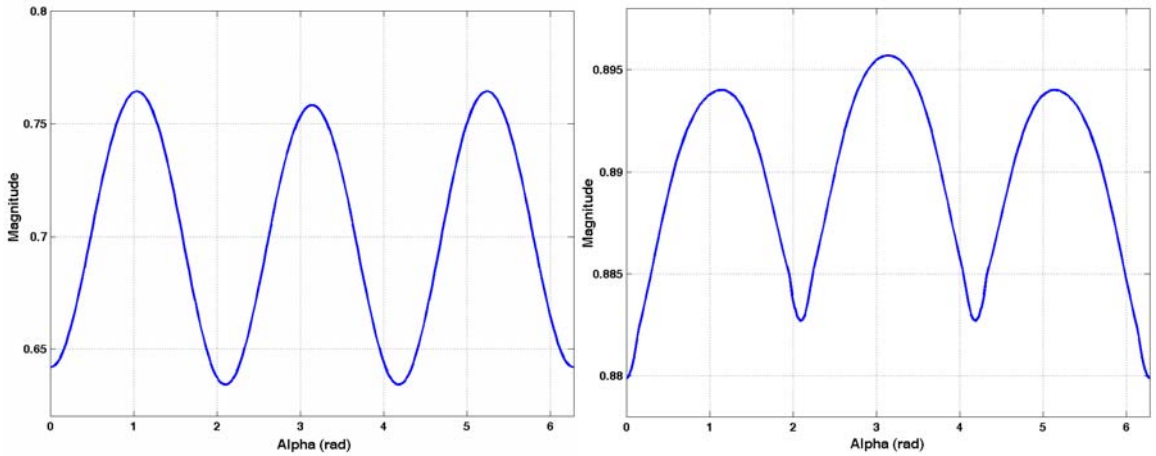


(a)




(b)

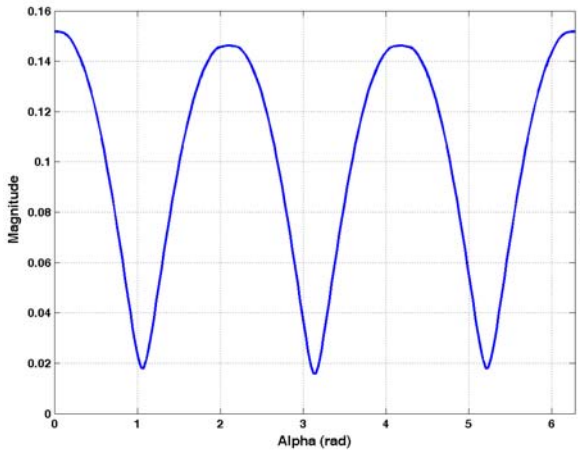


(c)

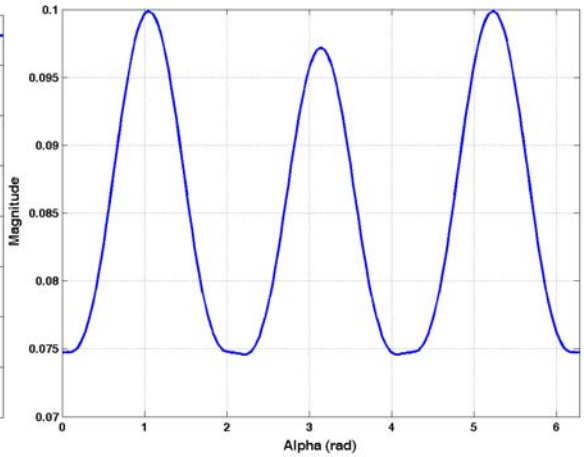


(d)

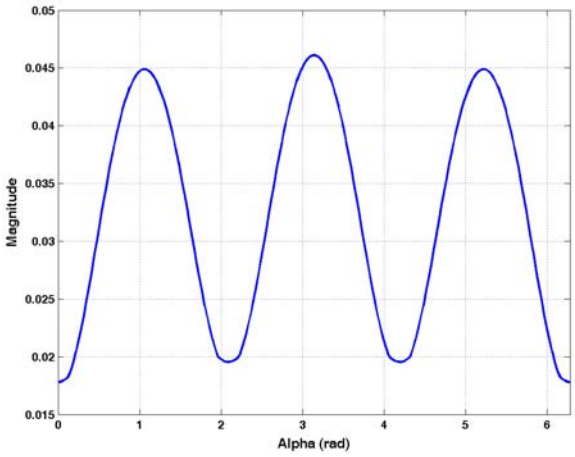


(e)

Figure 6.2: The influence of phase shift angle on the components of the saturated air-gap flux density. (a) Fundamental, (b) third, (c) fifth, (d) seventh, (e) ninth harmonics.

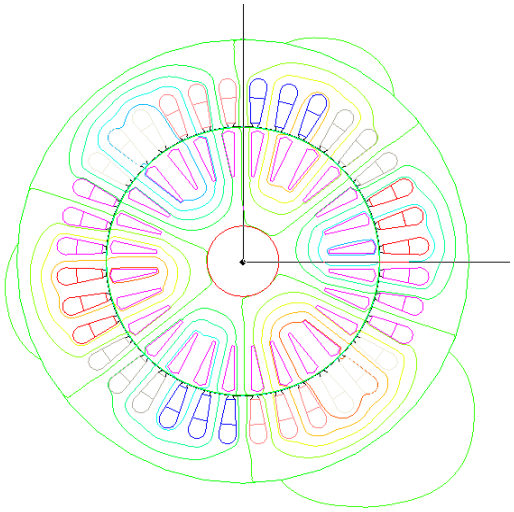

(a)

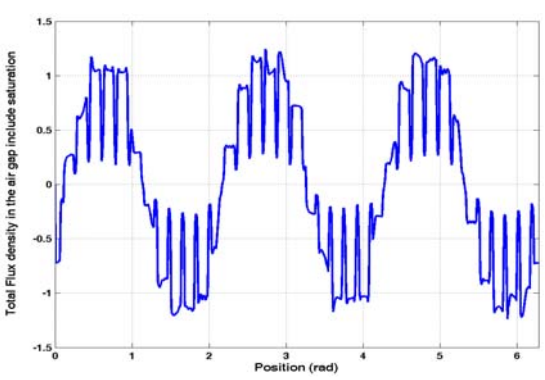


(b)

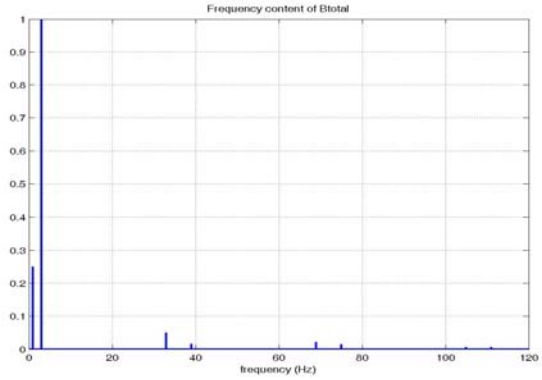


(c)

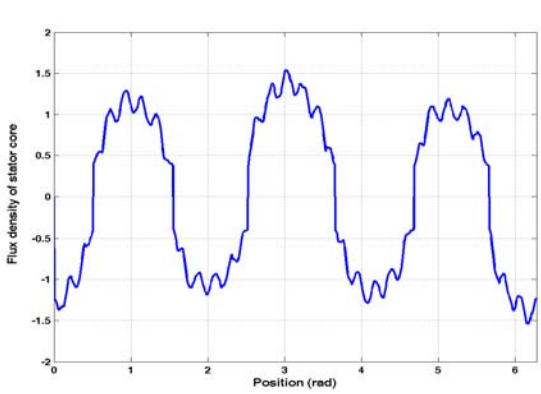


(d)

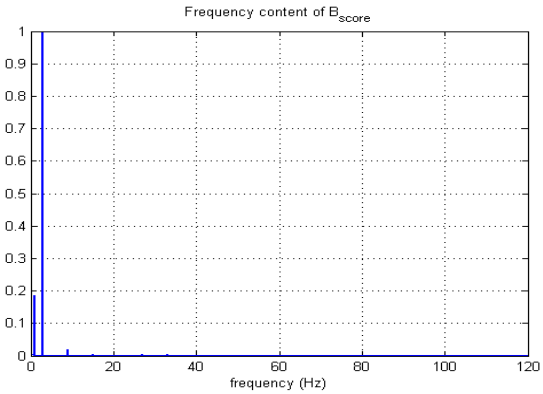


(e)

Figure 6.3: Finite Element Plots of a 2hp machine under rated condition and constant Volts/Hz operation. (a) Flux pattern, (b) air-gap flux density, (c) normalized spectrum of the air gap flux density, (d) stator core flux density as a function circumferential angle, (e) normalized spectrum of the stator core flux density.

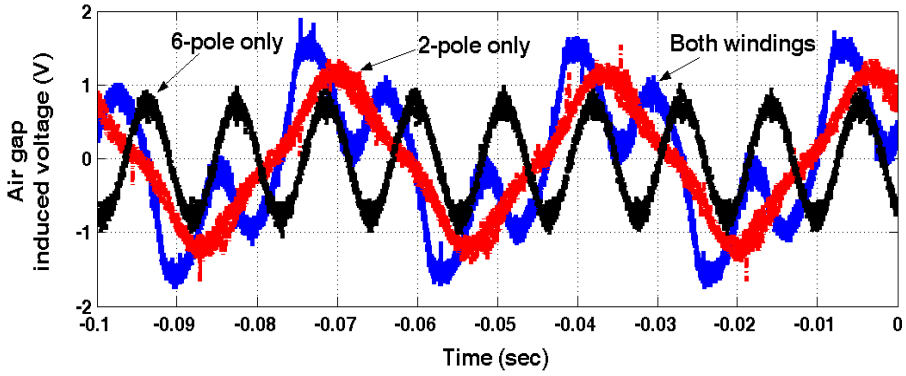


(a)

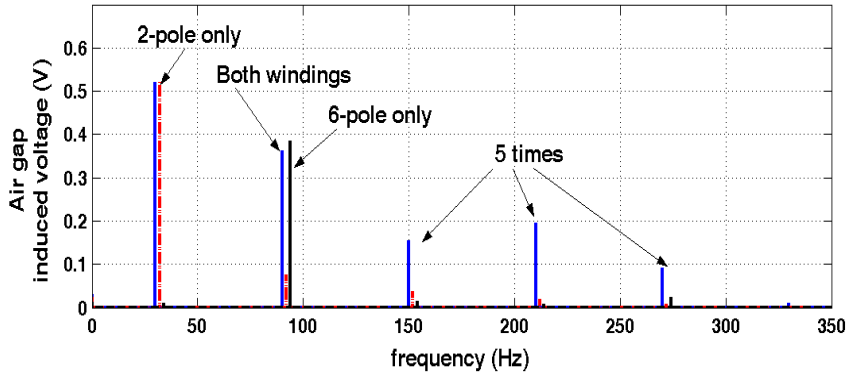


(b)

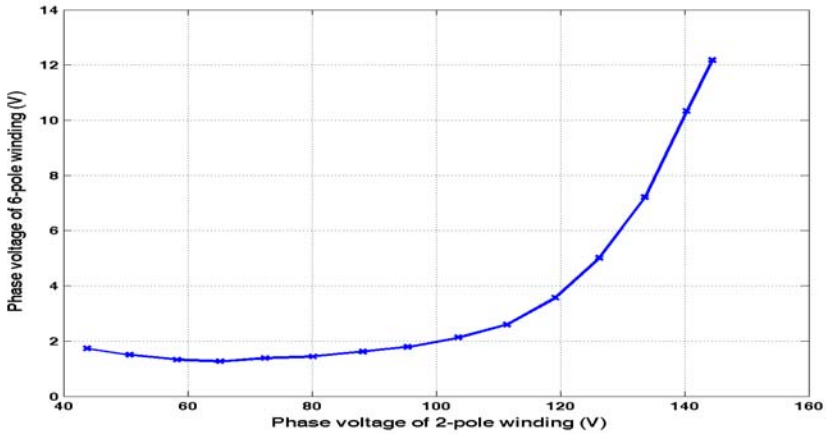


(c)

Figure 6.4: No load induced air-gap voltages. Winding ABC–phase voltage = 124 V, frequency = 30 Hz, winding XYZ—phase voltage = 124 V, frequency = 90 Hz (a) air gap induced voltage waveforms, (b) Fourier series of waveforms, (c) induced inter-winding voltage for varying 2-pole winding voltage.

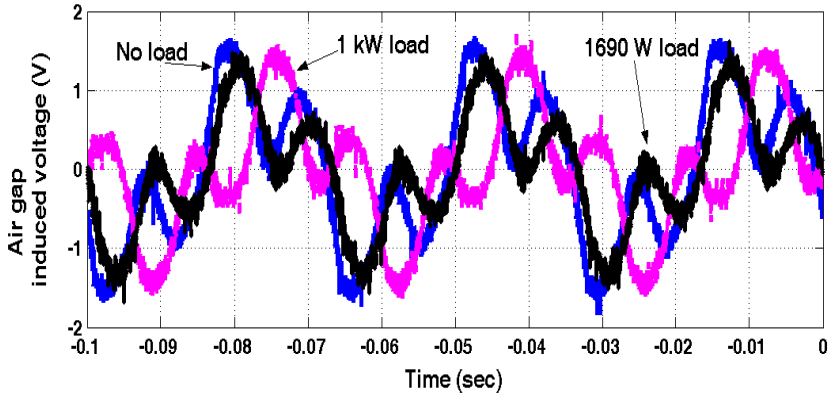


(a)

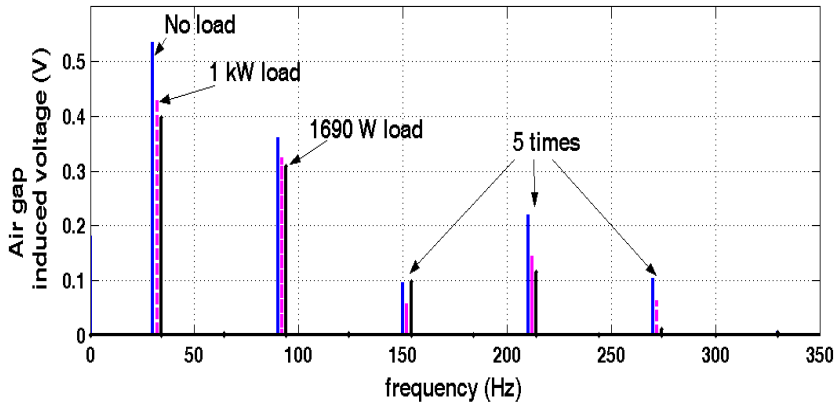


(b)

Figure 6.5: Induced air-gap voltages under load conditions. Winding ABC–phase voltage = 124 V, frequency = 30 Hz, winding XYZ—phase voltage = 124 V, frequency = 90 Hz (a) Voltage waveforms, (b) Fourier series.

In view of these simulation and experimental results, the inter-winding saturation induced voltages are not very significant under load conditions and may be excluded from the dynamic model of the machine with a minimal loss of prediction accuracy. Hence, on the fundamental component basis, the dual-stator winding squirrel-cage machine is considered to be analytically equivalent to two separate single stator winding

induction machines having the same air-gap flux MMF, but electrically and mechanical coupled through the rotor.

## 6.3 The Dynamic Model of the Machine

The voltage equations of dual stator winding induction machine can be expressed in the complex form as [1.10]:

$$V_{qdsi} = r_{si} i_{qdsi} + p\lambda_{qdsi} - j\omega\lambda_{qdsi} \tag{6.4}$$

$$V_{qdri} = r_{ri} i_{qdri} + p\lambda_{qdri} - j(\omega - \omega_{ri})\lambda_{qdri} = 0 \tag{6.5}$$

where, $i = 1, 2$ represents the (classical) parameters and state variables of ABC and XYZ winding set respectively; $\omega$ is the electrical rotating speed of the common reference frame; $\omega_{ri}$ is the electrical rotor speed. Since it is easier to account for the magnetic saturation of the main flux linkage using flux linkages as state variables, the currents in (6.4-6.5) are eliminated. The flux linkage equations given in terms of currents are :

$$\begin{bmatrix} \lambda_{qdsi} \\ \lambda_{qdri} \end{bmatrix} = \begin{bmatrix} L_{si} & L_{mi} \\ L_{mi} & L_{ri} \end{bmatrix} \times \begin{bmatrix} i_{qdsi} \\ i_{qdri} \end{bmatrix} \tag{6.6}$$

The stator and rotor currents from (6.6) can be expressed in terms of the flux linkages as:

$$i_{qdsi} = \frac{L_{ri}}{D_i}\lambda_{qdsi} - \frac{L_{mi}}{D_i}\lambda_{qdri}$$

$$i_{qdri} = \frac{L_{si}}{D_i}\lambda_{qdri} - \frac{L_{mi}}{D_i}\lambda_{qdsi} \tag{6.7}$$

where, $D_i = L_{si}L_{ri} - L_{mi}^2$ .

Substituting (6.7) into (6.4-6.6), the voltage equations become:

$$V_{qdsi} = \frac{r_{si}L_{ri}}{D_i}\lambda_{qdsi} - \frac{r_{si}L_{mi}}{D_i}\lambda_{qdri} + p\lambda_{qdsi} - j\omega\lambda_{qdsi} \tag{6.8}$$

$$0 = \frac{r_{ri}L_{si}}{D_i}\lambda_{qdri} - \frac{r_{ri}L_{mi}}{D_i}\lambda_{qdsi} + p\lambda_{qdri} - j(\omega - \omega_{ri})\lambda_{qdri} \tag{6.9}$$

The developed electromagnetic torque equation for each stator winding can be written in complex variable form as:

$$T_{ei} = \frac{3}{2}\frac{P_i}{2}\mathrm{Im}\left(\lambda_{qdsi}i^*_{qdsi}\right) \tag{6.10}$$

Hence, the total electromagnetic torque of the dual-stator winding induction machine is the sum of the torques due to both stator windings, which is given as:

$$T_e = T_{e1} + T_{e2} = \frac{3}{2}\frac{P_1}{2}\mathrm{Im}\left(\lambda_{qds1}i^*_{qds1}\right) + \frac{3}{2}\frac{P_2}{2}\mathrm{Im}\left(\lambda_{qds2}i^*_{qds2}\right) \tag{6.11}$$

The air gap flux linkage can be expressed as:

$$\lambda_{qdmi} = L_{mi}i_{qdsi} + L_{mi}i_{qdri} \tag{6.12}$$

Substituting (6.7) into (6.12) to eliminate the currents, the air gap flux linkage of each stator winding can be expressed in terms of the stator and rotor flux linkages as:

$$\lambda_{qdmi} = \frac{L_{lri}L_{mi}}{D_i}\lambda_{qdsi} + \frac{L_{lsi}L_{mi}}{D_i}\lambda_{qdri} \tag{6.13}$$

The total unsaturated air gap flux linkage is the sum of the two separate air-gap flux linkages which is expressed as:

$$\lambda_{qdm} = \frac{L_{lr1}L_{m1}}{D_1}\lambda_{qds1} + \frac{L_{ls1}L_{m1}}{D_1}\lambda_{qdr1} + \frac{L_{lr2i}L_{m2}}{D_2}\lambda_{qds2} + \frac{L_{ls2}L_{m2}}{D_2}\lambda_{qdr2} \tag{6.14}$$

If a common reference frame speed is properly chosen so that the total air gap flux linkage is aligned with the d-axis of the reference frame at all times, then the total air gap flux linkage on the q-axis and its derivative will always be zero [6.4]. Hence,

$$\lambda_{qm} = \frac{L_{lr1}L_{m1}}{D_1}\lambda_{qs1} + \frac{L_{ls1}L_{m1}}{D_1}\lambda_{qr1} + \frac{L_{lr2i}L_{m2}}{D_2}\lambda_{qs2} + \frac{L_{ls2}L_{m2}}{D_2}\lambda_{qr2} = 0 \tag{6.15}$$

If the leakage inductances are all assumed to be constant, the time derivative of the total air gap flux linkage on the q-axis is:

$$p\lambda_{qm} = \frac{L_{lr1}L_{m1}}{D_1}p\lambda_{qs1} + \frac{L_{ls1}L_{m1}}{D_1}p\lambda_{qr1} + \frac{L_{lr2i}L_{m2}}{D_2}p\lambda_{qs2} + \frac{L_{ls2}L_{m2}}{D_2}p\lambda_{qr2} = 0 \tag{6.16}$$

Substituting (6.8-6.9) into (6.16) to eliminate the derivative terms, then

$$\begin{aligned} &A_{r1}V_{qs1} - B_{rr1}\lambda_{qs1} + B_{rm1}\lambda_{qr1} - A_{r1}\omega\lambda_{ds1} - B_{ss1}\lambda_{qr1} + B_{sm1}\lambda_{qs1} \\ &- A_{s1}(\omega - \omega_{r1})\lambda_{dr1} + A_{r2}V_{qs2} - B_{rr2}\lambda_{qs2} + B_{rm2}\lambda_{qr2} - A_{r2}\omega\lambda_{ds2} \\ &- B_{ss2}\lambda_{qr2} + B_{sm2}\lambda_{qs2} - A_{s2}(\omega - \omega_{r2})\lambda_{dr2} = 0 \end{aligned} \tag{6.17}$$

where, $A_{ri} = \frac{L_{lri}L_{mi}}{D_i}$, $A_{si} = \frac{L_{lsi}L_{mi}}{D_i}$, $B_{rri} = A_{ri}\frac{r_{si}L_{ri}}{D_i}$, $B_{rmi} = A_{ri}\frac{r_{si}L_{mi}}{D_i}$, $B_{ssi} = A_{si}\frac{r_{si}L_{si}}{D_i}$,

$B_{smi} = A_{si}\frac{r_{si}L_{mi}}{D_i}$, $i = 1, 2$.

The electrical speed of common reference frame from (6.17) is given as:

$$\omega = \frac{\begin{aligned} &A_{r1}V_{qs1} - B_{rr1}\lambda_{qs1} + B_{rm1}\lambda_{qr1} - B_{ss1}\lambda_{qr1} + B_{sm1}\lambda_{qs1} + A_{s1}\omega_{r1}\lambda_{dr1} + \\ &A_{r2}V_{qs2} - B_{rr2}\lambda_{qs2} + B_{rm2}\lambda_{qr2} - B_{ss2}\lambda_{qr2} + B_{sm2}\lambda_{qs2} + A_{s2}\omega_{r2}\lambda_{dr2} \end{aligned}}{A_{r1}\lambda_{ds1} + A_{s1}\lambda_{dr1} + A_{r2}\lambda_{ds2} + A_{s2}\lambda_{dr2}} \tag{6.18}$$

Then substituting (6.15) into (6.18) to eliminate $\lambda_{qr2}$, the desired electrical speed of the common reference frame is obtained. By aligning the total air gap flux linkage to d-axis, the q-axis magnetizing inductances of the two sets of winding are constant at the unsaturated values. Then the total air gap flux linkage then becomes (6.19):

$$\lambda_m = \frac{L_{lr1}L_{m1}}{D_1}\lambda_{ds1} + \frac{L_{ls1}L_{m1}}{D_1}\lambda_{dr1} + \frac{L_{lr2i}L_{m2}}{D_2}\lambda_{ds2} + \frac{L_{ls2}L_{m2}}{D_2}\lambda_{dr2} \tag{6.19}$$

No load tests were conducted on an experimental 2 hp machine to determine the magnetizing inductances. The other parameters which are considered constant are determined using well-known methods of short circuit and dc tests. For the no-load test and the machine running at close to the synchronous speed, the phase voltage of the 2-pole winding set was varied while the 6-pole winding set was opened. In the second run, the 2-pole winding set was opened while the phase voltage of the 6-pole winding set was varied from zero to the rated value. Finally, the phase voltage of the 2-pole winding set was fixed at three values and for each fixed value, the phase voltage of the 6-pole winding set was varied from zero to the rated voltage. Similar experiments were conducted for three fixed values of the phase voltage of the 6-pole winding set.

The magnetizing inductances of the 2hp dual-stator winding induction machine are shown in Figure 6.6 for the various tests. Polynomials expressing the magnetizing inductances as a function of the unsaturated total air-gap flux linkage are determined. As shown in Figure 6.6, they closely follow the experimental data. In the presented computer simulations, the calculated total air-gap flux linkage is used with the polynomial equations to determine the correct d-axis magnetizing inductances as the two q-axis magnetizing inductances are held constant at the unsaturated no-load values.

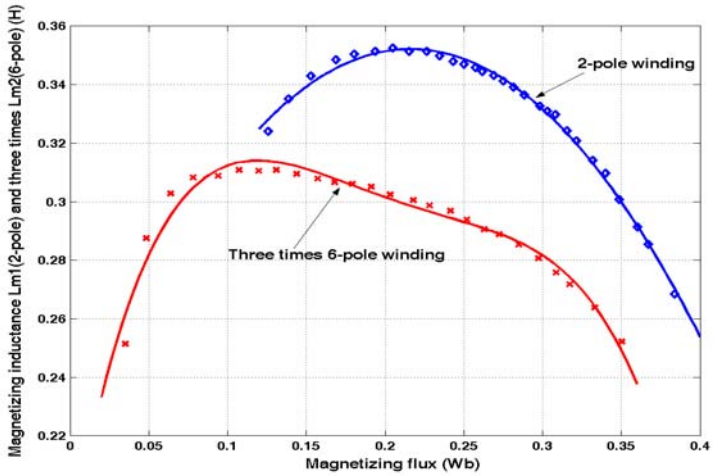


(a)

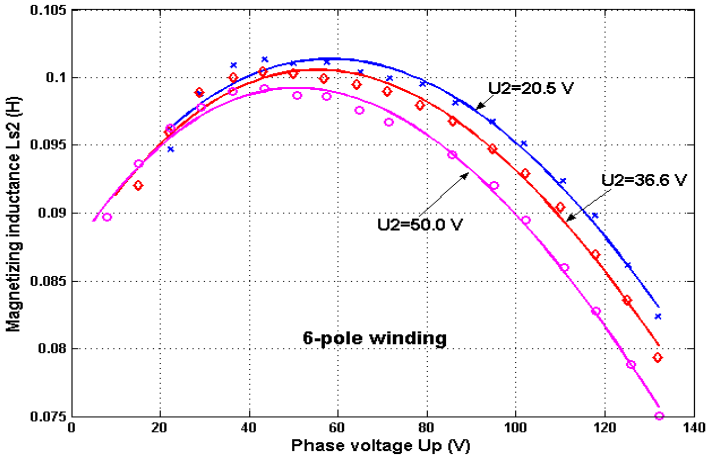


(b)

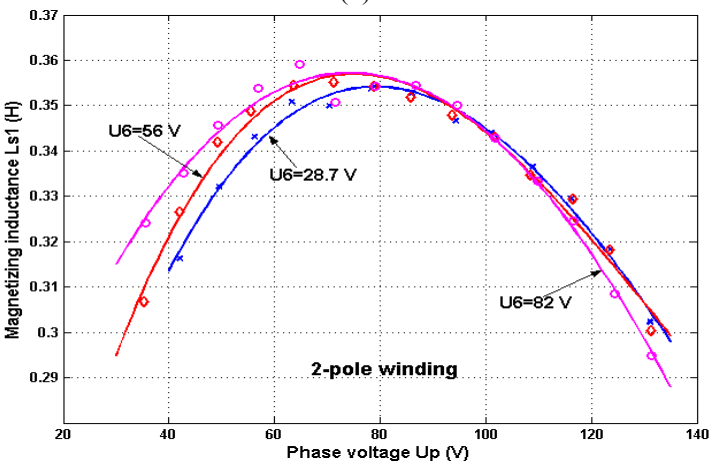


(c)

Figure 6.6: The magnetizing inductances of a 2hp, 2/6 dual-stator winding induction machine (a) From no-load test, (b) three fixed 2-pole winding voltages and variable phase voltages of 6-pole windings, (c) Three fixed phase voltages of the 6-pole windings and variable phase voltage of the 2-pole windings.

## 6.4 Simulation and Experimental Results

The impact of the main flux saturation on the transient and dynamic performance of the machine was investigated through the computer simulation of the machine using the air-gap flux linkage alignment methodology set forth in Section 6.3. The constant machine parameters are given in Table 6.1 and the values of the mutual inductances depend on the flux level. These can be calculated using the curves given in Figure 6.6. Figure 6.7 presents the simulation results of the free acceleration starting process of the saturated machine. The line-to-line voltages and its frequencies supplied to ABC winding set are 65V and 30 Hz, respectively, while the corresponding line-line voltages and frequency supplied to the XYZ winding set are 195V and 90 Hz respectively. Some comparative experimental results obtained under the same input voltage conditions are given in Figure 6.9 and are very similar to the simulation results. The dynamic responses of the machine to changes in load are shown in Figure 6.8. When the rotor speed is constant and in steady-state, the load torque is changed from 0 Nm to 5.5 Nm to show the effect of the main air-gap flux linkage saturation on the machine performance. The flux linkage on the q-axis is very small while the air gap flux linkage is aligned with the d-axis. The variations of the magnetizing inductances of two stator winding sets are shown in Figure 6.7 (g-h) and Figure 6.8 (g-h). Figure 6.10 illustrates experimentally the dynamics due to a load change, which also compares favorably with the computer simulations result when the saturation effect is accounted for.

Table 6.1 Experimental machine parameters

| | ABC winding | XYZ winding |
|---|---|---|
| Number of pole | 2 | 6 |
| Stator resistance | $r_{s1} = 3.4\,\Omega$ | $r_{s2} = 1.9\,\Omega$ |
| Leakage inductance | $L_{ls1} = 0.006\ H\ 6$ | $L_{ls2} = 0.009\ H$ |
| Rotor resistance | $r_{r1} = 0.61\,\Omega$ | $r_{r2} = 0.55\,\Omega$ |

The detailed waveforms of the d- and q-axis air gap magnetizing flux linkage, the common reference frame speed and the magnetizing inductances of both stator winding sets under no load steady-state operating condition are shown in Figure 6.11. The total magnetizing flux linkage and the reference frame speed are not constant evidently because of the absence of a common synchronous reference frame.

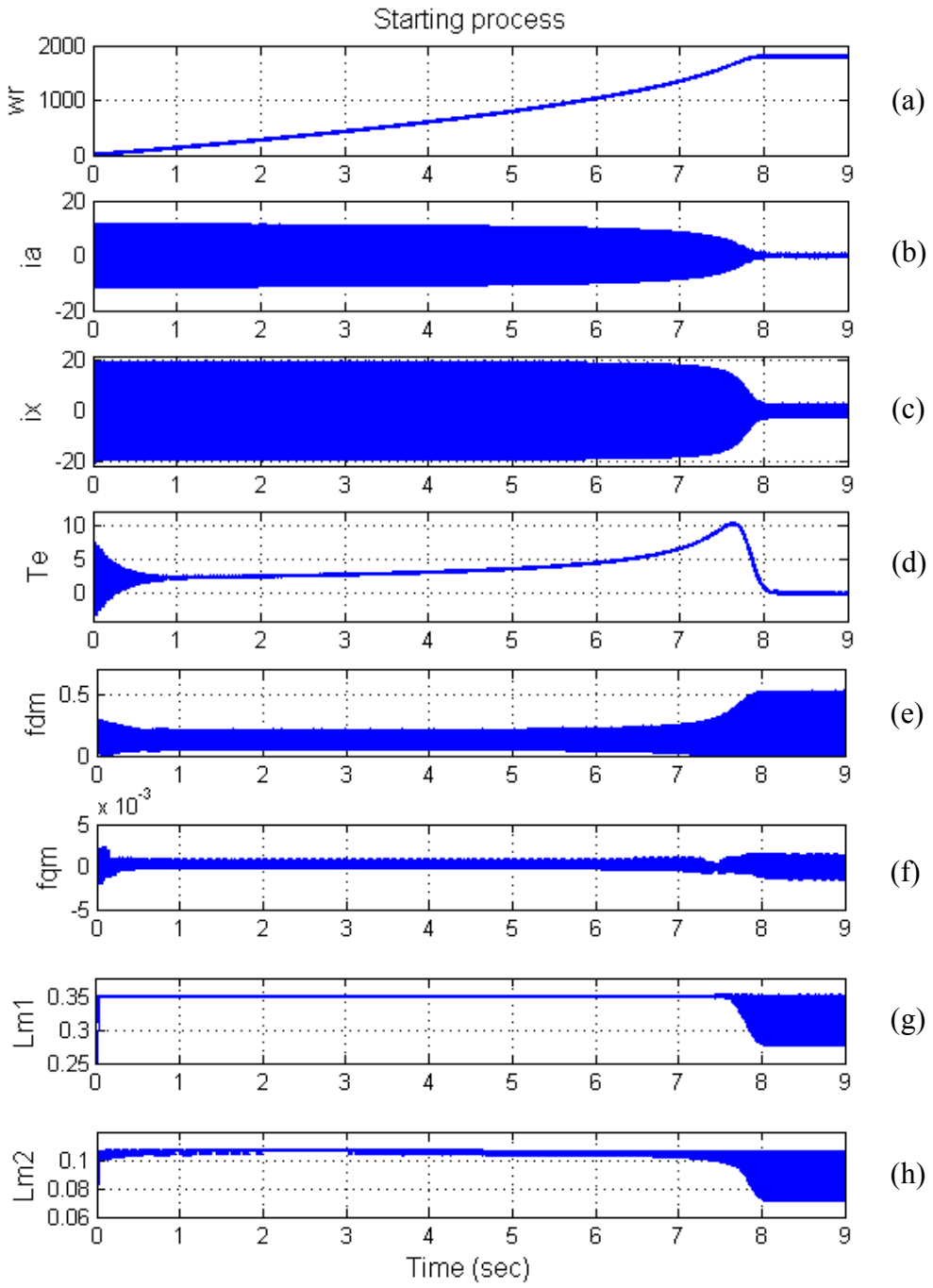


Figure 6.7 . Simulation results for starting process, from top: (a) rotor speed; (b) Phase 'A' current, (c) phase 'X' current, (d) electromagnetic torque, (e) d-axis magnetizing flux linkage, (f) q-axis magnetizing flux linkage, (g) magnetizing inductance for the ABC winding set, (h) magnetizing inductance for the XYZ winding set.

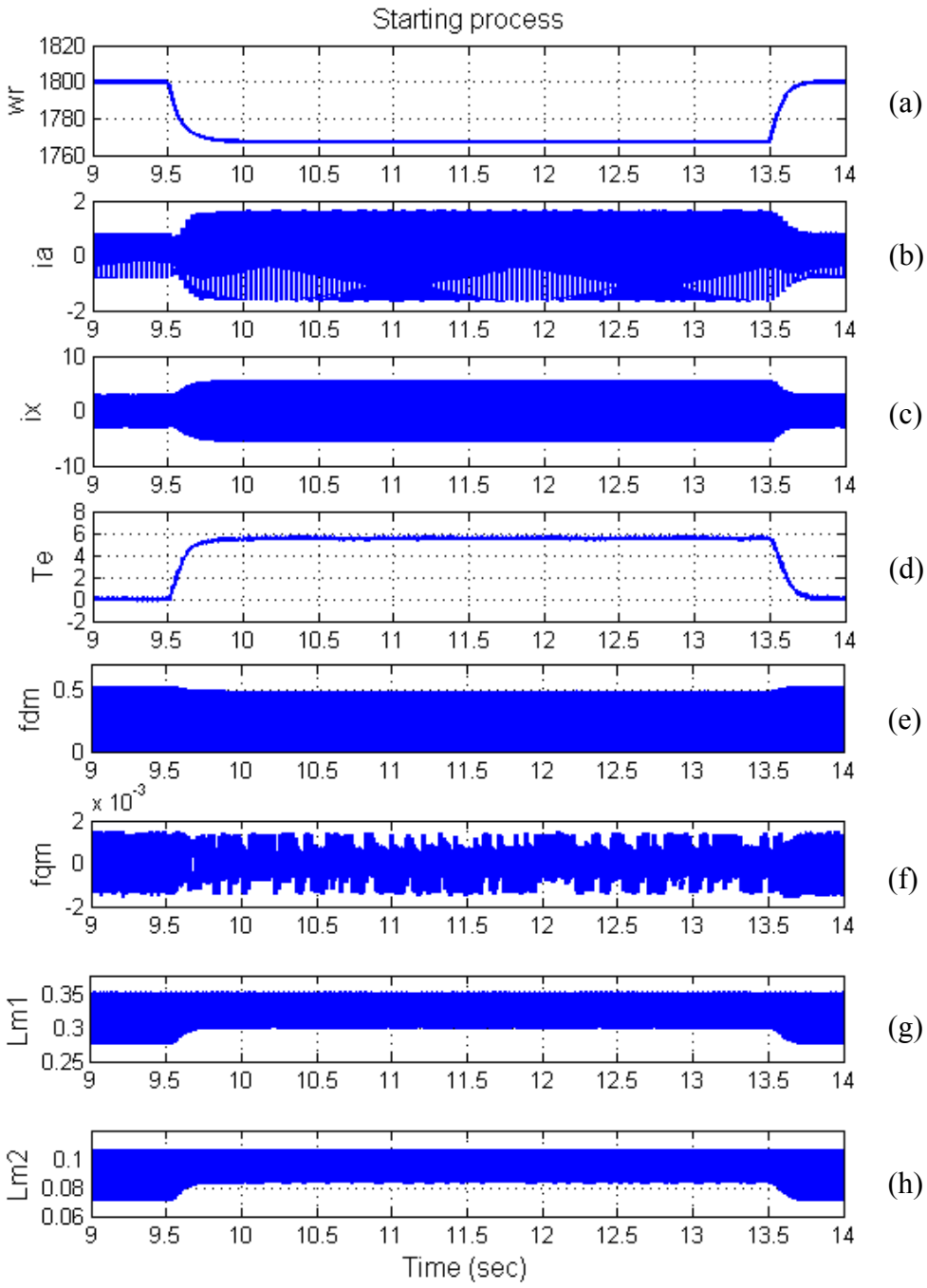


Figure 6.8. The dynamic response of changing load, from top: (a) rotor speed; (b) Phase 'A' current, (c) phase 'X' current, (d) electromagnetic torque, (e) d-axis magnetizing flux linkage, (f) q-axis magnetizing flux linkage, (g) magnetizing inductance for the ABC winding set, (h) magnetizing inductance for the XYZ winding set.

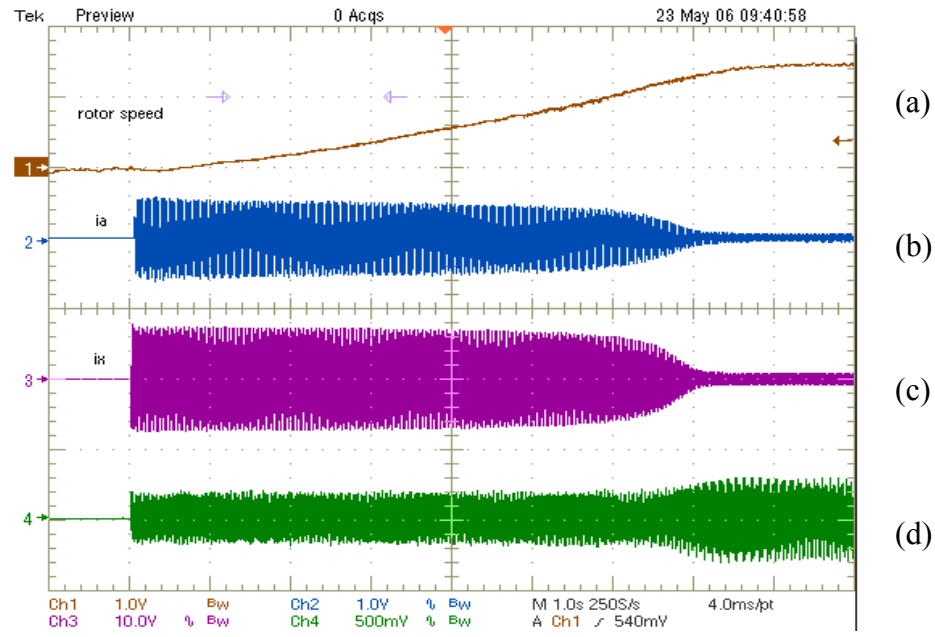


Figure 6.9 Experimental results for free acceleration process, from top: (a) rotor speed (1245 rpm/div), (b) phase A current (5.5 A/div), (c) phase X current (14.2 A/div), (d) induced voltage in 2-pole searching coil (0.5 V/div).

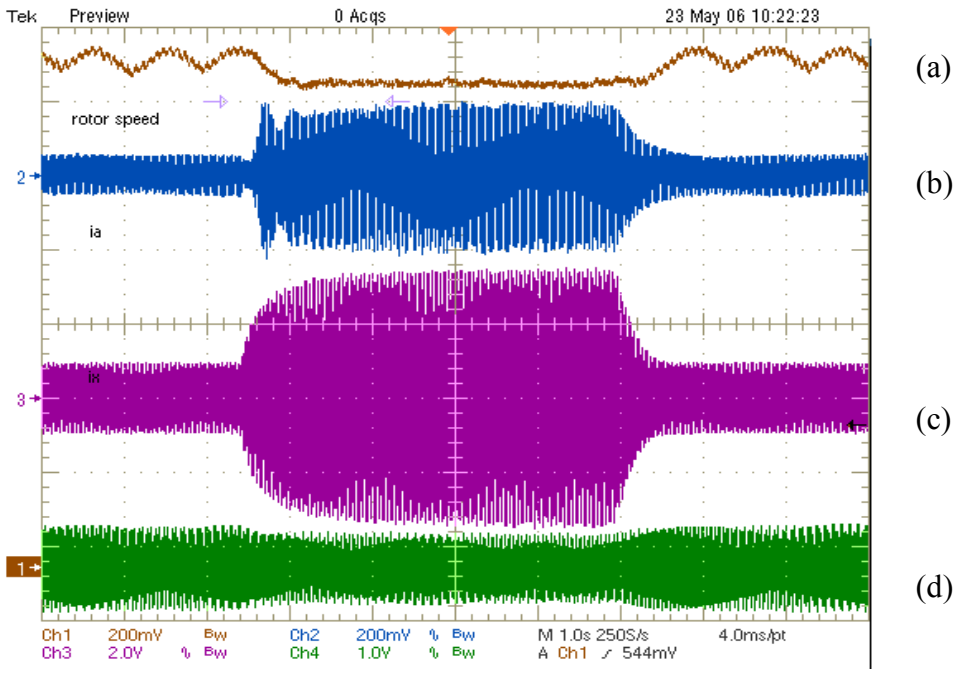


Figure 6.10 Experimental results for dynamic response, from top: (a) rotor speed, (b) phase A current (2.55 A/div), (c) phase X current (4.5 A/div), (d) induced voltage in 2-pole searching coil (0.5 V/div).

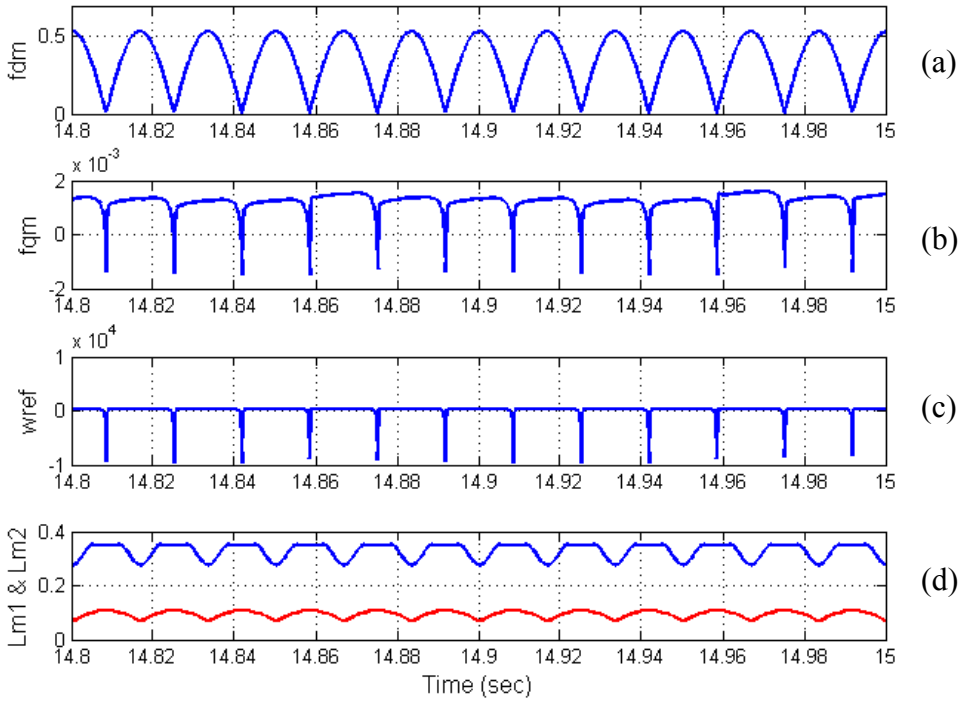


Figure 6.11 Simulation results under steady-state no load condition, from top: (a) d-axis magnetizing flux linkage, (b) q-axis magnetizing flux linkage, (c) common reference frame speed, (d) magnetizing inductances for two stator winding sets.

## 6.5 Conclusions

A study of the influence of magnetic circuit saturation on the main air-gap flux density comprising of flux density components having different pole numbers is set forth in which the consequences of the phase angle between the flux density components are explored. For the 2/6 pole dual-stator winding machine, the two pole winding set induces a voltage on the 6-pole winding set when the air-gap flux density saturates due to saturating rotor and stator teeth. The various air-gap space harmonics generated due to magnetic saturation for the 2/6 winding sets include prominent $5^{th}$, $7^{th}$ and $9^{th}$ components. There is an inter-winding induced flux linkage which may reinforce or

diminish the contribution of the 6-pole winding set to the effective air-gap flux density. This study indicates that an understanding of the nature and magnitudes of space harmonics in addition to the fundamental components rather than the peak values alone or generalized average values of the two dominant flux densities is important in the selection of the specific magnetic loading of the machine [6.5].

The dynamic model of a dual stator winding induction machine including the air gap main flux linkage saturation effect is also presented in this chapter. It is argued that in the light of experimental and simulation results, the inter-winding induced flux linkages can be ignored with little loss of prediction accuracy for the fundamental component state variables. A common reference frame speed is determined and chosen for computer simulations to ensure that the instantaneous total air gap flux linkage due to the contributions of the two windings of dissimilar pole numbers is aligned with the d-axis of the reference frame. Thus the main air-gap flux linkage saturation is included in the machine model by varying the saturation dependent d-axis magnetizing inductances and setting the constant q-axis magnetizing inductances to be equal to the unsaturated values. The resulting model is used to illustrate the differences in transient and dynamic performance measures with and without the inclusion of the saturation of the stator and rotor teeth reflected in the air-gap flux density. Experimental results for a 2hp, 2/6 machine validate the proposed simulation model.

The modeling methodology adopted in this chapter for the understanding and computer simulation of the influence of saturation effects on the effective air-gap flux density arising from the interactions of flux linkages due to windings of dissimilar pole numbers and fed with voltages of different frequencies should find utility in the analysis

of other electric machines in the same family such as the brushless doubly-fed induction machines with nested rotor circuitry, the doubly-fed synchronous reluctance machines and the general class of mixed pole windings machinery [6.5-6.7].

# CHAPTER 7

# STEADY STATE ANALYSIS OF A DUAL WINDING INDUCTION MACHINE

## 7.1 Introduction

In the discussions of previous research on the dual winding machine, it is seen that research has focused on the modeling and high performance control when operating as a motor [1.1]. However, the steady state analysis of the machine, which is important to give some insight into the machine operation, has not been considered thus far. In this chapter, the steady state analysis of dual stator winding induction machine is presented.

## 7.2 System Model

The complex form defines the variables using the 'j' operator that represents the variable as $90^o$ apart in space. The variables of the machine are defined in the complex form as below:

$$V_{qds} = V_{qs} + jV_{ds} \tag{7.1}$$

$$V_{qdr} = V_{qr} + jV_{dr} \tag{7.2}$$

$$\lambda_{qdr} = \lambda_{qr} + j\lambda_{dr} \tag{7.3}$$

$$\lambda_{qds} = \lambda_{qs} + j\lambda_{ds} \tag{7.4}$$

$$i_{qds} = i_{qs} + ji_{ds} \tag{7.5}$$

$$i_{qdr} = i_{qr} + ji_{dr} \tag{7.6}$$

where, $j$ is the complex operator; $V_{qs}$ and $V_{ds}$ are the q- and d-axis stator voltages respectively; $V_{qr}$ and $V_{dr}$ are the q- and d-axis rotor voltages respectively; $\lambda_{qs}$ and $\lambda_{ds}$ are the q- and d-axis stator flux linkages respectively; $\lambda_{qr}$ and $\lambda_{dr}$ are the q- and d-axis rotor flux linkages respectively; $i_{qs}$ and $i_{ds}$ are the q- and d-axis stator currents respectively; $i_{qr}$ and $i_{dr}$ are the q- and d-axis rotor currents respectively.

The steady state voltage equations of the dual stator winding induction machine can then be expressed in the complex variable form as:

$$V_{qdsi} = r_{si} \cdot i_{qdsi} - j\omega_{ei}\lambda_{qdsi} \tag{7.7}$$

$$V_{qdri} = r_{ri} \cdot i_{qdri} - j\omega_{si}\lambda_{qdri} = 0 \tag{7.8}$$

where, $i = 1, 2$ represent the variables of the ABC and XYZ winding sets respectively; $r_{si}$ is the stator resistance; $r_{ri}$ is the rotor resistance; $\omega_{ei}$ is the electric speed, $\omega_{si}$ is the slip, $\omega_{rm}$ is rotor mechanical speed and the slip of two windings can be expressed as $\omega_{s1} = \omega_{e1} - \frac{P_1}{2}\omega_{rm}$, $\omega_{s2} = \omega_{e2} - \frac{P_2}{2}\omega_{rm}$.

If the flux linkage equations in terms of currents are expressed in matrix form as:

$$\begin{bmatrix} \lambda_{qdsi} \\ \lambda_{qdri} \end{bmatrix} = \begin{bmatrix} L_{si} & L_{mi} \\ L_{mi} & L_{ri} \end{bmatrix} \times \begin{bmatrix} i_{qdsi} \\ i_{qdri} \end{bmatrix} \tag{7.9}$$

Then by calculating the inverse of the matrix, the stator and rotor currents can be expressed in terms of the flux linkages as:

$$i_{qdsi} = \frac{L_{ri}}{D_i}\lambda_{qdsi} - \frac{L_{mi}}{D_i}\lambda_{qdri} \tag{7.10}$$

$$i_{qdri} = \frac{L_{si}}{D_i}\lambda_{qdri} - \frac{L_{mi}}{D_i}\lambda_{qdsi} \tag{7.11}$$

where, $D_i = L_{si}L_{ri} - L_{mi}^2$.

Substituting (7.10) and (7.11) into the machine model equations (7.7) and (7.8), the voltage equations can be expressed in terms of the flux linkages as:

$$V_{qdsi} = (C_{si} - j\omega_{ei})\lambda_{qdsi} - A_{si}\lambda_{qdri} \tag{7.12}$$

$$0 = (B_{ri} - j\omega_{si})\lambda_{qdri} - A_{ri}\lambda_{qdsi} \tag{7.13}$$

where, $A_{ri} = \frac{r_{ri}L_{mi}}{D_i}$, $B_{ri} = \frac{r_{ri}L_{si}}{D_i}$, $A_{si} = \frac{r_{si}L_{mi}}{D_i}$, $C_{si} = \frac{r_{si}L_{ri}}{D_i}$

Substituting (7.13) into (7.12) to eliminate the rotor flux linkage, the stator voltage is expressed in term of the stator flux linkage as:

$$V_{qdsi} = \left(C_{si} - j\omega_{ei} - \frac{A_{ri}A_{si}}{B_{ri} - j\omega_{si}}\right)\lambda_{qdsi} \tag{7.14}$$

Then the magnitude of the stator flux linkage can be expressed as:

$$\left|\lambda_{qdsi}\right| = \frac{\left|V_{qdsi}\right|}{\sqrt{\left(C_{si} - \frac{A_{si}A_{ri}B_{ri}}{B_{ri}^2 + \omega_{si}^2}\right)^2 + \left(\omega_{ei} + \frac{A_{si}A_{ri}\omega_{si}}{B_{ri}^2 + \omega_{si}^2}\right)^2}} \tag{7.15}$$

Substituting (7.13) into (7.10) to obtain the relation between the stator current and the stator flux linkage as:

$$i_{qdsi} = \left(\frac{L_{ri}}{D_i} - \frac{L_{mi}}{D_i}\frac{A_{ri}}{B_{ri} - j\omega_{si}}\right)\lambda_{qdsi} \tag{7.16}$$

The electromagnetic torque equation for each stator winding set can be written in complex form as:

$$T_{ei} = \frac{3}{2}\frac{P_i}{2}\mathrm{Im}\left(\lambda_{qdsi} i^*_{qdsi}\right) \tag{7.17}$$

where, * represents complex conjugation of variables.

The total electromagnetic torque of the dual stator winding induction machine is the sum of the torques due to the two stator winding sets, which can be expressed as:

$$T_e = T_{e1} + T_{e2} = \frac{3}{2}\frac{P_1}{2}\mathrm{Im}\left(\lambda_{qds1} i^*_{qds1}\right) + \frac{3}{2}\frac{P_2}{2}\mathrm{Im}\left(\lambda_{qds2} i^*_{qds2}\right) \tag{7.18}$$

Then by substituting (7.15) and (7.16) into (7.18), the torque equation can be expressed in terms of the input voltages, input frequencies and machine parameters as:

$$\begin{aligned} T_e = {} & \frac{3}{2}\frac{P_1}{2}\frac{L_{m1}}{D_1}\frac{A_{r1}\omega_{s1}V_{s1}^2\left(B_{r1}^2+\omega_{s1}^2\right)}{\left(C_{s1}\left(B_{r1}^2+\omega_{s1}^2\right)-A_{s1}A_{r1}B_{r1}\right)^2+\left(\omega_{e1}\left(B_{r1}^2+\omega_{s1}^2\right)+A_{s1}A_{r1}\omega_{s1}\right)^2} \\ & + \frac{3}{2}\frac{P_2}{2}\frac{L_{m2}}{D_2}\frac{A_{r2}\omega_{s2}V_{s2}^2\left(B_{r2}^2+\omega_{s2}^2\right)}{\left(C_{s2}\left(B_{r2}^2+\omega_{s2}^2\right)-A_{s2}A_{r2}B_{r2}\right)^2+\left(\omega_{e2}\left(B_{r2}^2+\omega_{s2}^2\right)+A_{s2}A_{r2}\omega_{s2}\right)^2} \end{aligned} \tag{7.19}$$

If the machine parameters are assumed to be constant at any operating condition and the constant V/Hz control is applied to the machine, the variables in equation (7.19) are electromagnetic torque $T_e$, rotor mechanical speed $\omega_{rm}$, electric speed of the ABC winding set $\omega_{e1}$ and electric speed of the XYZ winding set $\omega_{e2}$. It should be noticed that only three of them are independent, which means that if any three of them are known, the last one is also fixed.

The complex power equation of the machine is given by

$$S_i = \frac{3}{2}\left(V_{qdsi} I^*_{qdsi}\right) \tag{7.20}$$

The power factor of the dual stator induction machine can then be expressed as:

$$Power\ Factor\ (PF) = \frac{\mathrm{Re}\left(S_i\right)}{Abs\left(S_i\right)} \tag{7.21}$$

Overall efficiency of the dual stator induction machine is given by,

$$\eta = \frac{T_e \cdot \omega_{rm}}{\mathrm{Re}(S_1) + \mathrm{Re}(S_2)} \tag{7.22}$$

The copper loss of dual stator winding induction machine is given as:

$$P_{copper} = \frac{3}{2} r_{s1} \left| i_{qds1} \right|^2 + \frac{3}{2} r_{s2} \left| i_{qds2} \right|^2 \tag{7.23}$$

The copper loss equation can also be expressed in terms of the stator voltages as

$$\begin{aligned} P_{copper} = {} & \frac{3}{2} r_{s1} \frac{\left[ \left( \frac{L_{r1}}{D_1} - \frac{L_{m1} A_{r1} B_{r1}}{D_1 \left( B_{r1}^2 + \omega_{s1}^2 \right)} \right)^2 + \left( \frac{L_{m1} A_{r1} \omega_{s1}}{D_1 \left( B_{r1}^2 + \omega_{s1}^2 \right)} \right)^2 \right] V_{s1}^2}{\left( C_{s1} - \frac{A_{s1} A_{r1} B_{r1}}{B_{r1}^2 + \omega_{s1}^2} \right)^2 + \left( \omega_{e1} + \frac{A_{s1} A_{r1} \omega_{s1}}{B_{r1}^2 + \omega_{s1}^2} \right)^2} \\ & + \frac{3}{2} r_{s2} \frac{\left[ \left( \frac{L_{r2}}{D_2} - \frac{L_{m2} A_{r2} B_{r2}}{D_2 \left( B_{r2}^2 + \omega_{s2}^2 \right)} \right)^2 + \left( \frac{L_{m2} A_{r2} \omega_{s2}}{D_2 \left( B_{r2}^2 + \omega_{s2}^2 \right)} \right)^2 \right] V_{s2}^2}{\left( C_{s2} - \frac{A_{s2} A_{r2} B_{r2}}{B_{r2}^2 + \omega_{s2}^2} \right)^2 + \left( \omega_{e2} + \frac{A_{s2} A_{r2} \omega_{s2}}{B_{r2}^2 + \omega_{s2}^2} \right)^2} \end{aligned} \tag{7.24}$$

## 7.3 Steady State Analysis

In the first part of steady state analysis, four typical steady state curves of the dual stator winding induction machine---the output electromagnetic torque vs speed curve, the input stator current vs speed curve, the input power factor vs speed curve and the efficiency vs rotor speed curve, are given. The constant V/Hz control is applied to the machine and the rated V/Hz value of 2.99V/Hz is used in the steady state analysis. Since the pole ratio between the two winding sets of the dual stator winding induction machine is 3, the input frequency ratio is normally kept to be 3 to avoid extreme losses. In the following analysis, different values of the input voltage frequency ratio of the dual stator

winding induction machine are given to show the influences of the frequency ratio. The rated frequency of the ABC winding set is 30 Hz and the corresponding value of the XYZ winding is 90 Hz.

### 7.3.1 $f_{abc} = 30$ Hz and $f_{xyz} = 90$

The steady state curves under this condition are given in Figures 7.1-7.3.

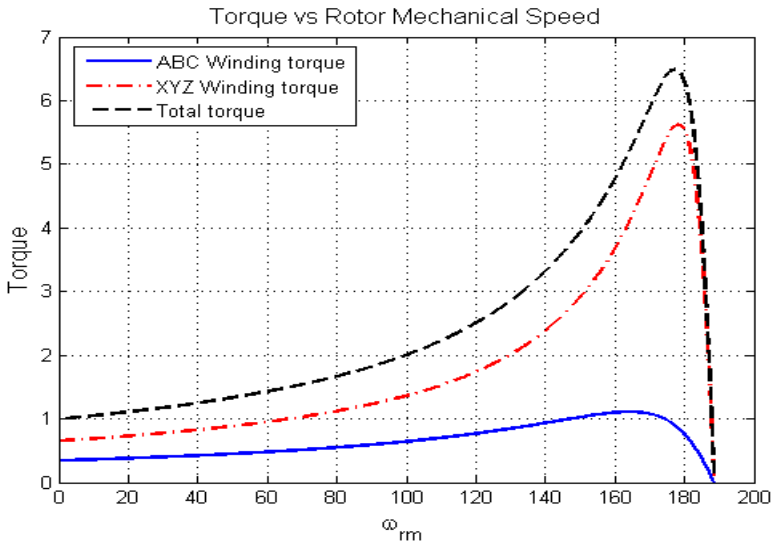


Figure 7.1 Torque speed characteristics when $f_{abc} = 30$ Hz and $f_{xyz} = 90$

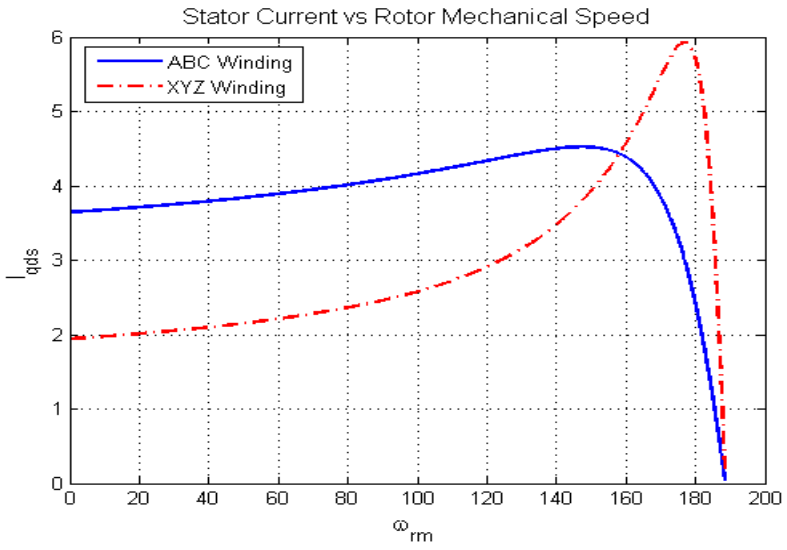


Figure 7.2 Stator current speed characteristics when $f_{abc} = 30$ Hz and $f_{xyz} = 90$

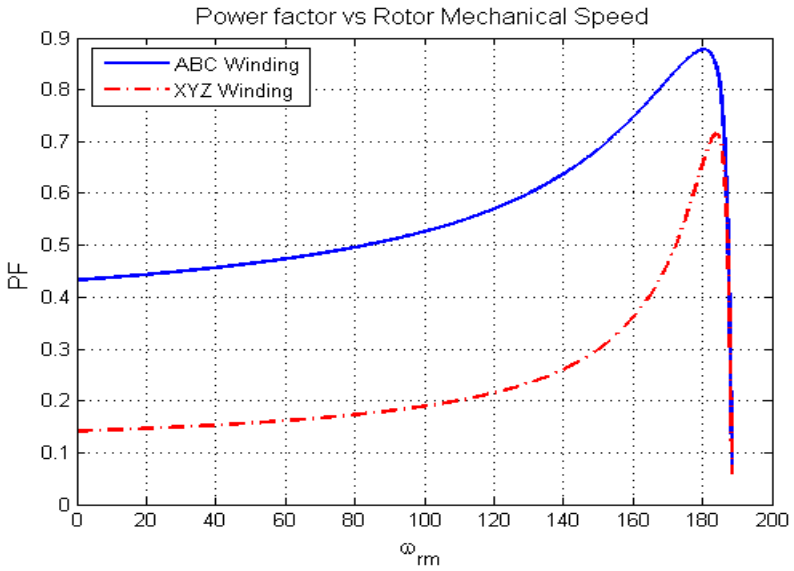


Figure 7.3 Power factor speed characteristics when $f_{abc} = 30$ Hz and $f_{xyz} = 90$

The synchronous speeds of the two winding sets have the same value at this condition. The machine performance is maximized if the two stator winding sets are properly designed such that the peak values of the electromagnetic torque occur at the same rotor mechanical speed.

### 7.3.2 $f_{abc} = 5\,\mathbf{Hz}$ and $f_{xyz} = 15\,\mathbf{Hz}$

The steady state curves are used to study the machine performance at low speed range. The simulation results under this condition are given in Figures 7.4-7.6.

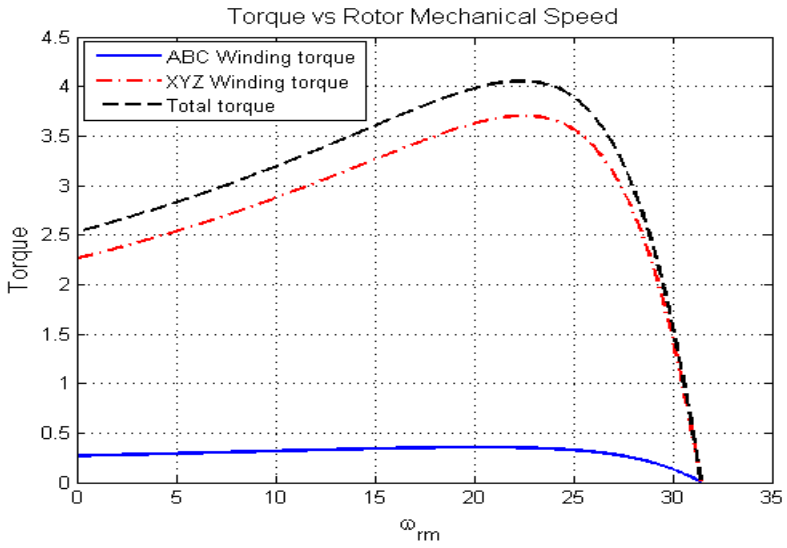


Figure 7.4 Torque speed characteristics when $f_{abc} = 5\,\text{Hz}$ and $f_{xyz} = 15\,\text{Hz}$

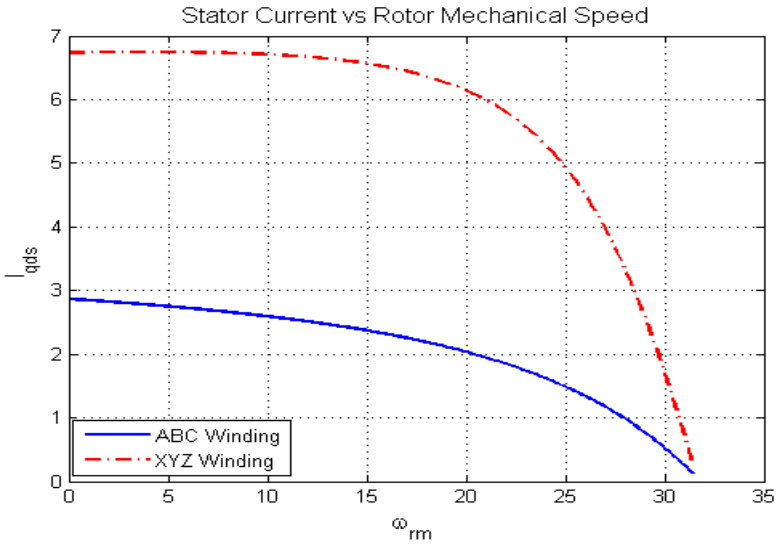


Figure 7.5 Stator current speed characteristics when $f_{abc} = 5\,\text{Hz}$ and $f_{xyz} = 15\,\text{Hz}$

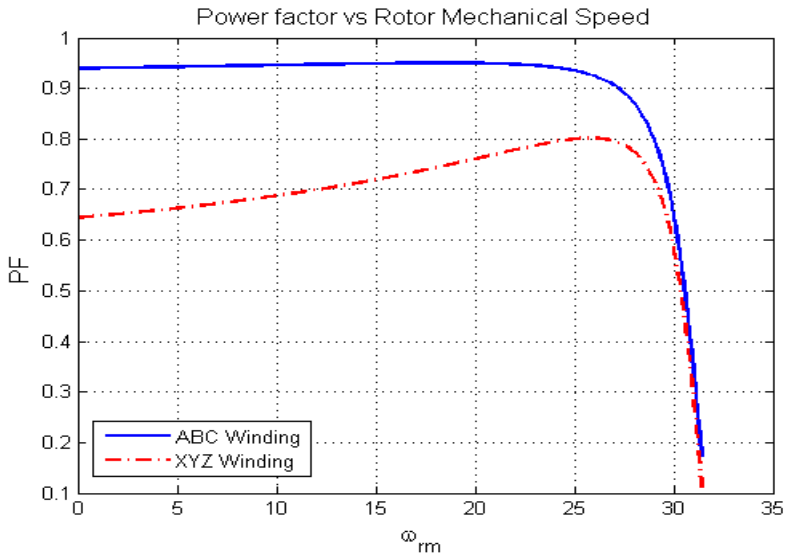


Figure 7.6 Power factor speed characteristics when $f_{abc} = 5\,\text{Hz}$ and $f_{xyz} = 15\,\text{Hz}$

The output torque of the dual winding induction machine is reduced at low speed range. The XYZ winding set carries most of the load torque under the same constant V/Hz condition.

### 7.3.3 $f_{abc} = 25\,$ Hz and $f_{xyz} = 90\,$ Hz

The frequency ratio is greater than 3 while the frequency of the ABC winding set is less than the rated value in this case. The steady state curves under this condition are given in Figures 7.7-7.9. The ABC winding set is generating when the rotor speed is greater than the synchronous speed of the ABC winding set while the XYZ winding set produces positive torque until the rotor speed reaches the synchronous speed of the XYZ winding set. The output torque of the dual stator winding induction machine is the sum of the electromagnetic torques contributed by the two winding sets.

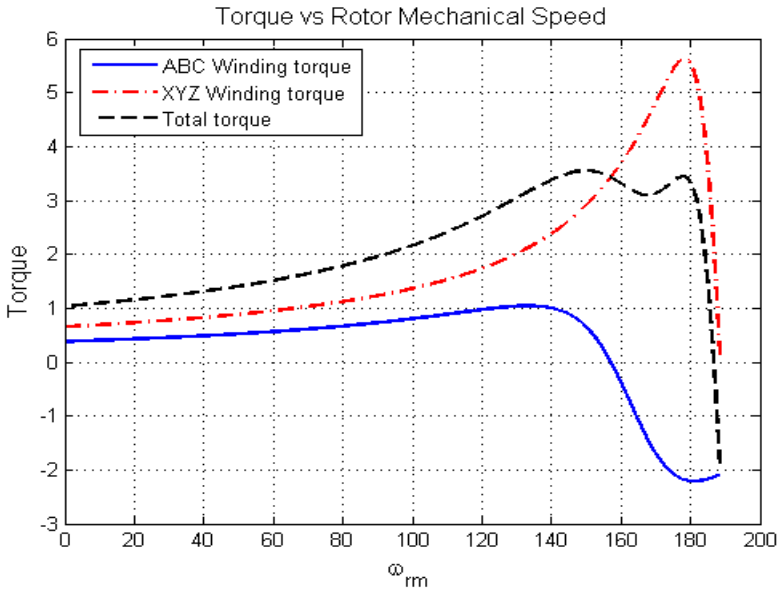


Figure 7.7 Torque speed characteristics when $f_{abc} = 25$ Hz and $f_{xyz} = 90$ Hz

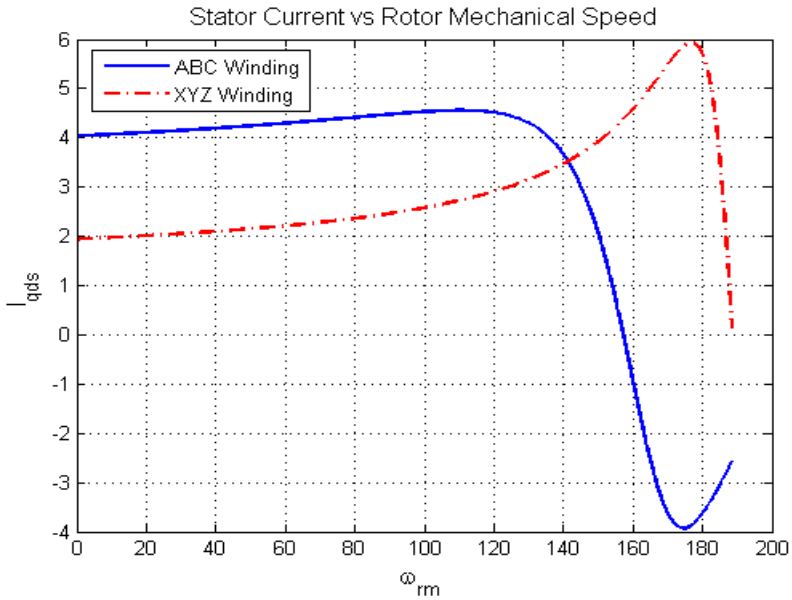


Figure 7.8 Stator current speed characteristics when $f_{abc} = 25$ Hz and $f_{xyz} = 90$ Hz

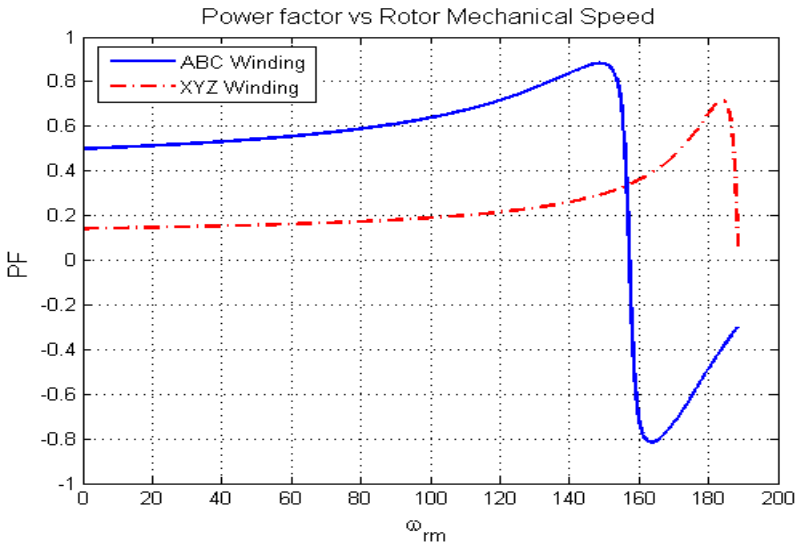


Figure 7.9 Power factor speed characteristics when $f_{abc} = 25$ Hz and $f_{xyz} = 90$ Hz

### 7.3.4 $f_{abc} = 30$ Hz and $f_{xyz} = 95$ Hz

The frequency ratio is greater than 3 while the frequency of the XYZ winding set is greater than the rated value. The steady state curves under this condition are given in Figures 7.10-7.12.

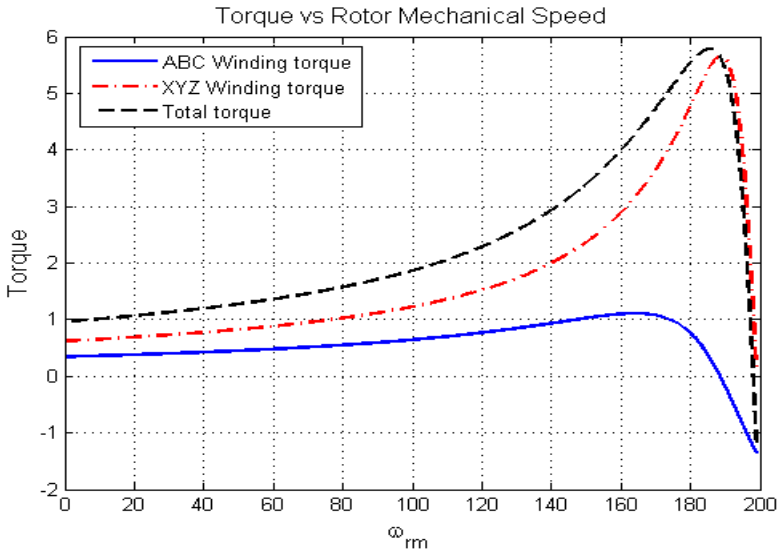


Figure 7.10 Torque speed characteristics when $f_{abc} = 30$ Hz and $f_{xyz} = 95$ Hz

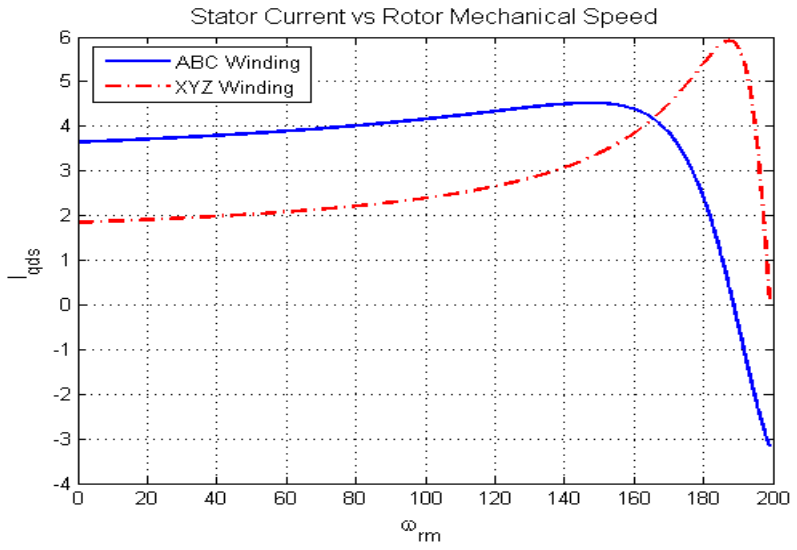


Figure 7.11 Stator current speed characteristics when $f_{abc} = 30\,\text{Hz}$ and $f_{xyz} = 95$ Hz

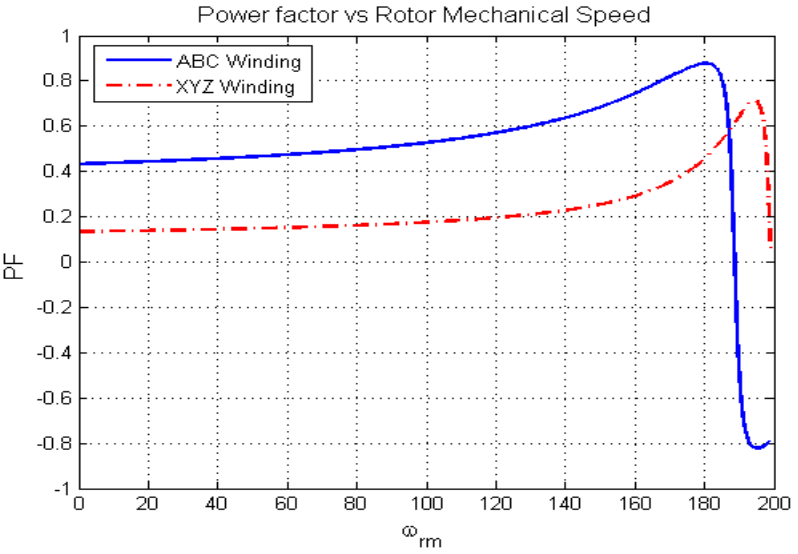


Figure 7.12 Power factor speed characteristics when $f_{abc} = 30\,\text{Hz}$ and $f_{xyz} = 95$ Hz

The simulation results in this case are similar to those in Section 7.3.3 because the frequency ratio of the XYZ and ABC winding sets is greater than 3.

### 7.3.5 $f_{abc} = 35$ Hz and $f_{xyz} = 90$ Hz

Since the frequency of the ABC winding set is greater than the rated value, the frequency ratio in this case is less than 3. The steady state curves under this condition are given in Figures 7.13-7.15.

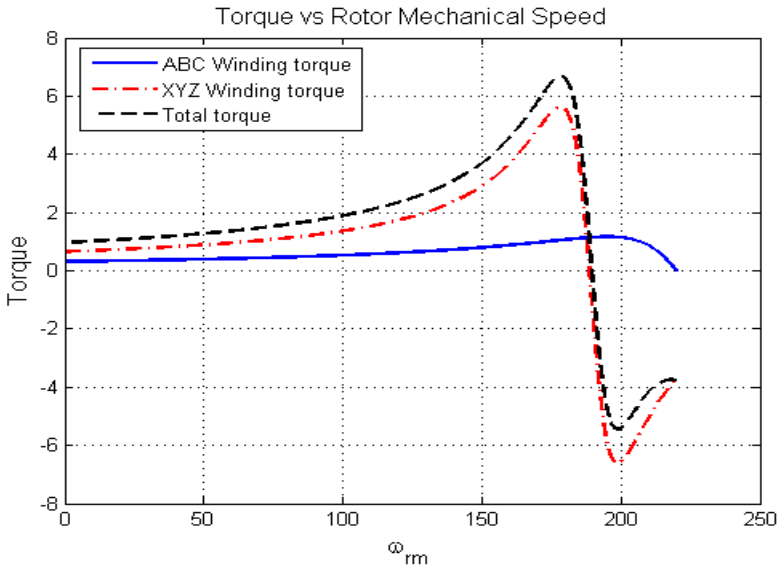


Figure 7.13 Torque speed characteristics when $f_{abc} = 35$ Hz and $f_{xyz} = 90$ Hz

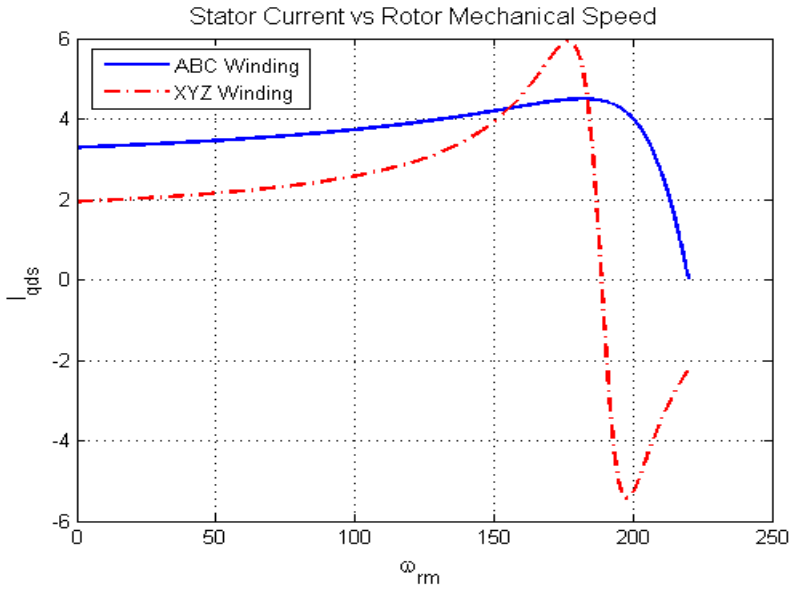


Figure 7.14 Stator current speed characteristics when $f_{abc} = 35$ Hz and $f_{xyz} = 90$ Hz

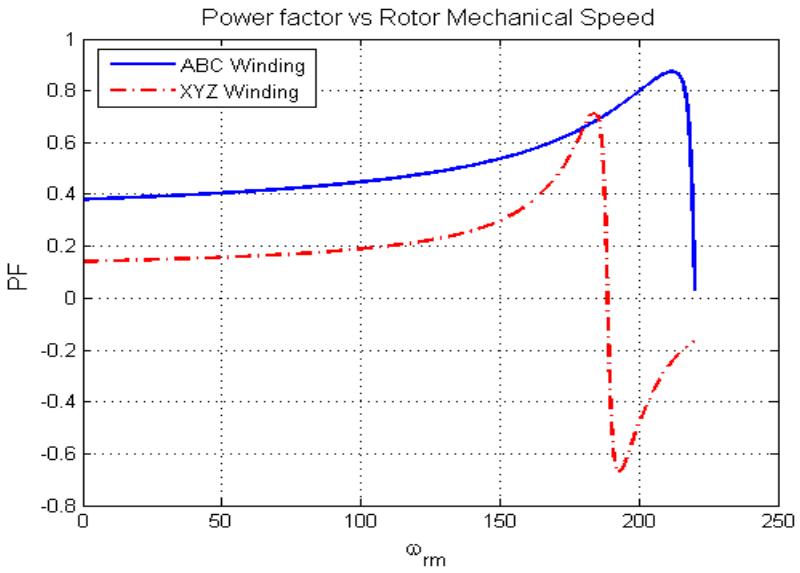


Figure 7.15 Power factor speed characteristics when $f_{abc} = 35$ Hz and $f_{xyz} = 90$ Hz

The XYZ winding set is generating when the rotor speed is greater than the synchronous speed of the XYZ winding set while the ABC winding set produces a positive torque until the rotor speed reaches the synchronous speed of the ABC winding set. The output torque of the dual stator winding induction machine is close to the output torque of the XYZ winding set since the electromagnetic torque contributed by the ABC winding set is relatively small.

### 7.3.6 $f_{abc} = 30$ Hz and $f_{xyz} = 85$ Hz

The frequency ratio is less than 3 while the frequency of the XYZ winding set is less than the rated value in this case. The steady state curves under this condition are given in Figures 7.16-7.18.

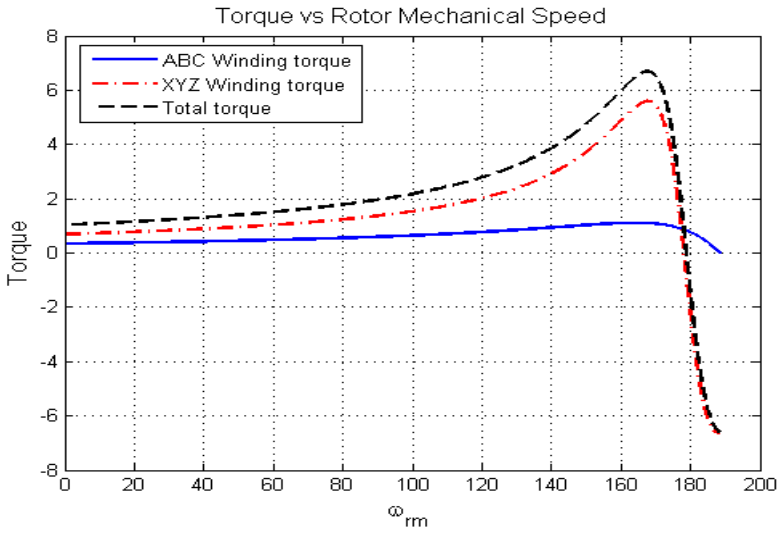


Figure 7.16 Torque speed characteristics when $f_{abc} = 30\,\text{Hz}$ and $f_{xyz} = 85$ Hz

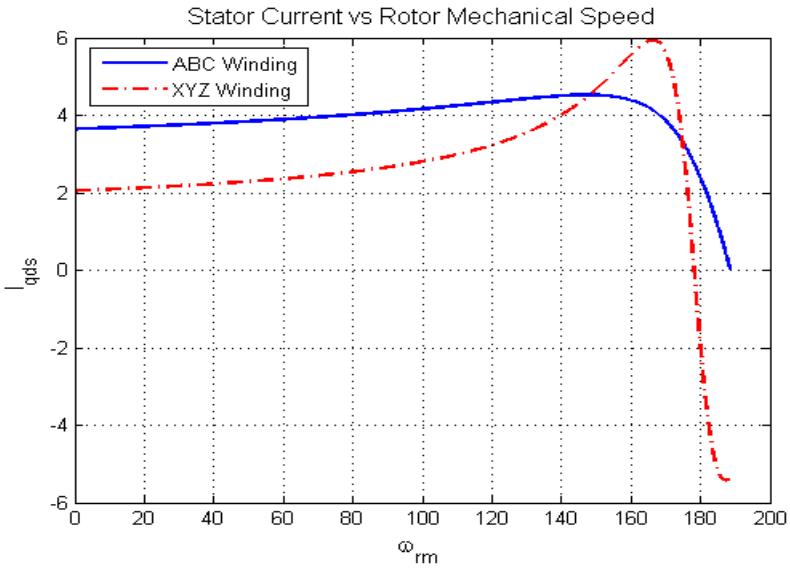


Figure 7.17 Stator current speed characteristics when $f_{abc} = 30\,\text{Hz}$ and $f_{xyz} = 85$ Hz

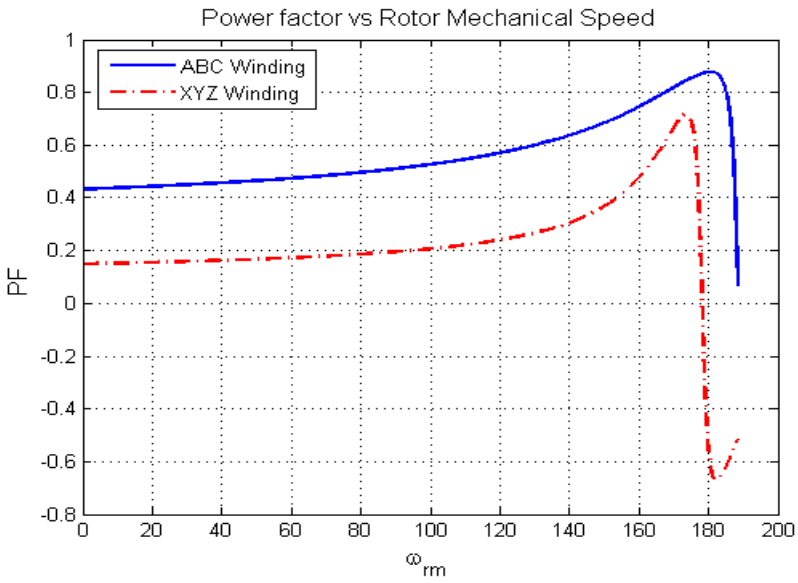


Figure 7.18 Power factor speed characteristics when $f_{abc} = 30\,\text{Hz}$ and $f_{xyz} = 85$ Hz

From the above simulation results, it is found that when the ratio of the input frequencies of the ABC and XYZ winding sets is 3, both winding sets are working in the motoring mode. However, when the frequency ratio is not 3, i.e. frequency synchronous operation, the synchronous speed of the dual stator winding induction machine depends on the two frequencies. The winding set that has input frequency less than the rated value works as a generator before reaching the synchronous speed. The power factor decreases when the rotor speed decreases.

In the second part of the steady state analysis, the relationships between slip frequency, rotor speed and electromagnetic torque are studied. There are four variables in the final torque equation--electromagnetic torque $T_e$, rotor mechanical speed $\omega_{rm}$, electric speed of ABC windings $\omega_{e1}$ and electric speed of XYZ windings $\omega_{e2}$. If any three of them are known, the last one can also be calculated. Different analysis results will be achieved if different conditions are applied. However, it should be noticed that

this conclusion is based on the assumption that the same constant V/Hz coefficients are applied to both winding sets and the machine parameters are all constants during the analysis.

### 7.3.7 Fix $\omega_{e1}$, $\omega_{e2}$ and $\omega_{rm}$, Find Electromagnetic Torque

If the rotor mechanical speed is 180 rad/s and the slip frequency of ABC windings and XYZ windings are varying in [-10 rad/s, 10 rad/s] and [-30 rad/s, 30 rad/s] respectively, the simulation results are given in Figure 7.19 and Figure 7.20.

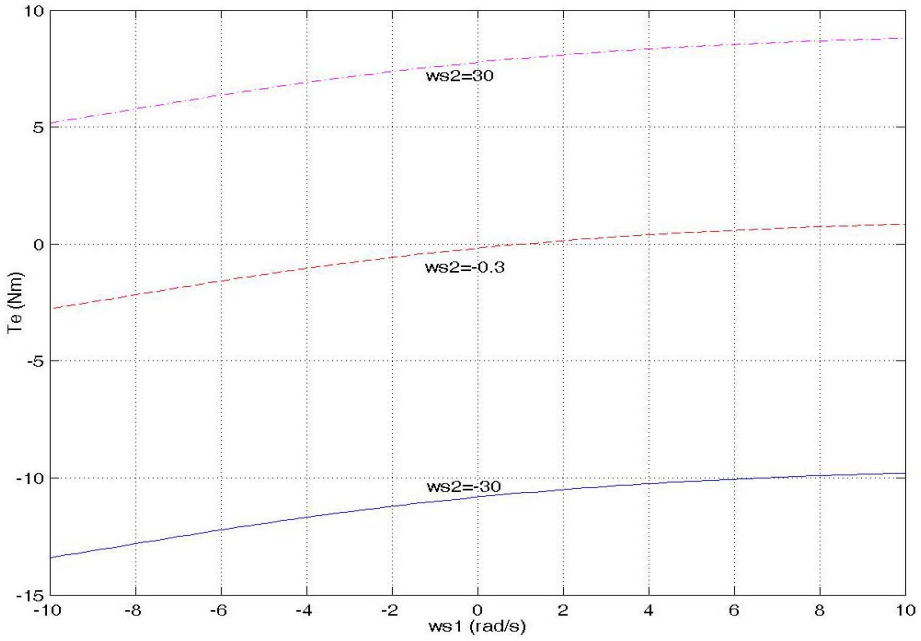


Figure 7.19. Electromagnetic torque of the machine when the slip frequency of the XYZ winding set is a constant value while the slip frequency of the ABC winding set is varied from –10 rad/s to 10 rad/s

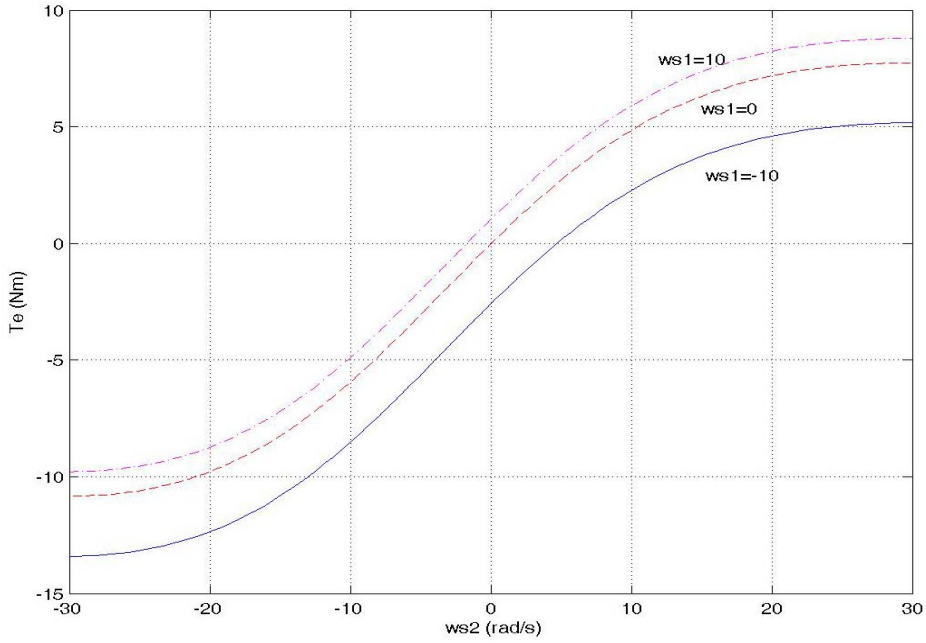


Figure 7.20. Electromagnetic torque of the machine when the slip frequency of the ABC winding set is a constant value while the slip frequency of the XYZ winding set is varied from –30 rad/s to 30 rad/s

The simulation results show that the 6-pole XYZ winding set contributes more torque than the 2-pole ABC winding set. When the V/Hz values of the stator winding sets are not equal, the output electromagnetic torques contributed by each stator winding can be controlled independently.

### 7.3.8 Fix $\omega_{e1}$, $\omega_{rm}$ and $T_e$, Find $\omega_{e2}$

If the output electromagnetic torque is 3 Nm and the rotor speed is kept constant during the analysis while the slip frequency of ABC winding set is varied from -10 rad/s to 10 rad/s, the simulation results are shown in Figure 7.21-7.24. The analysis results for a constant rotor speed at different electromagnetic torque values are given in Figure 7.25 and Figure 7.26.

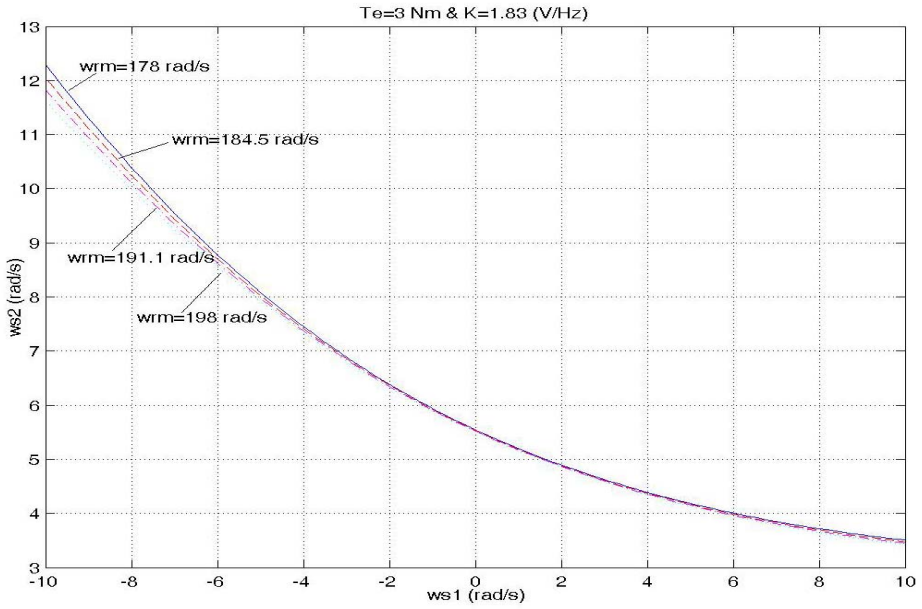


Figure 7.21. $\omega_{s1}$ vs $\omega_{s2}$ when total electromagnetic torque is constant but different rotor mechanical speeds.

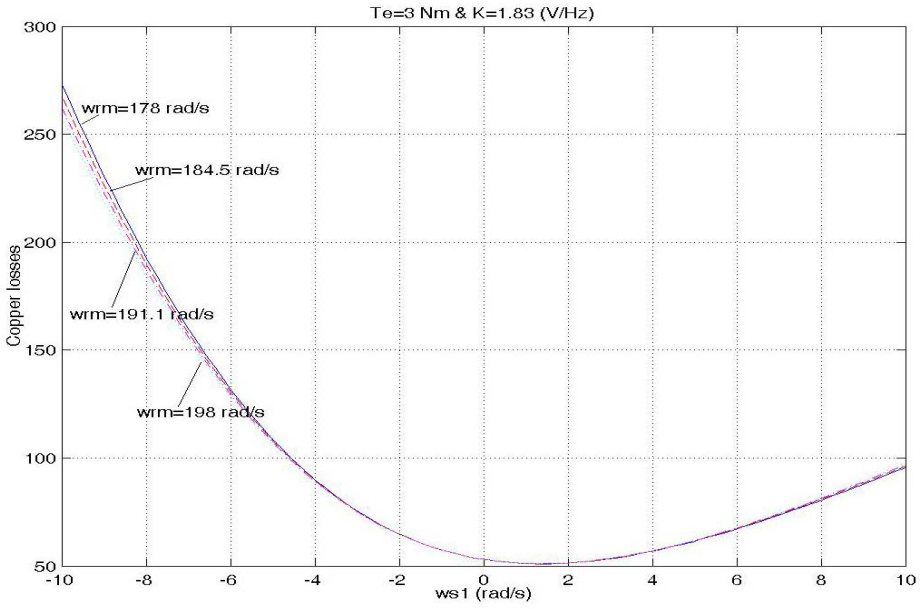


Figure 7.22. Copper losses of the machine when the total electromagnetic torque is a constant and different rotor mechanical speeds are given while the slip of ABC winding set $\omega_{s1}$ is varied from –10 rad/s to 10 rad/s.

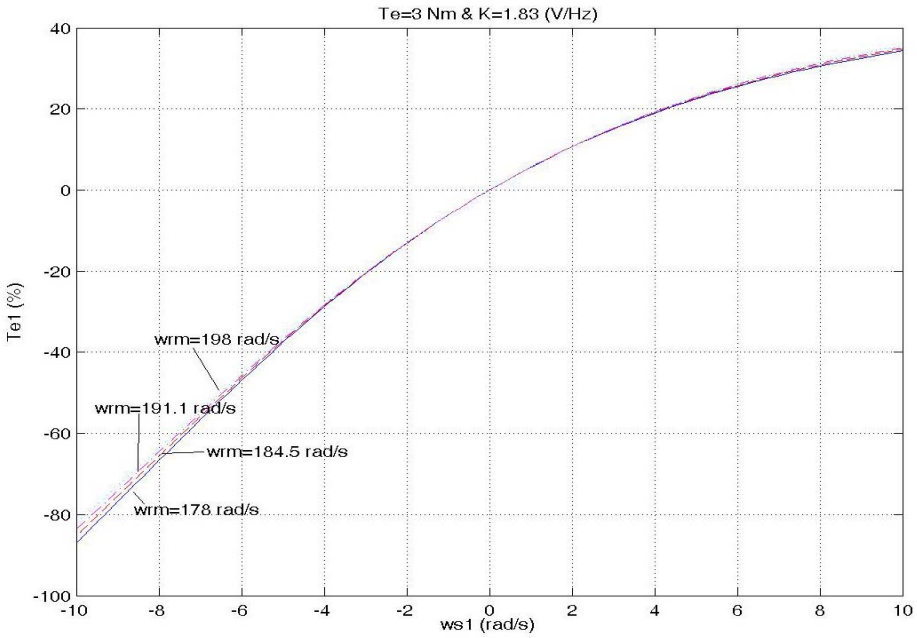


Figure 7.23. The percentage of the torque from the ABC winding set when total electromagnetic torque and rotor mechanical speed are constant while the slip frequency of the ABC winding set $\omega_{s1}$ is varied from –10 rad/s to 10 rad/s.

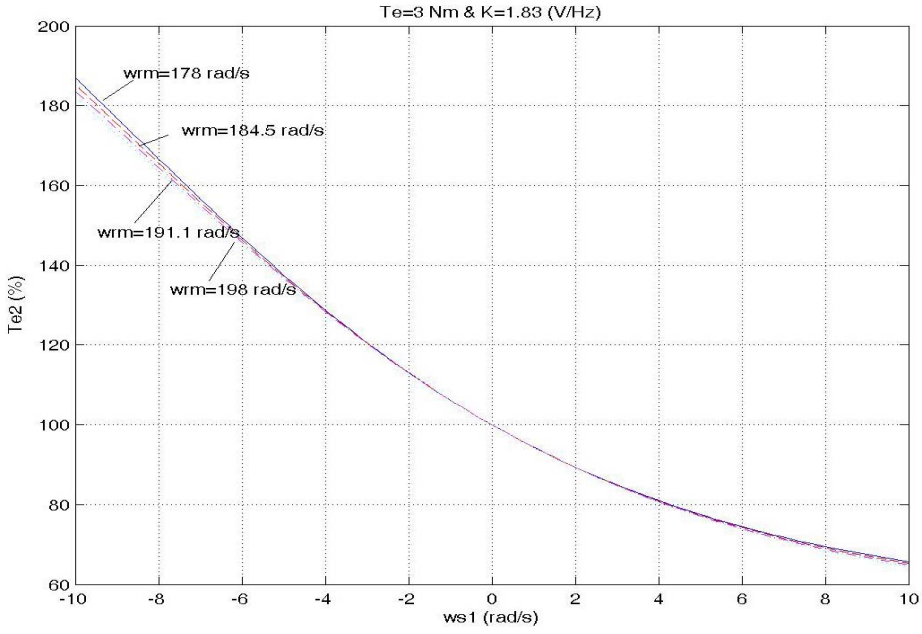


Figure 7.24. The percentage of the torque from the XYZ winding set when total electromagnetic torque and rotor mechanical speed are constant while the slip frequency of the ABC winding set $\omega_{s1}$ is varied from –10 rad/s to 10 rad/s.

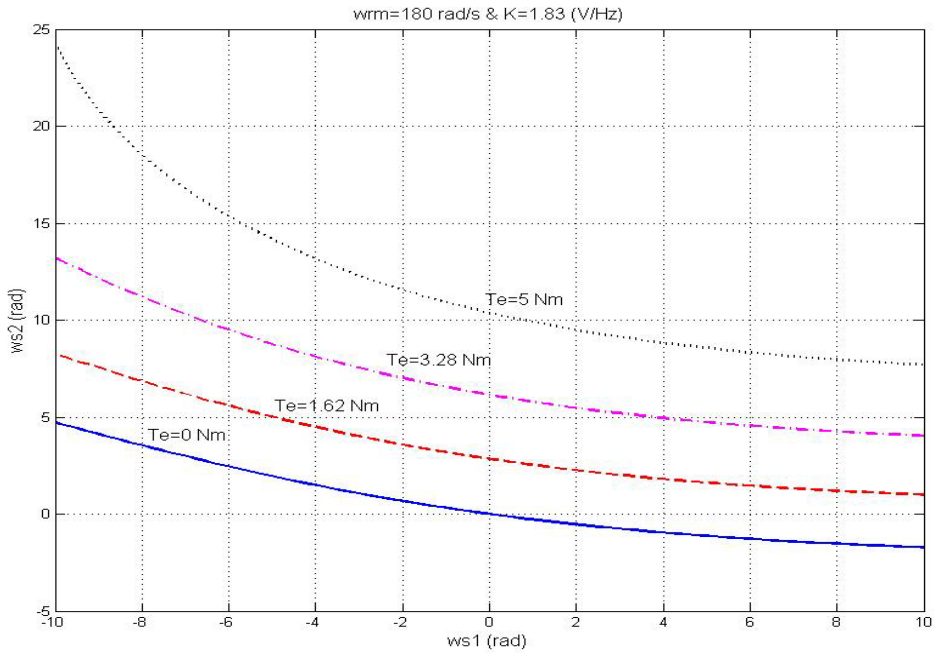


Figure 7.25 $\omega_{s1}$ vs $\omega_{s2}$ when the rotor mechanical speeds are constant and variable total electromagnetic torque values

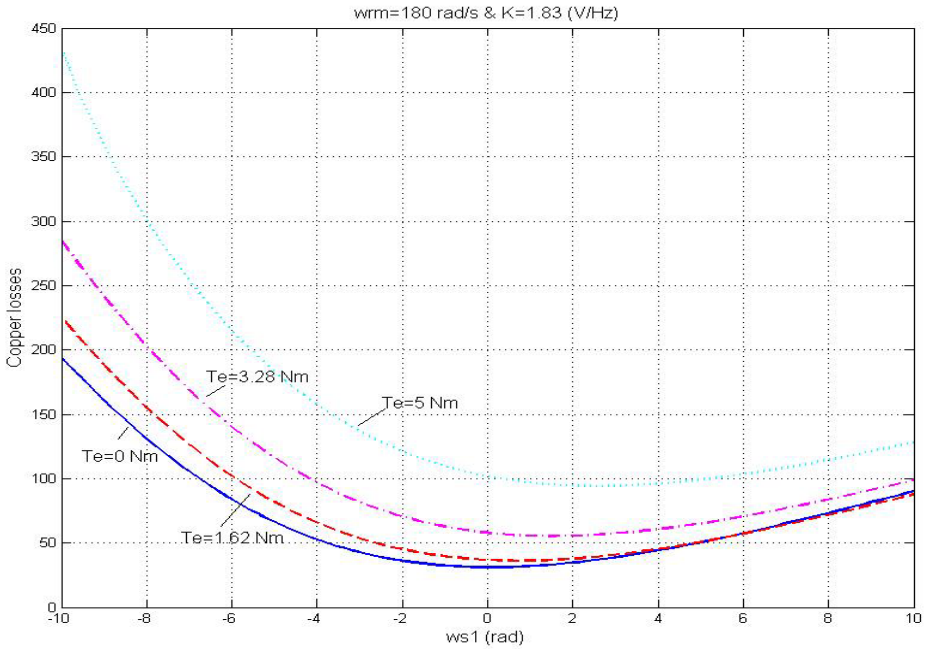


Figure 7.26 Copper losses of the machine when the rotor mechanical speed is constant and variable total electromagnetic torque values

The relationships between the two slip frequencies under different constant rotor mechanical speeds are shown clearly in Figure 7.21. It should be noticed that the slip

frequency of the XYZ winding set is always positive under this condition. From Figure 7.22, it is obvious that under constant output mechanical power condition a minimum copper loss operating point can be found. It is found that the optimal slip frequencies of the ABC winding set under different rotor speed conditions are very close to each other. The electromagnetic torque contributions of the ABC and XYZ winding sets are shown in Figure 7.23 and Figure 7.24 respectively. The comparison of slip frequencies under different total electromagnetic torque values for one constant rotor speed is given in Figure 7.25. The corresponding copper losses of the machine are compared as shown in Figure 7.26.

Since better controllability in the very low speed range is one of the advantages of this type of machine, the rotor speed of dual stator winding induction machine is forced in this speed range to analyze the machine performance under this operating condition. The simulation results are shown in Figure 7.27-7.30.

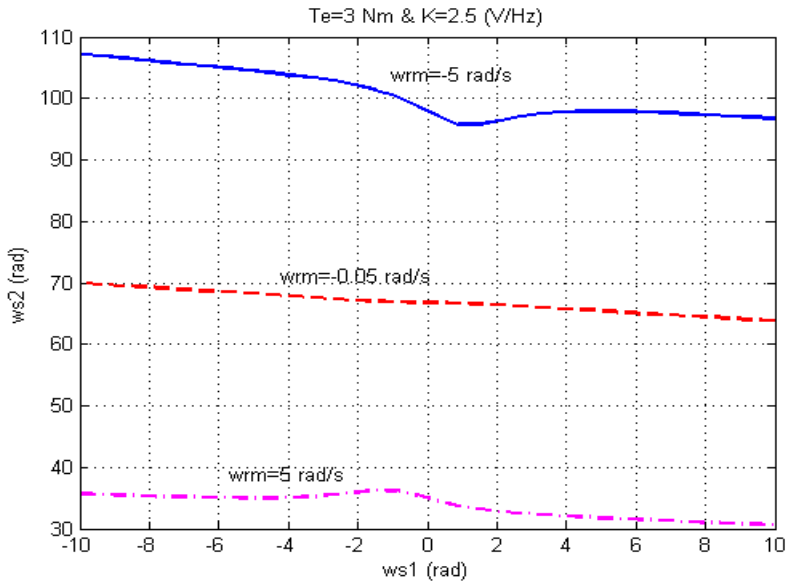


Figure 7.27. $\omega_{s1}$ vs $\omega_{s2}$ when the total electromagnetic torque and the rotor mechanical speed are constant.

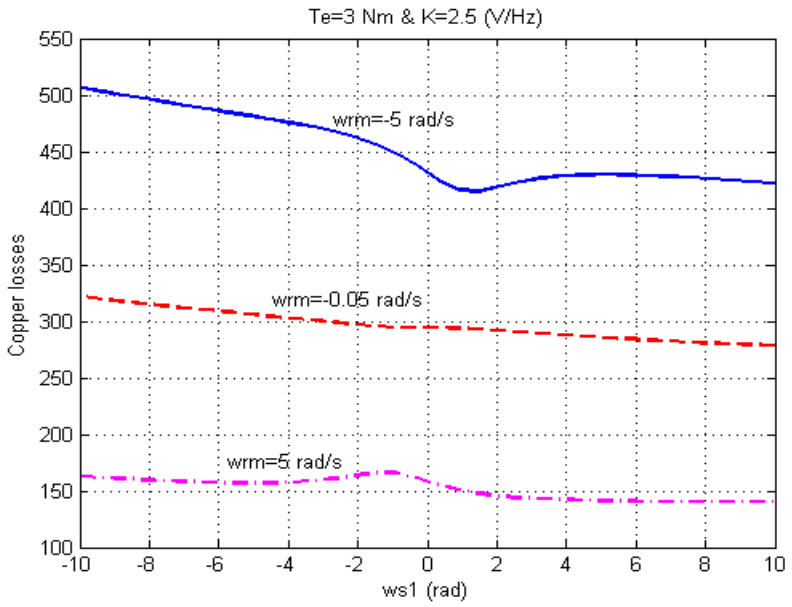


Figure 7.28. Copper losses of the machine when the total electromagnetic torque and the rotor mechanical speed are constant while the slip frequency of the ABC winding set $\omega_{s1}$ is varied from –10 rad/s to 10 rad/s.

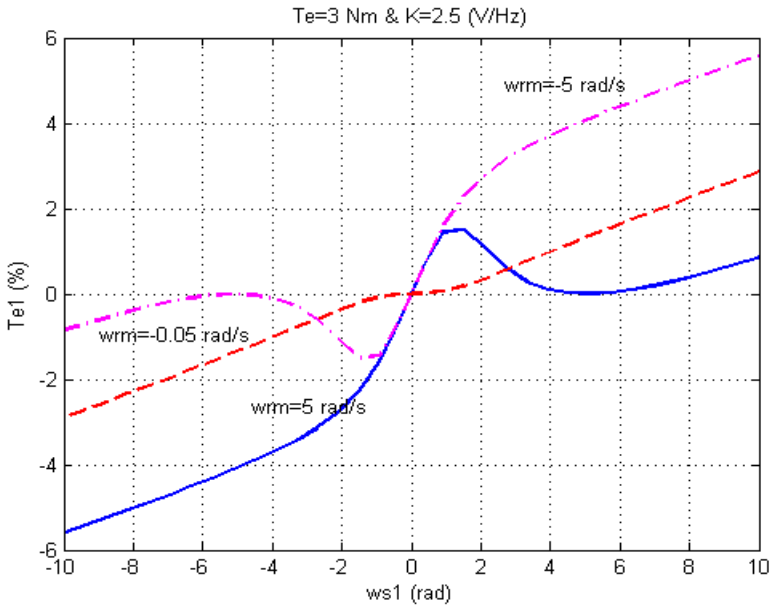


Figure 7.29. The percentage of the torque from the ABC winding set when the total electromagnetic torque and the rotor mechanical speed are constant while the slip frequency of the ABC winding set $\omega_{s1}$ is varied from –10 rad/s to 10 rad/s.

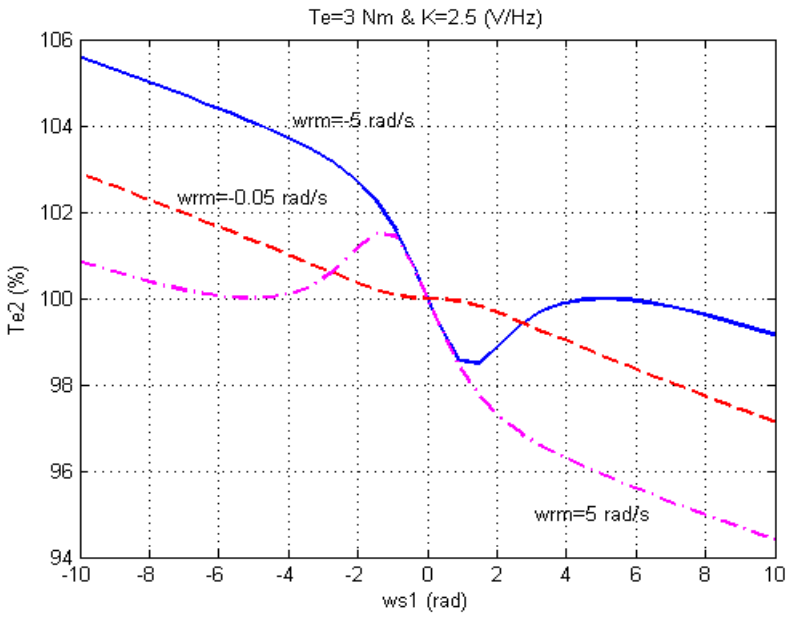


Figure 7.30. The percentage of the torque from the XYZ winding set when the total electromagnetic torque and the rotor mechanical speed are constant while the slip frequency of the ABC winding set $\omega_{s1}$ is varied from –10 rad/s to 10 rad/s.

In the low speed range, the relationship between two slip frequencies under different constant rotor mechanical speeds is shown in Figure 7.27. Similar to what it is found in Figure 7.21, the slip frequency of the XYZ winding set is always positive while the ABC winding set moves from generating condition to motor condition. In the low speed range, a minimum copper loss operating point can be found under a constant output mechanical power condition to greatly reduce the loss of the machine. The electromagnetic torque contributions of the ABC and XYZ winding set in the low speed range are shown in Figure 7.29 and Figure 7.30 respectively.

## 7.4 Conclusions

Based on the steady state machine model in the complex variable form, the steady state analysis of the dual stator winding induction machine to explore the operability regimes of the machine under constant V/Hz control scheme has been presented in this chapter. The relationship between the slip frequencies of two stator winding sets and the power contributions from each winding set have been clearly shown by the simulation results. The operating conditions for minimizing copper loss have also been determined.

# CHAPTER 8

# HIGH PERFORMACE CONTROL OF A DUAL STATOR WINDING DC POWER INDUCTION GENERATOR WITH PARALLEL CONNECTED PWM RECTIFIERS

## 8.1 Introduction

Dual-winding machines of various types are being considered for various motor and generating applications. Although the use of dual-winding machines is not new and has been investigated for a long time, the emergence of new motor topologies, the changing technical and economic context for motor drive applications and the improvement in analytical and electric drive control methodologies have given new impetus to the exploration of new applications for the machine.

The dual stator winding induction machine working as a generator is an area that has not been considered, however because of some common characteristics between the dual stator winding and the normal single winding induction machines, some of the analytic methods used for the normal induction machine can be adopted to the analysis of this new machine. Some previous works on induction generators have been described in Chapter 1.

The motivation behind the research effort leading to this chapter is to explore the advantages of using a single machine to efficiently and cheaply generate ac powers of different frequencies; obtain different dc voltage levels as may be required in automotive

applications and possible use as starter/alternator in four-wheel drive vehicles. In applications where only one dc output is required, the voltages of the two stator windings are processed with two ac-dc PWM boost rectifiers and connected in parallel to increase output current or to improve the system reliability. This is the subject of this chapter. However, two PWM rectifiers can also be series-connected to increase the output dc voltage or in applications where two or three different dc voltage levels are required. Generating system with series-connected PWM rectifiers will be discussed in the next chapter. The efficiency of this machine is not as high as that of the permanent magnet generator, however the opportunity to share the output power between two separate winding sets can improve overall efficiency, giving it a unique advantage. The system diagrams for both the parallel and series connections are shown in Figure 8.1.

This chapter explores the generating mode of operation of this new machine in the process of which the phenomenon of the steady-state converter excitation is explored. With the aid of the input-output linearization technique which enables the linearization and decoupling of the model equations in the synchronous reference frame, the control scheme for the dc voltage regulation with the potential of minimizing the total copper loss is set forth. Computer simulation results and experimental waveforms are presented to demonstrate the effectiveness of the control scheme as also the influence of the dynamic distribution of the input mechanical power between the two stator winding sets.

## 8.2 System Model

The dual stator winding induction generation system for parallel connected output ac-dc PWM rectifiers is shown in Figure 8.1.

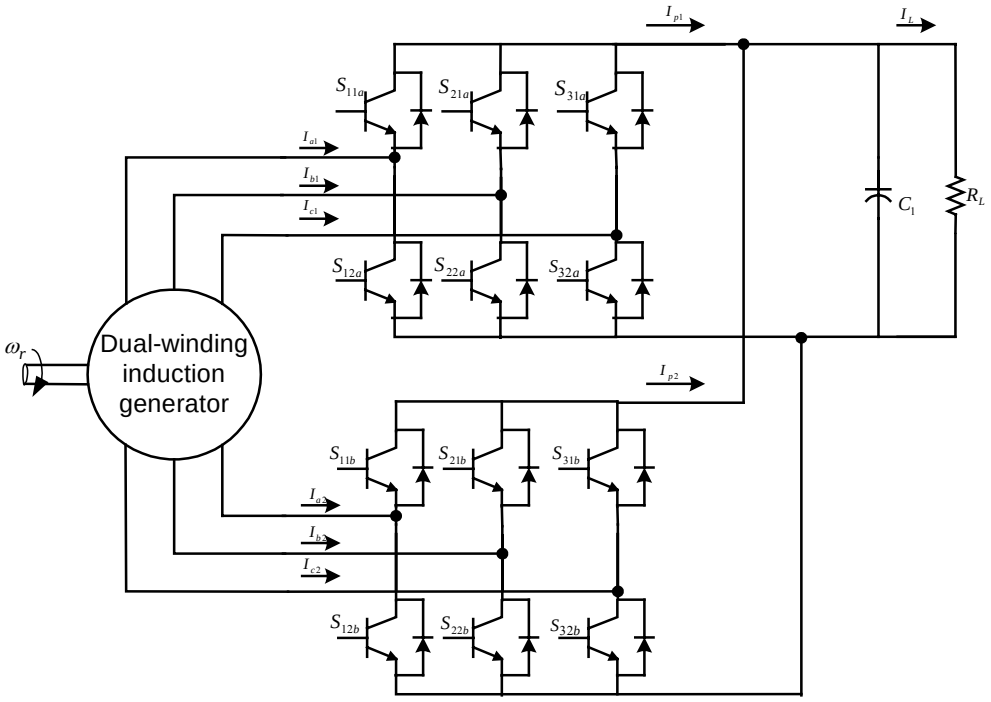


Figure 8.1. The dual winding induction generating system with parallel connected PWM rectifiers

For the parallel connection, only one load is added across the dc output. The qd0 voltage equations of a dual stator winding induction generator feeding two ac-dc boost PWM rectifiers expressed in the synchronous reference frame are given in (8.1-8.9). Since the state variables used in this analysis are q and d-axis stator currents and rotor flux linkages, the model equations (8.1-8.9) are obtained from the known model of the induction machine through state variable transformation. The subscripts 1 and 2 correspond to the parameters or state variables for $P_1$-pole winding and $P_2$-pole winding, respectively:

$$L_{\sigma 1} pI_{qs1} + r_1 I_{qs1} = V_{qs1} - \omega_{e1} L_{\sigma 1} I_{ds1} + \frac{r_{r1} L_{m1}}{L_{r1}^2} \lambda_{qr1} - \omega_{r1} \frac{L_{m1}}{L_{r1}} \lambda_{dr1} = \sigma_{qs1} \tag{8.1}$$

$$L_{\sigma 1} pI_{ds1} + r_1 I_{ds1} = V_{ds1} + \omega_{e1} L_{\sigma 1} I_{qs1} + \frac{r_{r1} L_{m1}}{L_{r1}^2} \lambda_{dr1} + \omega_{r1} \frac{L_{m1}}{L_{r1}} \lambda_{qr1} = \sigma_{ds1} \tag{8.2}$$

$$p\lambda_{qr1}+\frac{r_{r1}}{L_{r1}}\lambda_{qr1}=\frac{r_{r1}L_{m1}}{L_{r1}}I_{qs1}-(\omega_{e1}-\omega_{r1})\lambda_{dr1}=\sigma_{qr1} \tag{8.3}$$

$$p\lambda_{dr1}+\frac{r_{r1}}{L_{r1}}\lambda_{dr1}=\frac{r_{r1}L_{m1}}{L_{r1}}I_{ds1}+(\omega_{e1}-\omega_{r1})\lambda_{qr1}=\sigma_{dr1} \tag{8.4}$$

$$L_{\sigma 2}pI_{qs2}+r_2I_{qs2}=V_{qs2}-\omega_{e2}L_{\sigma 2}I_{ds2}+\frac{r_{r2}L_{m2}}{L_{r2}^2}\lambda_{qr2}-\omega_{r2}\frac{L_{m2}}{L_{r2}}\lambda_{dr2}=\sigma_{qs2} \tag{8.5}$$

$$L_{\sigma 2}pI_{ds2}+r_2I_{ds2}=V_{ds2}+\omega_{e2}L_{\sigma 2}I_{qs2}+\frac{r_{r2}L_{m2}}{L_{r2}^2}\lambda_{dr2}+\omega_{r2}\frac{L_{m2}}{L_{r2}}\lambda_{qr2}=\sigma_{ds2} \tag{8.6}$$

$$p\lambda_{qr2}+\frac{r_{r2}}{L_{r2}}\lambda_{qr2}=\frac{r_{r2}L_{m2}}{L_{r2}}I_{qs2}-(\omega_{e2}-\omega_{r2})\lambda_{dr2}=\sigma_{qr2} \tag{8.7}$$

$$p\lambda_{dr2}+\frac{r_{r1}}{L_{r1}}\lambda_{dr2}=\frac{r_{r2}L_{m2}}{L_{r2}}I_{ds2}+(\omega_{e2}-\omega_{r2})\lambda_{qr2}=\sigma_{dr2} \tag{8.8}$$

$$CpV_{dc}=-\frac{3}{2}\left(M_{qs1}I_{qs1}+M_{ds1}I_{ds1}+M_{qs2}I_{qs2}+M_{ds2}I_{ds2}\right)-\frac{V_{dc}}{R_L} \tag{8.9}$$

where $L_{\sigma 1}=L_{s1}-\frac{L_{m1}^2}{L_{r1}}, r_1=r_{s1}+\frac{r_{r1}L_{m1}^2}{L_{r1}^2}, M_{qs1}=2\frac{V_{qs1}}{V_{dc}}, M_{ds1}=2\frac{V_{ds1}}{V_{dc}}, L_{\sigma 2}=L_{s2}-\frac{L_{m2}^2}{L_{r2}},$

$r_2=r_{s2}+\frac{r_{r2}L_{m2}^2}{L_{r2}^2}, M_{qs2}=2\frac{V_{qs2}}{V_{dc}}, M_{ds2}=2\frac{V_{ds2}}{V_{dc}}, \omega_{r1}=\frac{p}{2}\omega_r, \omega_{r2}=\frac{q}{2}\omega_r$

The above model equations can be rewritten in matrix form as;

$$\dot{X}=f(X)+g(X)\cdot u \tag{8.10}$$

where, the state variable vector is $X$, the system input vector is $u$, $f(X)$.and $g(X)$ are the functions in terms of machine parameters, input frequencies and rotor electric speeds. The expressions of those vectors and functions are given as:

$$X=\begin{bmatrix} i_{qs1} & i_{ds1} & \lambda_{qr1} & \lambda_{dr1} & i_{qs2} & i_{ds2} & \lambda_{qr2} & \lambda_{dr2} & V_{dc}\end{bmatrix}$$

$$u=\begin{bmatrix} V_{qs1} & V_{ds1} & V_{qs2} & V_{ds1}\end{bmatrix}$$

$$f(X)=\begin{bmatrix}
-r_1 I_{qs1}-\omega_{e1}L_{\sigma1}I_{ds1}+\frac{r_{r1}L_{m1}}{L_{r1}^2}\lambda_{qr1}-\omega_{r1}\frac{L_{m1}}{L_{r1}}\lambda_{dr1}\\
-r_1 I_{ds1}+\omega_{e1}L_{\sigma1}I_{qs1}+\frac{r_{r1}L_{m1}}{L_{r1}^2}\lambda_{dr1}+\omega_{r1}\frac{L_{m1}}{L_{r1}}\lambda_{qr1}\\
-\frac{r_{r1}}{L_{r1}}\lambda_{qr1}+\frac{r_{r1}L_{m1}}{L_{r1}}I_{qs1}-(\omega_{e1}-\omega_{r1})\lambda_{dr1}\\
-\frac{r_{r1}}{L_{r1}}\lambda_{dr1}+\frac{r_{r1}L_{m1}}{L_{r1}}I_{ds1}+(\omega_{e1}-\omega_{r1})\lambda_{qr1}\\
-r_2 I_{qs2}-\omega_{e2}L_{\sigma2}I_{ds2}+\frac{r_{r2}L_{m2}}{L_{r2}^2}\lambda_{qr2}-\omega_{r2}\frac{L_{m2}}{L_{r2}}\lambda_{dr2}\\
-r_2 I_{ds2}+\omega_{e2}L_{\sigma2}I_{qs2}+\frac{r_{r2}L_{m2}}{L_{r2}^2}\lambda_{dr2}+\omega_{r2}\frac{L_{m2}}{L_{r2}}\lambda_{qr2}\\
-\frac{r_{r2}}{L_{r2}}\lambda_{qr2}+\frac{r_{r2}L_{m2}}{L_{r2}}I_{qs2}-(\omega_{e2}-\omega_{r2})\lambda_{dr2}\\
-\frac{r_{r1}}{L_{r1}}\lambda_{dr2}+\frac{r_{r2}L_{m2}}{L_{r2}}I_{ds2}+(\omega_{e2}-\omega_{r2})\lambda_{qr2}\\
-\frac{V_{dc}}{R_L}
\end{bmatrix}$$

$$g(X)=\begin{bmatrix}
1 & 0 & 0 & 0\\
0 & 1 & 0 & 0\\
0 & 0 & 0 & 0\\
0 & 0 & 0 & 0\\
0 & 0 & 1 & 0\\
0 & 0 & 0 & 1\\
0 & 0 & 0 & 0\\
0 & 0 & 0 & 0\\
-\frac{3}{C}\frac{I_{qs1}}{V_{dc}} & -\frac{3}{C}\frac{I_{ds1}}{V_{dc}} & -\frac{3}{C}\frac{I_{qs2}}{V_{dc}} & -\frac{3}{C}\frac{I_{ds2}}{V_{dc}}
\end{bmatrix}$$

The rotor mechanical speed is $\omega_r$. For the 2-pole ABC winding set, the electric rotor speed is $\omega_{r1}$, the angular frequency of the qd0 motor voltages is $\omega_{e1}$, the q-d rotor flux linkages are $\lambda_{qr1}$ and $\lambda_{dr1}$, respectively. The stator q and d axis currents are $I_{qs1}$ and $I_{ds1}$, respectively. For the 6-pole XYZ winding set, the electric rotor speed is $\omega_{r2}$, the angular frequency of the qd0 motor voltages is $\omega_{e2}$, the q-d rotor flux linkages are $\lambda_{qr2}$ and $\lambda_{dr2}$,

respectively. The stator q and d axis currents are $I_{qs2}$ and $I_{ds2}$, respectively. The qd modulation indexes for the two ac-dc rectifiers are $M_{qs1}$, $M_{ds1}$ and $M_{qs2}$, $M_{ds2}$, respectively.

No-load and short-circuit tests are used to measure the parameters of a 2 hp dual stator winding induction machine with the 2-pole and 6-pole winding sets. The magnetizing inductances of the two winding sets as a function of the magnetizing air-gap flux linkage are shown in Figure 8.2. Since the numbers of poles for both winding sets are different, the saturation characteristics of the windings are different and are not necessarily in phase.

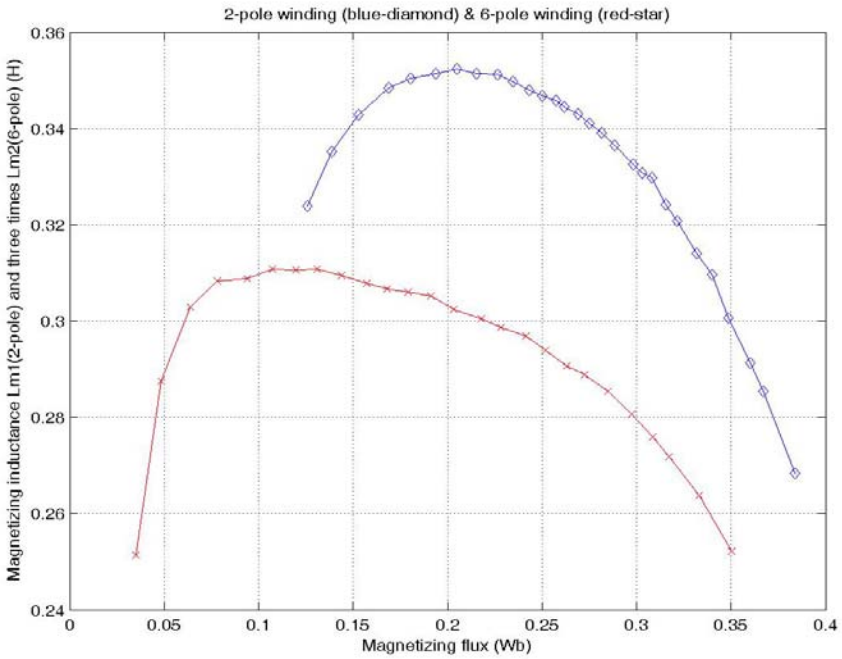


Figure 8.2. Experimental result of magnetizing flux vs magnetizing inductance $L_{m1}$ (2-pole winding) and three times magnetizing inductance $L_{m2}$ (6-pole winding)

## 8.3 Steady State Analysis

With the derivative terms in (8.1-8.9) set to be equal to zero, the system equations are used for the steady state analysis. If q- and d-axis stator and rotor fluxes are chosen as the state variables, the voltage equations for 2-pole ABC winding set are expressed in complex variable-form as :

$$\begin{aligned} V_{qds1} &= \frac{M_{qds1}}{2} \cdot V_{dc} \\ &= \left( \frac{r_{s1} L_{r1}}{L_{\delta 1}} - j\omega_{e1} \right) \cdot \lambda_{qds1} - \frac{r_{s1} L_{m1}}{L_{\delta 1}} \lambda_{qdr1} \end{aligned} \tag{8.11}$$

$$V_{qdr1} = 0 = \left( \frac{r_{r1} L_{s1}}{L_{\delta 1}} - j\omega_{e1} \right) \cdot \lambda_{qdr1} - \frac{r_{r1} L_{m1}}{L_{\delta 1}} \lambda_{qds1} \tag{8.12}$$

Similar equations are obtained for the 6-pole XYZ winding set,

$$\begin{aligned} V_{qds2} &= \frac{M_{qds2}}{2} \cdot V_{dc} \\ &= \left( \frac{r_{s2} L_{r2}}{L_{\delta 2}} - j\omega_{e2} \right) \cdot \lambda_{qds2} - \frac{r_{s2} L_{m2}}{L_{\delta 1}} \lambda_{qdr2} \end{aligned} \tag{8.13}$$

$$V_{qdr2} = 0 = \left( \frac{r_{r2} L_{s2}}{L_{\delta 2}} - j\omega_{e2} \right) \cdot \lambda_{qdr2} - \frac{r_{r2} L_{m2}}{L_{\delta 2}} \lambda_{qds2} \tag{8.14}$$

where, $L_{\delta 1} = L_{s1} L_{r1} - L_{m1}^2$ and $L_{\delta 2} = L_{s2} L_{r2} - L_{m2}^2$.

The dc capacitor voltage equation in steady state can be expressed in complex format as:

$$\frac{V_{dc}}{R_L} = -\frac{3}{2} \mathrm{Re}\left( M^*_{qds1} I_{qds1} + M^*_{qds2} I_{qds2} \right) \tag{8.15}$$

If the output powers of the 2-pole ABC winding set and the 6-pole XYZ winding set are defined as:

$$P_p = \frac{3}{2}\mathrm{Re}\left(V_{qds1} I_{qds1}^{*}\right) = \frac{3}{4} V_{dc}\ \mathrm{Re}\left(M_{qds1}^{*} I_{qds1}\right) \tag{8.16}$$

$$P_q = \frac{3}{2}\mathrm{Re}\left(V_{qds2} I_{qds2}^{*}\right) = \frac{3}{4} V_{dc}\ \mathrm{Re}\left(M_{qds2}^{*} I_{qds2}\right) \tag{8.17}$$

Then the output power ratio coefficient K between the 2-pole ABC winding set and the 6-pole XYZ winding set is expressed as:

$$K = \frac{P_q}{P_p} = \frac{\mathrm{Re}\left(M_{qds2}^{*} I_{qds2}\right)}{\mathrm{Re}\left(M_{qds1}^{*} I_{qds1}\right)}, \qquad \frac{P_p}{P_p + P_q} = \frac{1}{1+K} = \alpha \tag{8.18}$$

The rotor flux terms are eliminated in equation (8.11), and the equation expressed in terms of the stator fluxes is substituted in (8.15). This results in an equation that expresses the required excitation of each winding set in terms of the magnetizing flux linkage using the magnitude of the modulation index as a measure of the excitation.

$$\left|M_1\right|^2 = \frac{-2}{3R_L\left(1+K\right)} \mathrm{Re}\left\{ 2 \frac{\left[\left(A_{s1} - j\omega_{e1}\right) - \dfrac{B_{s1}B_{r1}}{A_{r1} - j\omega_{s1}}\right]}{\left[\dfrac{L_{r1}}{L_{\delta 1}} + \dfrac{L_{m1}B_{r1}}{L_{\delta 1}\left(A_{r1} - j\omega_{s1}\right)}\right]} \right\} \tag{8.19}$$

$$\left|M_2\right|^2 = \frac{-2K}{3R_L\left(1+K\right)} \mathrm{Re}\left\{ 2 \frac{\left[\left(A_{s2} - j\omega_{e2}\right) - \dfrac{B_{s2}B_{r2}}{A_{r2} - j\omega_{s2}}\right]}{\left[\dfrac{L_{r2}}{L_{\delta 2}} + \dfrac{L_{m2}B_{r2}}{L_{\delta 2}\left(A_{r2} - j\omega_{s2}\right)}\right]} \right\} \tag{8.20}$$

where, $\omega_{s1}$ is the slip frequency of the 2-pole ABC winding set and $\omega_{s2}$ is the slip frequency of the 6-pole XYZ winding set. The other variables are defined as follows:

$$A_{si} = \frac{r_{si}L_{ri}}{L_{\delta i}},\ A_{ri} = \frac{r_{ri}L_{si}}{L_{\delta i}},\ B_{si} = \frac{-r_i L_{mi}}{L_{\delta i}},\ B_{ri} = \frac{-r_{ri}L_{mi}}{L_{\delta i}},\ i = 1\ or\ 2\,.$$

Magnetizing flux linkage saturation reflected in the values of the magnetizing inductances of the machine (Figure 8.2) has an influence on the converter excitation

phenomenon as can be seen in (8.19-8.20). It is desirable to operate the generator and control the dc voltage when the total copper loss of the machine is minimized. Since the machine operates as two independent machines at steady state, the total copper loss is minimized when the copper loss due to each stator winding is minimized. This condition is obtained quantitatively, when the derivative of the expression of the copper loss for each machine with respect to the rotor slip is equated to zero (8.21).

$$s_i^* = -\frac{1}{\sqrt{\frac{\omega_{ri}^2}{r_{si}r_{ri}^2}\left(r_{si}L_{ri}^2 + r_{ri}L_{mi}^2\right) - 1}},\ i = 1\ or\ 2 \tag{8.21}$$

For the control scheme, the rotor flux reference is selected to achieve minimum total copper loss. The reference of the rotor flux linkage obtained from (8.11-8.14) as:

$$\lambda_{qdri} = \frac{-B_{ri}}{A_{ri} - j\frac{s_i^*}{1-s_i^*}\omega_{ri}}\lambda_{qdsi},\ i = 1\ or\ 2 \tag{8.22}$$

For the control scheme, instead of choosing the rotor flux reference to be a constant value, it can be adjusted on-line to further reduce the total loss including copper and core losses.

Figure 8.3(a) shows the relationship between the magnitudes of the modulation indexes ($M_1$, $M_2$) of the two boost rectifiers and the coefficient $\alpha = 1/(1+K)$ for a constant output power when the rotor speed is constant, the magnetizing flux $\lambda_m$ is set to a constant value of 0.25 Wb and the rotor slips are chosen to achieve minimum total copper loss. When α = 1, the 2-pole ABC winding set delivers all the dc power while in the extreme case the 6-pole XYZ winding set delivers the dc power alone when α = 0. Three different load resistance values—60 Ω, 80 Ω and 100 Ω, are chosen to show how

the modulation index of the rectifier and load resistance are constrained to achieve converter excitation. For constant total output power condition, a greater load resistance requires a smaller modulation index and the power distribution coefficient can be used to change the power ratios of both stator windings. Similarly, the effect of the magnetizing inductance on the magnitudes of the modulation indexes is shown in Figure 8.3(b), assuming a constant rotor speed of $\omega_r = 400$ rad/s and a constant load ($R_L$ =100 Ω). The optimal slip is calculated using (8.21). The variation of $M_1$ and $M_2$ with the change in the power distribution factor is also shown in Figure 8.3(b). Because of the saturation of the magnetizing inductance, two corresponding magnetizing flux linkage levels can be found for a given modulation index value. This implies that two different output dc voltages can be obtained for each of the resulting magnetizing flux linkages.

## 8.4 Input-Output Linearization

It is observed from the machine model that the model equations are nonlinear. Therefore, it is not easy to see how to control the behaviors of the outputs by using the input signals. If a direct and simple relationship between system inputs and outputs can be found, the difficulty of control design will be reduced. The input-output linearization approach is one of the methods for nonlinear control design. The fundamental idea is to transform a nonlinear system into a fully or partly linear one so that traditional linear control techniques can be applied for control design.

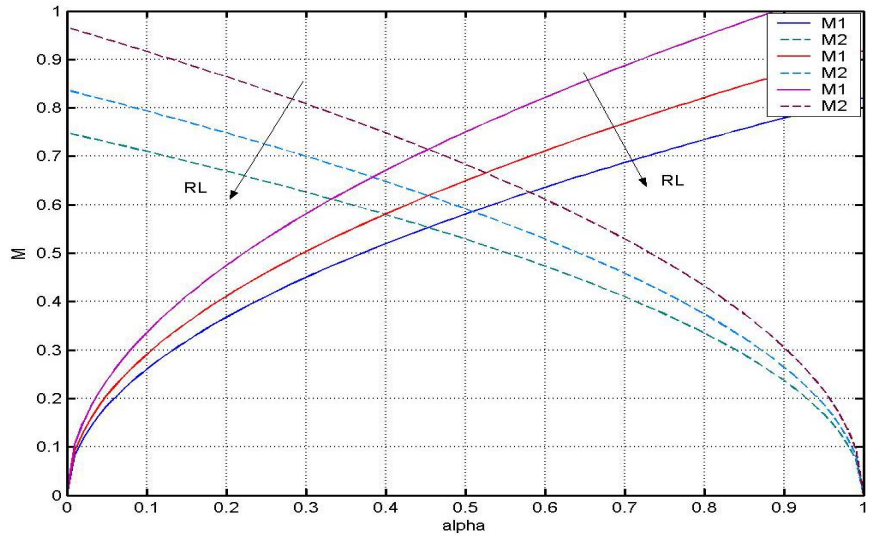


(a)

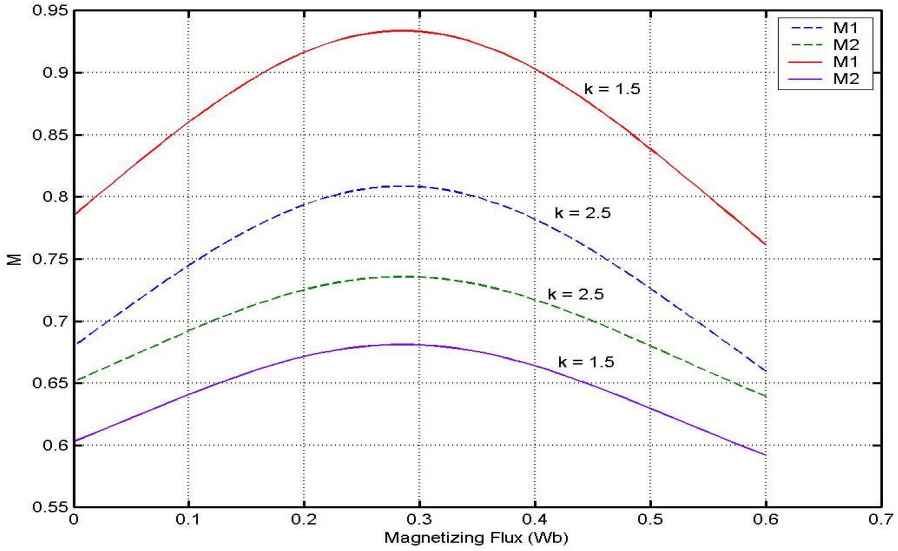


(b)

Figure 8.3: (a) Magnitude of modulation indexes of rectifiers and K, (b) Magnitude of modulation indexes of rectifiers and magnetizing flux

The simplest form of feedback linearization is to cancel the nonlinearities in a nonlinear system so that the closed-loop dynamics are in a linear form. The nonlinear system to be considered has the following form.

$$\dot{x} = f(x) + g(x)u \tag{8.23}$$

where, $x \in \Re^n$ is the vector of state variables and $u \in \Re^m$ is the input vector.

Lie derivative and relative order degree are the two important definitions in this analysis [8.1]. If $h:\Re^n \to \Re$ is a scalar function while $f:\Re^n \to \Re^n$ represents a vector field in $\Re^n$, then the Lie derivative of $h$ with respect to $f$ is a vector field defined as,

$$L_f h(x) = \frac{\partial h}{\partial x} f(x) \tag{8.24}$$

Then the Lie derivative $L_f h(x)$ is the directional derivative of $h$ along the direction of the vector $f$. If an explicit relationship between the output and input can only be obtained after differentiating the output of the system r times, the system is said to have relative degree r. The mathematical definition is given as follows. If $y = h(x)$ is a scalar output of a nonlinear system, the nonlinear system is said to have relative degree r in a region $\Omega$ if $L_g L_f^{r-1} h(x) \neq 0$ while $L_g h(x) = L_g L_f h(x) = \cdots = L_g L_f^{r-2} h(x) = 0$

For example, the single input single output case is firstly considered here. If the output $y = h(x)$ has a relative degree n, the expressions of all the derivatives are given as:

$$\begin{aligned}
\dot{y} &= L_f h(x) + L_g h(x) \cdot u = L_f h(x) \\
\ddot{y} &= L_f^2 h(x) + L_g L_f h(x) \cdot u = L_f^2 h(x) \\
\dddot{y} &= L_f^3 h(x) + L_g L_f^2 h(x) \cdot u = L_f^3 h(x) \\
&\vdots \\
y^n &= L_f^n h(x) + L_g L_f^{n-1} h(x) \cdot u
\end{aligned} \tag{8.25}$$

A new set of state variables is defined as:

$$\begin{aligned}
\dot{z}_1 &= z_2 \\
\dot{z}_2 &= z_3 \\
&\vdots \\
\dot{z}_{n-1} &= z_n \\
\dot{z}_n &= L_f^n h(x) + L_g L_f^{n-1} h(x) \cdot u = a(x) + b(x) \cdot u
\end{aligned} \tag{8.26}$$

The matrix form of the new state variables is given as:

$$\begin{pmatrix} z_1 \\ z_2 \\ \vdots \\ z_n \end{pmatrix} = \begin{pmatrix} h(x) \\ L_f h(x) \\ \\ L_f^{n-1} h(x) \end{pmatrix} = \phi(x) \tag{8.27}$$

where $\phi(x): \Re^n \to \Re^n$ is smooth locally invertible function in a neighborhood of $x = 0$. This is known as the controller canonical form, which has the exact same form as the linear system. The system input is defined as:

$$u = \frac{1}{b(x)}\left[-a(x) + v\right] \tag{8.28}$$

where, $v$ is a vector of control signals. Then a linear differential relationship is obtained and the resulting system equation is given as:

$$L_f^n z_1 = \dot{z}_n = v \tag{8.29}$$

which is the linear multiple-integrator relation. $v$ can be designed according to the system requirements.

For example, the controller that regulates the output $y = h(x)$ as desired constant value $y^*$ can be designed as:

$$v = -a_0\left(z_1 - y^*\right) - a_1 z_2 - \cdots - a_{n-1} z_n \tag{8.30}$$

Similarly, the tracking controller that makes a system output to track a smooth trajectory $y^*(t)$ can be designed by using the error dynamics $e(t) = y(t) - y^*(t)$.

$$\frac{d^n e(t)}{dt^n} = y^n(t) - y^{*(n)}(t) = \dot{z}_n - y^{*(n)}(t) = v - y^{*(n)}(t) \tag{8.31}$$

Therefore, the control signal to make the system track the desired trajectory is designed as:

$$v = y^{*(n)}(t) - a_0\left(z_1 - y^*\right) - a_1\left(z_2 - \dot{y}^*\right) - \cdots - a_{n-1}\left(z_n - y^{*(n)}\right) \tag{8.32}$$

The above algorithm requires that the output function $y = h(x)$ has a relative degree of $r = n$. If $r < n$, then the procedure can only proceed up to $r$ steps. Under this condition, part of the system dynamics described by the state components is "unobservable" in the input-output linearization. This part of the dynamics is called the internal dynamics and the issue of internal stability becomes important when a relative degree is less than the number of state variables.

The internal dynamics are simply determined by the locations of the zeros in the linear system, in which the internal dynamics are stable if all zeros are in the left-half plane. The system with negative real parts for all the zeros is also called "minimum-phase system". However, this cannot be directly used for the nonlinear system. In that case, the zero-dynamic is defined in the nonlinear system to determine the stability of the internal dynamics. When the system output is kept at zero by the input, it is internal dynamics of the nonlinear system. Hence the study of the internal dynamics stability can be simplified by studying that of the zero dynamics instead. A different control strategy has to be applied if the zero dynamics are unstable.

## 8.5 Control Scheme

Since the system equations of the dual stator winding induction machine given in (8.1-8.9) are nonlinear and coupled, the input-output linearization method with decoupling is used to remove the non-linearity and coupled terms permitting the classic linear system control methodology to be used to determine the parameters of the controllers. This method is possible since the input-output linearization and decoupling strategy ensure the linear relationship between the input control variables and the output

controlled variables with each output-input pair decoupled from each other. The control variables are $M_{qs1}$, $M_{ds1}$ and $M_{qs2}$, $M_{ds2}$ while the controlled variables are dc voltage $V_{dc}$, the rotor flux linkages of the 2-pole ABC winding $\lambda_{qr1}$ and $\lambda_{dr1}$ and the rotor flux linkages of the 6-pole XYZ winding $\lambda_{qr2}$ and $\lambda_{dr2}$. The above input-output linearization algorithm is simplified as a three-step process: (a) differentiate a controlled variable until an input variable appears, (b) choose the input variables to cancel nonlinear terms and guarantee tracking convergence, and (c) study the stability of the internal dynamics. The total number of differentiations for all controlled variables is called the relative order r, while the internal dynamics are composed of n-r states (n is the total number of the system dynamic states).

When operations (a-c) are performed on equations (8.1-8.9), the resulting equations are linearized and decoupled hence the system is input-output linearizable, decoupled with no internal dynamics. Any realistic dynamics can be imposed by means of linear controllers.

Multiplying (8.9) with $V_{dc}$ gives:

$$\frac{1}{2}CpV_{dc}^2 + \frac{V_{dc}^2}{R_L} = 3\left(V_{qs1}i_{qs1} + V_{ds1}i_{ds1} + V_{qs2}i_{qs2} + V_{ds2}i_{ds2}\right) = \sigma_{dc} \tag{8.33}$$

Assume the power ratio between the 6-pole XYZ winding set to the 2-pole winding set is K :

$$\left(V_{qs2}i_{qs2} + V_{ds2}i_{ds2}\right) = K \cdot \left(V_{qs1}i_{qs1} + V_{ds1}i_{ds1}\right) \tag{8.34}$$

Then the relationship between $\sigma_{dc}$ and the two controlled variables to the 2-pole ABC and 6-pole XYZ winding sets respectively are:

$$\frac{\sigma_{dc}}{1+K} = 3\left(V_{qs1} i_{qs1} + V_{ds1} i_{ds1}\right) = \sigma_{dc1} \tag{8.35}$$

$$\frac{K\sigma_{dc}}{1+K} = 3\left(V_{qs2} i_{qs2} + V_{ds2} i_{ds2}\right) = \sigma_{dc2} \tag{8.36}$$

K is the power distribution coefficient which is used to vary the output power of each winding set. If a constant power load is desired, the value of K can be varied to change the power generated by each winding in order to further improve the generator efficiency. Only the control design for the 2-pole ABC winding set is undertaken below. Similar analysis is done for the 6-pole XYZ winding. From (8.3-8.4), the slip frequency and the reference stator d-axis current of the 2-pole ABC winding set are :

$$\left(\omega_{e1} - \omega_{r1}\right) = -\frac{\sigma_{qr1}}{\lambda_{dr1}} + \frac{r_{r1} L_{m1}}{L_{r1}} \cdot \frac{I_{qs1}}{\lambda_{dr1}} \tag{8.37}$$

$$I_{ds1}^{*} = \left[\sigma_{dr1} - \left(\omega_{e1} - \omega_{r1}\right)\lambda_{qr1}\right] \frac{L_{r1}}{r_{r1} L_{m1}} \tag{8.38}$$

Since the optimal slip is determined by (8.21), equation (8.37) is used to calculate the reference rotor flux linkage value. The command (reference) q and d axis stator voltages of the 2-pole ABC winding set from (8.1-8.2) are expressed as :

$$V_{qs1}^{*} = \sigma_{qs1} + \omega_{e1} L_{\sigma 1} I_{ds1} - \frac{r_{r1} L_{m1}}{L_{r1}^2} \lambda_{qr1} + \omega_{r1} \frac{L_{m1}}{L_{r1}} \lambda_{dr1} \tag{8.39}$$

$$V_{ds1}^{*} = \sigma_{ds1} - \omega_{e1} L_{\sigma 1} I_{qs1} - \frac{r_{r1} L_{m1}}{L_{r1}^2} \lambda_{dr1} - \omega_{r1} \frac{L_{m1}}{L_{r1}} \lambda_{qr1} \tag{8.40}$$

The unknown quantities $\sigma_{qs1}$, $\sigma_{ds1}$, $\sigma_{qr1}$, $\sigma_{dr1}$ and $\sigma_{dc}$ are the outputs of controllers of the 2-pole winding set which are defined from (8.1-8.4, 8.9). If the traditional PI controllers are used and the parameters of the controllers are given as defined below (i.e.

$K_{pqs1}$ and $K_{iqs1}$ are the controller parameters for q-axis current controller), the transfer functions of the state variables are:

$$\frac{V_{dc}^2}{V_{dc}^{*2}} = \frac{K_{pdc}S + K_{idc}}{\frac{1}{2}CS^2 + \left(\frac{1}{R_L} + K_{pdc}\right)S + K_{idc}} \tag{8.41}$$

$$\frac{\lambda_{qr1}}{\lambda_{qr1}^*} = \frac{K_{pqr1}S + K_{iqr1}}{S^2 + \left(K_{pqr1} + \frac{r_{r1}}{L_{r1}}\right)S + K_{iqr1}} \tag{8.42}$$

$$\frac{\lambda_{dr1}}{\lambda_{dr1}^*} = \frac{K_{pdr1}S + K_{idr1}}{S^2 + \left(K_{pdr1} + \frac{r_{r1}}{L_{r1}}\right)S + K_{idr1}} \tag{8.43}$$

$$\frac{I_{qs1}}{I_{qs1}^*} = \frac{K_{pqs1}S + K_{iqs1}}{S^2 + \left(\frac{K_{pqs1}}{L_{\sigma 1}} + \frac{r_1}{L_{\sigma 1}}\right)S + \frac{K_{iqs1}}{L_{\sigma 1}}} \tag{8.44}$$

$$\frac{I_{ds1}}{I_{ds1}^*} = \frac{K_{pds1}S + K_{ids1}}{S^2 + \left(\frac{K_{pds1}}{L_{\sigma 1}} + \frac{r_1}{L_{\sigma 1}}\right)S + \frac{K_{ids1}}{L_{\sigma 1}}} \tag{8.45}$$

The Butterworth method is applied to design the parameters of the controllers, in which the gain parameters are selected to locate the eigen-values of the transfer functions uniformly in the left half of the s-plane, on a circle of radius $\omega_0$, with its center at the origin [8.2]. The second order Butterworth polynomial can be expressed as:

$$S^2 + \sqrt{2}\omega_0 S + \omega_0^2 = 0 \tag{8.46}$$

The values of $\omega_0$ for different controllers should be properly chosen. Generally, the inner loop controller should have a value of $\omega_0$ that is about 10 times higher than the one in the outer control loop. Controller parameters are calculated by comparing the

Butterworth polynomial with the denominator of the transfer functions. Similar transfer functions for the state variables are determined for the 6-pole XYZ winding set. The same design idea will be applied to calculate the parameters of the controllers for the 6-pole winding set. The zeros of the transfer functions also greatly influence the system performance. When any zero of a transfer function of a system has positive real part (the system is non-minimum phase), the closed-loop performance is compromised as the right half-plane zero induces additional phase shift of -180. The determination of controller parameters should ensure the minimum phase system requirement. In this case, the requirement can be ensured when $k_p$ and $k_i$ of a controller have the same sign. The controller parameters for the simulation of parallel connected generating system are given in Table 8.1. The final control scheme is shown in Figure 8.4. Since the equations for the d-axis current controller, the slip calculation and the command voltages calculations of the 6-pole XYZ winding set are similar to those of the 2-pole ABC winding set, they are eliminated in Figure 8.4.

To achieve field orientation control, the reference q-axis flux linkage is set equal to zero and the d-axis flux linkage reference is equal to the magnitude of the rotor flux linkage given in (8.21) while the dc voltage is regulated. Although the control structure and design set forth applies to the dual stator-winding connected to parallel connected rectifiers, the same approach applies for the machine with series connected rectifiers.

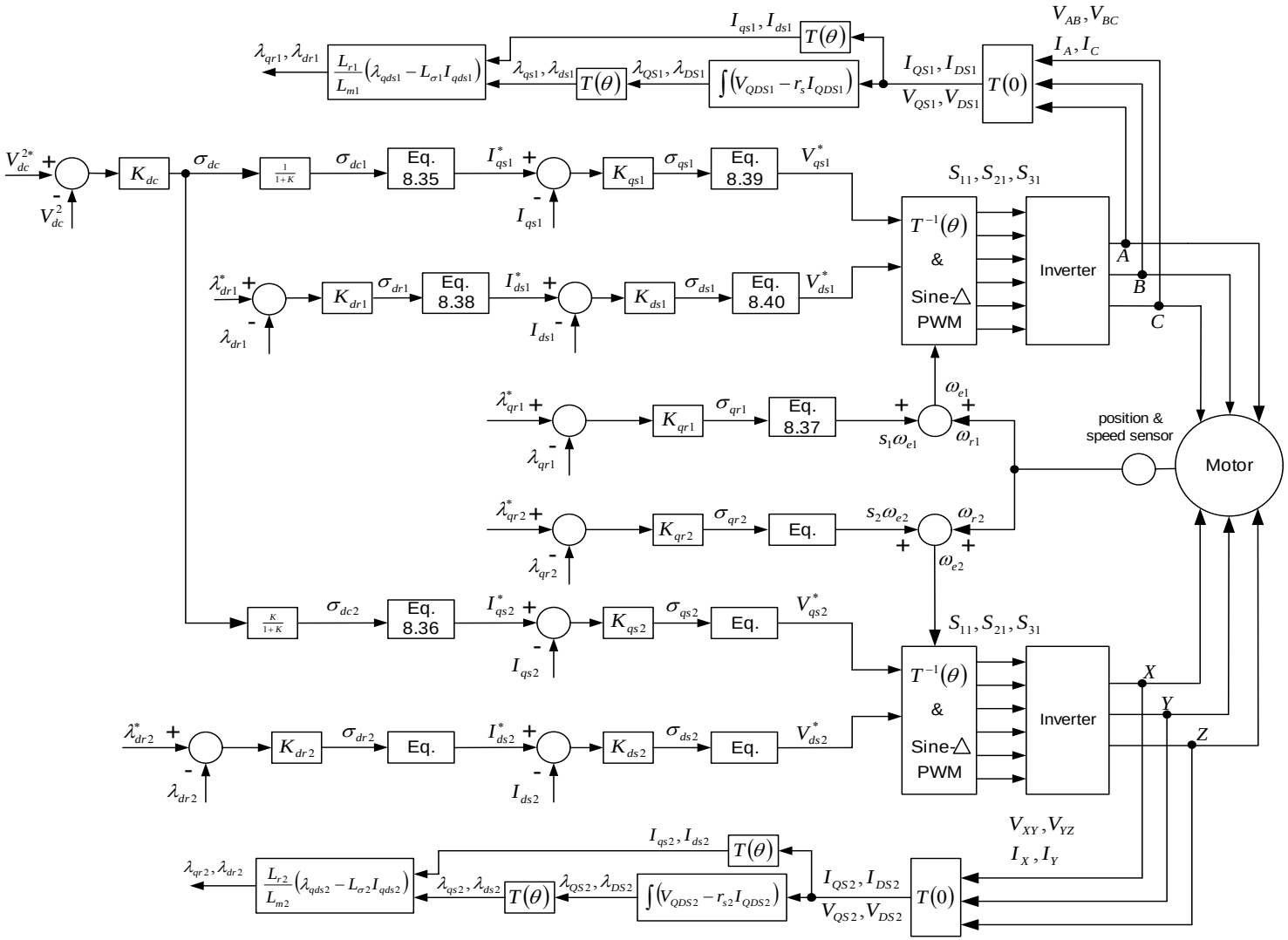


Figure 8.4. The control scheme of the proposed method

Table 8.1 Parameters of controllers in parallel-connected generating system

| Controller name | 2-pole ABC winding | 6-pole XYZ winding |
|---|---|---|
| Q-axis current | $k_{pqs1} = 24.18$, $k_{iqs1} = 19708$ | $k_{pqs2} = 21.92$, $k_{iqs2} = 17147$ |
| D-axis current | $k_{pds1} = 24.18$, $k_{ids1} = 19708$ | $k_{pds2} = 21.92$, $k_{ids2} = 17147$ |
| Q-axis rotor flux linkage | $k_{pqr1} = 13.2$, $k_{iqr1} = 100$ | $k_{pqr2} = 8.56$, $k_{iqr2} = 100$ |
| D-axis rotor flux linkage | $k_{pdr1} = 140.5$, $k_{idr1} = 10e4$ | $k_{pdr2} = 135.8$, $k_{idr2} = 10e4$ |
| DC voltage | $k_{pdc} = 0.0992$, $k_{idc} = 1.56$ | |

## 8.6 Flux Estimation

Flux linkages are required in the implementation of the control scheme. The values that can be used for flux estimation are the stator voltages and currents, which can be easily measured using voltage and current sensors.

Some observers or other methods have been proposed to estimate the rotor flux. The direct approach is to integrate the back-EMF in the stationary q-d reference frame.

The stator fluxes can be estimated from the stator voltage equations in the stationary reference frame by integrating back-EMF as:

$$\begin{aligned} \lambda_{qsi} &= \int \left( V_{qsi} - r_{si} I_{qsi} \right) \\ \lambda_{dsi} &= \int \left( V_{dsi} - r_{si} I_{dsi} \right) \end{aligned} \tag{8.47}$$

where, the subscripts $_{qsi}$ and $_{dsi}$ represent the stator q- and d-axis components for $i$ winding set respectively. The $i$ winding can be either the ABC winding set or the XYZ winding set.

Since the input quantities to be integrated are AC signals, drift and saturation problems cannot be avoided if pure integrators are used. The reasons for these problems can be addressed as: firstly, the starting point of integration is not always zero. It is not practicable to always start the integration when the integrated signal is exactly at zero. This is called the initial condition problem, which results in a DC offset after integration. Secondly, the actual input signal for integration is not a pure AC signal and it has a DC component. The DC component of the integrated signal is due to the distortion of the signal itself, the resolution of the sensors and the difference between the desired reference DC voltage and actual reference DC voltage. The DC offset will drift the integration and saturates the integrator. Finally, if the frequency of the integrated signal is low, the integration may be saturated even if the magnitude of the signal to be integrated is very small.

To solve the problems, it has been proposed in [10.11, 10.12] that the pure integrator is replaced by a Low Pass Filter (LPF). The transfer function of a LPF is $\frac{1}{s+a}$ while that of a pure integrator is given as $\frac{1}{s}$. The effectiveness of LPF to solve the problems of pure integration has been demonstrated by both simulation and experimental results [10.10, 10.11, 10.39]. By using the low pass filter, the small DC offset in the integrated signals cannot cause saturation although the estimated values are not correct at the very beginning. The DC offset in the outputs introduced by the initial values is eliminated. However, the introduction of $a$ (cut-off frequency) produces the magnitude and phase errors in the integration. The error will increase when $a$ is relatively large, which is

generally the case to get a good performance from the LPF. Hence the following gain ($G_i$) and phase compensations ($P_i$) are proposed to solve the problem:

$$\begin{aligned} G_i &= \frac{\sqrt{\omega_{ei}^2 + a_i^2}}{\omega_{ei}} \\ P_i &= \exp(-j\varphi_i) \end{aligned} \tag{8.48}$$

where, $\varphi_i = \tan^{-1}\left(\frac{a_i}{\omega_{ei}}\right)$ and $\omega_{ei}$ is the synchronous angular frequency.

These two compensations can be combined to be:

$$G_i \cdot P_i = \frac{1}{\omega_{ei}}(\omega_{ei} - j \cdot a_i) \tag{8.49}$$

If the pole of a LPF $a$ is varied proportionally to the synchronous motor speed, the ratio of the motor frequency to the cutoff frequency is constant. Then (8.49) is converted to a compensation with constant coefficients. If the constant coefficient is assumed to be $k_i = \frac{a_i}{\omega_{ei}}$, the compensation expression and the compensated flux linkages are given as:

$$\begin{aligned} \lambda_{qsi} + j\lambda_{dsi} &= (\lambda_{qsip} + j\lambda_{dsip}) \cdot (1 - j \cdot k_i) \\ \lambda_{qsi} &= \lambda_{qsip} + k_i \cdot \lambda_{dsip} \\ \lambda_{dsi} &= \lambda_{dsip} - k_i \cdot \lambda_{qsip} \end{aligned} \tag{8.50}$$

where, $\lambda_{qsip}$ and $\lambda_{dsip}$ are the estimated flux linkages using the Low Pass Filter (LPF); $\lambda_{qsi}$ and $\lambda_{dsi}$ are the flux linkages after compensation.

If the stator resistance is ignored, the complete model of the stator flux estimation is given as:

$$\frac{\lambda_{qdsi}}{V_{si}} = \frac{1}{s + a_i} \cdot \frac{\sqrt{\omega_{ei}^2 + a_i^2}}{\omega_{ei}} \cdot \exp(-j\varphi_i) \tag{8.51}$$

where, $\exp(-j\varphi_i)=\cos(\varphi_i)-j\sin(\varphi_i)$, $\cos(\varphi_i)=\frac{\omega_{ei}}{\sqrt{\omega_{ei}^2+a_i^2}}$ and $\sin(\varphi_i)=\frac{a_i}{\sqrt{\omega_{ei}^2+a_i^2}}$.

Then the rotor flux linkages are estimated using stator flux linkages as:

$$\begin{aligned}\lambda_{qri} &= \frac{L_{ri}}{L_{mi}}\cdot\left(\lambda_{qsi}-L_{\sigma i}I_{qsi}\right)\\ \lambda_{dri} &= \frac{L_{ri}}{L_{mi}}\cdot\left(\lambda_{dsi}-L_{\sigma i}I_{dsi}\right)\end{aligned} \tag{8.52}$$

where, $L_{\sigma i}=L_{si}-\frac{L_{mi}^2}{L_{ri}}$.

## 8.7 Simulation and Experimental Results

The models of the generator systems are built up using the MATLAB/SIMULINK to evaluate the proposed control scheme for the parallel rectifier. The parameters of the dual winding induction machine are given in Table 8.2.

The simulation results in Figure 8.5 show the starting process of the machine. The rotor speed is maintained at 188 rad/s. The reference dc voltage is set to be 240V. It is clearly shown that by using the proposed control scheme, the dc voltage is well regulated. The dynamic responses of the generation system to changes in load and portioning coefficient K are shown in Figure 8.6. When the rotor speed is constant and the system is running at the steady state, the load resistance is changed from 90 Ω to 60 Ω at 1.5 s, rotor speed changes to 168 rad/s from 2.2 s to 2.5 s, while the power distribution coefficient K is changed from 1 to 3 at 2.8 s to see how it influences the output power of each winding. The dc voltage adequately tracks the reference under the dynamic situation.

Table 8.2 Machine parameters for simulation and experimental implementation

| | ABC winding | XYZ winding |
|---|---|---|
| Number of pole | 2 | 6 |
| Stator resistance | $r_{s1} = 3.4\,\Omega$ | $r_{s2} = 1.9\,\Omega$ |
| Mutual inductance | $L_{m1} = 0.336\ H$ | $L_{m2} = 0.093\ H$ |
| Leakage inductance | $L_{ls1} = 0.006\ H$ 6 | $L_{ls2} = 0.009\ H$ |
| Rotor resistance | $r_{r1} = 0.61\,\Omega$ | $r_{r2} = 0.55\,\Omega$ |

Significant redistribution of required power from each stator winding is manifested in the value of the electromagnetic torque of each winding. For changes in load, power distribution coefficient and rotor speed, the controlled dc voltage effectively tracks the command.

The proposed input-output linearization method for controller design results in a decoupled q-d control scheme, however the calculations of the excitation input command voltages are dependent on the knowledge of the machine parameters, in which the magnetizing inductances, the stator and rotor resistances are parameters that vary under different operating conditions. The dynamic responses of the proposed control system to the changing parameters are simulated to check the robustness of the control scheme and the simulation results are shown in Figure 8.7. The magnetizing inductances of both stator winding sets are increased by 10% of their rated values while the rotor resistances increase by 50% of their rated values as shown in Figure 8.7 (h-k). When the parameters change, the dc voltage is well regulated to be constant. It is found from the simulation results that the change of the rotor resistance of the XYZ winding set has relatively

greater influences on the system, which can be seen from the waveforms of the voltages and currents. All the simulation results demonstrate the good performance of the proposed control scheme for parallel connection of the generating system.

The proposed control scheme for the regulation of the dc voltage using the parallel connection has been experimentally implemented for a 2 hp dual stator winding 2/6 pole machine. The central controller is DSP TMS320LF2407A EVM board while two PWM inverters are connected to the terminals of the stator winding sets. The dc buses of both inverters are connected in parallel. A dc motor coupled to the dual stator winding generator by the rotor shaft is the driver. The generating system driven by the dc motor achieves a steady state condition after the load capacitor voltage is initialized with a low voltage value. Under a steady-state condition, the power partition coefficient and the load resistor value are changed to demonstrate the dynamic responses of the system. Figure 8.8 shows the experimental results when the power coefficient constant K changes from 1 to 3. The output dc voltage of the rectifier is kept at 240 V and the load resistance is 60 Ω. Significant power distribution change of each stator winding is observed from the experimental results when K changes. The power contributed by the ABC winding set decreases to almost half of the previous value corresponding to the change of K, while the power output by the XYZ winding set is increased to keep the total power constant. The experimental results for changing load resistance have been shown in Figure 8.9 where the dc voltage is regulated at 240 V. Other state variables are also shown such as the redistribution of the power extracted from the two stator windings. The dc voltage is fairly well regulated under all the changes examined.

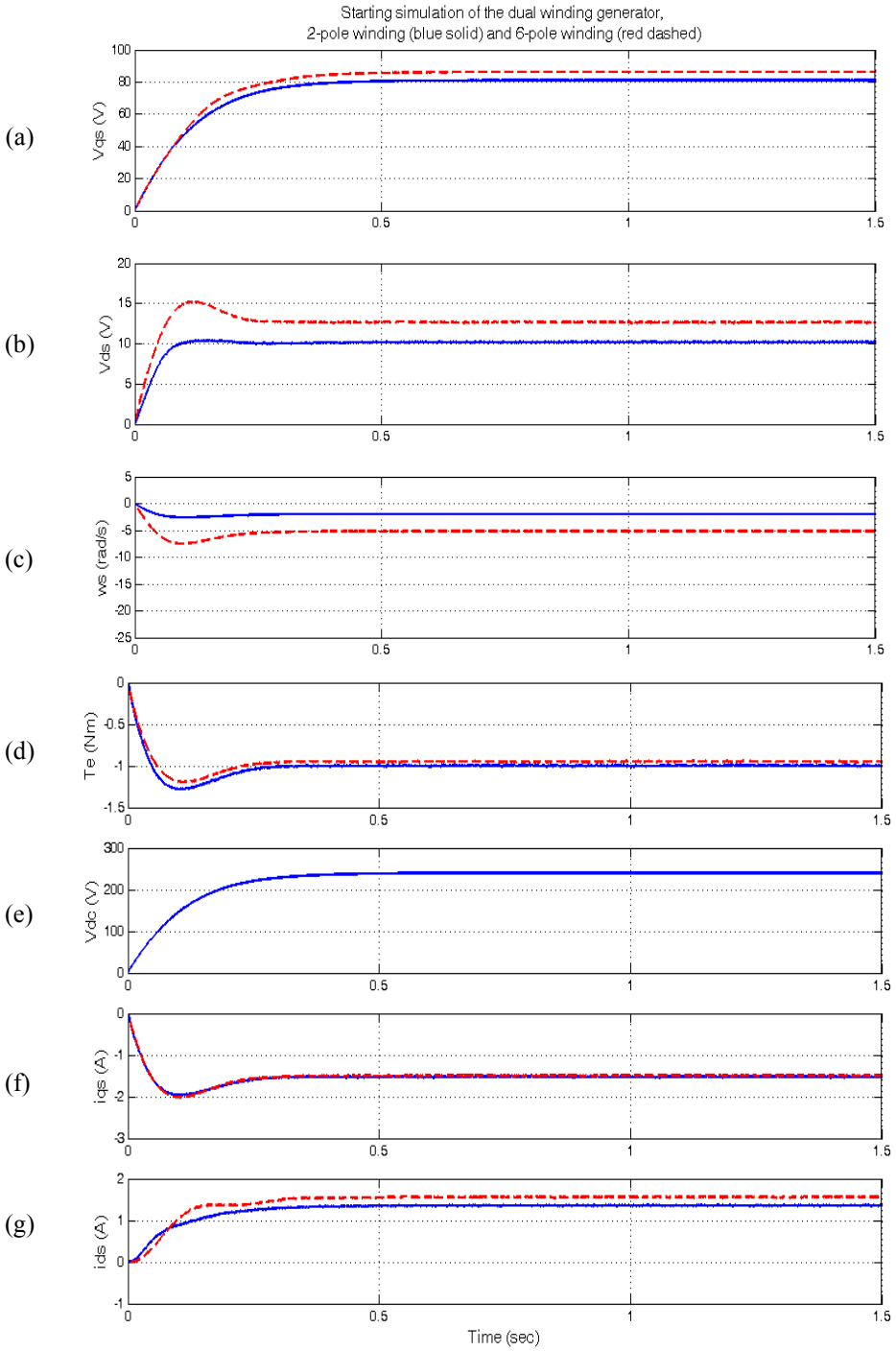


Figure 8.5. Simulation results of parallel connection for starting process, 2-pole winding is illustrated by blue solid line and 6-pole winding is illustrated by red dashed line. From top : (a) q-axis voltage $V_{qs}$; (b) d-axis voltage $V_{ds}$; (c) slip frequency $\omega_s$, (d) electromagnetic torque $T_e$; (e) dc voltage $V_{dc}$, (f) q-axis current $i_{qs}$, (g) d-axis current $i_{ds}$.

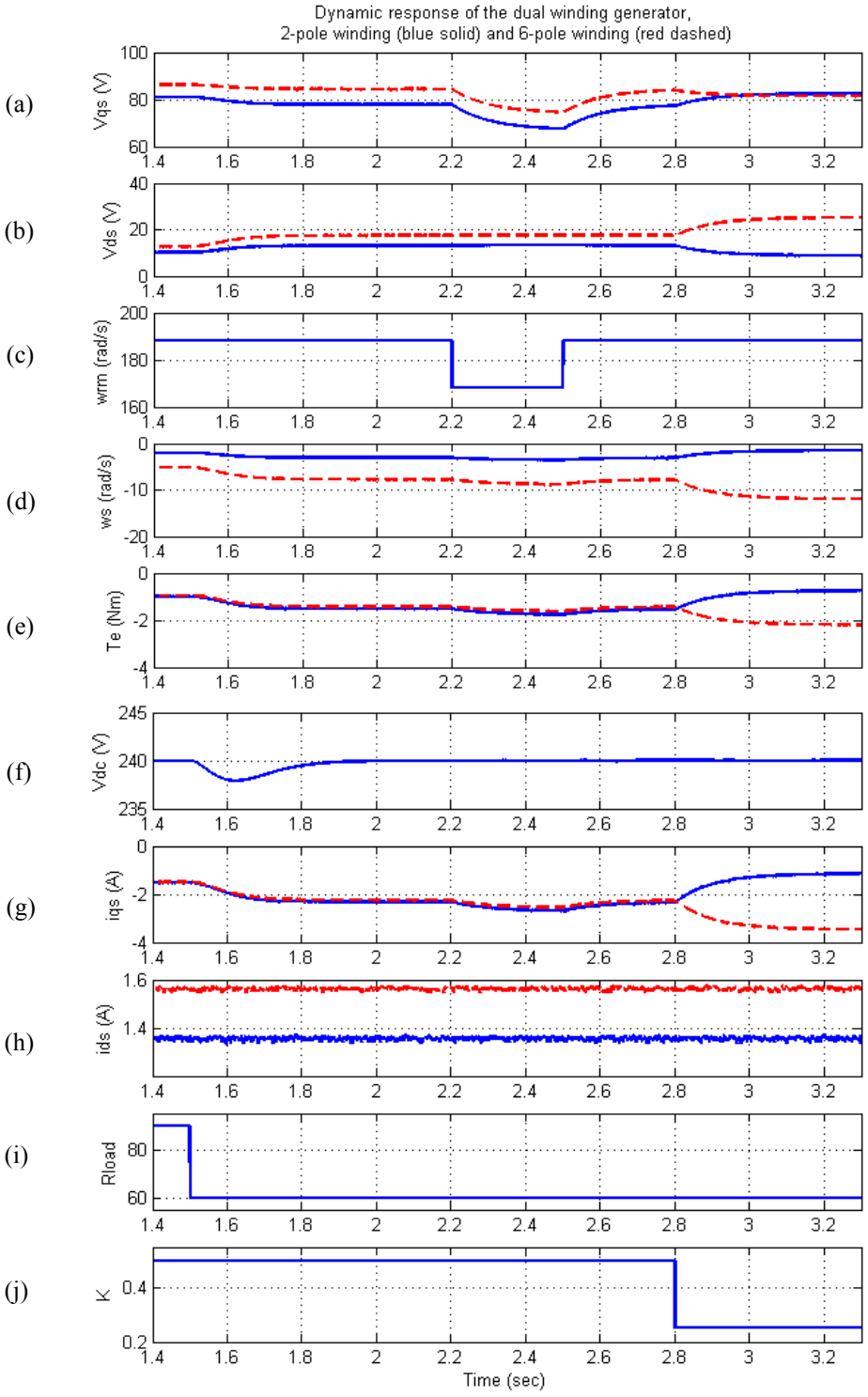


Figure 8.6. The dynamic response of parallel connection for changing load, rotor speed and K, 2-pole winding is illustrated by blue solid line and 6-pole winding is illustrated by red dashed line. From top : (a) q-axis voltage $V_{qs}$; (b) d-axis voltage $V_{ds}$; (c) rotor mechanical speed, (d) slip frequency $\omega_s$, (e) electromagnetic torque $T_e$; (f) dc voltage $V_{dc}$, (g) q-axis current $i_{qs}$, (h) d-axis current $i_{ds}$, (i) load resistance, (j) the value of K.

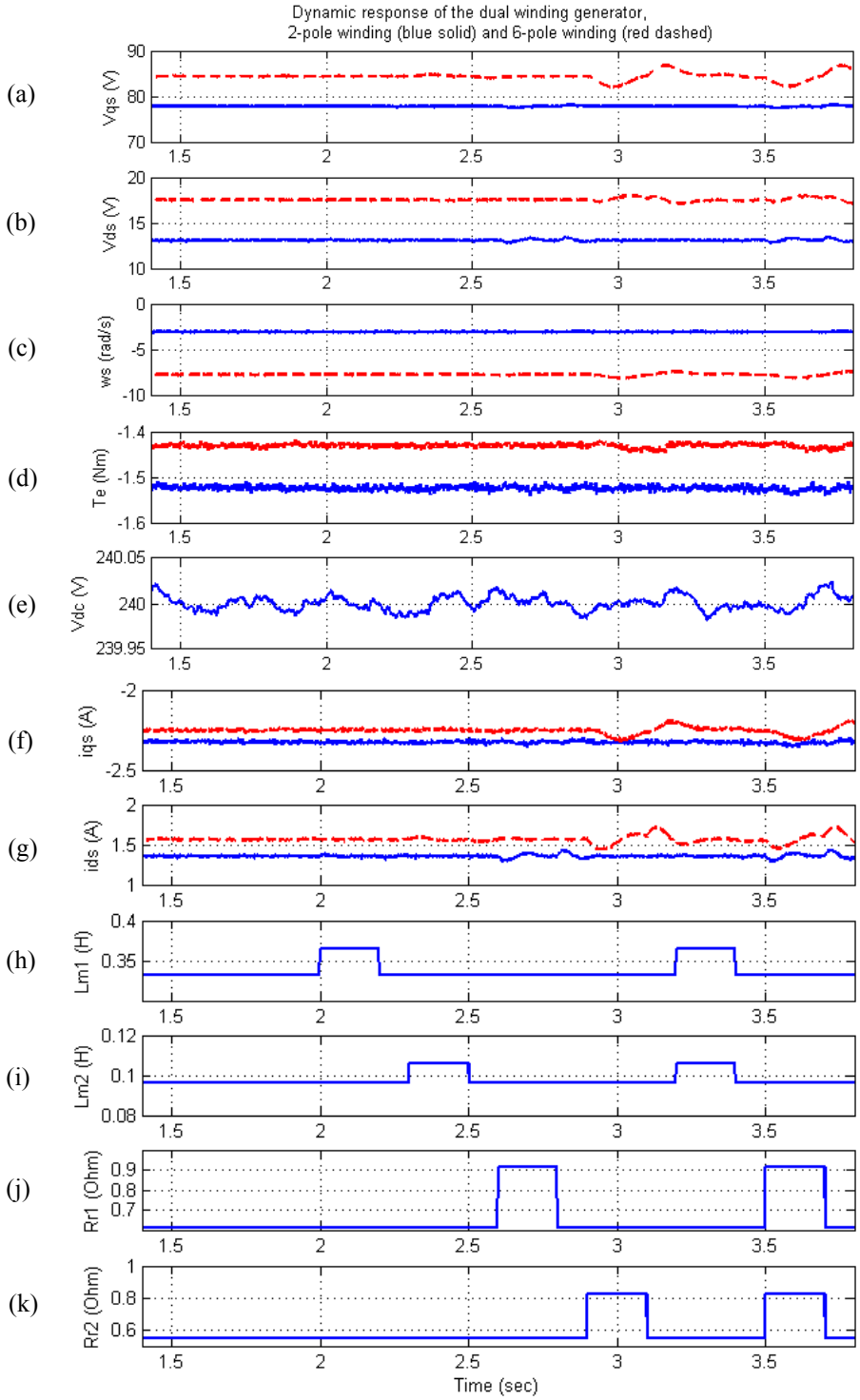


Figure 8.7. The dynamic response of parallel connection for changing parameters, 2-pole winding is illustrated by blue solid line and 6-pole winding is illustrated by red dashed line. From top : (a) q-axis voltage $V_{qs}$; (b) d-axis voltage $V_{ds}$; (c) slip frequency $\omega_s$, (d) electromagnetic torque $T_e$; (e) dc voltage $V_{dc}$, (f) q-axis current $i_{qs}$, (g) d-axis current $i_{ds}$,(h) magnetizing inductance of the ABC winding set $L_{m1}$, (i) magnetizing inductance of the XYZ winding set $L_{m2}$, (j) rotor resistance of the ABC winding set $R_{r1}$, (k) rotor resistance of the XYZ winding set $R_{r2}$.

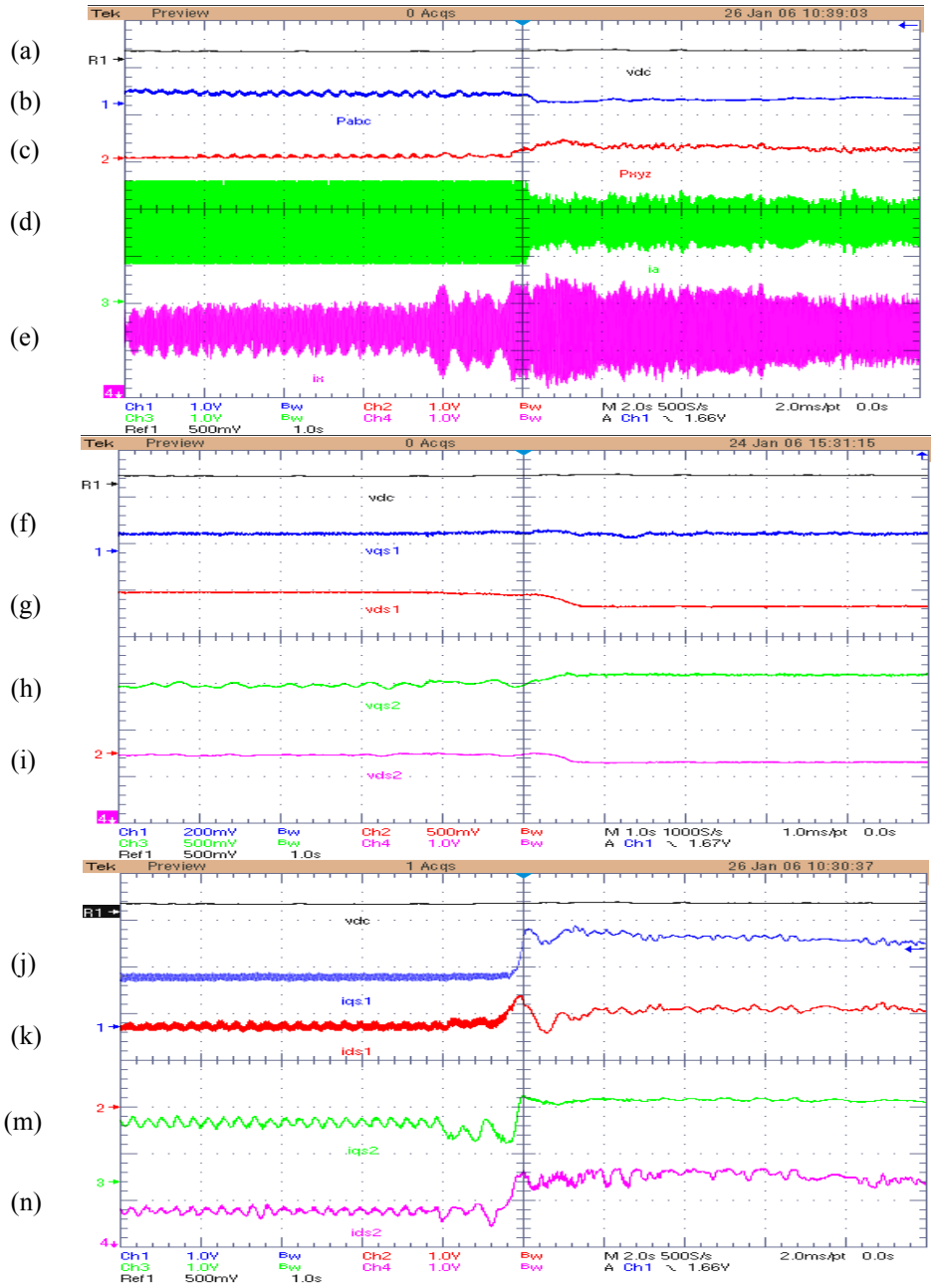


Figure 8.8 Experimental results for changing K from 1 to 3 when reference dc voltage is 240 V, load resistance is 60 Ω. from top. (a) dc voltage (240 V); (b) power of ABC windings (changes from 842 W to 483 W), (c) power of XYZ windings (changes from 454W to 873 W), (d) phase A current (change from 2.5A to 5.6 A), (e) phase X current (changes from 6.8 A to 3.2 A), (f) q-axis voltage of ABC windings $V_{qs1}$ (changes from 96 V to 94 V), (g) d-axis voltage of ABC windings $V_{ds1}$ (changes from –12 V to –31V), (h) q-axis voltage of XYZ windings $V_{qs2}$ (from 113 V to 135 V), (i) d-axis voltage of XYZ windings $V_{ds2}$ (changes from –25 V to –42 V), (j) q-axis current of ABC windings $i_{qs1}$ (changes from -2.4 A to –1.1 A), (k) d-axis current of ABC windings $i_{ds1}$ (changes from 1.8 A to 2.0 A), (m) q-axis current of XYZ windings $i_{qs2}$ (changes from –2.7 A to -2.1 A), (n) d-axis current of XYZ windings $i_{ds2}$(changes from 2.3 A to 3.6 A).

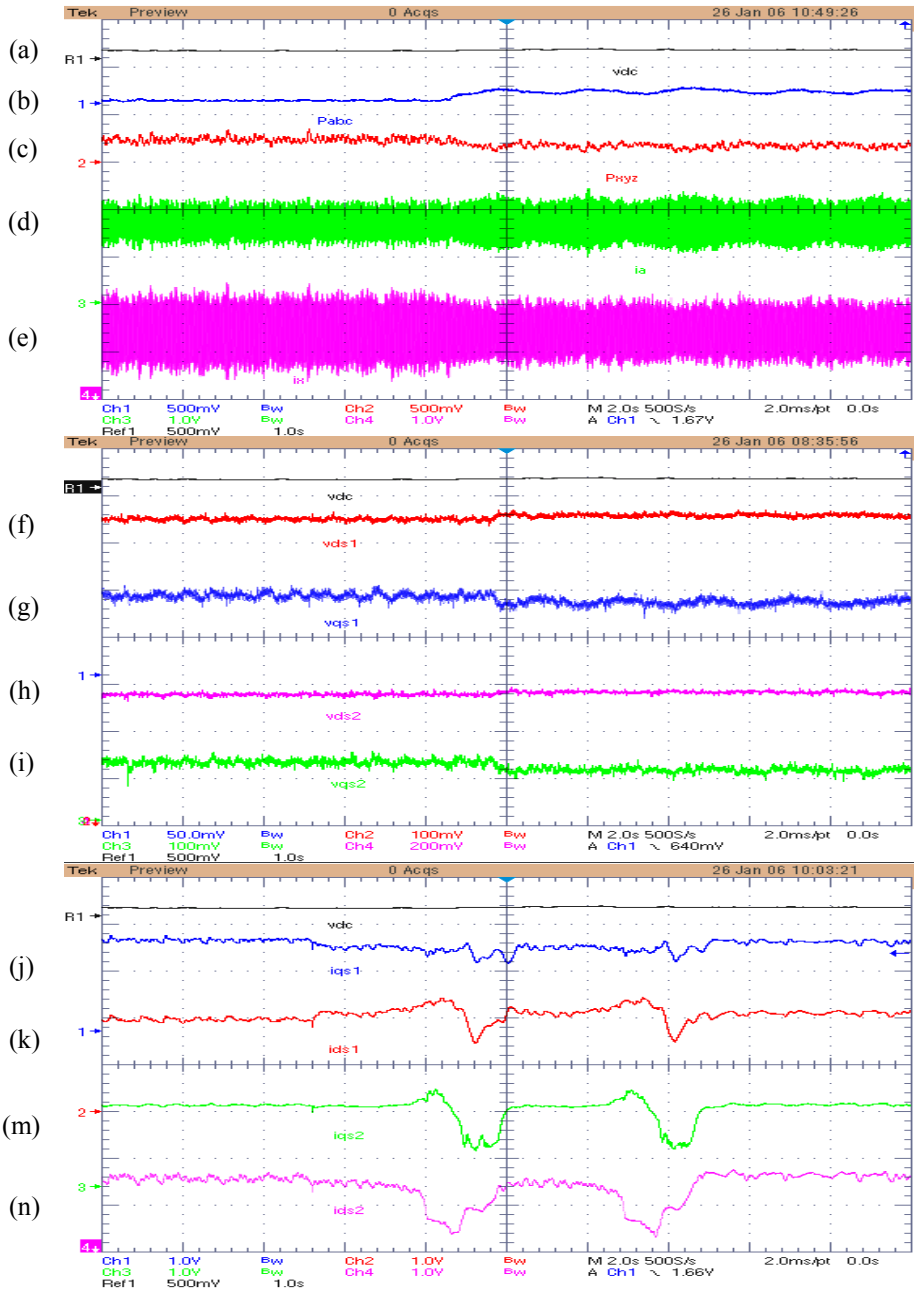


Figure 8.9 Experimental results for changing load resistance from 90 Ω to 60 Ω when reference dc voltage is 240 V, K is 3. from top. (a) dc voltage (almost 240 V); (b) power of ABC windings (changes from 304 W to 381 W), (c) power of XYZ windings (changes from 646 W to 724 W), (d) phase A current (change from 2.5A to 2.9 A), (e) phase X current (changes from 4.7 A to 4.1 A), (f) d-axis voltage of ABC windings $V_{ds1}$ (changes from –26 to -13 V), (g) q-axis voltage of ABC windings $V_{qs1}$ (changes from 86 V to 81 V), (h) d-axis voltage of XYZ windings $V_{ds2}$ (from -26 V to -24 V), (i) q-axis voltage of XYZ windings $V_{qs2}$ (changes from 104 V to 92 V), (j) q-axis current of ABC windings $i_{qs1}$ (changes from –1.2 A to –1.9 A), (k) d-axis current of ABC windings $i_{ds1}$ (changes from 1.7 A to 2.0 A), (m) q-axis current of XYZ windings $i_{qs2}$(changes from –2.2 A to -2.3 A), (n) d-axis current of XYZ windings $i_{ds2}$(changes from 2.3 A to 1.9 A).

## 8.8 Conclusions

The dynamic control scheme of the dual-winding induction generator producing dc load power using two parallel connected boost ac-dc PWM rectifiers has been set forth using the principles of input-output linearization control method. By properly choosing the power distribution coefficient K and the rotor d-axes reference flux linkages, the losses of the machine can be minimized. Simulation results validate the dc voltage control scheme proposed. Steady-state analysis further reveals the constraints on the load resistance, magnetizing flux linkage and rotor speed under which the rectifier excitation of the generator is possible. The control scheme has been implemented with a DSP in a 2hp dual stator-winding generator. Both simulation and experimental results validate the proposed control scheme.

# CHAPTER 9

# HIGH PERFORMANCE CONTROL OF A DUAL WINDING INDUCTION GENERATOR WITH SERIES CONNECTED BOOST RECTIFIERS

## 9.1 Introduction

The inherent advantages of dual-winding machines of various types have made them attractive in various motor and generating applications. In applications requiring dc voltages, the voltages of the two stator windings are processed with ac-dc PWM boost rectifiers and connected in parallel or series to the dc load. In the series connection, up to three dc outputs can be obtained while only two of them can be controlled independently. With appropriate winding design, this machine can be used as a starter-alternator for electric vehicles for future 42V applications, to produce 42V, 14V with/without 56V for various on-board applications.

The dual winding induction machine with parallel-connected output boost ac-dc rectifiers producing regulated dc voltage levels has been described in the previous chapter. The dual winding induction generator with two series connected rectifiers is the focus of this chapter. Very few published papers have focused on the use of series connected ac-dc boost rectifiers when compared to the relatively large body of work on paralleled ac-dc boost converters [9.1-9.5]. In [9.1], both parallel and series connected AC-DC rectifier systems using hysteresis current controls have been studied and stability

analysis results based on a very simple converter model have also been shown under the unity power factor condition.

In this chapter, a steady state analysis of the dual winding induction machine with series connected ac-dc boost rectifiers is presented for the first time with the high regulatory output dc voltage control scheme. Experimental and computer simulation results are provided to validate analysis and control methodologies. Application areas for this generating scheme may include hybrid electric vehicle starter-generator, battery charging facility for stand-alone systems and aerospace power dc power systems.

## 9.2 System Model

The proposed generation system is schematically shown in Figure 9.1. At most three output dc voltages can be obtained, however only two of them can be controlled independently.

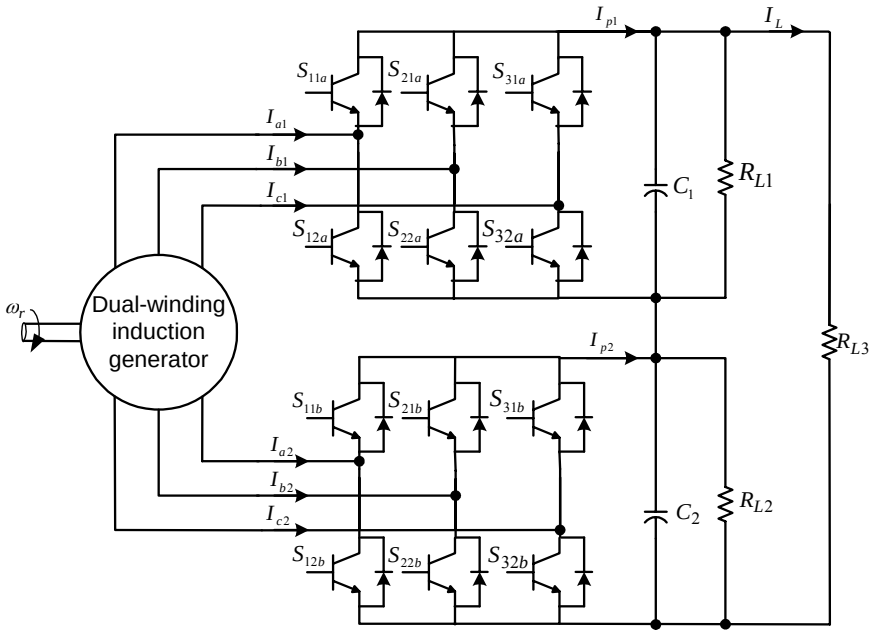


Figure 9.1. The Series connection of generation system diagram

The qd0 voltage equations of a dual winding induction generator feeding two ac-dc boost PWM rectifiers expressed in the synchronous reference frames of the winding rotor flux linkages are given in (9.1-9.10). The subscripts 1 and 2 correspond to the parameters or state variables for the 2-pole (ABC) three-phase winding set and the 6-pole (XYZ) three-phase winding set, respectively:

$$L_{\sigma 1} pI_{qs1} + r_1 I_{qs1} = V_{qs1} - \omega_{e1} L_{\sigma 1} I_{ds1} + \frac{r_{r1} L_{m1}}{L_{r1}^2} \lambda_{qr1} - \omega_{r1} \frac{L_{m1}}{L_{r1}} \lambda_{dr1} = \sigma_{qs1} \tag{9.1}$$

$$L_{\sigma 1} pI_{ds1} + r_1 I_{ds1} = V_{ds1} + \omega_{e1} L_{\sigma 1} I_{qs1} + \frac{r_{r1} L_{m1}}{L_{r1}^2} \lambda_{dr1} + \omega_{r1} \frac{L_{m1}}{L_{r1}} \lambda_{qr1} = \sigma_{ds1} \tag{9.2}$$

$$p\lambda_{qr1} + \frac{r_{r1}}{L_{r1}} \lambda_{qr1} = \frac{r_{r1} L_{m1}}{L_{r1}} I_{qs1} - (\omega_{e1} - \omega_{r1}) \lambda_{dr1} = \sigma_{qr1} \tag{9.3}$$

$$p\lambda_{dr1} + \frac{r_{r1}}{L_{r1}} \lambda_{dr1} = \frac{r_{r1} L_{m1}}{L_{r1}} I_{ds1} + (\omega_{e1} - \omega_{r1}) \lambda_{qr1} = \sigma_{dr1} \tag{9.4}$$

$$L_{\sigma 2} pI_{qs2} + r_2 I_{qs2} = V_{qs2} - \omega_{e2} L_{\sigma 2} I_{ds2} + \frac{r_{r2} L_{m2}}{L_{r2}^2} \lambda_{qr2} - \omega_{r2} \frac{L_{m2}}{L_{r2}} \lambda_{dr2} = \sigma_{qs2} \tag{9.5}$$

$$L_{\sigma 2} pI_{ds2} + r_2 I_{ds2} = V_{ds2} + \omega_{e2} L_{\sigma 2} I_{qs2} + \frac{r_{r2} L_{m2}}{L_{r2}^2} \lambda_{dr2} + \omega_{r2} \frac{L_{m2}}{L_{r2}} \lambda_{qr2} = \sigma_{ds2} \tag{9.6}$$

$$p\lambda_{qr2} + \frac{r_{r2}}{L_{r2}} \lambda_{qr2} = \frac{r_{r2} L_{m2}}{L_{r2}} I_{qs2} - (\omega_{e2} - \omega_{r2}) \lambda_{dr2} = \sigma_{qr2} \tag{9.7}$$

$$p\lambda_{dr2} + \frac{r_{r1}}{L_{r1}} \lambda_{dr2} = \frac{r_{r2} L_{m2}}{L_{r2}} I_{ds2} + (\omega_{e2} - \omega_{r2}) \lambda_{qr2} = \sigma_{dr2} \tag{9.8}$$

$$C_1 pV_{dc1} = -\frac{3}{2} \left( M_{qs1} I_{qs1} + M_{ds1} I_{ds1} \right) - \frac{V_{dc1}}{R_{L1}} - \frac{V_{dc1} + V_{dc2}}{R_{L3}} \tag{9.9}$$

$$C_2 pV_{dc2} = -\frac{3}{2} \left( M_{qs2} I_{qs2} + M_{ds2} I_{ds2} \right) - \frac{V_{dc2}}{R_{L2}} - \frac{V_{dc1} + V_{dc2}}{R_{L3}} \tag{9.10}$$

where, $K_{ei} = \frac{3P_i}{4J} \cdot \frac{L_{mi}}{L_{ri}}$, $L_{\sigma i} = L_{si} - \frac{L_{mi}^2}{L_{ri}}$, $r_i = r_{si} + \frac{r_{ri} L_{mi}^2}{L_{ri}^2}$. The subscript $i = 1 \; or \; 2$ represents the state variables of the ABC winding set and the XYZ winding set respectively. The q- and d-axis modulation indexes for the ac-dc PWM rectifiers are $M_{qsi} = 2V_{qsi}/V_{dci}$ and $M_{dsi} = 2V_{dsi}/V_{dci}$ respectively. The rotor speed is $\omega_{ri}$, the angular frequency of the qd0 motor voltages is $\omega_{ei}$, the q-d rotor flux linkages are $\lambda_{qri}$ and $\lambda_{dri}$, respectively. The stator q and d axis currents are $I_{qsi}$ and $I_{dsi}$, respectively. The output dc voltages are represented as $V_{dc1}$, $V_{dc2}$ and $V_{dc}$ , where $V_{dc} = V_{dc1} + V_{dc2}$.

The above model equations can be rewritten in matrix form as;

$$\dot{X} = f(X) + g(X) \cdot u \tag{9.11}$$

where, the state variable vector is $X$ , the system input vector is $u$, $f(X)$ .and $g(X)$ are the functions in terms of state variables, machine parameters, input frequencies and rotor electric speeds. Those vectors and functions are expressed as:

$$X = \begin{bmatrix} i_{qs1} & i_{ds1} & \lambda_{qr1} & \lambda_{dr1} & i_{qs2} & i_{ds2} & \lambda_{qr2} & \lambda_{dr2} & V_{dc1} & V_{dc2} \end{bmatrix}$$

$$u = \begin{bmatrix} V_{qs1} & V_{ds1} & V_{qs2} & V_{ds2} \end{bmatrix}$$

$$f(X)=\begin{bmatrix}
-r_1 I_{qs1}-\omega_{e1}L_{\sigma1}I_{ds1}+\dfrac{r_{r1}L_{m1}}{L_{r1}^2}\lambda_{qr1}-\omega_{r1}\dfrac{L_{m1}}{L_{r1}}\lambda_{dr1}\\
-r_1 I_{ds1}+\omega_{e1}L_{\sigma1}I_{qs1}+\dfrac{r_{r1}L_{m1}}{L_{r1}^2}\lambda_{dr1}+\omega_{r1}\dfrac{L_{m1}}{L_{r1}}\lambda_{qr1}\\
-\dfrac{r_{r1}}{L_{r1}}\lambda_{qr1}+\dfrac{r_{r1}L_{m1}}{L_{r1}}I_{qs1}-(\omega_{e1}-\omega_{r1})\lambda_{dr1}\\
-\dfrac{r_{r1}}{L_{r1}}\lambda_{dr1}+\dfrac{r_{r1}L_{m1}}{L_{r1}}I_{ds1}+(\omega_{e1}-\omega_{r1})\lambda_{qr1}\\
-r_2 I_{qs2}-\omega_{e2}L_{\sigma2}I_{ds2}+\dfrac{r_{r2}L_{m2}}{L_{r2}^2}\lambda_{qr2}-\omega_{r2}\dfrac{L_{m2}}{L_{r2}}\lambda_{dr2}\\
-r_2 I_{ds2}+\omega_{e2}L_{\sigma2}I_{qs2}+\dfrac{r_{r2}L_{m2}}{L_{r2}^2}\lambda_{dr2}+\omega_{r2}\dfrac{L_{m2}}{L_{r2}}\lambda_{qr2}\\
-\dfrac{r_{r2}}{L_{r2}}\lambda_{qr2}+\dfrac{r_{r2}L_{m2}}{L_{r2}}I_{qs2}-(\omega_{e2}-\omega_{r2})\lambda_{dr2}\\
-\dfrac{r_{r1}}{L_{r1}}\lambda_{dr2}+\dfrac{r_{r2}L_{m2}}{L_{r2}}I_{ds2}+(\omega_{e2}-\omega_{r2})\lambda_{qr2}\\
-\dfrac{V_{dc1}}{R_{L1}}-\dfrac{V_{dc1}+V_{dc2}}{R_{L3}}\\
-\dfrac{V_{dc2}}{R_{L2}}-\dfrac{V_{dc1}+V_{dc2}}{R_{L3}}
\end{bmatrix}$$

$$g(X)=\begin{bmatrix}
1 & 0 & 0 & 0\\
0 & 1 & 0 & 0\\
0 & 0 & 0 & 0\\
0 & 0 & 0 & 0\\
0 & 0 & 1 & 0\\
0 & 0 & 0 & 1\\
0 & 0 & 0 & 0\\
0 & 0 & 0 & 0\\
-\dfrac{3I_{qs1}}{V_{dc1}} & -\dfrac{3I_{ds1}}{V_{dc1}} & 0 & 0\\
0 & 0 & -\dfrac{3I_{qs2}}{V_{dc1}} & -\dfrac{3I_{ds2}}{V_{dc1}}
\end{bmatrix}$$

## 9.3 Steady State Analysis

With the derivative terms in (9.1-9.10) set to be equal to zero, the resulting equations are used for the steady state analysis that follows. The q-axis rotor flux linkage is zero when the rotor flux linkage is aligned to the d-axis. Under a steady state operating condition, the equations are simplified as:

$$V_{qsi} = r_i I_{qsi} + \omega_{ei} L_{\sigma i} I_{dsi} + \omega_{ri} \frac{L_{mi}}{L_{ri}} \lambda_{dri} \tag{9.12}$$

$$V_{dsi} = r_i I_{dsi} - \omega_{ei} L_{\sigma i} I_{qsi} - \frac{r_{ri} L_{mi}}{L_{ri}^2} \lambda_{dri} \tag{9.13}$$

$$\frac{r_{ri} L_{mi}}{L_{ri}} I_{qsi} - (\omega_{ei} - \omega_{ri}) \lambda_{dri} = 0 \tag{9.14}$$

$$\frac{r_{ri}}{L_{ri}} \lambda_{dri} = \frac{r_{ri} L_{mi}}{L_{ri}} I_{dsi} \tag{9.15}$$

$$-\frac{3}{2}\left(M_{qs1} I_{qs1} + M_{ds1} I_{ds1}\right) = \frac{V_{dc1}}{R_{L1}} + \frac{V_{dc1} + V_{dc2}}{R_{L3}} \tag{9.16}$$

$$-\frac{3}{2}\left(M_{qs2} I_{qs2} + M_{ds2} I_{ds2}\right) = \frac{V_{dc2}}{R_{L2}} + \frac{V_{dc1} + V_{dc2}}{R_{L3}} \tag{9.17}$$

Substituting (9.12-9.15) into the left hand side of (9.16-9.17) and eliminating the q- and d-axis modulation indexes and currents, the dc voltage equations are expressed in terms of the machine parameters, rotor flux linkages, rotor speed and slip frequencies as:

$$\frac{V_{dc1}^2}{R_{L1}} + \frac{V_{dc1} + V_{dc2}}{R_{L3}} V_{dc1} = -3\left[ r_1 \left( \frac{L_{r1} \lambda_{dr1}}{r_{r1} L_{m1}} \right)^2 \omega_{s1}^2 + \frac{\omega_{r1} \lambda_{dr1}^2}{r_{r1}} \omega_{s1} + r_1 \frac{\lambda_{dr1}^2}{L_{m1}^2} - \frac{r_{r1}}{L_{r1}^2} \lambda_{dr1}^2 \right] \tag{9.18}$$

$$\frac{V_{dc2}^2}{R_{L2}} + \frac{V_{dc1} + V_{dc2}}{R_{L3}} V_{dc2} = -3\left[ r_2 \left( \frac{L_{r2} \lambda_{dr2}}{r_{r2} L_{m2}} \right)^2 \omega_{s2}^2 + \frac{\omega_{r2} \lambda_{dr2}^2}{r_{r2}} \omega_{s2} + r_2 \frac{\lambda_{dr2}^2}{L_{m2}^2} - \frac{r_{r2}}{L_{r2}^2} \lambda_{dr2}^2 \right] \tag{9.19}$$

If the rotor speed and the rotor flux linkages are fixed to certain values and the slip frequencies of both stator windings are known, the corresponding dc voltages are expressed as:

$$V_{dc1}^2 = \frac{-b \pm \sqrt{b^2 - 4ac}}{2a} \tag{9.20}$$

$$V_{dc2} = \sqrt{\left( \frac{R_{L1} + R_{L3}}{R_{L1} R_{L3}} V_{dc1}^2 - \delta_1 + \delta_2 \right) \frac{R_{L2} R_{L3}}{R_{L2} + R_{L3}}} \tag{9.21}$$

where, $\delta_1 = -3\left[ r_1 \left( \frac{L_{r1} \lambda_{dr1}}{r_{r1} L_{m1}} \right)^2 \omega_{s1}^2 + \frac{\omega_{r1} \lambda_{dr1}^2}{r_{r1}} \omega_{s1} + r_1 \frac{\lambda_{dr1}^2}{L_{m1}^2} - \frac{r_{r1}}{L_{r1}^2} \lambda_{dr1}^2 \right]$,

$\delta_2 = -3\left[ r_2 \left( \frac{L_{r2} \lambda_{dr2}}{r_{r2} L_{m2}} \right)^2 \omega_{s2}^2 + \frac{\omega_{r2} \lambda_{dr2}^2}{r_{r2}} \omega_{s2} + r_2 \frac{\lambda_{dr2}^2}{L_{m2}^2} - \frac{r_{r2}}{L_{r2}^2} \lambda_{dr2}^2 \right]$,

$a = \frac{R_{L1} + R_{L3}}{R_{L1} R_{L3}^2} \frac{R_{L2}}{R_{L2} + R_{L3}} - \left( \frac{R_{L1} + R_{L3}}{R_{L1} R_{L3}} \right)^2$, $b = \frac{(\delta_2 - \delta_1) R_{L2}}{R_{L3} (R_{L2} + R_{L3})} + 2\delta_1 \frac{R_{L1} + R_{L3}}{R_{L1} R_{L3}}$ and

$c = -\delta_1^2$.

The contours of the dc voltages are shown in Figure 9.2 (a), where the contours of the ABC winding set rectifier output dc voltage are represented as slanting vertical dash lines while the contours of the dc output voltage of the rectifier connected to the XYZ winding set are represented as horizontal solid lines. The dc voltage generated by the rectifier connected to the ABC winding set depends significantly on the slip frequency of the ABC winding set and less on the slip frequency of the XYZ winding set. A similar conclusion applies to the second rectifier dc output voltage. To generate reasonable dc output voltages from (9.20-9.21), the condition $b^2 - 4ac \geq 0$ must be true, giving the

boundary of the rotor slip frequencies graphically illustrated in Figure 9.2 (b) for specific rotor speed and rotor flux references.

Reasonable dc voltages can only be obtained when the choice of slip frequencies for the winding sets is within the possible regions shown in Figure 9.2(b). However, the first quadrant is the feasible operability region. If the dc voltages and rotor speeds are known, the relationship between the slip frequencies and rotor flux linkages can be found as shown in Figure 9.3(a) for the rectifier connected to the XYZ winding set, where the set dc output voltage is 200V and five different rotor speeds ranging from 1200 rpm to 3600 rpm are considered.

If the value of d-axis flux linkage is given and the rectifier dc voltage of the ABC winding set is fixed, the boundary value of the rotor speed is expressed as:

$$\omega_{r1} = \sqrt{4r_1\left(\frac{L_{r1}}{L_{m1}}\right)^2\left[\frac{r_1}{L_{m1}^2} - \frac{r_{r1}}{L_{r1}^2} + \left(\frac{V_{dc1}^2}{R_{L1}} + \frac{V_{dc1}+V_{dc2}}{R_{L3}}V_{dc1}\right)\Big/ 3\lambda_{dr1}^2\right]} \tag{9.22}$$

A similar boundary equation can be derived for the rectifier connected to the XYZ winding set. The boundaries for the possible generated dc voltages are shown in Figure 9.3 (b), where the solid line represents the boundary for the rectifier connected to the ABC winding set while the dashed line gives the limits of the rectifier connected to the XYZ winding set. The right hand side of the boundary lines gives the possible operating range for the two rectifiers.

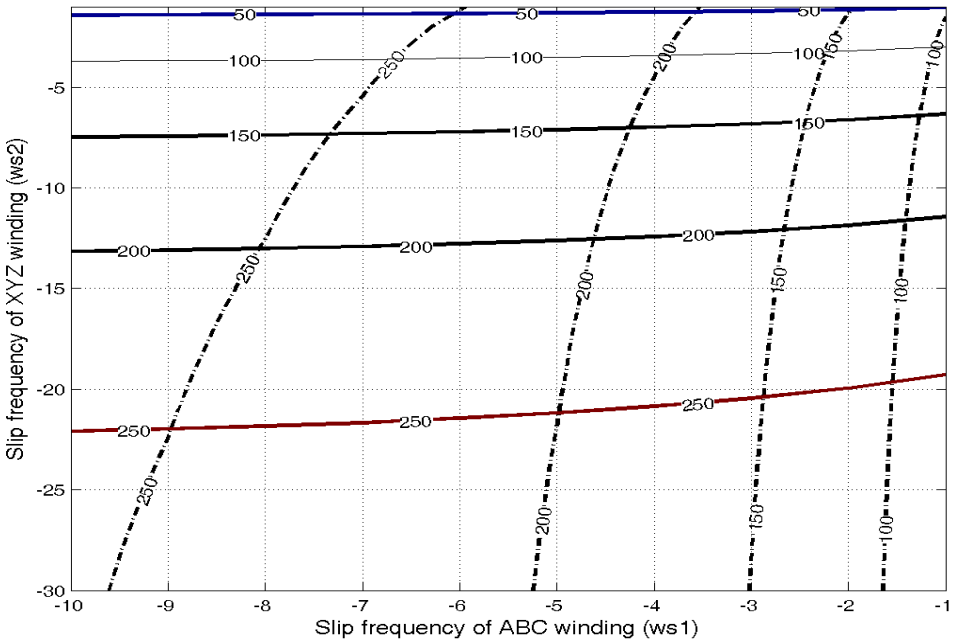


(a) $V_{dc1}$ and $V_{dc2}$ contour

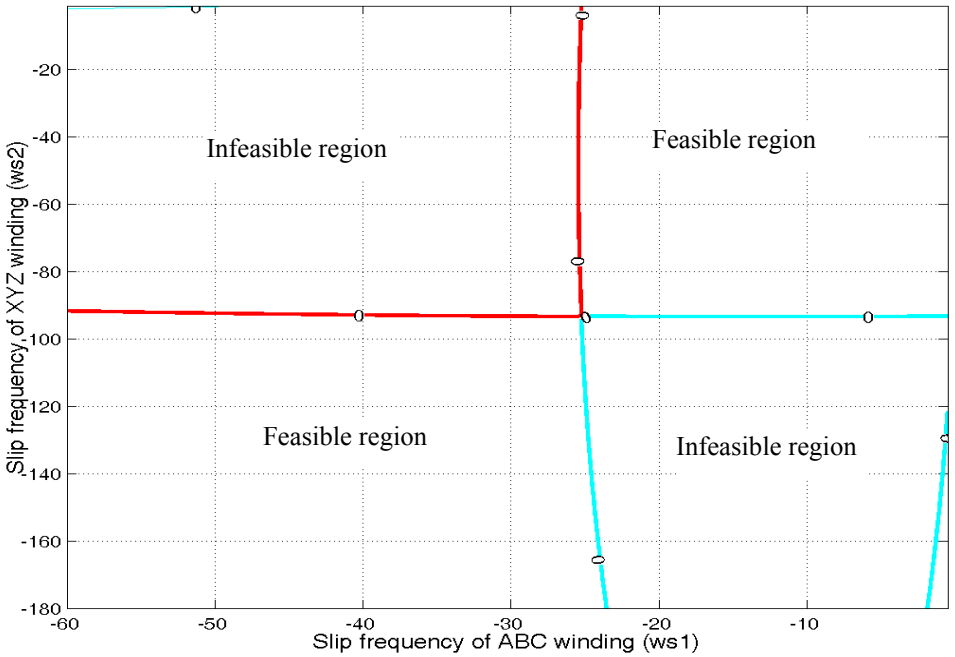


(b) Slip boundary for the existence of the dc voltage

Figure 9.2. Steady state operation of a dual winding induction machine with two series connected rectifiers. (a) contour of dc voltages; (b) the operating boundaries of the slip frequencies of the windings for dc voltage.

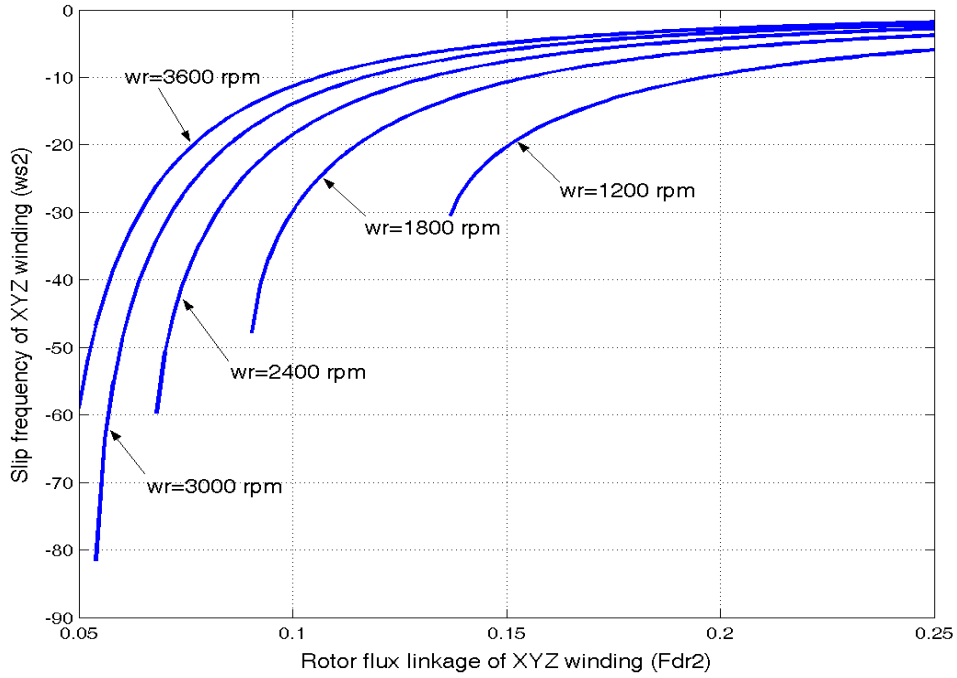


(a)

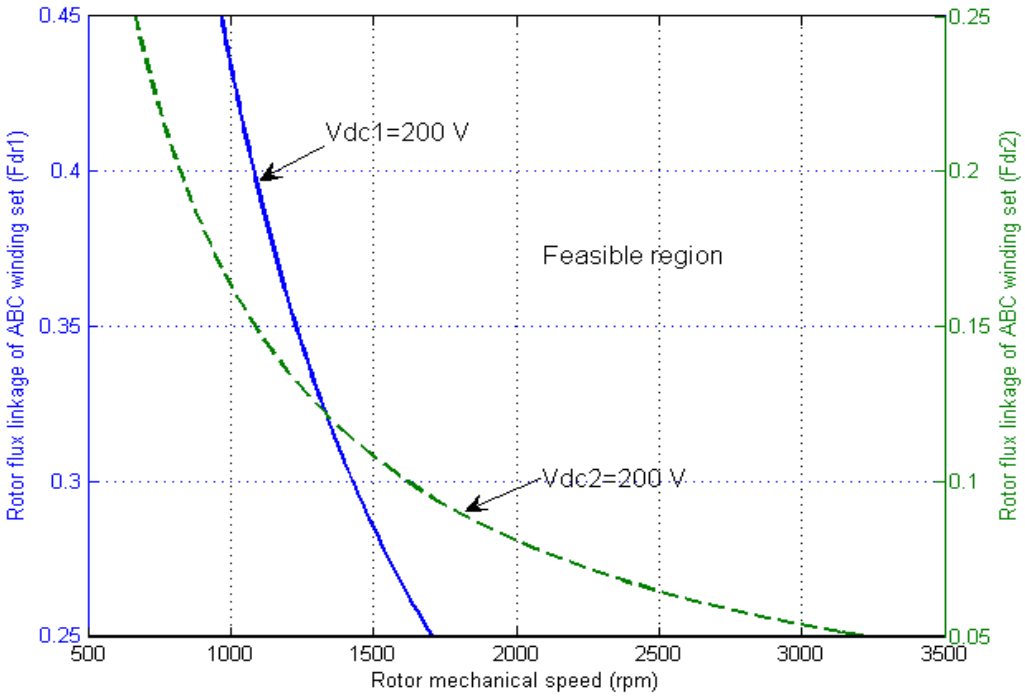


(b)

Figure 9.3. Operability region of a dual winding induction machine with two series connected rectifiers under a constant dc voltage condition. (a) Relationship between slip frequency and rotor flux density under constant dc voltage for the XYZ windings; (b) Boundary of generator operation under constant dc voltage

The influences of the saturation of the magnetizing flux linkage and the ratio of each rectifier dc voltage with respect to the total dc voltage on generator performance are considered. The relationship between the output rectifier dc voltage of the ABC winding set and the total output dc voltage is $V_{dc1} = \gamma \cdot V_{dc}$, where $\gamma$ ranges between 0 and 1. The modulation magnitudes of the rectifiers ($M_1$, $M_2$) are given as:

$$\left|M_1\right|^2 = \frac{-4}{3}\left(\frac{1}{R_{L1}} + \frac{1}{\gamma \cdot R_{L3}}\right) \Bigg/ \operatorname{Re}\left\{\frac{\left[\frac{L_{r1}}{D_1} - \frac{L_{m1}A_{r1}}{D_1\left(B_{r1} - j\omega_{s1}\right)}\right]}{\left[C_{s1} - \frac{A_{s1}A_{r1}}{B_{r1} - j\omega_{s1}} - j\omega_{e1}\right]}\right\} \tag{9.23}$$

$$\left|M_2\right|^2 = \frac{-4}{3}\left(\frac{1}{R_{L2}} + \frac{1}{(1-\gamma)R_{L3}}\right) \Bigg/ \operatorname{Re}\left\{\frac{\left[\frac{L_{r2}}{D_2} - \frac{L_{m2}A_{r2}}{D_2\left(B_{r2} - j\omega_{s2}\right)}\right]}{\left[C_{s2} - \frac{A_{s1}A_{r1}}{B_{r2} - j\omega_{s2}} - j\omega_{e2}\right]}\right\} \tag{9.24}$$

where, $A_{si} = \frac{r_{si}L_{ri}}{L_{\delta i}}$, $A_{ri} = \frac{r_{ri}L_{si}}{L_{\delta i}}$, $B_{si} = \frac{-r_i L_{mi}}{L_{\delta i}}$, $B_{ri} = \frac{-r_{ri}L_{mi}}{L_{\delta i}}$, $C_{si} = \frac{r_{si}L_{ri}}{D_i}$,

$D_i = L_{si}L_{ri} - L_{mi}^2$, $i = 1 \; or \; 2$.

The stator current is expressed in complex variable form in term of stator flux linkages as:

$$I_{qdsi} = \left(\frac{L_{ri}}{D_i} + \frac{L_{mi}}{D_i}\frac{A_{ri}}{B_{ri} - j\omega_{si}}\right)\lambda_{qdsi} \tag{9.25}$$

The magnetizing flux linkage is expressed in terms of stator flux linkages as:

$$\lambda_{qdmi} = \frac{L_{mi}}{D_i}\left(L_{lri} + L_{lsi}\frac{A_{ri}}{B_{ri} - j\omega_{si}}\right)\lambda_{qdsi} \tag{9.26}$$

The total dc voltage equation now expressed in terms of the variables of the ABC winding set becomes:

$$V_{dc} = -\frac{3R_{L3}R_{L1}}{2\left(R_{L1}+\gamma\cdot R_{L3}\right)}\mathrm{Re}\left[M^{*}_{qds1}\lambda_{qdm1}\frac{L_{lr1}+L_{m1}\dfrac{A_{r1}}{B_{r1}-j\omega_{s1}}}{L_{m1}\left(L_{lr1}+L_{ls1}\dfrac{A_{r1}}{B_{r1}-j\omega_{s1}}\right)}\right] \tag{9.27}$$

A similar equation can be obtained from the XYZ winding set as shown in (9.28).

$$V_{dc} = -\frac{3R_{L3}R_{L2}}{2\left(R_{L2}+(1-\gamma)R_{L3}\right)}\mathrm{Re}\left[M^{*}_{qds2}\lambda_{qdm2}\frac{L_{lr2}+L_{m2}\dfrac{A_{r2}}{B_{r2}-j\omega_{s2}}}{L_{m2}\left(L_{lr2}+L_{ls2}\dfrac{A_{r2}}{B_{r2}-j\omega_{s2}}\right)}\right] \tag{9.28}$$

The saturation effect of the induction generator is included in the analysis by varying the magnetizing inductance with the magnetizing flux linkage. The main flux saturation curve fit of the experimental results of 2-pole ABC winding set is shown in Figure 9.4(a). Fixing the coefficient $\gamma$, the slip and the load resistances to be constant and varying the magnetizing flux linkage, the variation of the magnitude of the modulation index with the magnetizing flux can be found from (9.23-9.24) is displayed in Figure 9.4(a). Three different load resistance values have been given to $R_{L1}$ to demonstrate the influence of the load resistance on dc voltage generation. The ellipses relating the dc voltage and q-axis modulation index of the ABC winding set at different load resistance values are shown in Figure 9.4 (b). Similar curves for the rectifier connected to the XYZ windings can be calculated using (9.28). Under constant $\gamma$, constant slip, constant magnetizing flux linkage and a constant load resistance condition, by varying the q-axis modulation index, the variation of dc voltage of the rectifier connected to the ABC winding set is in the form of ellipse shown in Figure 9.5(a). Note that equations (9.26-9.27) independently define the same output dc voltage $V_{dc}$. It follows that the feasible values are defined by the overlapping regions of the two curves. As can be seen from the Figure 9.4(b) and

Figure 9.5(a), by varying the q-axis modulation index, a maximum output dc voltage corresponding to a certain magnetizing flux value can be generated under a constant slip and constant load resistance condition. The variation of the maximum output dc voltage with the magnetizing flux linkage for a constant slip and a constant load resistance is shown in Figure 9.5(b). The load resistance $R_{L3}$ is also constant in Figure 9.5. It should be noted that equations (9.18-9.19) are mutually constrained, defined in (9.29), so that the slip frequencies of two winding sets depend on each other if the rotor speed, the rotor flux linkages of both winding sets and coefficient $\gamma$ are all fixed.

$$\begin{aligned}&\left[r_1\left(\frac{L_{r1}\lambda_{dr1}}{r_{r1}L_{m1}}\right)^2\omega_{s1}^2+\frac{\omega_{r1}\lambda_{dr1}^2}{r_{r1}}\omega_{s1}+r_1\frac{\lambda_{dr1}^2}{L_{m1}^2}-\frac{r_{r1}}{L_{r1}^2}\lambda_{dr1}^2\right]\frac{\gamma^2}{1/R_{L1}+1/(\gamma\cdot R_{L3})}\\&=\left[r_2\left(\frac{L_{r2}\lambda_{dr2}}{r_{r2}L_{m2}}\right)^2\omega_{s2}^2+\frac{\omega_{r2}\lambda_{dr2}^2}{r_{r2}}\omega_{s2}+r_2\frac{\lambda_{dr2}^2}{L_{m2}^2}-\frac{r_{r2}}{L_{r2}^2}\lambda_{dr2}^2\right]\frac{(1-\gamma)^2}{1/R_{L2}+1/[(1-\gamma)R_{L3}]}\end{aligned}\tag{9.29}$$

This constraint is applied in the selection of slip frequencies in the above analysis. The simulation results of equation (9.29) under different rotor speed conditions are given in Figure 9.6 when $\lambda_{dr1}=0.45$ Wb, $\lambda_{dr2}=0.15$ Wb, $\gamma=0.6$, $R_{L1}=80\,\Omega$, $R_{L2}=80\,\Omega$ and $R_{L3}=200\,\Omega$.

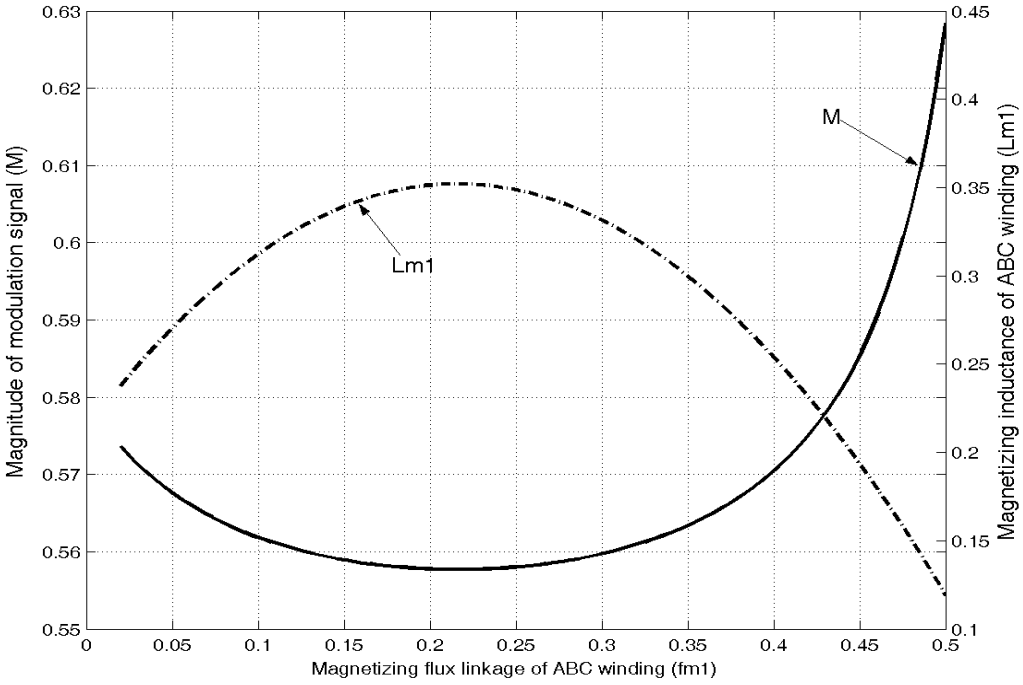


(a)

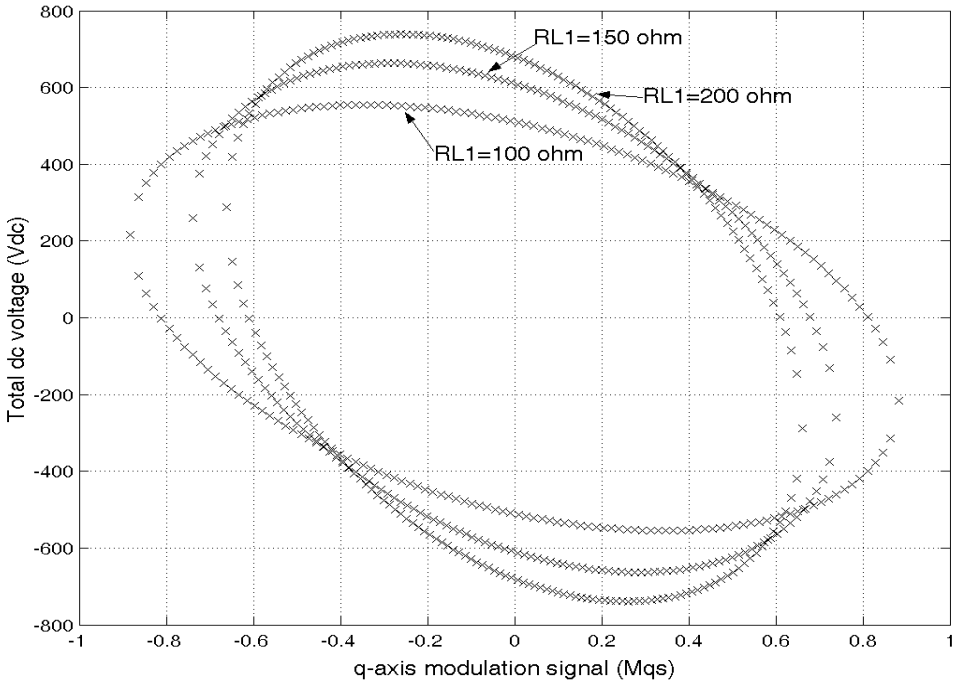


(b)

Figure 9.4 Steady state analysis, (a) the magnetizing inductance and magnitude of modulation index vs magnetizing flux, (b) dc voltage and q-axis modulation index for the ABC winding set under different load conditions.

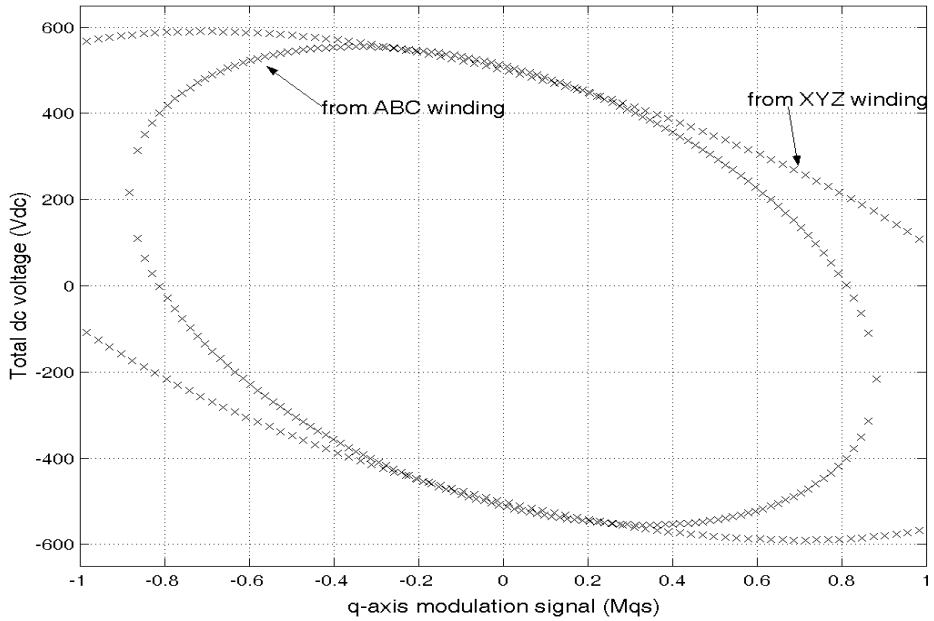


(a)

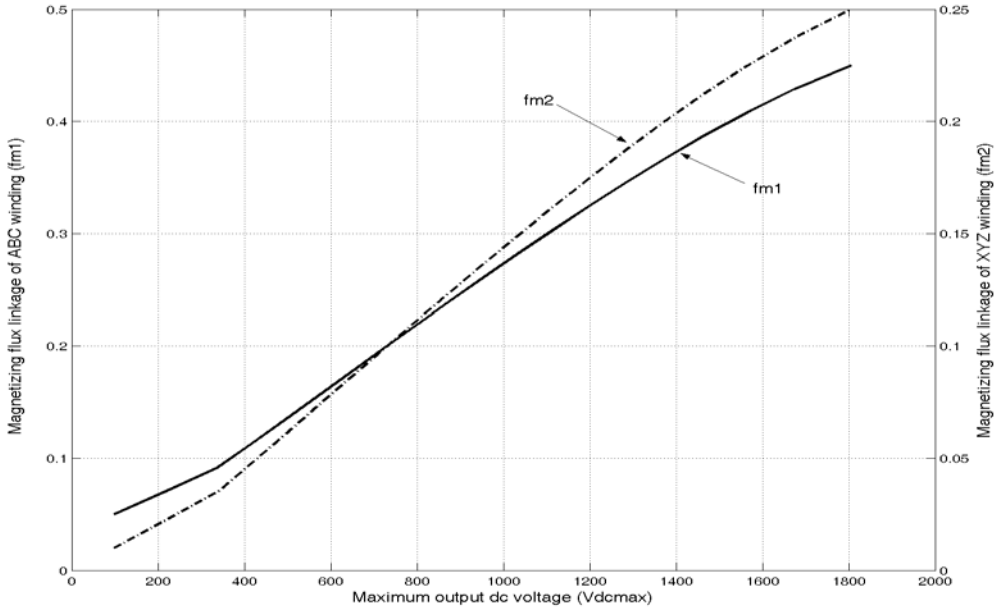


(b)

Figure 9.5 Steady state analysis, (a) dc voltage and q-axis modulation index for both (ABC and XYZ) winding sets, (b) maximum dc voltage and magnetizing flux of both stator winding sets

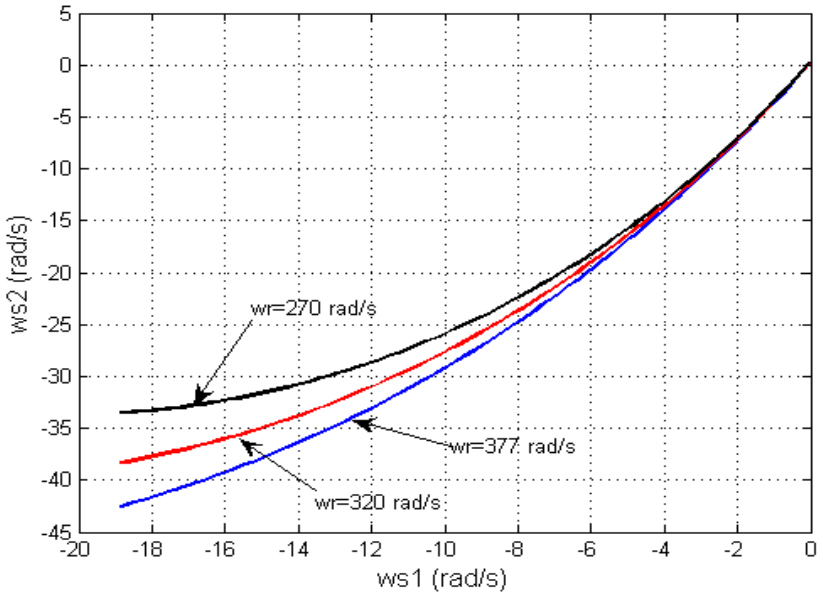


Figure 9.6 The relationship between the slip frequencies of two stator winding sets under different rotor speeds

## 9.4 Control Scheme

The input-output linearization method with decoupling is used to remove the non-linearity and model interacting terms. Hence, the classic linear system control methodology can be used to determine the parameters of the controllers. The control variables here are $M_{qs1}$, $M_{ds1}$ and $M_{qs2}$, $M_{ds2}$. The controlled variables are the dc voltages $V_{dc1}$, $V_{dc2}$ , the rotor flux linkages of the ABC winding set $\lambda_{qr1}$ and $\lambda_{dr1}$, the rotor flux linkages of the XYZ winding set $\lambda_{qr2}$ and $\lambda_{dr2}$. The input-output linearization process has been described in Chapter 8.

Multiplying (9.9) and (9.10) with $V_{dc1}$ and $V_{dc2}$ respectively and replacing the modulation signals with the corresponding q- and d-axis voltages we have,

$$\frac{1}{2}C_1 pV_{dc1}^2 + \frac{V_{dc1}^2}{R_{L1}} + \frac{V_{dc1}^2}{R_{L3}} + \frac{(1-K)V_{dc1}^2}{KR_{L3}} = \frac{3}{2}\left(V_{qs1}i_{qs1} + V_{ds1}i_{ds1}\right) = \sigma_{dc1} \tag{9.30}$$

$$\frac{1}{2}C_2 pV_{dc2}^2 + \frac{V_{dc2}^2}{R_{L2}} + \frac{V_{dc2}^2}{R_{L3}} + \frac{KV_{dc2}^2}{(1-K)R_{L3}} = \frac{3}{2}\left(V_{qs2}i_{qs2} + V_{ds2}i_{ds2}\right) = \sigma_{dc2} \tag{9.31}$$

From (9.3-9.4), the slip frequency and the reference stator d-axis current of the 2-pole (ABC) winding set are given as :

$$\left(\omega_{e1} - \omega_{r1}\right) = -\frac{\sigma_{qr1}}{\lambda_{dr1}} + \frac{r_{r1}L_{m1}}{L_{r1}} \cdot \frac{I_{qs1}}{\lambda_{dr1}} \tag{9.32}$$

$$I_{ds1}^* = \left[\sigma_{dr1} - \left(\omega_{e1} - \omega_{r1}\right)\lambda_{qr1}\right]\frac{L_{r1}}{r_{r1}L_{m1}} \tag{9.33}$$

The command (reference) q and d axis stator voltages of the 2-pole winding set from (9.1-9.2) are expressed as :

$$V_{qs1}^* = \sigma_{qs1} + \omega_{e1}L_{\sigma 1}I_{ds1} - \frac{r_{r1}L_{m1}}{L_{r1}^2}\lambda_{qr1} + \omega_{r1}\frac{L_{m1}}{L_{r1}}\lambda_{dr1} \tag{9.34}$$

$$V_{ds1}^* = \sigma_{ds1} - \omega_{e1}L_{\sigma 1}I_{qs1} - \frac{r_{r1}L_{m1}}{L_{r1}^2}\lambda_{dr1} - \omega_{r1}\frac{L_{m1}}{L_{r1}}\lambda_{qr1} \tag{9.35}$$

The unknown quantities $\sigma_{qs1}$, $\sigma_{ds1}$, $\sigma_{qr1}$, $\sigma_{dr1}$ and $\sigma_{dc1}$ are the outputs of controllers of the ABC winding set which are defined from (9.1-9.4, 9.30). A similar analysis undertaken for the ABC winding set also gives the controller structure for the XYZ winding set The complete control strategy and the open-loop flux estimation scheme are given in Figure 9.7. The equations for the d-axis current controller, the slip calculation and the command voltages calculations of the 6-pole XYZ winding set are eliminated in Figure 9.7 to avoid repetition. To achieve field orientation control, the reference q-axis flux linkages are set equal to zero and the d-axis flux linkage references are either fixed or manipulated to achieve minimum motor loss while the dc voltages are regulated.

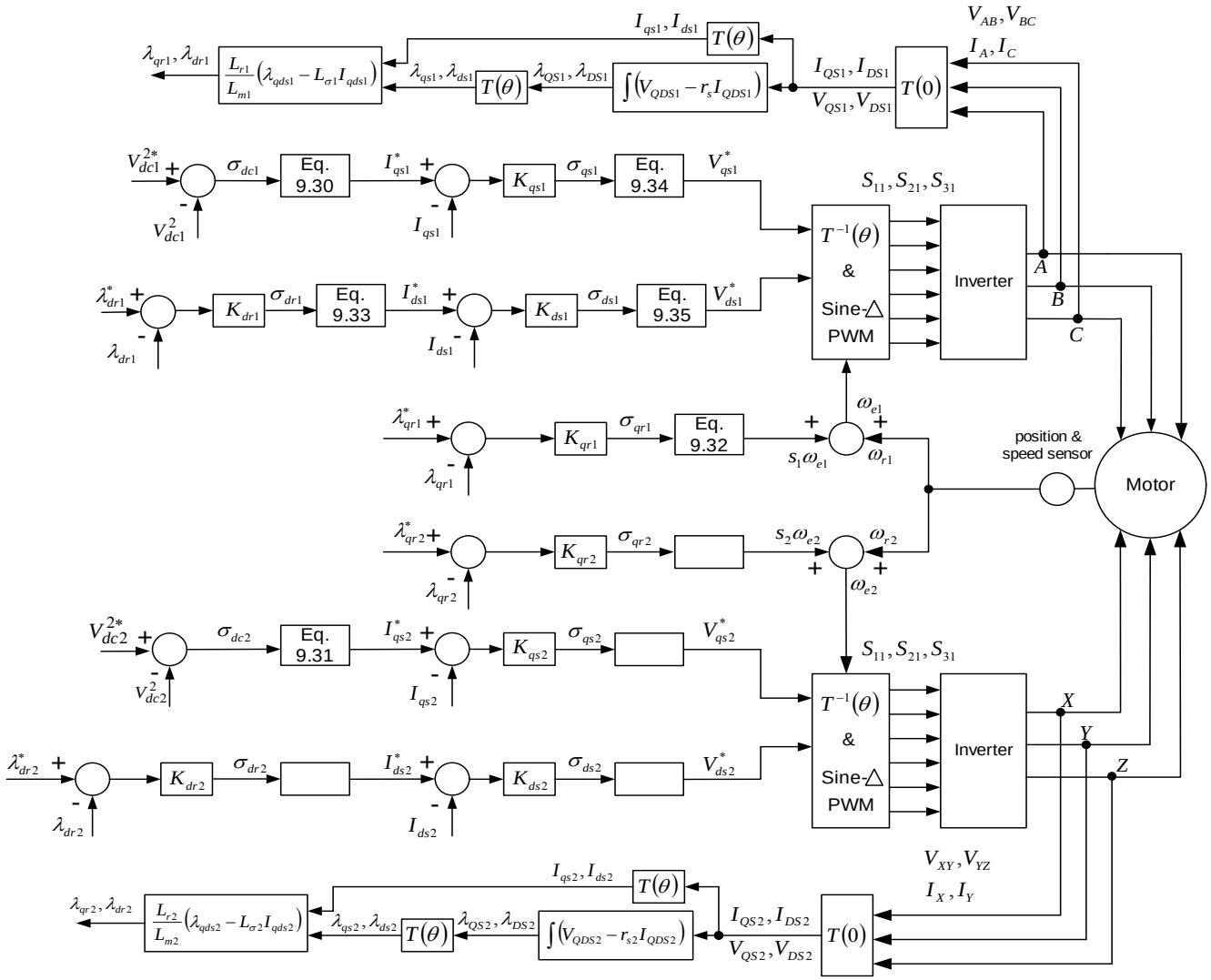


Figure 9.7. The control scheme of the purposed method

If the PI controllers are used and the parameters of the controllers are given as defined below (i.e. $K_{pqs1}$ and $K_{iqs1}$ are the controller parameters for q-axis current controller), the transfer functions of the state variables are:

$$\frac{V_{dc1}^2}{V_{dc1}^{*2}} = \frac{K_{p1}p + K_{i1}}{\frac{1}{2}C_1 p^2 + \left(1/R_{L1} + 1/KR_{L3} + K_{p1}\right)p + K_{i1}} \tag{9.36}$$

$$\frac{\lambda_{qr1}}{\lambda_{qr1}^*} = \frac{K_{pqr1}p + K_{iqr1}}{p^2 + \left(K_{pqr1} + r_{r1}/L_{r1}\right)p + K_{iqr1}} \tag{9.37}$$

$$\frac{\lambda_{dr1}}{\lambda_{dr1}^*} = \frac{K_{pdr1}p + K_{idr1}}{p^2 + \left(K_{pdr1} + r_{r1}/L_{r1}\right)p + K_{idr1}} \tag{9.38}$$

$$\frac{I_{qs1}}{I_{qs1}^*} = \frac{K_{pqs1}p + K_{iqs1}}{p^2 + \left(K_{pqs1}/L_{\sigma 1} + r_1/L_{\sigma 1}\right)p + K_{iqs1}/L_{\sigma 1}} \tag{9.39}$$

$$\frac{I_{ds1}}{I_{ds1}^*} = \frac{K_{pds1}p + K_{ids1}}{p^2 + \left(K_{pds1}/L_{\sigma 1} + r_1/L_{\sigma 1}\right)p + K_{ids1}/L_{\sigma 1}} \tag{9.40}$$

The Butterworth method is applied to design the parameters of the controllers. Controller parameters are calculated by comparing the Butterworth polynomial with the denominator of the transfer functions. The zeros of the transfer functions can influence the system performance. The determination of controller parameters should ensure the minimum phase system requirement (all the zeros have negative real parts), which can be ensured in this case when $k_p$ and $k_i$ of a controller have the same sign. Normally, these control parameters are all chosen to be positive. The controller parameters in the simulation are given in Table 9.1

Table 9.1 Parameters of controllers in series-connected generating system

| Controller name | 2-pole ABC winding | 6-pole XYZ winding |
|---|---|---|
| Q-axis current | $k_{pqs1} = 24.18$, $k_{iqs1} = 19708$ | $k_{pqs2} = 21.92$, $k_{iqs2} = 17147$ |
| D-axis current | $k_{pds1} = 24.18$, $k_{ids1} = 19708$ | $k_{pds2} = 21.92$, $k_{ids2} = 17147$ |
| Q-axis rotor flux linkage | $k_{pqr1} = 13.2$, $k_{iqr1} = 100$ | $k_{pqr2} = 8.56$, $k_{iqr2} = 100$ |
| D-axis rotor flux linkage | $k_{pdr1} = 140.5$, $k_{idr1} = 10e4$ | $k_{pdr2} = 135.8$, $k_{idr2} = 10e4$ |
| DC voltage | $k_{pdc} = 0.0396$, $k_{idc} = 0.1053$ | |

## 9.5 Simulation and Experimental Results

The proposed control scheme has been simulated in MATLAB/SIMULINK. The machine parameters are the same as the parameters given in Table 8.2. The computer simulation results in Figure 9.8 show the starting process of the generator. The rotor ramps up from 955 to 1600 rpm from 0 to 0.34 seconds and is maintained at 1600 rpm thereafter. The dynamic responses of the control scheme to changes in load, portioning voltage coefficient $\gamma$ and rotor speed are also shown in Figure 9.9. At t = 3 seconds the coefficient $\gamma$ is changed from 0.5 to 0.3. At t = 2.5 seconds, the rotor speed is changed to 1791 rpm and returns to 1600 rpm at t=3 second as shown in Figure 9.9(c). The load resistance $R_{L3}$ is changed from 600 Ω to 300 Ω at t = 2 seconds, then the load resistance $R_{L1}$ is then changed from 300 Ω to 120 Ω at t = 3.5 seconds, and finally the load resistance $R_{L2}$ is changed from 400 Ω to 200 Ω at t = 4 seconds to observe how these changes influence the developed torque of each winding and the output dc voltage

regulation capabilities of the controllers. The variations of the load resistance are given in Figure 9.9(q). Significant redistribution of active power from each stator winding set is manifested in the value of the electromagnetic torques. For changes in load resistances, output dc voltage distribution coefficient ($\gamma$) or rotor speed, the controlled dc voltage effectively tracks the commands. The simulation results of the dynamic responses of the system to the changing parameters, which are given in Figure 9.10, are used to check the robustness of the control scheme. The magnetizing inductances of both stator winding sets are increased by 10% of their rated values while the rotor resistances increase by 50% of their rated values as shown in Figure 8.7 (n, p and q). During the variations of all these parameters, the output dc voltage is well regulated to be constant. It is observed from the simulation results that the changes of the rotor resistances of both winding set have bigger influences to the system than those of the variation of magnetizing inductances, which can be observed from the waveforms of the corresponding voltages. The proposed system and its control scheme have been experimentally implemented using TMS320LF2407A DSP. Two voltage source inverters are serially connected while each of them feeds a stator winding set as shown in Figure 9.1. The dual winding induction generator is coupled with a dc machine by the rotor shaft and the dc machine is used to drive the generating system. At the beginning, the rotor speed of generator is fixed at 1600 rpm. Small initial voltages are supplied to the capacitors of the PWM rectifiers connected to the both winding sets. Then the DSP controller starts to send out the control PWM signals. The starting processes of the ABC and XYZ winding sets are shown in Figure 9.11(a) and (b) respectively. The dc voltages ramp from 0 to 200 V. The steady state waveforms of the generator windings are shown in Figure 9.12 (a-b).

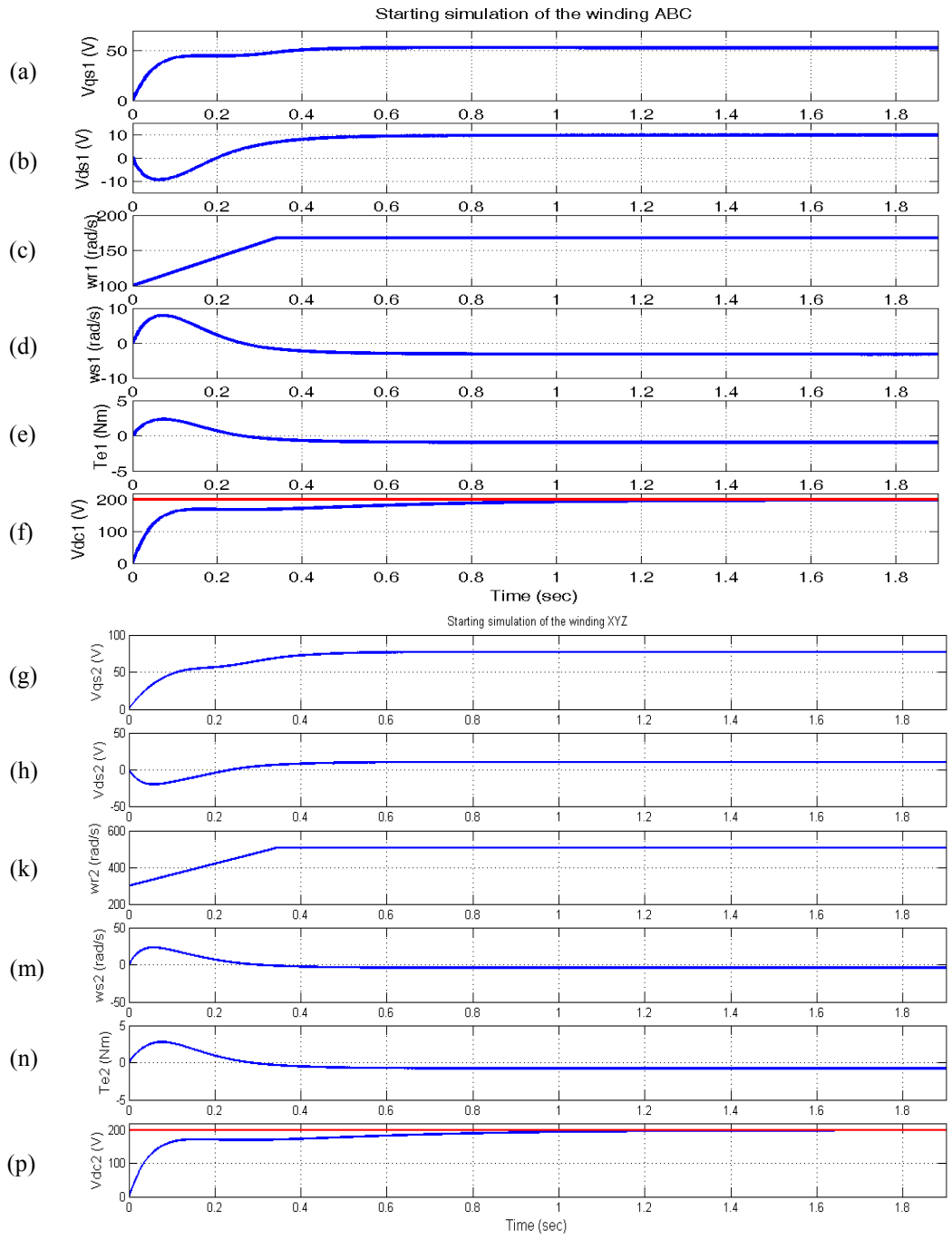


Figure 9.8. Simulation results for starting process, from top: (a) q-axis voltage $V_{qs1}$ of ABC windings, (b) d-axis voltage $V_{ds1}$ of ABC windings, (c) rotor electric speed $\omega_{r1}$ of ABC windings, (d) slip frequency $\omega_{s1}$ of ABC windings, (e) electromagnetic torque $T_{e1}$ of ABC windings, (f) command and actual dc voltage $V_{dc1}$, (g) q-axis voltage $V_{qs2}$ of XYZ windings, (h) d-axis voltage $V_{ds2}$ of XYZ windings, (k) rotor electric speed $\omega_{r2}$ of XYZ windings, (m) slip frequency $\omega_{s2}$ of XYZ windings, (n) electromagnetic torque $T_{e2}$ of XYZ windings, (p) command and actual dc voltage $V_{dc2}$.

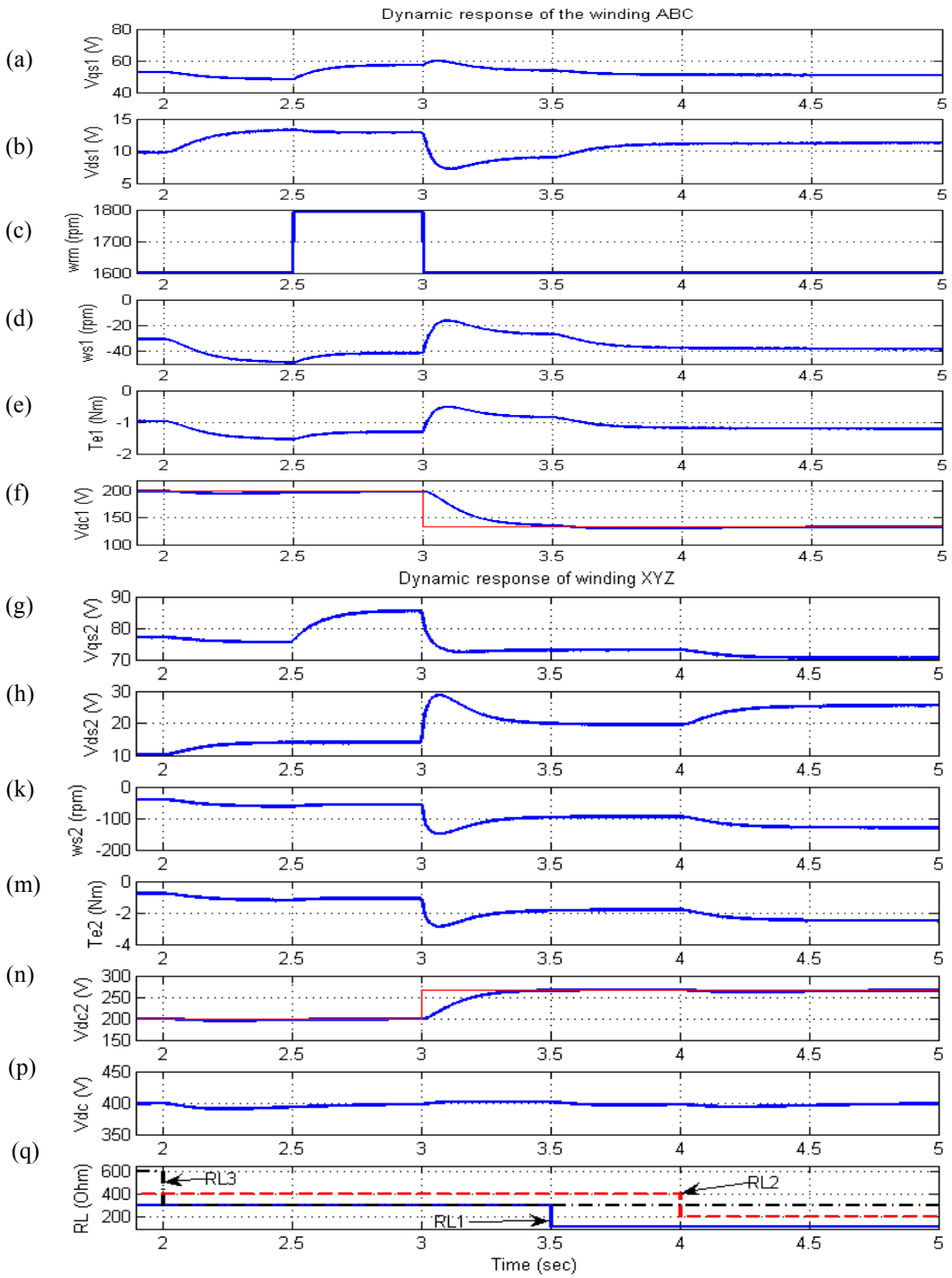


Figure 9.9. The dynamic response of changing load, $\gamma$ and the rotor speed, from top: (a) q-axis voltage $V_{qs1}$ of ABC windings, (b) d-axis voltage $V_{ds1}$ of ABC windings, (c) rotor mechanical speed $\omega_{rm}$, (d) slip frequency $\omega_{s1}$ of ABC windings, (e) electromagnetic torque $T_{e1}$ of ABC windings, (f) command and actual dc voltage $V_{dc1}$, (g) q-axis voltage $V_{qs2}$ of XYZ windings, (h) d-axis voltage $V_{ds2}$ of XYZ windings, (k) slip frequency $\omega_{s2}$ of XYZ windings, (m) electromagnetic torque $T_{e2}$ of XYZ windings, (n) command and actual dc voltage $V_{dc2}$, (p) total dc voltage, (q) load resistances.

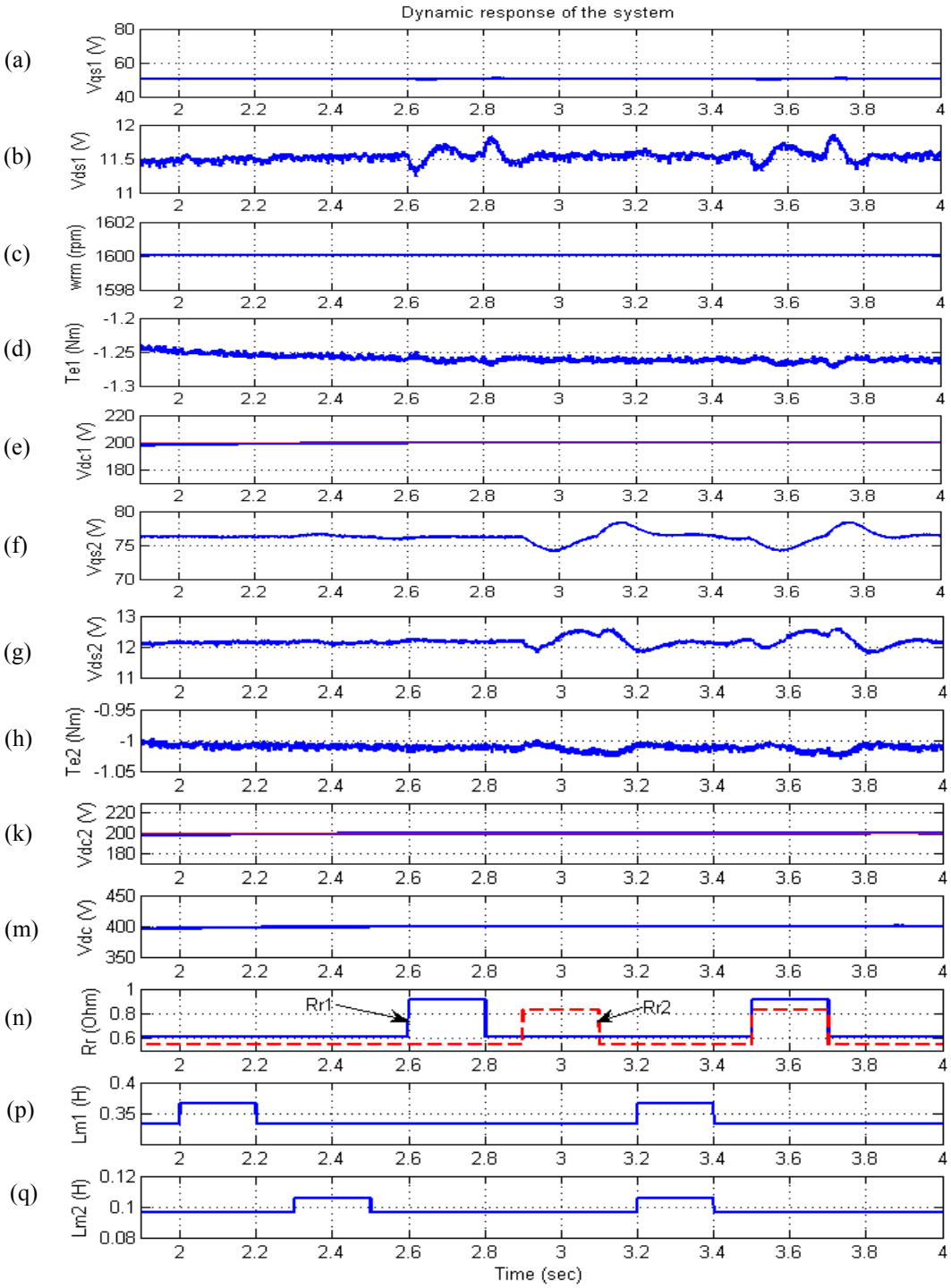


Figure 9.10. The dynamic response of changing parameters, from top: (a) q-axis voltage $V_{qs1}$ of ABC windings, (b) d-axis voltage $V_{ds1}$ of ABC windings, (c) rotor mechanical speed $\omega_{rm}$, (d) electromagnetic torque $T_{e1}$ of ABC windings, (e) command and actual dc voltage $V_{dc1}$, (f) q-axis voltage $V_{qs2}$ of XYZ windings, (g) d-axis voltage $V_{ds2}$ of XYZ windings, (h) electromagnetic torque $T_{e2}$ of XYZ windings, (k) command and actual dc voltage $V_{dc2}$, (m) total dc voltage, (n) rotor resistances, (p) magnetizing inductance of ABC windings, (q) magnetizing inductance of XYZ windings

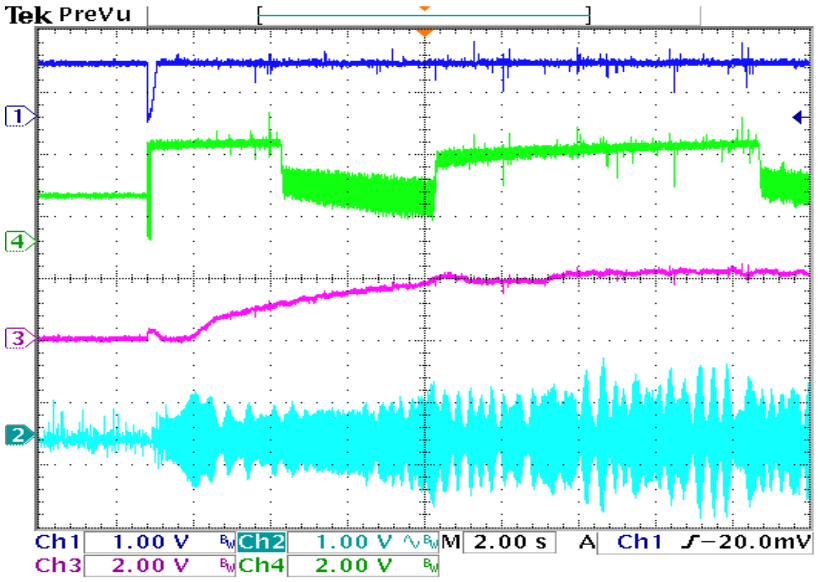


(a)

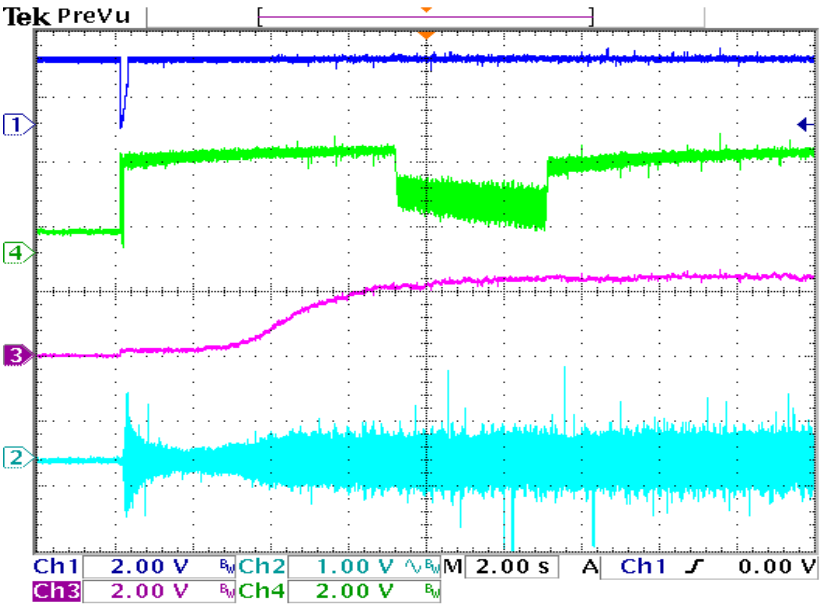


(b)

Figure 9.11. The starting process of the dual winding generator, (a) Starting process of ABC windings, from top: (1) d-axis voltage $V_{ds1}$; (2) q-axis voltage $V_{qs1}$; (3) dc voltage $V_{dc1}$ (200 V/div); (4) phase A current $I_a$ (4 A/div), (b) XYZ windings, from top (1) d-axis voltage $V_{ds2}$; (2) q-axis voltage $V_{qs2}$; (3) dc voltage $V_{dc2}$ (167 V/div); (4) phase X current $I_x$ (4.5 A/div).

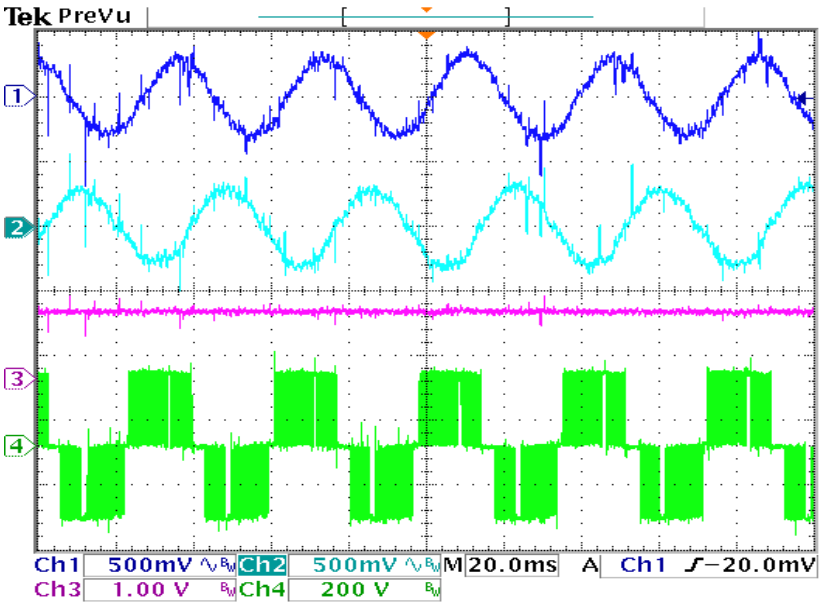


(a)

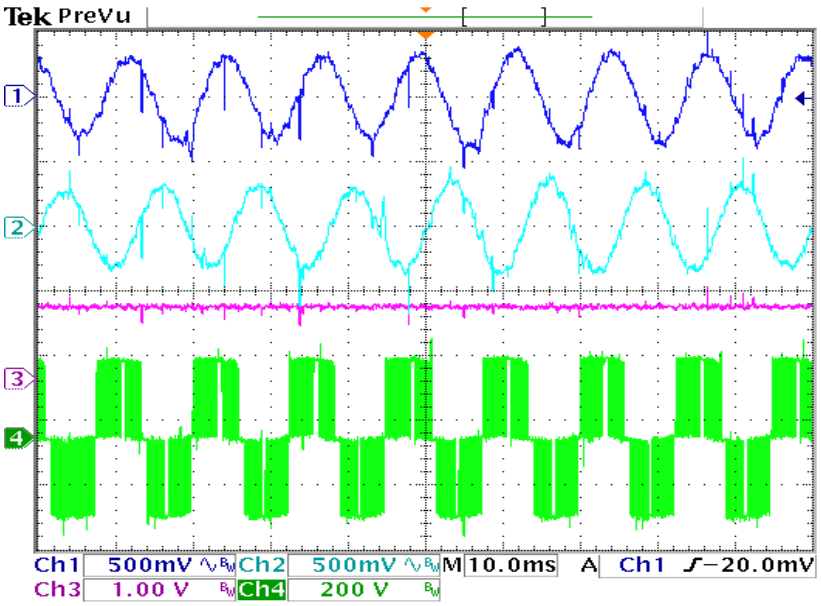


(b)

Figure 9.12. The steady state waveforms of the dual winding generator, (a) ABC windings, from top: (1) phase A current $I_a$ (4.3 A/div); (2) phase B current $I_b$ (4.3 A/div); (3) dc voltage $V_{dc1}$ (200 V/div); (4) line-to-line voltage $V_{bc}$ (200 V/div), (b) XYZ windings, from top: (1) phase X current $I_x$ (4.3 A/div); (2) phase Y current $I_y$ (4.3 A/div); (3) dc voltage $V_{dc2}$ (200 V/div); (4) line-to-line voltage $V_{yz}$ (200 V/div).

## 9.6 Conclusions

The high performance control scheme of the dual-winding induction generator with two series connected ac-dc PWM boost rectifiers has been outlined. The steady state analysis exploring the influences of the main flux saturation and operational boundaries under various dc output voltages have been set forth. Based on the input-output linearization technique, a control scheme is proposed to regulate the dc output voltages. The controller design methodology based on the Butterworth method has been described. Simulation and experimental results are provided to validate the analysis and control system design methodology adopted.

# CHAPTER 10

# DUAL STATOR WINDING INDUCTION MOTOR DRIVE

## 10.1 Introduction

The dual stator winding induction machine working as a motor is another potential application area of this machine. Two stator winding sets offer more flexibility and controllability when this type of dual winding machine is compared with a normal single winding induction machine. For example, at low speed, one stator winding set works under the motoring condition and outputs a positive torque while the other winding set can work as a generator producing a negative torque such that the motoring stator winding has to carry the load torque and the negative torque is contributed by the other winding. This operating condition has been experimentally implemented in [1.11] and better torque controllability is the advantage of this operating condition. Since the output torques from both winding sets are independently controllable, a relatively high input voltage magnitude can be obtained at a very low speed. In this situation, the instability problems associated with the sensorless control of a single winding induction machine disappear in the sensorless control of dual stator winding induction machine. Obviously, the losses of the dual stator winding induction machine under this operating condition will be higher, however this operating condition generally only occurs for a short period of time.

Because of the similarities between the dual stator winding induction machine and the single winding induction machine, the control methodologies of a single winding

induction machine are applicable to the dual stator winding induction machine with necessary modifications. A brief introduction and literature review of induction machine control have been given in chapter 1. The constant V/Hz control of the dual stator winding induction machine was proposed and experimentally implemented in [1.11] because of the simplicity and robustness of this scalar control scheme. However, the well known constant V/Hz control scheme with its poor dynamic response has limited the application to low performance drives such that a high performance vector control of the machine is necessary for precise speed and torque requirements. An indirect field orientation control has been proposed in [1.1, 1.11], in which the two stator winding sets cooperated by a master-slaver control model and only the torque control of the machine is studied. In the proposed vector control, the input voltage frequency ratio of the two windings is always kept at 3 so that the slips of both winding sets are equal at any time [1.11]. The equal slip condition does simplify the control scheme, however the control options are limited and the machine performance is reduced. In this chapter, a speed control of the dual stator winding induction machine is proposed. The frequencies of input voltages of two stator winding sets will be controlled independently so that an optimizing operating point may be obtained at a particular speed by using the proper control scheme. A torque partition factor K has been introduced to modify the electromagnetic torque distribution of each winding set so that each winding set can move smoothly from motoring condition to generating condition by changing the value of K. The principles of input-output linearization are applied in the control system design and the controller design methodology based on the Butterworth method is used to design

the controllers. Because of the good performance and simple system hardware requirement, the indirect rotor field orientation control scheme is adopted in this work.

The full-order observer based on Model Reference Adaptive Scheme (MRAS) is used to estimate the flux linkages and stator currents using the measured stator voltage and stator current signals of the motor. There are two sets of currents in the system, one is the set of measured or actual currents and the other is the set of estimated currents. The error between the actual stator currents and the estimated stator currents is used in a specialized error function to calculate an estimation error between the observer and the actual physical system. Then the output of the error function is fed to the speed estimator to estimate the rotor speed. The adaptive mechanism is established when the rotor speed estimated from this error is used as the feedback. The estimated rotor speed is equal to the actual speed when this error is reduced to zero. This method is a closed loop estimation scheme, which is different from flux estimation using the stator voltage equations.

In this chapter, a speed sensorless control scheme based on a full-order flux observer using MRAS technique has been analyzed. A novel error function has been proposed to ensure the stability within ultra-low speed range. The Butterworth method is used to design the observer gains. The transfer function of the estimated and actual speeds is derived based on the error analysis, and is used to determine the parameters of the speed estimator for the sensorless control. The D-decomposition method is the design methodology for both speed estimator and speed controller. Both the rotor speed and slip frequency are varied within the possible operating range to ensure the stability of the system based on the selected parameters.

In section 10.2, the fundamentals of vector control and indirect rotor flux orientation control are introduced based on the induction machine dynamic model. Then the derivation of the indirect rotor flux orientation control scheme is presented in section 10.3. The design methods for current controllers, flux controller and speed controller are discussed in section 10.4. In section 10.5, computer simulation results of indirect rotor flux orientation control of the dual stator winding induction machine are shown. Full-order flux observer design and determination of observer gains are the topics of section 10.6 and 10.7 respectively. The sensorless control scheme uses a flux observer and a speed estimator instead of the encoder. The methodology for properly choosing the observer gains is presented in section 10.7. A brief introduction of D-decomposition method is given in section 10.8. Controller design methods for the speed estimator is the topic of section 10.9. The speed controller design method is described in section 10.10. Finally, the simulation results for sensorless control are given in section 10.11 and conclusions can be found in section 10.12.

## 10.2 Indirect Flux Orientation Control

The original idea of vector control for induction machines comes from the model of dc machines. In the dc machine, the electromagnetic torque results from the interaction between excitation field and armature current, which can be controlled independently. The excitation field is the result of field current or a permanent magnet. The torque equation of dc machines is given as:

$$T_e = \frac{P}{2}\lambda_{af} i_a \tag{10.1}$$

where, $P$ is the number of poles, $\lambda_{af}$ is the flux produced by the field current that links the armature winding, $i_a$ is the armature current. The difference between the field flux and the flux linked with the armature winding is the leakage flux, which can be represented by a leakage inductance.

The excitation flux axis and the axis of MMF due to the armature current are orthogonal to each other, which are enforced by the structure of dc machines. The advantage of this orthogonality removes the possible coupling interaction between the excitation flux and the MMF from the armature current. Since the field flux can be controlled independently by adjusting the value of the field current while the armature current of the dc machine is independently controlled, the torque control of dc machine is simple and good dynamic response can be achieved. For example, when the flux linking the armature winding is kept constant, the output torque of dc machine will linearly depend on the armature current so that the torque control of the dc machine becomes a simple control of the armature current.

However, the same control method of dc machine is not applicable to ac machines, since the field and armature current do not exist anymore. Before this problem was solved, the speed control of induction machine was obtained by simple constant V/Hz control. The emergence of the field orientation control or vector control solved the problem and brought us the idea that the independent torque control of ac machines is similar to what is known for dc machines. High performance independent torque control of ac machines is obtained by external control algorithms although the method is more complex than that of dc machines.

The vector control of an induction machine is based on the synchronous reference frame transformation, in which the state variables in the abc stationary reference frame are transformed into an orthogonal q-d reference frame that rotates at the synchronous speed. One of the important advantages of this transformation is that all the state variables are dc quantities in steady state after the transformation, which greatly simplifies the controller design so that all the traditional controller design methodologies applicable to dc signals can be used in ac machine control. The other advantage gained from the transformation is that the coupling between the stator windings is totally removed because of the orthogonality of q-d reference frame. The torque equation of induction machine will be given to explain the similarity between the dc machine control and vector control of an induction machine. The torque equation of an induction machine in terms of rotor flux linkages and stator currents is given as:

$$T_e = \frac{3P}{4}\frac{L_m}{L_r}\left(\lambda_{dr} i_{qs} - \lambda_{qr} i_{ds}\right) \tag{10.2}$$

where, $P$ is the number of poles, $L_m$ is the mutual inductance, $L_r$ is the rotor inductance, $\lambda_{qr}$ and $\lambda_{dr}$ are the q- and d-axis rotor flux linkage respectively, $i_{qs}$ and $i_{ds}$ are the q- and d-axis stator currents respectively. It should be noted that the electromagnetic torque equation given in (10.2) is satisfactory for an arbitrary reference frame, however the synchronous reference frame transformation ensures that all the variables will be dc quantities in steady state.

If the rotor flux linkage is aligned with the d-axis, which means

$$\begin{cases} \lambda_{dr} = \lambda_r \\ \lambda_{qr} = 0 \end{cases} \tag{10.3}$$

Then the torque equation (10.2) can be simplified as;

$$T_e = \frac{3P}{4}\frac{L_m}{L_r}\lambda_r i_{qs} \tag{10.4}$$

The torque equation in this form is similar to the one for dc machines. So if the rotor flux linkage $\lambda_r$ is regulated to be constant, the output electromagnetic torque of an induction machine will linearly depend on the q-axis current in the synchronous reference frame. To achieve good dynamic performance, the synchronous reference frame transformation that decouples the state variables, independent control of rotor flux linkages and stator currents are the important issues that need to be dealt with.

The instant angle for the synchronous reference frame with respect to the stationary reference frame is the only quantity needed for the synchronous reference frame transformation. Depending upon the method of getting this rotor flux position angle, the vector control schemes are divided into two categories: direct and indirect vector control. The rotor flux position angle is determined from the direct flux measurements using flux sensing techniques in direct vector control while in the indirect vector control scheme the angle is computed from the measured rotor position and the calculated slip, which is expressed as:

$$\begin{aligned}\theta_e &= \theta_r + \theta_{sl} \\ &= \int (\omega_r + \omega_s) dt\end{aligned} \tag{10.5}$$

where, $\omega_r$ is the rotor speed and $\omega_s$ is the slip frequency.

Hence the indirect field orientation is basically achieved by controlling the slip frequency to satisfy the specified slip condition calculated from the induction machine model. Increasing the complexity of the system by adding flux sensors or windings to the induction machine not only increases the cost of the system but also increases the

possibilities for fault conditions, which make direct vector control unattractive for most application areas. The most popular vector control scheme for an induction machine is the indirect vector control, in which the rotor speed sensor is necessary and a machine parameters dependent slip calculation is utilized. The indirect vector control of the dual stator winding induction machine is derived in the following section.

## 10.3 Formulation of Indirect Vector Control Scheme

The indirect vector control scheme for the dual stator winding induction machine is based on the assumption that the machine can be treated as two independent induction machines coupled through the same rotor shaft as shown in chapter 5 and also given in [1.1, 1.11]. To avoid unnecessary repetition, all the derivations are made for the *i* winding set, which can be either the 2-pole ABC winding set or the 6-pole XYZ winding set.

The dual stator winding induction machine model in synchronous reference frame is given as:

$$V_{qsi} = r_{si} I_{qsi} + p\lambda_{qsi} + \omega_{ei}\lambda_{dsi} \tag{10.6}$$

$$V_{dsi} = r_{si} I_{dsi} + p\lambda_{dsi} - \omega_{ei}\lambda_{qsi} \tag{10.7}$$

$$0 = r_{ri} I_{qri} + p\lambda_{qri} + (\omega_{ei} - \omega_{ri})\lambda_{dri} \tag{10.8}$$

$$0 = r_{ri} I_{dri} + p\lambda_{dri} - (\omega_{ei} - \omega_{ri})\lambda_{qri} \tag{10.9}$$

$$T_{ei} = \frac{3P}{4}\frac{L_{mi}}{L_{ri}}\left(\lambda_{dri} i_{qsi} - \lambda_{qri} i_{dsi}\right) \tag{10.10}$$

where, $V_{qsi}$ and $V_{dsi}$ are the stator q- and d-axis voltages respectively, $I_{qsi}$ and $I_{dsi}$ are the stator q- and d-axis currents respectively, $\lambda_{qsi}$ and $\lambda_{dsi}$ are the stator q- and d-axis flux linkages respectively, $I_{qri}$ and $I_{dri}$ are the rotor q- and d-axis currents respectively, $\lambda_{qri}$ and $\lambda_{dri}$ are the rotor q- and d-axis flux linkages respectively; $i=1$ or 2 represents the ABC winding set or the XYZ winding set respectively.

Based on the two independent machine assumptions, the total electromagnetic torque of the dual stator winding induction machine is given as:

$$T_e = T_{e1} + T_{e2} \tag{10.11}$$

If the stator currents and rotor flux linkages are chosen as state variables, the stator flux linkages and rotor currents can be expressed in terms of state variables as;

$$I_{qri} = \frac{\lambda_{qri} - L_{mi} I_{qsi}}{L_{ri}} \tag{10.12}$$

$$I_{dri} = \frac{\lambda_{dri} - L_{mi} I_{dsi}}{L_{ri}} \tag{10.13}$$

$$\lambda_{qsi} = L_{si} I_{qsi} + \frac{L_{mi}}{L_{ri}} \left( \lambda_{qri} - L_{mi} I_{qsi} \right) \tag{10.14}$$

$$\lambda_{dsi} = L_{si} I_{dsi} + \frac{L_{mi}}{L_{ri}} \left( \lambda_{dri} - L_{mi} I_{dsi} \right) \tag{10.15}$$

Substituting (10.12-10.15) into (10.6-10.9), the induction machine model in terms of those state variables is given as:

$$L_{\sigma i}\, pI_{qsi} = V_{qsi} - r_i I_{qsi} - \omega_{ei} L_{\sigma i} I_{dsi} + \frac{r_{ri} L_{mi}}{L_{ri}^2} \lambda_{qri} - \frac{\omega_{ri} L_{mi}}{L_{ri}} \lambda_{dri} \tag{10.16}$$

$$L_{\sigma i}\, pI_{dsi} = V_{dsi} - r_i I_{dsi} + \omega_{ei} L_{\sigma i} I_{qsi} + \frac{r_{ri} L_{mi}}{L_{ri}^2} \lambda_{dri} + \frac{\omega_{ri} L_{mi}}{L_{ri}} \lambda_{qri} \tag{10.17}$$

$$p\lambda_{qri} = \frac{-r_{ri}}{L_{ri}}\lambda_{qri} + \frac{r_{ri}L_{mi}}{L_{ri}}I_{qsi} - (\omega_{ei} - \omega_{ri})\lambda_{dri} \tag{10.18}$$

$$p\lambda_{dri} = \frac{-r_{ri}}{L_{ri}}\lambda_{dri} + \frac{r_{ri}L_{mi}}{L_{ri}}I_{dsi} + (\omega_{ei} - \omega_{ri})\lambda_{qri} \tag{10.19}$$

where, $L_{\sigma i} = L_{si} - \frac{L_{mi}^2}{L_{ri}}$ and $r_i = r_{si} + \frac{r_{ri}L_{mi}^2}{L_{ri}^2}$.

The mechanical rotor speed dynamic equation is:

$$p\omega_{rm} = \frac{K_{e1}}{J}\left(\lambda_{dr1}I_{qs1} - \lambda_{qr1}I_{ds1}\right) + \frac{K_{e2}}{J}\left(\lambda_{dr2}I_{qs2} - \lambda_{qr2}I_{ds2}\right) - \frac{T_L}{J} \tag{10.20}$$

where, $K_{e1} = \frac{3P_1}{4}\cdot\frac{L_{m1}}{L_{r1}}$, $K_{e2} = \frac{3P_2}{4}\cdot\frac{L_{m2}}{L_{r2}}$, $P_1$ and $P_2$ are the numbers of poles for the ABC winding set and the XYZ winding set respectively; $\omega_{rm}$ is the rotor mechanical speed; the electric rotor speed of each stator winding set can be expressed in term of rotor mechanical speed as: $\omega_{r1} = \frac{P_1}{2}\cdot\omega_{rm}$ and $\omega_{r2} = \frac{P_2}{2}\cdot\omega_{rm}$.

When the rotor flux linkage is aligned with the d-axis of the synchronous reference frame, q-axis rotor flux linkage and its derivative are zero, which can be expressed as:

$$\lambda_{dri} = \lambda_{ri} \tag{10.21}$$

$$\lambda_{qri} = p\lambda_{qri} = 0 \tag{10.22}$$

Substituting (10.21-10.22) into the model equations (10.16-10.20), the simplified model equations are:

$$L_{\sigma i}pI_{qsi} = V_{qsi} - r_iI_{qsi} - \omega_{ei}L_{\sigma i}I_{dsi} - \frac{\omega_{ri}L_{mi}}{L_{ri}}\lambda_{ri} \tag{10.23}$$

$$L_{\sigma i}pI_{dsi} = V_{dsi} - r_iI_{dsi} + \omega_{ei}L_{\sigma i}I_{qsi} + \frac{r_{ri}L_{mi}}{L_{ri}^2}\lambda_{ri} \tag{10.24}$$

$$0 = \frac{r_{ri} L_{mi}}{L_{ri}} I_{qsi} - (\omega_{ei} - \omega_{ri}) \lambda_{ri} \tag{10.25}$$

$$p\lambda_{ri} = \frac{-r_{ri}}{L_{ri}} \lambda_{ri} + \frac{r_{ri} L_{mi}}{L_{ri}} I_{dsi} \tag{10.26}$$

$$p\omega_{rm} = \frac{K_{e1}}{J} (\lambda_{r1} I_{qs1}) + \frac{K_{e2}}{J} (\lambda_{r2} I_{qs2}) - \frac{T_L}{J} \tag{10.27}$$

Equation (10.25) yields the expression of the slip frequency required for indirect field orientation control, which is given as:

$$\omega_{ei} - \omega_{ri} = \frac{r_{ri} L_{mi}}{L_{ri} \lambda_{ri}} I_{qsi} \tag{10.28}$$

The input-output linearization method is used to design the control scheme of the dual stator winding induction machine. If the nonlinear terms are moved to the left side of the equations, the machine model equations are expressed as:

$$L_{\sigma i} p I_{qsi} + r_i I_{qsi} = V_{qsi} - \omega_{ei} L_{\sigma i} I_{dsi} - \frac{\omega_{ri} L_{mi}}{L_{ri}} \lambda_{ri} = \sigma_{qsi} \tag{10.29}$$

$$L_{\sigma i} p I_{dsi} + r_i I_{dsi} = V_{dsi} + \omega_{ei} L_{\sigma i} I_{qsi} + \frac{r_{ri} L_{mi}}{L_{ri}^2} \lambda_{ri} = \sigma_{dsi} \tag{10.30}$$

$$p\lambda_{ri} + \frac{r_{ri}}{L_{ri}} \lambda_{ri} = \frac{r_{ri} L_{mi}}{L_{ri}} I_{dsi} = \sigma_{ri} \tag{10.31}$$

$$p\omega_{rm} = \frac{K_{e1}}{J} (\lambda_{r1} I_{qs1}) + \frac{K_{e2}}{J} (\lambda_{r2} I_{qs2}) - \frac{T_L}{J} = \sigma_{\omega} \tag{10.32}$$

where, $\sigma_{qsi}$ is the output of the q-axis current controller, $\sigma_{dsi}$ is the output of the d-axis current controller, $\sigma_{ri}$ is the output of the rotor flux linkage controller and $\sigma_{\omega}$ is the output of the speed controller. The expressions of the outputs of these controllers are given as:

$$\sigma_{qsi} = K_{qsi} \cdot \left( I_{qsi}^{*} - I_{qsi} \right) \tag{10.33}$$

$$\sigma_{dsi} = K_{dsi} \cdot \left( I_{dsi}^{*} - I_{dsi} \right) \tag{10.34}$$

$$\sigma_{ri} = K_{ri} \cdot \left( \lambda_{ri}^{*} - \lambda_{ri} \right) \tag{10.35}$$

$$\sigma_{\omega} = K_{\omega} \cdot \left( \omega_{rm}^{*} - \omega_{rm} \right) \tag{10.36}$$

Where, $K_{qsi}$, $K_{dsi}$, $K_{ri}$ and $K_{\omega}$ are the transfer functions of controllers for q-axis current, d-axis current, rotor flux and rotor speed respectively. The traditional PI controller structure is used for all the controllers.

Since the nonlinear terms of the system model have been embedded in the nonlinear controllers, the system is linearized and linear system control methodologies can be used to determine the parameters of the controllers.

The d-axis stator current command is determined from (10.31):

$$i_{dsi}^{*} = \sigma_{ri} \frac{L_{ri}}{r_{ri} L_{mi}} \tag{10.37}$$

The desired q- and d-axis voltages are calculated from (10.29-10.30) as:

$$V_{qsi}^{*} = \sigma_{qsi} + \omega_{ei} L_{\sigma i} I_{dsi} + \frac{\omega_{ri} L_{mi}}{L_{ri}} \lambda_{ri} \tag{10.38}$$

$$V_{dsi}^{*} = \sigma_{dsi} - \omega_{ei} L_{\sigma i} I_{qsi} - \frac{r_{ri} L_{mi}}{L_{ri}^{2}} \lambda_{ri} \tag{10.39}$$

The calculation of q-axis stator current command needs the speed controller output. However, it should be noticed that the two stator winding sets have the same rotor mechanical speed such that the q-axis stator current commands of both winding sets have to share the same speed controller output. A variable coefficient called torque distribution factor K is introduced to partition the electromagnetic torque for each winding set.

The expression of torque distribution factor is expressed as:

$$K = \frac{T_{e1}}{T_{e1} + T_{e2}} \tag{10.40}$$

where, $T_{e1}$ and $T_{e2}$ are the electromagnetic torque from ABC winding set and XYZ winding set respectively.

From (10.40), the electromagnetic torque of ABC winding is given as:

$$\begin{aligned} T_{e1} &= K_{e1}\lambda_{r1}i_{qs1} \\ &= K \cdot \left(K_{e1}\lambda_{r1}i_{qs1} + K_{e2}\lambda_{r2}i_{qs2}\right) \end{aligned} \tag{10.41}$$

Replacing the total torque with the output of speed controller and the load torque, (10.41) becomes:

$$\begin{aligned} T_{e1} &= K_{e1}\lambda_{r1}i_{qs1} \\ &= K \cdot \left(J \cdot \sigma_{\omega} + T_L\right) \end{aligned} \tag{10.42}$$

The expression of the q-axis current command for the ABC winding set is given as:

$$i_{qs1}^{*} = \frac{K \cdot \left(J \cdot \sigma_{\omega} + T_L\right)}{K_{e1}\lambda_{r1}} \tag{10.43}$$

Similarly, the expression of the q-axis current command for the XYZ winding set is determined by:

$$i_{qs2}^{*} = \frac{\left(1-K\right) \cdot \left(J \cdot \sigma_{\omega} + T_L\right)}{K_{e2}\lambda_{r2}} \tag{10.44}$$

By properly choosing the torque distribution factor K, the command q-axis currents of both stator winding sets can be determined. In the case where the machine is running at a very low speed and one of the stator winding set needs to generate negative torque, K can be chosen as a negative value so that the ABC winding set is generating or K can be greater that 1 to force the XYZ winding set to generate.

In the proposed control scheme, rotor speed and rotor flux linkage level are the control objectives and are achieved by proper control of the q- and d-axis currents. An indirect current control method is used in this control scheme in such a manner that the desired q- and d-axis currents are controlled through the proper control of q- and d-axis voltage commands. An alternative way can also be used to achieve the same goal by regulating the current directly. The diagram of the proposed control scheme is given in Figure 10.1.

For each stator winding set, there are three controllers, which include a controller for flux control and two controllers for the q- and d-axis currents. Two stator winding sets share the same speed controller and receive their individual inputs after the partition factor K. The parameters of the controllers need to be properly determined to meet the stability and dynamic requirements. The design methodologies for the controllers are introduced in the next section.

## 10.4 Controller Design

Controller parameter design is an essential part of control system determination. Different controller structures are available such as Proportion-Integral controller (PI), Integration-Proportional controller (IP), Proportional-Integral-Derivative controller (PID), Proportion-Derivative controller (PD) etc, but not all of them are applicable to a particular control system. The stability constraint is the most important consideration for the controller design. The diagrams of different controllers are given in Figure 10.2.

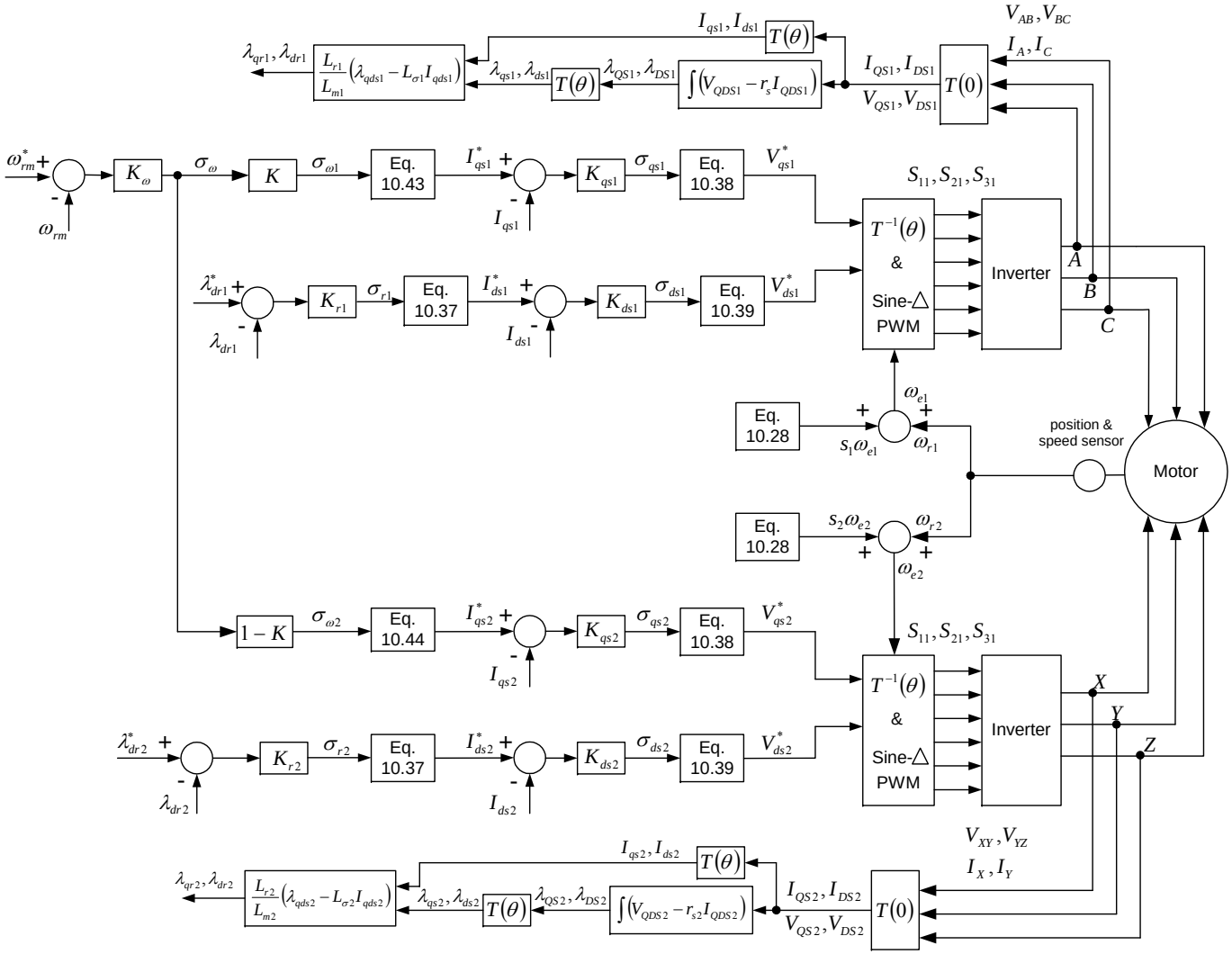


Figure 10.1 The diagram of control scheme

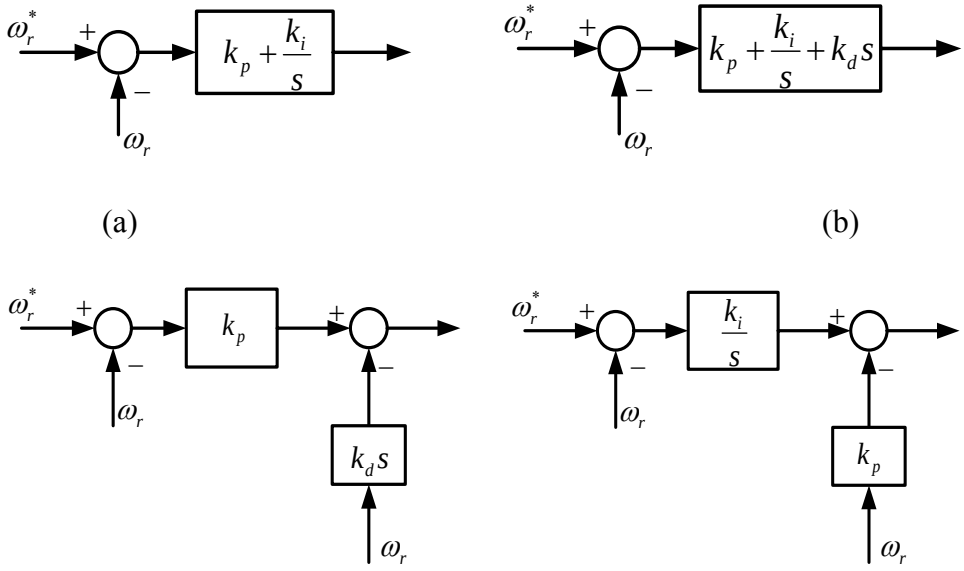


Figure 10.2 Controller structures, (a) diagram of PI controller, (b) diagram of PID controller, (c) diagram of PD controller, (d) diagram of IP controller.

The pole placement method used in this design is called the Butterworth method, in which the parameters are selected to locate the eigen-values of the transfer function uniformly in the left half of the s-plane, on a circle of radius $\omega_0$, with its center at the origin. The poles are evenly distributed around the circle. The example of pole placement for a second order system is given in Figure 10.3.

The design steps using the Butterworth method are: firstly, the transfer function of the controller is obtained; then the denominator of the transfer function is compared with the Butterworth polynomial by equaling the coefficient of each term. Since the Butterworth polynomial is expressed only in term of $\omega_0$, if the value of $\omega_0$ is selected, all the controller parameters can be obtained.

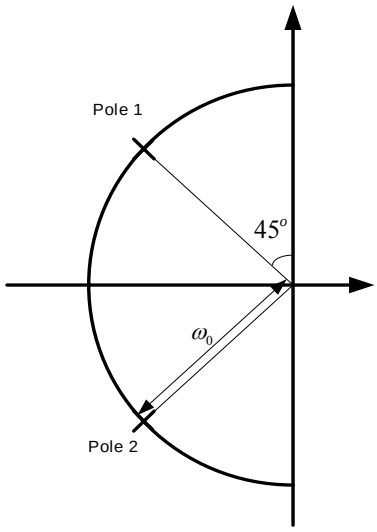


Figure 10.3 Diagram of pole placement using Butterworth method

The zeros of transfer function can also greatly influence the system performance. It is well known that when any zero of a transfer function of a system has a positive real part (the system is non-minimum phase), the closed-loop performance is compromised as the right half-plane zero induces an additional phase shift of -180. The determination of controller parameters should ensure the minimum phase system requirement.

The design methodology of the Butterworth method requires that none of the terms in the denominator is missing. This becomes the limitation for the controller determination. The reason for this limitation is simple. For example, the second order Butterworth polynomial is given as:

$$S^2 + \sqrt{2}\omega_0 S + \omega_0^2 = 0 \tag{10.45}$$

The absence of any term in (10.45) leads to the conclusion that $\omega_0$ has to be zero, which yields unreasonable controller parameters. On the other hand, zero value for $\omega_0$ means that the poles of the controllers overlap the original point, which makes the system unstable for practical purposes.

The value of $\omega_0$ determines the dynamic response of the controller. It should be noticed that in a control system with multiple controllers, the values of $\omega_0$ for different controllers must be properly designed. Generally, the inner loop controller should have a value of $\omega_0$ about 10 times higher than the one in the outer control loop.

The PI controller structure is used for which the design process is given in the following sub-sections.

### 10.4.1 Speed Controller Design

The transfer function for a PI controller is expressed as:

$$G_{pi} = k_p + \frac{k_i}{s} \tag{10.46}$$

Substituting the transfer function of the PI controller into (10.36), the speed controller equation can be expressed as:

$$s\omega_{rm} = \left( k_{p\omega} + \frac{k_{i\omega}}{s} \right) \cdot \left( \omega_{rm}^* - \omega_{rm} \right) \tag{10.47}$$

Then the transfer function of the speed controller is given as:

$$\frac{\omega_{rm}}{\omega_{rm}^*} = \frac{k_{p\omega} s + k_{i\omega}}{s^2 + k_{p\omega} s + k_{i\omega}} \tag{10.48}$$

The second order Butterworth polynomial has been given in (10.46). The comparison between the denominator of the transfer function with the Butterworth polynomial yields the parameters of the controller, which are given as:

$$\begin{cases} k_{p\omega} = \sqrt{2}\omega_0 \\ k_{i\omega} = \omega_0^2 \end{cases} \tag{10.49}$$

### 10.4.2 Flux Controller Design

Substituting the transfer function of PI controller into the flux controller, the transfer function becomes:

$$s\lambda_{dri} + \frac{r_{ri}}{L_{ri}}\lambda_{dri} = \left(k_{pr} + \frac{k_{ir}}{s}\right)\cdot\left(\lambda_{dri}^{*} - \lambda_{dri}\right)$$

$$\frac{\lambda_{dri}}{\lambda_{dri}^{*}} = \frac{sk_{pr} + k_{ir}}{s^2 + \left(\frac{r_{ri}}{L_{ri}} + k_{pr}\right)s + k_{ir}} \tag{10.50}$$

Apply the Butterworth method, the flux controller parameters are calculated as:

$$\begin{cases} k_{pr} = \sqrt{2}\omega_0 - \dfrac{r_{ri}}{L_{ri}} \\ k_{ir} = \omega_0^2 \end{cases} \tag{10.51}$$

### 10.4.3 Stator Q-axis Current Controller Design

If the traditional PI controller is used, the transfer function of the q-axis current controller is expressed as:

$$L_{\sigma i}si_{qsi} + r_{si}i_{qsi} = \left(k_{pq} + \frac{k_{iq}}{s}\right)\cdot\left(i_{qsi}^{*} - i_{qsi}\right)$$

$$\frac{i_{qsi}}{i_{qsi}^{*}} = \frac{\frac{k_{pq}}{L_{\sigma i}}s + \frac{k_{iq}}{L_{\sigma i}}}{s^2 + \frac{r_{si} + k_{pq}}{L_{\sigma i}}s + \frac{k_{iq}}{L_{\sigma i}}} \tag{10.52}$$

Then the controller parameters are determined using the Butterworth method as:

$$\begin{cases} k_{pq} = \sqrt{2}\omega_0 L_{\sigma i} - r_{si} \\ k_{iq} = \omega_0^2 L_{\sigma i} \end{cases} \tag{10.53}$$

### 10.4.4 Stator D-axis Current Controller Design

The transfer function for the d-axis current controller is similar to the one of the q-axis current and will not be repeated here. The designed parameters can be found as:

$$\begin{cases} k_{pd} = \sqrt{2}\omega_0 L_{\sigma i} - r_{si} \\ k_{id} = \omega_0^2 L_{\sigma i} \end{cases} \tag{10.54}$$

The stability issue in the control design has been considered in previous work by locating the poles of the transfer function at the left-side of s-plane. However, the zeros of transfer functions can also greatly influence the system performance. Hence to improve the system dynamic performance, the zeros of the transfer functions should have negative real parts also. In all above controller designs, the negative real part of zeros can be ensured when $k_p$ and $k_i$ of a controller have the same sign. Normally, these control parameters are all chosen to be positive.

## 10.5 Simulation and Experimental Results for Indirect Flux Orientation Control

The proposed control scheme has been simulated using MATLAB/SIMULINK. Both the starting process and dynamic response of the system have been given to validate the effectiveness of the proposed control scheme. The parameters of the controllers are shown in Table 10.1

Table 10.1 Parameters of controllers in simulation

| | 2-pole ABC winding | 6-pole XYZ winding |
|---|---|---|
| Q-axis current controller | $k_{pq} = 3.8$, $k_{iq} = 1018.9$ | $k_{pq} = 3.8$, $k_{iq} = 1018.9$ |
| D-axis current controller | $k_{pd} = 0.20$, $k_{id} = 254.7$ | $k_{pd} = 0.20$, $k_{id} = 254.7$ |
| Rotor flux linkage controller | $k_{pr} = 5.0$, $k_{ir} = 25$ | $k_{pr} = 5.0$, $k_{ir} = 25$ |
| Speed controller | $k_{\omega p} = 70.71$, $k_{\omega i} = 2500$ | |

The values of $\omega_0$ for controllers are given as:

Speed controller : $\omega_0 = 50$ Flux controller : $\omega_0 = 5$

q-axis current controller : $\omega_0 = 200$ d-axis current controller : $\omega_0 = 100$

The simulation results for the starting process of the dual stator winding induction motor are shown in Figure 10.4, where the simulation results for the ABC winding set (2-pole) are represented by blue solid line while the simulation results for the XYZ winding set (6-pole) are represented by red dashed line. The DC bus voltage is kept to be constant 300 V and 2 Nm load torque is added to the system at 4.5 seconds. The torque distribution factor K is 0.5 during the starting process. The reference rotor speed ramps up from 0 to 126 rad/s and is kept at 126 rad/s after that. It is found from the simulation results that the actual speed tracks the command speed very well and the system runs at the steady state. The torque distribution factor K works very well so that the electromagnetic torques from both winding sets are equal when K = 0.5. The dynamic responses of the system are given in Figure 10.5. The rotor speed ramps down and up and down between 126 rad/s and -126 rad/s while the torque distribution factor K changes from 0.5 to 0.25 at 18 seconds. During all these dynamic changes, the rotor speed accurately tracks the speed command. The torque distribution factor works effectively as shown in the simulation results.

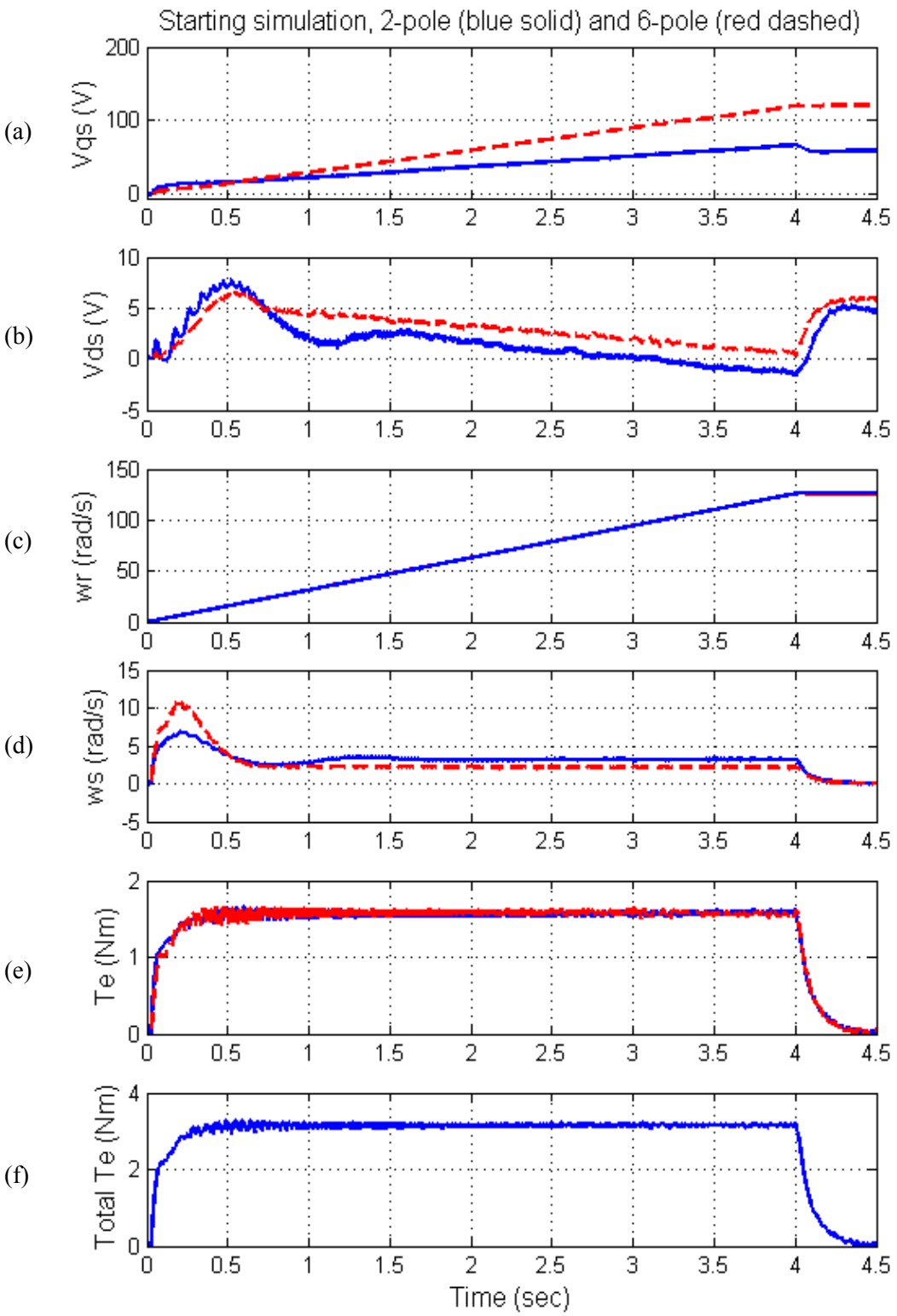


Figure 10.4 Starting process of dual stator winding induction motor, (a) q-axis voltage $V_{qsi}$, (b) d-axis voltage $V_{dsi}$, (c) reference and actual rotor mechanical speed $\omega_{rm}$, (d) slip frequency $\omega_{sli}$, (e) electromagnetic torque $T_{ei}$, (f) total torque $T_e$.

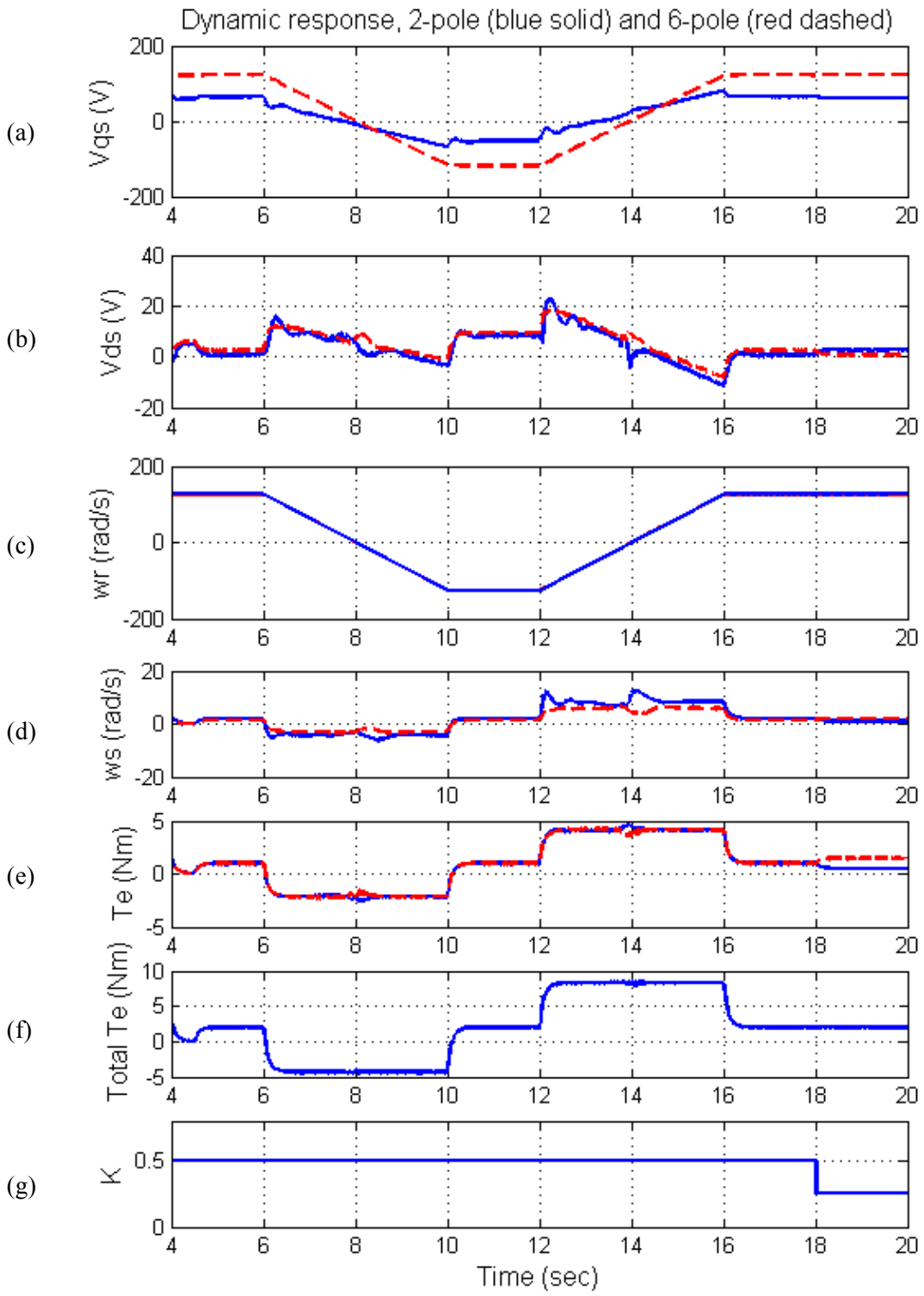


Figure 10.5 Dynamic response of dual stator winding induction motor, (a) q-axis voltage $V_{qsi}$, (b) d-axis voltage $V_{dsi}$, (c) reference and actual rotor mechanical speed $\omega_{rm}$, (d) slip frequency $\omega_{sli}$, (e) electromagnetic torque $T_{ei}$, (f) total torque $T_e$, (g) torque distribution factor K.

The proposed control scheme has also been checked at low speed. The torque distribution factor K is set to be a negative value when the rotor speed is within a certain low speed area. The starting process and dynamic response of the system are shown in Figure 10.6 and Figure 10.7. DC bus voltage is 300 V and 2 Nm load torque is added to the machine at 4.5 second. The rotor speed ramps up from 0 to 37 rad/s during the starting process. During the dynamic changing process, the rotor speed ramps down from 37 rad/s to zero speed and remains there for one second. After that, the rotor speed keeps decreasing to -37 rad/s, remains there for 2 seconds and ramps up to 37 rad/s. During the ramping up process, the rotor speed is also kept at zero speed for a while to check the system performance at that particular operating condition. When the absolute value of rotor mechanical speed is within 10 rad/s, the torque distribution factor K changes from 0.5 to -0.2 so that the ABC winding set generates power and output negative torque while the XYZ winding set has to carry the sum of the load torque and the negative torque generated by ABC winding set. This operating condition increases the output torque of one winding set so that the input voltage magnitude of the winding set is increased. It is well known that the main difficulty of sensorless induction machine control is the very weak input signals at very low speed due to the low input voltage magnitude. By using the proposed control method, the input voltage of one winding set is increased so that the difficulty of sensorless control in a single winding induction machine is overcome without any hardware or software modifications. The actual rotor speed tracks the command rotor speed within the whole speed range including zero speed in the computer simulation results. The simulation results validate the proposed control scheme.

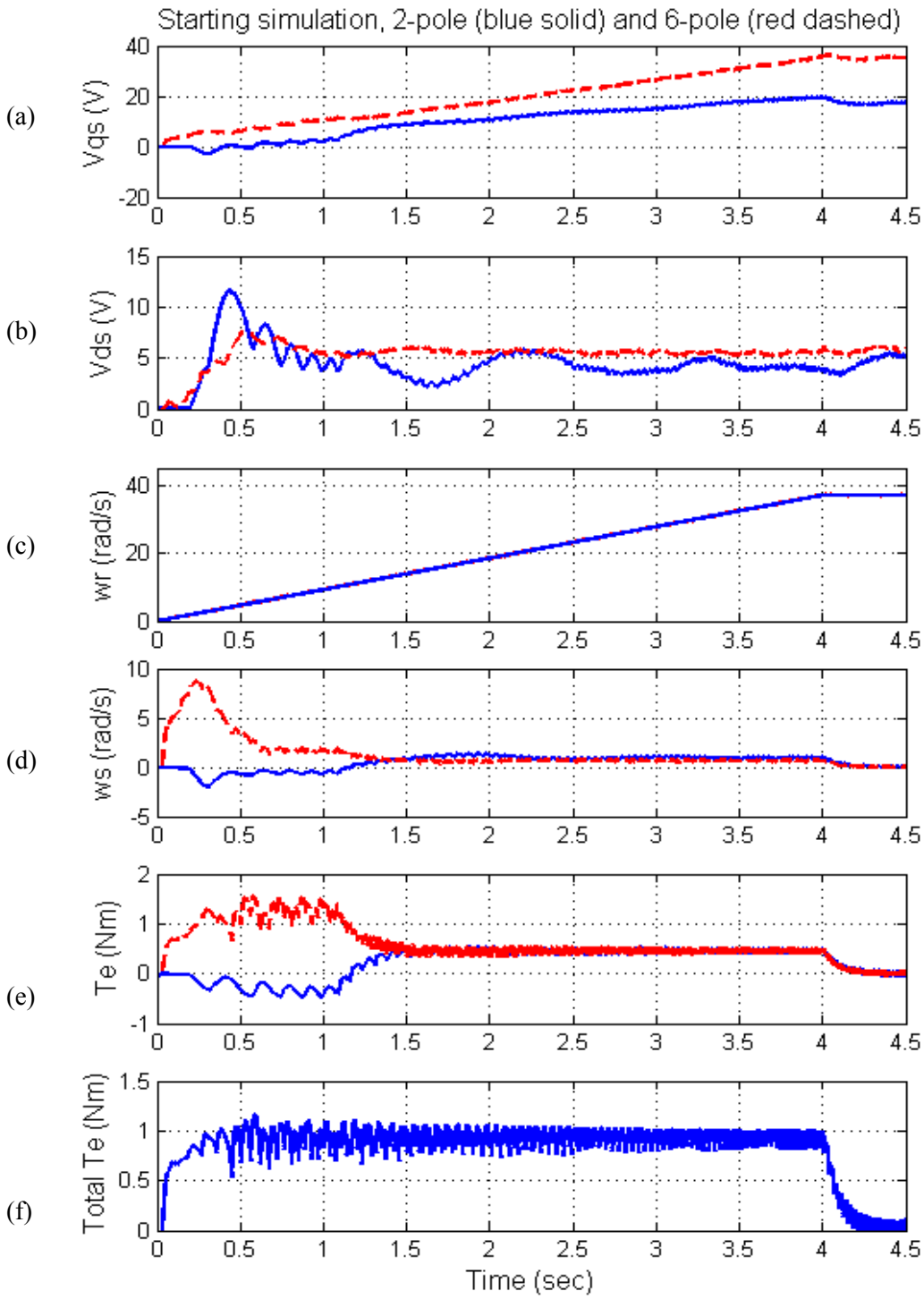


Figure 10.6 Starting process of dual stator winding induction motor within low speed range, (a) q-axis voltage $V_{qsi}$, (b) d-axis voltage $V_{dsi}$, (c) reference and actual rotor mechanical speed $\omega_{rm}$, (d) slip frequency $\omega_{sli}$, (e) electromagnetic torque $T_{ei}$, (f) total torque $T_e$.

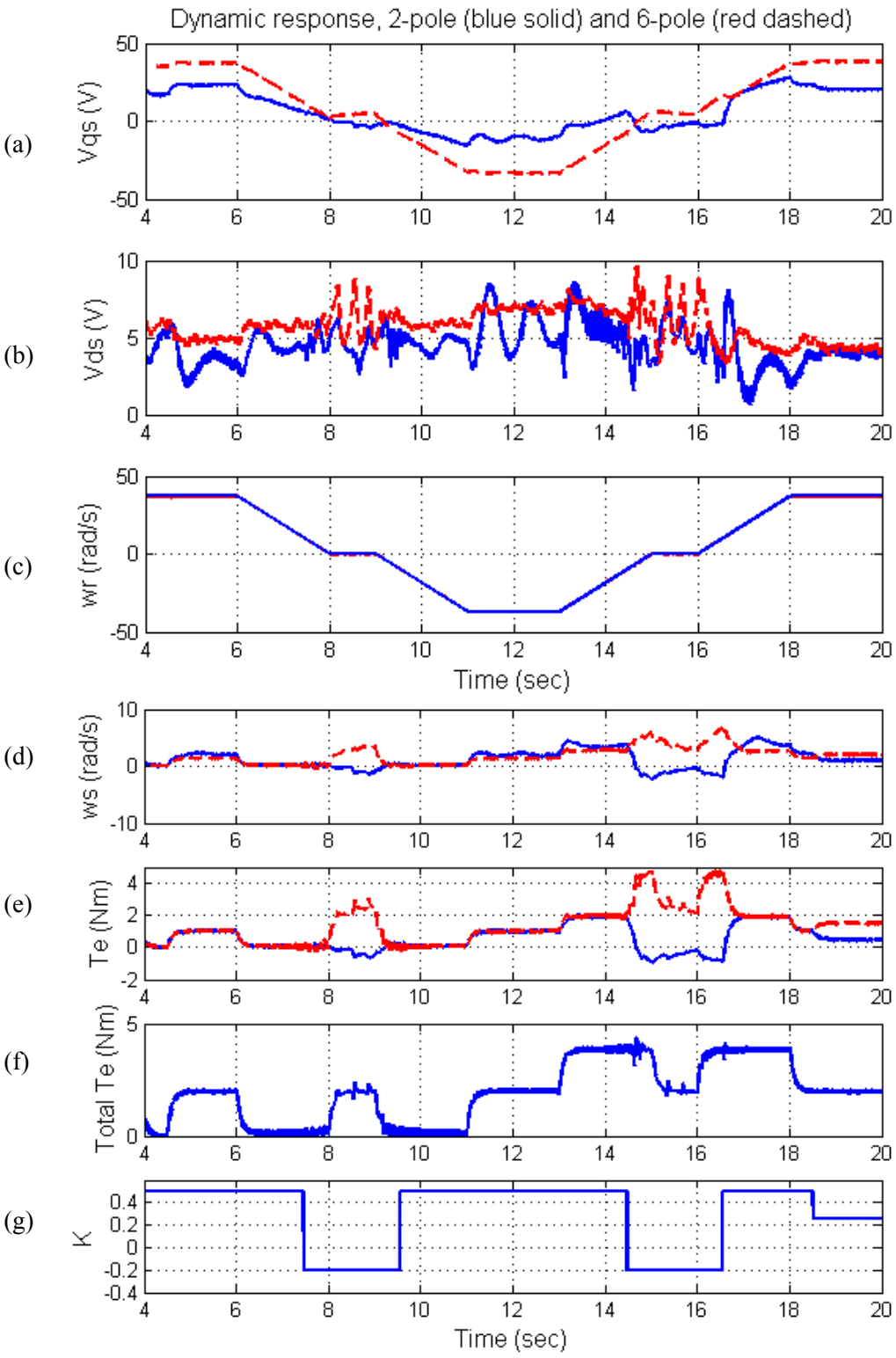


Figure 10.7 Dynamic response of dual stator winding induction motor within low speed range, (a) q-axis voltage $V_{qsi}$, (b) d-axis voltage $V_{dsi}$, (c) reference and actual rotor mechanical speed $\omega_{rm}$, (d) slip frequency $\omega_{sli}$, (e) electromagnetic torque $T_{ei}$, (f) total torque $T_e$, (g) torque distribution factor K.

Experimental results of the starting process are given in Figure 10.8, in which the reference speed ramps up from 0 to 126 rad/sec (1200 rpm). The actual speed accurately tracks the speed command.

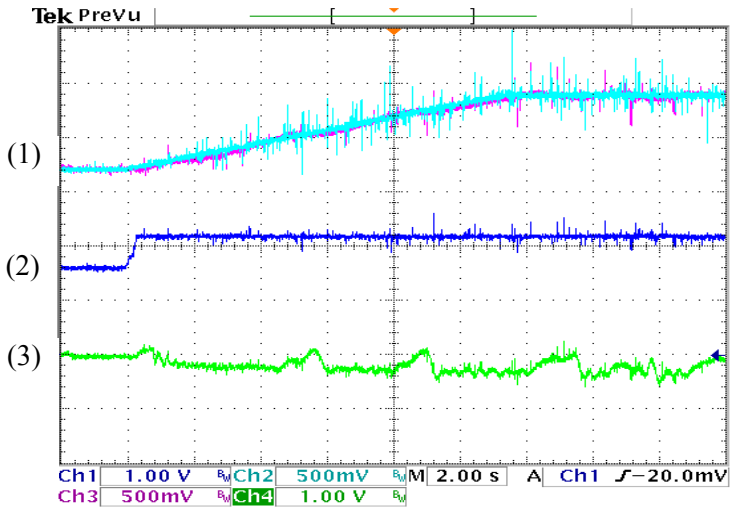


(a)

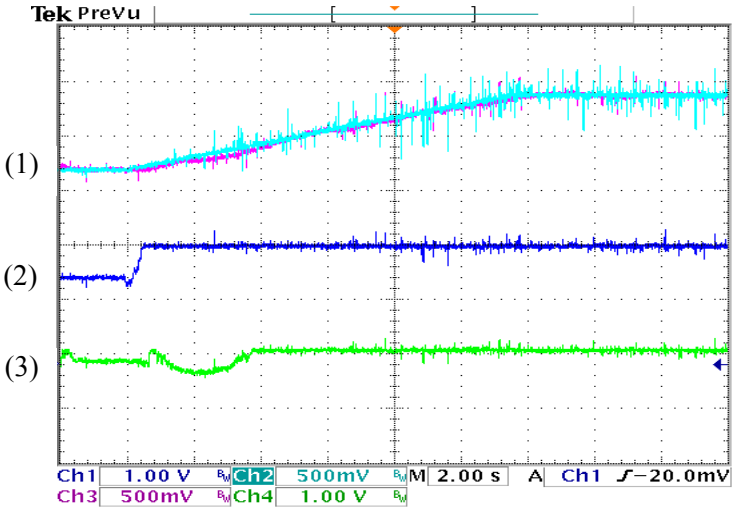


(b)

Figure 10.8 Experimental results of the dual stator winding induction machine, (a) the starting process of the ABC winding set, from top: (1) reference and actual rotor speed (1500 rpm/div), (2) $V_{qs1}$ (100 V/div), (3) $F_{dr1}$ (0.3 Wb/div); (b) the starting process of the XYZ winding set, from top: (1) reference and actual rotor speed(1500 rpm/div), (2) $V_{qs2}$ (100 V/div), (3) $F_{dr2}$ (0.1 Wb/div).

## 10.6 Full-order Flux Observer

The control scheme for dual stator winding induction machine with a speed sensor has been derived and simulated in the previous section. The existence of the speed sensor not only increases the cost but also decreases the reliability of the whole system. For example, in the power train application, the environment for encoder is normally hostile so that more than one encoder will need to be installed in the system. At any point in time, only one of the encoders is working while the others are the backup of the primary one in case any failure is found in the primary encoder. Industrial drive applications require the sensorless technique rather than the use of encoder. Generally speaking, two techniques have been proposed. One of them is machine model based methods and the other one is magnetic structure based methods. A brief introduction of the sensorless control of induction machine has been given in chapter 1.

From the review of the previous work on the full-order observers, some important issues related to the selection of observer gains and the determination of speed estimator parameters have not been clearly and adequately addressed. A relatively comprehensive methodology for the design of full-order flux observer and the speed adaptive mechanism are defined [10.39]. The observer gains are designed based on the Butterworth polynomials. The transfer function between the estimated speed and actual speed is derived in the synchronous reference frame, which are used to select appropriate PI controller parameters for the speed estimation. The D-decomposition method is applied to determine the stable and unstable regions of the transfer function. However, the designed system parameters have only been checked for a particular rotor speed with variable slip frequencies so that stability within the whole operating speed range cannot be guaranteed.

In this chapter, the flux observer parameters have been designed to ensure the stability over the whole speed range. The stability problem for sensorless control are demonstrated by the pole-zero maps under the rotor speed varying within the whole speed range. Two observer gain design methods have been studied and compared. A new speed adaptive speed estimator is proposed and its effectiveness is validated by the pole-zero map of the whole system.

This section is organized as follows: first of all, the machine model and full-order flux observer model in matrix form are derived. Then based on the error analysis, the transfer function of estimated speed and actual rotor speed is obtained. The observer gains are determined from the transfer function of the estimated speed and actual rotor speed while the determination of the speed estimator gains is based on the transfer function of estimated rotor speed and reference rotor speed. The D-decomposition method is adopted to ensure the stability of the system. The whole controlled system is simulated in both motoring and generating modes. It has been demonstrated that the whole system remains stable within the whole speed range, all the controllers work properly and the rotor speed is well regulated under different load conditions, validating the proposed method of designing full-order flux observer, speed estimator and speed controller.

### 10.6.1 Machine Model

The complex variable form of the voltage equations for the dual stator winding induction machine expressed in the synchronous reference frames are given in (10.55-10.56). The three-phase windings wound for $P_1$ poles is called the ABC winding set

while the second three-phase winding set wound for $P_2$ poles is called the XYZ winding set.

$$V_{qdsi} = r_{si} i_{qdsi} + p\lambda_{qdsi} - j\omega_{ei}\lambda_{qdsi} \tag{10.55}$$

$$0 = r_{ri} i_{qdri} + p\lambda_{qdri} - j(\omega_{ei} - \omega_{ri})\lambda_{qdri} \tag{10.56}$$

where, the complex variable forms of the voltages and flux linkages are defined as $V_{qdsi} = V_{qsi} + jV_{dsi}$, $V_{qdri} = V_{qri} + jV_{dri}$, $\lambda_{qdri} = \lambda_{qri} + j\lambda_{dri}$, $\lambda_{qdsi} = \lambda_{qsi} + j\lambda_{dsi}$. The frequencies of the supply voltages are $\omega_{ei}$ and the rotor electric speeds are $\omega_{ri}$. In all these and subsequent equations, $i = 1,2$ represent the state variables for ABC winding set and XYZ winding set respectively.

The stator and rotor currents are expressed in terms of the flux linkages as:

$$i_{qdsi} = \frac{L_{ri}}{D_i}\lambda_{qdsi} - \frac{L_{mi}}{D_i}\lambda_{qdri} \tag{10.57}$$

$$i_{qdri} = \frac{L_{si}}{D_i}\lambda_{qdri} - \frac{L_{mi}}{D_i}\lambda_{qdsi} \tag{10.58}$$

where, $D_i = L_{si}L_{ri} - L_{mi}^2$

Substituting equations (10.57-10.58) into (10.55-10.56) to eliminate the currents, the voltage equations can be expressed in terms of flux linkages as:

$$V_{qdsi} = \frac{r_{si}L_{ri}}{D_i}\lambda_{qdsi} - \frac{r_{si}L_{mi}}{D_i}\lambda_{qdri} + p\lambda_{qdsi} - j\omega_{ei}\lambda_{qdsi} \tag{10.59}$$

$$0 = \frac{r_{ri}L_{si}}{D_i}\lambda_{qdri} - \frac{r_{ri}L_{mi}}{D_i}\lambda_{qdsi} + p\lambda_{qdri} - j(\omega_{ei} - \omega_{ri})\lambda_{qdri} \tag{10.60}$$

If the stator and rotor flux linkages are chosen as state variables,

$$X_i = \begin{bmatrix} \lambda_{qdsi} \\ \lambda_{qdri} \end{bmatrix},\ B = \begin{bmatrix} 1 & 0 \\ 0 & 1 \end{bmatrix},\ U_i = \begin{bmatrix} V_{qdsi} \\ 0 \end{bmatrix}$$

The system equation in matrix form becomes:

$$\dot{X} = A_i X_i + BU_i \tag{10.61}$$

where, $A_i = \begin{bmatrix} -\frac{r_{si}L_{ri}}{D_i} + j\omega_{ei} & \frac{r_{si}L_{mi}}{D_i} \\ \frac{r_{ri}L_{mi}}{D_i} & -\frac{r_{ri}L_{si}}{D_i} + j(\omega_{ei} - \omega_{ri}) \end{bmatrix}$.

The stator currents are expressed in terms of flux linkages as:

$$i_{qdsi} = C_i X_i \tag{10.62}$$

where, $C_i = \begin{bmatrix} \frac{L_{ri}}{D_i} & -\frac{L_{mi}}{D_i} \end{bmatrix}$

The electromagnetic torque due to each winding set expressed in terms of the flux linkages is given as :

$$T_{ei} = \frac{3P}{4}\frac{L_{ri}}{D_i}\left(\lambda_{dri}\lambda_{qsi} - \lambda_{qri}\lambda_{dsi}\right) \tag{10.63}$$

The total electromagnetic torque of the dual stator winding induction machine is the sum of the electromagnetic torque components due to the interaction of the separate two three-phase winding sets with the squirrel-cage rotor.

### 10.6.2 Full Order Observer Model

The full-order flux observer equations of the machine are defined as:

$$p\hat{\lambda}_{qsi} = V_{qsi} - \frac{r_{si}L_{ri}}{D_i}\hat{\lambda}_{qsi} + \frac{r_{si}L_{mi}}{D_i}\hat{\lambda}_{qri} - \omega_{ei}\hat{\lambda}_{dsi} + K_{11i}\cdot\left(i_{qsi} - \hat{i}_{qsi}\right) \tag{10.64}$$

$$p\hat{\lambda}_{dsi} = V_{dsi} - \frac{r_{si}L_{ri}}{D_i}\hat{\lambda}_{ds} + \frac{r_{si}L_{mi}}{D_i}\hat{\lambda}_{dri} + \omega_{ei}\hat{\lambda}_{qsi} + K_{12i}\cdot\left(i_{dsi} - \hat{i}_{dsi}\right) \tag{10.65}$$

$$p\hat{\lambda}_{qri} = -\frac{r_{ri}L_{si}}{D_i}\hat{\lambda}_{qri} + \frac{r_{ri}L_{mi}}{D_i}\hat{\lambda}_{qsi} - (\omega_{ei} - \omega_{ri})\hat{\lambda}_{dri} + K_{21i}\cdot(i_{qsi} - \hat{i}_{qsi}) \tag{10.66}$$

$$p\hat{\lambda}_{dri} = -\frac{r_{ri}L_{si}}{D_i}\hat{\lambda}_{dri} + \frac{r_{ri}L_{mi}}{D_i}\hat{\lambda}_{dsi} + (\omega_{ei} - \omega_{ri})\hat{\lambda}_{qri} + K_{22i}\cdot(i_{dsi} - \hat{i}_{dsi}) \tag{10.67}$$

where, ^ represents the estimated quantities.

$$\hat{i}_{qdsi} = \frac{L_{ri}}{D_i}\hat{\lambda}_{qds} - \frac{L_{mi}}{D_i}\hat{\lambda}_{qdr} \tag{10.68}$$

The full-order flux observer is expressed in matrix form as:

$$\begin{aligned} \dot{\hat{X}}_i &= \hat{A}_i\hat{X}_i + BU_i + K_i(i_{qdsi} - \hat{i}_{qdsi}) \\ \hat{i}_{qdsi} &= \hat{C}_i\hat{X}_i \end{aligned} \tag{10.69}$$

where, $\hat{A}_i = \begin{bmatrix} -\frac{\hat{r}_{si}\hat{L}_{ri}}{\hat{D}_i} + j\omega_{ei} & \frac{\hat{r}_{si}\hat{L}_{mi}}{\hat{D}_i} \\ \frac{\hat{r}_{ri}\hat{L}_{mi}}{\hat{D}_i} & -\frac{\hat{r}_{ri}\hat{L}_{si}}{\hat{D}_i} + j(\omega_{ei} - \hat{\omega}_{ri}) \end{bmatrix}$, $\hat{C}_i = \begin{bmatrix} \frac{\hat{L}_{ri}}{\hat{D}_i} & -\frac{\hat{L}_{mi}}{\hat{D}_i} \end{bmatrix}$

The comparisons between the machine model and model equations of full-order flux observer show the similarities between them. Because of these similarities, it is described in some papers that the mechanism of full-order flux observer is basically an integration of simulating and controlling the machine within one micro-controller.

The difference between the machine model and observer model lies in the scalar coefficient matrix $K_i$, which may be time-varying matrix or constant values. The design methodology of $K_i$ will be introduced in the next section.

## 10.7 Observer Gain Design

The scalar coefficient $K_i$ is called observer gain. The definition of the observer gain is given as:

$$K_i = \begin{bmatrix} K_{11i} + jK_{12i} \\ K_{21i} + jK_{22i} \end{bmatrix} \tag{10.70}$$

The error between the actual and estimated states is defined as :

$$e_i = X_i - \hat{X}_i \tag{10.71}$$

Substituting the expressions of states into (10.71), the derivative of the error is expressed as:

$$\begin{aligned} \dot{e}_i &= \dot{X}_i - \dot{\hat{X}}_i \\ &= (A_i - K_i \cdot C_i) X_i - (\hat{A}_i - K_i \cdot \hat{C}_i) \hat{X}_i \\ &= (A_i - K_i \cdot C_i) X_i - (A_i - \Delta A_i - K_i \cdot C_i + K_i \cdot \Delta C_i) \hat{X}_i \\ &= (A_i - K_i \cdot C_i) e_i + (\Delta A_i - K_i \cdot \Delta C_i) \cdot \hat{X}_i \end{aligned} \tag{10.72}$$

where $\Delta A_i = A_i - \hat{A}_i = \gamma_{1i} - \begin{bmatrix} 0 & 0 \\ 0 & j(\omega_{ri} - \hat{\omega}_{ri}) \end{bmatrix}$, $\Delta C_i = C_i - \hat{C}_i$,

and $\gamma_i = \begin{bmatrix} -\frac{r_{si} L_{ri}}{D_i} + \frac{\hat{r}_{si} \hat{L}_{ri}}{\hat{D}_i} & \frac{r_{si} L_{mi}}{D_i} - \frac{\hat{r}_{si} \hat{L}_{mi}}{\hat{D}_i} \\ \frac{r_{ri} L_{mi}}{D_i} - \frac{\hat{r}_{ri} \hat{L}_{mi}}{\hat{D}_i} & -\frac{r_{ri} L_{si}}{D_i} + \frac{\hat{r}_{ri} \hat{L}_{si}}{\hat{D}_i} \end{bmatrix}$.

Then the characteristic equation of the error function is expressed as:

$$\lambda_i = \left| p \cdot I - A_i + K_i \cdot C_i \right| \tag{10.73}$$

Substituting the expressions of the matrices $A_i$, $K_i$ and $C_i$ into (10.72), the characteristic equation becomes:

$$
\begin{aligned}
&\left[p\cdot I - A_i + K_i\cdot C_i\right] \\
&= \begin{bmatrix} p & 0 \\ 0 & p \end{bmatrix} - \begin{bmatrix} -\frac{r_{si}L_{ri}}{D_i} + j\omega_{ei} & \frac{r_{si}L_{mi}}{D_i} \\ \frac{r_{ri}L_{mi}}{D_i} & -\frac{r_{ri}L_{si}}{D_i} + j\left(\omega_{ei}-\omega_{ri}\right) \end{bmatrix} + \begin{bmatrix} K_{11i} + jK_{12i} \\ K_{21i} + jK_{22i} \end{bmatrix}\cdot\begin{bmatrix} \frac{L_{ri}}{D_i} & -\frac{L_{mi}}{D_i} \end{bmatrix} \\
&= \begin{bmatrix} p + \frac{r_{si}L_{ri}}{D_i} - j\omega_{ei} & -\frac{r_{si}L_{mi}}{D_i} \\ -\frac{r_{ri}L_{mi}}{D_i} & p + \frac{r_{ri}L_{si}}{D_i} - j\left(\omega_{ei}-\omega_{ri}\right) \end{bmatrix} + \begin{bmatrix} \left(K_{11i} + jK_{12i}\right)\cdot\frac{L_{ri}}{D_i} & \left(K_{11i} + jK_{12i}\right)\cdot\left(-\frac{L_{mi}}{D_i}\right) \\ \left(K_{21i} + jK_{22i}\right)\cdot\frac{L_{ri}}{D_i} & \left(K_{21i} + jK_{22i}\right)\cdot\left(-\frac{L_{mi}}{D_i}\right) \end{bmatrix} \\
&= \begin{bmatrix} p + \frac{r_{si}L_{ri}}{D_i} - j\omega_{ei} + \left(K_{11i} + jK_{12i}\right)\cdot\frac{L_{ri}}{D_i} & -\frac{r_{si}L_{mi}}{D_i} + \left(K_{11i} + jK_{12i}\right)\cdot\left(-\frac{L_{mi}}{D_i}\right) \\ -\frac{r_{ri}L_{mi}}{D_i} + \left(K_{21i} + jK_{22i}\right)\cdot\frac{L_{ri}}{D_i} & p + \frac{r_{ri}L_{si}}{D_i} - j\left(\omega_{ei}-\omega_{ri}\right) + \left(K_{21i} + jK_{22i}\right)\cdot\left(-\frac{L_{mi}}{D_i}\right) \end{bmatrix} \\
&= \begin{bmatrix} p + \frac{r_{si}L_{ri}}{D_i} + \frac{K_{11i}L_{ri}}{D_i} + j\left(\frac{K_{12i}L_{ri}}{D_i} - \omega_{ei}\right) & -\frac{r_{si}L_{mi}}{D_i} - \frac{K_{11i}L_{mi}}{D_i} - j\frac{K_{12i}L_{mi}}{D_i} \\ -\frac{r_{ri}L_{mi}}{D_i} + \frac{K_{21i}L_{ri}}{D_i} + j\frac{K_{22i}L_{ri}}{D_i} & p + \frac{r_{ri}L_{si}}{D_i} - \frac{K_{21i}L_{mi}}{D_i} - j\left(\omega_{ei} - \omega_{ri} + \frac{K_{22i}L_{mi}}{D_i}\right) \end{bmatrix} \\
&= \begin{bmatrix} P_{11i} & P_{12i} \\ P_{21i} & P_{22i} \end{bmatrix}
\end{aligned}
\tag{10.74}
$$

If $P_{11i}P_{22i} - P_{12i}P_{21i} = t_{1i} + jt_{2i}$, then,

$$
\begin{aligned}
t_{1i} &= \left(p + \frac{r_{si}L_{ri}}{D_i} + \frac{K_{11i}L_{ri}}{D_i}\right)\cdot\left(p + \frac{r_{ri}L_{si}}{D_i} - \frac{K_{21i}L_{mi}}{D_i}\right) + \left(\frac{K_{12i}L_{ri}}{D_i} - \omega_{ei}\right)\cdot\left(\omega_{ei} - \omega_{ri} + \frac{K_{22i}L_{mi}}{D_i}\right) \\
&\quad - \left(-\frac{r_{si}L_{mi}}{D_i} - \frac{K_{11i}L_{mi}}{D_i}\right)\cdot\left(-\frac{r_{ri}L_{mi}}{D_i} + \frac{K_{21i}L_{ri}}{D_i}\right) - \frac{K_{12}L_{mi}}{D_i}\frac{K_{22i}L_{ri}}{D_i} \\
&= p^2 + t_{1ai}p + t_{1bi}
\end{aligned}
\tag{10.75}
$$

where,

$$
t_{1ai} = \frac{1}{D_i}\left(r_{si}L_{ri} + r_{ri}L_{si} + K_{11i}L_{ri} - K_{21i}L_{mi}\right) \tag{10.76}
$$

$$
\begin{aligned}
t_{1bi} &= \left(\frac{r_{si}L_{ri}}{D_i}+\frac{K_{11i}L_{ri}}{D_i}\right)\cdot\left(\frac{r_{ri}L_{si}}{D_i}-\frac{K_{21i}L_{mi}}{D_i}\right)+\left(\frac{K_{12i}L_{ri}}{D_i}-\omega_{ei}\right)\cdot\left(\omega_{ei}-\omega_{ri}+\frac{K_{22i}L_{mi}}{D_i}\right)\\
&\quad-\left(-\frac{r_{si}L_{mi}}{D_i}-\frac{K_{11i}L_{mi}}{D_i}\right)\cdot\left(-\frac{r_{ri}L_{mi}}{D_i}+\frac{K_{21i}L_{ri}}{D_i}\right)-\frac{K_{12i}L_{mi}}{D_i}\frac{K_{22i}L_{ri}}{D_i}\\
&=\frac{1}{D_i^2}\left(r_{si}L_{ri}+K_{11i}L_{ri}\right)\cdot\left(r_{ri}L_{si}-K_{21i}L_{mi}\right)+\left(\frac{K_{12i}L_{ri}}{D_i}-\omega_{ei}\right)\cdot\left(\omega_{ei}-\omega_{ri}\right)\\
&\quad-\omega_{ei}\frac{K_{22i}L_{mi}}{D_i}-\frac{1}{D_i^2}\left(r_{si}L_{mi}+K_{11i}L_{mi}\right)\cdot\left(r_{ri}L_{mi}-K_{21i}L_{ri}\right)\\
&=\frac{1}{D_i^2}\left(r_{si}L_{ri}r_{ri}L_{si}+K_{11i}L_{ri}r_{ri}L_{si}-r_{si}L_{mi}^2r_{ri}-K_{11i}L_{mi}^2r_{ri}\right)+\left(\frac{K_{12i}L_{ri}}{D_i}-\omega_{ei}\right)\cdot\left(\omega_{ei}-\omega_{ri}\right)-\omega_{ei}\frac{K_{22i}L_{mi}}{D_i}\\
&=\frac{1}{D_i}\left(r_{si}r_{ri}+K_{11i}r_{ri}\right)+\left(\frac{K_{12i}L_{ri}}{D_i}-\omega_{ei}\right)\cdot\left(\omega_{ei}-\omega_{ri}\right)-\omega_{ei}\frac{K_{22i}L_{mi}}{D_i}
\end{aligned}
\tag{10.77}
$$

Then

$$
\begin{aligned}
t_{2i} &= -\left(p+\frac{r_{si}L_{ri}}{D_i}+\frac{K_{11i}L_{ri}}{D_i}\right)\cdot\left(\omega_{ei}-\omega_{ri}+\frac{K_{22i}L_{mi}}{D_i}\right)+\left(p+\frac{r_{ri}L_{si}}{D_i}-\frac{K_{21i}L_{mi}}{D_i}\right)\cdot\left(\frac{K_{12i}L_{ri}}{D_i}-\omega_{ei}\right)\\
&\quad-\left(-\frac{r_{si}L_{mi}}{D_i}-\frac{K_{11i}L_{mi}}{D_i}\right)\cdot\frac{K_{22i}L_{ri}}{D_i}+\left(-\frac{r_{ri}L_{mi}}{D_i}+\frac{K_{21i}L_{ri}}{D_i}\right)\frac{K_{12i}L_{mi}}{D_i}\\
&=t_{2ai}\,p+t_{2bi}
\end{aligned}
\tag{10.78}
$$

where,

$$
\begin{aligned}
t_{2ai} &= -\left(\omega_{ei}-\omega_{ri}+\frac{K_{22}L_{mi}}{D_i}\right)+\left(\frac{K_{12}L_{ri}}{D_i}-\omega_{ei}\right)\\
&=\frac{K_{12i}L_{ri}+K_{22i}L_{mi}}{D_i}+\omega_{ri}-2\cdot\omega_{ei}
\end{aligned}
\tag{10.79}
$$

$$
\begin{aligned}
t_{2bi} &= -\left(\frac{r_{si}L_{ri}}{D_i}+\frac{K_{11i}L_{ri}}{D_i}\right)\cdot\left(\omega_{ei}-\omega_{ri}+\frac{K_{22i}L_{mi}}{D_i}\right)+\left(\frac{r_{ri}L_{si}}{D_i}-\frac{K_{21i}L_{mi}}{D_i}\right)\cdot\left(\frac{K_{12i}L_{ri}}{D_i}-\omega_{ei}\right) \\
&\quad -\left(-\frac{r_{si}L_{mi}}{D_i}-\frac{K_{11i}L_{mi}}{D_i}\right)\cdot\frac{K_{22i}L_{ri}}{D_i}+\left(-\frac{r_{ri}L_{mi}}{D_i}+\frac{K_{21i}L_{ri}}{D_i}\right)\frac{K_{12i}L_{mi}}{D_i} \\
&= -\left(\frac{r_{si}L_{ri}}{D_i}+\frac{K_{11i}L_{ri}}{D_i}\right)\cdot\left(\omega_{ei}-\omega_{ri}\right)-\left(\frac{r_{ri}L_{si}}{D_i}-\frac{K_{21i}L_{mi}}{D_i}\right)\cdot\left(\omega_{ei}\right)+\frac{r_{ri}L_{si}K_{12i}L_{ri}}{D_i^2}-\frac{r_{ri}K_{12i}L_{mi}^2}{D_i^2} \\
&= -\left(\frac{r_{si}L_{ri}}{D_i}+\frac{K_{11i}L_{ri}}{D_i}\right)\cdot\left(\omega_{ei}-\omega_{ri}\right)-\left(\frac{r_{ri}L_{si}}{D_i}-\frac{K_{21i}L_{mi}}{D_i}\right)\cdot\left(\omega_{ei}\right)+\frac{r_{ri}K_{12i}}{D_i}
\end{aligned}
\tag{10.80}
$$

The observer gain design is based on the characteristic equation of the observer so that the selected observer gains ensure the stability within the entire possible operating speed range. It should be noted that both the constant rotor speed with variable slip frequency condition and the constant slip frequency with variable rotor speed condition should be considered in the stability analysis.

Two pole placement methods have been used to design the observer gain. The first one is Butterworth method, which has been used in the controller design and has been described in [10.39]. The other method is called pole-shift method, which has been proposed in [10.25] and has also been adopted for observer gain design in [10.34]. The results from both methods have been compared and the Butterworth method is finally used to design the observer gain.

### 10.7.1 Butterworth Method

The Butterworth polynomial is used to locate the poles of the characteristic function. Since the complex form is used in the transfer function, there are only two poles. However the complex conjugates of these two poles yield other two poles [10.39]. The

main idea of the Butterworth method is to place the poles evenly on a half circle of radius $\omega_0$ in the left s-plane, with its center at origin. The four poles are given as:

$$p_1 = \omega_0 \cdot e^{j\frac{5\pi}{8}},\ p_2 = \omega_0 \cdot e^{j\frac{7\pi}{8}},\ p_3 = \omega_0 \cdot e^{j\frac{9\pi}{8}},\ p_4 = \omega_0 \cdot e^{j\frac{11\pi}{8}}$$

The first two poles are used to construct the Butterworth equation in complex form, which is given as:

$$(p - p_1)(p - p_2) = p^2 + \omega_0(1.3066 - j1.3066)p - j \cdot \omega_0^2 \tag{10.81}$$

The observer characteristic equation is compared with Butterworth equation to find the observer gains,

$$\begin{aligned}&\frac{r_{si}L_{ri}}{D_i} + \frac{r_{ri}L_{si}}{D_i} + \frac{L_{ri}}{D_i}(K_{11} + j \cdot K_{12}) - j \cdot (2\omega_{ei} - \omega_{ri}) - \frac{L_{mi}}{D_i}(K_{21} + j \cdot K_{22}) \\ &= \omega_0(1.3066 - j1.3066)\end{aligned} \tag{10.82}$$

$$\begin{aligned}&\frac{r_{si}r_{ri}}{D_i} + \frac{r_{ri}}{D_i}(K_{11} + j \cdot K_{12}) - j\frac{r_{si}L_{ri}}{D_i}(\omega_{ei} - \omega_{ri}) - j\omega_{ei}\frac{r_{ri}L_{si}}{D_i} \\ &+ j\omega_{ei}\frac{L_{mi}}{D_i}(K_{21} + j \cdot K_{22}) - j(\omega_{ei} - \omega_{ri})\frac{L_{ri}}{D_i}(K_{11} + j \cdot K_{12}) - \omega_{ei}(\omega_{ei} - \omega_{ri}) \\ &= -j \cdot \omega_0^2\end{aligned} \tag{10.83}$$

Both the imaginary and real parts of (10.82-10.83) need to be equal, which are expressed as:

$$\frac{r_{si}L_{ri}}{D_i} + \frac{r_{ri}L_{si}}{D_i} + \frac{L_{ri}}{D_i}(K_{11}) - \frac{L_{mi}}{D_i}(K_{21}) = 1.3066 \cdot \omega_0 \tag{10.84}$$

$$\frac{L_{ri}}{D_i}(K_{12}) - (2\omega_{ei} - \omega_{ri}) - \frac{L_{mi}}{D_i}(K_{22}) = -1.3066 \cdot \omega_0 \tag{10.85}$$

$$\frac{r_{si}r_{ri}}{D_i} + \frac{r_{ri}}{D_i}(K_{11}) - \omega_{ei}\frac{L_{mi}}{D_i}(K_{22}) + (\omega_{ei} - \omega_{ri})\frac{L_{ri}}{D_i}(K_{12}) - \omega_{ei}(\omega_{ei} - \omega_{ri}) = 0 \tag{10.86}$$

$$\frac{r_{ri}}{D_i}(K_{12}) - \frac{r_{si}L_{ri}}{D_i}(\omega_{ei} - \omega_{ri}) - \omega_{ei}\frac{r_{ri}L_{si}}{D_i} + \omega_{ei}\frac{L_{mi}}{D_i}(K_{21}) - (\omega_{ei} - \omega_{ri})\frac{L_{ri}}{D_i}(K_{11}) = -\omega_0^2 \tag{10.87}$$

Then the four observer gains can be determined from (10.84-10.87) as:

$$K_{11} = \frac{\left(-r_{ri}D_i\omega_{ei}^2 + 1.3066r_{ri}D_i\omega_{ei}\omega_0 + 1.3066L_{ri}\omega_{ri}\omega_{ei}\omega_0 D_i - L_{ri}D_i\omega_{ri}\omega_0^2\right)}{r_{ri}^2 + L_{ri}^2\omega_{ri}^2} - r_{si} \tag{10.88}$$

$$K_{12} = \frac{D_i\left(L_{ri}\omega_{ri}\omega_{ei}^2 - 1.3066L_{ri}\omega_{ri}\omega_{ei}\omega_0 + 1.3066r_{ri}\omega_{ei}\omega_0 - r_{ri}\omega_0^2\right)}{r_{ri}^2 + L_{ri}^2\omega_{ri}^2} \tag{10.89}$$

$$\begin{aligned} K_{21} = {} & \frac{\left(-r_{ri}L_{ri}D_i\omega_{ei}^2 + 1.3066r_{ri}L_{ri}D_i\omega_{ei}\omega_0 + 1.3066L_{ri}^2\omega_{ri}\omega_{ei}\omega_0 D_i - L_{ri}^2D_i\omega_{ri}\omega_0^2\right)}{\left(r_{ri}^2 + L_{ri}^2\omega_{ri}^2\right)L_{mi}} \\ & + \frac{r_{ri}L_{si}}{L_{mi}} - 1.3066\frac{\omega_0 D_i}{L_{mi}} \end{aligned} \tag{10.90}$$

$$\begin{aligned} K_{22} = {} & \frac{D_i\left(\omega_{ri}L_{ri}^2\omega_{ei}^2 - 1.3066\omega_{ri}L_{ri}^2\omega_{ei}\omega_0 + 1.3066L_{ri}\omega_{ei}\omega_0 r_{ri} - L_{ri}r_{ri}\omega_0^2\right)}{\left(r_{ri}^2 + L_{ri}^2\omega_{ri}^2\right)L_{mi}} \\ & - (2\omega_{ei} - \omega_{ri})\frac{D_i}{L_{mi}} + 1.3066\frac{\omega_0 D_i}{L_{mi}} \end{aligned} \tag{10.91}$$

The value of $\omega_0$ is obtained from the poles of the open loop induction machine model, whose characteristic equation is expressed as:

$$\begin{aligned} & p^2 + \left[\frac{r_{si}L_{ri}}{D_i} + \frac{r_{ri}L_{si}}{D_i} - j(2\omega_{ei} - \omega_{ri})\right]\cdot p \\ & + \left[\frac{r_{si}r_{ri}}{D_i} - j\frac{r_{ri}L_{si}\omega_{ei}}{D_i} - j(\omega_{ei} - \omega_{ri})\frac{r_{si}L_{ri}}{D_i} - \omega_{ei}(\omega_{ei} - \omega_{ri})\right] = 0 \end{aligned} \tag{10.92}$$

When $\omega_0$ is assumed to be the sum of the imaginary parts of the machine poles, the expression of $\omega_0$ is,

$$\omega_0 = 2\omega_{ei} - \omega_{ri} \tag{10.93}$$

If the rotor speed and the electric speed are known, the observer gains are functions of $\omega_0$. The variations of observer gains in terms of $\omega_0$ for the 2-pole winding set are given in Figure 10.9 when $\omega_{e1} = 377$ and $\omega_{r1} = 375$.

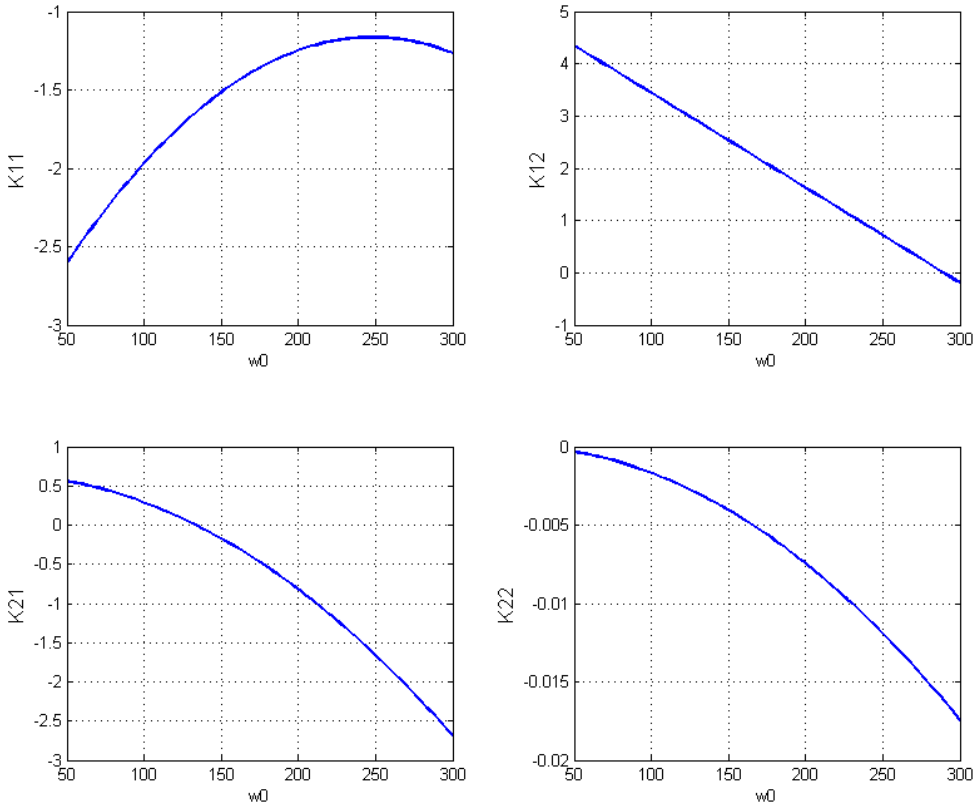


Figure 10.9 The variations of the observer gains in terms of $\omega_0$ for the 2-pole winding set

If the observer gains are chosen to be the values when $\omega_0 = 300$, the poles of machine model and observer models with the designed observer gains under varying rotor speed condition are shown in Figure 10.10(a) and Figure 10.10(b) respectively. The poles with positive slip frequency (motoring) are blue while and the poles with negative slip frequency (generating) are marked as red. Since the operating slip of the induction machine is within 0.03~0.05, depending on the load condition, the slip value in the analysis is chosen to be 0.05 to simulate the heavily loaded condition. The simulation

results show that the selected observer gains of the 2-pole winding set ensure the stability of the 2-pole winding observer within the whole operating range.

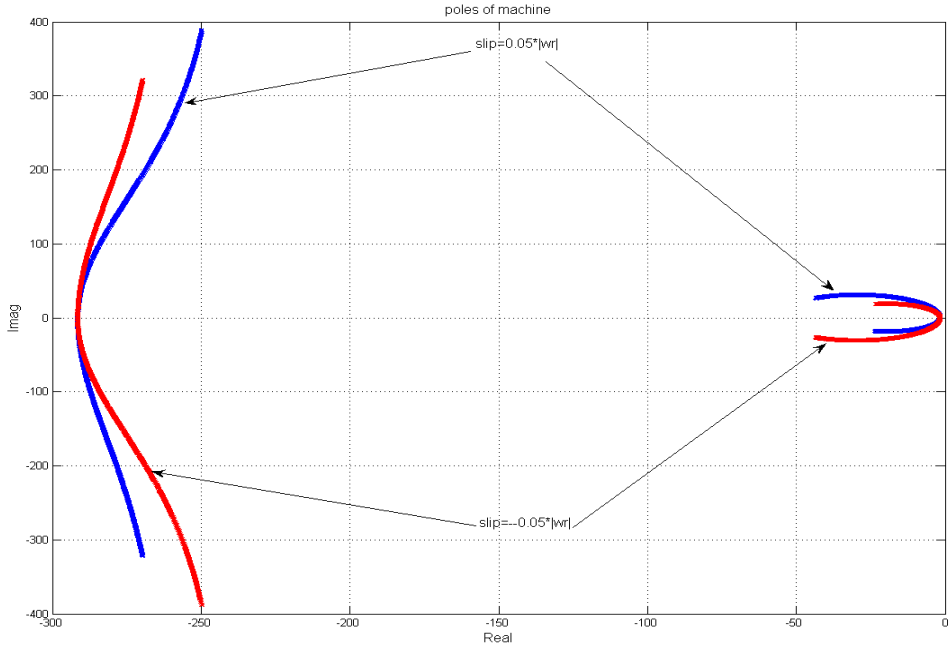


(a)

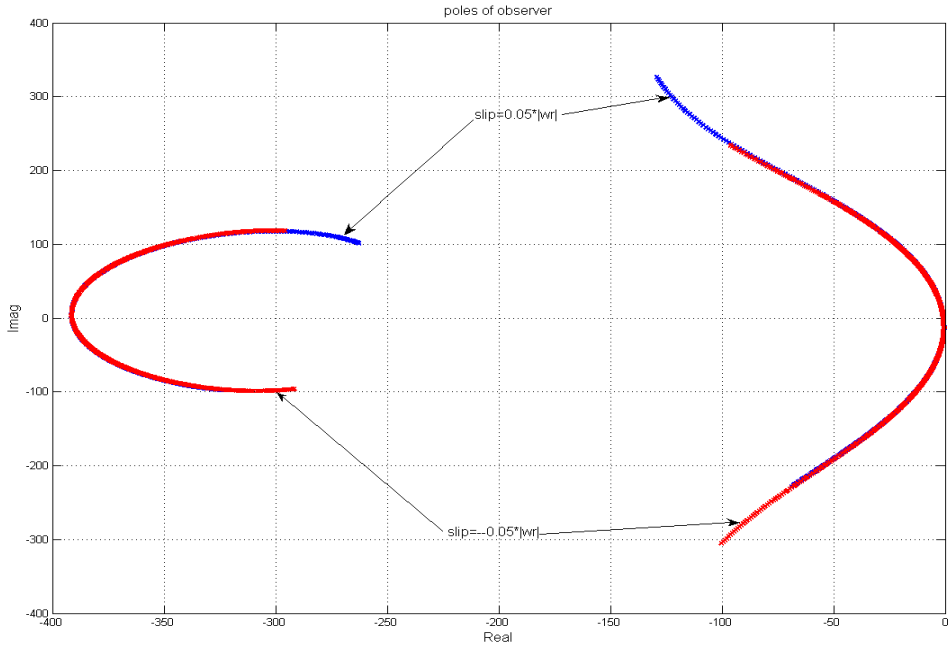


(b)

Figure 10.10 Pole placement, (a) the poles of the 2-pole winding set, (b) the observer poles of the 2-pole winding set

The variations of observer gains in terms of $\omega_0$ for the 6-pole winding set are shown in Figure 10.11 when $\omega_{e1} = 377$ and $\omega_{r1} = 375$.

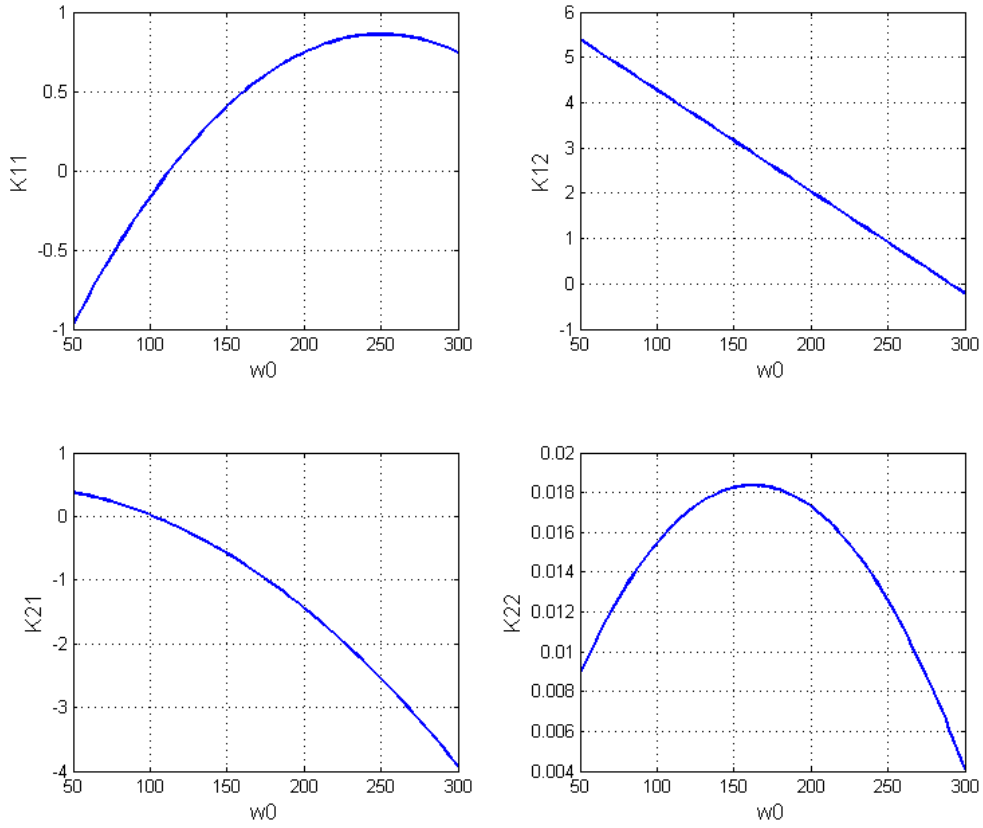


Figure 10.11 The variations of the observer gains in terms of $\omega_0$ for the 6-pole winding set

If the observer gains are chosen to be the values when $\omega_0 = 300$, the machine poles and the observer poles with the selected observer gains for the 6-pole winding set are shown in Figure 10.12 and Figure 10.13 respectively. The poles with positive slip frequency (motoring) is blue while and the poles with negative slip frequency (generating) is marked as red. The stability of the observer for the 6-pole winding set within the whole speed range has been confirmed by these simulation results.

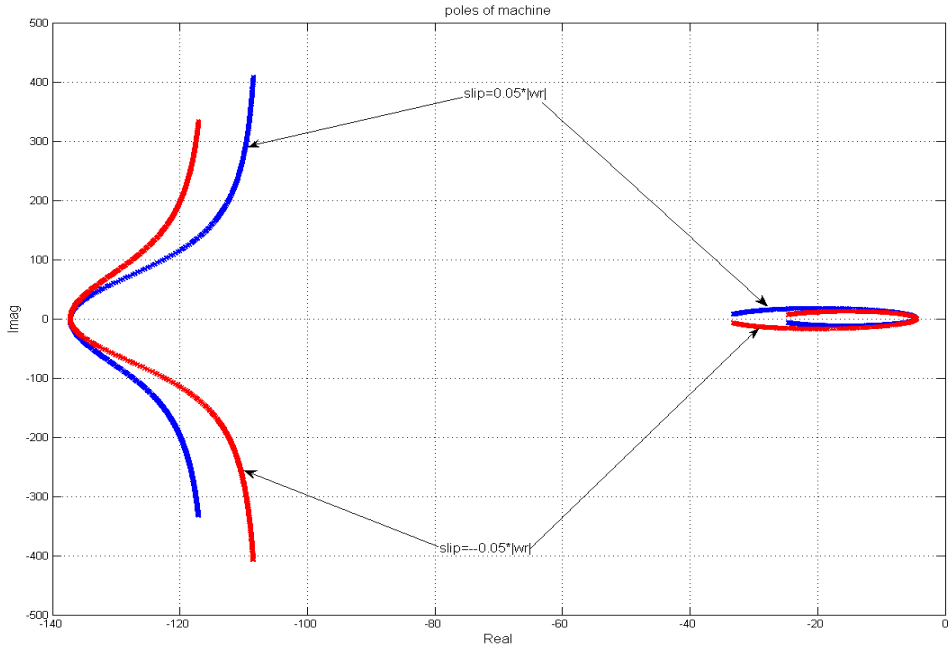


Figure 10.12 The poles of the 6-pole winding set

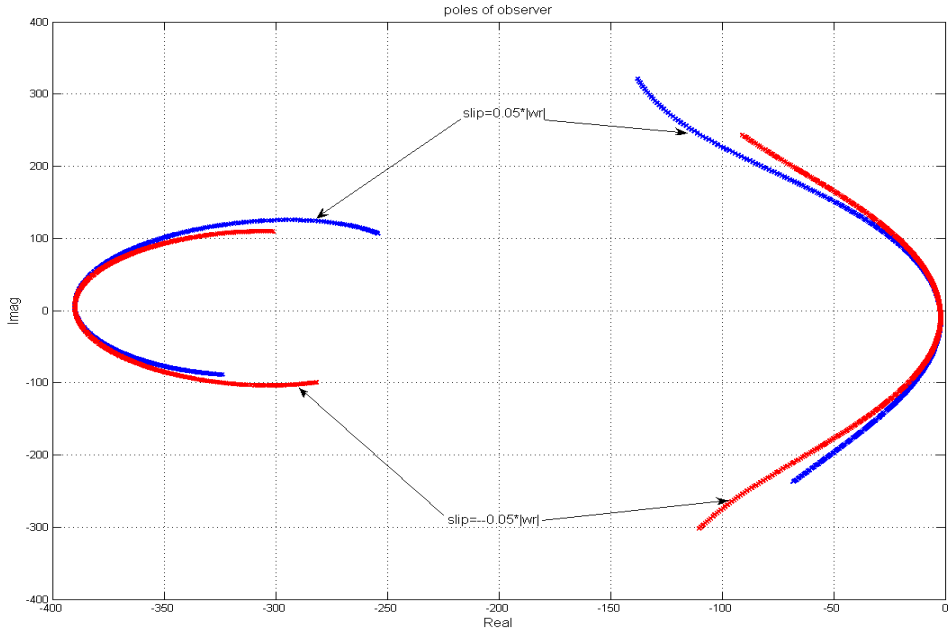


Figure 10.13 The observer poles of the 6-pole winding set

From the simulation results for both stator winding sets, it is found that one of the poles from each winding set will approach the imaginary axis when the rotor speed is

close to zero, confirming the instability problems observed when operating in the low speed range reported in many recent publications.

### 10.7.2 Pole-shift Method

The pole placement method in [10.25] is used to place the poles of the full-order observer. The coefficients of the observer are calculated at the base speed $\omega_b$ so that the observer poles are shifted to the left by the amount $k_s$ with respect to motor poles, that is $p_o(\omega_b) = p_m(\omega_b) - k_s$, with $k_s > 0$.

The characteristic equation for an induction motor is given as:

$$\begin{aligned} |p \cdot I - A| &= \left| \begin{bmatrix} p & 0 \\ 0 & p \end{bmatrix} - \begin{bmatrix} -\frac{r_{si}L_{ri}}{D_i} + j\omega_{ei} & \frac{r_{si}L_{mi}}{D_i} \\ \frac{r_{ri}L_{mi}}{D_i} & -\frac{r_{ri}L_{si}}{D_i} + j(\omega_{ei} - \omega_{ri}) \end{bmatrix} \right| \\ &= \begin{vmatrix} p + \frac{r_{si}L_{ri}}{D_i} - j\omega_{ei} & -\frac{r_{si}L_{mi}}{D_i} \\ -\frac{r_{ri}L_{mi}}{D_i} & p + \frac{r_{ri}L_{si}}{D_i} - j(\omega_{ei} - \omega_{ri}) \end{vmatrix} \end{aligned} \tag{10.94}$$

If E and F are assumed to be the poles of the machine, the characteristic equations can be expressed as:

$$\left(p + \frac{r_{si}L_{ri}}{D_i} - j\omega_{ei}\right) \cdot \left(p + \frac{r_{ri}L_{si}}{D_i} - j(\omega_{ei} - \omega_{ri})\right) - \frac{r_{si}L_{mi}}{D_i}\frac{r_{ri}L_{mi}}{D_i} = (p - E) \cdot (p - F) \tag{10.95}$$

If the poles of the observer are shifted left with $k_s$, the characteristic equation is given as:

$$\lambda = (p - E + k_s) \cdot (p - F + k_s) \tag{10.96}$$

Substituting (10.95) into (10.96),

$$
\begin{aligned}
\lambda &= \left(p - E + k_s\right)\cdot\left(p - F + k_s\right) \\
&= \left(p - E\right)\cdot\left(p - F\right) + \left(2p - E - F\right)\cdot k_s + k_s^2 \\
&= \left(p + \frac{r_{si}L_{ri}}{D_i} - j\omega_{ei}\right)\cdot\left(p + \frac{r_{ri}L_{si}}{D_i} - j\left(\omega_{ei} - \omega_{ri}\right)\right) - \frac{r_{si}L_{mi}}{D_i}\frac{r_{ri}L_{mi}}{D_i} + 2k_s p \\
&\quad + \left(\frac{r_{si}L_{ri}}{D_i} - j\omega_{ei} + \frac{r_{ri}L_{si}}{D_i} - j\left(\omega_{ei} - \omega_{ri}\right)\right)\cdot k_s + k_s^2 \\
&= p^2 + \left(\frac{r_{si}L_{ri}}{D_i} - j\omega_{ei} + \frac{r_{ri}L_{si}}{D_i} - j\left(\omega_{ei} - \omega_{ri}\right) + 2k_s\right)\cdot p \\
&\quad + \left(\frac{r_{si}L_{ri}}{D_i} - j\omega_{ei}\right)\cdot\left(\frac{r_{ri}L_{si}}{D_i} - j\left(\omega_{ei} - \omega_{ri}\right)\right) - \frac{r_{si}L_{mi}}{D_i}\frac{r_{ri}L_{mi}}{D_i} \\
&\quad + \left(\frac{r_{si}L_{ri}}{D_i} - j\omega_{ei} + \frac{r_{ri}L_{si}}{D_i} - j\left(\omega_{ei} - \omega_{ri}\right)\right)\cdot k_s + k_s^2 \\
&= p^2 + t_{s1}p + t_{s2}
\end{aligned}
\tag{10.97}
$$

where, $t_{s1} = \dfrac{r_{si}L_{ri}}{D_i} - j\omega_{ei} + \dfrac{r_{ri}L_{si}}{D_i} - j\left(\omega_{ei} - \omega_{ri}\right) + 2k_s$ and

$$
\begin{aligned}
t_{s2} &= \left(\frac{r_{si}L_{ri}}{D_i} - j\omega_{ei}\right)\cdot\left(\frac{r_{ri}L_{si}}{D_i} - j\left(\omega_{ei} - \omega_{ri}\right)\right) - \frac{r_{si}L_{mi}}{D_i}\frac{r_{ri}L_{mi}}{D_i} \\
&\quad + \left(\frac{r_{si}L_{ri}}{D_i} - j\omega_{ei} + \frac{r_{ri}L_{si}}{D_i} - j\left(\omega_{ei} - \omega_{ri}\right)\right)\cdot k_s + k_s^2
\end{aligned}
$$

The characteristic equation of observer with the feedback observer gains is given as:

$$
\begin{aligned}
\lambda &= \left|p\cdot I - A + K\cdot C\right| \\
&= \begin{bmatrix} P_{11} & P_{12} \\ P_{21} & P_{22} \end{bmatrix} \\
&= \begin{bmatrix} p + \dfrac{r_{si}L_{ri}}{D_i} + \dfrac{K_{11i}L_{ri}}{D_i} + j\left(\dfrac{K_{12i}L_{ri}}{D_i} - \omega_{ei}\right) & -\dfrac{r_{si}L_{mi}}{D_i} - \dfrac{K_{11i}L_{mi}}{D_i} - j\dfrac{K_{12i}L_{mi}}{D_i} \\ -\dfrac{r_{ri}L_{mi}}{D_i} + \dfrac{K_{21i}L_{ri}}{D_i} + j\dfrac{K_{22i}L_{ri}}{D_i} & p + \dfrac{r_{ri}L_{si}}{D_i} - \dfrac{K_{21i}L_{mi}}{D_i} - j\left(\omega_{ei} - \omega_{ri} + \dfrac{K_{22i}L_{mi}}{D_i}\right) \end{bmatrix} \\
&= p^2 + t_1 p + t_2
\end{aligned}
\tag{10.98}
$$

where,

$$
\begin{aligned}
&p^2 + t_1 p + t_2 \\
&= \left[ p + \frac{r_{si} L_{ri}}{D_i} + \frac{K_{11i} L_{ri}}{D_i} + j\left( \frac{K_{12i} L_{ri}}{D_i} - \omega_{ei} \right) \right] \cdot \left[ p + \frac{r_{ri} L_{si}}{D_i} - \frac{K_{21i} L_{mi}}{D_i} - j\left( \omega_{ei} - \omega_{ri} + \frac{K_{22i} L_{mi}}{D_i} \right) \right] \\
&- \left( - \frac{r_{si} L_{mi}}{D_i} - \frac{K_{11i} L_{mi}}{D_i} - j \frac{K_{12i} L_{mi}}{D_i} \right) \cdot \left( - \frac{r_{ri} L_{mi}}{D_i} + \frac{K_{21i} L_{ri}}{D_i} + j \frac{K_{22i} L_{ri}}{D_i} \right) \\
&= p^2 + \left[ \frac{r_{si} L_{ri}}{D_i} + \frac{K_{11i} L_{ri}}{D_i} + j\left( \frac{K_{12i} L_{ri}}{D_i} - \omega_{ei} \right) + \frac{r_{ri} L_{si}}{D_i} - \frac{K_{21i} L_{mi}}{D_i} - j\left( \omega_{ei} - \omega_{ri} + \frac{K_{22i} L_{mi}}{D_i} \right) \right] \cdot p \\
&+ \left[ \frac{r_{si} L_{ri}}{D_i} + \frac{K_{11i} L_{ri}}{D_i} + j\left( \frac{K_{12i} L_{ri}}{D_i} - \omega_{ei} \right) \right] \cdot \left[ \frac{r_{ri} L_{si}}{D_i} - \frac{K_{21i} L_{mi}}{D_i} - j\left( \omega_{ei} - \omega_{ri} + \frac{K_{22i} L_{mi}}{D_i} \right) \right] \\
&- \left( - \frac{r_{si} L_{mi}}{D_i} - \frac{K_{11i} L_{mi}}{D_i} - j \frac{K_{12i} L_{mi}}{D_i} \right) \cdot \left( - \frac{r_{ri} L_{mi}}{D_i} + \frac{K_{21i} L_{ri}}{D_i} + j \frac{K_{22i} L_{ri}}{D_i} \right)
\end{aligned}
$$

(10.99)

$$
\begin{aligned}
t_1 &= \frac{r_{si} L_{ri}}{D_i} + \frac{K_{11i} L_{ri}}{D_i} + j\left( \frac{K_{12i} L_{ri}}{D_i} - \omega_{ei} \right) + \frac{r_{ri} L_{si}}{D_i} - \frac{K_{21i} L_{mi}}{D_i} - j\left( \omega_{ei} - \omega_{ri} + \frac{K_{22i} L_{mi}}{D_i} \right) \\
&= \frac{r_{si} L_{ri}}{D_i} + \frac{r_{ri} L_{si}}{D_i} + \frac{L_{ri}}{D_i}\left( K_{11i} + j \cdot K_{12i} \right) - j \cdot \left( 2\omega_{ei} - \omega_{ri} \right) - \frac{L_{mi}}{D_i}\left( K_{21i} + j \cdot K_{22i} \right)
\end{aligned}
$$

(10.100)

$$
\begin{aligned}
t_2 &= \left[ \frac{r_{si} L_{ri}}{D_i} + \frac{L_{ri}}{D_i}\left( K_{11i} + j \cdot K_{12i} \right) - j\omega_{ei} \right] \cdot \left[ \frac{r_{ri} L_{si}}{D_i} - \frac{L_{mi}}{D_i}\left( K_{21i} + j \cdot K_{22i} \right) - j\left( \omega_{ei} - \omega_{ri} \right) \right] \\
&- \left[ - \frac{r_{si} L_{mi}}{D_i} - \frac{L_{mi}}{D_i}\left( K_{11i} + j \cdot K_{12i} \right) \right] \cdot \left[ - \frac{r_{ri} L_{mi}}{D_i} + \frac{L_{ri}}{D_i}\left( K_{21i} + j \cdot K_{22i} \right) \right] \\
&= \frac{r_{si} r_{ri}}{D_i} + \frac{r_{ri}}{D_i}\left( K_{11i} + j \cdot K_{12i} \right) - j \frac{r_{si} L_{ri}}{D_i}\left( \omega_{ei} - \omega_{ri} \right) - j\omega_{ei} \frac{r_{ri} L_{si}}{D_i} + j\omega_{ei} \frac{L_{mi}}{D_i}\left( K_{21i} + j \cdot K_{22i} \right) \\
&- j\left( \omega_{ei} - \omega_{ri} \right) \frac{L_{ri}}{D_i}\left( K_{11i} + j \cdot K_{12i} \right) - \omega_{ei}\left( \omega_{ei} - \omega_{ri} \right)
\end{aligned}
$$

(10.101)

The characteristic equation (10.97) and (10.98) will be equal if the following conditions are met,

$$\begin{cases} t_{s1} = t_1 \\ t_{s2} = t_2 \end{cases} \tag{10.102}$$

Then the constant coefficients are obtained from:

$$\begin{aligned} &\frac{r_{si}L_{ri}}{D_i} + \frac{r_{ri}L_{si}}{D_i} + \frac{L_{ri}}{D_i}\left(K_{11i} + j\cdot K_{12i}\right) - j\cdot\left(2\omega_{ei} - \omega_{ri}\right) - \frac{L_{mi}}{D_i}\left(K_{21i} + j\cdot K_{22i}\right) \\ &= \frac{r_{si}L_{ri}}{D_i} - j\omega_{ei} + \frac{r_{ri}L_{si}}{D_i} - j\left(\omega_{ei} - \omega_{ri}\right) + 2k_s \end{aligned} \tag{10.103}$$

$$\begin{aligned} &\frac{r_{si}r_{ri}}{D_i} + \frac{r_{ri}}{D_i}\left(K_{11i} + j\cdot K_{12i}\right) - j\frac{r_{si}L_{ri}}{D_i}\left(\omega_{ei} - \omega_{ri}\right) - j\omega_{ei}\frac{r_{ri}L_{si}}{D_i} \\ &+ j\omega_{ei}\frac{L_{mi}}{D_i}\left(K_{21i} + j\cdot K_{22i}\right) - j\left(\omega_{ei} - \omega_{ri}\right)\frac{L_{ri}}{D_i}\left(K_{11i} + j\cdot K_{12i}\right) - \omega_{ei}\left(\omega_{ei} - \omega_{ri}\right) \\ &= \left(\frac{r_{si}L_{ri}}{D_i} - j\omega_{ei}\right)\cdot\left(\frac{r_{ri}L_{si}}{D_i} - j\left(\omega_{ei} - \omega_{ri}\right)\right) - \frac{r_{si}L_{mi}}{D_i}\frac{r_{ri}L_{mi}}{D_i} \\ &+ \left(\frac{r_{si}L_{ri}}{D_i} - j\omega_{ei} + \frac{r_{ri}L_{si}}{D_i} - j\left(\omega_{ei} - \omega_{ri}\right)\right)\cdot k_s + k_s^2 \end{aligned} \tag{10.104}$$

Since both the imaginary and real parts of (10.103-10.104) must be equal, the four equations are given as:

$$\frac{L_{ri}}{D_i}K_{11i} - \frac{L_{mi}}{D_i}K_{21i} = 2k_s \tag{10.105}$$

$$\frac{L_{ri}}{D_i}K_{12i} - \frac{L_{mi}}{D_i}K_{22i} = 0 \tag{10.106}$$

$$\begin{aligned} &\frac{r_{ri}}{D_i}K_{11i} - \omega_{ei}\frac{L_{mi}}{D_i}K_{22i} + \left(\omega_{ei} - \omega_{ri}\right)\frac{L_{ri}}{D_i}K_{12i} \\ &= \left(\frac{r_{si}L_{ri}}{D_i} + \frac{r_{ri}L_{si}}{D_i}\right)\cdot k_s + k_s^2 \end{aligned} \tag{10.107}$$

$$\begin{aligned} &\frac{r_{ri}}{D_i}K_{12i} + \omega_{ei}\frac{L_{mi}}{D_i}K_{21i} - \left(\omega_{ei} - \omega_{ri}\right)\frac{L_{ri}}{D_i}K_{11i} \\ &= -\left(2\omega_{ei} - \omega_{ri}\right)\cdot k_s \end{aligned} \tag{10.108}$$

When $k_s = 100$, the simulation results of the pole-shift method with a positive slip frequency (corresponding to the motoring condition) and negative slip frequency (corresponding to the generating condition) are given in Figure 10.14 and Figure 10.15 respectively. The poles of the machine are blue while the poles of the observer are marked in red in the figures.

The effectiveness of the pole-shift method for high rotor speed are demonstrated in the simulation results given in Figure 10.14 and Figure 10.15, however the method does not work well at the low speed range since one of the poles from both the machine model and the observer approach the imaginary axis when rotor speed is close to zero.

Since the pole-shift method cannot achieve the desired pole movement at the low speed range, the Butterworth method, which is straightforward and simpler to use, has been chosen as the design method adopted.

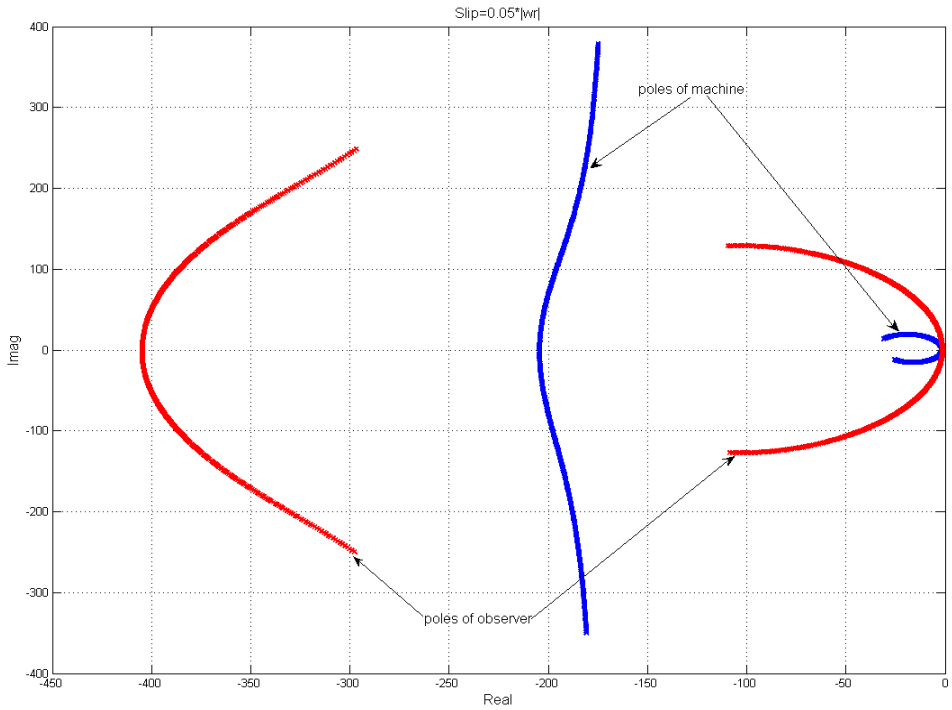


Figure 10.14 The poles of the machine and the observer under motoring condition for the 2-pole winding set

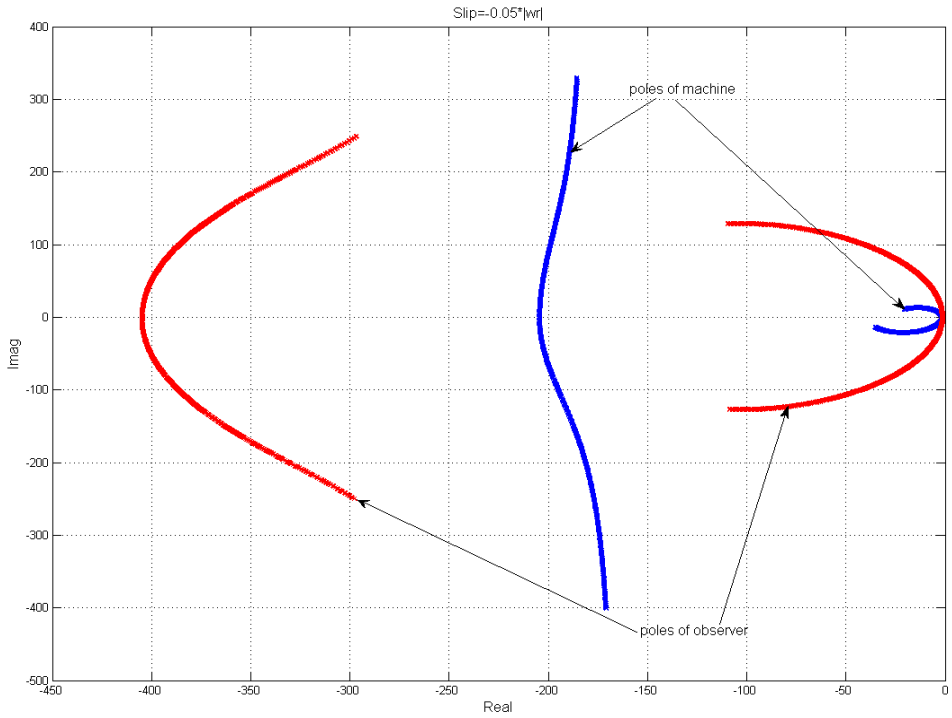


Figure 10.15 The poles of the machine and the observer under generating condition for the 2-pole winding set

## 10.8 D-decomposition Method

The challenging problem for controller design is to determine a set of control parameters, which ensure the stability of the system and achieve good dynamic responses. The system stability is the primary issue considered in the design. The general solution of stability problem has been given by the stability criteria of Routh, Hurwitz, Nyquist and Mikhailov. However, the stability criteria do not constitute a completely satisfactory theory for the design of feedback system. Thus the development of refined techniques for the analysis and design of feedback control system was necessary. The idea of investigating the system response characteristics was first introduced by Vishnegradsky. Then Neimark generalized the Vishnegradsky approach for the case of

nth-degree algebraic equations in his D-decomposition method. Here D-decomposition is applied to determine the boundary of stable and unstable resigns from the system characteristic equation in system parameter domain.

Consider a real polynomial, which is corresponding to the characteristic equation of a transfer function,

$$F(s)=\sum_{i=0}^{n} a_i \cdot s^i = 0 \tag{10.109}$$

where, $s=\sigma+j\omega$ is the complex variable and the coefficients $a_i$ are the continuous function of $r$ system parameters $p$, which is expressed as $a_i = a_i(p_1, p_2, \cdots, p_r)$.

Then the r-dimensional vector space can be decomposed into sets denoted by $D(m, n-m)$, which represent the polynomial having $m$ zeros with negative real parts and $n-m$ zeros with positive real parts. Such a decomposition of the parameter space into sets is called the D-decomposition.

The boundary of the sets $D(m, n-m)$ consists of surfaces determined by:

$$a_0 = 0, \quad a_n = 0 \tag{10.110}$$

The surface determined by $a_0 = 0$ corresponds to a zero at the origin of the $s$ plane while the surface determined by $a_n = 0$ corresponds to the zero at infinity of the $s$ plane.

The boundary also consists of the surface determined by:

$$\begin{aligned} R &= \sum_{i=0}^{n} a_i X_i = 0 \\ I &= \sum_{i=0}^{n} a_i Y_i = 0 \end{aligned} \tag{10.111}$$

where $a_i$ are the coefficients of $F(s)$ and

$$X_i = X_i(\sigma, \omega)$$
$$Y_i = Y_i(\sigma, \omega) \tag{10.112}$$

are functions defined by the complex variable expression $s = \sigma + j\omega$ and

$$s^i = X_i + jY_i \tag{10.113}$$

$X_i$ and $Y_i$ can be obtained by applying the recurrence formulas as:

$$X_{i+2} - 2\sigma X_{i+1} + \omega^2 X_i = 0$$
$$Y_{i+2} - 2\sigma Y_{i+1} + \omega^2 Y_i = 0 \tag{10.114}$$

where, $X_0 = 1$, $X_1 = 0$, $Y_0 = 0$, $Y_{01} = \omega$.

If the value of $\sigma$ is zero in (10.111-10.114), the surface determined by (10.111) corresponds to the zeros of $F(s)$ that have zero real parts.

If the system parameters in the space are chosen from the set $D(n,0)$, the stability of a linear system with characteristic polynomial $F(s)$ is assured. The points on the boundary of the set $D(n,0)$ will satisfy the condition.

The general definition of D-decomposition is within an $n$ dimension parameter space, however it is convenient to apply it to two-parameter problems since the stability boundary of two-parameter problems can be graphically shown. In the case of two parameters, the boundary of the stable and unstable regions can be determined from (10.110) and (10.111). The conditions for (10.111) are equivalent to the $F(s)$ with substituting $s = j\omega$. Certain D-decomposition curve can be drawn by varying $\omega$, in which the two unknown parameters are the real and imaginary axis. The curve will divide the system parameter plane into the stable and unstable regions. The stable region is determined by following a certain shading rule [10.66]. In the *s*-plane, the stable area is on the left half plane while the corresponding stable area in the parameter plane is

determined by calculating the determinant of the Jacobian matrix. In the case of the two parameters ($\alpha$ and $\beta$) problem, the Jacobian matrix is defined as

$$J = \begin{vmatrix} \dfrac{\partial R}{\partial \alpha} & \dfrac{\partial R}{\partial \beta} \\ \dfrac{\partial I}{\partial \alpha} & \dfrac{\partial I}{\partial \beta} \end{vmatrix} \tag{10.115}$$

where $R$ and $I$ are the real and imaginary parts of the characteristic equation when $s = j\omega$ is substituted into $F(s)$. If determinant of $J$ ($\det(J) > 0$) is greater than 0, the stable area in the parameter plane will be on the left hand side of the D-decomposition curve when $\omega$ is increasing; if $\det(J) < 0$, then the stable area in the parameter plane will be on the right hand side of the D-decomposition curve when $\omega$ is increasing. When the D-decomposition curve is complicated, it is better to double check the stable and unstable regions by calculating the real parts of the roots of the characteristic equations in each individual region.

## 10.9 Speed Estimator Design

The full-order observer system based on Model Reference Adaptive Scheme (MRAS) is used to estimate the flux linkages, the stator currents and rotor speed using the measured stator voltage and stator current signals of the motor. The error between the actual stator currents and the estimated stator currents is used in a specialized error function to calculate an estimation error between the observer and the actual physical system. Then the output of the error function is fed to the speed estimator to estimate the rotor speed. The adaptive mechanism is established when the rotor speed estimated from

this error is used as the feedback. The estimated rotor speed is equal to the actual speed when this error is minimized to be zero. This method is a closed loop estimation scheme, which is different from the open loop flux estimation using the stator voltage equations.

The speed error is known to converge to zero when the speed estimator structure is a Proportion-Integral (PI) [10.17]. The error function, which yields the error signal, plays a very important role in the speed estimator design. Different error functions have been proposed in previous work and a brief introduction can be found in Chapter 1.

The error function proposed in [10.39] is given as:

$$\varepsilon = k\,\mathrm{Im}\left[\hat{\lambda}^{*}_{qdri}\left(i_{qdsi} - \hat{i}_{qdsi}\right)\right] + (1-k)\,\mathrm{Re}\left[\hat{\lambda}^{*}_{qdri}\left(i_{qdsi} - \hat{i}_{qdsi}\right)\right] \tag{10.116}$$

where, $0 \le k \le 1$.

The drawback of this error function lies in the fact that when the weight of reactive power increases, the weight of active power has to be reduced. It is found that the reduction of active power at any rotor speed cannot enhance the system stability and can only make the stability problem worse. If only the reactive power is used in the error function, it is found from the stability analysis using D-decomposition that the stable regions for different slip frequencies with the same set of speed estimator parameters will conflict with each other. For example, if the rotor speed is adjusted within the whole speed range so that the parameters of speed estimator are chosen to stabilize the system in slip frequency A, it may be unstable when the motor is operated under slip frequency B. However, by adding the reactive power in a specific manner, the system stability can be improved.

A novel error function is proposed in this dissertation to improve the stability of the speed estimator within the whole operating speed range. The proposed error function is defined as:

$$\begin{aligned}\varepsilon = k\left\{ \mathrm{Im}\left[\hat{\lambda}^{*}_{qdr1}\left(i_{qds1}-\hat{i}_{qds1}\right)\right]+k_1\,\mathrm{Re}\left[\hat{\lambda}^{*}_{qdr1}\left(i_{qds1}-\hat{i}_{qds1}\right)\right]\right\} \\ +\left(1-k\right)\left\{ \mathrm{Im}\left[\hat{\lambda}^{*}_{qdr2}\left(i_{qds2}-\hat{i}_{qds2}\right)\right]+k_2\,\mathrm{Re}\left[\hat{\lambda}^{*}_{qdr2}\left(i_{qds2}-\hat{i}_{qds2}\right)\right]\right\}\end{aligned} \tag{10.117}$$

where, $k$ is a binary variable used to partition the error signals from two stator windings and $k = 0\ or\ 1$; $k_1$ is used to change the effects of reactive power of the ABC winding set; $k_2$ is used to change the effect of reactive power of the XYZ winding set.

If the PI controller is used to generate the speed estimation, the estimated speed can be expressed as:

$$\begin{aligned}\hat{\omega}_{rm} &= G\cdot\varepsilon \\ &= G_p\cdot\varepsilon + G_i\cdot\int\varepsilon\,dt\end{aligned} \tag{10.118}$$

where, $\hat{\omega}_{rm}$ is estimated rotor mechanical speed.

The error between the actual and estimated states is needed to determine the transfer function of the speed estimation. The error function definition and its derivative have been given in (10.71-10.72).

The derivative of the state error can also be given as :

$$\dot{e}_i = \left(A_i - K_i\cdot C_i\right)\cdot e_i + \alpha_i\cdot\hat{X}_i - \underbrace{\begin{bmatrix}0\\ j\lambda_{qdri}\end{bmatrix}}_{Z_i}\left(\omega_{ri}-\hat{\omega}_{ri}\right) \tag{10.119}$$

where $\alpha_i = \gamma_i - K_i\cdot\Delta C_i$.

Hence,

$$e_i = \left[p\cdot I - A_i + K_i\cdot C_i\right]^{-1}\cdot\left[\alpha_i\cdot\hat{X}_i - Z_i\cdot\left(\omega_{ri}-\hat{\omega}_{ri}\right)\right] \tag{10.120}$$

The output error is expressed in terms of the speed information and states in (10.121).

$$\begin{aligned} i_{qdsi} - \hat{i}_{qdsi} &= C_i \cdot X_i - \hat{C}_i \cdot \hat{X}_i \\ &= (C_i - \Delta C_i) \cdot e_i + \Delta C_i \cdot X_i \\ &= (C_i - \Delta C_i) \cdot [p \cdot I - A_i + K_i \cdot C_i]^{-1} \left[\alpha_i \cdot \hat{X}_i - Z_i \cdot (\omega_{ri} - \hat{\omega}_{ri})\right] + \Delta C_i \cdot X_i \end{aligned}$$

(10.121)

The speed estimation using (10.117) and (10.121) becomes:

$$\begin{aligned} \hat{\omega}_{rm} &= G \cdot k \left\{ \mathrm{Im}\left[\hat{\lambda}^*_{qdr1} \left(i_{qds1} - \hat{i}_{qds1}\right)\right] + k_1 \,\mathrm{Re}\left[\hat{\lambda}^*_{qdr1} \left(i_{qds1} - \hat{i}_{qds1}\right)\right] \right\} \\ &\quad + (1-k) \left\{ \mathrm{Im}\left[\hat{\lambda}^*_{qdr2} \left(i_{qds2} - \hat{i}_{qds2}\right)\right] + k_2 \,\mathrm{Re}\left[\hat{\lambda}^*_{qdr2} \left(i_{qds2} - \hat{i}_{qds2}\right)\right] \right\} \\ &= G \cdot k \left\{ \begin{array}{l} \mathrm{Im}\left[ \begin{array}{l} \hat{\lambda}^*_{qdr1} \cdot (C_1 - \Delta C_1) \cdot [p \cdot I - A_1 + K_1 \cdot C_1]^{-1} \left[\alpha_1 \cdot \hat{X}_1 - Z_1 \cdot (\omega_{r1} - \hat{\omega}_{r1})\right] \\ + \hat{\lambda}^*_{qdr1} \cdot \Delta C_1 \cdot X_1 \end{array} \right] \\ + k_1 \,\mathrm{Re}\left[ \begin{array}{l} \hat{\lambda}^*_{qdr1} (C_1 - \Delta C_1) \cdot [p \cdot I - A_1 + K_1 \cdot C_1]^{-1} \left[\alpha_1 \cdot \hat{X}_1 - Z_1 \cdot (\omega_{r1} - \hat{\omega}_{r1})\right] \\ + \hat{\lambda}^*_{qdr1} \cdot \Delta C_1 \cdot X_1 \end{array} \right] \end{array} \right\} \\ &\quad + G \cdot (1-k) \left\{ \begin{array}{l} \mathrm{Im}\left[ \begin{array}{l} \hat{\lambda}^*_{qdr2} \cdot (C_2 - \Delta C_2) \cdot [p \cdot I - A_2 + K_2 \cdot C_2]^{-1} \left[\alpha_2 \cdot \hat{X}_2 - Z_2 \cdot (\omega_{r2} - \hat{\omega}_{r2})\right] \\ + \hat{\lambda}^*_{qdr2} \cdot \Delta C_2 \cdot X_2 \end{array} \right] \\ + k_2 \,\mathrm{Re}\left[ \begin{array}{l} \hat{\lambda}^*_{qdr2} \cdot (C_2 - \Delta C_2) \cdot [p \cdot I - A_2 + K_2 \cdot C_2]^{-1} \left[\alpha_2 \cdot \hat{X}_2 - Z_2 \cdot (\omega_{r2} - \hat{\omega}_{r2})\right] \\ + \hat{\lambda}^*_{qdr2} \cdot \Delta C_2 \cdot X_2 \end{array} \right] \end{array} \right\} \end{aligned}$$

(10.122)

To simplify the analysis that follows, the motor parameters are assumed to be constant, which means $\Delta C_i = 0$ and $\alpha_i = 0$. Hence, the speed estimation is simplified as in (10.123).

$$\begin{aligned} \hat{\omega}_{rm} &= -G \cdot k \left\{ \begin{array}{l} \mathrm{Im}\left[\hat{\lambda}^*_{qdr1} \cdot (C_1) \cdot [p \cdot I - A_1 + K_1 \cdot C_1]^{-1} [Z_1 \cdot (\omega_{r1} - \hat{\omega}_{r1})]\right] \\ + k_1 \,\mathrm{Re}\left[\hat{\lambda}^*_{qdr1} (C_1) \cdot [p \cdot I - A_1 + K_1 \cdot C_1]^{-1} [Z_1 \cdot (\omega_{r1} - \hat{\omega}_{r1})]\right] \end{array} \right\} \\ &\quad - G \cdot (1-k) \left\{ \begin{array}{l} \mathrm{Im}\left[\hat{\lambda}^*_{qdr2} \cdot (C_2) \cdot [p \cdot I - A_2 + K_2 \cdot C_2]^{-1} [Z_2 \cdot (\omega_{r2} - \hat{\omega}_{r2})]\right] \\ + k_2 \,\mathrm{Re}\left[\hat{\lambda}^*_{qdr2} \cdot (C_2) \cdot [p \cdot I - A_2 + K_2 \cdot C_2]^{-1} [Z_2 \cdot (\omega_{r2} - \hat{\omega}_{r2})]\right] \end{array} \right\} \end{aligned}$$

(10.123)

If the relationship between rotor mechanical speed $\omega_{rm}$, rotor speed of ABC winding set $\omega_{r1}$ and rotor speed of XYZ winding set $\omega_{r2}$ are expressed as:

$$\begin{aligned}\omega_{r1} &= P_1 \cdot \omega_{rm} \\ \omega_{r2} &= P_2 \cdot \omega_{rm}\end{aligned} \tag{10.124}$$

where, $P_1$ and $P_2$ are the pole pair numbers of ABC and XYZ winding sets respectively.

Then (10.123) can be rewritten in terms of rotor mechanical speed $\omega_{rm}$ as:

$$\begin{aligned}\hat{\omega}_{rm} &= -G \cdot P_1 \cdot k\left\{\begin{array}{l}\mathrm{Im}\left[\hat{\lambda}^*_{qdr1} \cdot (C_1) \cdot \left[p \cdot I - A_1 + K_1 \cdot C_1\right]^{-1}\left[Z_1 \cdot (\omega_{rm} - \hat{\omega}_{rm})\right]\right] \\ + k_1\,\mathrm{Re}\left[\hat{\lambda}^*_{qdr1}(C_1) \cdot \left[p \cdot I - A_1 + K_1 \cdot C_1\right]^{-1}\left[Z_1 \cdot (\omega_{rm} - \hat{\omega}_{rm})\right]\right]\end{array}\right\} \\ &\quad - G \cdot P_2 \cdot (1-k)\left\{\begin{array}{l}\mathrm{Im}\left[\hat{\lambda}^*_{qdr2} \cdot (C_2) \cdot \left[p \cdot I - A_2 + K_2 \cdot C_2\right]^{-1}\left[Z_2 \cdot (\omega_{rm} - \hat{\omega}_{rm})\right]\right] \\ + k_2\,\mathrm{Re}\left[\hat{\lambda}^*_{qdr2} \cdot (C_2) \cdot \left[p \cdot I - A_2 + K_2 \cdot C_2\right]^{-1}\left[Z_2 \cdot (\omega_{rm} - \hat{\omega}_{rm})\right]\right]\end{array}\right\} \\ &= -G \cdot P_1 \cdot k\{\,\mathrm{Im}[H_1] + k_1\,\mathrm{Re}[H_1]\} - G \cdot P_2 \cdot (1-k)\{\,\mathrm{Im}[H_2] + k_2\,\mathrm{Re}[H_2]\}\end{aligned} \tag{10.125}$$

where, $H_i = \hat{\lambda}^*_{qdri} \cdot (C_i) \cdot \left[p \cdot I - A_i + K_i \cdot C_i\right]^{-1}\left[Z_i \cdot (\omega_{rm} - \hat{\omega}_{rm})\right]$.

The expression of $\left[p \cdot I - A_i + K_i \cdot C_i\right]$ is given in (10.74). Then the expression of $H_i$ is given as:

$$\begin{aligned}H_i &= \hat{\lambda}^*_{qdri} C_i \frac{\begin{bmatrix} P_{22i} & -P_{12i} \\ -P_{21i} & P_{11i}\end{bmatrix}}{P_{11i}P_{22i} - P_{12i}P_{21i}} Z_i(\omega_{rm} - \hat{\omega}_{rm}) \\ &= -\left|\hat{\lambda}_{qdri}\right|^2 \cdot (\omega_{rm} - \hat{\omega}_{rm}) \cdot j \cdot \frac{\left(\frac{L_{ri}}{D_i}P_{12i} + \frac{L_{mi}}{D_i}P_{11i}\right)}{P_{11i}P_{22i} - P_{12i}P_{21i}} \\ &= -\left|\hat{\lambda}_{qdri}\right|^2 \cdot (\omega_{rm} - \hat{\omega}_{rm}) \cdot \frac{L_{mi}}{D_i} \cdot j \cdot \frac{p - j\omega_{ei}}{P_{11i}P_{22i} - P_{12i}P_{21i}} \\ &= -\left|\hat{\lambda}_{qdri}\right|^2 \cdot (\omega_{rm} - \hat{\omega}_{rm}) \cdot \frac{L_{mi}}{D_i} \cdot j \cdot \frac{p - j\omega_{ei}}{t_{1i} + jt_{2i}}\end{aligned} \tag{10.126}$$

The expressions of $t_{1i}$ and $t_{2i}$ are given in (10.75-10.80). Equation (10.119) can also be function expressed as:

$$H_i = -\left|\hat{\lambda}_{qdri}\right|^2 \cdot \left(\omega_{rm} - \hat{\omega}_{rm}\right) \cdot \frac{L_{mi}}{D_i} \cdot \frac{\left(\omega_{ei} t_{1i} + p t_{2i}\right) + j\left(p t_{1i} - \omega_{ei} t_{2i}\right)}{t_{1i}^2 + t_{2i}^2}. \tag{10.127}$$

Then the imaginary and real parts of (10.127) are given as:

$$\mathrm{Im}\left(H_i\right) = -\left|\hat{\lambda}_{qdri}\right|^2 \cdot \left(\omega_{rm} - \hat{\omega}_{rm}\right) \cdot \frac{L_{mi}}{D_i} \cdot \frac{p t_{1i} - \omega_{ei} t_{2i}}{t_{1i}^2 + t_{2i}^2} \tag{10.128}$$

$$\mathrm{Re}\left(H_i\right) = -\left|\hat{\lambda}_{qdri}\right|^2 \cdot \left(\omega_{rm} - \hat{\omega}_{rm}\right) \cdot \frac{L_{mi}}{D_i} \cdot \frac{\omega_{ei} t_{1i} + p t_{2i}}{t_{1i}^2 + t_{2i}^2} \tag{10.129}$$

To simplify the analysis, the following definitions are made:

$$f_{1i}(p) = \left|\hat{\lambda}_{qdri}\right|^2 \cdot \frac{L_{mi}}{D_i} \cdot \frac{p t_{1i} - \omega_{ei} t_{2i}}{t_{1i}^2 + t_{2i}^2} \tag{10.130}$$

$$f_{2i}(p) = \left|\hat{\lambda}_{qdri}\right|^2 \cdot \frac{L_{mi}}{D_i} \cdot \frac{p t_{2i} + \omega_{ei} t_{1i}}{t_{1i}^2 + t_{2i}^2} \tag{10.131}$$

Then (10.125) can be rewritten as:

$$\begin{aligned} \hat{\omega}_{rm} = {} & G \cdot P_1 \cdot k\left\{ f_{11}(p) + k_1 \cdot f_{21}(p)\right\} \cdot \left(\omega_{rm} - \hat{\omega}_{rm}\right) \\ & + G \cdot P_2 \cdot (1-k)\left\{ f_{12}(p) + k_2 \cdot f_{22}(p)\right\} \cdot \left(\omega_{rm} - \hat{\omega}_{rm}\right) \end{aligned} \tag{10.132}$$

The first idea of speed estimation is an adjustable combination of the error signals from both stator winding sets. The computed error function is expressed as:

$$\begin{aligned} \varepsilon = {} & k\left\{ k_1 \,\mathrm{Im}\left[\hat{\lambda}_{qdr1}^{*}\left(i_{qds1} - \hat{i}_{qds1}\right)\right] + (1-k_1)\,\mathrm{Re}\left[\hat{\lambda}_{qdr1}^{*}\left(i_{qds1} - \hat{i}_{qds1}\right)\right]\right\} \\ & + (1-k)\left\{ k_2 \,\mathrm{Im}\left[\hat{\lambda}_{qdr2}^{*}\left(i_{qds2} - \hat{i}_{qds2}\right)\right] + (1-k_2)\,\mathrm{Re}\left[\hat{\lambda}_{qdr2}^{*}\left(i_{qds2} - \hat{i}_{qds2}\right)\right]\right\} \end{aligned} \tag{10.133}$$

where, $k$ is used to partition the error signals from two stator windings and $0 \le k \le 1$; $k_1$ is used to partition the active power and reactive power of ABC winding set and

$0 \le k_1 \le 1$; $k_2$ is used to partition the active power and reactive power of XYZ winding set and $0 \le k_2 \le 1$.

However, it is found that when two error signals are combined together, the speed estimation scheme becomes much more complex. To simplify the analysis, the error function uses the error signal from one winding at any point in time, however the winding that provides the error signals may change at different times and different operating conditions. The derivation of the speed estimation is now simplified to be the same as that of the single winding induction machine except that a binary variable k is used to determine the winding set that provides the speed estimation error signal.

Since at any point in time, only one error signal is applied to the speed estimation, (10.133) can be simplified as:

$$\hat{\omega}_{rm} = G \cdot \left[ f_{1i}(p) + k_i \cdot f_{2i}(p) \right] \cdot \left( \omega_{rm} - \hat{\omega}_{rm} \right) \tag{10.134}$$

Define $f_i(p) = f_{1i}(p) + k_i \cdot f_{2i}(p)$, then the transfer function becomes,

$$\frac{\hat{\omega}_{rm}}{\omega_{rm}} = \frac{G \cdot f_i(p)}{1 + G \cdot f_i(p)} \tag{10.135}$$

where,

$$\begin{aligned} f_i(p) &= f_{1i}(p) + k_i \cdot f_{2i}(p) \\ &= \left| \hat{\lambda}_{qdri} \right|^2 \cdot \frac{L_{mi}}{D_i} \cdot \frac{p t_{1i} - \omega_{ei} t_{2i}}{t_{1i}^2 + t_{2i}^2} + k_i \cdot \left| \hat{\lambda}_{qdri} \right|^2 \cdot \frac{L_{mi}}{D_i} \cdot \frac{p t_{2i} + \omega_{ei} t_{1i}}{t_{1i}^2 + t_{2i}^2} \\ &= \left| \hat{\lambda}_{qdri} \right|^2 \cdot \frac{L_{mi}}{D_i} \cdot \left[ \frac{p t_{1i} - \omega_{ei} t_{2i}}{t_{1i}^2 + t_{2i}^2} + k_i \cdot \frac{p t_{2i} + \omega_{ei} t_{1i}}{t_{1i}^2 + t_{2i}^2} \right] \\ &= K_{fi} \cdot \frac{a_{3i} p^3 + a_{2i} p^2 + a_{1i} p + a_{0i}}{p^4 + b_{3i} p^3 + b_{2i} p^2 + b_{1i} p + b_{0i}} \end{aligned} \tag{10.136}$$

$$
\begin{aligned}
a_{3i} &= 1 \\
a_{2i} &= t_{1ai} + k_i \cdot \left(t_{2ai} + \omega_{ei}\right) \\
a_{1i} &= \left(t_{1bi} - \omega_{ei} \cdot t_{2ai}\right) + k_i \cdot \left(t_{2bi} + \omega_{ei} t_{1ai}\right) \\
a_{0i} &= -\omega_{ei} \cdot t_{2bi} + k_i \cdot \omega_{ei} \cdot t_{1bi}
\end{aligned}
\tag{10.137}
$$

$$
\begin{aligned}
b_{3i} &= 2t_{1ai} \\
b_{2i} &= 2t_{1bi} + t_{1ai}^2 + t_{2ai}^2 \\
b_{1i} &= 2t_{1ai} t_{1bi} + 2t_{2ai} t_{2bi} \\
b_{0i} &= t_{1bi}^2 + t_{2bi}^2
\end{aligned}
\tag{10.138}
$$

$$
K_{fi} = \left|\hat{\lambda}_{qdri}\right|^2 \cdot \frac{L_{mi}}{D_i} \tag{10.139}
$$

If the controller structure is a Proportion-Integral (PI), the transfer function becomes,

$$
\begin{aligned}
\frac{\hat{\omega}_{rm}}{\omega_{rm}} &= \frac{\left(G_{pi} + \dfrac{G_{ii}}{p}\right) \cdot f_i(p)}{1 + \left(G_{pi} + \dfrac{G_{ii}}{p}\right) \cdot f_i(p)} \\
&= \frac{A_{4i} p^4 + A_{3i} p^3 + A_{2i} p^2 + A_{1i} p + A_{0i}}{p^5 + B_{4i} p^4 + B_{3i} p^3 + B_{2i} p^2 + B_{1i} p + B_{0i}} = \frac{A_i(p)}{B_i(p)}
\end{aligned}
\tag{10.140}
$$

where,

$$
\begin{aligned}
A_{4i} &= a_{3i} G_{pi} K_{fi} \\
A_{3i} &= a_{2i} G_{pi} K_{fi} + a_{3i} G_{ii} K_{fi} \\
A_{2i} &= a_{1i} G_{pi} K_{fi} + a_{2i} G_{ii} K_{fi} \\
A_{1i} &= a_{0i} G_{pi} K_{fi} + a_{1i} G_{ii} K_{fi} \\
A_{0i} &= a_{0i} G_{ii} K_{fi}
\end{aligned}
\tag{10.141}
$$

$$
\begin{aligned}
B_{4i} &= b_{3i} + a_{3i} G_{pi} K_{fi} \\
B_{3i} &= b_{2i} + a_{2i} G_{pi} K_{fi} + a_{3i} G_{ii} K_{fi} \\
B_{2i} &= b_{1i} + a_{1i} G_{pi} K_{fi} + a_{2i} G_{ii} K_{fi} \\
B_{1i} &= b_{0i} + a_{0i} G_{pi} K_{fi} + a_{1i} G_{ii} K_{fi} \\
B_{0i} &= a_{0i} G_{ii} K_{fi}
\end{aligned}
\tag{10.142}
$$

The control parameters of a PI controller have to be properly selected to regulate the error function of the Model Reference Adaptive Scheme (MRAS), yield accurate estimated rotor speed and maintain the stability of the whole motor drive. The stability of the system in the whole variable speed range is the first concern and the condition required to achieve stability is that all the poles of the transfer function should be in the left half s-plane, which also implies that all the poles should have negative real parts. In the real applications, from the system noise point of view, the real parts of the poles cannot be too large. The zeroes of the transfer function also need to have negative real parts to ensure that the system is the minimum phase system.

Several approaches have been proposed to select the control parameters and ensure the stability of the system. The Routh criteria is one of those methods, in which the coefficients of the transfer function are used to build up a Routh table, and the stability conditions can be found from the Routh table. However, because of the complexity of the coefficients, the Routh criteria is not applicable in this case. The D-decomposition is applied to select the parameters of the PI controller. Basically, the boundary of the stability region is found in the control parameters plane and the parameters within the stability region are applied to the system. There are two critical conditions that need to be examined. The first case is the condition in which the poles located at the origin of the s-plane, which can be expressed as:

$$p = 0 \tag{10.143}$$

The second condition is that the poles are located at the imaginary axis of s-plane. The expression for this case is:

$$p = \pm j\omega_0 \tag{10.144}$$

The transfer function of rotor speed is given as:

$$\frac{\hat{\omega}_{rm}}{\omega_{rm}} = \frac{A_{4i}p^4 + A_{3i}p^3 + A_{2i}p^2 + A_{1i}p + A_{0i}}{p^5 + B_{4i}p^4 + B_{3i}p^3 + B_{2i}p^2 + B_{1i}p + B_{0i}}$$

The condition that satisfies the first condition is:

$$\begin{aligned} &B_{0i} = 0 \Rightarrow a_{0i} = 0 \Rightarrow \\ &-\omega_{ei} \cdot t_{2bi} + k_i \cdot \omega_{ei} \cdot t_{1bi} = 0 \end{aligned} \tag{10.145}$$

Equation (10.145) is a function of the observer gains, machine parameters and the error function partition coefficient of active and reactive power. Since the observer gains have been determined in the previous section and the machine parameters are all known and assumed to be constant here, (10.138) becomes the function of error function partition coefficients ($k$, $k_1$ and $k_2$).

Substituting (10.144) into the denominator of (10.140), the expression satisfying the second condition is given as:

$$\begin{cases} \omega_0^4 - B_{3i} \cdot \omega_0^2 + B_{1i} = 0 \\ B_{4i} \cdot \omega_0^4 - B_{2i} \cdot \omega_0^2 + B_{0i} = 0 \end{cases} \tag{10.146}$$

Since all the B coefficients in (10.146) are functions of the controller parameters $G_{pi}$ and $G_{ii}$, the boundary of the controller parameters can be obtained when $\omega_0$ is changed.

The boundaries of the controller parameters should be found under different slip conditions and different values of factor $k_i$ so that the controller parameters chosen guarantee stability under all operating conditions.

The stability issue using only active power has been studied by plotting the zeros and poles of the transfer function for speed estimation. The observer gains and parameters of the speed estimator are kept to be constant and factor $k_i$ is set equal to zero, the poles and

zeros of the transfer function are plotted when the operating rotor speed changes from 377 to -377. The slip is kept constant during the speed changes and the expression of the slip frequency is given as:

$$\omega_{si} = 0.05 \cdot \left|\omega_{ri}\right| \tag{10.147}$$

One of the reasons to use this kind of slip frequency expression is because most of the induction machines are operated within the slip range $[-0.05, 0.05]$ and the second reason is that this kind of slip definition matches approximately the constant torque operating condition.

When $k_i$ is equal to zero, the pole-zero maps under different rotor speeds with different constant slip conditions are given in Figure 10.16(a-d). It is found that the poles and zeros of the speed estimator approach the imaginary axis when the rotor speed moves close to zero no matter the value of the operation slip. That might explain why the speed estimation scheme is always unstable at low speed range.

The effects of coefficient $k_i$ under different rotor speeds and slip frequency conditions are demonstrated in Figures 10.17 - 10.20.

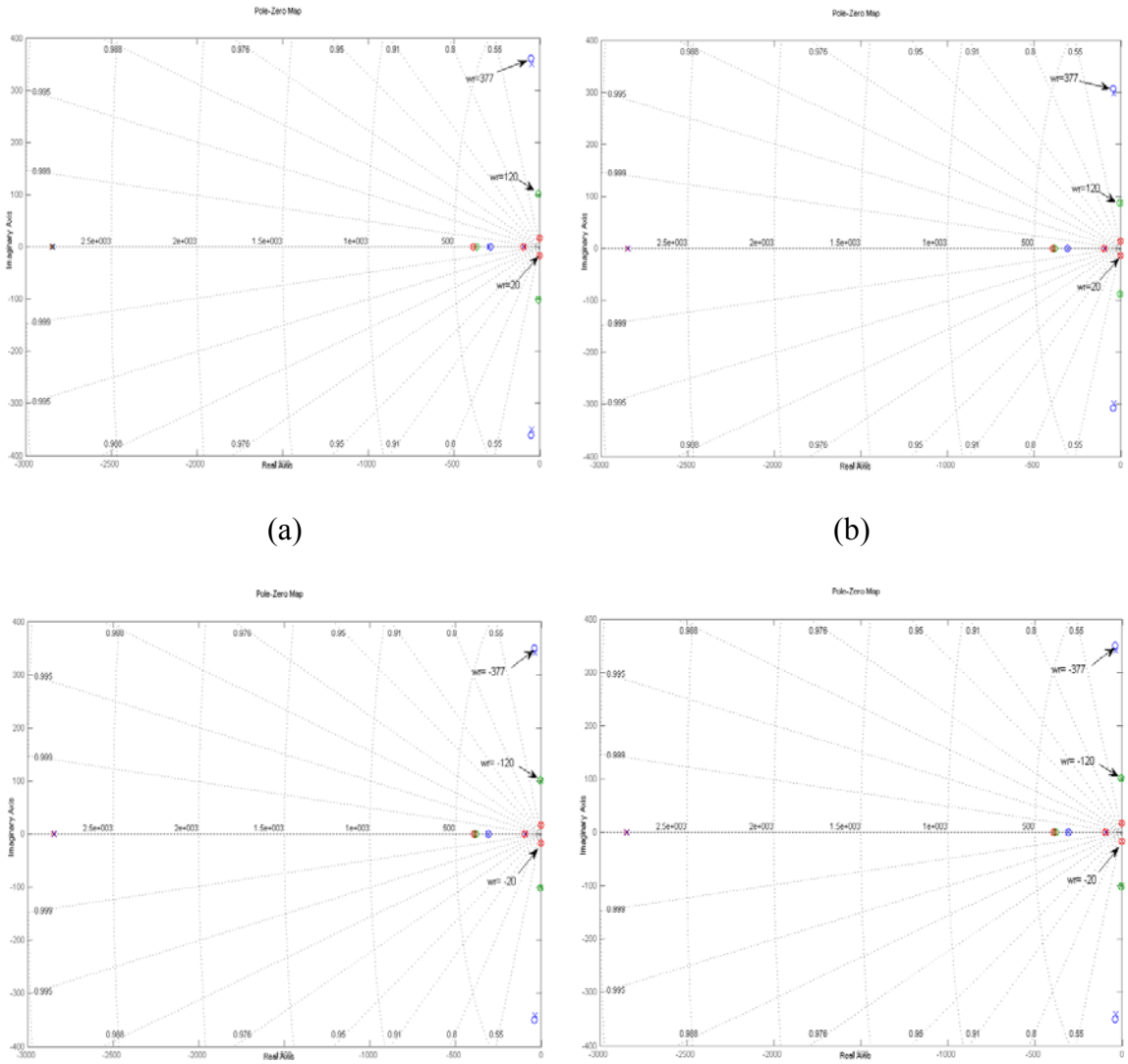


Figure 10.16 Pole-zero maps under different operating conditions, (a) positive rotor speed when slip=0.05, (b) positive rotor speed when slip=-0.05, (c) negative rotor speed when slip=0.05, (d) negative rotor speed when slip=-0.05.

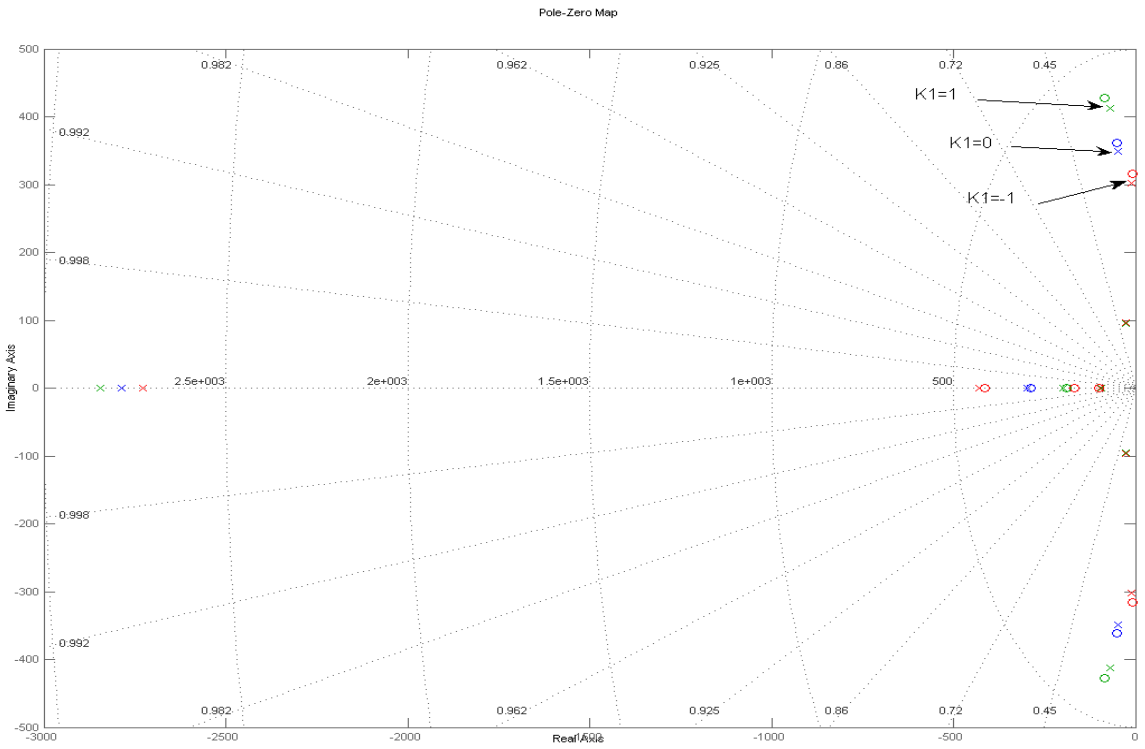


Figure 10.17 Pole-zero maps with different $k_i$ values when $\omega_{r1} = 377$ and slip =0.05

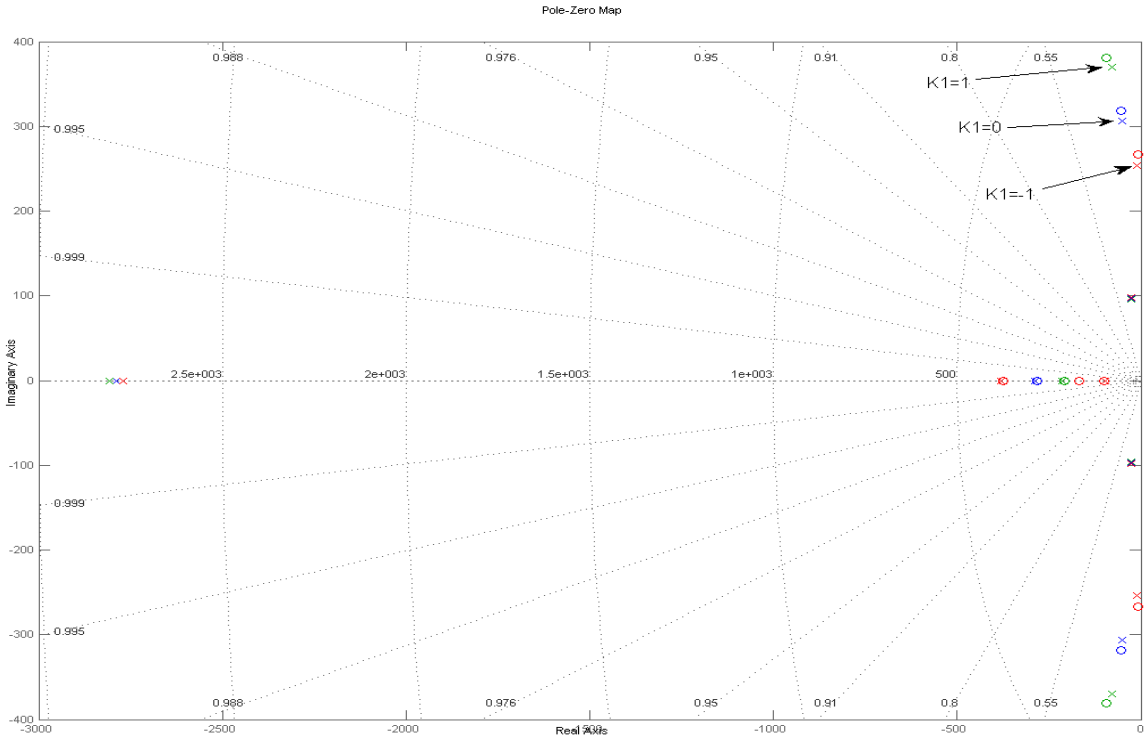


Figure 10.18 Pole-zero maps with different $k_i$ values when $\omega_{r1} = 377$ and slip =-0.05

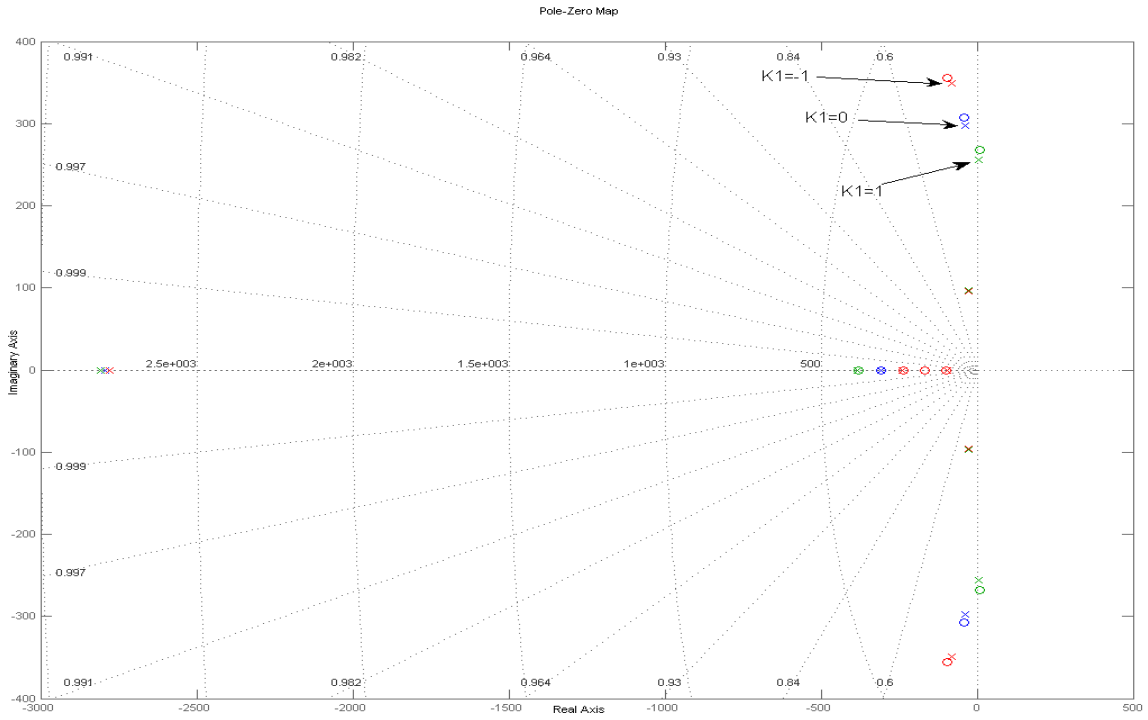


Figure 10.19 Pole-zero maps with different $k_i$ values when $\omega_{r1} = -377$ and slip =0.05

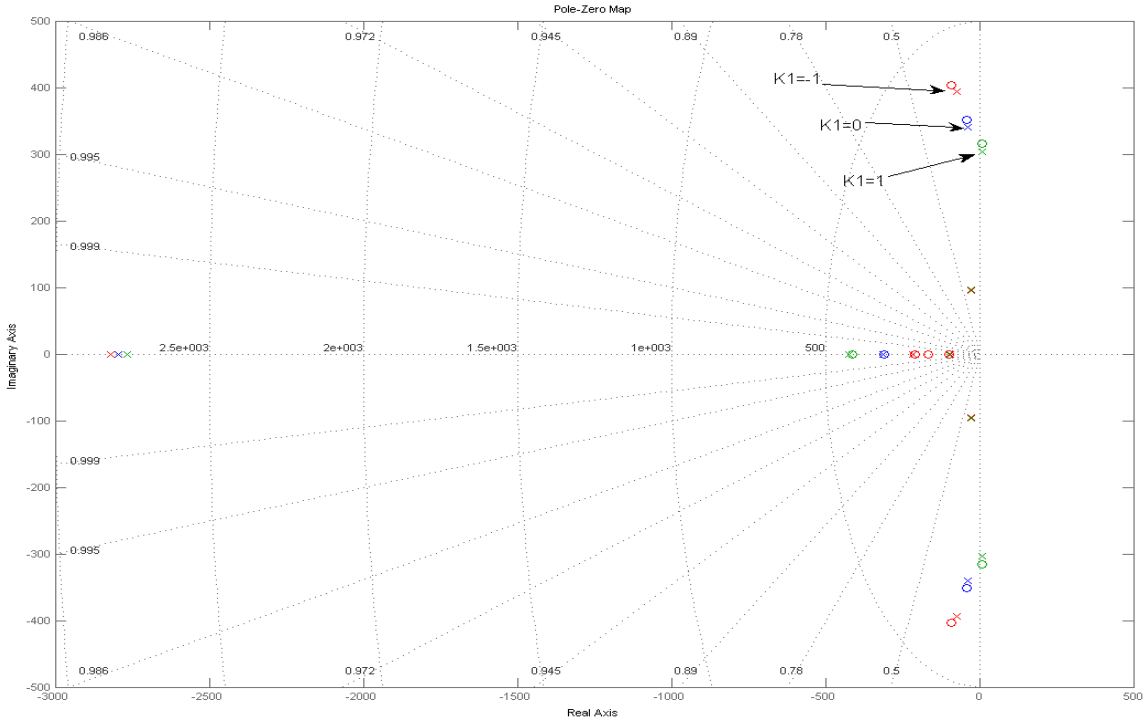


Figure 10.20 Pole-zero maps with different $k_i$ values when $\omega_{r1} = -377$ and slip =-0.05

It can be concluded that when the rotor speed is greater than zero, a positive $k_i$ value will enhance the stability of the speed estimator. However, when the rotor speed is negative, a negative value of $k_i$ enhances the system stability.

Since the instability of the system is always found at low speed under the generating condition, the same method is applied to that condition to check the effect of $k_i$. Simulation results for the middle speed and the low speed range are given in Figure 10.21 and Figure 10.22 respectively.

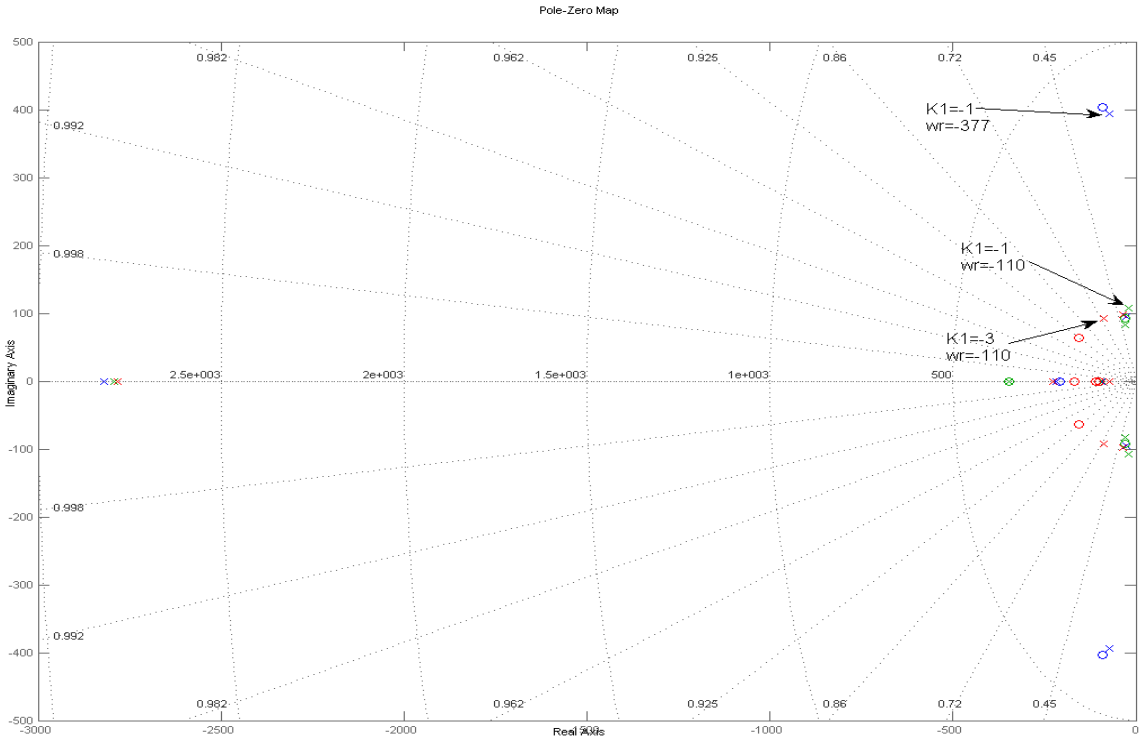


Figure 10.21 Pole-zero maps with different $k_i$ values $k_i = -1 \; or \; -3$ when $\omega_{r1} = -377$ rad/s and $\omega_{r1} = -110$ rad/s while the slip = - 0.05

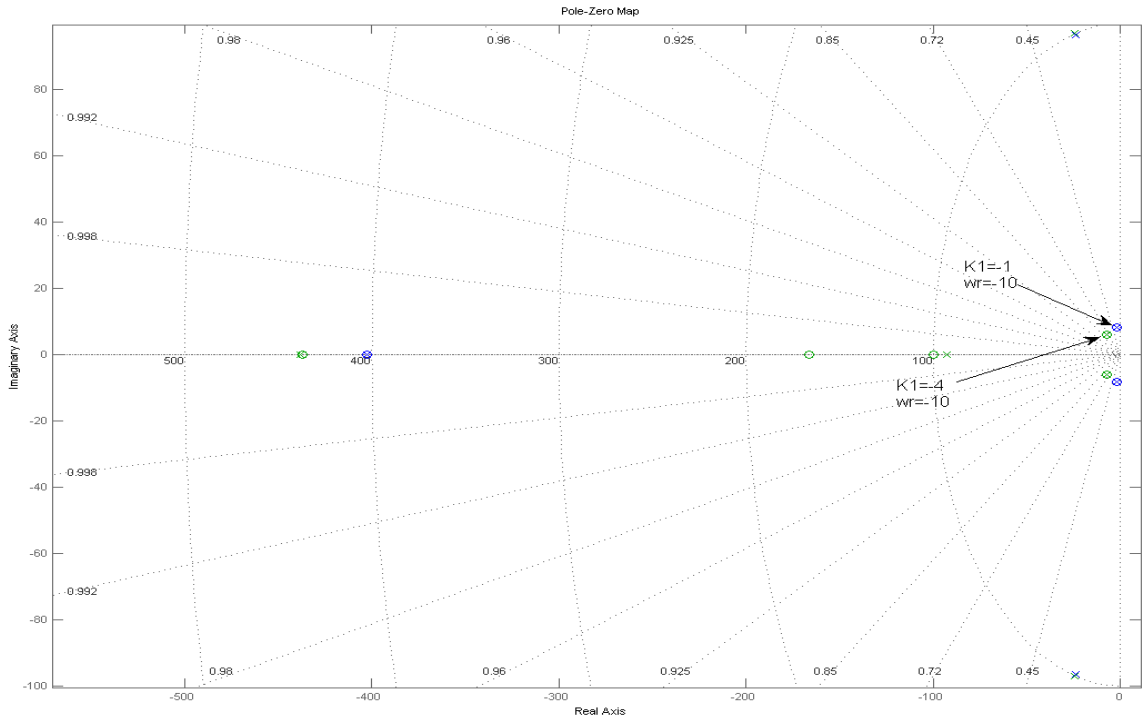


Figure 10.22 Pole-zero maps with different $k_i$ values $k_i = -1 \, or \, -4$ when $\omega_{r1} = -10$ rad/s and the slip = - 0.05.

The effects of $k_i$ under the middle and the low speed generating conditions are shown in Figure 10.21 and Figure 10.22 respectively. Increasing $k_i$ value shifts the poles of the speed estimator to the left half plane under a low speed generating condition which enhances the system stability.

In the proposed error function, the active power term remains unchanged while a variable amount of reactive power is added into or subtracted from the error function to stabilize the system by changing the value and sign of factor $k_i$.

The boundary of $G_{pi}$ and $G_{ii}$ is calculated from (10.140). The boundaries of the speed estimation parameters for the 2-pole winding set under different slip conditions are shown in Figure 10.23 and Figure 10.24.

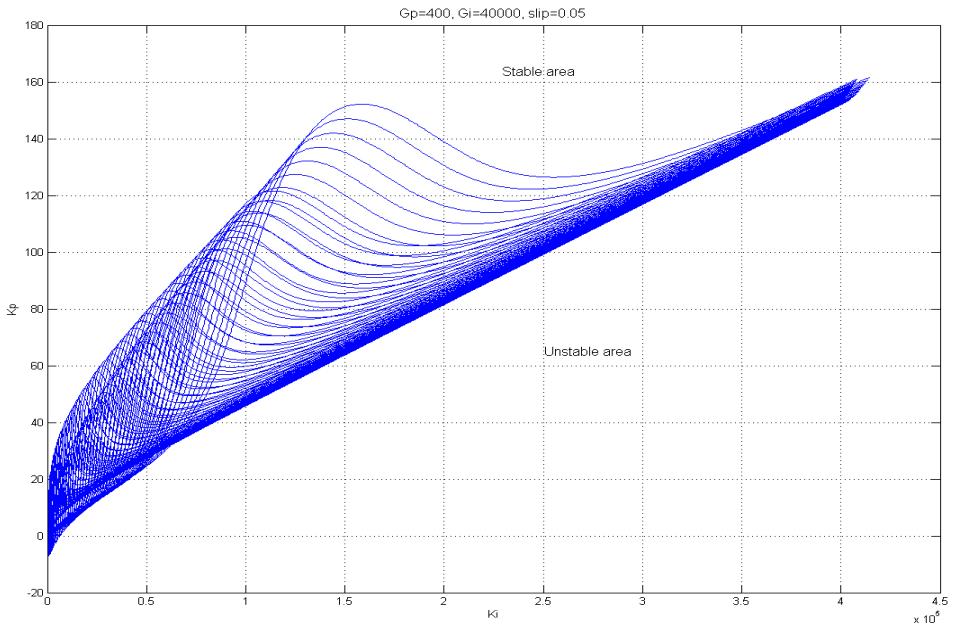


Figure 10.23 Boundary of speed estimator when slip = 0.05

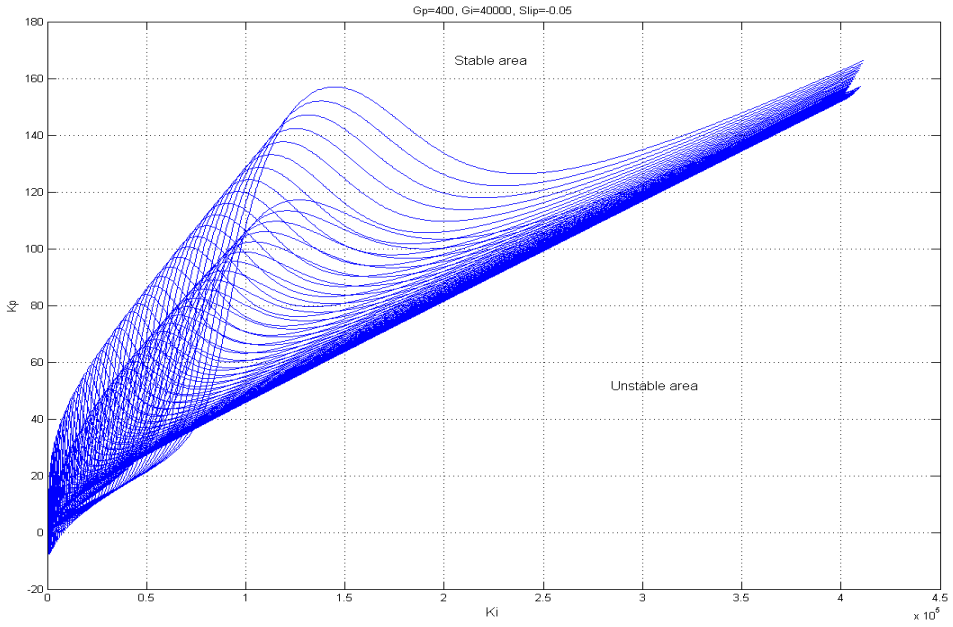


Figure 10.24 Boundary of speed estimator when slip = - 0.05

From the simulation results, it is found that changing the slip does not change the shape of the boundary significantly, however the selected speed estimator parameters

should ensure the stability under all the slip values when rotor speed changes from -377 rad/s to 377 rad/s.

The methodology for speed estimator design based on D-decomposition method has been described clearly in this section. A novel error function has been proposed for the speed estimation, which has been demonstrated by simulation results. The boundary of the speed estimator parameters is calculated using D-decomposition method and simulation results have been shown in Figure 10.23 and Figure 10.24.

It should be noted that the system performance is also due to the placements of zeros. When any zero of the system transfer function has a positive real part (the system is non-minimum phase), the closed-loop performance is compromised as the right half-plane zero induces an additional phase shift of –180 degrees. Hence the designed speed estimator gains should be substituted back into the transfer function to ensure the minimum-phase system requirement.

## 10.10 Speed Controller Design

The above analysis focuses only on the parameter design for the speed estimation. When the estimated speed is used as the feedback for rotor speed control, the transfer function of the speed control changes so that a new speed controller design process becomes necessary. The adopted speed controller design strategy is introduced in this section. The basic idea of the controller parameters determination is also based on the transfer function of the speed controller and the D-decomposition method.

When the estimated rotor speed is used as feedback, the transfer function between the reference speed and the rotor speed is defined as:

$$\sigma_\omega = p\omega_r = K_\omega \cdot \left(\omega_r^* - \hat{\omega}_r\right) = K_\omega \cdot \left(\omega_r^* - \frac{A_i(p)}{B_i(p)}\omega_r\right)$$

$$\frac{\omega_r}{\omega_r^*} = \frac{K_\omega B_i(p)}{pB_i(p) + K_\omega A_i(p)} \tag{10.148}$$

A PI controller is adopted in (10.148),

$$K_\omega = k_{wp} + \frac{k_{wi}}{S} \tag{10.149}$$

Substituting (10.149) into (10.148), the transfer function of the speed controller becomes:

$$\begin{aligned}\frac{\omega_r}{\omega_r^*} &= \frac{\left(pk_{\omega p} + k_{\omega i}\right)B_i(p)}{p^2 B_i(p) + \left(pk_{\omega p} + k_{\omega i}\right)A_i(p)} \\ &= \frac{\begin{array}{l} k_{\omega p}A_{4i}p^5 + \left(k_{\omega p}A_{3i} + k_{\omega i}A_{4i}\right)p^4 + \left(k_{\omega p}A_{2i} + k_{\omega i}A_{3i}\right)p^3 \\ + \left(k_{\omega p}A_{1i} + k_{\omega i}A_{2i}\right)p^2 + \left(k_{\omega p}A_{0i} + k_{\omega i}A_{1i}\right)p + k_{\omega i}A_{0i}\end{array}}{\begin{array}{l} p^7 + B_{4i}p^6 + \left(B_{3i} + k_{\omega p}A_{4i}\right)p^5 + \left(B_{2i} + k_{\omega p}A_{3i} + k_{\omega i}A_{4i}\right)p^4 \\ + \left(B_{1i} + k_{\omega p}A_{2i} + k_{\omega i}A_{3i}\right)p^3 + \left(B_{0i} + k_{\omega p}A_{1i} + k_{\omega i}A_{2i}\right)p^2 + \left(k_{\omega p}A_{0i} + k_{\omega i}A_{1i}\right)p + k_{\omega i}A_{0i}\end{array}}\end{aligned} \tag{10.150}$$

The D-decomposition method is used to plot the boundary of the stable region,

$$\begin{aligned}&-j\omega_0^7 - B_{4i}\omega_0^6 + j\left(B_{3i} + k_{\omega p}A_{4i}\right)\omega_0^5 + \left(B_{2i} + k_{\omega p}A_{3i} + k_{\omega i}A_{4i}\right)\omega_0^4 - j\left(B_{1i} + k_{\omega p}A_{2i} + k_{\omega i}A_{3i}\right)\omega_0^3 \\ &-\left(B_{0i} + k_{\omega p}A_{1i} + k_{\omega i}A_{2i}\right)\omega_0^2 + j\left(k_{\omega p}A_{0i} + k_{\omega i}A_{1i}\right)\omega_0 + k_{\omega i}A_{0i} = 0\end{aligned} \tag{10.151}$$

Separating (10.151) into imaginary and real parts, then

$$\begin{cases} -B_{4i}\omega_0^6 + \left(B_{2i} + k_{\omega p}A_{3i} + k_{\omega i}A_{4i}\right)\omega_0^4 - \left(B_{0i} + k_{\omega p}A_{1i} + k_{\omega i}A_{2i}\right)\omega_0^2 + k_{\omega i}A_{0i} = 0 \\ -\omega_0^6 + \left(B_{3i} + k_{\omega p}A_{4i}\right)\omega_0^4 - \left(B_{1i} + k_{\omega p}A_{2i} + k_{\omega i}A_{3i}\right)\omega_0^2 + \left(k_{\omega p}A_{0i} + k_{\omega i}A_{1i}\right) = 0 \end{cases} \tag{10.152}$$

The boundary of the speed controller parameters can be calculated using (10.152). When the observer gains and speed estimator parameters are all fixed while the rotor speed changes from -377 rad/s to 377 rad/s and $\omega_0$ of the speed controller is varying within [0, 600], the boundary of the speed controller parameters for the 2-pole winding set is obtained using (10.152) as shown in Figure 10.25. Similarly, the boundary of the speed controller parameters for the 6-pole winding set is given in Figure 10.26. Because the error signal used for speed estimation switches between both winding sets, the speed controller parameters should be chosen within the common stable region of both sets so that the selected controller parameters ensure the system stability under any operating condition.

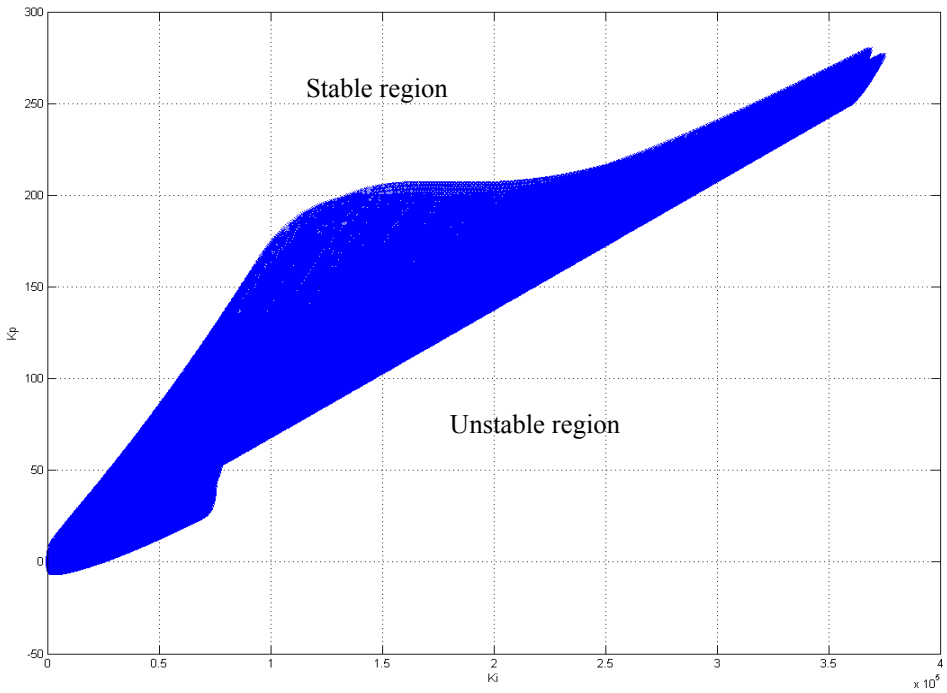


Figure 10.25 The boundary of speed controller parameters for the 2-pole winding set

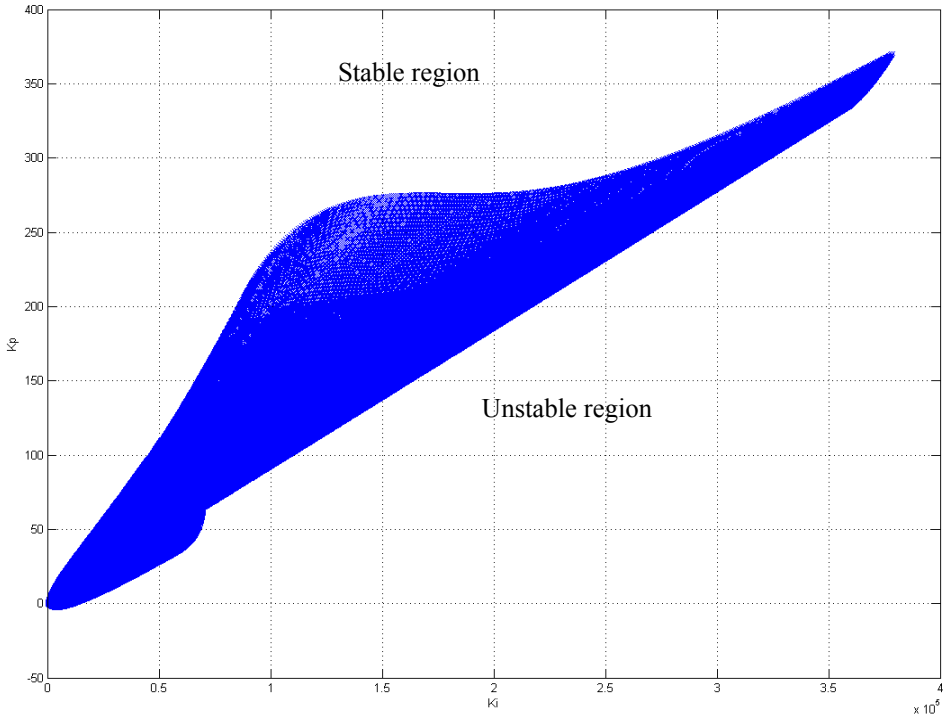


Figure 10.26 The boundary of speed controller parameters for the 6-pole winding set

The stability boundary from the D-decomposition method divides the whole region into two parts. The stable region is found using the rule defined in the D-decomposition method in section 10.8. It is found from simulation results that the upper side is the stable region while the lower side is the unstable region, which verifies that arbitrarily large parameters of PI controller can be chosen. However, noise causes significant problems when large values are used in the DSP hardware implementation. The selected speed controller parameters should be substituted back into the transfer function to ensure that all the zeros have negative real parts.

## 10.11 Simulation Results for Sensorless Control

The proposed control scheme and speed estimation strategy have been simulated using MATLAB/SIMULINK, in which the proposed design methodologies are used to determine the parameters of the controllers and estimators. The machine parameters are given in Table 8.2 and some of the controller parameters are the same as those in Table 10.1. The parameters of controller, which are different from Table 10.1, are shown in Table 10.2.

Firstly, the speed estimation strategies for both stator winding sets are simulated separately. The rotor mechanical speed command ramps up from 0 to 126 rad/sec within 4 seconds. After the rotor speed command is maintained constant for 2 seconds, the speed command ramps down and up between -126 rad/sec and 126 rad/sec. The estimated speed and actual speed are compared during the simulation. For the 2-pole winding set, the simulation results of speed estimation with constant $k_1 = 0$ and $k_1 = 0.5$ have been given in Figure 10.27 and Figure 10.28 respectively. In both Figure 10.27 and Figure 10.28, significant instability can be observed, however the oscillation under the generating condition is worse as demonstrated in Figure 10.28. The simulation results of the proposed variation of $k_1$ for the 2-pole winding are given in Figure 10.29, in which the estimated rotor speed tracks the actual speed very well.

Table 10.2 Parameters of speed estimator and controller

| | |
|---|---|
| Speed estimator | $k_{\omega estp} = 100$, $k_{\omega esti} = 40000$ |
| Speed controller | $k_{\omega p} = 80$, $k_{\omega i} = 2500$ |

The comparison between the simulation results with different $k_1$ values show that the speed estimations have oscillation at low speed when $k_1 = 0$ and the estimated speed is totally different during generating condition when $k_1 = 0.5$ while the proposed adaptive value of $k_1$ effectively stabilizes the speed estimation within the low speed range under both motoring and generating conditions.

A small oscillation of the estimated rotor speed, which may due to the initial errors of integrators in the observer model, can be found during the starting process at the first 0.2 second in Figure 10.29. The estimated rotor speed matches the actual rotor speed very well after that transient process.

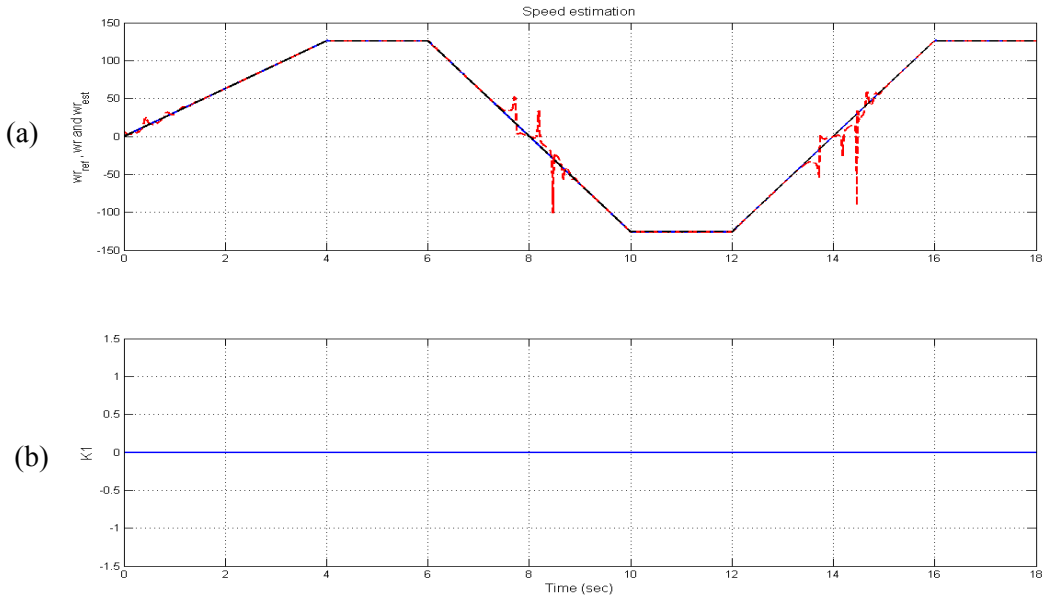


Figure 10.27 Speed estimation for 2-pole winding set with constant $k_1 = 0$, (a) actual rotor speed and estimated rotor speed, (b) reactive power factor $k_1$.

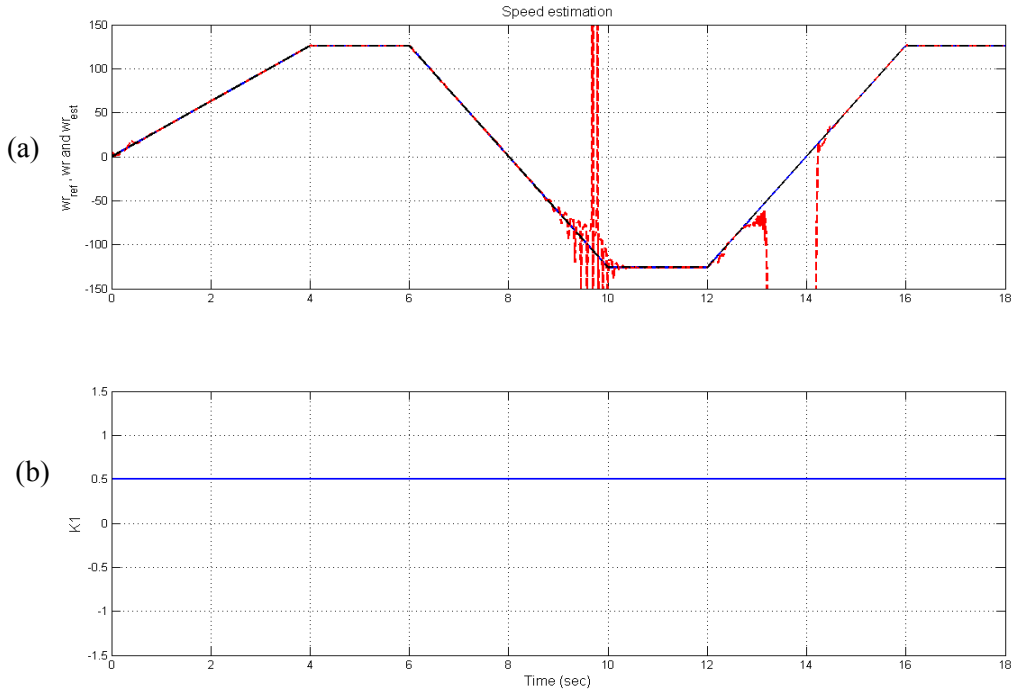


Figure 10.28 Speed estimation for 2-pole winding set with constant $k_1 = 0.5$, (a) actual rotor speed and estimated rotor speed, (b) reactive power factor $k_1$

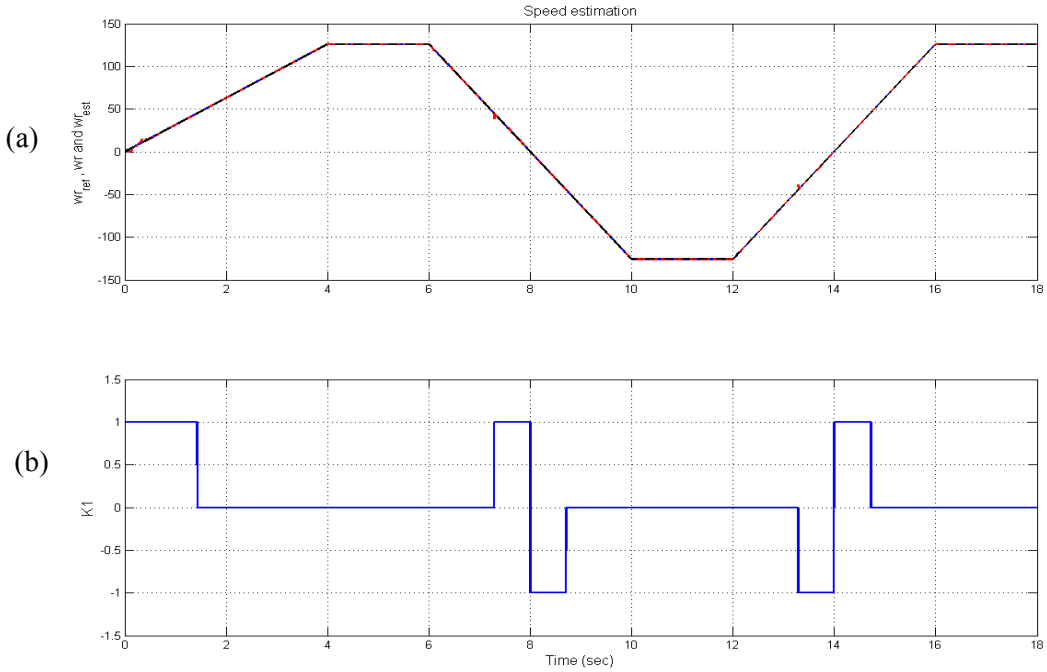


Figure 10.29 Speed estimation for the 2-pole winding set with proposed varied $k_1$, (a) Actual rotor and estimated rotor speeds, (b) reactive power factor $k_1$.

It should be noticed that the simulation results and discussions are only for the 2-pole winding set. When the same design process is applied to the 6-pole winding set, the simulation results with constant $k_2 = 0$ and varied $k_2$ for the 6-pole winding set are given in Figure 10.30 and Figure 10.31 respectively.

From the simulation results, it is observed that the difference between the speed estimation with constant $k_2$ and proposed speed adaptive $k_2$ is almost invisible for 6-pole winding. The characteristics of the speed estimators of 2-pole winding set and 6-pole winding set are different. The reasons for that lie in the fact that the electrical frequency of 6-pole winding set is almost three times higher than the one for 2-pole winding set and the machine inductances of the 6-pole winding set is only one third of the corresponding inductances of the 2-pole winding set.

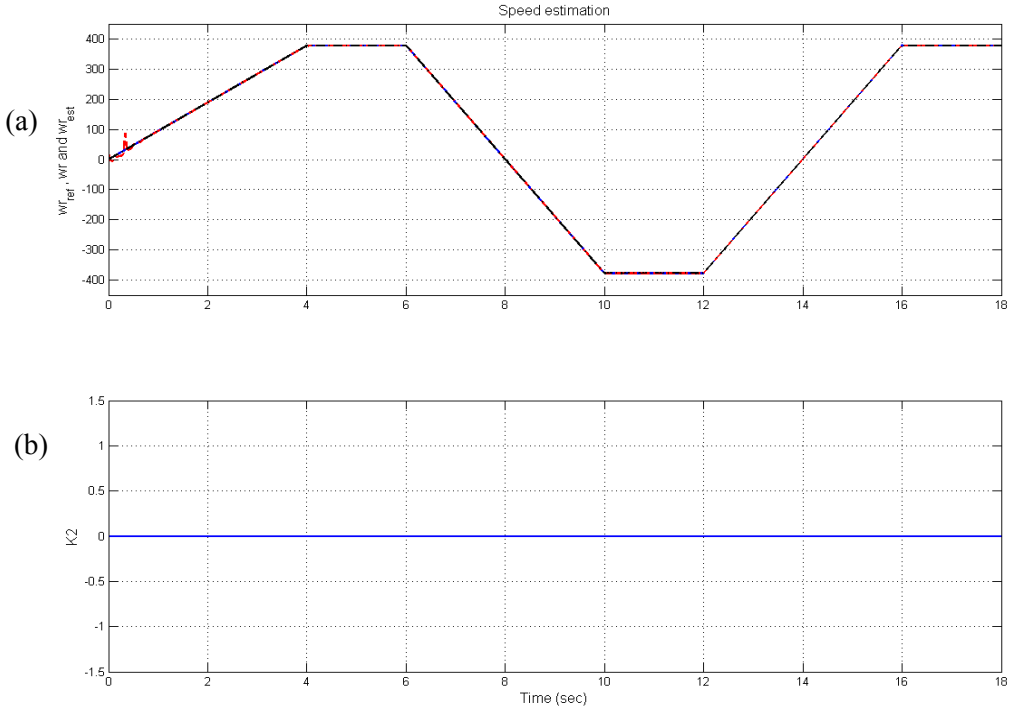


Figure 10.30 Speed estimation for the 6-pole winding set with constant $k_2$, (a) Actual rotor and estimated rotor speeds, (b) reactive power factor $k_2$.

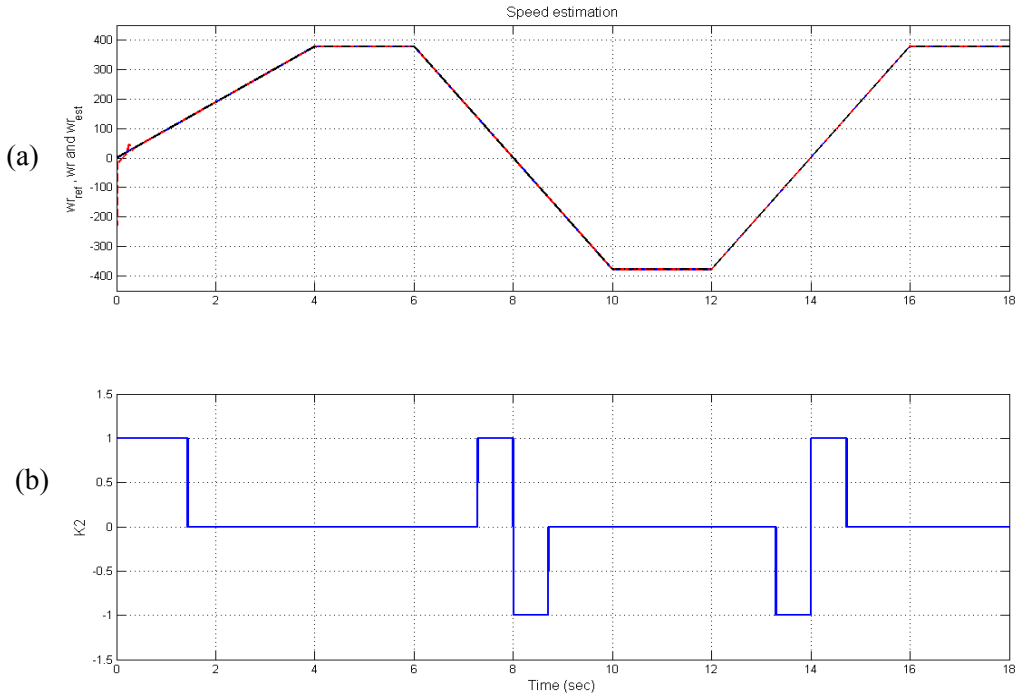


Figure 10.31 Speed estimation for the 6-pole winding set with proposed varied $k_2$, (a) actual rotor speed and estimated rotor speed, (b) reactive power factor $k_2$.

It seems that using the error signal from the 6-pole winding set to do the speed estimation of the dual stator winding induction machine may be a good choice for the sensorless control. However, it should be noticed that the error signal from the error function reflects the error between the actual rotor speed and estimated rotor speed, also a greater speed estimation error leads to a bigger error signal. Based on the above analysis, the maximum value of the two error signals is fed to the speed estimator and used to estimate rotor mechanical speed.

The estimated rotor speed is used as feedback in the speed control scheme and the simulation results of starting process and dynamic responses are shown in Figure 10.32 and Figure 10.33 respectively. During the starting process, the rotor speed command ramps up from 0 to 126 rad/sec and maintained at 126 rad/sec thereafter. A 3 Nm load is

added to the system at t = 4 seconds. In the dynamic responses of the system, rotor speed command ramps down and up between -126 rad/sec and 126 rad/sec. The torque partition factor is 0.5 from 0 to 18 seconds except that when the absolute value of rotor speed is within 30 rad/sec torque partition factor changes to be -0.2. The proposed reactive power factor is applied to the system and the expression for that factor is given as:

$$\begin{cases} k_i = 0 & |\omega_r| \geq 45\ rad/\sec \\ k_i = sig(\omega_r) & |\omega_r| < 45\ rad/\sec \end{cases}$$

where, the subscript i=1 or 2, which represents the reactive power factor for 2-pole winding set and 6-pole winding set respectively. It should be noticed that both reactive power factors can be adjusted independently to achieve best performance. In Figure 10.32-10.33, the variables for 2-pole winding set are represented by blue solid line while the variables from 6-pole winding set are represented by red dashed line. The actual and estimated stator currents and rotor flux linkage for both winding sets are shown in Figure 10.34 and 10.35 with blue-solid line and red-dashed line respectively. All the simulation results validate the proposed sensorless control scheme and the design methodologies.

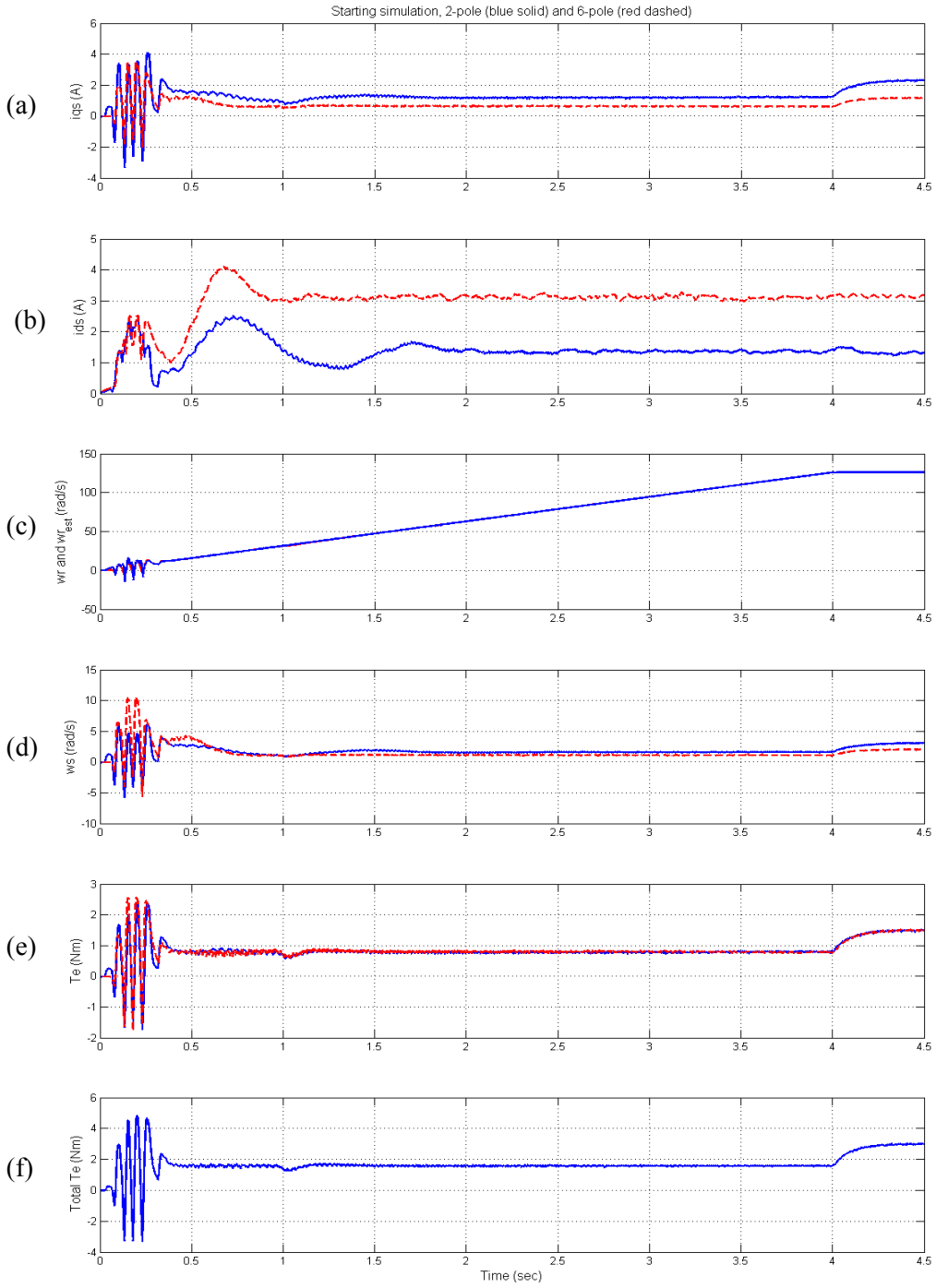


Figure 10.32 Starting process of the sensorless dual winding induction machine drive, (a) q-axis current $i_{qsi}$, (b) d-axis current $i_{dsi}$, (c) actual and estimated rotor speeds, (d) slip frequency $\omega_{si}$, (e) electromagnetic torque from each winding $T_{ei}$, (f) total electromagnetic torque.

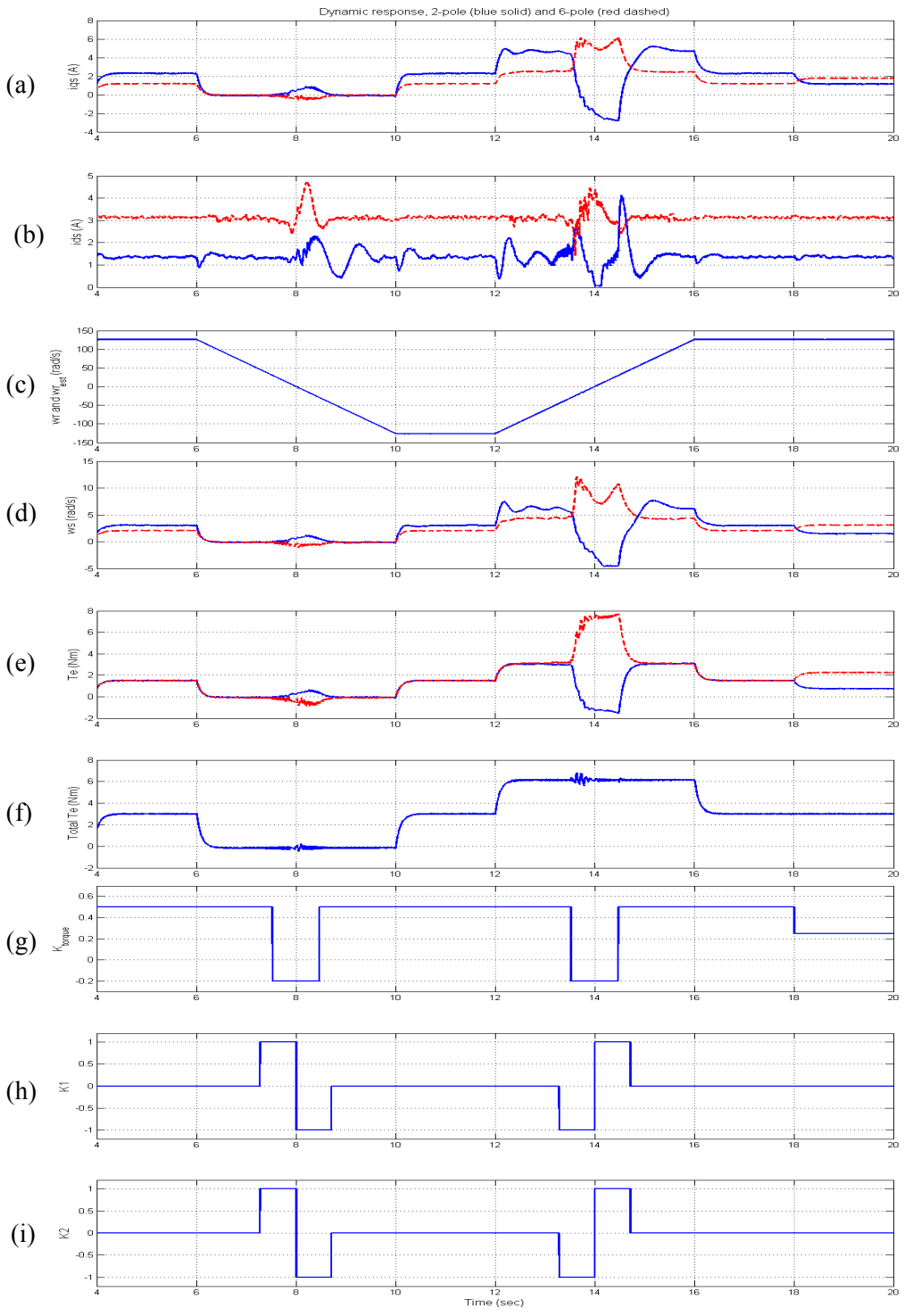


Figure 10.33 Dynamic responses of the sensorless dual winding induction machine drive, (a) q-axis current $i_{qsi}$, (b) d-axis current $i_{dsi}$, (c) actual and estimated rotor speeds, (d) slip frequency $\omega_{si}$, (e) electromagnetic torque from each winding $T_{ei}$, (f) total electromagnetic torque, (g) torque partition factor $K_{tor}$, (h) reactive power factor $K_1$, (i) reactive power factor $K_2$.

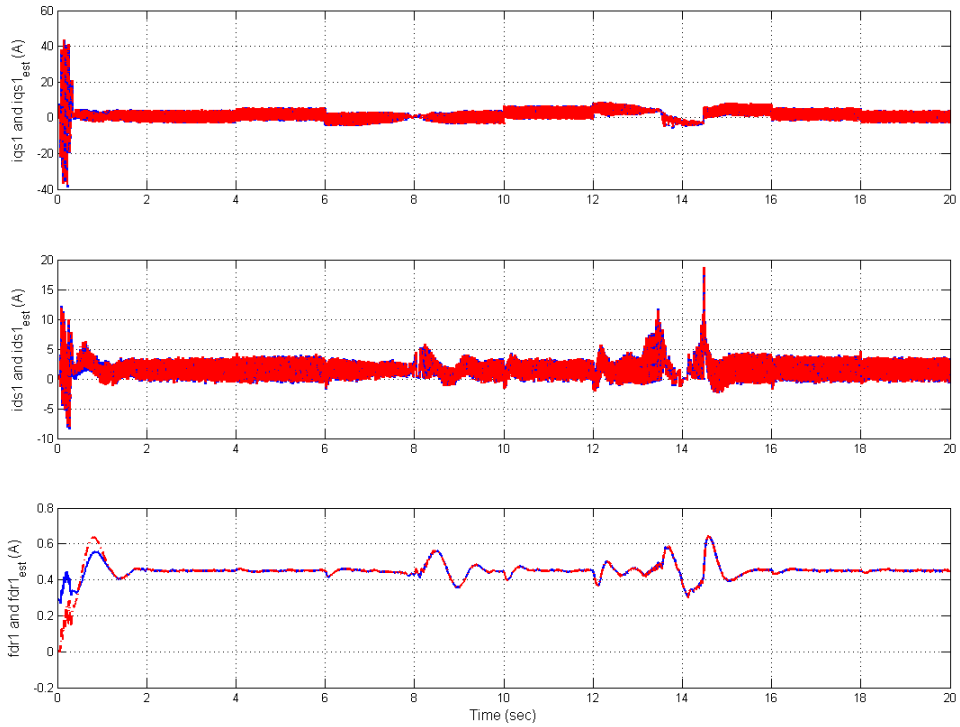


Figure 10.34 Actual and estimated variables for the 2-pole winding set, (a) q-axis current $i_{qs1}$, (b) d-axis current $i_{ds1}$, (c) rotor flux linkage $f_{dr1}$.

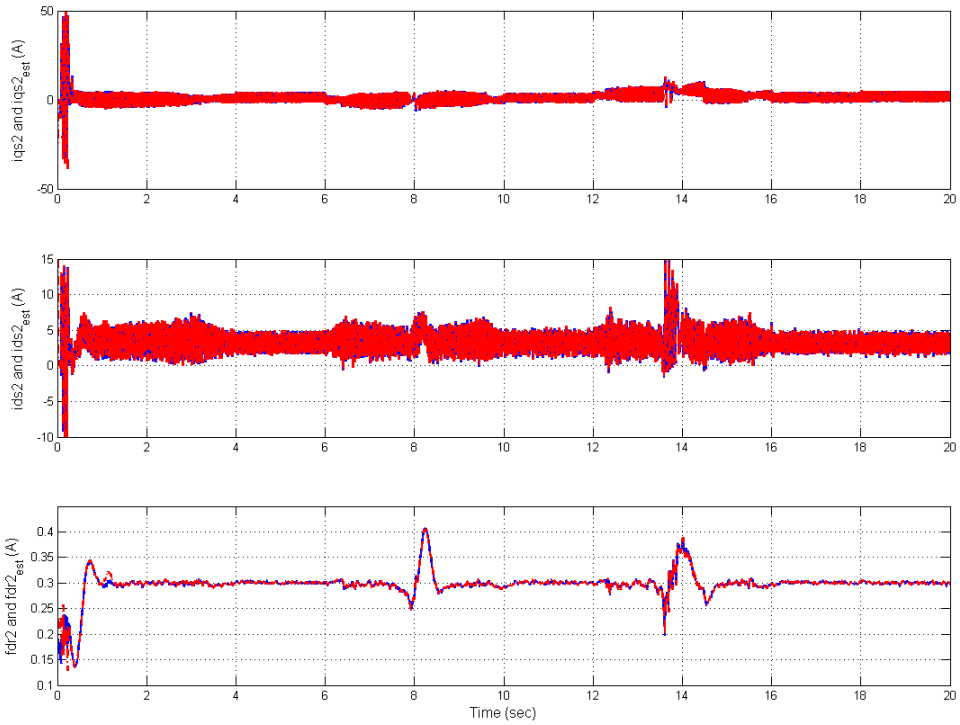


Figure 10.35 Actual and estimated variables for the 6-pole winding set, (a) q-axis current $i_{qs2}$, (b) d-axis current $i_{ds2}$, (c) rotor flux linkage $f_{dr2}$.

## 10.12 Conclusions

In the first part of this chapter, a speed control scheme for the dual winding induction machine with a speed sensor has been proposed. The principles of input-output linearization have been applied to the control system design so that the coupling and interaction terms are removed and the classic linear design methods are applied for controller design. The controller design methodology based on the Butterworth method has been adopted. A torque partition factor K has been introduced to distribute the electromagnetic torque to each of the winding sets. By changing the value of K, one winding set can move smoothly from motoring condition into generating condition. The effectiveness of the torque partition factor has been demonstrated by simulation results. In the second part of this chapter, a speed sensorless control scheme based on full-order flux observer using MRAS technique has been analyzed. A novel error function has been proposed to ensure stability within the ultra-low speed range. The Butterworth method is used to design the observer gains. The transfer function of the estimated and actual speeds is derived based on the error analysis, which is used to determine the parameters of the speed estimator for the sensorless control. The D-decomposition method is the design methodology for both the speed estimator and the speed controller. Both the rotor speed and slip frequency are varied within the possible operating range to ensure the stability of the system based on the selected parameters. The whole system is simulated in both motoring and generating modes. The controllers are shown to work properly and the rotor speed is regulated accurately, validating the proposed full-order flux observer and speed estimation methodologies.

# CHAPTER 11

# HARDWARE IMPLEMENTATION

## 11.1 Introduction

The nature of the hardware implementation for the experimental verification in all the previous work is described in this chapter.

The machine parameters are determined using traditional dc test, open circuit test and short circuit test. The description of those tests and their corresponding equivalent circuits are presented in section 11.2.

Based on the EVM board of TI TMS320LF2407A fixed point DSP with 40 MHz CPU frequency, the implementation has been carried out on a 2 hp dual stator winding induction machine. The diagrams of experimental setups can be found in section 11.3.

The control schemes are experimentally implemented by the software written in assembly language. Some of the important issues regarding the software implementation are described in section 11.4, 11.5 and 11.6. The voltage and current measurements are introduced in section 4 while the rotor speed measurement is the topic of section 11.5. The program flowcharts are given in section 11.6.

## 11.2 Parameters Measurement

Basically, the dual stator winding induction machine can be treated as two independent induction machines coupled by the rotor shaft as proven in chapter 5 and the similar conclusion can also be found in [1.1] and [1.11]. Hence the parameter

determination method of the dual stator winding induction machine is similar to the one for the normal single winding induction machine.

For a normal single stator winding squirrel-cage rotor induction machine, the parameters are determined by three different tests, namely the dc test, blocked rotor test, and no-load test. The per-phase equivalent circuit of a three-phase squirrel cage induction machine, which is the core of these tests, is shown in Figure 11.1.

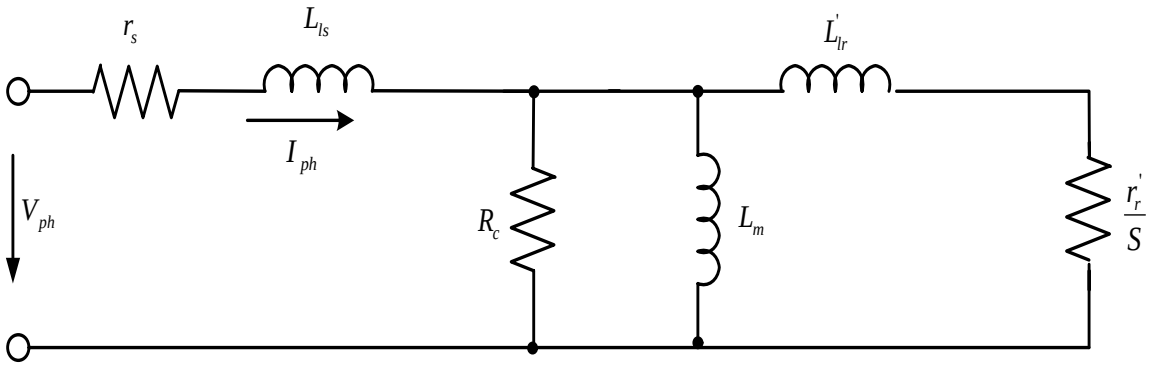


Figure 11.1: Per phase equivalent circuit of a three phase induction machine including the core loss resistance

Generally, the stator and rotor leakage inductances are assumed to be equal in the calculation of the different parameters of the equivalent circuit. The parameters determination is based on the equivalent circuit model of the induction machine shown in Figure 11.1.

### 11.2.1 Stator Resistance Measurement

The dc test is used to determine the stator resistance. The test involves applying a dc voltage across any of the two of the three terminals of the induction machine. The voltage applied divided by the current flowing through the two winding sets gives the sum of the

resistance for two phase windings. The expression for per phase stator resistance is given as:

$$r_s = \frac{1}{2}\frac{V_{dc}}{I_{dc}} \tag{11.1}$$

To reduce the random error during the test, the same test was taken three times and the average value is used as the stator resistance.

### 11.2.2 Open Circuit Test

In the open circuit test, three-phase balance voltages are supplied to the three phase induction machine and the machine is running without any load. Thus, the rotor speed is close to the synchronous speed so that the slip of the induction machine is very small $(s \approx 0)$ and the rotor current can be assumed to be zero. From equivalent circuit view of point, $\frac{r_r}{S} \approx \infty$ when $S \approx 0$, The modified equivalent circuit for open circuit test is given in Figure 11.2.

If the equivalent impedance for the open circuit test is assumed as:

$$Z_o = \frac{V_o}{I_o} = R_o + jX_o \tag{11.2}$$

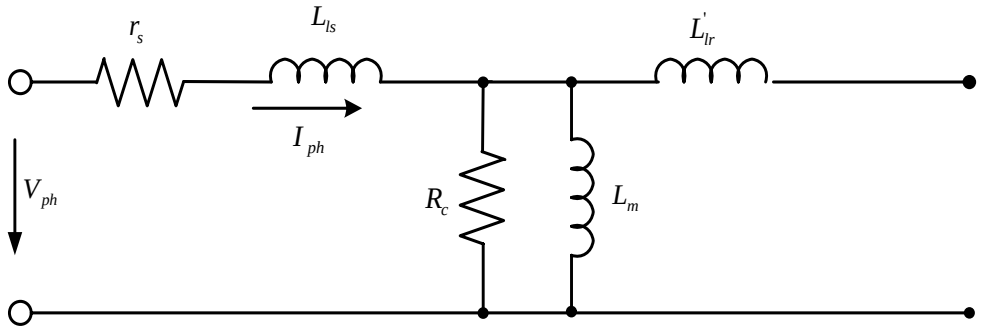


Figure 11.2 Per phase equivalent circuit of an induction machine for the open circuit test

The assumption in the calculations are the core loss resistance is so big compared with the impedance of the mutual inductance that the voltage drops on the stator resistance can be neglect at this time. Then, the open circuit equivalent resistance is equal to the stator resistance and the reactance is equal to the sum of the stator leakage reactance and magnetizing reactance. As the stator leakage reactance and resistance have been calculated from the other two tests performed, the magnetizing reactance is calculated.

$$r_s = R_o \tag{11.3}$$

$$X_m = X_o - X_{1s} \tag{11.4}$$

$$L_m = \frac{X_m}{2\pi f} \tag{11.5}$$

$f$ = supply frequency = 60 Hz

$$P_{input} = 3r_s I_o^2 + 3\frac{V_o^2}{R_c}\frac{X_m}{2\pi f} \tag{11.6}$$

Both the magnetizing inductance and the core loss resistance can be calculated by the open circuit test. The input terminal voltage for the open circuit test ramps down from 1.2 times of rated voltage and stop when the phase current increases instead of decreasing. The Experimental results of magnetizing flux vs magnetizing inductance $L_{m1}$ (2-pole winding set) and three times magnetizing inductance $L_{m2}$ (6-pole winding set) are shown in Figure 8.2.

### 11.2.3 Short Circuit Test

The short circuit test is used to calculate the leakage inductance and the rotor resistance. The test is performed by blocking the rotor so it cannot rotate while a three-phase balanced voltage is applied to the stator winding sets. The input active power, input voltage and phase current are measured. In this case, since the slip of the machine is equal to one, the impedance of the core loss resistance and the mutual inductance are so big compared with the impedance of the rotor leakage inductance and rotor resistance that the current flowing through the impedance of the core loss resistance and the mutual inductance can be ignored. The equivalent circuit of the short circuit test is shown in Figure 11.3.

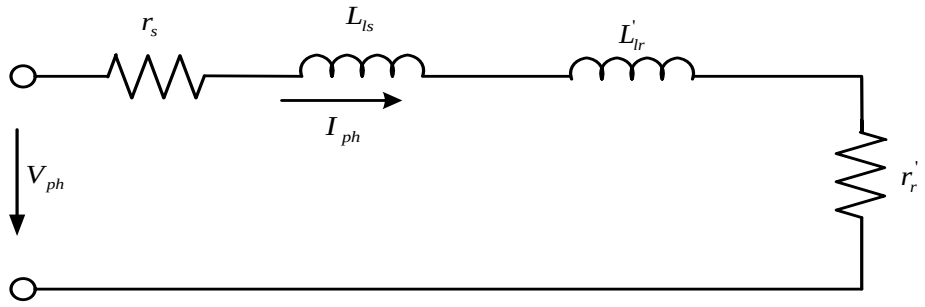


Figure 11.3 Per phase equivalent circuit of an induction machine for the short circuit test

Therefore the machine parameters can be calculated by:

$$\frac{V_{sc}}{I_{sc}} = \left(r_s + r_r'\right) + j\left(X_{ls} + X_{lr}\right) = \left(r_s + r_r'\right) + j2X_{ls} \tag{11.7}$$

$$P_{sc} = 3\left(r_s + r_r\right)I_{sc}^2 \tag{11.8}$$

Since the stator resistance has been calculated in the dc voltage test, the rotor resistance, the stator leakage inductance and the rotor leakage inductances are obtained by the short circuit test.

### 11.2.4 Parameters Measurement with Two Winding Excitation

Using the same parameter measurement method for the single winding induction machine, the dual stator winding induction machine parameters measurements have been done without considering the saturation effect. However, since two stator winding sets share the same stator core, the saturation in the stator core is supposed to be serious and dissimilar pole number winding sets give different affects of stator saturation. Some of the machine parameters such as the magnetizing inductance and the core loss resistor are saturation dependable. How the parameters of the machine change under different saturation conditions can only be found under two stator winding sets excitation condition. The block representation of the experimental setup is shown in Figure 11.4.

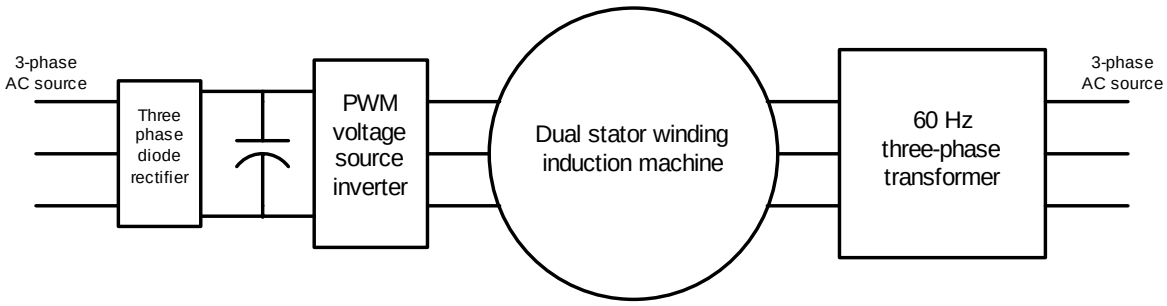


Figure 11.4 The block representation of experimental setup for the dual winding excited parameter measurement

When the input voltages of 2-pole ABC winding set are modulated by 60 Hz three-phase transformer from high to low, the 6-pole XYZ winding set is fed by a PWM voltage inverter with different output voltage magnitudes. Similarly, when the input voltages of 6-pole XYZ winding set are adjusted by 60 Hz three transformer from high to low, the 2-pole ABC winding set is fed by a PWM voltage inverter with different output voltage magnitudes. The frequency ratio between the 2-pole ABC winding set and the 6-pole XYZ winding set is kept to be 1:3 in this experiment to avoid big phase currents. The experimental results are shown in Figure 6.6(b) and Figure 6.6(c). It is shown from the experimental results that the magnetizing inductance of the winding A decreases if the input voltage of the winding B increases, in which A and B represent either the 2-pole ABC winding set or the 6-pole XYZ winding set.

## 11.3 Experimental Setup

The block diagram representation of the experimental setup for the dual stator winding induction generator with parallel connected PWM boost rectifier is shown in Figure 11.5. Two line-to-line voltages, two phase currents, the dc voltage and the rotor speed are the input signals to DSP and all of them are measured by the corresponding sensors or encoder. The single phase rectifier with single phase ac input voltage connected is used to apply a low initial voltage for the dc capacitor during the starting process of generator operation. The clamped diode $D_1$ ensures the current direction and disconnects the capacitor with the initial changing circuit when the capacitor voltage is greater than the initial voltage.

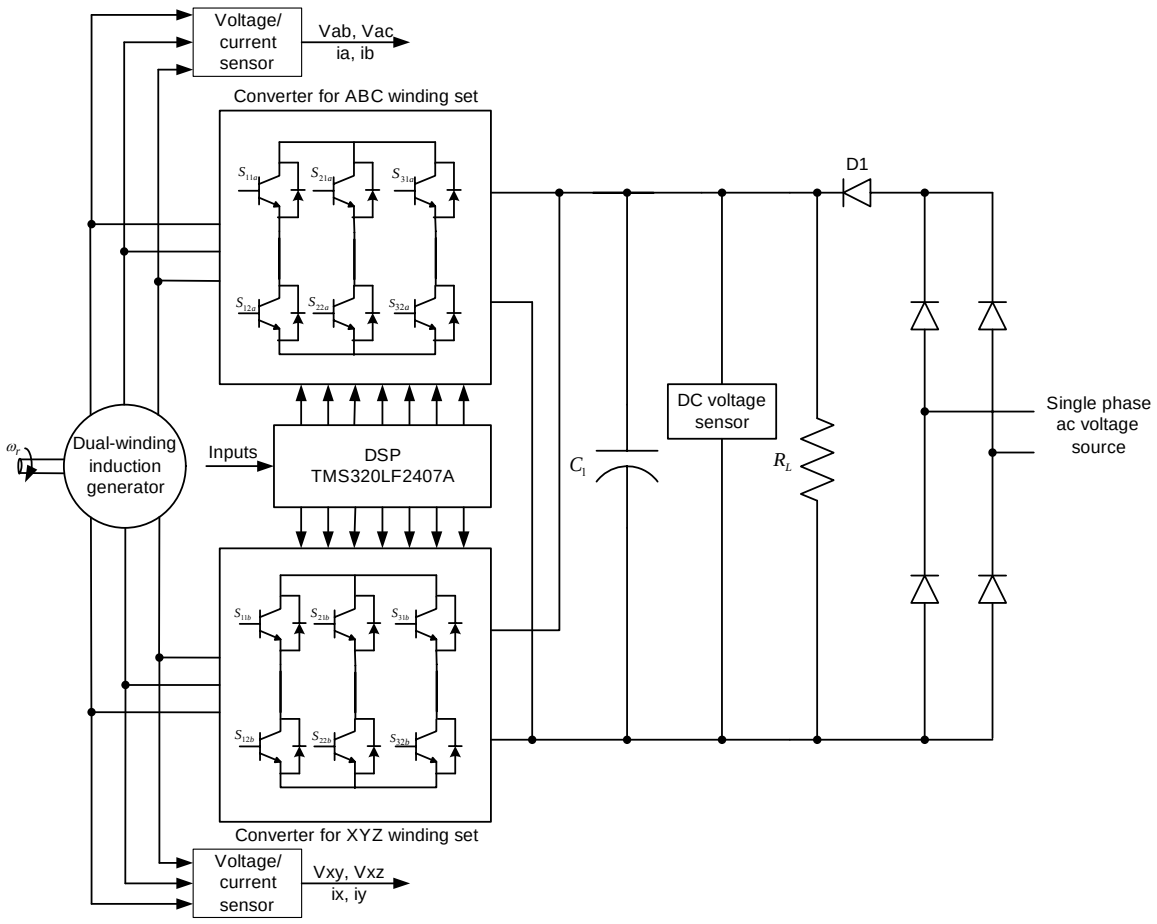


Figure 11.5 The block diagram of the experimental setup for the dual stator winding induction generator with parallel connected PWM boost rectifier

Similar setup for the dual stator winding induction generator with series connected PWM boost rectifier is given in Figure 11.6. It should be noted that two independent ac voltage sources are necessary to supply two independent initial dc voltages. If only one initial voltage is given, since the air gap flux linkage building processes for two stator winding sets have different time constants, the winding set that has faster flux building process will occupy the whole initial dc voltage and generates the command dc voltage such that the initial dc voltage circuit will be disconnected and the other winding set can not generate any power at all. This has been observed from the experiments that one

winding set is generating and the other one will not have any output voltage. Two independent initial dc voltage charging circuits ensure the generating operation of both stator winding sets.

The block diagram representation of the experimental setup for the dual stator winding induction motor can be found in Figure 11.7, where a dc machine is coupled with the dual stator winding induction machine through the rotor shaft and works as a variable load of the dual winding machine.

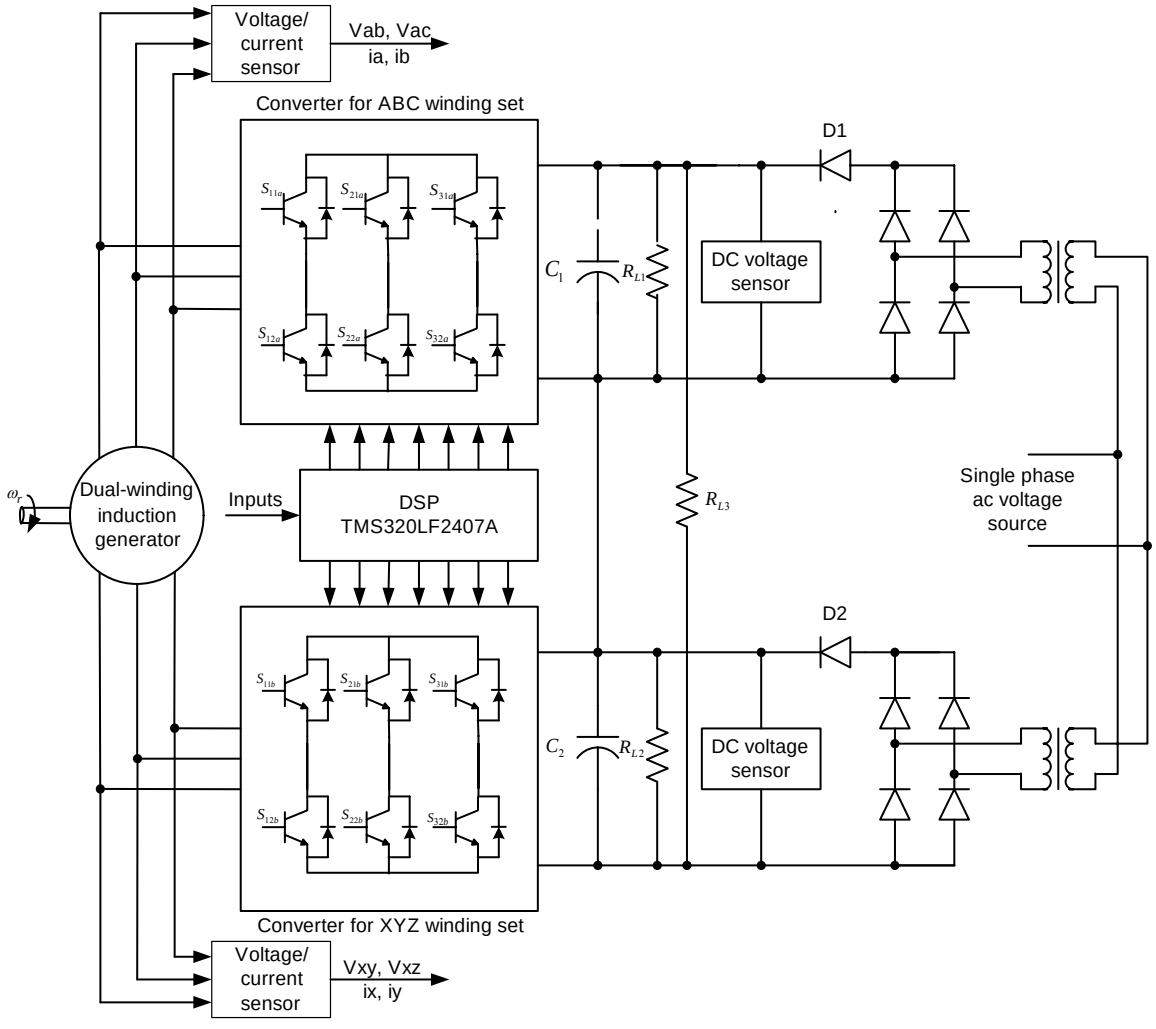


Figure 11.6 The block diagram of the experimental setup for the dual stator winding induction generator with series connected PWM boost rectifier

A variable three phase voltages will supply the dc voltage through a three phase diode rectifier. The speed of dual stator winding induction machine is measured by an encoder.

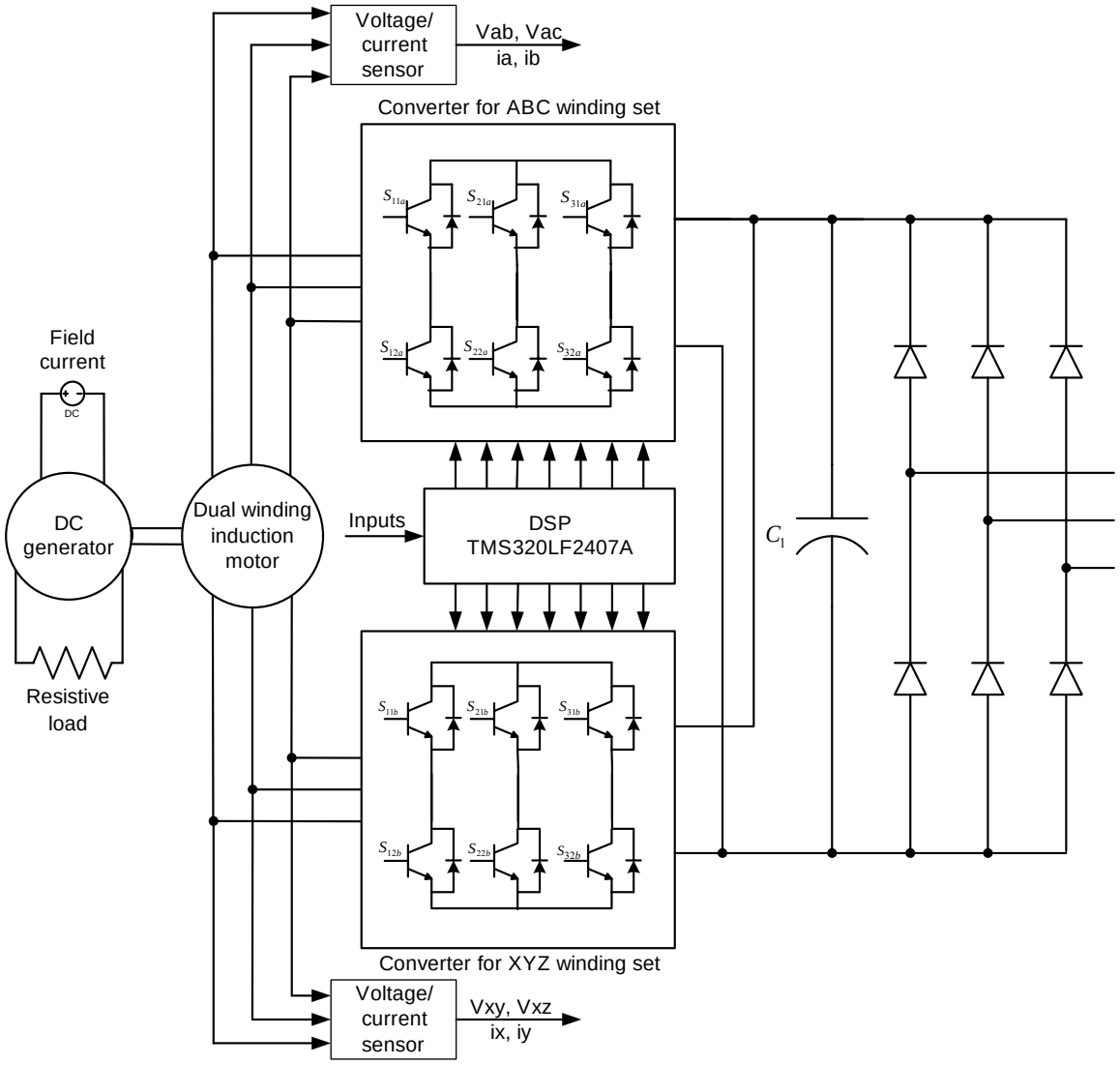


Figure 11.7 The block diagram of the experimental setup for the dual stator winding induction motor

## 11.4 Per Unit Model

For the fixed point DSP--TMS320LF2407A, a per unit model of the motor is always used to compromise both accuracy and measurement range. All the quantities of the model have to be referred to the base values. Generally speaking, the base values of the model can be chosen arbitrary. However, the traditional method that the base values are determined from the nominal values of the machine is more meaningful and has been adopted in all the implementations. If the base values of voltage, current, electrical speed and resistance are represented by $V_b$, $I_b$, $\omega_b$ and $Z_b$ respectively, the expressions for the calculations of base values are given as:

$$V_b = \sqrt{2} \cdot V_p \tag{11.9a}$$

$$I_b = \sqrt{2} \cdot I_p \tag{11.9b}$$

$$\omega_b = 2\pi f_p \tag{11.9c}$$

$$Z_b = \frac{V_b}{I_b} \tag{11.9d}$$

where, $V_p$ and $I_p$ represent the RMS value of rated phase voltage and rated phase current respectively; $f_p$ is the rated operating frequency.

The real quantities that are implemented in the DSP software are defined as:

$$v = \frac{V_{real}}{V_b} \tag{11.10a}$$

$$i = \frac{I_{real}}{I_b} \tag{11.10b}$$

$$\omega = \frac{\omega_{real}}{\omega_b} \tag{11.10c}$$

$$r = \frac{r_{real}}{Z_b} \tag{11.10d}$$

where, $v$, $i$, $\omega$ and $r$ are per unit value of voltage, current, electrical speed and resistance respectively; $V_{real}$, $I_{real}$, $\omega_{real}$ and $r_{real}$ represent the actual values of voltage, current, electrical speed and resistance respectively.

## 11.5 Numerical Consideration

The per unit model has been developed so that the software representation of current is one when the actual current is equal to the base value of current. It should be noted that the actual current may be greater than the based value during the overload condition or the starting process so that the overflow will appear in the software representation of current when all the 15 lower bit are used to represent the per unit current value. Similar condition is applicable for voltage, flux, rotor speed and etc. So a proper definition of numeric format in the fixed point DSP is necessary. It has been found from the experiences that the per unit value in the machine model is within the range from -4 to 4 at most of times. The selection of a demonstration range of [-8; 8] ensures that the software values can handle each drive control quantity, not only during the steady state operation but also during the transient operation. So the numeric format Q12 is used in this application, which means that the four highest bits are dedicated to the integer part including the representation of the sign of the number by the highest one bit while the twelve lowest bits are dedicated to the fractional part. This format is also called 4.12f in some other references. The representation range of this format is from $-2^3$ to $2^3$ and the resolution for this format is:

$$\frac{1}{2^{12}} = 0.0024414$$

The transformation from the actual number to the number in Q12 format is given as:

$$X_{Q12} = 2^{12} \cdot X \tag{11.11}$$

where, $X$ is the actual number and $X_{Q12}$ is the number in Q12 format.

## 11.6 Current/Voltage Measurement

The proposed control scheme requires two line-to-line voltages and two phase currents as inputs. Therefore, two LEM type voltage and current transducers are used to sense these voltages and currents. The current sensors and voltage sensors are LA 55-P and LV 100-1000 respectively.

Since the A/D conversion ports of the DSP have the voltage range [0 V; 3.3 V], the current sensors have been designed for operation in the desired output voltage region by varying the number of turns and measuring resistance values. Similarly, the voltage sensors have been properly designed for operation in the desired voltage region by varying the primary side resistor value and the value of measuring resistance. It should be noted that because of the bipolarity of the current and voltage signals, the actual output voltage range of current and voltage sensor should be [-1.65 V; 1.65 V]. Then the voltage and current sensor outputs therefore need to be rearranged and scaled so that it can be used by the control software as Q12 format values. The complete processes of acquiring the voltages and currents are depicted in the Figure 11.8 and Figure 11.9 respectively. The process of dc voltage measurement is a little different from the ac voltage and ac current measurement and its block diagram is shown in Figure 11.10.

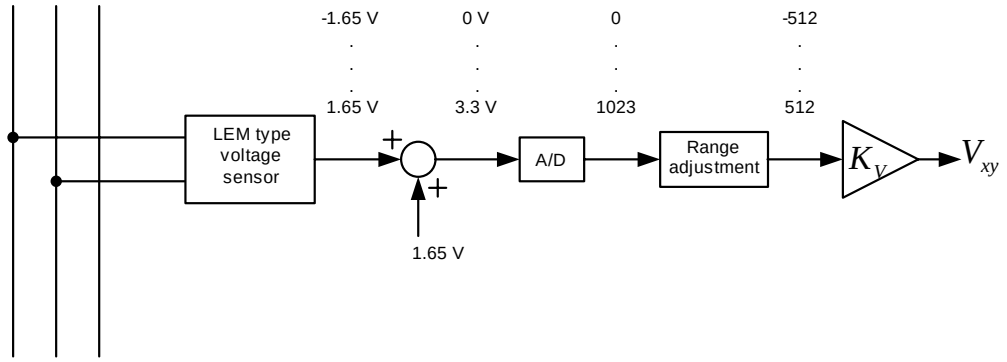


Figure 11.8 Voltage sensing and scaling block diagram

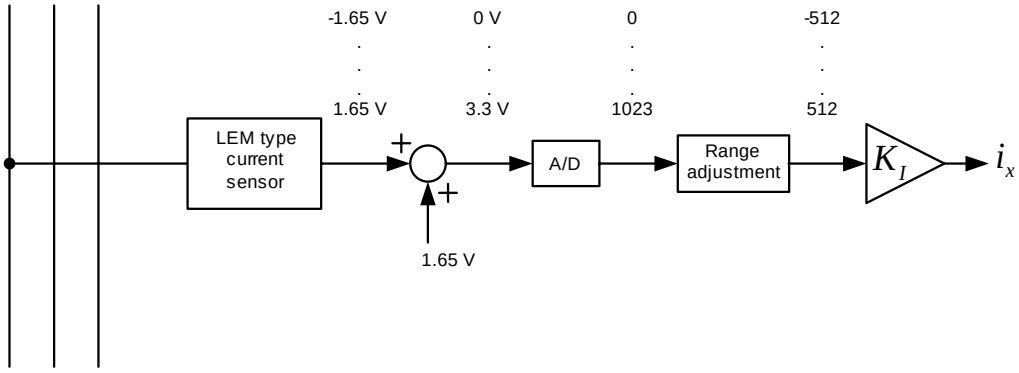


Figure 11.9 Current sensing and scaling block diagram

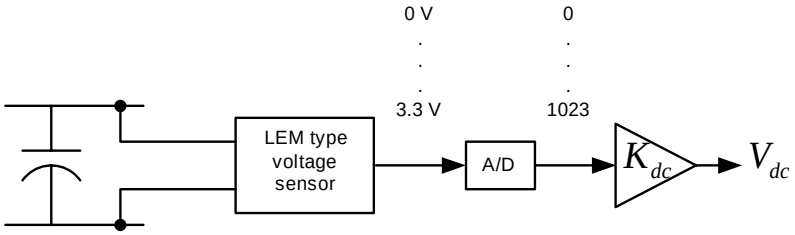


Figure 11.10 DC voltage sensing and scaling block diagram

Then the voltages and currents must be expressed with the per unit model and be converted into the Q12 format. Notice that the per unit representation of the voltages/currents are defined as the ratio between the measured voltage/current and the

base values of voltage/current. The maximum voltage/current handled by the hardware is represented by 512 in digital format and 1.65V in analog circuits. The voltage/current conversion into the Q12 format is achieved by multiplying the sensed voltage/current with the following constants:

$$K_V = \frac{4096}{512 \cdot \frac{V_b}{V_{\max}}} \tag{11.12}$$

$$K_I = \frac{4096}{512 \cdot \frac{I_b}{I_{\max}}} \tag{11.13}$$

$$K_{dc} = \frac{4096}{1024 \cdot \frac{V_b}{V_{\max}}} \tag{11.14}$$

It should be noticed that in one single multiplication, this constant performs not only the per unit modeling but also the numerical conversion into Q12 format.

## 11.7 Position/Speed Measurement

A 4096 pulse absolute encoder with binary code is used to measure the rotor speed in this application. Twelve digital I/O ports of the TMS320LF2407A are used for reading the outputs of the encoder. Generally speaking, the mechanical time constant is much lower than the electrical one, so the frequency of the speed regulation loop can be lower than the frequency of the current loop. This can be achieved by means of a software counter. This counter takes the clock of PWM interrupt as the input and the speed is calculated every 50 cycles. If the gray code encoder is used, a logic conversion code that

transfers the gray code to binary code is necessary and can be embedded into the DSP code. The block diagram of speed sensing and scaling is shown in Figure 11.11.

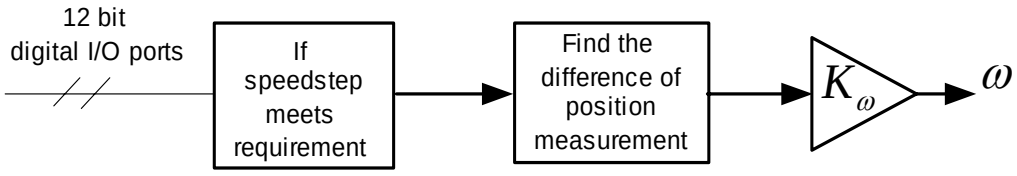


Figure 11.11 Speed sensing and scaling block diagram

The speed of the rotor is basically calculated by dividing the difference between the rotor positions with time. The speed sensing and scaling coefficient is given as:

$$K_\omega = \frac{4096}{\Delta_{rated}} \tag{11.15}$$

where, $\Delta_{rated}$ is the difference of rotor positions at rated rotor speed.

## 11.8 Program Flowchart

The main program flowchart of the software for DSP implementation is shown in Figure 11.12. The flowchart of the interrupt service program is given in Figure 11.13. All the DSP codes are written using assembly language to achieve high execute efficiency.

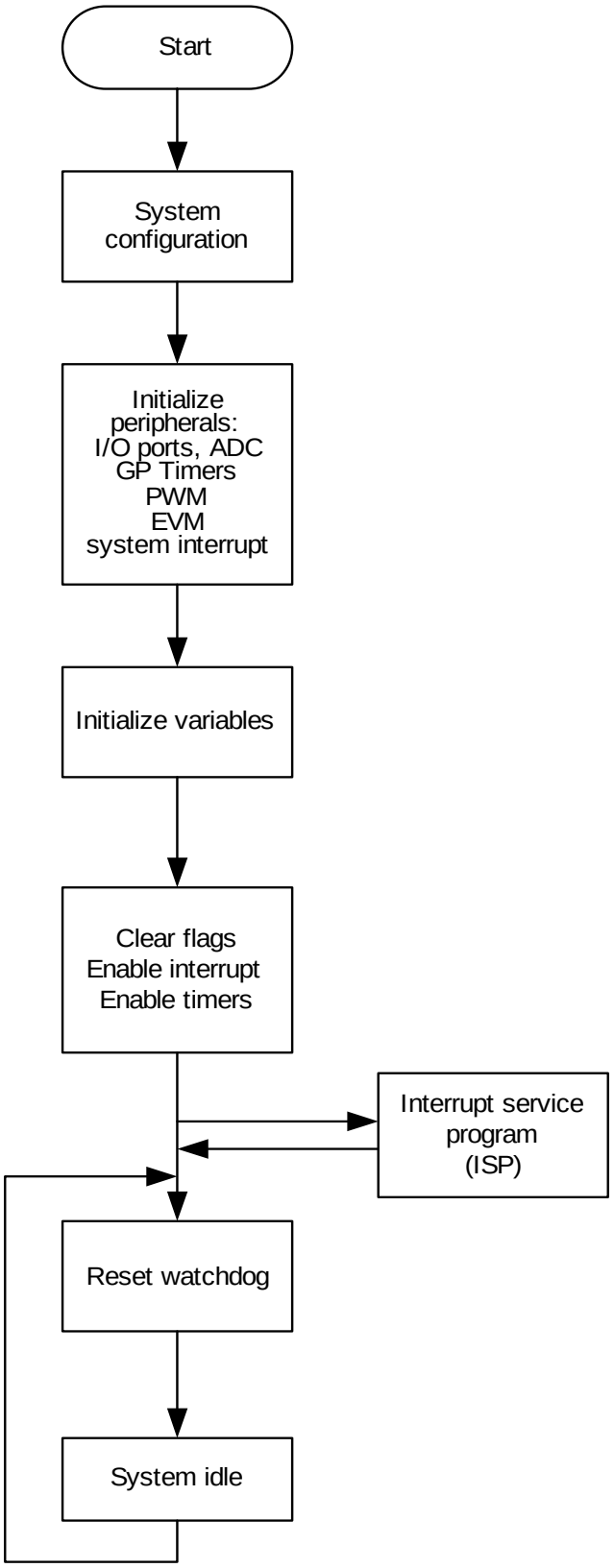


Figure 11.12 Main program flowchart

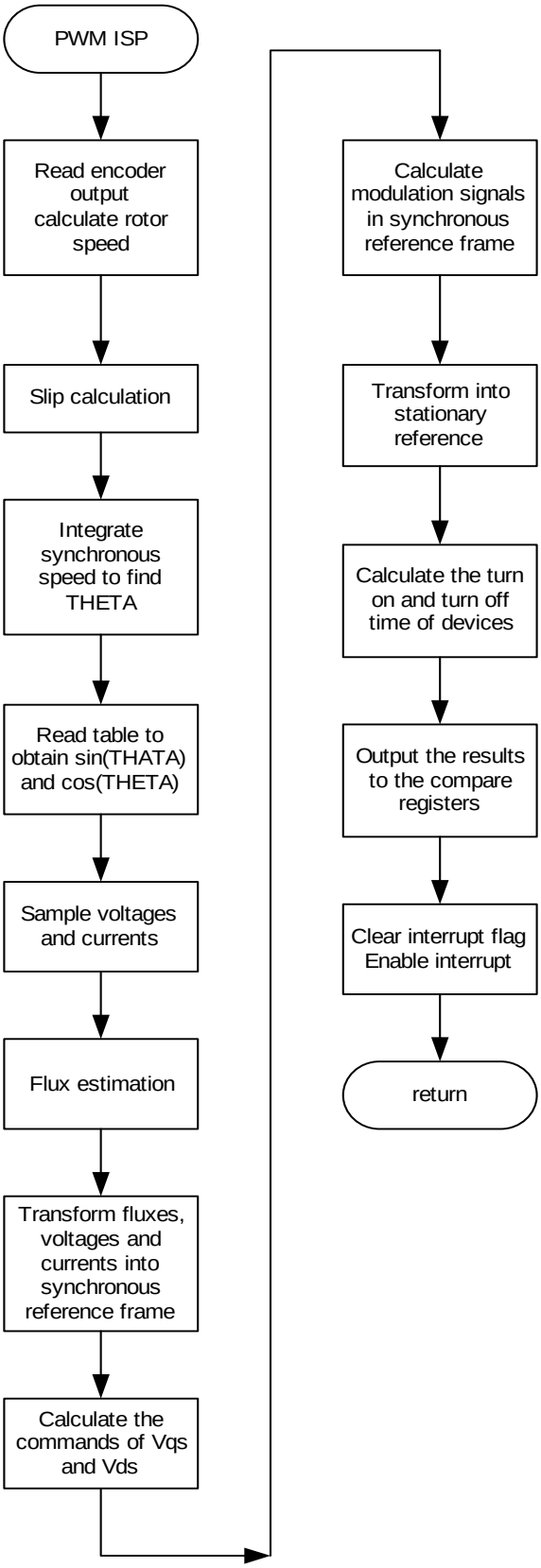


Figure 11.13 ISP flowchart

# CHAPTER 12

# CONCLUSIONS AND FUTURE WORK

The contributions of this dissertation are summarized in this chapter. Different paragraph represents the contributions in different areas of this project. Some previous work done in this area or relative areas has been detailed in Chapter 1 to establish some background on the work carried out in this thesis. Based on the work that has been developed, the scope of future work is discussed.

## 12.1 Conclusions

A detailed design procedure of the dual stator winding induction machine is clearly laid out. The idea of rewinding a standard cage-rotor induction machine stator to be the stator suitable for dual winding induction machine reduces the cost of the machine and simplifies the production procedure. The ways to evaluate the magnetic loading have been summarized and the procedure of designing the magnetic loading for each winding set has been clearly presented. The method of estimating the equivalent parameters of the dual winding machine has also been presented.

The simulation model of the dual stator winding induction machine in which the space harmonics of the stator windings and those of the rotor circuits are accounted has been presented. The complications involved with the definition of the winding function when the air gap length is not constant have been highlighted. This method was used to calculate the self and mutual inductances in the stator windings, the rotor circuits and the

mutual inductances between the stator windings and the rotor circuits. The phase voltage and torque equations thus obtained are further transformed to the rotor reference frame to facilitate simplicity of model and ease computational efforts. A new approach, using the stator windings and rotor bar currents determined from the coupled-circuit model and the winding functions of the stator windings and the rotor loops to generate the air gap flux density, has been presented for the first time. A simplified correction scheme, using the B-H curve of the magnetic steel material to account for magnetic saturation in the air gap was introduced, improving the prediction accuracy. Some measurements of no-load and full load flux densities largely confirm the simulation and FEA results.

An analysis of a dual stator winding induction machine under rotor eccentricity conditions is presented. The method of calculating the inductances is based on the general winding function definition and the winding function approach. The calculation and waveforms of stator, rotor and mutual inductances under rotor static, dynamic and mixed eccentricity conditions are clearly set forth and illustrated for the first time. The 2-pole winding set of the induction machine has the worst performance in terms of generating more harmonic inductance components and harmonic currents under rotor eccentricity conditions when it is compared to the other higher pole number stator winding set. Computer simulation of the starting transient is presented under mixed eccentricity condition as also the steady-state performance. The components of the currents and electromagnetic torque are given indicating the presence of non-fundamental and low order harmonics in currents and torque induced by the presence of the eccentricity conditions.

Using the rotating-field theory and coupling magnetic circuit theory, a fundamental understanding of the generated voltages and possible developed electromagnetic torque components of the dual stator winding squirrel-cage induction machine has been set forth for the first time. The advantage of this method is the opportunity to clearly show all the frequency components and the corresponding magnitudes of induced voltages, unsaturated air-gap flux linkages and components of the developed electromagnetic torque. The development of the torque equations show that under certain operating conditions, some additional torque components may be created only during the transient process, however the average torque will disappear under steady state condition. Relevant computer simulation resulting from two different machine models are provided to show the possible equal slip frequency operating condition of the motor to yield an additional torque component during the transient process. This operational mode is not predicted when the dual stator winding induction machine is modeled and analyzed as two independent induction machines coupled by the rotor shaft since the generated torque components are due to the stator winding currents of the individual winding sets interacting with the total rotor currents.

A study of the influence of magnetic circuit saturation on the main air-gap flux density comprising of flux density components having different pole numbers has been set forth in which the consequences of the phase angle between the flux density components are explored. For the 2/6 pole dual-stator winding machine, the two pole winding set induces a voltage on the 6-pole winding set when the air-gap flux density saturates due to saturating rotor and stator teeth. The various air-gap space harmonics generated due to magnetic saturation for the 2/6 winding sets have been discussed. There is an inter-

winding induced flux linkage which may reinforce or diminish the contribution of the 6-pole winding set to the effective air-gap flux density. The study indicates that an understanding of the nature and magnitudes of space harmonics in addition to the fundamental components rather than the peak values alone or generalized average values of the two dominant flux densities are important in the selection of the specific magnetic loading of the machine. The dynamic model of a dual stator winding induction machine including the air gap main flux linkage saturation effect has also been presented. It is argued that in the light of experimental and simulation results, the inter-winding induced flux linkages can be ignored with little loss of prediction accuracy for the fundamental component state variables. A common reference frame speed is determined and chosen for computer simulations to ensure that the instantaneous total air gap flux linkage due to the contributions of the two windings of dissimilar pole numbers is aligned with the d-axis of the reference frame. Thus the main air-gap flux linkage saturation is included in the machine model by varying the saturation dependent d-axis magnetizing inductances and setting the constant q-axis magnetizing inductances to be equal to the unsaturated values. The resulting model is used to illustrate the differences in transient and dynamic performance measures with and without the inclusion of the saturation of the stator and rotor teeth reflected in the air-gap flux density.

Based on the steady state machine model in complex variable form, the steady state analysis of dual stator winding induction machine to explore the operability regimes of the machine under constant Volt/Hz control scheme has been presented. The relationship between the slip frequencies of two stator windings and the power contributions from

each winding have been clearly shown by simulation results. The operating conditions for minimum copper loss conditions have been determined.

The loss minimization dynamic control scheme of the dual-winding induction generator producing dc load power using two parallel connected boost ac-dc PWM rectifiers has been set forth using the principles of input-output linearization control principles. By properly choosing the power distribution coefficient K and the rotor d-axes reference flux linkages, a minimum loss operation strategy has been developed. Steady-state analysis further reveals the constraints on the load resistances, magnetizing flux linkage and rotor speed under which the rectifier excitation of the generator is possible. The control scheme has been implemented with a DSP in a 2hp dual stator-winding generator. Both simulation and experimental results validate the proposed control scheme.

The high performance control scheme of the dual-winding induction generator with two series connected ac-dc PWM boost rectifiers scheme delivering three regulated dc voltages has been outlined. The steady analysis exploring the influences of the main flux saturation and operational boundaries under various dc output voltages have been set forth. Simulation and experimental results are provided to validate some of the analyses and control system design methodology adopted.

Finally, a speed control scheme of dual winding induction machine with speed sensor has been proposed. The principles of input-output linearization have been applied to the control system design such that the coupling and interaction terms are removed and the classic linear design method can be applied for controller design. The controller design methodology based on Butterworth method has been used to design the controllers. A

torque partition factor K has been introduced to distribute the electromagnetic torque to the two winding sets. By changing the value of K, one winding set can move smoothly from motoring condition into generating condition. The effectiveness of the torque partition factor has been demonstrated by the simulation results. Secondly, a speed sensorless control scheme based on full-order flux observer using MRAS technique has been analyzed. A novel error function has been proposed to ensure the stability within ultra-low speed range. The Butterworth method is used to design the observer gains. The transfer function of the estimated and actual speeds is derived based on the error analysis, which is used to determine the parameters of speed estimator. The D-decomposition method is adopted as the design methodology for both speed estimator and speed controller. The whole system is simulated in both motoring and regenerating modes. The controllers are working properly and the rotor speed is regulated very well, which validate the proposed full-order flux observer and speed estimation. Experimental results validate these simulation results.

## 12.2 Future Work

There are still several possible areas for the future research on the dual stator winding induction machine. The proposed future work is discussed in this section.

Although a coupled circuit model of the dual stator winding induction machine has been developed and validated by the simulation and experimental results, the saturation effect is not included into the model. Some steps for better understanding and modeling of saturation effect have been made in this dissertation, however because of the complexity of flux linkages due to windings of dissimilar pole numbers and fed with

voltages of different frequencies, a good saturation modeling method accounting for harmonic flux linkage components needs to be developed. The field analysis method may be one of the approaches that can be applied to study the saturation effect of the induction machine. In previous work, a modified air gap function has been proposed to model the saturation effect of single stator winding induction machine. If the same modified air gap function is included in the field analysis, a new methodology for saturation analysis will be obtained. Instead of changing the air gap function, the air gap permeability can be modified to achieve a similar result for saturation modeling. The advantage of varying air gap permeability is that the air gap function can be modified to include the eccentricity in the modeling and analysis. So if the air gap permeability function reflects the saturation effect and the air gap length function reflects the eccentricity effect, these two conditions can be included in the analysis at the same time to find the harmonics of a saturated induction machine with rotor eccentricity, which may be useful for induction machine fault diagnosis. The results from the saturation modeling will also directly affect the machine design methodology of dual winding induction machine.

The stability analysis of dual stator winding induction machine is another area for future work. When a converter fed dual stator winding induction machine works as a motor, system instability has been experimentally observed. The analysis results on the instability range in motoring condition under either constant V/f control or vector control will be helpful to the real industry application. Instability when the dual stator winding induction generator is fed with series connected boost PWM rectifiers has been observed during the experiments. The stability analysis for that system configuration has not yet been studied.

The field analysis method has been applied to the dual stator winding induction machine. The advantage of this method is the ability to clearly show all the frequency components and the corresponding magnitudes of induced voltages, unsaturated air-gap flux linkages and components of the developed electromagnetic torque. It may be possible to use some of these induced voltages and air-gap flux linkages by virtue of their dependencies on the rotor speed to estimate the rotor speeds (from zero to high speed) for a sensorless speed and/or torque control. This possibility is a subject of future research and experimentation.

The field analysis approach and coupled-circuit model simulation method are powerful analysis tools for electric machines and the same methodology and derivation steps can be applied to the analysis of other electric machines.

When the dual stator winding induction machine system is desired to be fault-tolerant, a new control algorithm that enables the machine to deliver the best performance under various fault conditions must be implemented. This is a possible area of future research. The objectives of the control algorithm must also include the protection of the system from further damage.

# REFERENCES

[1.1]. A. R. Muñoz and T. A. Lipo, “Dual stator winding induction machine drive,” *IEEE Transactions on Industry Applications*, vol. 36, pp. 1369-1379, Sep./Oct. 2000.

[1.2]. P. L. Alger, E. H. Freiburghouse and D. D. Chase, “Double windings for turbine alternators,” *AIEE Transactions*, vol. 49, pp. 226 – 244, Jan. 1930.

[1.3]. P. W. Franklin, “A theoretical study of the three phase salient pole type generator with simultaneous AC and bridge rectified DC output,” *IEEE Transactions on Power Apparatus and Systems*, vol. PAS-92, no. 2, pp. 543 – 557, Mar./Apr. 1973.

[1.4]. J. C. Salmon and B. W. Williams, “A split-wound induction motor design to improve the reliability of PWM inverter drives,” *IEEE Transactions Industry Applications*, vol. IA-26, no. 1, pp. 143–150, Jan./Feb. 1990.

[1.5]. O. Ojo and I. E. Davidson, “PWM-VSI inverter-assisted stand-alone dual stator winding generator,” *IEEE Transactions on Industry Applications*, vol. 36, no. 6, pp. 1604- 1611, Nov./Dec. 2000.

[1.6]. L. J. Hunt, “A new type of induction motor,” *Journal of Institute of Electrical Engineers*, vol. 39, pp. 648 – 677, 1907.

[1.7]. A. R. W. Broadway, “Self-cascaded machine: a low-speed motor or high-frequency brushless alternator,” *Proc. IEE*, vol. 117, No. 7, pp. 1277–1290, July 1970.

[1.8]. S. Williamson, A. C. Ferreira and A. K. Wallace, “Generalized theory of the brushless doubly-fed machine. Part 1: Analysis,” *IEE Proceedings – Electric Power Applications*, vol. 144, no. 2, pp. 111 – 122, Mar. 1997.

[1.9]. R. Li, R. Spee, A. K. Wallace and G. C. Alexander, “ Synchronous drive performance of brushless doubly-fed motors,” *IEEE Transactions on Industry Applications*, vol. 30, no. 4, pp. 963 – 970, Jul./Aug. 1994.

[1.10]. A. R. Muñoz and T. A. Lipo, “Complex vector model of the squirrel cage induction machine including instantaneous rotor bar currents,” *IEEE Transactions on Industry Applications*, vol. 35, no. 6, pp. 1332–1340, Nov./Dec. 1999.

[1.11]. A. R. Muñoz, "**Analysis and Control of a Dual Stator Winding Squirrel Cage Induction Machine Drive**," Ph.D dissertation, University of Wisconsin, Madison, WI, 1999.

[2.1]. A. R. W. Broadway, "Brushless cascade alternator," *Proceedings IEE*, Vol. 121, No. 12, Dec., 1974

[2.2]. P. C. Roberts, "**A Study of Brushless Doubly-Fed (Induction) Machines**," Ph.D dissertation, University of Cambridge, 2005.

[2.3]. T. A. Lipo, **Introduction to AC Machine Design**, Madison, WI: University of Wisconsin Press, 1996.

[3.1]. Siemens Brothers and co. Ltd. And Francis Lydall, Improvement in polyphase induction motors. British Patent No. : 16839, July 1902.

[3.2]. F. Creedy, "Some development in multi-speed cascade induction motors," *Journal of the Institution of Electrical Engineers*, Vol. 59, pp. 511- 532, 1921.

[3.3]. R. Li, A. Wallace, R. Spee and Y. Wang, "Two axis model development of cage-rotor brushless doubly-fed machines," *IEEE Transactions on Energy Conversion*, Vol. 6, No. 3, pp. 453 – 460, September 1991.

[3.4]. S. Willamson, "Generalised harmonic analysis for the steady-state performance of sinusoidally-excited cage induction motors," *IEE Proceedings*, Vol. 132, No. 3, pp. 157 – 163, May 1985.

[3.5]. X. Luo, Y. Liao, H. A. Toliyat, A.El-Antably and T. A. Lipo, "Multiple coupled circuit modeling of induction machines," *IEEE Transactions on Industry Applications*, Vol. 31, No. 2, pp. 311-318, Mar./Apr. 1995.

[3.6]. N. L. Schmidt and D. W. Novotny, **Introductory Electromechanics**, Ronald Press, 1965.

[3.7]. H. Toliyat, M. S. Afrefeen and A. G. Parlos, "A Method for dynamic simulation of air-gap eccentricity in induction machines," *IEEE Transactions on Industry Applications*, Vol. 32, No. 4, pp. 910-918, July/Aug. 1996.

[3.8]. N. A. Al-Nuaim and H. Toliyat, "A novel method for modeling dynamic air-gap eccentricity in synchronous machines based on modified winding function theory," *IEEE Transactions on Energy Conversion*, Vol. 13, No. 2, pp. 156-162, June 1998.

[3.9]. J. Faiz and I. Tabatabaei, "Extension of winding function theory for non-uniform air gap in electric machinery," *IEEE Transactions on Magnetics*, Vol. 38, No. 6, pp. 3654-3657, Nov. 2002.

[3.10]. D. W. Novotny and T. A. Lipo, **Vector Control and Dynamics of AC Drives**, Clarendon Press, Oxford, 1996

[3.11]. H. R. Fudeh and C. M. Ong, "Modeling and analysis of induction machines containing space harmonics, Parts I-III: modeling and transformation," *IEEE Transactions on Power Apparatus and System*, Vol. PAS-102, No. 8, pp. 2608 – 2628, Aug. 1983.

[3.12]. G. J. Retter, **Matrix and Space-Phasor Theory of Electrical Machines**, Academiai Kiado, Budapest, 1987.

[4.1]. S. Nandi, S. Ahmed and H. Toliyat, "Detection of Rotor Slot and Other Eccentricity Related Harmonics in a Three Phase Induction Motor with Different Rotor Cages," *IEEE Transactions on Energy Conversion*, Vol. 16, No. 3, pp. 253-260, Sep. 2001.

[4.2]. G. M. Joksimovic, M. D. Durovic, J. Penman and NeilArthur, "Dynamic Simulation of Dynamic Eccentricity in Induction Machines-Winding Function Approach," *IEEE Transactions on Energy Conversion*, Vol. 15, No. 2, pp. 143-148, June 2000.

[4.3]. H. Meshgin-Kelk, J. Milimonfared and H. Toliyat, "A Comprehensive Method for the Calculation of Inductance Coefficients of Cage Induction Machines," *IEEE Transactions on Energy Conversion*, Vol. 18, No. 2, pp. 187-193, June 2003.

[4.4]. J. Faiz, I. T. Ardekanei and H. Toliyat, "An Evaluation of Inductances of a Squirrel-Cage Induction Motor Under Mixed Eccentric Conditions," *IEEE Transactions on Energy Conversion*, Vol. 18, No. 2, pp. 252-258, June 2003.

[4.5]. S. Nandi, S. Ahmed and H. Toliyat, "Performance Analysis of a Three-Phase Induction Motor Under Mixed Eccentricity Condition," *IEEE Transactions on Energy Conversion*, Vol. 17, No. 3, pp. 392-399, Sep. 2002.

[4.6]. G. M. Joksimovic, "Dynamic simulation of cage induction machine with air gap eccentricity," *IEE proceedings-Electric Power Applications*, Vol. 152, No. 4, pp. 803-811, July 2005

[4.7]. P. Penfield, **Frequency- Power Formulas**, MIT and John Wiley and Sons, New York, 1960.

[4.8]. A. P. Russell and I. E. D. Pickup, “An analysis of the induction motor, Part 3 – Power/frequency relationships,” *IEE Proceedings*, vol. 129, Part B, pp. 243 – 247, September, 1982.

[4.9]. J. O. Ojo, V. Ostovic , T. A. Lipo and J. C. White, “ Measurement and Computation of Starting Torque Pulsations of Salient-Pole Synchronous Motors,” *IEEE Transactions on Energy Conversion*, Vol. 5, No. 1, pp. 176 – 182, March 1990.

[5.1]. S. Williamson, "Power-factor Improvement in Cage-rotor Induction Motors," *IEE Proceedings,* Vol. 130, Pt. B, No. 2, pp.121-129, Mar. 1983.

[5.2]. P. C. Roberts, R. A. McMahon, P. J. Tavner, J. M. Maciejowski and T. J. Flack, “ Equivalent circuit for the brushless doubly-fed machine (BDFM) including parameter estimation,” *IEE Proceedings-Electric Power Applications*, Vol. 152, No. 4, pp. 933 – 942, July 2005.

[5.3]. R. A. McMahon, P. C. Roberts, X. Wang and P. J. Tavner, "Performance of BDFM as generator and motor," *IEE Proceedings-Electric Power Applications*, Vol. 153, No. 2, pp. 289 – 299, March 2005.

[5.4]. Z. Wu and O. Ojo, "Coupled circuit model simulation and air gap field calculation of a dual stator winding induction machine," *IEE Proceedings-Electric Power Applications*, Vol. 153, No. 3, pp. 387 – 400, May 2006.

[6.1]. Z. Wu, O. Ojo and J. Sastry, "Control of a dual stator winding induction machine as a source of dc power," Conference Record of *IEEE Industry Applications Conference*, vol. 2, pp. 1089 – 1096, 2-6 Oct. 2005.

[6.2]. Z. Wu and O. Ojo, "High performance control of a dual winding induction generator with series connected boost rectifiers," Conference Record of *37th IEEE Power Electronics Specialists Conference*, Jun. 18-22, Korea, 2006.

[6.3]. A. C. Ferreira and S. Williamson, "Time-stepping finite-element analysis of brushless doubly fed machine taking iron loss and saturation into account," *IEEE Transactions on Industry Applications*, vol. 35, no. 3, pp. 583-588, May./Jun. 1999.

[6.4]. O. Ojo, "Dynamics and system bifurcation in autonomous induction generators," *IEEE Transactions on Industry Applications*, vol. 31, no. 4, pp. 918-924, Jul./Aug. 1995.

[6.5]. R. A. McMahon, P. C. Roberts, X. Wang and P. J. Tavner, " Performance of BDFM as generator and motor," *IEE Proceedings- Electric Power Applications*, vol. 153, no. 2, pp. 289 -298, March 2005.

[6.6]. P. C. Roberts, R. A. McMahon, P. J. Tavner, J. M. Maciejowski and T. J. Flack, "Equivalent circuit for the brushless doubly-fed machine (BDFM) including parameter estimation," *IEE Proceedings – Electric Power Applications*, vol. 152, no. 4, pp. 933-942, July 2005.

[6.7]. E. Spooner, A. C. Williamson, "Mixed pole windings and some applications," *IEE Proceedings – Electric Power Applications*, vol. 137, no. 2, pp. 89-97, March 1990.

[8.1]. J-J Slotine and W. Li, **Applied Nonlinear Control**, Prentice-Hall, Eaglewood Cliffs, New Jersey, 1991.

[8.2]. B. Friedland, **Control System Design, An Introduction to State-Space Methods**, McGraw-Hill Inc., New York, 1986.

[8.3]. R. C. Bansal, " Three-phase self-excited induction generator: an overview," *IEEE Transactions on Energy Conversion*, Vol. 20, No. 2, pp. 292-299, Jun. 2005.

[8.4]. L. Wang and J. Su, "Effect of long shunt and short shunt connection on voltage variations of a self excited induction generator," *IEEE Transactions on Energy Conversion*, Vol. 12, No. 4, pp. 368-374, Dec. 1997.

[8.5]. L. Shridhar, B. Singh, C. S. Jha, B. P. Singh and S. S. Murthy, "Selection of capacitors for the self regulated short shunt self excited induction generator," *IEEE Transactions on Energy Conversion*, Vol. 10, No. 1, pp. 10-17, Mar. 1995.

[8.6]. A. M. Eltamaly, "New formulation to determine the minimum capacitance required for self-excited induction generator," conference record of *IEEE power electronics specialist conference*, pp. 106-110, June 23-27, Cairns, Australia 2002.

[8.7]. O. Ojo, "Minimum air gap flux linkage requirement for self-excitation in stand-alone induction generators," *IEEE Transactions on Energy Conversion*, Vol. 10, No. 3, pp. 484-492, Sep. 1995.

[8.8]. L. Wang and C. Lee, "A novel analysis on the performance of an isolated self-excited induction generator," *IEEE Transactions on Energy Conversion*, Vol. 12, No. 2, pp109-117, Jun. 1997.

[8.9]. A. Kh. Al Jabri and A. I. Alolah, "Limits on the performance of the three-phase self-excited induction generator," *IEEE Transactions on Energy Conversion*, Vol. 5, No. 2, pp. 350-356, Jun. 1990.

[8.10]. T. F. Chan, "Self-excited induction generators driven by regulated and unregulated turbines," *IEEE Transactions on Energy Conversion*, Vol. 11, No. 2, pp. 338-343, Jun. 1996.

[8.11]. S. P. Singh, S. K. Jain and J. Sharma, "Voltage regulation optimization of compensated self-excited induction generator with dynamic load," *IEEE Transactions on Energy Conversion*, Vol. 19, No. 4, pp. 724-732, Dec. 2004.

[8.12]. S. S. Murthy, B. P. Singh, C. Nagamani and K. V. V. Satyanarayana, "Studies on the use of conventional induction motors as self-excited induction generator," *IEEE Transactions on Energy Conversion*, Vol. 3, No. 4, pp. 842-848, Dec. 1988.

[8.13]. L. Shridhar, B. Singh and C. S. Jha, "A step towards improvements in the characteristic of self-excited induction generator," *IEEE Transactions on Energy Conversion*, Vol. 8, No. 1, pp. 40-46, Mar. 1993.

[8.14]. O. Ojo, "Dynamic and system bifurcation in autonomous induction generators," *IEEE Transactions on Industry Applications*, Vol. 31, No. 4, pp.918-924, July/Aug. 1995.

[8.15]. O. Ojo, "The transient and qualitative performance of a self-excited single-phase induction generator," *IEEE Transactions on Energy Conversion*, Vol. 10, No. 3, pp. 493-501, Sep. 1995.

[8.16]. O. Ojo and I. Bhat, "An analysis of self-excited single-phase induction generators: model development and steady-state calculations," *IEEE Transactions on Energy Conversion*, Vol. 10, No. 2, pp. 254-260, Jun. 1995.

[8.17]. O. Ojo, "Performance of self-excited single-phase induction generators with shunt, short-shunt and long-shunt excitation connections," *IEEE Transactions on Energy Conversion*, Vol. 11, No. 3, pp. 477-482, Sep. 1996.

[8.18]. M. S. Miranda, R. O. C. Lyra and S. R. Silva, "An alternative isolated winding electric pumping system using induction machines," *IEEE Transactions on Energy Conversion*, Vol. 14, No. 4, pp. 1611-1616, Dec. 1999.

[8.19]. B. Singh, S. S. Murthy and S. Gupta, "Analysis and design of STACOM-based voltage regulator for self-excited induction generators," *IEEE Transactions on Energy Conversion*, Vol. 19, No. 4, pp. 783-790, Dec. 2004.

[8.20]. L. A. C. Lopes and R. G. Almeida, "Wind-driven self-excited induction generator with voltage and frequency regulated by a reduced-rating voltage source invter," *IEEE Transactions on Energy Conversion*, Vol. 21, No. 2, pp. 297-304, Jun. 2006.

[8.21]. D. W. Novotny. D. J. Gritter and G. H. Studtmann, "Self-excitation in inverter driven induction machines," *IEEE Transactions on power Apparatus and Systems*, Vol. PAS-96, No. 4, pp. 1117-1125, July/Aug., 1977.

[8.22]. R. Leidhold, G. Garcia and M. I. Valla, "Field-oriented controlled induction generator with loss minimization," *IEEE Transactions on Industrial Electronics*, Vol. 49, No. 1, pp. 147-156, Feb. 2002.

[8.23]. M. Karrari, W. Rosehart and O. P. Malik, "Comprehensive control strategy for a variable speed cage machine wind generation unit," *IEEE Transactions on Energy Conversion*, Vol. 20, No. 2, pp. 415-423, Jun. 2005.

[8.24]. M. Naidu and J. Walters, "A 4-kW 42-V induction –machine-based automotive power generation system with a diode bridge rectifier and a PWM inverter," *IEEE Transactions on Industry Applications,* vol. 39, No. 5, pp. 1287 -1293, Sep./Oct. 2003.

[9.1]. J. W. Dixon and B. T. Ooi, "Series and parallel operation of hysteresis current-controlled PWM rectifiers," *IEEE Transactions on Industry Applications,* vol. 25, pp. 644 -651, July/August 1989.

[9.2]. Z. Ye, D. Boroyevich, J. Choi and F. C. Lee, "Control of Circulating Current in Two Parallel Three-Phase Boost Rectifiers*," IEEE Transactions on Power Electronics,* vol. 17, no. 5, pp. 609–615, September. 2002.

[9.3]. P. M. Barbosa and F. C. Lee, "Design Aspects of Paralleled Three-Phase DCM Boost Rectifiers, 30th Annual *IEEE Power Electronics Specialists Conference*, vol. 1, pp. 331-336, 1999, Kobe, Japan.

[9.4]. K. Xing, F. C. Lee, D. Borojevic, Z. Ye, S. Mazumder, "Interleaved PWM with discontinuous space-vector modulation," *IEEE Transactions on Power Electronics*, vol. 14, no. 5, pp. 906 – 917, September 1999.

[9.5]. S. K. Mazumder, "A novel discreet control strategy for independent stabilization of parallel three-phase boost converters by combining space-vector modulation with variable-structure control," *IEEE Transactions on Power Electronics*, vol. 18, no. 4, pp. 1070 – 1083, July 2003.

[9.6]. A. Isidori, **Nonlinear Control Systems**, Springer-Verlag, New York, 1989.

[9.7]. S. Ogasawara, J. Takagaki, H. Akagi and A. Nabae, "A novel control scheme of a parallel current-controlled PWM inverter," *IEEE Transactions on Industry Applications,* vol. 28, No. 5, pp. 1023 -1030, Sep./Oct. 1992.

[9.8]. S. K. Mazumder, " Continuous and discrete variable-structure controls for parallel three-phase boost rectifier," *IEEE Transactions on Industrial Electronics*, Vol. 52, No. 2, pp 340-354, April, 2005.

[9.9]. T. Kawabata and S. Higashino, "Parallel operation of voltage source inverters," *IEEE Transactions on Industry Applications,* vol. 24, No. 2, pp. 281 -287, Mar./Apr. 1992.

[9.10]. J. Thunes, R. Kerkman, D. Schlegel and T. Rowan, "Current regulator instabilities on parallel voltage-source inverters," *IEEE Transactions on Industry Applications,* vol. 35, No. 1, pp. 70 -77, Jan./Feb. 1999.

[9.11]. H. Mori, K. Matsui, K. Kondo, I. Yamamoto and M. Hasegawa, "Parallel-connected five-level PWM inverters," *IEEE Transactions on Power Electronics,* vol. 18, No. 1, pp. 173 -179, Jan. 2003.

[10.1]. A. B. Plunkett and T. A. Lipo, "New methods of induction motor torque regulation," IEEE transactions on Industry Applications, Vol. IA-12, No. 1, pp. 47-55, Jan./Feb. 1976.

[10.2]. R. J. Kerkman and T. M. Rowan, "Voltage controlled current regulated PWM inverter," IEEE transactions on Industry Applications, Vol. 26, No. 2, pp. 244-251, Mar./Apr. 1990.

[10.3]. R. H. Nelson, T. A. Lipo and P. C. Krsuae, "Stability analysis of a symmetrical induction machine," IEEE Transactions on Power App. And System, Vol. PAS-88, No. 11, pp. 1710-1717, Nov. 1969.

[10.4]. C. Wang, D. W. Novotny and T. A. Lipo, "An automated rotor time constant measurement system for indirect field oriented drive," IEEE transactions on Industry Applications, Vol. 24, No. 1, pp. 151-159, Jan./Feb. 1988.

[10.5]. J. C. Moreira, K. T. Hung, T. A. Lipo and R. D. Lorenz, "A simple and robust adaptive controller for detuning correction in field oriented induction machines," IEEE transactions on Industry Applications, Vol. 28, No. 6, pp. 1359-1366, Nov./Dec. 1992.

[10.6]. T. M. Rowan, R. J. Kerkman and D. Leggate, "A simple on-line adaption for indirect field orientation of an induction machine," IEEE transactions on Industry Applications, Vol. 27, No. 4, pp. 720-727, Jul./Aug. 1991.

[10.7]. K. Tungpimolrut, F. X. Peng and T. Fukao, " Robust vector control of induction motor without using stator and rotor circuit time constants," IEEE transactions on Industry Applications, Vol. 30, No. 5, pp. 1241-1246, Sep./Oct. 1994.

[10.8]. D. Zinger, F. Profumo, T. A. Lipo and D. W. Novotny, "A direct field oriented controller for induction motor drives using tapped stator windings," IEEE Transactions on Power Electronics, Vol. 5, No. 4, pp. 446-453, Oct. 1990.

[10.9]. T. A. Lipo, " Flux sensing and control of static AC drives by the use of flux coils," IEEE Transactions on Magnetics, Vol. MAG-13, No. 5, pp. 1403-1408, 1977.

[10.10].T. Ohtani, T. Ohtani, N. Takada, and K. Tanaka, "Vector control of induction motor without shaft encoder," *IEEE Transactions on Industry Applications*, Vol. 28, No. 1, pp. 157–164, Jan./Feb. 1992.

[10.11].J. Hu and B. Wu, "New integration algorithms for estimating motor flux over a wide speed range," *IEEE Transactions on Power Electronics*, Vol. 13, No. 5, pp. 969-977, Sep. 1998.

[10.12].M-H. Shin, D-S Hyun, S-B Cho and S-Y Choe, "An improved stator flux estimation for speed sensorless statpr flux orientation control of induction motors," *IEEE Transactions on Power Electronics*, Vol. 15, No. 2, pp. 312-318, Mar. 2000.

[10.13].I. Takahashi and T. Noguchi, "A new quick-response and high-efficiency control strategy of an induction motor," *IEEE Transactions on Industry Applications*, vol. IA-22, No. 5, pp. 820–827, Sept./Oct. 1986.

[10.14].P. L. Jansen and R. D. Lorenz, "A physically insightful approach to the design and accuracy assessment of flux observers for field oriented induction machine drives," *IEEE Transactions on Industry Applications,* Vol. 30, No. 1, pp. 101–110, Jan./Feb. 1994.

[10.15].J. Kim, J. Choi and S. Sul, "Novel rotor-flux observer using observer characteristic function in complex vector space for field-oriented induction motor drives," *IEEE Transactions on Industry Applications,* Vol. 38, No. 5, pp. 1334–1343, Sep./Oct. 2002.

[10.16].Y. Kim, S. Sul and M. Park, "Speed sensorless vector control of induction motor using extended Kalman filter,*"* *IEEE Transactions on Industry Applications,* Vol. 30, No. 5, pp. 1225–1233, Sep./Oct. 1994.

[10.17].C. Schauder, "Adaptive speed identification for vector control of induction motors without rotational transducers," *IEEE Transactions on Industry Applications*, vol. 28, pp. 1054–1061, Sep./Oct. 1992.

[10.18].H. Tajima and Y. Hori, "Speed sensorless field-orientation control of the induction machine," *IEEE Transactions on Industry Applications*, vol. 29, No. 1, pp. 175–180, Jan./Feb. 1993.

[10.19].E. D. Mitronikas and A. N. Safacas, "An improved snesorless vector-control method for an induction motor drive," *IEEE Transactions on Industrial Electronics*, Vol. 52, No. 6, pp. 1660–1668, December 2005.

[10.20].H. Kubota, K. Matsuse, and T. Nakano, "DSP-based speed adaptive flux observer of induction motor," *IEEE Transactions on Industry Applications*, vol. 29, pp. 344–348, March/April 1993.

[10.21].G. Yang and T.-H. Chin, "Adaptive-speed identification scheme for a vector controlled speed sensorless inverter-induction motor drive," *IEEE Transactions on Industry Applications*, vol. 29, No. 4, pp. 820–825, July/August 1993.

[10.22].H. Kubota, I. Sato, Y. Tamura, K. Matsuse, H. Ohta and Y. Hori, "Stable operation of adaptive observer based sensorless induction motor drives in regenerating mode at low speeds," Proceeding IAS Annual Meeting, pp. 469-474, Chicago, IL, USA, 2001.

[10.23].H. Kubota, I. Sato, Y. Tamura, K. Matsuse, H. Ohta and Y. Hori, "Regenerating-mode low-speed operation of sensorless induction motor drive with adaptive observer," *IEEE Transactions on Industry Applications*, Vol. 38, No. 4, pp. 1081–1086, Jul./Aug. 2002.

[10.24].F-Z Peng, and T. Fukao, "Robust speed identification for speed-sensorless vector control of induction motors," *IEEE Transactions on Industry Applications*, Vol. 30, No. 5, pp. 1234–1240, Sep./Oct. 1994.

[10.25].J. Maes and J. Melkebeek, "Speed-sensorless direct torque control of induction motors using an adaptive flux observers," *IEEE Transactions on Industry Applications*, Vol. 36, No. 3, pp. 778–785, May/June 2000.

[10.26].H. Hofmann and S. R. Sanders, "Speed-sensorless vector torque control of induction machines using a two-time-scale approach," *IEEE Transactions on Industry Applications*, vol. 34, No. 1, pp. 169–177, Jan./Feb. 1998.

[10.27].M. Hinkkanen, “Analysis and design of full-order flux observers for sensorless induction motors,” *IEEE Transactions on Industrial Electronics*, Vol. 51, No. 5, pp. 1033–1040, October 2004.

[10.28].M. Hinkkanen and J. Luomi, “Parameter sensitivity of full-order flux observers for induction motors,” *IEEE Transactions on Industry Applications*, Vol. 39, No. 4, pp. 1127–1135, Jul./Aug. 2003.

[10.29].M. Hinkkanen and J. Luomi, “Stabilization of regenerating-mode operation in sensorless induction motor drives by full-order flux observer design,” *IEEE Transactions on Industrial Electronics*, vol. 51, no. 6, pp. 1318–1328, December 2004.

[10.30].L. Harnefors, “Instability phenomena and remedies in sensorless indirect field oriented control,” *IEEE Transactions on Power Electronics*, Vol. 15, No. 4, pp. 733-743, July. 2000.

[10.31].S. Suwankawin and S. Sangwongwanich, “A speed-sensorless IM drive with decoupling control and stability analysis of speed estimation,” *IEEE Transactions on Industrial Electronics*, Vol. 49, No. 2, pp. 444–455, April 2002.

[10.32].S. Suwankawin and S. Sangwongwanich, “Design strategy of an adaptive full-order observer for speed-sensorless induction-motor drives-tracking performance and stabilization,” *IEEE Transactions on Industrial Electronics*, Vol. 53, No. 1, pp. 96–119, February 2006.

[10.33].M. Saejia and S. Sangwongwanich, “Averaging analysis approach for stability analysis of speed-sensorless induction motor drives with stator resistance estimation,” *IEEE Transactions on Industrial Electronics*, Vol. 53, No. 1, pp. 162–177, February 2006.

[10.34].C. Lascu, I. Boldea and F. Blaabjerg, “Comparative study of adaptive and inherently sensorless observers for variable-speed induction-motor drives,” *IEEE Transactions on Industrial Electronics*, Vol. 53, No. 1, pp. 57–65, February 2006.

[10.35].K. Ohyama, G. A. Asher and M. Sumner, “Comparative analysis of experimental performance and stability of snesorless induction motor drives,” *IEEE Transactions on Industrial Electronics*, Vol. 53, No. 1, pp. 178–186, February 2006.

[10.36].M. Rashed and A.F. Stronach, “A stable back-EMF MRAS-based sensorless lowspeed induction motor drive insensitive to stator resistance variation,” *IEE Proceeding – Electrical Power Applications*, vol. 151, no. 6, pp. 685–693, November 2004.

[10.37].M. Rashed P. F. A. MacConnell and A.F. Stronach, "Nonlinear adaptive state-feedback speed control of a voltage-fed induction motor with varying parameters," *IEEE Transactions on Industry Applications*, Vol. 42, No. 3, pp. 723–732, May/Jun. 2006.

[10.38].M. Hasegawa, "Robust-adaptive-observer design based on γ-positive real problem for sensorless induction-motor drives," *IEEE Transactions on Industrial Electronics*, Vol. 53, No. 1, pp. 76–85, February 2006.

[10.39].G. Dong, "**Sensorless and efficiency optimized induction machine control with associated converter PWM modulation schemes**," Ph.D dissertation, Tennessee Technological University, Cookeville, TN, 2005.

[10.40].M. Depenbrock and C. Evers, "Model-based speed identification for induction machines in the whole operating range," *IEEE Transactions on Industrial Electronics*, Vol. 53, No. 1, pp. 31–40, February 2006.

[10.41].M. Boussak and K. Jarray, "A high-performance sensorless indirect stator flux orientation control of induction motor drive," *IEEE Transactions on Industrial Electronics*, Vol. 53, No. 1, pp. 41–49, February 2006.

[10.42].C. Lascu, I. Boldea and F. Blaabjerg, "Direct torque control of sensorless induction motor drives: A sliding-mode approach," *IEEE Transactions on Industry Applications*, Vol. 40, No. 2, pp. 582–590, Mar./Apr. 2004.

[10.43].J. Li, L. Xu and Z. Zhang, "An adaptive sliding-mode observer for induction motor sensorless speed control," *IEEE Transactions on Industry Applications*, Vol. 41, No. 4, pp. 1039–1046, Jul./Aug. 2005.

[10.44].M. Rashed, K. B. Goh, M. W. Dunnigan, P. F. A. MacConnell, A.F. Stronach and B. W. Williams, "Sensorless second-order sliding mode speed control of a voltage-fed induction-motor drive using nonlinear state feedback," *IEE Proceeding – Electrical Power Applications*, vol. 152, no. 5, pp. 1127–1136, September 2005.

[10.45].G. Edelbaher, K. Jezernik and E. Urlep, "Low-spees sensorless control of induction machine," *IEEE Transactions on Industrial Electronics*, Vol. 53, No. 1, pp. 120-129, February 2006.

[10.46].M. Comanescu and L. Xu, "Sliding-mode MRAS speed estimations for sensorless vector control of induction machine," *IEEE Transactions on Industrial Electronics*, Vol. 53, No. 1, pp. 146-153, February 2006.

[10.47].C. Lascu, I. Boldea and F. Blaabjerg, "Very-low-speed variable-structure control of sensorless induction machine drives without signal injection," *IEEE Transactions on Industry Applications*, Vol. 41, No. 2, pp. 591–598, Mar./Apr. 2005.

[10.48].K. Lee and F. Blaabjerg, "Reduced-order extended Luenberger observer based sensorless vector control driven by Matrix converter with nonlinearity compensation," *IEEE Transactions on Industrial Electronics*, Vol. 53, No. 1, pp. 66-75, February 2006.

[10.49].M. Cirrincione and M. Pucci, G. Cirrincione and G. Gapolino, "An adaptive speed observer based on a new total least-squares neuron for induction machine drives," *IEEE Transactions on Industry Applications*, Vol. 42, No. 1, pp. 89-104, Jan./Feb. 2006.

[10.50].M. Comanescu and L. Xu, "An improved flux observer based on PLL frequency estimator for sensorless vector control of induction motors," *IEEE Transactions on Industrial Electronics*, Vol. 53, No. 1, pp. 50-56, February 2006.

[10.51].K. Ide, J. Ha and M. Sawamura, "A hybrid speed estimator of flux observer for induction motor drives," *IEEE Transactions on Industrial Electronics*, Vol. 53, No. 1, pp. 130-137, February 2006.

[10.52].R. Cardenas and R. Pena, "Sensorless vector control of induction machines for variable-speed wind energy application," *IEEE Transactions on Energy Conversion*, Vol. 19, No. 1, pp. 196-205, March 2004.

[10.53].R. Cardenas, R. Pena, J. Proboste, G. Asher and J. Clare, "MRAS observer for sensorless control of standalone doubly fed induction generator," *IEEE Transactions on Energy Conversion*, Vol. 20, No. 4, pp. 710-718, December 2005.

[10.54].G. Poddar and V. T. Ranganathan, "sensorless double-inverter-fed wound-rotor induction-machine drive," *IEEE Transactions on Industrial Electronics*, Vol. 53, No. 1, pp. 86-95, February 2006.

[10.55].L. Kreindler, J. C. Moreira, A. Telsa and T. A. Lipo, "direct field orientation using the stator phase voltage third harmonics," *IEEE Transactions on Industry Applications,* Vol. 30, No. 2, pp. 441–447, Mar./Apr. 1994.

[10.56].M. D. Manjrekar, T. A. Lipo, S. Chang and K. Kim, "Flux tracking methods for direct field orientation," International Conference on Electrical Machines, Turky, pp. 1022-1029, Sep. 1998.

[10.57].J. Ha and S. Sul, " Sensorless field-orientation control of an induction machine by high-frequency signal injection," *IEEE Transactions on Industry Applications,* Vol. 35, No. 1, pp. 45–51, Jan./Feb. 1999.

[10.58].N. Teske, G. M. Asher, M. Sumner and K. J. Bradley, "Encoderless postion estimation for symmetric cage induction machines under loaded conditions," *IEEE Transactions on Industry Applications,* Vol. 37, No. 6, pp. 1793–1800, Nov./Dec. 2001.

[10.59].T. Tera, Y. Yamauchi, A. Chiba, T. Fukao and M. A. Rahman, "Performance of bearingless and sensorless induction motor drive based on mutual inductances and rotor displacements estimation," *IEEE Transactions on Industrial Electronics,* Vol. 53, No. 1, pp. 187–194, Feb. 2006.

[10.60].C. Caruana, G. M. Asher and M. Sumner, "Performance of HF signal injection techniques for zero-low-frequency vector control of induction machines under sensorless conditions," *IEEE Transactions on Industrial Electronics,* Vol. 53, No. 1, pp. 225–238, Feb. 2006.

[10.61].C. Spiteri, C. Caruana, G. M. Asher and M. Sumner, "Sensorless control of induction machines at zero and low frequency using zero sequence currents," *IEEE Transactions on Industrial Electronics,* Vol. 53, No. 1, pp. 195–206, Feb. 2006.

[10.62].A. Consoli, G. Scarcella, G. Bottiglieri, G. Scelba, A. Testa and D. A. Triolo, "Low-frequency signal-demodulation-based sensorless technique for induction motor drives at low speed," *IEEE Transactions on Industrial Electronics,* Vol. 53, No. 1, pp. 207–215, Feb. 2006.

[10.63].V. Leppanen and J. Luomi, "Oberver using low-frequency injection for sensorless induction motor control—parameter sensitivity analysis," *IEEE Transactions on Industrial Electronics,* Vol. 53, No. 1, pp. 216–224, Feb. 2006.

[10.64].J. Cilia, G. M. Asher, K. J. Bradley and M. Sumner, " Sensorless position detection for vector-controlled induction motor drives using an asymmetrica outer-section cage," *IEEE Transactions on Industry Applications,* Vol. 33, No. 5, pp. 1162–1169, Sep./Oct. 1997.

[10.65].J. Holtz, "Sensorless control of induction machines—with or without signal injection?," *IEEE Transactions on Industrial Electronics*, Vol. 53, No. 1, pp. 7-30, February 2006.

[10.66].D. D. Siljak, **Nonlinear System: The Parameter Analysis and Design**, John Wiley & Sons, McGraw-Hill, New York, 1969.

[10.67].Elena N. Gryazina, Boris T. Polyak, "Stability regions in the parameter space: D-decomposition revisited," Automatica, vol. 42, no. 1, pp. 13-26, January 2006.

# VITA

Zhiqiao Wu was born in Shashi, Hubei, China, in 1978. He received his B.S. and M.S. degrees in electrical engineering from Huazhong University of Science and Technology, Wuhan, Hubei, China in 1999 and 2002 respectively. He is currently working towards his Doctorate of Philosophy degree in Engineering at Tennessee Technological University. His research interests include power electronics, electrical machines and motor drive.

.

# PUBLICATIONS

Journals

1. Zhiqiao Wu, O. Ojo and J. Sastry, "High Performance Control of a Dual Stator Winding DC Power Induction Generator," has been accepted for publication in IEEE Transactions on Industry Applications.

2. Zhiqiao Wu and O. Ojo, "Coupled Circuit Model Simulation and Air Gap Field Calculation of a Dual Stator Winding Induction Machine," IEE Proceedings: Electric Power Applications, Vol. 153, Issue 3, May 2006 pp. 387 – 400.

3. O. Ojo, Zhiqiao Wu, Gan Dong and Sheetal Asuri, "High Performance Speed Sensor-less Control of an Induction Motor Drive using a Minimalist Single-Phase PWM Converter," IEEE Transactions on Industry Applications, Volume 41, Issue 4, July-Aug., 2005, pp. 996 - 1004.

4. J. Sastry, O. Ojo and Zhiqiao Wu "High Performance Control of A Boost AC-DC PWM Rectifier-Induction Generator System," IEEE Transactions on Industry Applications, Volume 42, Issue 5, Sep.-Oct., 2006, pp. 1146-1154.

5. O. Ojo, Sheetal Asuri, Gan Dong and Zhiqiao Wu, "Control of an Induction Motor Drive Fed with a Single-Phase Fed Sparse PWM Rectifier/Inverter," IEE Proceedings part-B, Volume 152, Issue 3, May-June, 2005, pp. 526 - 534.

Conferences

1. Zhiqiao Wu and O. Ojo, "Modeling of a Dual Stator Winding Induction Machine Including the Effect of Main Flux Linkage Magnetic Saturation," Conference Record of the Industry Applications Society Annual meeting, Oct. 8-12, 2006, Tampa, Florida, USA.

2. O. Ojo, G. Dong and Zhiqiao Wu, "Pulse-Width Modulation for Five-Phase Converters Based on Device Turn-on Times," Conference Record of the Industry Applications Society Annual meeting, Oct. 8-12, 2006, Tampa, Florida, USA.

3. Zhiqiao Wu and O. Ojo, "High Performance Control of a Dual Winding Induction Generator with Series Connected Boost Rectifiers," Conference Record of IEEE Power Electronics Specialists Conference, Jun. 18-22, 2006, Korea.

4. B Mwinyiwiwa, O. Ojo and Zhiqiao Wu, "A Five Phase Three-level Neutral Point Clamped Converter using DSP and FPGA based Control Scheme," Conference Record of IEEE Power Electronics Specialists Conference, Jun. 18-22, 2006, Korea.

5. Zhiqiao Wu, O. Ojo and J. Sastry "High Performance Control of a Dual Stator Winding DC Power Induction Generator," Conference Record of the Industry Applications Society Annual meeting, Oct. 2-6, 2005, Hongkong.

6. Zhiqiao Wu and O. Ojo "Power Factor Control of a Three-Phase Boost Rectifier with Specific Power Factor under Asymmetrical," Conference Record of the Industry Applications Society Annual meeting, Oct. 2-6, 2005, Hongkong.

7. J. Sastry, O. Ojo and Zhiqiao Wu "High Performance Control of A Boost AC-DC PWM Rectifier-Induction Generator System," Conference Record of the Industry Applications Society Annual meeting, Oct. 2-6, 2005, Hongkong.

8. O. Ojo and Zhiqiao Wu, "A Speed Control of an Interior Permanent Magnet Motor Drive Ensuring Minimum Electrical Loss," Conference Record of International Electric Machines and Drives Conference, May. 15-18, 2005, San Antonio, TX, USA.

9. O. Ojo and Zhiqiao Wu, Gan Dong and Sheetal Asuri, "Variable Frequency Control of an Induction Motor Drive With Reduced Switching Devices," Conference Record of International Electric Machines and Drives Conference, May. 15-18, 2005, San Antonio, TX, USA.

10. O. Ojo and Zhiqiao Wu, "A New Controller for Three-phase Boost Rectifiers Lacking Balance in Source Voltages and Impedances," Conference Record of Applied Power Electronics Conference and Exposition, March 6-10, 2005, Austin, Texas, USA.

11. O. Ojo, Zhiqiao Wu and Gan Dong, "High Performance Speed Sensor-less Control of an Induction Motor Drive using a Minimalist Single-Phase PWM Converter," Conference Record of the Industry Applications Society Annual meeting, Oct. 3-7, 2004, Seattle, WA, USA.

12. O. Ojo, F. Osaloni, Zhiqiao Wu and M. Omoigui, "A Control Strategy for Optimum Efficiency Operation of High Performance Interior Permanent Magnet Motor Drives," Conference Record of the Industry Applications Society Annual meeting, Oct. 13-17, 2003, Salt Lake City, UT, USA.

13. O. Ojo, F. Osaloni, Zhiqiao Wu and M. Omoigui, "The Influence of Magnetic Saturation and Armature Reaction on the Performance of Interior Permanent Magnet Machines," Conference Record of the Industry Applications Society Annual meeting, Oct. 13-17, 2003, Salt Lake City, UT, USA.